

**Dottorato di Ricerca in Scienze Chimiche**  
**Ciclo XXVII**

**Settore Concorsuale di afferenza: CHIM 03**

**Settore Scientifico disciplinare: 03/B1**

***Homo- and Heterometal Carbonyl Nanoclusters***

Presentato da:  
**Iacopo Ciabatti**

Relatore  
**Prof. Stefano Zacchini**

Coordinatore Dottorato  
**Prof. Aldo Roda**

Co-relatore  
**Prof. Giuliano Longoni**

**Anno 2015**



*A Corinna*



# Homo- and Heterometal Carbonyl Nanoclusters

## Contents

<b>1 Historical Introduction</b> .....	7
<b>2 Metal Carbonyl Nanoclusters</b> .....	19
<b>3 New Platinum Carbonyl Clusters</b> .....	29
3.1 New Platinum Heteroleptic Carbonyl Clusters Stabilized by Phosphine Ligands .....	30
3.2 Reactions of $[\text{Pt}_{12}(\text{CO})_{24}]^{2-}$ Chini's Cluster with Bidentate Phosphines .....	43
3.3 Surface Decorated Platinum Carbonyl Clusters .....	56
<b>4 High Nuclearity Bimetallic Nickel Carbonyl Clusters</b> .....	67
4.1 Mixed Ni-Co Carbide Carbonyl Clusters .....	68
4.2 Bimetallic Ni-Cu Carbide Carbonyl Clusters with Vacant Ni(CO) Fragments .....	83
<b>5 New Bimetallic Carbonyl Clusters Containing Au(I) Units</b> .....	101
5.1 Investigation on the Redox Condensation of $[\text{Ni}_6(\text{CO})_{12}]^{2-}$ with Au(III) Salts .....	103
5.2 $\text{Co}_6\text{C}$ Carbide Carbonyl Clusters Decorated by Gold(I) Phosphine Fragments .....	117
5.3 Isolation of the Unprecedented New $\text{Co}_5\text{C}$ Square-Pyramidal Clusters.....	129
<b>6 Metal Segregation in Bimetallic Co-Pd Carbide Carbonyl Clusters</b> .....	149
<b>7 Carbides and Hydrides Contained in Small Cages</b> .....	173
7.1 Surface Decorated Nickel Carbide Carbonyl Clusters .....	174
7.2 Interstitial Hydride into Tetrahedral Cavity .....	187
<b>8 Final Remarks</b> .....	198
<b>9 Experimental Section</b> .....	205

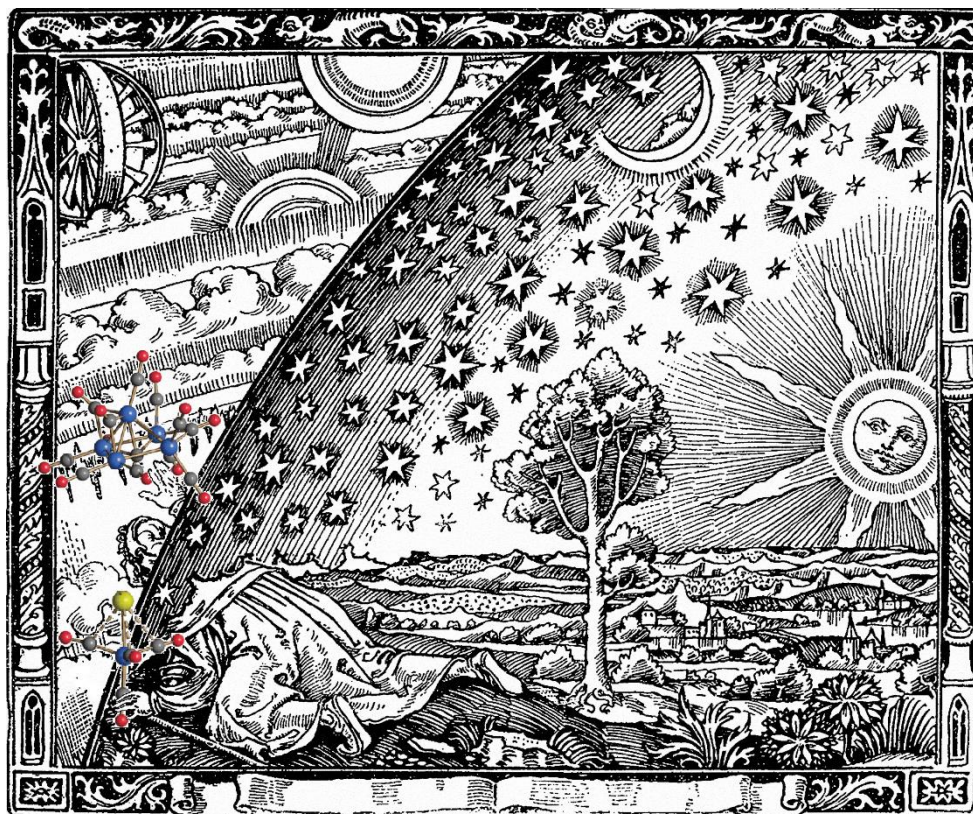


## CHAPTER 1

# Historical Introduction

## Landmarks in metal carbonyl compounds

At the end of 19th century, an unknown artist painted a man peering through the Earth's atmosphere the borders of the world as symbol of the human limits. The illustration known as Flammarion's engraving, represents the human thirst for knowledge. According to this representation, scientific knowledge consists of familiar things whereas the infinity is inaccessible to direct experience. Often, the combination of many factors such as intuition, chance and perseverance has been the turning point for going beyond scientific restrictions. In the same way, famous discoveries in the field of metal carbonyl compounds were the results of a fortunate combination between imagination and scientific ability, with the intuition suggesting the right experiment at the right time.



### 1.1 Ludwig Mond and the Serendipitous Discovery of Nickel Tetracarbonyl

Although platinum carbonyls of Schützenberger were the first metal carbonyls to be discovered, for fifty years “potassium carbonyl” was confused with a true carbonyl species [1]. Actually, as early as 1834, Justus von Liebig (1803-1873) carried out the reaction of molten potassium with carbon monoxide obtaining a new compound, which could be represented by the empirical formula KCO. Only later Nietski and Benckiser identified the product as the potassium salt of hexahydroxybenzene [2].

In 1868 Paul Schützenberger (1829-1897) reported the synthesis of a new compound by passing a mixture of carbon monoxide and chlorine over platinum black at a temperature range of 240-250°C [3]. The melting point of the product indicated that it was a mixture of species; through the aid of fractional crystallization, he was able to separate two complexes with the formulas  $\text{Pt}(\text{CO})\text{Cl}_2$  and  $\text{Pt}(\text{CO})_2\text{Cl}_2$  [4]. Schützenberger reported this brilliant observation as follows [4]:

*“They are readily convertible into each other, the former into the latter by saturating it with carbonic oxide at 150°C, and the latter into the former by heating it to 250°C.”*

Several years passed before confirming that the “monocarbonyl compound” was indeed a chloro-bridged dimer with formula  $\text{Pt}_2(\text{CO})_2\text{Cl}_4$  [5]. These are the first isolated approaches to the chemistry of carbonyl compounds, which did not involve relevant scientific developments. It is a paradox that the main compound for the beginning of a systematic study was due to an accidental discovery.

In 1890, Ludwig Mond (1839-1909) with his collaborators Carl Langer and Friedrich Quincke announced the discovery of nickel tetracarbonyl  $\text{Ni}(\text{CO})_4$  [6], whose fascinating stories deserves a more detailed description. Mond wanted to produce chlorine directly from the ammonium chloride obtained as waste from the Solvay process.<sup>1</sup>

The promising studies carried out in the laboratory immediately presented problems at industrial scale. In particular, the plant required the use of valves for switching from ammonium chloride vapors to hot air [7]:

*“On the laboratory scale these nickel valves worked perfectly, but when I applied them on a manufacturing scale I found them to be acted upon and very soon to become leaky. The*

---

<sup>1</sup> The recovery consisted in vaporizing ammonium chloride into ammonia and hydrochloric acid. Ammonia was reintegrated in the process while vapors of HCl were passed over metallic oxides, which was later submitted to the reaction of air in order to generate chloride at suitable temperature.

*faces became covered with a black crust, which, on examination, was found to contain carbon."*

Initially the source of this carbon seemed mysterious; the only difference in the scale up was the quality of the CO<sub>2</sub>, that was used to eject the ammonia chloride vapors:

*"...on a small scale we swept the ammonia out of the apparatus before admitting the hot air by means of pure CO<sub>2</sub>, while on the large scale we used the gases from a lime kiln, containing a few per cent. of CO."*

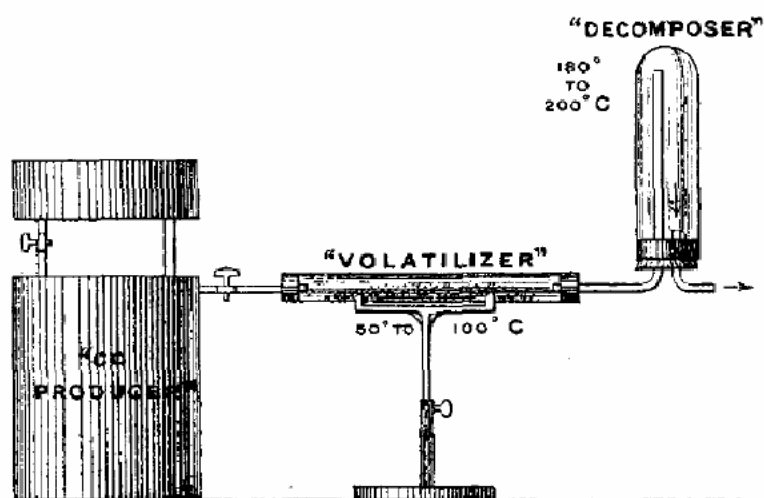


**Figure 1.1** Ludwig Mond and the representation of Langer's equipment for the synthesis (volatilizer) and the decomposition (decomposer) of the nickel tetracarbonyl [8].

The following studies pointed out the corrosive action of carbon monoxide when the valves were made of nickel. It is clear that the solution of the problem was simply the use of valves made of a different material. In an attempt to shed light on the nature of the corrosion of the nickel valves, Mond continued his studies in collaboration with Langer, hoping for the possibility to exploit it for the purification of hydrogen from CO.<sup>2</sup> The discovery of nickel tetracarbonyl occurred in the course of these experiments. Mond and his collaborators treated finely divided nickel with a static pressure of pure CO at variable temperatures. After the treatment, the apparatus was cooled with a flow of CO and, on the basis of its toxicity, the escaping gas was burned:

<sup>2</sup> They noted with satisfaction that by passing gases containing hydrogen, CO and steam over finely-divided nickel at a temperature of 400°C it was possible to obtain the complete conversion of CO into CO<sub>2</sub> with formation of an equivalent amount of hydrogen. In view of the acid nature of CO<sub>2</sub>, it can be readily separated from the gas mixture.

*To our surprise we found that, while the apparatus was cooling down, the flame of the escaping gas became luminous and increased in luminosity as the temperature got below 100°C. On a cold plate of porcelain put into this luminous flame, metallic spots were deposited...and on heating the tube through which the gas was escaping we obtained a metallic mirror, while the luminosity disappeared”.*

In the attempt to isolate this “*curious and interesting substance*” Langer projected a new apparatus where the nickel tetracarbonyl was synthesized in a *volatizer* at a range of temperature of 50-100°C and finally it was decomposed to nickel [8]. With the thermal decomposition, Mond deduced the empiric formula of the compound observing that one volume of Ni(CO)<sub>4</sub> generated four volumes of carbon monoxide.

It is interesting to observe that Langer’s apparatus is a simple small scale version of the process for the industrial refining of nickel extracted from mines in the International Nickel Company. The atypical high volatility of nickel tetracarbonyl with a boiling point of 43°C led Lord Kelvin to the famous statement that Mond had “given wings to the metals”.

Stimulated by these amazing scientific results, several other laboratories focused their attention on the synthesis of new metal carbonyls. In 1891, Mond and Berthelot disclosed their independent discovery of iron pentacarbonyl obtained as the synthesis of Ni(CO)<sub>4</sub>, with direct carbonylation of the metal, although more forced condition were required [9]. The reluctance of the other metals to form carbonyl compounds led to a general disaffection of the chemical community. After the death of Mond, the research on metal carbonyls suffered a sudden setback. In 1927/1928 the lack of attention concerning the discovery of Cr(CO)<sub>6</sub> and W(CO)<sub>6</sub> attests a widespread indifference [10]. It was necessary to overcome the fright of dealing with substances that seemed so difficult to rationalize.

### **1.2 The Fundamental Contribution of Walter Hieber**

Around the same time the experimental research of Walter Otto Hieber, the *Father of Metal Carbonyl Chemistry*,<sup>3</sup> (1895-1976) was initiated. The impressive number of publications, some of which are milestones in the academic research, documents his extraordinary contribution [11]. When Hieber carried out his first reaction on Fe(CO)<sub>5</sub>, the number of known carbonyl compounds was very small, but enough to rationalize their chemistry.

Systematic studies on the reactivity of these compounds were not carried out before, although they showed peculiar properties of scientific interest. In such atmosphere of doubt and

---

<sup>3</sup> The famous phrase of Dahl at a symposium on metal carbonyls organized by the American Chemical Society in 1964.

uncertainty, it was necessary the genius of Hieber in order to obtain a radical change as it is documented in his personal account [12]:

“... it was only in the autumn of 1927 at the Institute of Chemistry of the University of Heidelberg that I took up research experiments with iron pentacarbonyl, which was kindly provided by Dr. A. Mittasch of BASF ... On the basis of his own experience with nickel carbonyl he warned me emphatically of the danger inherent in the use of these highly toxic substance, coupling his warning with the comment that in this field one could only expect a great deal of trouble and results of little scientific value!”



1868	Pt(CO) <sub>2</sub> Cl <sub>2</sub>	M.P. Schützenberger
1890	Ni(CO) <sub>4</sub>	L. Mond et al.
1891	Fe(CO) <sub>5</sub>	L. Mond, F. Quinke, M. Berthelot
1905	Fe <sub>2</sub> (CO) <sub>9</sub>	J. Dewar, H.O. Jones
1907	[Fe <sub>3</sub> (CO) <sub>12</sub> ]*	
1910	Co <sub>2</sub> (CO) <sub>8</sub>	L. Mond et al.
	Co <sub>4</sub> (CO) <sub>12</sub>	
1910	Mo(CO) <sub>6</sub>	
1927/28	Cr(CO) <sub>6</sub>	A. Job et al.
	W(CO) <sub>6</sub>	

**Figure 1.2** Hieber with his assistant during a lecture on the laboratory course at Technische Hochschule München. In the right, the list of metal carbonyls discovered before the beginning of Hieber’s works.

\* At that time the compound was formulated as [Fe(CO)<sub>4</sub>]<sub>n</sub> (n = 20).

After Hieber, the unusual composition and properties of metal carbonyls did not allow them to be classified with other known compounds, and in the literature of that time, there are strange formulations [13]. The resemblance to organic compounds as the manner in which they react, led Mond to propose a chain structure. According to Reihlen, they were metal salts neutralized by oxygen atoms of organic pseudo-acids, in contrast Hieber considered them as organometallic complexes. In 1909, A. von Werner had just suggested the possibility that they can be coordination compounds without any experimental evidence: it was more a fan’s speculation than scientific supposition. Differently, the Hieber’s assumption was based on systematic investigations obtained by experimental techniques, considered “sophisticated” at those times, that have become standard today. He started to study the “*Reaktionen und Derivate des Eisencarbonyls*” observing that carbon monoxide of Fe(CO)<sub>5</sub> was replaced by chelating bases such as ethylenediamine leading to the production of deep-red solutions [14]. These products were described as amine-substituted iron carbonyls in contrast to their real anionic nature, some of those were low nuclearity “clusters” such as [Fe<sub>2</sub>(CO)<sub>8</sub>]<sup>2-</sup>, [Fe<sub>3</sub>(CO)<sub>11</sub>]<sup>2-</sup> and [Fe<sub>4</sub>(CO)<sub>13</sub>]<sup>2-</sup>. The anionic nature of these compounds were inferred by means of osmotic and

molar conductivity measurements.<sup>4</sup> Although the formulations of these compounds were incorrect at that time, the possibility that carbon monoxide could be displaced by other ligands is an idea of great significance.

Although Hieber did not recognize their possible applications, in the second part of his academic career, several physical-chemical characterization techniques such as magnetic and dipole measurements and, since 1957, IR spectroscopy, became available.

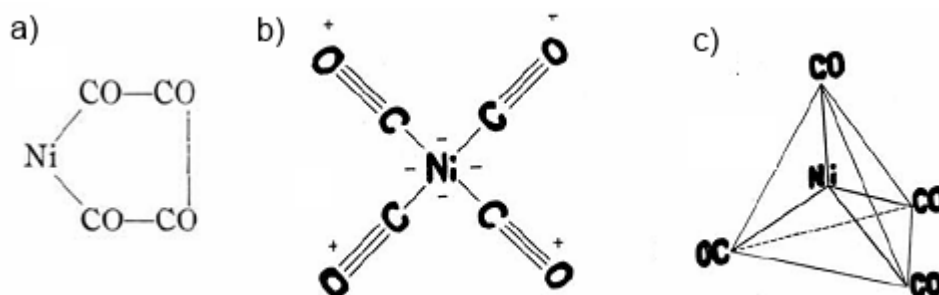


**Figure 1.3** a) Cyclic structure proposed by Mond in 1892. b) Nickel tetracarbonyl representation as planar coordination compound according to Werner-Hieber-Manchot theory. c) The real tetrahedral model.

It is amazing that Hieber predicted the correct structures of complicated compounds, many of those had been later characterized by X-ray diffraction. In this regard, the characterizations of iron and cobalt carbonyl hydrides represent the most relevant results [12]:

*“I can still remember the day when I was able to freeze out a volatile water-clear liquid from the decomposition of the ethylenediamine containing iron carbonyl, identifying it as  $H_2Fe(CO)_4$ ”*

On the basis of the similar properties of  $H_2Fe(CO)_5$ ,  $HCo(CO)_4$  and  $Ni(CO)_4$ , Hieber postulated a direct hydrogen-metal bond considering the  $H_2Fe$  and  $HCo$  units as pseudo-nickel atoms in agreement with the effective atomic number rule. Owing to the impossibility to register the NMR and IR spectra, the scientific community refused Hieber’s ideas. Indeed, it was a widespread opinion that the more electropositive hydrogen atom must be linked to an electronegative one such as the oxygen of the CO ligand. Although this general skepticism, Hieber’s postulate was supported by Hein with this brilliant experimental consideration [15]:

*“The hydrogen must be in some way directly involved in the coordination sphere of the respective metal which, inter alia, would explain the low stability as well as the great*

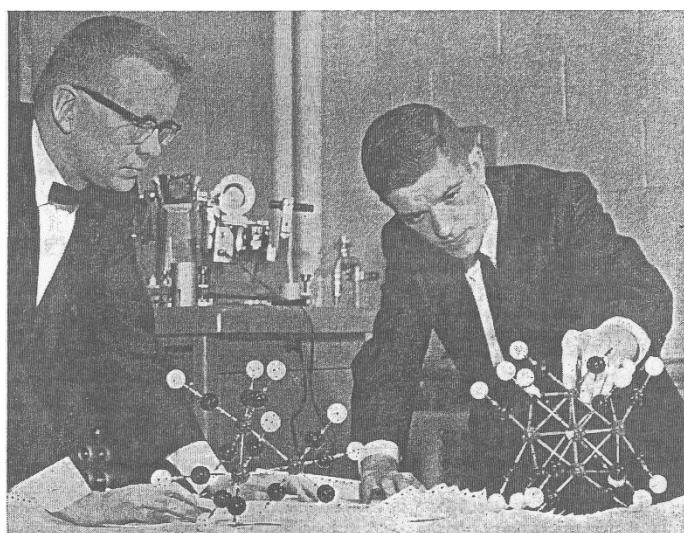
<sup>4</sup> Just by way of explanation, it is important to point out that a general monomeric compound such as  $Ni_2(CO)_2L_2$  shows the same elemental analysis of the  $[NiL_6]^{2+}[Ni_2(CO)_6]^{2-}$  salt, therefore it is necessary to measure their conductivity in order to discriminate between them.

*tendency to give binary carbonyls such as  $[\text{Co}(\text{CO})_4]_2$  by elimination of elemental hydrogen.”*

It took several years to confirm by X-Ray diffraction the structure proposed by Hieber. The striking logic in order to understand the unusual structures of carbonyl compounds on the basis of their reactivity, melting point, empiric formula and molecular weight is, without any doubt, one of the most important triumph of human mind.

### 1.3 The Fundamental Contribution of Crystallography

Single crystal x-ray diffraction has been a fundamental tool for the correct characterization of the first low nuclearity carbonyl clusters. After the crystallographic evidence, many scientists represented these compounds as polynuclear complexes whose architecture was supported by bridging M-(CO)-M carbonyl ligands [13]. The properties of these complexes were attributed to the metal-ligand interactions, whereas the metal-metal bonds were not considered.



#### Study Shows New Type of Metal Carbonyl

Molecular structure of  $\text{Rh}_6(\text{CO})_{16}$  shown by x-ray analysis; compound is first known example of a hexanuclear metal carbonyl

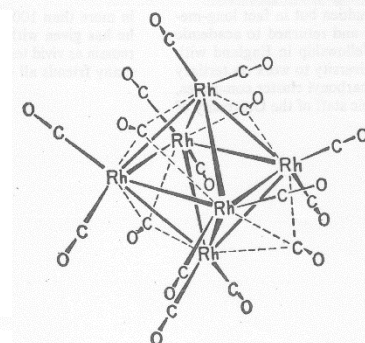


**Figure 1.4** L.F. Dahl (left) and E.R. Corey examine a molecular model of the first known hexanuclear metal carbonyl cluster. The x-ray study had shown that the compound previously reported as  $\text{Rh}_4(\text{CO})_{11}$ , on the basis of elemental analysis, had instead the molecular formula  $\text{Rh}_6(\text{CO})_{16}$ .

The first evidence of a short distance (*ca.* 2.5 Å) between two metals in a polynuclear carbonyl compound was observed by a structural determination of  $\text{Fe}_2(\text{CO})_9$  in 1939 [16]. In the literature of that time, the presence of M-M bond was recognized despite the concomitant connection of the two metals with bridging carbonyl ligands [17]. Maybe, the structural characterization of  $\text{Mn}_2(\text{CO})_{10}$  in 1957, in the absence of bridging carbonyls, represents the first undisputed evidence of a M-M bond [18]. Moreover, the comparative study of M-C and C-O

distances in the carbonyl ligands lead to conclude the presence of a  $\sigma/\pi$  synergic effect on the metal-carbonyl bonds.

Sometimes, the structural x-ray determinations of some clusters<sup>5</sup> were possible thanks to the countless tries and attempts. The problems could be due to many reasons as the crystal size or the instability of carbonyl compounds during x-ray data collection.

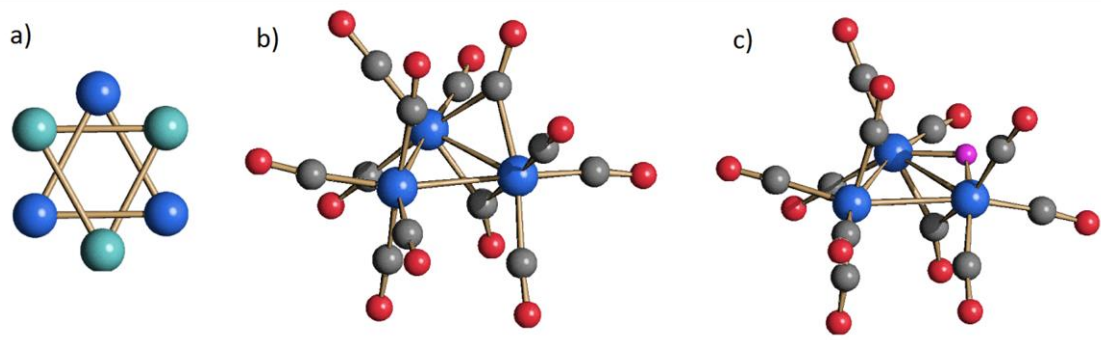


**Figure 1.5** a) “Star of David” arrangement due to the overlap of two  $\text{Fe}_3(\text{CO})_{12}$  units related by an inversion center: the two orientations are indicated with different blue colors. **b-c)** Crystallographic structures of  $\text{Fe}_3(\text{CO})_{12}$  and  $[\text{HFe}_3(\text{CO})_{11}]^-$ .

Generally, the change of the cations is a useful way to overcome the symmetry problems in crystallographic characterizations. Unfortunately, when the target is a neutral compound, this friendly trick loses its power. In this regard, one of the most fascinating examples of frustrating x-ray characterization is triiron dodecarbonyl cluster of L.F. Dahl. Indeed, the crystal disorder gave rise to a “Star of David” arrangement with six half iron atoms [19]. On the base on Mössbauer and solid-state IR data, in 1965 Dahl proposed the structural analogy between the  $\text{Fe}_3(\text{CO})_{12}$  and the previous characterized  $[\text{HFe}(\text{CO})_{11}]^-$  anionic cluster by the formal substitution of the bridging hydride with a bridging carbonyl [20]. The scientific community did not accept his correct postulate because too speculative. The “definitive” structural resolution had happen in 1974 by Cotton by means of a modern computational simulation [21].

#### 1.4 Metal Carbonyl Cluster: the Milano’s school

In the last three decades of the twentieth century, following Walter Hieber’s retirement, the metal carbonyl history recorded the chemical contribution of many research groups, some of these were meteors. On the contrary, systematic studies were started by the research group of B. F. G. Johnson and J. Lewis in Cambridge and Paolo Chini (1928-1980) in Milano. The synthetic strategies and the nature of metals used by the two groups were different and so there were not

<sup>5</sup> In the field of metal carbonyl compounds, the term cluster defines any compounds containing a finite group of metal atoms, which are mainly held together by direct metal-metal bonds. Sometimes, in the literature there is an incorrect use of the term cluster when it is related to polynuclear complex where there are not M-M bonds.

conflicts in their research topics. Indeed, the Milan's group synthesized nickel, platinum, cobalt and rhodium anionic clusters while at Cambridge osmium and ruthenium were the main core elements of neutral carbonyl clusters.

Despite his premature death, Chini played a key role in the development of high nuclearity metal carbonyl clusters. The scientific community will always remember Paolo Chini as a man of singular intelligence; his personality is fully represented by the biographical memory of Calderazzo [22]:

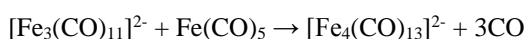
*“he was a straightforward and frank person. It was easy to see what he thought and meant, both in science and in his relationship with other people; ... he regarded personal ambition as beneficial as long as it did not become predominant and therefore detrimental to the progress of science.”*



**Figure 1.6** Left: Chini's research group. From the left: Alessandro Ceriotti, Alessandro Fumagalli, Secondo Martinengo, Giuliano Longoni and Paolo Chini. Right: Lord Jack Lewis.

Chini recognized the possibility to modulate the clusters' nuclearity through the change of their redox state. He used the term *redox condensation*<sup>6</sup> concerning the reactions where the cluster is formed by the comproportion of two reagents at different redox potentials [24]. He was interested in the development and improvement of methods for the synthesis of large carbonyl clusters, such as thermal degradation. He observed that the reaction selectivity increases with the charge of the precursor. Today these methods are still the main approaches to the synthesis of high nuclearity heterometallic clusters [25]. His first studies started in 1958, in the attempt to repeat a patent that claimed an improved selectivity in hydroformylation.

<sup>6</sup> The first example of redox condensation was reported by Hieber and Schubert in 1965 for the synthesis of  $[\text{Fe}_4(\text{CO})_{13}]^{2-}$  [23]:



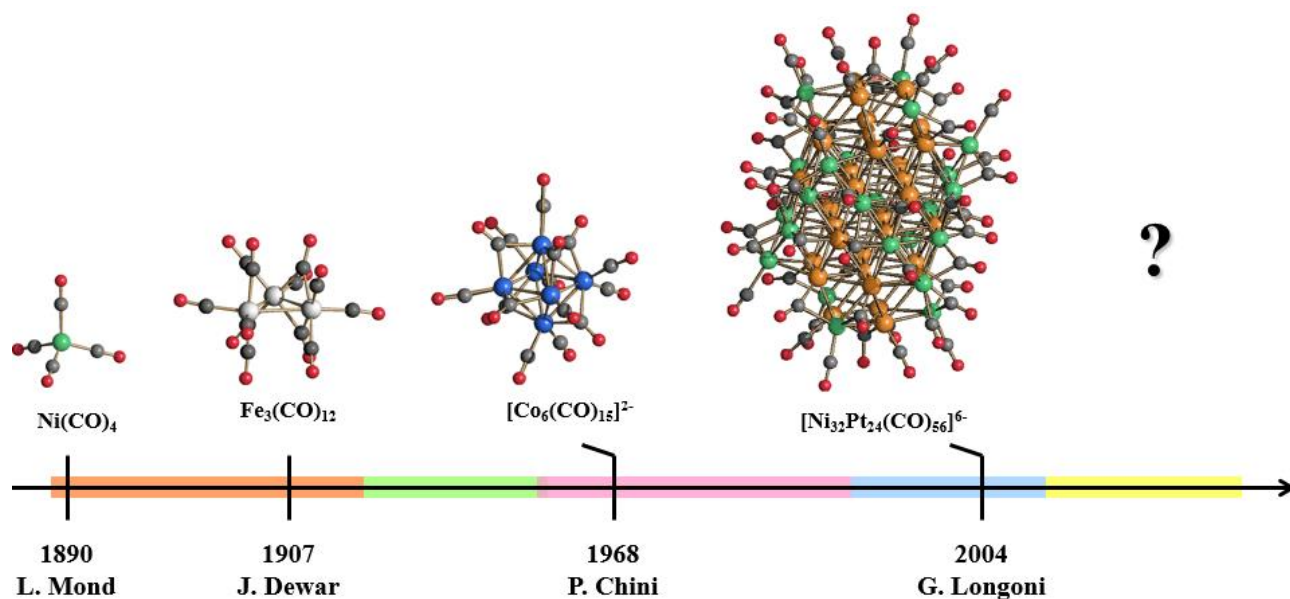


**Figure 1.7** The discovery of some key compounds related to technological scientific progress. — Measure of surface tension for the estimation of the parachor, molecular refraction, temperature, pressure and volume. — IR, Raman and NMR spectroscopy, conductivity and osmometric measurements. — Single crystal x-ray diffraction. — Use of CCD (charge-coupled-device) detector for x-ray diffractometer. — New type of analytical instruments or techniques.

From a mixture of iron and cobalt carbonyls the first bimetallic metal carbonyl  $\text{HFeCo}_3(\text{CO})_{12}$  was obtained [26]. Similar to this case, most syntheses of clusters set out with a product in mind, but in many cases the reaction takes a very different course (see box 1.1). A few months later, in an analogous way, on the attempt to synthesize a bimetallic Co-Cr cluster, he carried out a reaction with a mixture of  $\text{Co}_2(\text{CO})_8$  and  $\text{Cr}(\text{CO})_6$  that produced the new  $[\text{Co}_6(\text{CO})_{15}]^{2-}$  cluster with an octahedral metal cage<sup>7</sup> [27]. This frustrating condition had contributed to a negative affection to the cluster's chemistry, as it was underlined by F. A. Cotton [28]:

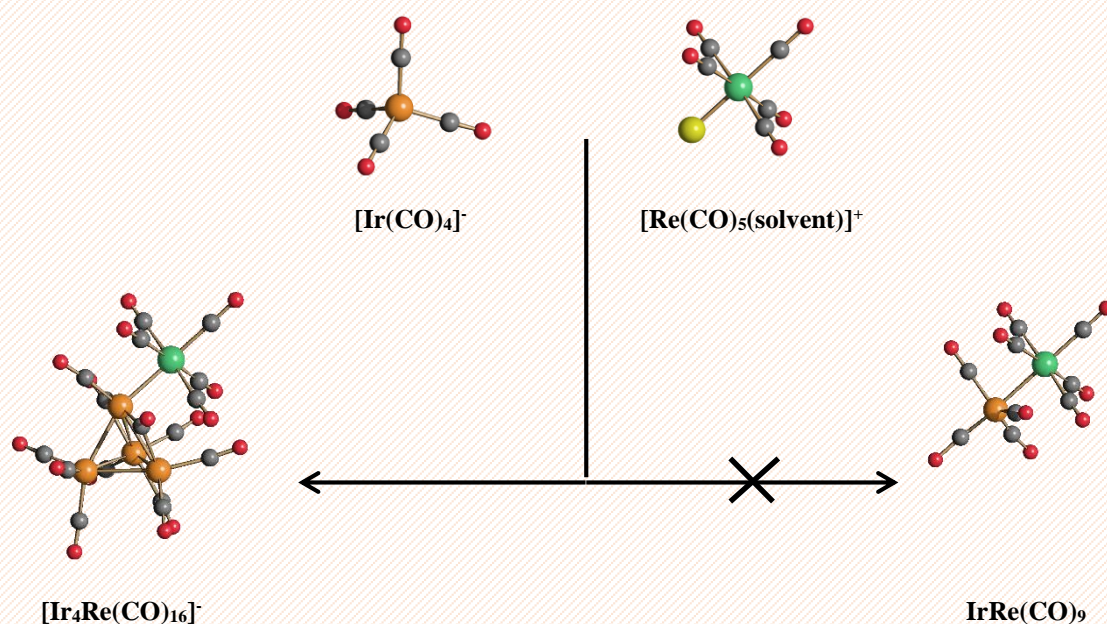
*“There does not yet appear to be any instance in which a synthetic reaction (or series of reactions) was deliberately designed to produce a particular cluster compound from molecular starting material. On the contrary, all known clusters were discovered by chance or prepared unwittingly. Thus the student of cluster chemistry is in somewhat the position of the collector of lepidoptera or meteorites, skipping observantly over the*

<sup>7</sup> From a historical-semantic perspective, the term *cage* is often used incorrectly. The clusters are generally packed so closely that they cannot be described as cages; moreover, the term is inappropriate for ternuclear clusters. On the base of this consideration it is more reasonable to use the term *skeleton*.

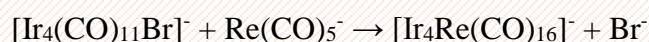
*countryside and exclaiming with delight when fortunate enough to encounter a new specimen.”*

### Box 1.1 Syntheses of clusters: only serendipitous reactions?

Generally, the different course of a cluster's synthesis is due to the unpredictable existence of the targets. In the literature, several examples of serendipitous syntheses that have been replaced by other ones with higher yields are reported. On the basis of this important progress, Cotton's statement can be considered as outdated.



A representative example is the serendipitous isolation of  $[\text{Ir}_4\text{Re}(\text{CO})_{16}]^-$  whose synthesis was subsequently rationalized on the basis of isolobal analogy. The original reaction was carried out with a mixture 1:1 of  $[\text{Ir}(\text{CO})_4]^-$  and  $[\text{Re}(\text{CO})_5]^-$  in order to obtain the unknown  $\text{Ir}(\text{CO})_4\text{-Re}(\text{CO})_5$ . From the initial failure, it was possible to rationalize a new improved reaction:



In the literature, the publications of crystallographic structures of clusters without other chemical information such as reactivity or physical properties aggravated the cluster's popularity. As the years passed, the characterization of many clusters contributed to create a clear view about their chemistry. This important result was achieved without being noticed and the due recognition. In particular, during the nineties the new interest in cluster science was due to the technological enhancement of the diffractometer: the CCD detector allowed the reduction of

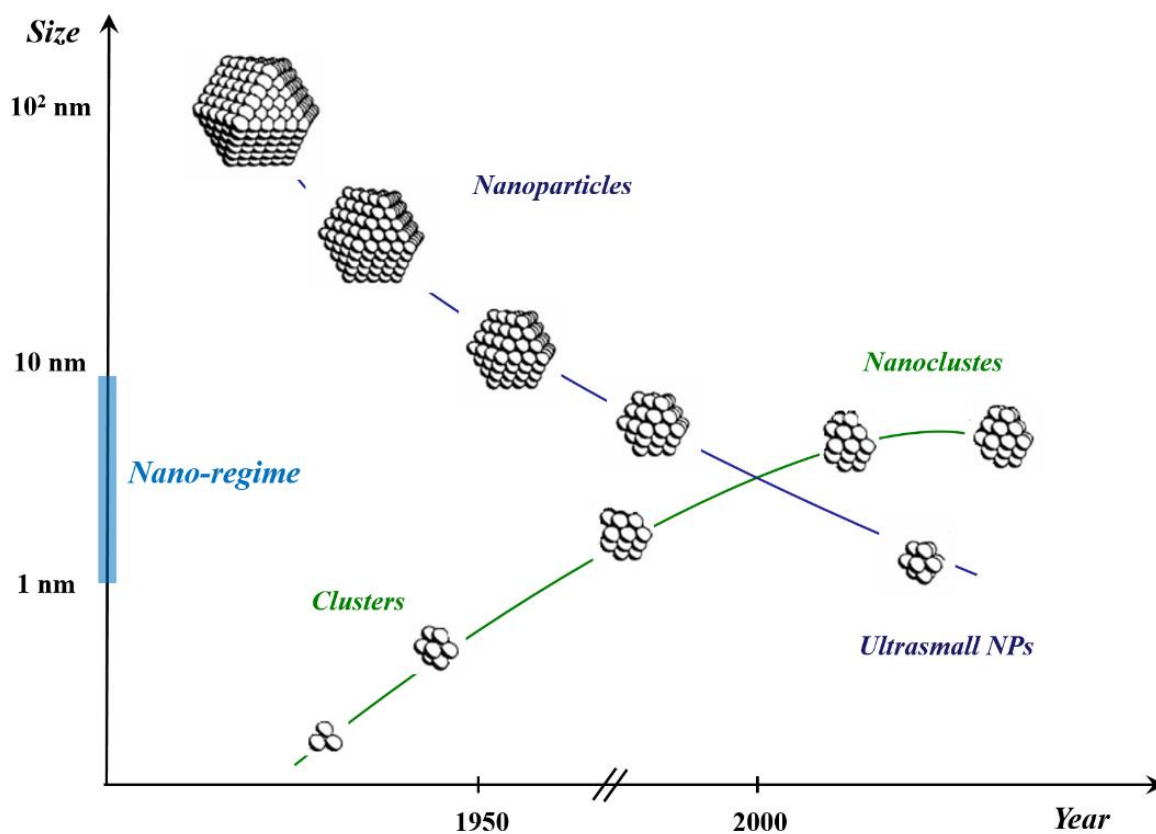
harvest time. Recently, high nuclearity metal clusters play a fundamental role in both nanosciences and nanotechnology [29].

The fascinating development of the metal carbonyl chemistry provides an indelible example of the fact that the progress in science often results from discoveries that, at first sight, are difficult or even impossible to understand. The famous discoveries in the field of metal carbonyl compounds were the results of a combination between imagination and scientific ability supported by the technological advance. In the future, *“new instruments and techniques are critical to the discovery process by which progress is measured.”* [19].

The development of metal carbonyls has played a key in the field of catalytic and industrial processes, in the development of bonding and the electronic counting theories, it has presented new questions and so new answers. Moreover, it proves the fundamental role that the academic research plays on the field of pioneering studies, always an adventure in the scientific unknown.

# Metal Carbonyl Nanoclusters

This chapter gives a brief account of high nuclearity metal carbonyl clusters (MCCs) that can be viewed as ultrasmall perfectly monodisperse ligand-stabilized metal nanoparticles. The structures, syntheses and physical properties such as multivalence and magnetism will be described. Finally, the role that bimetallic clusters play in catalysis as precursors of nanoparticles with controlled composition will be outlined.



## 2.1 Introduction

The word *cluster* means different things to different people. For instance in astronomy is referred to an aggregation of stars or galaxies moving together through space [31]. In chemistry the word *cluster* was introduced by F.A. Cotton in 1966 to refer to a class of compounds “*containing a finite group of metal atoms which are held together entirely, mainly, or at least to a significant extent, by bonds directly between the metal atoms even though some non-metal atoms may be associated intimately with the cluster*” [28].

Nowadays, several types of metal clusters are known, which may be classified on the basis of the metal present, their oxidation state and/or the ligands employed to stabilize them. Herein, we will focus on a particular class of metal clusters, *i.e.*, metal carbonyl clusters (MCCs).

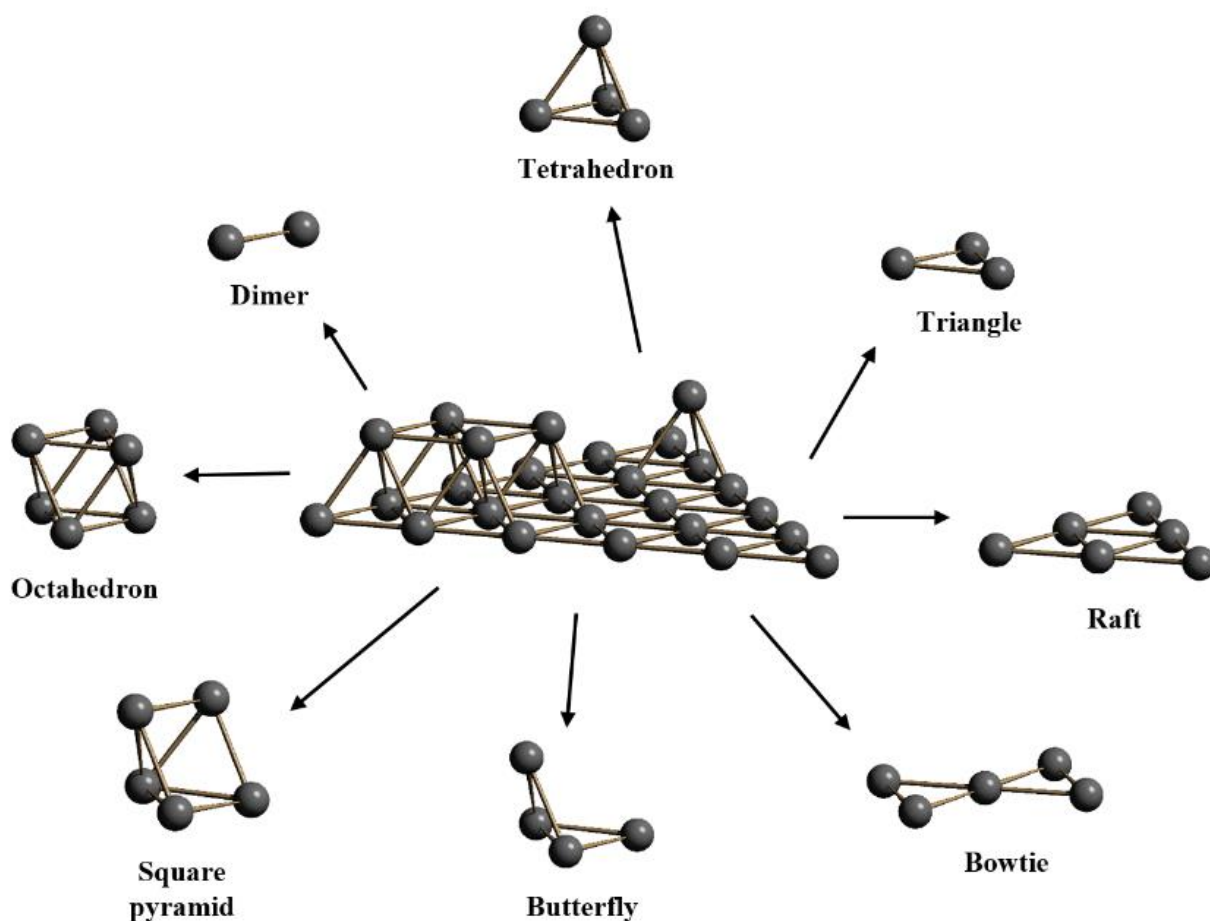


**Figure 2.1** Comparison between fragments of a bulk metal and the metal frameworks of carbonyl clusters.

These are low valent clusters based on late transition metals and stabilized by carbon monoxide. Developments in cluster synthesis and structural determination by X-ray

crystallography over the past decades have produced a wide number of high nuclearity<sup>8</sup> clusters with metal cores resembling chunks of crystal lattices (figure 2.1).

Other MCCs have little or no structural features in common with that of the bulky material. This is due to the fact that, in a cluster, the structural and/or electronic constraints imposed by the bulk phase are partially or completely absent. It is noteworthy that this comparison between clusters and bulky materials is only structural and other speculative analogies need to be carefully considered.

The interest in clusters is due to the intermediated dimensions between organometallic compounds and colloids exhibiting different chemical and physical properties [29]. The possibility of tuning these properties by varying some parameters such as the size and metal composition makes these compounds very attractive. On the basis of these peculiar properties, with well-defined atomic-like orbitals, cluster can be considered as “superatoms” [32]. The largest species studied to date already have nanometric dimensions, similar to those of ultrasmall nanoparticles. Thus, by increasing the nuclearity of molecular clusters and reducing the dimensions of metal nanoparticles, now these two words start to overlap.

## 2.2 Nanocapacitor behavior of metal carbonyl clusters

A molecular cluster is defined as multivalent if it can undergo several reversible redox processes without any major structural rearrangement. It has been shown that redox properties of MCCs can be due either to ad hoc conditions or incipient metallization of their metal core [30].

In some low nuclearity MCCs, ad hoc conditions arise from the presence of a nonbonding or weakly antibonding molecular orbital within an otherwise large HOMO-LUMO gap. However, as the nuclearity increases, multivalence becomes very common. This is confirmed by EHMO calculations, which indicate a progressive reduction of the HOMO-LUMO gap with the increase of the nuclearity. The incipient metallization of these high nuclearity MCCs is further corroborated by the fact that the voltammetric profiles of the largest species display almost equally spaced redox waves, as in the case of  $[\text{Ni}_{32}\text{C}_6(\text{CO})_{36}]^{6-}$  reported in figure 2.3 [33]. This

---

<sup>8</sup> *How much is high nuclearity?* There is not an unambiguous answer to this semantic question. From a historical perspective, clusters with 5 or more metal atoms are often considered as high nuclearity compounds since it is from this point that the metal-metal bonds often deviate from two centre/two electron bonds and the 18-electron or effective atomic number rules break down. Over the years, this value was progressively raised passing through 13, the lowest nuclearity necessary to obtain one fully interstitial metal atom at last. However, today there are so many much larger clusters and the term is more commonly used to describe clusters with 20 or more metal atoms.

means that the pairing energy within a single molecular orbital is very similar to the energy gap between a pair of them.

The gap between the pairs of redox waves decreases as the MMC nuclearity increases and, by extrapolation, it should be almost in the order of thermal energy at a nuclearity of approximately 60-70, indicating that complete metallization should occur at this nuclearity [30]. In these conditions, such MMCs should undergo spontaneous auto-disproportionation equilibria in solution. Above this limit, even a single atomically monodisperse molecular MCC would be “ionically” polydisperse hampering the isolation of single crystals suitable for X-ray crystallography.

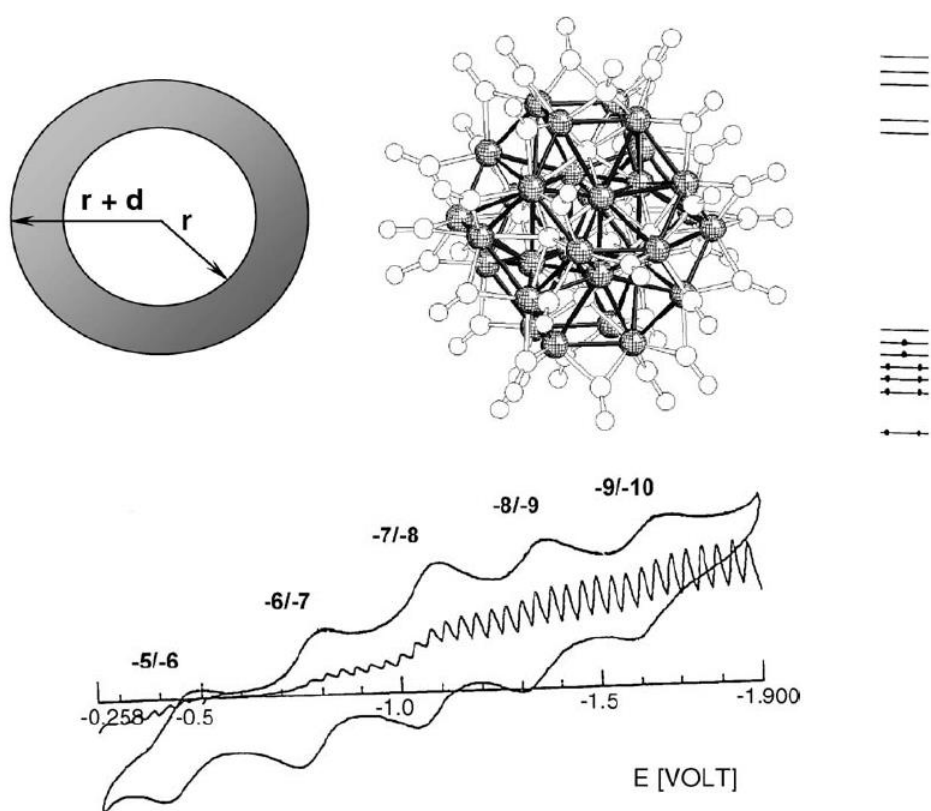


**Figure 2.3** Molecular structure, EHMO frontier region and voltammetric profile of  $[\text{Ni}_{132}\text{C}_6(\text{CO})_{36}]^{6-}$ . The molecule may be viewed as a spherical nano-capacitor.

This results in a limited number of large MCCs completely characterized. Indeed, as demonstrated by a search on the Cambridge Structural Database, the entries of the MCCs exponentially decrease as function of their nuclearity (figure 2.4).

So far, the largest homoleptic MCC characterized is the bimetallic Ni-Pt  $[\text{Ni}_{132}\text{Pt}_{24}(\text{CO})_{56}]^{6-}$  [25]. The problems in characterising larger MCCs are paralleled by analogous problems in the total structural determination of ultra-small metal nanoparticles and, in particular

Au-thiolate nanoclusters. Thus, despite major efforts in the scientific community, only five Au-thiolate nanoclusters have been crystallographically characterised and they display nuclearities in the range 24-102 [34-36].

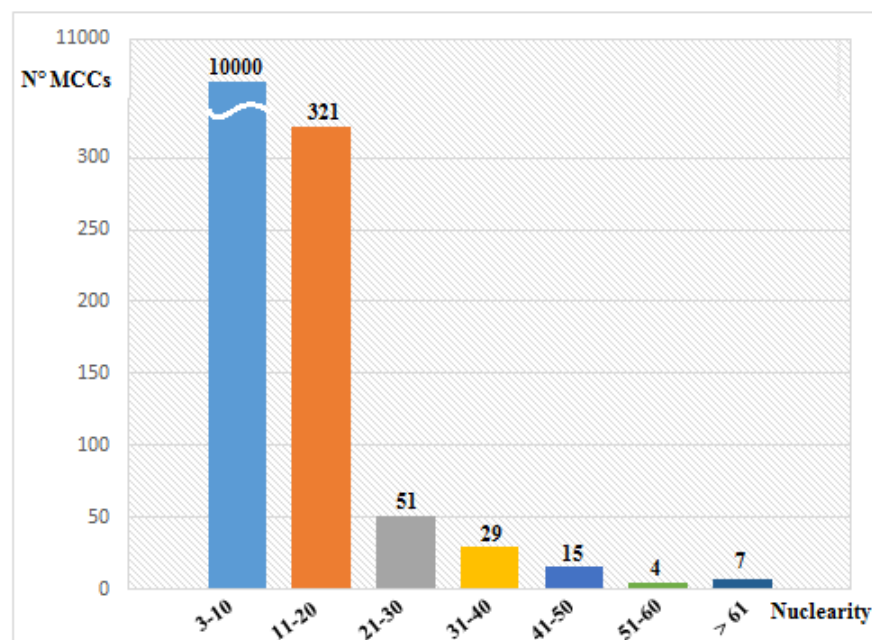


**Figure 2.4** Number of structurally characterized MCCs as a function of their nuclearity.

### 2.3 Magnetic properties of metal carbonyl clusters

As for electrochemical properties, the magnetic behavior of even-electron MCCs may arise either from had hoc conditions, stabilizing two or more almost degenerate molecular orbitals, or from incipient metallization of the metal core, reducing the energy gap of molecular orbitals to  $kT$  [29].

Odd-electron MCCs displaying one unpaired electron are paramagnetic species, as confirmed experimentally in several cases. Conversely, the magnetic behavior of even-electron MCCs is rather controversial. For instance, the paramagnetism of the odd-electron  $[\text{Co}_8\text{Pt}_4\text{C}_2(\text{CO})_{24}]^-$  monoanion is due to the presence of one unpaired electron in the SOMO, resulting in a doublet state ( $S = 1/2$ ). Conversely, the paramagnetic behavior displayed by the even-electron species  $[\text{Co}_8\text{Pt}_4\text{C}_2(\text{CO})_{24}]^{2-}$  dianion arises from triplet state ( $S = 1$ ), as indisputably pointed out by its EPR spectrum [37].

### 2.4 The problems of detecting hydrides in high nuclearity MCCs via $^1\text{H}$ NMR

The  $^1\text{H}$  NMR spectra of low-nuclearity clusters species are diagnostic for the presence of hydride ligands and support the IR evidences in demonstrating the occurrence in solution of protonation-

deprotonation equilibria. Unfortunately, beyond a nuclearity of *ca.* 20, several spin-active nuclei such as  $^1\text{H}$  in MCCs become partially or completely silent in NMR experiments and it is rather difficult to decide whether the different changes observed in the IR spectrum are due to redox or acid-base reactions.<sup>9</sup> The complete absence of any proton resonance in the hydride region is likely to be due to the fact that their resonance become so broad to be lost in the baseline of the spectrum, even if at the moment, there is not a satisfactory physical explanation for this phenomenon. Although the hydride nature of a large cluster can be indirectly inferred from joined chemical and electrochemical experiments, without NMR evidence the absolute number of hydride ligands is not known for sure. In general, when the NMR experiment is silent, we consider the species with the highest negative charge as hydride free.

The most remarkable exception to the above trend is represented by the neutral  $\text{H}_{12}\text{Pd}_{28}\text{Pt}_{13}(\text{PPh}_3)_{12}(\text{PMe}_3)(\text{CO})_{27}$  that displays a non-binomial triplet for the hydrides due to their coupling with  $^{195}\text{Pt}$  suggesting their localization inside the  $\text{PtPd}_5$  octahedral moieties of the cluster [38]. The high number of equivalent hydride atoms is a non-satisfactory explanation: the greater abundance of hydride atoms is probably compensated by the higher solubility of several anionic clusters where there is not NMR signal evidence.

The case study of  $[\text{H}_{4-n}\text{Ni}_{22}(\text{C}_2)_4(\text{CO})_{28}(\text{CdBr})_2]^{n-}$  ( $n = 2-4$ ) is very interesting, since the proton resonance of the di- and tri-anions could be observed by using a long collection time [39]. The resonances are broad and temperature-dependent with a drift of *ca.* 0.23 ppm/K, which is comparable to that of proteins which aggregate in solution via hydrogen bonds. Dynamic site-exchange processes alone seem inadequate to justify both the great broadness of all peaks as well as their unprecedented drift in chemical shift with change in solvent and temperature and the completely disappearance of all NMR resonances in larger compounds.

On the basis of these experimental evidences, G. Longoni speculates that in the case of anionic clusters, in solution there is self-aggregation of chunks of ionic lattice owing the electrostatic interaction among the clusters and the cations. As a result, their solutions are intrinsically anisotropic and this may lead to extreme broadening of all NMR resonances, up to their disappearance in the baseline [40].

However, similar behaviors are also documented for nanoparticles stabilized in a ligand shell. The debated question whether thiols or thiolates constitute the ligand shell of colloidal

---

<sup>9</sup> Many clusters contain hydrogen atoms attached directly to one or more metal centers. The hydrogen atom is more electronegative than the metal implying a  $\delta^-$  charge on the hydride. However, in many systems, the electron withdrawing properties of the other ligands in the molecule mean that the metal-bound hydrogen atom can be removed by treatment with bases, or introduced by reaction of cluster with acids.

particles is a typical example. It may seem that, the absence of NMR signals is due to the presence of a paramagnetic species due to the incipient metallization of the cluster. Indeed, with the formal grow of the particles, the energy of HOMO-LUMO gap decreases approaching to the  $KT$  value [29].

## 2.5 Heterometallic carbonyl clusters

Since ancient times, the desire to fabricate materials with well-defined properties has led to the obtainment of new materials by taking mixtures of elements to generate intermetallic compounds and alloys. In many cases, there is an enhancement in specific properties upon alloying due to synergic effects that have led to widespread applications in electronics, engineering and catalysis. The flexibility afforded by intermetallic materials coupled to the nanometer scale has generated interest in heterometallic nanoclusters. One of the major reasons of interest for heterometallic compounds is the fact that their chemical and physical properties may be tuned not only by varying the size of the clusters as we have discussed for homometallic species, but also with changing their composition and the atomic ordering. Indeed, heterometallic nanoclusters display different properties from the corresponding bulk alloys due to finite size effects and the stabilizing role of the carbonyl ligands, *e.g.*, iron and silver are immiscible in the bulk but they may be mixed in a cluster. In addition, heterometallic clusters often display different properties than homometallic species and can more easily reach higher nuclearities.

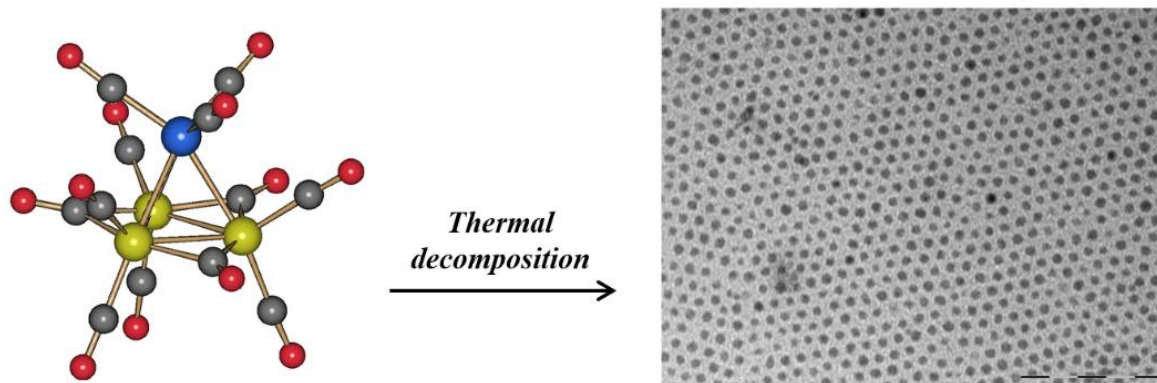


**Figure 2.5** Synthesis of bimetallic nanoparticles with controlled composition from metal carbonyl clusters.

On the basis of the intimately associated combinations of the metal components, bimetallic carbonyl clusters can be valuable precursors for the preparation of metal nanoparticles with controlled composition [29]. Nonetheless, other applications in nanosciences are scarcely described in the literature, apart from their application as precursors for the preparation of

supported metal nanoparticles to be used in catalysis (figure 2.5). These new catalysts represent one of the most interesting frontiers for heterogeneous catalysis research today [41].

## 2.6 Structures of bimetallic clusters

The phase diagrams of bulk alloys do not give reliable predictions about possible mixing in bimetallic clusters. Many simple questions about bimetallic  $A_mB_n$  clusters are still open. One would like to know if A and B segregate or if they mix to form a nanoalloy. Although several guidelines are known, it is not always possible to predict the final structure of the products except in the case of simple reactions such as fragment condensations that are based on the isolobal analogy. Indeed, in the case of redox condensation (see chapter 2.7), the comparison of the A-A, A-B and B-B bond energies and the individual affinity with carbonyl ligands provide only a rough idea of the resulting structures. However, the structures of bimetallic  $A_mB_n$  clusters, in general, belong to one of these two macro-categories: segregated and mixed structures (figure 2.6).

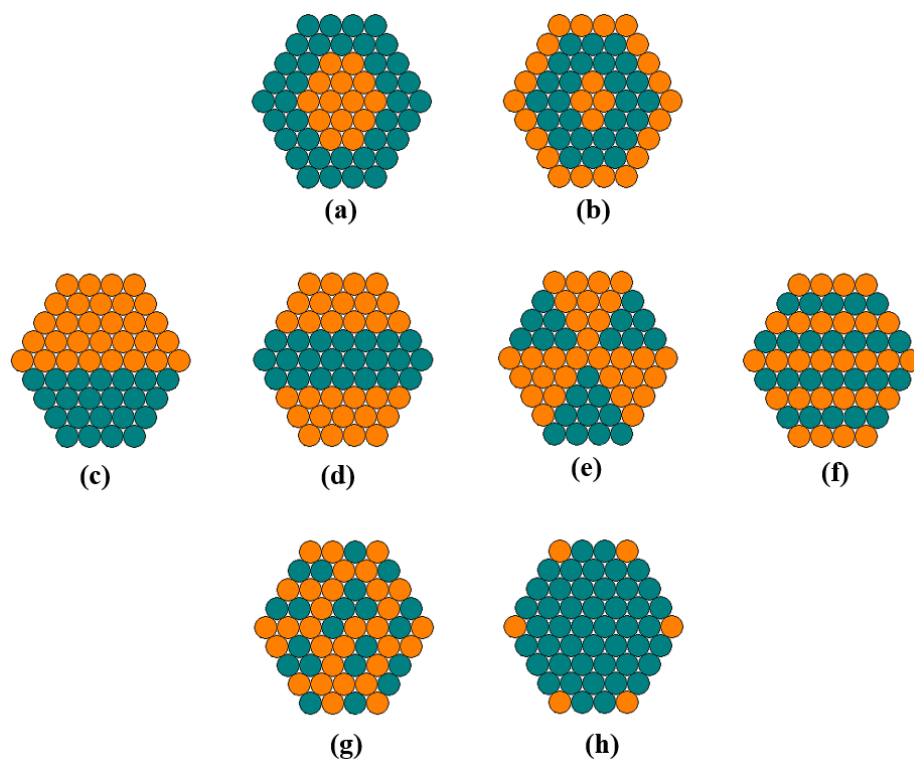


**Figure 2.6** Schematic representation of the possible structures of bimetallic carbonyl clusters: (a) core-shell, (b) multi-shell (three), (c) segregated right-left, (d) segregated sandwich, (e) cluster-in-cluster, (f) segregated layer, (g) random alloy and (h) surface decorated. The pictures show cross sections of the clusters.

The former structure can be further divided into core-shell, cluster-in-cluster or sub-cluster segregated, left-right segregated, layer segregated and sandwich type. In the core-shell architecture one metal is in the core and the other forms a shell around the first. Multi-shell clusters with onion-like alternating -A-B-A- shells, such as  $[\text{Sn}@\text{Cu}_{12}@\text{Sn}_{20}]^{12-}$ , are rare and examples of MCCs are not known. In the other cases of bimetallic segregated architectures the less restrictive definitions lead to different ways to describe the same structure. For instance left-right segregated and sandwich type are a particular case of cluster-in-cluster architecture which consist of A and B subclusters shared in one and two mixed interface respectively. Layer-segregated carbonyl clusters are well documented in the literature and multi-shell architecture may be viewed as its related 3D extension.

Mixed A-B alloy is often used in the field of nanoparticles and it may be ordered or random. It is noteworthy that synthesis and structural characterization of large clusters is required in order to observe the difference between ordered and random systems. However, the molecular or quasi-molecular feature of MCCs leads to the intermediate case of quasi-random alloys. In these systems only a limited number of *composomers*<sup>10</sup> are possible and a judicious change of the experimental conditions can lead to their different distribution (more common) or a selective synthesis of one (less common).

Surface decorated carbonyl cluster is a very interesting class of bimetallic clusters where the first metal A decorates the surface of the other metal B. Point staple motifs are present without any metal A-A bonds. However metal A-A bonds may be present as preformed staple motifs or induced by ad hoc conditions of the molecule and or crystalline packing. Generally the two metals A and B are bonded to different ligands resulting in heteroleptic clusters.

## 2.7 Synthesis of high nuclearity MCCs

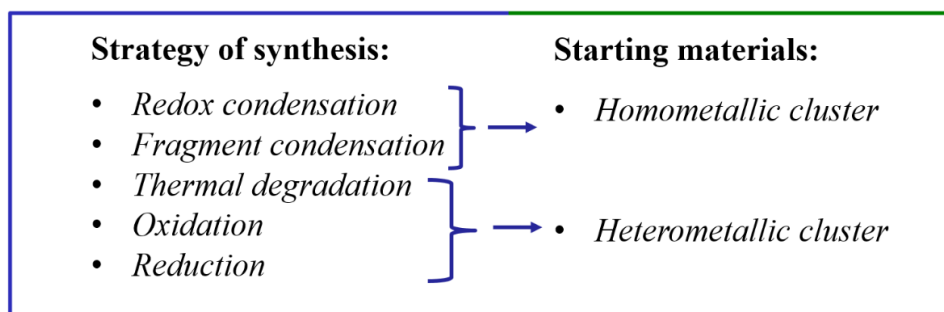
Several routes for the synthesis of high nuclearity heterometallic MCCs are known. Generally, in order to obtain new high nuclearity MCCs, preformed clusters that may be obtained in large-scale and high yields, *e.g.*,  $[\text{Ni}_6(\text{CO})_{12}]^{2-}$ ,  $[\text{Co}_6\text{C}(\text{CO})_{15}]^{2-}$ ,  $[\text{Pt}_{3n}(\text{CO})_{6n}]^{2-}$  ( $n = 2-6$ ) and  $\text{Rh}_4(\text{CO})_{12}$  are used as starting materials. The types of reactions may be classified on the basis of the nature (homo- or heterometallic) of the starting materials (scheme 2.1).

<sup>10</sup> The term *composomer* has been introduced by Johnston and Belchior to refer to clusters with the same number of atoms ( $N = N_A + N_B$ ) and metal framework but different composition ( $N_A/N_B$ ). From a theoretical point of view, the number of composomers can be calculated with the following equation:

$${}^N P_{A,B} = \frac{N!}{N_A! N_B!}$$

where  $N$  is the total number of atoms,  $N_A$  and  $N_B$  are the number of atoms of type A and B respectively. It is noteworthy that the point group symmetry of the molecule reduces the number of composomers.

The reactions starting from preformed heterometallic clusters are usually thermal degradations<sup>11</sup> and oxidations. In the *thermal degradation*, both the solvent and the choice of the counter-cation may have a significant influence on the products obtained. In general, the selectivity of the reaction increases by using a more reduced (anionic) starting material. Indeed, as demonstrated by Chini and Martinengo [42], in the case of neutral clusters, the selectivity of the reaction may be enhanced by introducing a reducing agent, *e.g.*, sodium hydroxide. Generally, the *oxidation* of heterometallic clusters consists in another alternative approach in order to increase the nuclearity. The formation of new M-M bonds with or without CO loss, may be carried out with innocent reagents, *e.g.*, ferricinium ions or using coordinating oxidants, *e.g.*, H<sup>+</sup>. In the last case, the coordinative properties of the oxidant may lead to acid-base adducts.



**Scheme 2.1** Main types of reactions routinely used in order to prepare bimetallic carbonyl clusters.

The latter process has been used to obtain surface decorated carbonyl clusters starting from homometallic species (Lewis base) with the addition a small number of [M<sub>x</sub>L<sub>y</sub>]<sup>n+</sup> fragments (Lewis acid). The reactivity of the starting clusters decreases with the increase of its nuclearity or increase of charge density. On the basis of these considerations, although *fragment condensation* is widely used, high nuclearity products are rarely obtained.

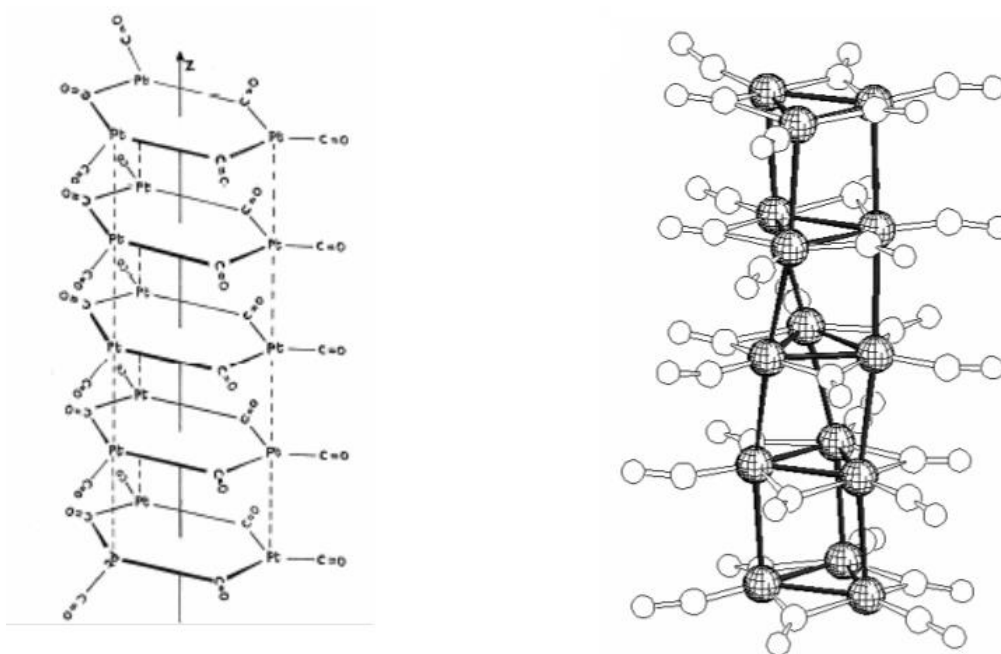
Generally, *redox condensation* is the most useful procedure for approaching the nanosize regime. For heterometallic clusters, it consists in the reactions of a reduced metal carbonyl anion with a more oxidized species, *i.e.*, another carbonyl cluster or a metal salt. The driving force of these reactions is the different redox potentials of the two starting materials.

<sup>11</sup> The thermal degradation may be carried out heating in solid state (pyrolysis) or solvent media (thermolysis). In this thesis the thermal degradation denotes thermolysis reactions.

## CHAPTER THREE

# New Platinum Carbonyl Clusters

In this chapter, the synthesis of new homometallic platinum carbonyl clusters is presented. First, the reactions of Chini's clusters with monodentate (section 3.1) and bidentate (section 3.2) phosphine ligands will be described. Finally, the synthesis of new bimetallic Pt-Cd carbonyl clusters is reported outlining their relationship with other surface decorated and nanometallic MCCs (section 3.3).



*Left: sketch of the columnar structure proposed by P. Chini for  $[Pt_{15}(CO)_{30}]^{2-}$  (from G. Longoni thesis, 1967). Right: molecular structure of  $[Pt_{15}(CO)_{30}]^{2-}$  inferred from x-ray crystallography studies (1974).*

## New Platinum Heteroleptic Carbonyl Clusters Stabilized by Phosphine Ligands

### 3.1.1 The $[\text{Pt}_{3n}(\text{CO})_{6n}]^{2-}$ ( $n = 1-10$ ) Chini's Clusters

Platinum carbonyls with formula  $\text{Pt}(\text{CO})\text{Cl}_2$  and  $\text{Pt}(\text{CO})_2\text{Cl}_2$  reported by Schützenberger have been the first metal carbonyls which have been discovered (see chapter 1). Nonetheless, only a small number of platinum carbonyl clusters have been fully characterized despite the huge efforts of several chemists such as P. Chini, G. Longoni and A. Ceriotti [40].

The synthesis and characterization of the platinum carbonyl dianions  $[\text{Pt}_{3n}(\text{CO})_{6n}]^{2-}$  ( $n = 1-10$ ) is recognized by the scientific community as the most spectacular result of Chini's work (figure 3.1.1). This series of inorganic oligomers was prepared either by reduction of  $\text{Pt}(\text{CO})_2\text{Cl}_2$  with alkali metals in the presence of CO or, more conveniently, by reduction of  $[\text{PtCl}_6]^{2-}$  with carbon monoxide and NaOH in methanol at atmospheric pressure and room temperature.

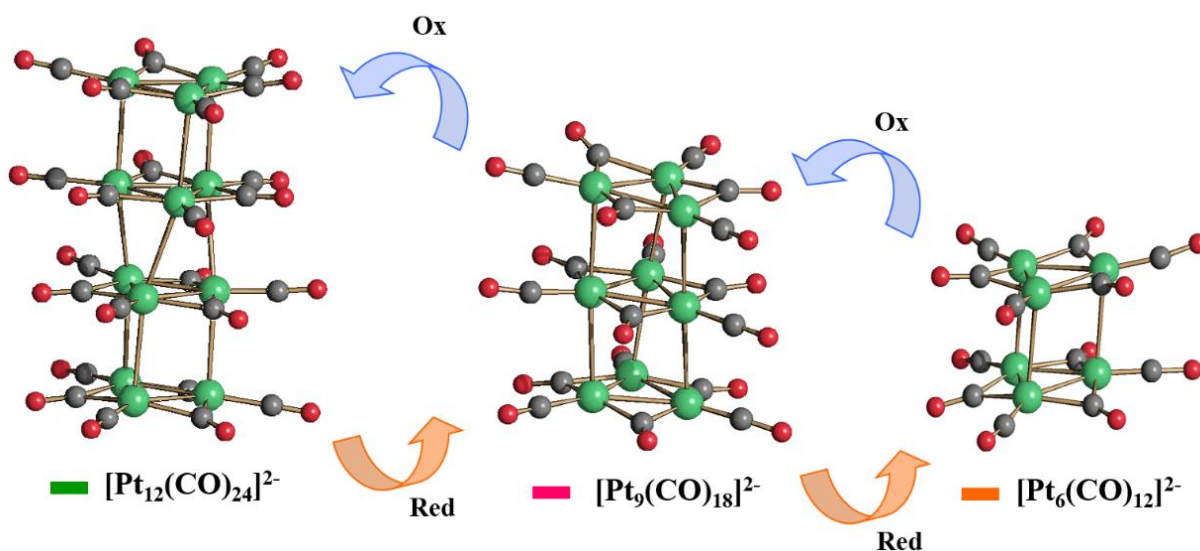


**Figure 3.1.1** Molecular structures and stepwise oxidation of  $[\text{Pt}_{3n}(\text{CO})_{6n}]^{2-}$  ( $n = 2-4$ ) clusters (Pt, green; C, grey; O, red).

The first crystallographic studies revealed that the structures of the  $[\text{Pt}_6(\text{CO})_{12}]^{2-}$ ,  $[\text{Pt}_9(\text{CO})_{18}]^{2-}$ ,  $[\text{Pt}_{15}(\text{CO})_{30}]^{2-}$  and  $[\text{Pt}_{18}(\text{CO})_{36}]^{2-}$  clusters result from the stacking of  $\text{Pt}_3(\text{CO})_3(\mu_2\text{-CO})_3$  triangular units along the pseudo-threefold axis [43]. The compromise between electronic

and steric (due to repulsions between the carbonyl ligands) effects appears to favor a regular trigonal-eclipsed metal geometry. Despite the efforts and the extensive attempts with miscellaneous tetra-substituted ammonium, phosphonium and arsonium cations, for a long time these four clusters were the only oligomers characterized. Recently, several other oligomers have been fully characterized, *i.e.*,  $[\text{Pt}_{12}(\text{CO})_{24}]^{2-}$  [44],  $[\text{Pt}_{21}(\text{CO})_{42}]^{2-}$  and  $[\text{Pt}_{24}(\text{CO})_{48}]^{2-}$ .

Concerning the reactions with phosphines, it has been previously reported that the addition of  $\text{PPh}_3$  to  $[\text{Pt}_{3n}(\text{CO})_{6n}]^{2-}$  ( $n = 2-6$ ) results in the elimination of  $\text{Pt}(\text{PPh}_3)_2(\text{CO})_2$  and formation of lower nuclearity  $[\text{Pt}_{3(n-1)}(\text{CO})_{6(n-1)}]^{2-}$  species [43]:

*“With triphenylphosphine the disproportion occurs with formation of Pt(0) species according to eq 7:*



*However, the stoichiometry of this reaction is further complicates by the equilibrium between  $\text{Pt}(\text{PPh}_3)_2(\text{CO})_2$  and  $\text{Pt}(\text{PPh}_3)_3(\text{CO})$ .”*

Supposing that these reactions might proceed initially *via* gradual substitution of up to three CO ligands with  $\text{PPh}_3$  followed by inter-triangular Pt-Pt bond cleavage and elimination of  $\text{Pt}(\text{PPh}_3)_2(\text{CO})_2$ , we decided to re-investigate the above reaction by stepwise addition of  $\text{PPh}_3$  to  $[\text{Pt}_{3n}(\text{CO})_{6n}]^{2-}$  ( $n = 2-6$ ).

### 3.1.2 Reactions of metal carbonyl clusters with phosphines

Phosphine ligands are good  $\sigma$ -donors and poor  $\pi$ -acceptors and are found only in terminal coordination sites. Their ability to back-donate to the metal can be increased by using more electronegative substituents, *e.g.*,  $\text{P}(\text{OR})_3$  or  $\text{PF}_3$ . In general, the addition of phosphines to metal carbonyl clusters may follow three common reaction pathways:

- simple addition;
- substitution of one or more carbonyl ligands;
- degradation to lower nuclearity species or mononuclear compounds.

Unsaturated clusters may add ligands without any major structural rearrangement. There are several examples of reactions where the carbonyls are replaced by phosphine ligands. It must be remarked that these studies have been mainly carried out on neutral clusters. Conversely, the replacement of CO with  $\text{PR}_3$  in anionic carbonyl clusters is not an obvious reaction, since the anionic charge should favor the presence of the more acidic CO compared to stronger  $\sigma$ -donors such as phosphines. At the moment, there is not in the literature any systematic study on the reactivity of high nuclearity anionic carbonyl clusters with phosphines and also the examples reported are scarce, compared to neutral clusters.

Large anionic carbonyl clusters do not react with phosphines or the reaction results in degradation to lower nuclearity species. In some cases, this process has been used for the selective synthesis of homoleptic carbonyl clusters, such as the conversion of  $[\text{Ni}_{13}\text{Sb}_2(\text{CO})_{24}]^{3-}$  into  $[\text{Ni}_{11}\text{Sb}_2(\text{CO})_{18}]^{3-}$  by addition of  $\text{PPh}_3$  and elimination of  $\text{Ni}(\text{CO})_3(\text{PPh}_3)$ . In very few cases, an opposite process has been observed, *i.e.*, cluster condensation to higher nuclearity species upon treatment with  $\text{PPh}_3$ , such for instance the formation of  $[\text{Ni}_{16}(\text{C}_2)_2(\text{CO})_{23}]^{4-}$  [45] by reacting  $[\text{Ni}_{10}(\text{C}_2)(\text{CO})_{16}]^{2-}$  with  $\text{PPh}_3$  (figure 3.1.2).

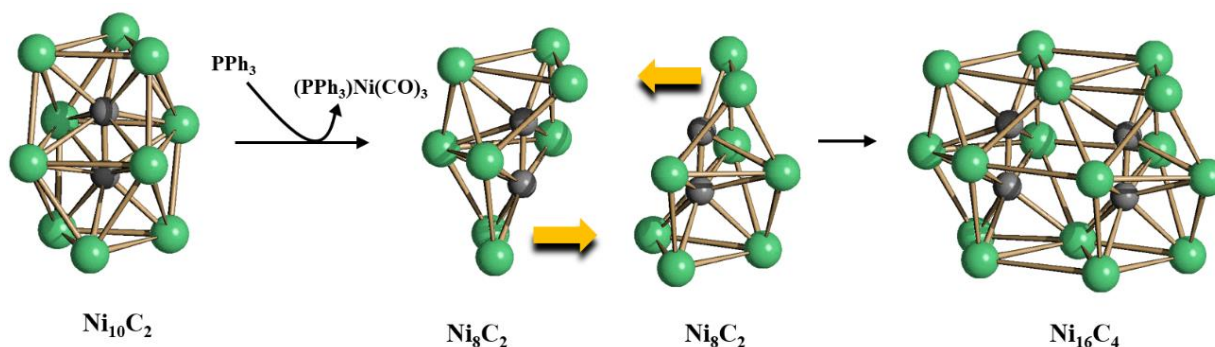


**Figure 3.1.2** The  $\text{Ni}_{16}\text{C}_4$  framework of  $[\text{Ni}_{16}(\text{C}_2)_2(\text{CO})_{23}]^{4-}$  may be viewed as the formal condensation of two unsaturated  $\text{Ni}_8\text{C}_2$  fragments obtained by the elimination of Ni atoms as  $\text{Ni}(\text{CO})_3(\text{PPh}_3)$  from  $[\text{Ni}_{10}(\text{C}_2)(\text{CO})_{16}]^{2-}$  (Ni, green; C, grey) [45].

### 3.1.3 Phosphine-substituted Pt carbonyl clusters

Several examples of homoleptic and heteroleptic metal clusters stabilized by phosphine ligands are known, in which the metal displays an oxidation state close to zero. Focusing our attention on heteroleptic  $\text{PR}_3/\text{CO}$  clusters of Group 10 metals, the most notable examples are the  $\text{Pd}/\text{CO}/\text{PR}_3$  clusters, which include several species with nuclearities ranging from 10 to 165 [46]. It is noticeable that these heteroleptic Pd clusters may reach very high nuclearities, even if no homoleptic Pd/CO cluster is known. In addition, it must be remarked that most of the species reported to date are neutral and only six examples of anionic Pd/CO/PR<sub>3</sub> clusters are known.

On the contrary, the chemistry of Pt/CO/PR<sub>3</sub> clusters is not so developed as for the fascinating Pd-analogues, even if richer than Ni. It mostly includes low nuclearity species such as  $\text{Pt}_3(\text{CO})_3(\text{PR}_3)_3$ ,  $\text{Pt}_3(\text{CO})_3(\text{PR}_3)_4$ ,  $\text{Pt}_4(\text{CO})_5(\text{PR}_3)_4$ ,  $\text{Pt}_5(\text{CO})_6(\text{PR}_3)_4$  (figure 3.1.3 a) and  $\text{Pt}_6(\text{CO})_6(\text{dppm})_3$ , as well as a few larger neutral clusters [40]. The neutral  $\text{Pt}_{15}(\text{CO})_8(\text{tBu}_3\text{P})_6$  (figure 3.1.3 b) and  $\text{Pt}_{17}(\text{CO})_{12}(\text{PEt}_3)_8$  are particularly worth of mention. They may be also envisioned as surface-decorated clusters. Indeed the structures of  $\text{Pt}_{17}(\text{CO})_{12}(\text{PEt}_3)_8$  consists of a Pt-centered  $\text{Pt}_{12}$  icosahedron decorated by two  $\text{Pt}_2(\text{PEt}_3)_2(\text{CO})$  units whereas the structure of  $\text{Pt}_{15}(\text{CO})_8(\text{tBu}_3\text{P})_6$  may be viewed as Pt-centered  $\text{Pt}_{12}$  anticuboctahedron decorated by two  $\text{Pt}(\text{tBu}_3\text{P})$  wings [40].

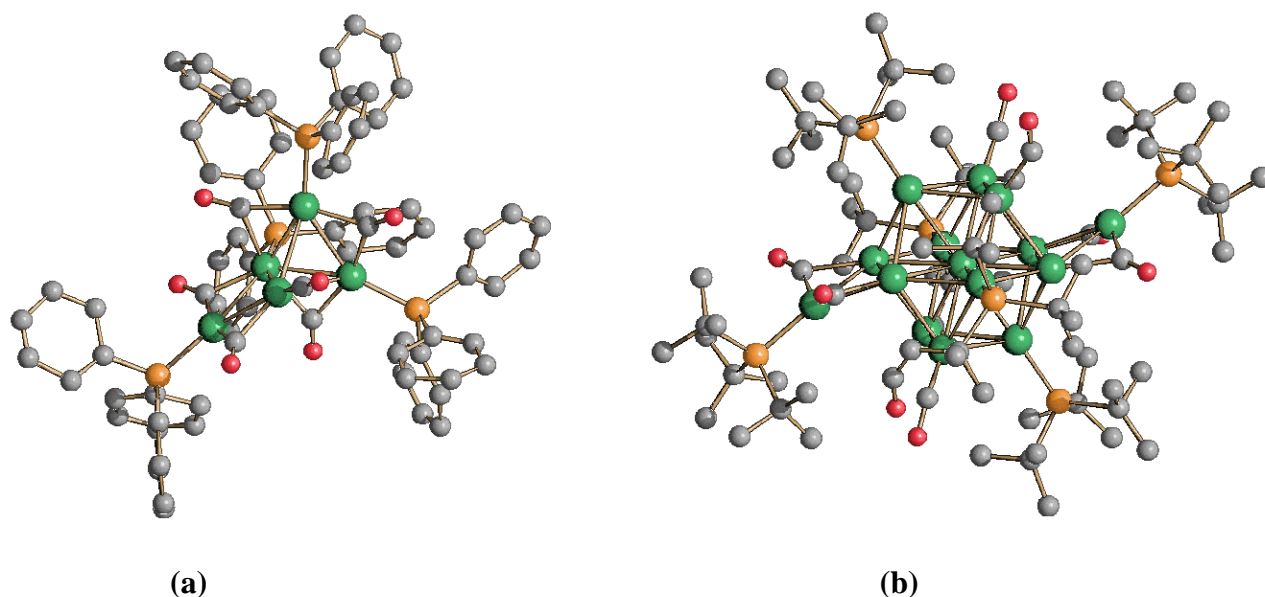


**Figure 3.1.3** Molecular structure of (a)  $\text{Pt}_5(\text{CO})_6(\text{PR}_3)_4$  and (b)  $\text{Pt}_{15}(\text{CO})_8(\text{tBu}_3\text{P})_6$  neutral clusters. It should be noted the presence in both cases of the same staple motif  $\text{Pt}(\text{PR}_3)$  that decorates the tetrahedral (a) and the Pt-centered  $\text{Pt}_{12}$  icosahedron (b) metal cores, respectively. H atoms have been omitted for clarity (Pt, green; P, orange; C, grey; O, red).

### 3.1.4 General results

The addition of small amounts of  $\text{PPh}_3$  to an acetone solution of  $[\text{Pt}_{12}(\text{CO})_{24}]^{2-}$  results in the gradual and continuous lowering of both terminal and bridging  $\nu(\text{CO})$  stretchings, as depicted in figure 3.1.4 [47]. The general outcome of the reaction is summarized in figure 3.1.5.

After the addition of one equivalent of  $\text{PPh}_3$  to  $[\text{Pt}_{12}(\text{CO})_{24}]^{2-}$ , the  $\nu(\text{CO})$  bands are lowered to 2042(s) and 1854(m)  $\text{cm}^{-1}$ , which is perfectly in the middle between the  $\nu(\text{CO})$  stretchings displayed by  $[\text{Pt}_{12}(\text{CO})_{24}]^{2-}$  and the structurally characterized  $[\text{Pt}_{12}(\text{CO})_{22}(\text{PPh}_3)_2]^{2-}$ . This suggests the formation of the mono-substituted anion  $[\text{Pt}_{12}(\text{CO})_{23}(\text{PPh}_3)]^{2-}$  (see below). The probable associative mechanism of the reaction is speculated in box 1.1. In order to substantiate this conclusion, the same solution has been analyzed *via*  $^{31}\text{P}\{^1\text{H}\}$  NMR spectroscopy (table 3.1.1 and 3.1.2). The  $^{31}\text{P}\{^1\text{H}\}$  NMR spectrum shows the presence of two main species in a 3 : 1 ratio. The minor product, which shows a multiplet centered at  $\delta_{\text{P}}$  50.6 ppm, is  $[\text{Pt}_{12}(\text{CO})_{22}(\text{PPh}_3)_2]^{2-}$  as indicated by comparison to the spectrum of the pure species (see section 3.1.6). The major species displays a similar pattern at  $\delta_{\text{P}}$  49.4 ppm with  $^1J_{\text{Pt-P}} = 5081$  Hz (to one Pt) and  $^2J_{\text{Pt-P}} = 551$  Hz (to two equivalent Pt-atoms), in agreement with the formation of  $[\text{Pt}_{12}(\text{CO})_{23}(\text{PPh}_3)]^{2-}$ , in which the  $\text{PPh}_3$  ligand is terminally bonded to a  $\text{Pt}_3$  triangle. The ESI-MS spectrum of a  $\text{CH}_3\text{CN}$  solution containing  $[\text{Pt}_{12}(\text{CO})_{24}]^{2-}$  and one equivalent of  $\text{PPh}_3$  displays peaks at  $m/z$  (relative intensity in parentheses) 1506(100), 1130(10), 1625(5) and 1883(5) attributable to  $[\text{Pt}_{12}(\text{CO})_{24}]^{2-}$ ,  $[\text{Pt}_9(\text{CO})_{18}]^{2-}$ ,  $[\text{Pt}_{12}(\text{CO})_{23}(\text{PPh}_3)]^{2-}$ ,  $[\text{Pt}_{15}(\text{CO})_{30}]^{2-}$ .

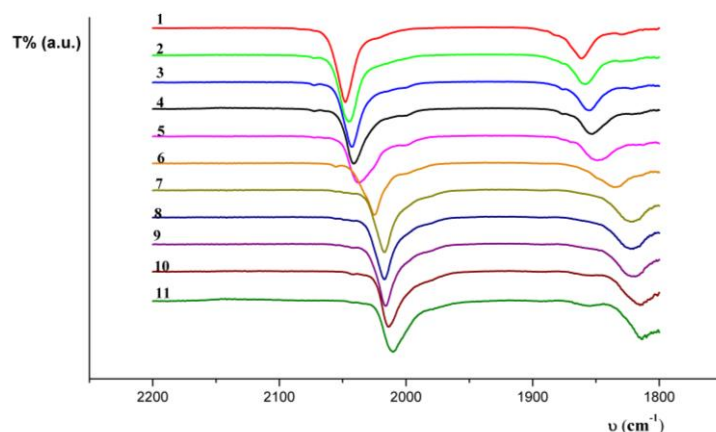


**Figure 3.1.4** IR spectra in the  $\nu(\text{CO})$  region obtained by the stepwise addition of  $\text{PPh}_3$  to an acetone solution of  $[\text{Pt}_{12}(\text{CO})_{24}]^{2-}$ : 1) starting material; 2) +0.5 equiv.; 3) +1.0 equiv.; 4) +1.5 equiv.; 5) + 2.0 equiv.; 6) +3.0 equiv.; 7) +3.5 equiv.; 8) +4.5 equiv.; 9) +5.0 equiv.; 10) +6.5 equiv.; 11) +7.5 equiv.

The compositions of the solution determined by  $^{31}\text{P}\{^1\text{H}\}$  NMR spectroscopy and ESI-MS are very different, and this is probably due to the different sensitivity of these techniques and to the fact that some reactions may occur during ionization. Therefore, the  $^{31}\text{P}\{^1\text{H}\}$  NMR data are more reliable in order to determine the species present in solution, being this technique less invasive. Nonetheless, ESI-MS data confirm the formation of a mono-substituted  $[\text{Pt}_{12}(\text{CO})_{23}(\text{PPh}_3)]^{2-}$  species. In addition, the spectroscopic data indicate that after the addition of one equivalent of  $\text{PPh}_3$  to  $[\text{Pt}_{12}(\text{CO})_{24}]^{2-}$  a mixture of products is present. Therefore, the first and second CO substitutions occur partially in parallel and not perfectly in sequence.

Similarly, the  $^{31}\text{P}\{^1\text{H}\}$  NMR spectrum recorded after the addition of two equivalents of  $\text{PPh}_3$  to an acetone solution of  $[\text{Pt}_{12}(\text{CO})_{24}]^{2-}$  shows the presence of a mixture where the  $\text{PPh}_3$ -derivatives are mainly  $[\text{Pt}_{12}(\text{CO})_{22}(\text{PPh}_3)_2]^{2-}$ ,  $[\text{Pt}_9(\text{CO})_{16}(\text{PPh}_3)_2]^{2-}$  and  $[\text{Pt}_9(\text{CO})_{17}(\text{PPh}_3)]^{2-}$ . Simulations have been used in order to confirm the assignments, since the spectra are complicated because of the different isotopes of platinum. The solutions containing  $[\text{Pt}_{12}(\text{CO})_{24}]^{2-}$ ,  $[\text{Pt}_{12}(\text{CO})_{23}(\text{PPh}_3)]^{2-}$  and  $[\text{Pt}_{12}(\text{CO})_{22}(\text{PPh}_3)_2]^{2-}$  as the major species display a typical green color.

After the addition of 3 equivalents of  $\text{PPh}_3$  to  $[\text{Pt}_{12}(\text{CO})_{24}]^{2-}$  the solution turns from green to red and the  $\nu(\text{CO})$  bands are shifted to 2024(s) and 1830(m)  $\text{cm}^{-1}$  significantly below the values reported for the red  $[\text{Pt}_9(\text{CO})_{18}]^{2-}$  anion [ $\nu(\text{CO})$  2029(s), 1839(m)  $\text{cm}^{-1}$ ].  $^{31}\text{P}\{^1\text{H}\}$  NMR spectroscopy shows the presence of a major species at  $\delta_{\text{P}}$  53.7 ppm with  $^1J_{\text{Pt-P}} = 5022$  Hz (to one Pt) and  $^2J_{\text{Pt-P}} = 556$  Hz (to two equivalent Pt-atoms), attributable to  $[\text{Pt}_9(\text{CO})_{17}(\text{PPh}_3)]^{2-}$ .

Formation of  $[\text{Pt}_9(\text{CO})_{17}(\text{PPh}_3)]^{2-}$  starting from  $[\text{Pt}_{12}(\text{CO})_{24}]^{2-}$  may be described by equation (1):

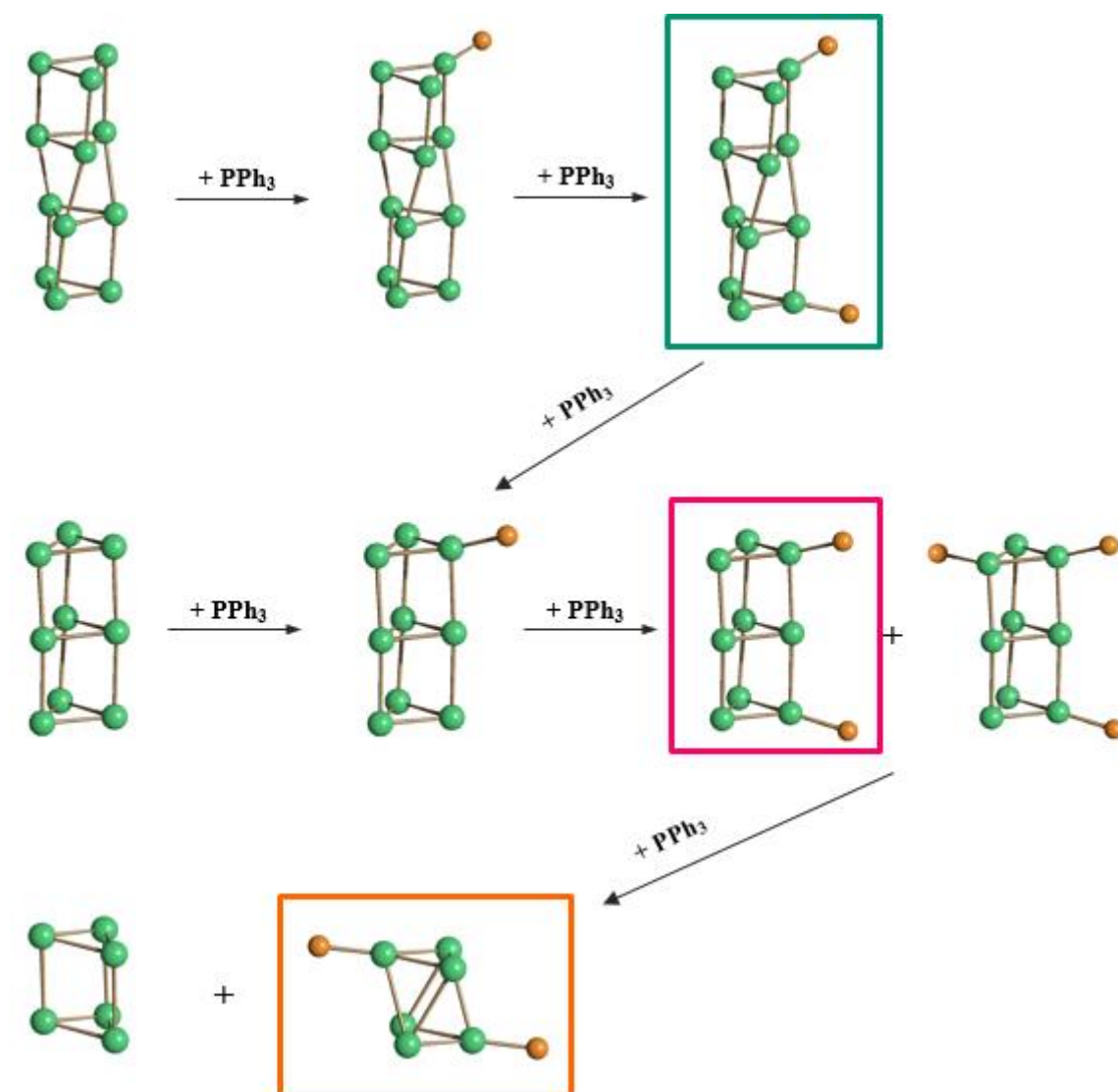


**Figure 3.1.5** Reaction of  $[\text{Pt}_{3n}(\text{CO})_{6n}]^{2-}$  ( $n = 2-4$ ) Chini's Clusters with increasing amount of  $\text{PPh}_3$ . For the sake of clarity, only the Pt-P frameworks are reported (Pt, green; P, orange).

### Box 3.1.1 Reaction of Chini's clusters with $\text{PPh}_3$ : mechanism of substitution

Substitution of CO by phosphine nucleophiles can involve an associative or dissociative reaction mechanism. In general, the two different mechanisms are governed by the nature of the ligand and the ability of the cluster to undergo M-M bond breaking. In detail, the basicity and the cone angle of the ligand are the main affecting parameters. In the associative reaction mechanism, the addition of the phosphine ligand leads to M-M bond breaking with a relative carbonyl rearrangement. The intermediate maintains the same electron count at each metal centre and subsequent loss of a CO ligand is accompanied by reformation of the M-M bond and isolation of the substitution product.

The dissociative mechanism requires dissociation of one CO ligand with a formation of an unsaturated species followed by coordination of PPh<sub>3</sub>. In the case of [Pt<sub>3n</sub>(CO)<sub>6n</sub>]<sup>2-</sup> (*n* = 2-6) Chini's Clusters the stability under *vacuum* suggests that the reaction should occur with an associative mechanism.

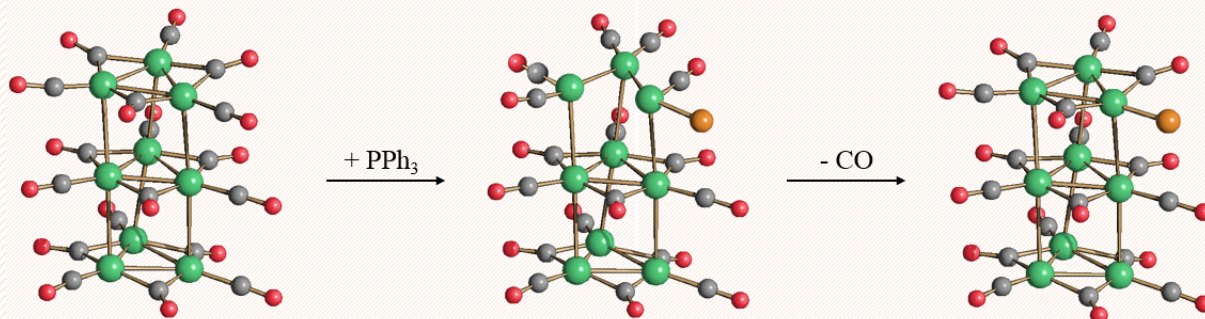


**Figure Box 3.1.1** The supposed associative mechanism for PPh<sub>3</sub> substitution in [Pt<sub>9</sub>(CO)<sub>18</sub>]<sup>2-</sup>. In the first step, the addition of the phosphine ligand lead to Pt-Pt bond breaking followed by the loss of a CO ligand. The cone angle of PPh<sub>3</sub> is 145° in the middle of the typical range of the phosphines, *i.e.*, from 106° for PPhH<sub>2</sub> to 182° for P(<sup>t</sup>Bu)<sub>3</sub> (Pt, green; P, orange; C, grey; O, red; H, white).

Indeed, under *vacuum* condition, equilibria between the cluster and the decarbonylated species (instable) should lead to high or nuclearity tridimensional carbonyl clusters as observed in the case of thermal degradation.

Compound	$\delta_P$ (ppm)	$^1J_{Pt-P}$ (Hz)	$^2J_{Pt-P}$ (Hz)
[Pt <sub>12</sub> (CO) <sub>23</sub> (PPh <sub>3</sub> ) <sup>2-</sup>	49.4	5081	551
[Pt <sub>12</sub> (CO) <sub>22</sub> (PPh <sub>3</sub> ) <sub>2</sub> ] <sup>2-</sup>	50.6	5102	551
[Pt <sub>9</sub> (CO) <sub>17</sub> (PPh <sub>3</sub> ) <sup>2-</sup>	53.7	5022	556
[Pt <sub>9</sub> (CO) <sub>16</sub> (PPh <sub>3</sub> ) <sub>2</sub> ] <sup>2-</sup>	54.3	5144	556
[Pt <sub>9</sub> (CO) <sub>15</sub> (PPh <sub>3</sub> ) <sub>3</sub> ] <sup>2-</sup>	55.0 <sup>a</sup>	5338	549
[Pt <sub>6</sub> (CO) <sub>11</sub> (PPh <sub>3</sub> ) <sup>2-</sup>	57.3 <sup>b</sup>	5215	530
[Pt <sub>6</sub> (CO) <sub>10</sub> (PPh <sub>3</sub> ) <sub>2</sub> ] <sup>2-</sup>	55.6	5222	540
[Pt <sub>6</sub> (CO) <sub>10</sub> (PPh <sub>3</sub> ) <sub>2</sub> ] <sup>2-</sup>	56.5	5301	566

**Table 3.1.1** <sup>31</sup>P{<sup>1</sup>H} NMR data of PPh<sub>3</sub>-derivatives of [Pt<sub>3n</sub>(CO)<sub>6n</sub>]<sup>2-</sup> (*n* = 2-4) Chini's Clusters recorded at room temperature in deuterated acetone. <sup>a</sup> Corresponding to a single P-atom. <sup>b</sup> Corresponding to two P-atoms. <sup>3</sup>J<sub>P-P</sub> = 50 Hz.

Formation of Pt<sub>3</sub>(CO)<sub>3</sub>(PPh<sub>3</sub>)<sub>3</sub> as side product was confirmed by IR and <sup>31</sup>P{<sup>1</sup>H} NMR spectroscopy. Moreover, the same compound [Pt<sub>9</sub>(CO)<sub>17</sub>(PPh<sub>3</sub>)<sup>2-</sup> may be obtained by the reaction of [Pt<sub>9</sub>(CO)<sub>18</sub>]<sup>2-</sup> with one equivalent of PPh<sub>3</sub>. In this case, the <sup>31</sup>P{<sup>1</sup>H} NMR spectrum

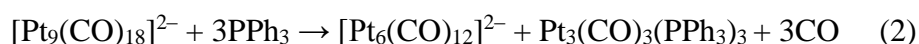
of a solution shows that  $[\text{Pt}_9(\text{CO})_{17}(\text{PPh}_3)]^{2-}$  and  $[\text{Pt}_9(\text{CO})_{16}(\text{PPh}_3)_2]^{2-}$  are the major species present in a *ca.* 2 : 1 ratio.

Reagents		Products *				
Starting Material	PPh <sub>3</sub> eq	Pt <sub>12</sub> L	Pt <sub>12</sub> L <sub>2</sub>	Pt <sub>9</sub> L	Pt <sub>9</sub> L <sub>2</sub>	Pt <sub>9</sub> L <sub>3</sub>
$[\text{Pt}_{12}(\text{CO})_{24}]^{2-}$	1	75	25	/	/	/
	2	t	48	20	32	/
$[\text{Pt}_9(\text{CO})_{18}]^{2-}$	1	t	t	66	34	/
	2	/	t	t	66	34

**Table 3.1.2** Most relevant data of the reaction of  $[\text{Pt}_{12}(\text{CO})_{24}]^{2-}$  or  $[\text{Pt}_9(\text{CO})_{18}]^{2-}$  with an increasing amount of PPh<sub>3</sub> (t = trace; Pt<sub>12</sub>L,  $[\text{Pt}_{12}(\text{CO})_{23}\text{L}]^{2-}$ ; Pt<sub>12</sub>L<sub>2</sub>,  $[\text{Pt}_{12}(\text{CO})_{22}\text{L}_2]^{2-}$ ; Pt<sub>9</sub>L,  $[\text{Pt}_9(\text{CO})_{17}\text{L}]^{2-}$ ; Pt<sub>9</sub>L<sub>2</sub>,  $[\text{Pt}_9(\text{CO})_{16}\text{L}_2]^{2-}$ ; Pt<sub>9</sub>L<sub>3</sub>,  $[\text{Pt}_9(\text{CO})_{15}\text{L}_3]^{2-}$ ). \* Percentage of PPh<sub>3</sub>-derivatives without taking into account the presence of the other homoleptic species as inferred by  $^{31}\text{P}\{^1\text{H}\}$  NMR experiments.

The addition of four equivalents or two equivalents of PPh<sub>3</sub>, respectively, to  $[\text{Pt}_{12}(\text{CO})_{24}]^{2-}$   $[\text{Pt}_9(\text{CO})_{18}]^{2-}$  results in a mixture of products containing  $[\text{Pt}_9(\text{CO})_{16}(\text{PPh}_3)_2]^{2-}$  and  $[\text{Pt}_9(\text{CO})_{15}(\text{PPh}_3)_3]^{2-}$  as the major species together with minor amounts of  $[\text{Pt}_9(\text{CO})_{17}(\text{PPh}_3)]^{2-}$  and  $[\text{Pt}_{12}(\text{CO})_{22}(\text{PPh}_3)_2]^{2-}$  as determined by  $^{31}\text{P}\{^1\text{H}\}$  NMR spectroscopy. The IR of this solution display  $\nu(\text{CO})$  bands formally attributable to  $[\text{Pt}_9(\text{CO})_{16}(\text{PPh}_3)_2]^{2-}$ . This is further corroborated by the fact that  $[\text{Pt}_9(\text{CO})_{16}(\text{PPh}_3)_2]^{2-}$  has been isolated in crystalline sample (see section 3.1.6) from the reaction of  $[\text{Pt}_9(\text{CO})_{18}]^{2-}$  with two equivalent of PPh<sub>3</sub>. These results further confirm that the first and second CO substitution reactions occur partially in parallel. Moreover, a third CO may be replaced, affording  $[\text{Pt}_9(\text{CO})_{15}(\text{PPh}_3)_3]^{2-}$ . Its  $^{31}\text{P}\{^1\text{H}\}$  NMR spectrum shows two multiplets in a 2 : 1 ratio centered at  $\delta_{\text{P}}$  57.3 and 55.0 ppm, respectively. The former displays  $^1J_{\text{Pt-P}} = 5215$  Hz (to one Pt atom),  $^2J_{\text{Pt-P}} = 530$  Hz (to two Pt-atoms) and  $^3J_{\text{P-P}} = 50$  Hz (to one P-atom), whereas the latter resonance displays the same pattern as the mono- and di-substituted clusters, with  $^1J_{\text{Pt-P}} = 5338$  Hz (to one Pt atom) and  $^2J_{\text{Pt-P}} = 549$  Hz (to two Pt-atoms).

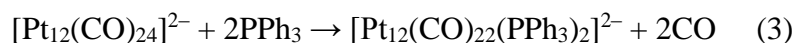
These data suggest that in the structure of  $[\text{Pt}_9(\text{CO})_{15}(\text{PPh}_3)_3]^{2-}$  two PPh<sub>3</sub> ligands are bonded to one external triangle and the third phosphine ligand to the other external Pt<sub>3</sub>-triangle. P-P coupling is present between the two PPh<sub>3</sub> ligands on the same triangle, whereas no inter-triangular P-P nor P-Pt coupling has been detected. The possible isomer in which each Pt<sub>3</sub> triangle bears a single PPh<sub>3</sub> ligand can be ruled out on the basis of the observed  $^{31}\text{P}\{^1\text{H}\}$  NMR pattern, whereas the isomer containing three PPh<sub>3</sub> ligands bonded to the same triangle would show a single resonance. Further addition of PPh<sub>3</sub> results in an orange solution displaying  $\nu(\text{CO})$  stretchings at 2001(s) and 1800(m)  $\text{cm}^{-1}$ , corresponding to  $[\text{Pt}_6(\text{CO})_{12}]^{2-}$ . Its formation is in accord to equation (2):



The formation of  $\text{Pt}_3(\text{CO})_3(\text{PPh}_3)_3$  has been confirmed by means of IR and  $^{31}\text{P}\{^1\text{H}\}$  NMR spectroscopy. Addition of  $\text{PPh}_3$  to  $[\text{Pt}_6(\text{CO})_{12}]^{2-}$  does not result in any significant change in its  $\nu(\text{CO})$  bands and, only after the addition of a large excess of phosphine (>15 equivalents),  $[\text{Pt}_6(\text{CO})_{12}]^{2-}$  is degraded to  $\text{Pt}_3(\text{CO})_3(\text{PPh}_3)_3$ ,  $\text{Pt}(\text{PPh}_3)_2(\text{CO})_2$  and  $\text{Pt}(\text{PPh}_3)_3(\text{CO})$ , as indicated by IR and  $^{31}\text{P}\{^1\text{H}\}$  NMR spectroscopy. The transformation of  $\text{Pt}_3(\text{CO})_3(\text{PPh}_3)_3$  into  $\text{Pt}(\text{PPh}_3)_2(\text{CO})_2$ ,  $\text{Pt}(\text{PPh}_3)_3(\text{CO})$  and other low nuclearity neutral Pt/CO/ $\text{PPh}_3$  clusters after reaction with  $\text{PPh}_3$  has been previously described in the literature. It is noteworthy that after the addition of 5 equivalents of  $\text{PPh}_3$  to  $[\text{Pt}_6(\text{CO})_{12}]^{2-}$  in acetone, the solution displays  $\nu(\text{CO})$  bands at 2001(s) and 1800(m)  $\text{cm}^{-1}$ , confirming that  $[\text{Pt}_6(\text{CO})_{12}]^{2-}$  is the major species present in solution. Nonetheless, the  $^{31}\text{P}\{^1\text{H}\}$  NMR spectrum reveals the presence also of  $[\text{Pt}_6(\text{CO})_{11}(\text{PPh}_3)]^{2-}$  and  $[\text{Pt}_9(\text{CO})_{16}(\text{PPh}_3)_2]^{2-}$  (ca. 5 : 1 ratio) together with a minor amount of  $[\text{Pt}_6(\text{CO})_{10}(\text{PPh}_3)_2]^{2-}$ . Moreover, crystals of  $[\text{Pt}_6(\text{CO})_{10}(\text{PPh}_3)_2]^{2-}$  have been obtained by slow diffusion of n-hexane on solutions containing  $[\text{Pt}_6(\text{CO})_{12}]^{2-}$  and 10 equivalents of  $\text{PPh}_3$ , even if IR spectroscopy indicated that  $[\text{Pt}_6(\text{CO})_{12}]^{2-}$  was the major species present in solution.

### 3.1.5 Synthesis and characterization of $[\text{Pt}_{12}(\text{CO})_{22}(\text{PPh}_3)_2]^{2-}$

$[\text{Pt}_{12}(\text{CO})_{24}]^{2-}$  reacts with two equivalents of  $\text{PPh}_3$  affording the new  $[\text{Pt}_{12}(\text{CO})_{22}(\text{PPh}_3)_2]^{2-}$  (figure 3.1.6 and table 3.1.3) anion in accord to equation (3):



The substitution of two CO ligands with the more basic  $\text{PPh}_3$  is confirmed by the lowering of the  $\nu(\text{CO})$  stretchings. X-ray quality crystals of  $[\text{NEt}_4]_2[\text{Pt}_{12}(\text{CO})_{22}(\text{PPh}_3)_2]$  have been obtained by slow diffusion of n-hexane on the acetone solution.

It must be noticed that the crystals of  $[\text{NEt}_4]_2[\text{Pt}_{12}(\text{CO})_{22}(\text{PPh}_3)_2]$  have been obtained in mixture with an amorphous powder containing  $[\text{Pt}_9(\text{CO})_{16}(\text{PPh}_3)_2]^{2-}$  and  $[\text{Pt}_9(\text{CO})_{17}(\text{PPh}_3)]^{2-}$ . A few crystals have been mechanically separated from the amorphous solid for spectroscopic characterization.  $[\text{NEt}_4]_2[\text{Pt}_{12}(\text{CO})_{22}(\text{PPh}_3)_2]$  displays  $\nu(\text{CO})$  at 2032(s), 2002(w), 1825(s) and 1780(s) in nujol mull, and 2036(s), 1848(m)  $\text{cm}^{-1}$  in acetone. Its  $^{31}\text{P}\{^1\text{H}\}$  NMR spectrum in deuterated acetone is similar to the one of  $[\text{Pt}_9(\text{CO})_{16}(\text{PPh}_3)_2]^{2-}$  showing a multiplet at  $\delta_{\text{P}}$  50.6 ppm with  $^1J_{\text{Pt-P}} = 5102$  Hz (to one Pt) and  $^2J_{\text{Pt-P}} = 551$  Hz (to two equivalent Pt-atoms).

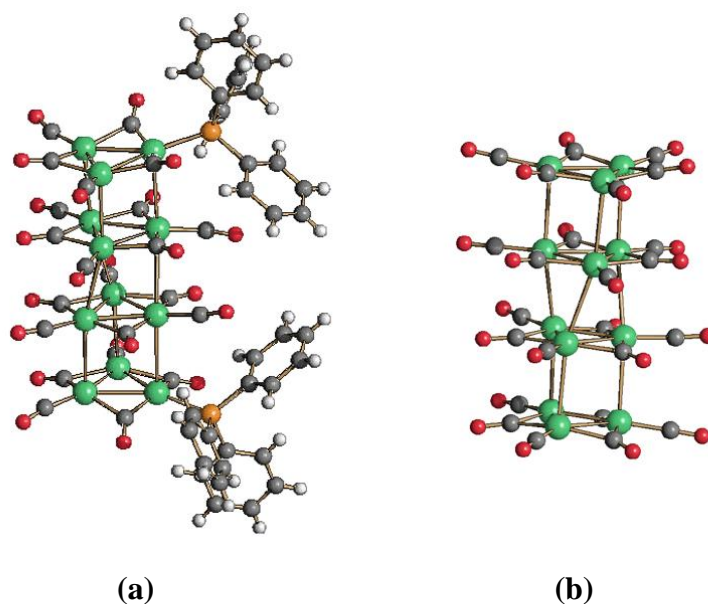


**Figure 3.1.6** Molecular structures of (a)  $[\text{Pt}_{12}(\text{CO})_{22}(\text{PPh}_3)_2]^{2-}$  and (b)  $[\text{Pt}_{12}(\text{CO})_{24}]^{2-}$  (Pt, green; P, orange; C, grey; O, red; H, white).

The molecular structure of  $[\text{Pt}_{12}(\text{CO})_{22}(\text{PPh}_3)_2]^{2-}$  is very similar to the parent  $[\text{Pt}_{12}(\text{CO})_{24}]^{2-}$  dianion, being the replacement of two terminal CO with two  $\text{PPh}_3$  ligands the main difference. One terminal position of both external triangular units is occupied by a  $\text{PPh}_3$  ligand. The two  $\text{PPh}_3$  ligands are in a relative pseudo *cis*-position.

	Pt-Pt		Pt-P
	Intra-triangular	Inter-triangular <sup>(a)</sup>	
$[\text{Pt}_{12}(\text{CO})_{22}(\text{PPh}_3)_2]^{2-}$	2.6539(9)-2.6756(9) Average 2.666(2)	3.0184(9)-3.2067(11) Average 3.086(2)	2.281(4)
$[\text{Pt}_{12}(\text{CO})_{24}]^{2-}$ <sup>(b)</sup>	2.6587(5)-2.6707(5) Average 2.6656(12)	3.0465(5)-3.0597(5) Average 3.0535(12)	-
$[\text{Pt}_9(\text{CO})_{16}(\text{PPh}_3)_2]^{2-}$	2.6597(8)-2.6814(9) Average 2.670(2)	3.0015(9)-3.1098(8) Average 3.043(2)	2.265(4)-2.287(4) Average 2.276(6)
$[\text{Pt}_9(\text{CO})_{18}]^{2-}$ <sup>(b)</sup>	2.65(2)-2.67(8) Average 2.66(9)	3.04(2)-3.06(2) Average 3.05(4)	-
$[\text{Pt}_6(\text{CO})_{10}(\text{PPh}_3)_2]^{2-}$ <sup>(c)</sup>	2.6558(6)-2.6743(6) Average 2.6644(10)	3.0353(6) <sup>(e)</sup>	2.240(3)
$[\text{Pt}_6(\text{CO})_{10}(\text{PPh}_3)_2]^{2-}$ <sup>(d)</sup>	2.6584(6)-2.6787(6) Average 2.6694(10)	3.1380(6)-3.2079(6) Average 3.1729(8) <sup>(f)</sup>	2.247(3)
$[\text{Pt}_6(\text{CO})_{12}]^{2-}$ <sup>(b)</sup>	2.644(7)-2.659(3) Average 2.653(10)	3.026(16)-3.049(17) Average 3.03(3)	-

**Table 3.1.3** Main bond distances of  $[\text{Pt}_{3n}(\text{CO})_{6n}]^{2-}$  ( $n = 2-4$ ) and their  $\text{PPh}_3$ -derivatives. <sup>(a)</sup> Only Pt-Pt interactions  $\leq 3.34$  Å have been included. <sup>(b)</sup> From ref. [43], [44]. <sup>(c)</sup> As found in  $[\text{NBu}_4]_2[\text{Pt}_6(\text{CO})_{10}(\text{PPh}_3)_2]$ . <sup>(d)</sup> As found in  $[\text{NBu}_4]_2[\text{Pt}_6(\text{CO})_{10}(\text{PPh}_3)_2] \cdot 2\text{thf}$ . <sup>(e)</sup> Three sets of inter-triangular Pt-Pt contacts are present: 3.0353(6), 3.3581(6), 3.5070(6) Å. <sup>(f)</sup> Three sets of inter-triangular Pt-Pt contacts are present: 3.1380(6), 3.2079(6), 3.4310(6) Å.

The intra-triangular Pt-Pt bonding distances and the the inter-triangular contacts of  $[\text{Pt}_{12}(\text{CO})_{22}(\text{PPh}_3)_2]^{2-}$  compare very well to that ones found in the parent  $[\text{Pt}_{12}(\text{CO})_{24}]^{2-}$  dianion for what concerns their ranges and average values. This suggests that the replacement of CO with  $\text{PPh}_3$  does not alter the intra- and the inter-triangular bonding contacts.

### 3.1.6 Synthesis and characterization of $[\text{Pt}_9(\text{CO})_{16}(\text{PPh}_3)_2]^{2-}$

The reaction of  $[\text{Pt}_9(\text{CO})_{18}]^{2-}$  in acetone with two equivalents of  $\text{PPh}_3$  results in the immediate formation of the new species  $[\text{Pt}_9(\text{CO})_{16}(\text{PPh}_3)_2]^{2-}$  in accord to equation (4):



The substitution of two CO ligands with the more basic  $\text{PPh}_3$  is confirmed by the lowering of the  $\nu(\text{CO})$  stretchings. Moreover, single crystals suitable for X-ray analyses of  $[\text{NBu}_4]_2[\text{Pt}_9(\text{CO})_{16}(\text{PPh}_3)_2]$  have been obtained by slow diffusion of n-hexane on the acetone solution.

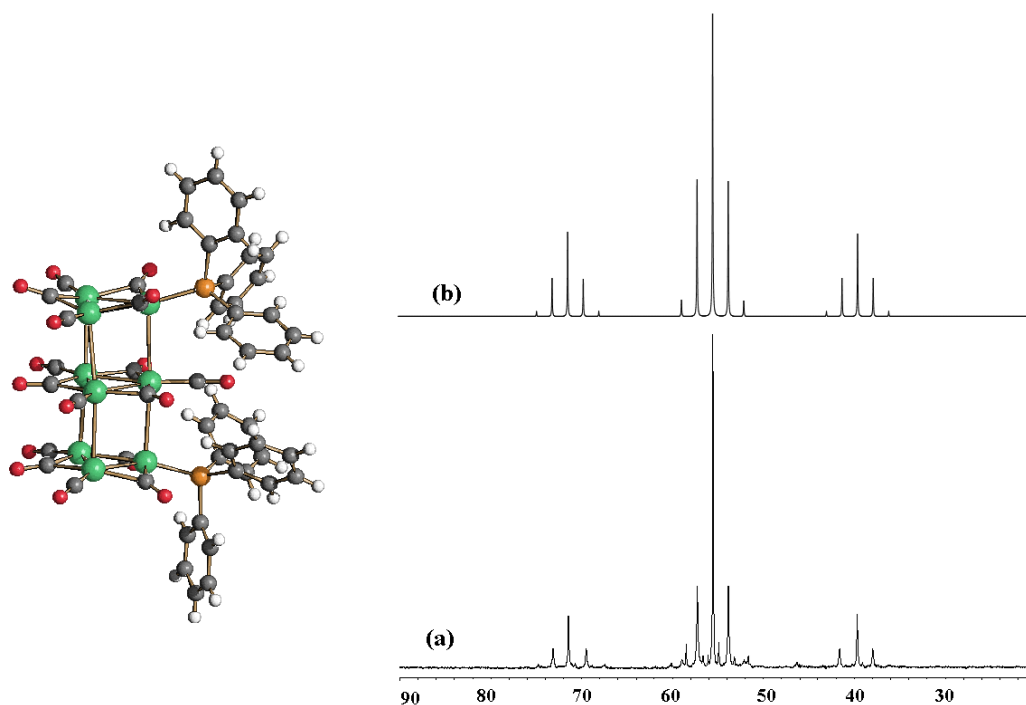


**Figure 3.1.7** Molecular structure of  $[\text{Pt}_9(\text{CO})_{16}(\text{PPh}_3)_2]^{2-}$  (left) and its  $^{31}\text{P}\{^1\text{H}\}$  NMR spectrum in deuterated acetone at room temperature (right): (a) experimental and (b) simulated with gNMR 5.0.6.0. (Pt, green; P, orange; C, grey; O, red; H, white).

The  $^{31}\text{P}\{^1\text{H}\}$  NMR spectrum of  $[\text{Pt}_9(\text{CO})_{16}(\text{PPh}_3)_2]^{2-}$  fully agrees with its solid state structure and it is remarkable that the presence of a single species indicates that no exchange process is present in solution (figure 3.1.7 right). Because of the isotopic distribution of Pt, the two equivalent phosphine ligands display a complex multiplet centered at  $\delta_{\text{P}} 54.3$  ppm with  $^1J_{\text{Pt}}$

$\nu_{\text{Pt-P}} = 5144$  Hz (to one Pt) and  ${}^2J_{\text{Pt-P}} = 556$  Hz (to two equivalent Pt-atoms). Each  $\text{PPh}_3$  ligand is coupled to three Pt-atoms of the same triangle, whereas no coupling to the internal triangle is present. A similar situation has been previously found for the  ${}^{13}\text{C}$  and  ${}^{195}\text{Pt}$  NMR spectra of  $[\text{Pt}_{3n}(\text{CO})_{6n}]^{2-}$  ( $n = 2-6$ ). This is due to the fact that the inter-triangular Pt-Pt bonds are considerably weaker than the intra-triangular ones.

As for  $[\text{Pt}_{12}(\text{CO})_{22}(\text{PPh}_3)_2]^{2-}$ , the molecular structure of  $[\text{Pt}_9(\text{CO})_{16}(\text{PPh}_3)_2]^{2-}$  is similar to the parent homoleptic dianion and the two  $\text{PPh}_3$  ligands are in a relative pseudo *cis*-position (figure 3.1.7 left).

### 3.1.7 Synthesis and characterization of $[\text{Pt}_6(\text{CO})_{10}(\text{PPh}_3)_2]^{2-}$

A few single crystals of  $[\text{NBu}_4]_2[\text{Pt}_6(\text{CO})_{10}(\text{PPh}_3)_2]$  and  $[\text{NBu}_4]_2[\text{Pt}_6(\text{CO})_{10}(\text{PPh}_3)_2] \cdot 2\text{thf}$  have been obtained by slow diffusion of n-hexane on acetone and thf solutions, respectively, containing  $[\text{Pt}_6(\text{CO})_{12}]^{2-}$  and 10 equivalents of  $\text{PPh}_3$ .

It must be remarked that the majority of the solid was composed of amorphous  $[\text{Pt}_6(\text{CO})_{12}]^{2-}$  and traces of  $[\text{Pt}_9(\text{CO})_{16}(\text{PPh}_3)_2]^{2-}$ ,  $[\text{Pt}_9(\text{CO})_{15}(\text{PPh}_3)_3]^{2-}$  and  $[\text{Pt}_6(\text{CO})_{11}(\text{PPh}_3)]^{2-}$ . This indicates that substitution of CO with  $\text{PPh}_3$  is more difficult in the small  $[\text{Pt}_6(\text{CO})_{12}]^{2-}$  anion compared to higher nuclearity clusters having the same total charge. Thus, the reaction occurs only to a small extent, whereas the unsubstituted anion remains the predominant species.

The crystals of  $[\text{NBu}_4]_2[\text{Pt}_6(\text{CO})_{10}(\text{PPh}_3)_2]$  and  $[\text{NBu}_4]_2[\text{Pt}_6(\text{CO})_{10}(\text{PPh}_3)_2] \cdot 2\text{thf}$  display  $\nu(\text{CO})$  at 1973(s), 1960(vs), 1794(m) and 1756(vs) in nujol mull. The  ${}^{31}\text{P}\{^1\text{H}\}$  NMR spectrum of  $[\text{Pt}_6(\text{CO})_{10}(\text{PPh}_3)_2]^{2-}$  (in deuterated acetone) displays a pattern very similar to the ones reported for  $[\text{Pt}_{12}(\text{CO})_{22}(\text{PPh}_3)_2]^{2-}$  and  $[\text{Pt}_9(\text{CO})_{16}(\text{PPh}_3)_2]^{2-}$ , displaying a multiplet centered at  $\delta_{\text{P}} 56.5$  ppm with  ${}^1J_{\text{Pt-P}} = 5301$  Hz (to one Pt) and  ${}^2J_{\text{Pt-P}} = 566$  Hz (to two equivalent Pt-atoms), in agreement with its solid state structure.

The structure of  $[\text{Pt}_6(\text{CO})_{10}(\text{PPh}_3)_2]^{2-}$  (figure 3.1.8), as found in the two solvates, significantly differs from  $[\text{Pt}_{12}(\text{CO})_{22}(\text{PPh}_3)_2]^{2-}$  and  $[\text{Pt}_9(\text{CO})_{16}(\text{PPh}_3)_2]^{2-}$ , as well as the parent  $[\text{Pt}_6(\text{CO})_{12}]^{2-}$ . In particular the last is a trigonal prism composed of two  $\text{Pt}_3(\mu\text{-CO})_3(\text{CO})_3$  units with ideal  $D_{3h}$  symmetry. Conversely,  $[\text{Pt}_6(\text{CO})_{10}(\text{PPh}_3)_2]^{2-}$ , as found in both salts, is composed of two  $\text{Pt}_3(\mu\text{-CO})_3(\text{CO})_2(\text{PPh}_3)$  units, which are rotated by  $180^\circ$  (taking the two  $\text{PPh}_3$  ligands as references), ideally originating a trigonal anti-prism which should include six inter-triangular Pt-Pt bonds.

The structures of the  $[\text{Pt}_6(\text{CO})_{10}(\text{PPh}_3)_2]^{2-}$  anions depart from the ideal one, since only two inter-triangular Pt-Pt contacts in the  $[\text{NBu}_4]_2[\text{Pt}_6(\text{CO})_{10}(\text{PPh}_3)_2]$  salt and four in  $[\text{NBu}_4]_2[\text{Pt}_6(\text{CO})_{10}(\text{PPh}_3)_2] \cdot 2\text{thf}$  are at bonding distances, whereas the other ones are basically

non-bonding. The fact that only  $[\text{Pt}_6(\text{CO})_{10}(\text{PPh}_3)_2]^{2-}$  shows a different geometry from the parent  $[\text{Pt}_6(\text{CO})_{12}]^{2-}$ , whereas all higher nuclearity substituted and unsubstituted clusters are almost isostructural, is likely to be originated by steric repulsion between the two bulky  $\text{PPh}_3$  ligands in the smaller  $\text{Pt}_6$  cluster (figure 3.1.9).

The slightly different structures found for  $[\text{Pt}_6(\text{CO})_{10}(\text{PPh}_3)_2]^{2-}$  in the two salts are due to different packing effects resulting from inclusion of thf in one salt. This points out that the inter-triangular bonds are rather weak and easily deformed by small changes in the van der Waals forces within the crystal.

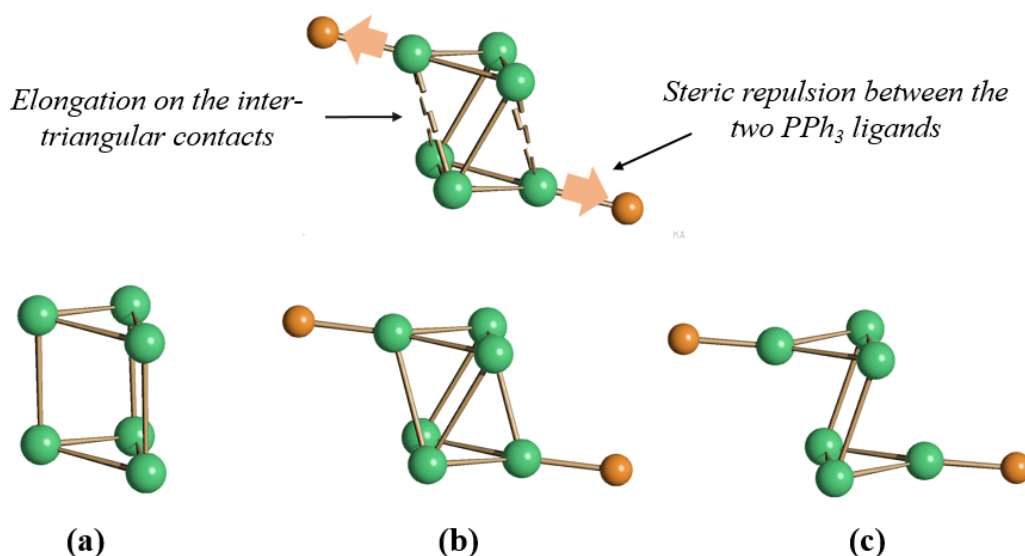


**Figure 3.1.9** Metal frameworks of  $[\text{Pt}_6(\text{CO})_{12}]^{2-}$  (a) and  $[\text{Pt}_6(\text{CO})_{10}(\text{PPh}_3)_2]^{2-}$  as found in  $[\text{NBu}_4]_2[\text{Pt}_6(\text{CO})_{10}(\text{PPh}_3)_2] \cdot 2\text{thf}$  (b) and  $[\text{NBu}_4]_2[\text{Pt}_6(\text{CO})_{10}(\text{PPh}_3)_2]$  (c). It has been arbitrarily decided to represent Pt-Pt bonds up to 3.34 Å, which is slightly below twice the van der Waals radius of Pt and ca. 20 % greater than twice its covalent radius (covalent radius 1.36 Å; van der Waals radius 1.72 Å; Pt, green; P, orange).

## Reactions of $[\text{Pt}_{12}(\text{CO})_{24}]^{2-}$ Chini's Cluster with Bidentate Phosphines

### 3.2.1 MCCs containing bidentate phosphines: a brief overview

Polydentate phosphine ligands are well known. The most common ones are bidentate phosphines linked by short spacers (*e.g.*,  $-\text{CH}_2-$  and  $-\text{NR}-$ ), flexible unit (*e.g.*,  $-(\text{CH}_2)_n-$  and  $-(\text{C}_5\text{H}_4)\text{Fe}(\text{C}_5\text{H}_4)-$ ) and rigid units (*e.g.*,  $-\text{C}_6\text{H}_4-$  and  $-\text{CH}=\text{CH}-$ ). The different nature of these spacers strongly influences the bonding mode. Indeed, bidentate phosphines can chelate a single metal atom in the cluster, bridge across a metal-metal bond, or form an intermolecular link between clusters (figure 3.2.1). For instance,  $\text{Ph}_2\text{PCH}=\text{CHPPh}_2$  prefers to form a five-membered ring with the metal whereas  $\text{Ph}_2\text{PCH}_2\text{PPh}_2$  prefers to bridge a metal-metal edge, also forming a stable five-membered ring. Instead, the stereochemistry and rigidity of  $\text{Ph}_2\text{P}(1,4\text{-C}_6\text{H}_4)\text{PPh}_2$  are ideal in order to obtain an intermolecular bond between two (dimer) or more clusters (polymer).

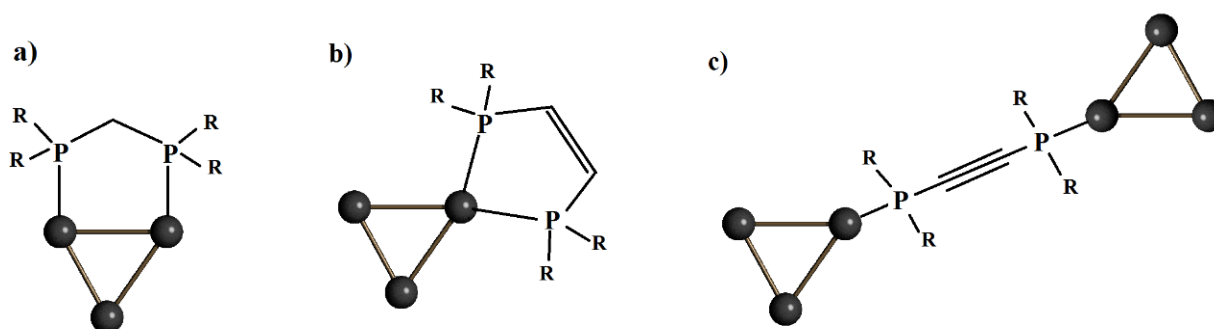


**Figure 3.2.1** Possible coordination modes of bidentate phosphines to metal clusters: **a)** bridging a metal-metal bond, **b)** chelating a metal centre and **c)** bridging two clusters.

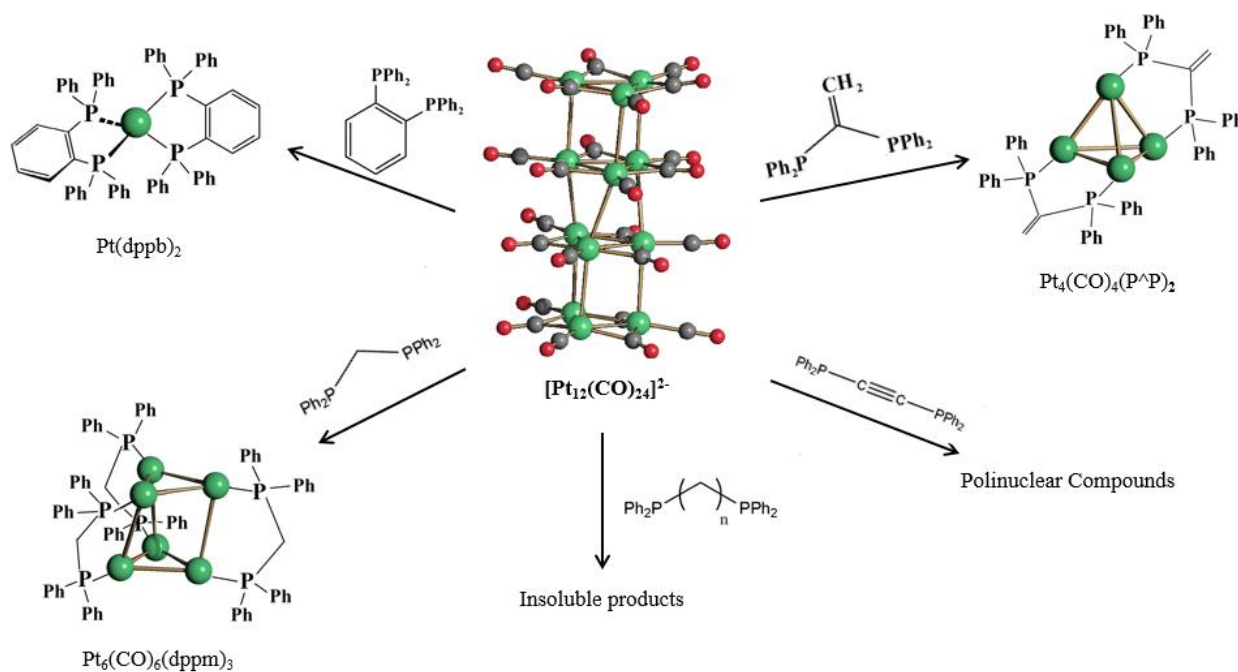
The countless cases of studies reported in the literature have contributed to have general guidelines for the synthesis of bidentate phosphines derivatives obtained by reaction of homoleptic carbonyl clusters. However, the predictions of these syntheses are not always simple and sometimes, more isomers can be obtained.<sup>12</sup> Moreover, the modulation of the nature of the phosphine is a simple way to obtain new clusters with performing properties in term of solubility,

<sup>12</sup> Curiously, two isomers of  $\text{H}_4\text{Ru}_4(\text{CO})_{10}(\text{Ph}_2\text{PCH}_2\text{CH}_2\text{PPh}_2)$  are known where the bidentate phosphine bridges across a Ru-Ru bond or chelates a Ru atom [48].

reactivity and stability. Substitution of carbonyl ligands with chiral phosphines leads to chiral clusters and in this regard the reaction of  $\text{H}_4\text{Ru}_4(\text{CO})_{12}$  with DIPAMP (ethane-1,2-diylbis[(2-methoxyphenyl)phenylphosphane]) represents a very interesting case of study in asymmetric homogenous catalysis [49].

### 3.2.2 General Results

The following sections illustrate the investigation of the reactions of  $[\text{Pt}_{12}(\text{CO})_{24}]^{2-}$  with different bidentate phosphines, *i.e.*,  $\text{CH}_2=\text{C}(\text{PPh}_2)_2$  ( $\text{P}^\wedge\text{P}$ ),  $\text{Ph}_2\text{PCH}_2\text{PPh}_2$  (dppm),  $\text{Ph}_2\text{PCH}_2\text{CH}_2\text{PPh}_2$  (dppe), *o*- $\text{C}_6\text{H}_4(\text{PPh}_2)_2$  (dppb),  $\text{Ph}_2\text{P}(\text{CH}_2)_4\text{PPh}_2$  (dppb\*) and  $\text{Ph}_2\text{PC}_2\text{PPh}_2$  (P-P) (scheme 3.2.1) [50].

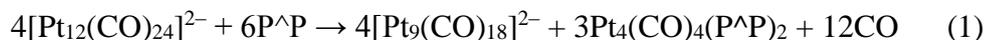


**Scheme 3.2.1** Reactions of  $[\text{Pt}_{12}(\text{CO})_{24}]^{2-}$  with different bidentate phosphines. For the sake of clarity, some carbonyl and phosphine ligands are represented with wireframe style (Pt, green; C, grey; O, red).  $n = 4$ .

The reactions with  $\text{P}^\wedge\text{P}$  and dppm have been fully investigated and lead to new lower nuclearity clusters. Conversely, the reaction of  $[\text{Pt}_{12}(\text{CO})_{24}]^{2-}$  with P-P does not result in dimers or polymers, as it might have been expected, but a complex polynuclear compound is formed. The use of *o*- $\text{C}_6\text{H}_4(\text{PPh}_2)_2$  results in complete degradation of the cluster leading to a mononuclear complex. Finally, the reactions with dppb\* and dppe result in uncharacterized polymeric amorphous compounds that are insoluble in all common solvents.

### 3.2.3 Synthesis of $[\text{H}_n\text{Pt}_4(\text{CO})_4(\text{P}^\wedge\text{P})_2]^{n+}$ ( $n = 0-2$ ) clusters

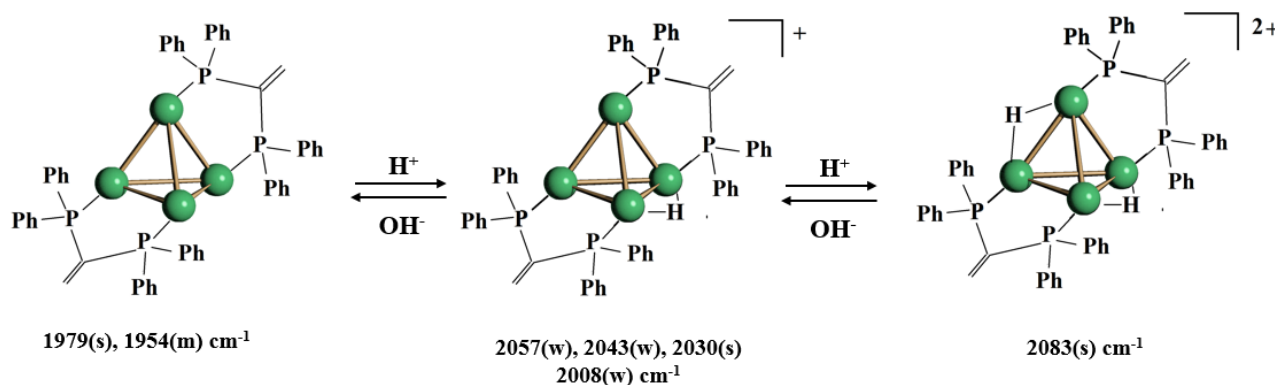
The reactions of  $[\text{Pt}_{12}(\text{CO})_{24}]^{2-}$  with *ca.* 1.5 equivalents of  $\text{P}^\wedge\text{P}$  in acetone results in the neutral compound  $\text{Pt}_4(\text{CO})_4(\text{P}^\wedge\text{P})_2$  according to equation (1):



Thus, after the addition of  $\text{P}^\wedge\text{P}$ , the green solution of  $[\text{Pt}_{12}(\text{CO})_{24}]^{2-}$  turns red in agreement with formation of  $[\text{Pt}_9(\text{CO})_{18}]^{2-}$  and the scarcely soluble  $\text{Pt}_4(\text{CO})_4(\text{P}^\wedge\text{P})_2$  starts to separate out as an orange microcrystalline solid. The reaction is completed after 2 days and complete precipitation of  $\text{Pt}_4(\text{CO})_4(\text{P}^\wedge\text{P})_2$  may be accomplished by addition of dmf to the acetone solution. Crystals of  $\text{Pt}_4(\text{CO})_4(\text{P}^\wedge\text{P})_2$  suitable for X-ray analyses can be obtained by slow diffusion of n-hexane on the acetone solution.

Under these conditions, the two compounds can be easily separated by filtration.  $\text{Pt}_4(\text{CO})_4(\text{P}^\wedge\text{P})_2$  is almost insoluble in polar solvents such as  $\text{CH}_3\text{CN}$  and dmf, scarcely soluble in less polar solvents such as acetone and thf, and partially soluble in  $\text{CH}_2\text{Cl}_2$  (solubility  $1.8 \times 10^{-3}$  M).

The neutral cluster  $\text{Pt}_4(\text{CO})_4(\text{P}^\wedge\text{P})_2$  is protonated by strong acids such as  $\text{HBF}_4 \cdot \text{Et}_2\text{O}$  in  $\text{CH}_2\text{Cl}_2$  resulting, after the addition of one equivalent of acid, in the  $[\text{HPT}_4(\text{CO})_4(\text{P}^\wedge\text{P})_2]^+$  mono-hydride mono-cation which is completely soluble in  $\text{CH}_2\text{Cl}_2$  (scheme 3.2.2).

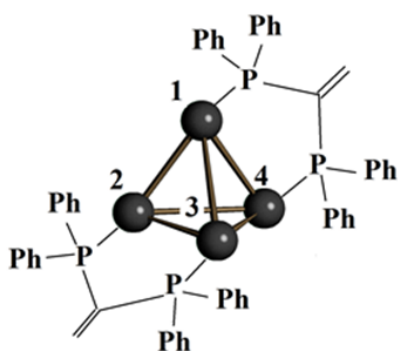


**Scheme 3.2.2** Protonation and deprotonation equilibria of  $[\text{H}_n\text{Pt}_4(\text{CO})_4(\text{P}^\wedge\text{P})_2]^{n+}$  ( $n = 0-2$ ). The  $\nu(\text{CO})$  stretchings have been recorded in  $\text{CH}_2\text{Cl}_2$ . For the sake of clarity, carbonyls are not represented and phosphine ligands are sketched with wireframe style (Pt, green).

Further addition of 3-4 equivalents of the same acid to  $[\text{HPT}_4(\text{CO})_4(\text{P}^\wedge\text{P})_2]^+$  results in the formation of the  $[\text{H}_2\text{Pt}_4(\text{CO})_4(\text{P}^\wedge\text{P})_2]^{2+}$  di-hydride di-cation. As expected, the  $\nu(\text{CO})$  stretchings are moved towards higher wavenumbers after each protonation step, in view of the increased positive charge. Crystals suitable for X-ray studies of  $[\text{HPT}_4(\text{CO})_4(\text{P}^\wedge\text{P})_2][\text{BF}_4] \cdot x\text{CH}_2\text{Cl}_2$  ( $x = 1.47$ ) and  $[\text{H}_2\text{Pt}_4(\text{CO})_4(\text{P}^\wedge\text{P})_2][(\text{BF}_4)_2\text{H}]_2$  have been obtained by slow diffusion of n-hexane on their  $\text{CH}_2\text{Cl}_2$  solution.

Structure and NMR characterization of  $Pt_4(CO)_4(P^AP)_2$ 

The neutral  $Pt_4(CO)_4(P^AP)_2$  cluster consists of a tetrahedral  $Pt_4$  core elongated along its  $C_2$  axis (figure 3.2.2 e table 3.2.1). The two edges of the elongated tetrahedron perpendicular to the  $C_2$  axis are bridged by two  $P^AP$  ligands and the coordination sphere of the cluster is completed by four terminal CO ligands, one per each Pt-atom.



	$Pt_4(CO)_4(P^AP)_2$	$[HPt_4(CO)_4(P^AP)_2]^+$	$[H_2Pt_4(CO)_4(P^AP)_2]^{2+}$
Pt <sub>1</sub> -Pt <sub>2</sub>	2.6110(8)	2.8246(6)	2.8406(8)
Pt <sub>3</sub> -Pt <sub>4</sub>	2.6110(8)	2.6034(6)	2.8192(10)
Pt <sub>1</sub> -Pt <sub>4</sub>	2.5932(8)	2.5992(7)	2.5922(9)
Pt <sub>2</sub> -Pt <sub>3</sub>	2.5932(8)	2.6062(6)	2.6138(9)
Pt <sub>1</sub> -Pt <sub>3</sub>	3.0339(11)	3.0375(6)	3.1356(9)
Pt <sub>2</sub> -Pt <sub>4</sub>	3.0947(11)	3.0470(7)	3.0378(9)

**Table 3.2.1** Main Pt-Pt distances (Å) of  $[H_nPt_4(CO)_4(P^AP)_2]^{n+}$  ( $n = 0-2$ ) clusters.

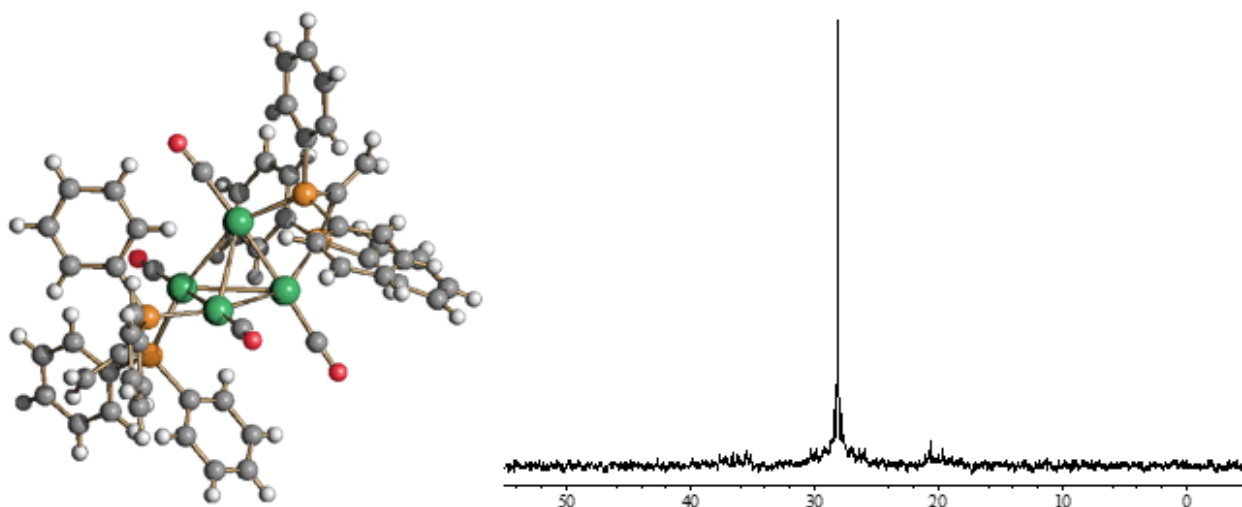


**Figure 3.2.2** Molecular structure and  $^{31}P\{^1H\}$  NMR spectrum of  $Pt_4(CO)_4(P^AP)_2$  in  $CD_2Cl_2$  at 298 K (Pt, green; P, orange; C, grey; O, red; H, white).

The six Pt-Pt contacts are divided into three sets consisting of two bonds each. The shortest contacts are those bridged by the  $P^AP$  ligands whereas the two bonds almost parallel to the  $C_2$  axis have intermediate values.<sup>13</sup> These are very important in order to understand the structures of the protonated clusters, since the hydride ligands are added to these two edges.

<sup>13</sup> These Pt-Pt contacts of *ca.* 3.03-3.10 Å are considered bonding on the basis of the inter-planar distances between the triangular units in  $[Pt_{3n}(CO)_{6n}]^{2-}$  ( $n = 2-8$ ) clusters.

Conversely, the two diagonals of the elongated tetrahedron are the loosest Pt-Pt contacts. The tetrahedral geometry is in agreement with the fact that the cluster possesses 56 CVE as predicted on the basis of theoretical considerations (see box 3.2.1).

### Box 3.2.1 Tetrahedral Geometry in Platinum Carbonyl Clusters

The most common geometries observed for tetra-nuclear clusters are the tetrahedron and the butterfly, and, to a minor extent, the rectangle and spiked triangle. The tetrahedral geometry is widely documented in metal cluster chemistry, with more than 1400 examples reported to date in the Cambridge Crystallographic Database. However, tetrahedral Pt clusters are rather rare, and only two structures of Pt-CO clusters displaying a tetrahedral geometry are known, *i.e.*,  $[\text{HPt}_4(\text{CO})_7(\text{PCy}_3)_4]^+$  and  $\text{Pt}_4(\text{CO})_2(\text{PCy}_3)_4(\text{ReO}_4)_2$ . More often, tetra-nuclear Pt carbonyl clusters show a butterfly or a square geometry. In this respect, it is noticeable that the 58-electron butterfly  $\text{Pt}_4(\text{CO})_5(\text{PPhMe}_2)_4$  cluster reported in 1969 by Dahl *et al.* displays, as expected, five short Pt-Pt interactions, whereas the sixth Pt...Pt distance is nonbonding [51]. The situation is not so clear in other reported 58-electron butterfly Pt carbonyl clusters, such as  $[\text{Pt}_4(\text{CO})_3(\text{PPh}_3)(\text{dppm})_3]^{2+}$ . In these cases, five Pt-Pt contacts are well below 3 Å and, thus, at bonding distances, whereas the sixth contact may be or may be not considered as a bond.

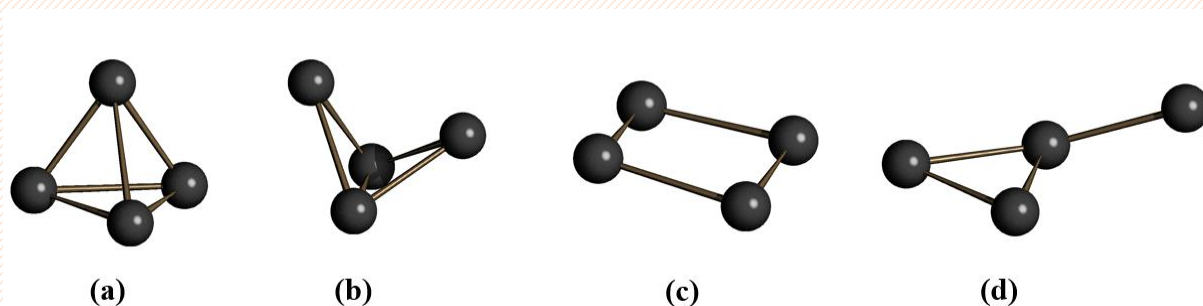


**Figure Box 3.2.1** Structural types of tetra-nuclear metal carbonyl cluster: (a) tetrahedral, (b) butterfly, (c) square and (d) spiked triangle.

An electron count of 56 or 54 for tetranuclear Pt clusters in tetrahedral geometry is predicted by theoretical studies based on  $\text{Pt}(\text{PH}_3)_2$  fragments. The above mentioned  $[\text{HPt}_4(\text{CO})_7(\text{PCy}_3)_4]^+$  as well as the poly-hydride cluster  $\text{H}_8\text{Pt}_4(\text{P}^i\text{Pr}_2\text{Ph})_4$  display the expected tetrahedral geometry with an electron count of 56 Cluster Valence Electrons (CVE). Conversely,  $\text{Pt}_4(\text{CO})_2(\text{PCy}_3)_4(\text{ReO}_4)_2$  and  $[\text{H}_7\text{Pt}_4(\text{PBu}_3)_4]^+$  are tetrahedral with 54 CVE and also some examples of electron poorer tetrahedral Pt clusters are known, *e.g.*,  $[\text{H}_2\text{Pt}_4(\text{PBu}_3)_4]^{2+}$  (48 CVE) and  $\text{H}_2\text{Pt}_4(\text{PBu}_3)_4$  (50 CVE). Tetra-nuclear Pt clusters with 58 CVE usually display a butterfly metal core, even if some care may be taken, as described above, whereas a rectangular structure

is expected in the case of 60 CVE, *e.g.*,  $[\text{H}_2\text{Pt}_4(\text{dppm})_2(\text{PPh}_2)_2(\mu\text{-I})_2]^{2+}$ . Nonetheless, the deprotonated species  $\text{Pt}_4(\text{dppm})_2(\text{PPh}_2)_2\text{I}_2$  displays a butterfly structure (sixth Pt...Pt contact 4.69 Å) despite its electron count of 56 CVE.

In view of these considerations, it seems that there is not a clear-cut between tetrahedral and butterfly geometry in the above tetranuclear clusters. Of course, it must also be considered that sometime short Pt-Pt contacts might be due not to bonding interactions, but to sterical effects, especially in the presence of bidentate ligands. All these data suggest that, despite their apparent simplicity, tetranuclear Pt clusters are far from simple and a more accurate interpretation is needed.

The  $^{31}\text{P}$   $\{^1\text{H}\}$  NMR spectrum of  $\text{Pt}_4(\text{CO})_4(\text{P}^{\wedge}\text{P})_2$  recorded at 298 K in  $\text{CD}_2\text{Cl}_2$  displays a complex multiplet centred at  $\delta_{\text{P}}$  28.1 ppm. Coordination of  $\text{P}^{\wedge}\text{P}$  to the cluster results in a considerable shift towards higher frequencies of the  $^{31}\text{P}$  resonance, since the free ligand shows a sharp singlet at -4.0 ppm. Due to the low solubility of the cluster, the quality of the spectrum is not very high and, thus, it has been possible to assign only the  $^1\text{J}_{\text{PtP}} = 2712$  Hz. This shows a typical value for a phosphine ligand directly bonded to a Pt cluster. The  $^1\text{H}$  NMR spectrum shows, as expected, the resonances due to aromatic protons in the range 7.1-7.8 ppm (40H) and a broad multiplet at 5.65 ppm (4H) due to  $=\text{CH}_2$ .

#### *Structure and NMR characterization of $[\text{HPt}_4(\text{CO})_4(\text{P}^{\wedge}\text{P})_2]^+$*

The molecular structure of the  $[\text{HPt}_4(\text{CO})_4(\text{P}^{\wedge}\text{P})_2]^+$  mono-hydride cluster has been determined as its  $[\text{HPt}_4(\text{CO})_4(\text{P}^{\wedge}\text{P})_2][\text{BF}_4] \cdot x\text{CH}_2\text{Cl}_2$  ( $x = 1.47$ ) and  $[\text{HPt}_4(\text{CO})_4(\text{P}^{\wedge}\text{P})_2][\text{B}_2\text{F}_7]$  salts that contain exactly the same molecular cluster (figure 3.2.3).  $[\text{HPt}_4(\text{CO})_4(\text{P}^{\wedge}\text{P})_2]^+$  mainly differs from the parent  $\text{Pt}_4(\text{CO})_4(\text{P}^{\wedge}\text{P})_2$  cluster because of the presence of a  $\mu\text{-H}$  bridging the  $\text{Pt}_1\text{-Pt}_2$  edge resulting in its elongation compared to the neutral molecule (table 3.2.1). Elongation of M-M bonds after addition of a  $\mu\text{-H}$  ligand has been explained on the basis of the three centre/two electron bond description.

The  $^1\text{H}$  NMR spectrum shows a resonance centred at  $\delta$  -2.40 ppm composed of several lines, due to the coupling of the hydride with four equivalent Pt-atoms ( $^{\text{av}}\text{J}_{\text{PtH}} = 286$  Hz) and four equivalent P-atoms ( $^{\text{av}}\text{J}_{\text{PH}} = 37$  Hz). This assignment has been corroborated by simulating the  $^1\text{H}$  NMR spectrum with the program gNMR 5.0.6.0. The  $\text{J}_{\text{PtH}}$  and  $\text{J}_{\text{PH}}$  are lower than expected for a direct coupling, since the larger  $^1\text{J}_{\text{PtH}}$  and  $^2\text{J}_{\text{PH}}$  coupling constants are time-averaged with smaller multiple bond coupling constants.

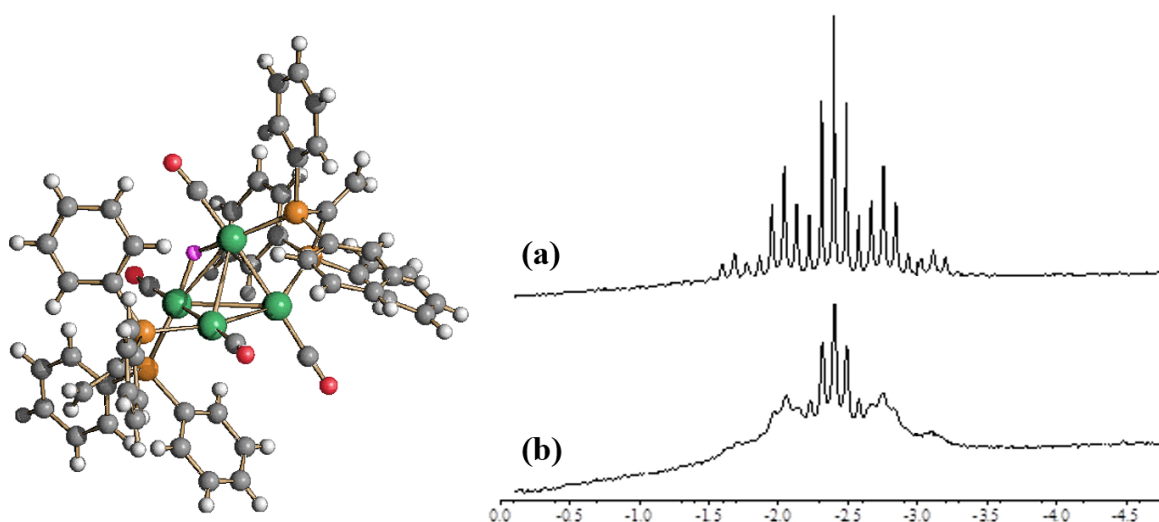
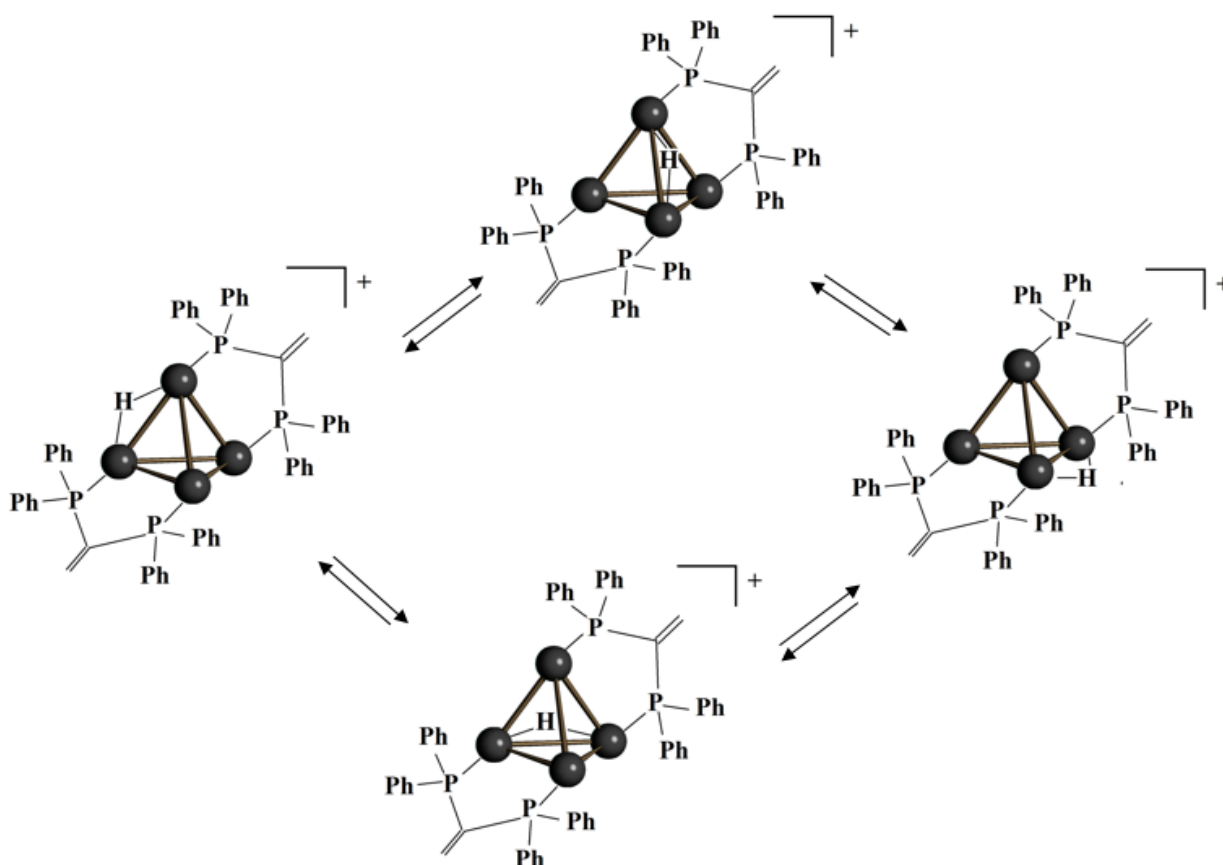


**Figure 3.2.3** Molecular structure and  $^1\text{H}$  NMR spectra of  $[\text{HPt}_4(\text{CO})_4(\text{P}^{\wedge}\text{P})_2]^+$  in  $\text{CD}_2\text{Cl}_2$  at (a) 298 K and (b) 173 K. The hydride ligand is shown in purple (Pt, green; P, orange; C, grey; O, red; H, white,  $\text{H}_{\text{hydride}}$ , purple).



**Scheme 3.2.3** Possible mechanism for the fluxionality of hydride in  $[\text{HPt}_4(\text{CO})_4(\text{P}^{\wedge}\text{P})_2]^+$  (Pt, black).

Unfortunately, it has not been possible to freeze the fluxionality even at low temperature and, thus, to fully assign all the coupling constants of this  $\text{AA}'\text{BB}'\text{MXX}'\text{YY}'$  system (A, B are P's; M is H; X and Y are Pt's). Similarly, the  $^{31}\text{P}$   $\{^1\text{H}\}$  NMR spectrum recorded at 298 K displays

a single resonance at 16.8 ppm with  $^1J_{\text{PtP}} = 3010$  Hz, whereas the other coupling constants could not be resolved. Coalescence in the  $^{31}\text{P}\{^1\text{H}\}$  NMR spectrum is observed only at 183 K and, at 173 K two very broad resonances start to appear at  $\delta_{\text{P}}$  6.4 and 23.4 ppm. Conversely, the  $^1\text{H}$  NMR spectrum at 173 K is still fluxional and shows a pattern similar to that observed at 298 K, only much broader.

Considering that both  $\text{Pt}_4(\text{CO})_4(\text{P}^{\wedge}\text{P})_2$  and  $[\text{H}_2\text{Pt}_4(\text{CO})_4(\text{P}^{\wedge}\text{P})_2]^{2+}$  (see below) are not fluxional, it is possible to conclude that the dynamic behaviour observed for  $[\text{HPt}_4(\text{CO})_4(\text{P}^{\wedge}\text{P})_2]^+$  is due to the movement of the hydride ligand from one edge to the other of the tetrahedron without losing the Pt-P interaction (scheme 3.2.3). In agreement with this, the  $J_{\text{PtH}}$  and  $J_{\text{PH}}$  are averaged at 298 K as well as  $\delta_{\text{P}}$ , whereas  $^1J_{\text{PtP}}$  seems not to be affected by the exchange.

### Structure and NMR characterization of $[\text{H}_2\text{Pt}_4(\text{CO})_4(\text{P}^{\wedge}\text{P})_2]^{2+}$

The molecular structure of the  $[\text{H}_2\text{Pt}_4(\text{CO})_4(\text{P}^{\wedge}\text{P})_2]^{2+}$  di-hydride di-cationic cluster has been determined as its  $[\text{H}_2\text{Pt}_4(\text{CO})_4(\text{P}^{\wedge}\text{P})_2][(\text{BF}_4)_2\text{H}]_2$  salt (figure 3.2.4).<sup>14</sup>

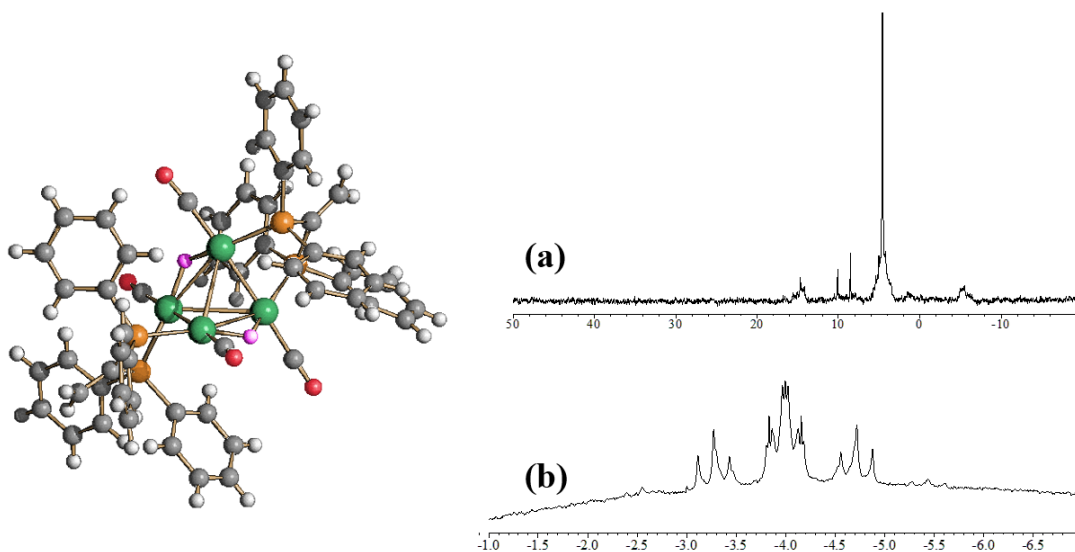


**Figure 3.2.4** Left: molecular structure of  $[\text{H}_2\text{Pt}_4(\text{CO})_4(\text{P}^{\wedge}\text{P})_2]^{2+}$  cluster. Right: (a)  $^1\text{H}$  NMR and (b)  $^{31}\text{P}\{^1\text{H}\}$  NMR spectra of  $[\text{H}_2\text{Pt}_4(\text{CO})_4(\text{P}^{\wedge}\text{P})_2]^{2+}$  in  $\text{CD}_2\text{Cl}_2$  at 298 (Pt, green; P, orange; C, grey, O, red; H, white,  $\text{H}_{\text{hydride}}$ , purple).

This contains the unusual  $[(\text{BF}_4)_2\text{H}]^-$  H-bonded anion. The  $[\text{H}_2\text{Pt}_4(\text{CO})_4(\text{P}^{\wedge}\text{P})_2]^{2+}$  di-hydride di-cationic cluster is obtained from the mono-hydride mono-cation by addition of a

<sup>14</sup> The  $[(\text{BF}_4)_2\text{H}]^-$  anion is the result of the formation of an adduct between  $\text{BF}_4^-$  and unreacted  $\text{HBF}_4$  in accord with the following equation:



second  $\mu$ -H ligand on Pt<sub>3</sub>-Pt<sub>4</sub>. This restores the symmetrical structure of the Pt<sub>4</sub>(CO)<sub>4</sub>(P<sup>^</sup>P)<sub>2</sub> parent neutral cluster, with the six Pt-Pt bonds two by two equivalent. Regarding the Pt-Pt contacts, the main difference in comparison to the neutral cluster is that both Pt<sub>1</sub>-Pt<sub>2</sub> and Pt<sub>3</sub>-Pt<sub>4</sub> are considerably elongated because of the presence of the bridging hydrides, whereas all other Pt-Pt bonds are almost unchanged (table 3.2.1).

The <sup>1</sup>H NMR spectrum of [H<sub>2</sub>Pt<sub>4</sub>(CO)<sub>4</sub>(P<sup>^</sup>P)<sub>2</sub>]<sup>2+</sup> shows a broad resonance at  $\delta_{\text{H}}$  9.52 ppm attributable to the [(BF<sub>4</sub>)<sub>2</sub>H]<sup>-</sup> anion, and a complex multiplet at -4.00 ppm due to the hydride ligands (<sup>1</sup>J<sub>PtH</sub> = 579 Hz; <sup>2</sup>J<sub>PtH</sub> = 25 Hz; <sup>2</sup>J<sub>PH</sub> = 64 Hz; <sup>3</sup>J<sub>PH</sub> = 11 Hz).<sup>15</sup> The cluster contains four P-atoms, two hydrides and four Pt-atoms which are chemically equivalent but not magnetically equivalent, resulting in a very complex AA'A''A'''MM'XX'X''X''' second order system (A = P, M = H; X = Pt). Simulation of the <sup>1</sup>H NMR spectrum with the above parameters supports the assignment of the coupling constants.

The <sup>31</sup>P {<sup>1</sup>H} NMR spectrum in CD<sub>2</sub>Cl<sub>2</sub> at 298 K displays a unique complex resonance at  $\delta_{\text{P}}$  4.6 with <sup>1</sup>J<sub>PtP</sub> = 3178 Hz. Due to the complexity of the system and the poor resolution of the spectrum, it has not been possible to determine the smaller coupling constants. It is noteworthy that, at difference from [HPt<sub>4</sub>(CO)<sub>4</sub>(P<sup>^</sup>P)<sub>2</sub>]<sup>+</sup>, both <sup>1</sup>H and <sup>31</sup>P {<sup>1</sup>H} NMR spectra of [H<sub>2</sub>Pt<sub>4</sub>(CO)<sub>4</sub>(P<sup>^</sup>P)<sub>2</sub>]<sup>2+</sup> are not fluxional, as found also for the neutral Pt<sub>4</sub>(CO)<sub>4</sub>(P<sup>^</sup>P)<sub>2</sub>. This suggests that the fluxionality observed for [HPt<sub>4</sub>(CO)<sub>4</sub>(P<sup>^</sup>P)<sub>2</sub>]<sup>+</sup> is due to its non-symmetrical structure.

#### *Synthesis of [H<sub>x</sub>Pt<sub>6</sub>(CO)<sub>6</sub>(P<sup>^</sup>P)<sub>3</sub>]<sup>y+</sup> by oxidation of [HPt<sub>4</sub>(CO)<sub>4</sub>(P<sup>^</sup>P)<sub>2</sub>]<sup>+</sup>*

The reaction of [HPt<sub>4</sub>(CO)<sub>4</sub>(P<sup>^</sup>P)<sub>2</sub>]<sup>+</sup> with Au(PPh<sub>3</sub>)Cl leads to a new compound with formula [H<sub>x</sub>Pt<sub>6</sub>(CO)<sub>6</sub>(P<sup>^</sup>P)<sub>3</sub>]<sup>y+</sup> (figure 3.2.5).

Unfortunately, the reaction is irreproducible and all attempts to find a new synthetic route have failed. Indeed, the use of different oxidizing agents such as tropylium (excess) and ferricinium leads to uncharacterized compounds. Finally, the thermal degradation of [HPt<sub>4</sub>(CO)<sub>4</sub>(P<sup>^</sup>P)<sub>2</sub>]<sup>+</sup> results in its complete decomposition.

Preliminary X-ray studies show a Pt<sub>6</sub> octahedral core to which are coordinated six terminal CO ligands and three P<sup>^</sup>P ligands bridging across the Pt-Pt bonds.

<sup>15</sup> Their values are in keeping with those reported for other Pt-containing clusters with bridging hydrides. In particular, <sup>1</sup>J<sub>PtH</sub> (579 Hz) displays the typical value for a direct H-Pt coupling in  $\mu$ -H hydride clusters, whereas the lower value of <sup>2</sup>J<sub>PtH</sub> (25 Hz) is in accord with the nearly *cis* arrangement of the hydride and the two-bonds Pt-atoms (H-Pt-Pt *ca.* 90°). Conversely, the relatively large value of <sup>2</sup>J<sub>PH</sub> (64 Hz) is in keeping with the nearly *trans* arrangement of the two atoms found in the solid state structure (H-Pt-P *ca.* 160°).

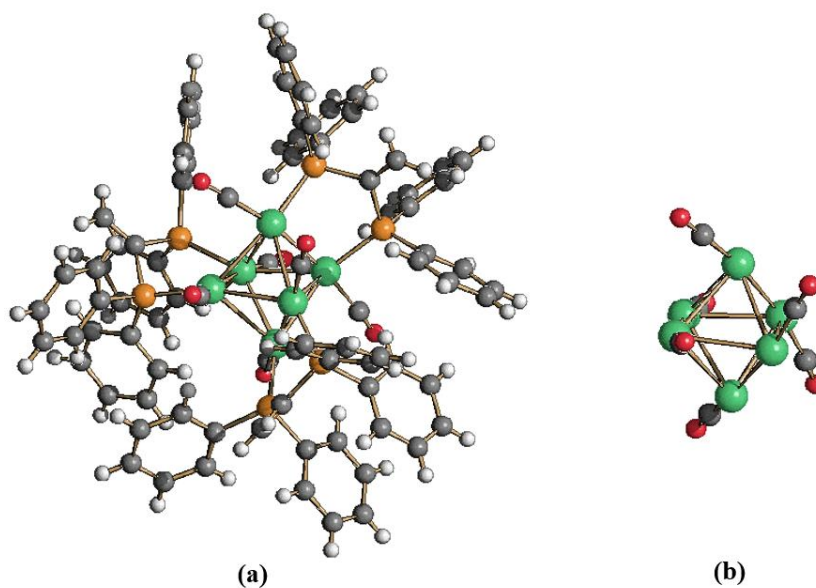


**Figure 3.2.5** (a) Molecular structure of  $[\text{H}_x\text{Pt}_6(\text{CO})_6(\text{P}^{\wedge}\text{P})_2]^y+$  and (b) its  $\text{Pt}_6(\text{CO})_6(\text{P}^{\wedge}\text{P})_3$  core (Pt, green; P, orange; C, grey; O, red; H, white).

### 3.2.4 Synthesis and characterization of $\text{Pt}_6(\text{CO})_6(\text{dppm})_3$

The reaction of  $[\text{Pt}_{12}(\text{CO})_{24}]^{2-}$  in acetone with *ca.* 2 equivalents of dppm results in the formation of a dark red-purple precipitate of  $\text{Pt}_6(\text{CO})_6(\text{dppm})_3$  (figure 3.2.6) and a red solution containing  $[\text{Pt}_9(\text{CO})_{18}]^{2-}$ , according to equation (2):

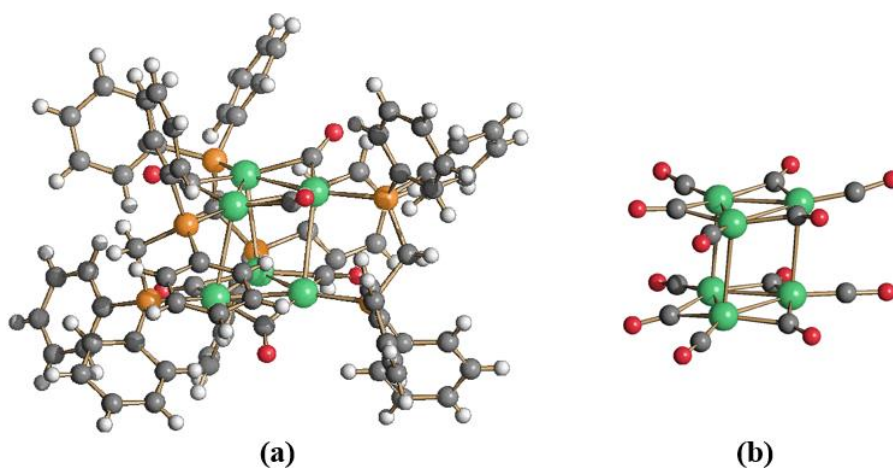
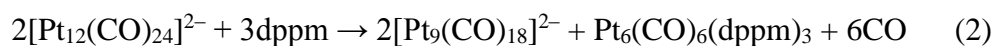


**Figure 3.2.6** Molecular structures of (a)  $\text{Pt}_6(\text{CO})_6(\text{dppm})_3$  and (b)  $[\text{Pt}_6(\text{CO})_{12}]^{2-}$  (Pt, green; P, orange; C, grey; O, red; H, white).

The two compounds may be separated by filtration and the solid dissolved in CH<sub>2</sub>Cl<sub>2</sub>, where it displays  $\nu(\text{CO})$  at 1836(w), 1795(s) and 1751(m) cm<sup>-1</sup>, as previously reported for Pt<sub>6</sub>(CO)<sub>6</sub>(dppm)<sub>3</sub>.<sup>16</sup>

The crystal structure of Pt<sub>6</sub>(CO)<sub>6</sub>(dppm)<sub>3</sub> fully confirms the one proposed in the original paper, and the cluster is isostructural with the palladium analog. This is composed of a Pt<sub>6</sub> trigonal prismatic core possessing *D*<sub>3h</sub> symmetry to which are coordinated six  $\mu$ -CO ligands bridging intra-triangular Pt-Pt edges and three  $\mu$ -dppm ligands bridging the three inter-triangular edges of the prism. The structure of the cluster and the bonding parameters closely resemble to those of [Pt<sub>6</sub>(CO)<sub>12</sub>]<sup>2-</sup>.

### 3.2.5 Reaction of [Pt<sub>12</sub>(CO)<sub>24</sub>]<sup>2-</sup> with other bidentate phosphines

The reaction of [Pt<sub>12</sub>(CO)<sub>24</sub>]<sup>2-</sup> in acetone with increasing amounts of *o*-C<sub>6</sub>H<sub>4</sub>(PPh<sub>2</sub>)<sub>2</sub> (dppb) is apparently similar to the ones described above for dppm and P<sup>^</sup>P, but it results in different products. Thus, after the addition of a few equivalents of dppb, an orange precipitate starts to separate out and the solution turns from green to red, in agreement with the transformation of [Pt<sub>12</sub>(CO)<sub>24</sub>]<sup>2-</sup> into [Pt<sub>9</sub>(CO)<sub>18</sub>]<sup>2-</sup>. The reaction is fully accomplished after the addition of *ca.* 8-10 equivalents of dppb.

The solid was separated by filtration, dried under *vacuo* and dissolved in CH<sub>2</sub>Cl<sub>2</sub> where it surprisingly does not display any  $\nu(\text{CO})$  band. Thus, in order to shed some light on its nature, crystals suitable for X-ray analyses were grown by slow diffusion of n-hexane on the CH<sub>2</sub>Cl<sub>2</sub> solution, showing that it consists of a tetrahedral Pt(dppb)<sub>2</sub> complex. Its formation may be explained by equation (3):



The Pt(dppb)<sub>2</sub> complex shows a tetrahedral structure as expected for a zerovalent Pt(LL)<sub>2</sub> complex. The stratification of the crude solution with hexane resulted in the formation of crystals of [NBu<sub>4</sub>]<sub>2</sub>[Pt<sub>9</sub>(CO)<sub>18</sub>] (major product) and a very few crystals of [Pt(dppb)<sub>2</sub>][Pt<sub>9</sub>(CO)<sub>18</sub>]·2CH<sub>3</sub>COCH<sub>3</sub> (figure 3.2.7). Probably, the presence of traces of air forces the partial oxidation of the platinum complex affording the [Pt(dppb)<sub>2</sub>]<sup>2+</sup> cation. The salt consists on a square-planar [Pt(dppb)<sub>2</sub>]<sup>2+</sup> cation and a trigonal prismatic [Pt<sub>9</sub>(CO)<sub>18</sub>]<sup>2-</sup> anion.

<sup>16</sup> Pt<sub>6</sub>(CO)<sub>6</sub>(dppm)<sub>3</sub> was originally obtained in high yields by the reduction of equimolar amounts of PtCl<sub>2</sub>(SMe<sub>2</sub>)<sub>2</sub> and PtCl<sub>2</sub>(dppm) with NaBH<sub>4</sub> under CO atmosphere. This represents a bottom-up reaction compared to our top-down synthesis.

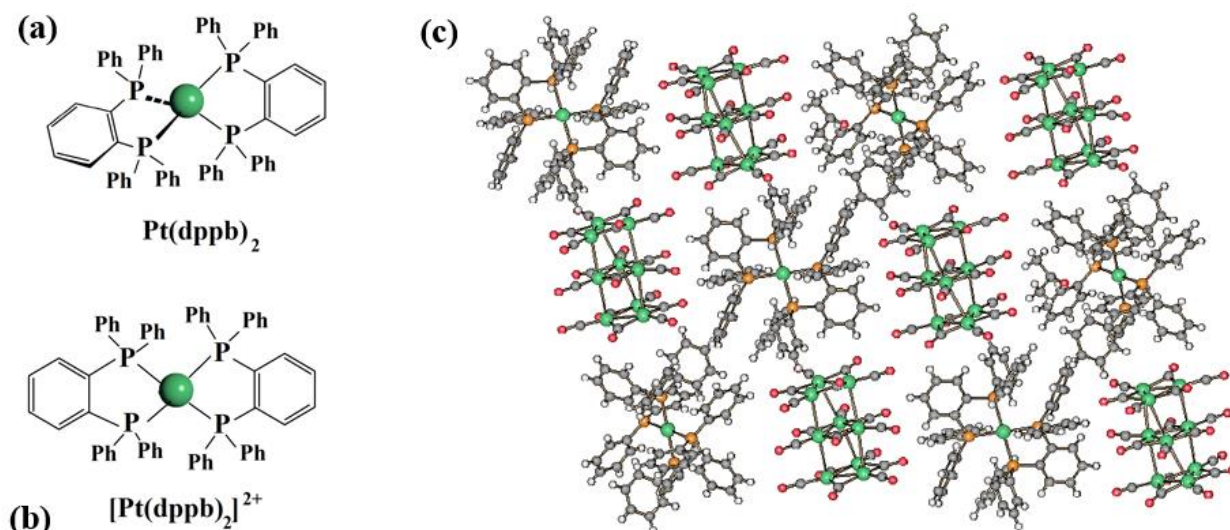


**Figure 3.2.7** Molecular structures of (a) Pt(dppb)<sub>2</sub>, (b) [Pt(dppb)<sub>2</sub>]<sup>2+</sup> and (c) view of the of crystal packing [Pt<sub>9</sub>(CO)<sub>18</sub>][Pt(dppb)<sub>2</sub>]<sup>2+</sup>·2acetone (acetone molecules have been omitted; Pt, green; P, orange; C, grey; O, red; H, white).

On the attempt to obtain a copolymer consisting of the periodic alternation of phosphine and cluster units, we investigated the reaction of [Pt<sub>12</sub>(CO)<sub>24</sub>]<sup>2-</sup> with Ph<sub>2</sub>PC≡CPh<sub>2</sub>. This bidentate phosphine is an ideal candidate on the basis of its rigid scaffold that prevents an intramolecular bond. Differently to our expectations, the reaction leads to a polynuclear complex with formula Pt<sub>8</sub>(CO)<sub>6</sub>(Ph<sub>2</sub>PC≡CPh<sub>2</sub>)<sub>2</sub>(C≡CPh<sub>2</sub>)<sub>2</sub>(PPh<sub>2</sub>)<sub>2</sub> resulting from partial C-P cleavage of the phosphine promoted by Pt (figure 3.2.8). The molecule is centrosymmetric and results from partial fragmentation of the bidentate phosphines with C-P bond cleavage. This results in the formation of PPh<sub>2</sub> and C≡CPh<sub>2</sub> units that act as ligands in the complex. The Ph<sub>2</sub>PC≡CPh<sub>2</sub>, C≡CPh<sub>2</sub> and PPh<sub>2</sub> units donate 6, 5 and 3 electrons respectively. Assuming only covalent interactions, the molecule possesses 128 Cluster Valence Electrons according to equation (4):

$$8(\text{Pt}) \times 10 + 6(\text{CO}) \times 2 + 2(\text{Ph}_2\text{PC}\equiv\text{CPh}_2) \times 6 + 2(\text{C}\equiv\text{CPh}_2) \times 5 + 2(\text{PPh}_2) \times 3 = 128 e^- \quad (4)$$

The number of electrons associated with each Pt is 16 according to the presence of 4 Pt-Pt bonds [(128-8)/8].

At last, the reactions of [Pt<sub>12</sub>(CO)<sub>24</sub>]<sup>2-</sup> with dppb\* and dppe give uncharacterized amorphous products that are completely insoluble in all solvents. In the case of dppb\*, the product displays ν(CO) bands in Nujol mull at 2012(s), 1830(m) similar to those shown by [Pt<sub>9</sub>(CO)<sub>16</sub>(PPh<sub>3</sub>)<sub>2</sub>]<sup>2-</sup>. On the basis of this spectroscopic evidence, it is possible to speculate that the compound is probably an anionic {Pt<sub>9</sub>(CO)<sub>16</sub>(dppb)<sup>2-</sup>}<sub>∞</sub> infinite polymer with the dppb\* ligands bridging between clusters units.

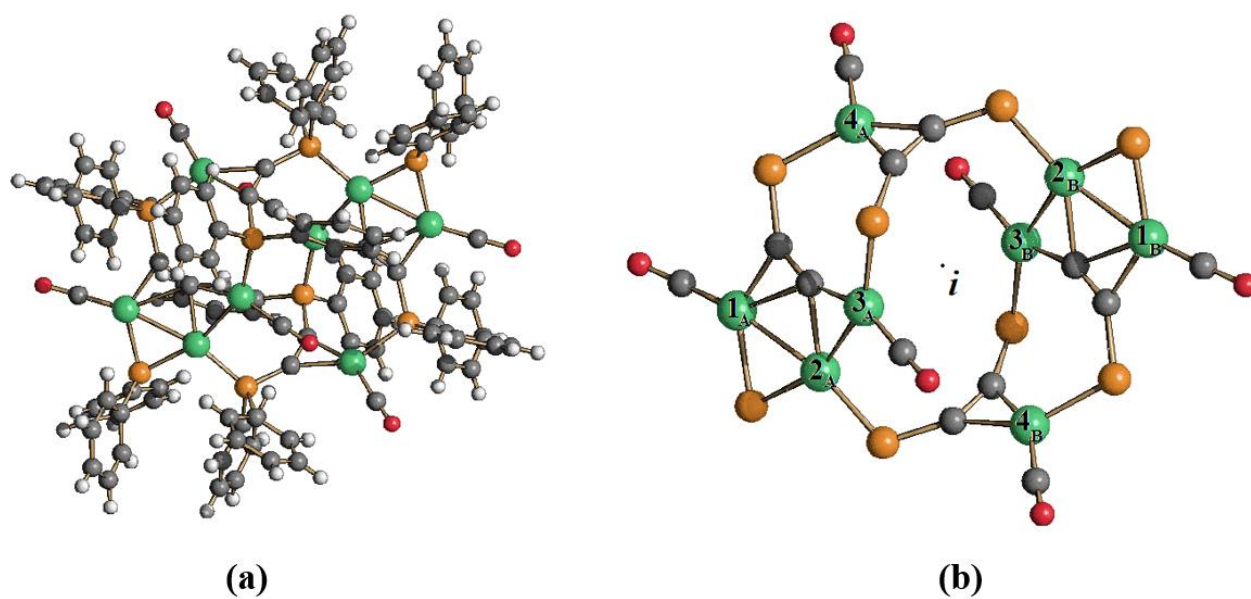


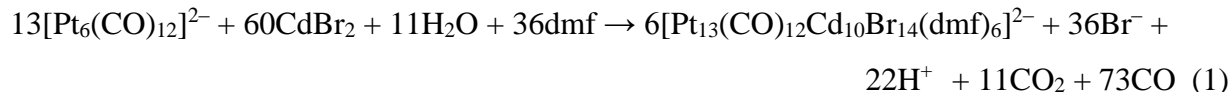
**Figure 3.2.8** (a) Molecular structures of  $\text{Pt}_8(\text{CO})_6(\text{Ph}_2\text{PC}\equiv\text{CPh}_2)_2(\text{C}\equiv\text{CPh}_2)_2(\text{PPh}_2)_2$  its (b)  $\text{Pt}_8(\text{CO})_6(\text{PC}\equiv\text{CPP})_2(\text{C}\equiv\text{CP})_2(\text{P})_2$  core as found in  $\text{Pt}_8(\text{CO})_6(\text{Ph}_2\text{PC}\equiv\text{CPh}_2)_2(\text{C}\equiv\text{CPh}_2)_2(\text{PPh}_2)_2\cdot\text{CH}_3\text{COCH}_3$ . The  $\text{Pt}_A$  and  $\text{Pt}_B$  atoms are related by the inversion centre ( $i$ ) (Pt, green; P, orange; C, grey, O, red; H, white).

## Surface Decorated Platinum Carbonyl Clusters

### 3.3.1 State of the art of the bimetallic Pt-Cd clusters

It is known that  $\text{CdX}_2 \cdot n\text{H}_2\text{O}$  salts ( $\text{X} = \text{Cl}, \text{Br}, \text{I}$ ) may act as oxidants and/or Lewis acids towards MCCs. Their oxidising power is due to the presence of hydration water and to the  $\text{H}^+/\text{H}_2$  redox couple, since the  $\text{Cd}^{2+}/\text{Cd}(0)$  couple is a poorer oxidant. A combination of oxidation and coordination has been observed, for instance, in the case of the reaction between  $[\text{Pt}_6(\text{CO})_{12}]^{2-}$  and  $\text{CdCl}_2 \cdot n\text{H}_2\text{O}$  to give  $\{[\text{Pt}_9(\text{CO})_{18}(\mu_3\text{-CdCl}_2)_2]^{2-}\}_\infty$  infinite chains, *via* oxidation of  $[\text{Pt}_6(\text{CO})_{12}]^{2-}$  to  $[\text{Pt}_9(\text{CO})_{18}]^{2-}$  and coordination of  $\text{CdCl}_2$  to the latter [52].

Conversely, the reaction of  $[\text{Pt}_6(\text{CO})_{12}]^{2-}$  with an excess of  $\text{CdX}_2 \cdot n\text{H}_2\text{O}$  in dmf at  $120^\circ\text{C}$  afforded  $[\text{Pt}_{13}(\text{CO})_{12}\{\text{Cd}_5(\mu\text{-Br})_5\text{Br}_2(\text{dmf})_3\}_2]^{2-}$  [53] according to equation (1):



An excess of  $\text{CdX}_2 \cdot n\text{H}_2\text{O}$  was used in order to avoid the formation of brown homometallic Pt-clusters, which are usual products of the thermal decomposition of Chini's clusters.

The core of the cluster is composed by a Pt-centred  $\text{Pt}_{13}$  icosahedron sandwiched between two  $\text{Cd}_5(\mu\text{-Br})_5\text{Br}_2(\text{dmf})_3$  fragments (figure 3.3.1). Each of the 12 Pt-atoms on the surface of the icosahedron are bonded to one terminal CO, whereas the  $\text{Cd}_5(\mu\text{-Br})_5\text{Br}_2(\text{dmf})_3$  fragments are coordinated to the  $\text{Pt}_{13}$ -core via face-bridging Cd-Pt<sub>3</sub> interactions, originating a  $D_{5d}$   $\text{Pt}_{13}\text{Cd}_{10}$  metal frame.

Differently, the reaction of  $[\text{Pt}_9(\text{CO})_{18}]^{2-}$  with  $\text{CdBr}_2 \cdot \text{H}_2\text{O}$  at  $120^\circ\text{C}$  leads the larger  $[\text{Pt}_{19}(\text{CO})_{17}\{\text{Cd}_5(\mu\text{-Br})_5\text{Br}_3(\text{Me}_2\text{CO})_2\}\{\text{Cd}_5(\mu\text{-Br})_5\text{Br}(\text{Me}_2\text{CO})_4\}]^{2-}$  nanocluster (figure 3.3.2) [53]. The molecular structure of this cluster anion consists of a  $\text{Pt}_{19}$  interpenetrated double-icosahedron sandwiched along the unique idealised  $\text{C}_5$  axis by one  $\text{Cd}_5(\mu\text{-Br})_5\text{Br}_3(\text{Me}_2\text{CO})_2$  and one  $\text{Cd}_5(\mu\text{-Br})_5\text{Br}(\text{Me}_2\text{CO})_4$  ring. These are similar to the  $\text{Cd}_5(\mu\text{-Br})_5\text{Br}_2(\text{dmf})_3$  rings found

in  $[\text{Pt}_{13}(\text{CO})_{12}\{\text{Cd}_5(\mu\text{-Br})_5\text{Br}_2(\text{dmf})_3\}_2]^{2-}$ , apart from the different distribution of Br and solvent molecules.

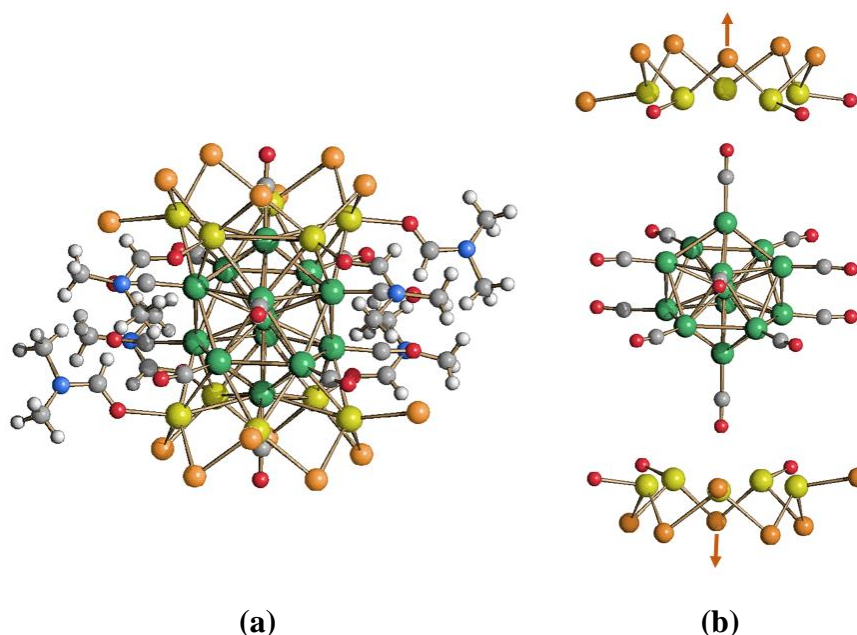


**Figure 3.3.1** (a) Molecular structure of  $[\text{Pt}_{13}(\text{CO})_{12}\{\text{Cd}_5(\mu\text{-Br})_5\text{Br}_2(\text{dmf})_3\}_2]^{2-}$ . (b) Its  $[\text{Pt}_{13}(\text{CO})_{12}]^{8-}$  core and the two  $[\text{Cd}_5(\mu\text{-Br})_5\text{Br}_2(\text{dmf})_3]^{3+}$  moieties (Pt, green; Cd, yellow; Br, orange; N, blue; C, grey; O, red; H, white).

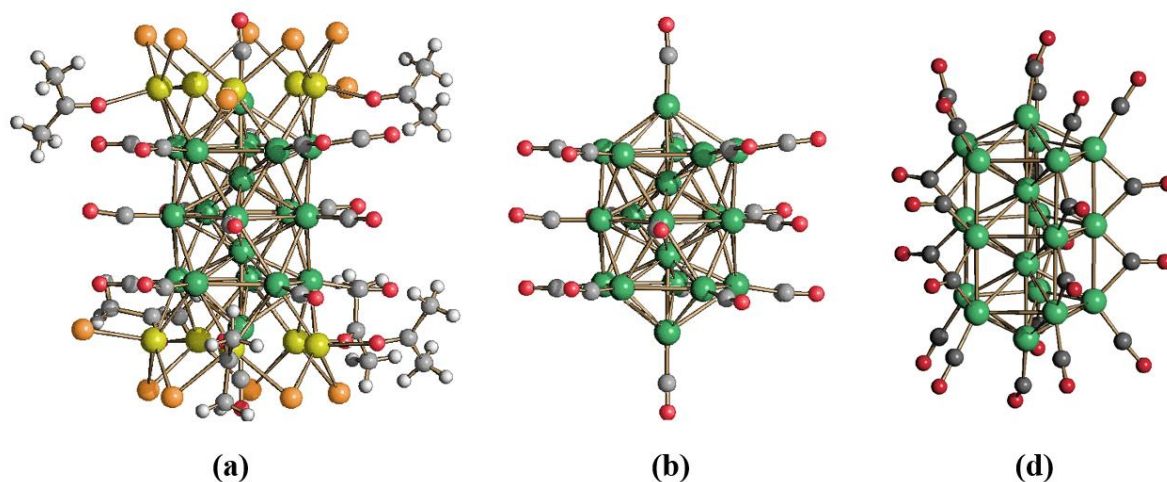


**Figure 3.3.2** (a) Molecular structure of  $[\text{Pt}_{19}(\text{CO})_{17}\{\text{Cd}_5(\mu\text{-Br})_5\text{Br}_3(\text{Me}_2\text{CO})_2\}\{\text{Cd}_5(\mu\text{-Br})_5\text{Br}(\text{Me}_2\text{CO})_4\}]^{2-}$ , (b) its  $[\text{Pt}_{19}(\text{CO})_{17}]^{8-}$  core compared to (c)  $[\text{Pt}_{19}(\text{CO})_{22}]^{4-}$  homometallic cluster (Pt, green; Cd, yellow; Br, orange; C, grey; O, red; H, white).

The  $\text{Pt}_{19}$  core contains two fully interstitial Pt atoms, whereas the 17 Pt on the surface are coordinated each to one terminal CO ligand. The different architecture of the  $[\text{Pt}_{19}(\text{CO})_{17}\{\text{Cd}_5(\mu\text{-Br})_5\text{Br}_3(\text{Me}_2\text{CO})_2\}\{\text{Cd}_5(\mu\text{-Br})_5\text{Br}(\text{Me}_2\text{CO})_4\}]^{2-}$  compared to the analogous isonuclear

$[\text{Pt}_{19}(\text{CO})_{22}]^{4+}$  [54] species indicates that the coordination of the Cd-Br moieties is not innocent and influences the final structure (see box 3.3.1).

### Box 3.3.1

#### Surface decorated clusters: stabilization of unprecedented or unstable compounds?

The different architectures of bimetallic Pt-Cd clusters compared to homometallic species indicates that the coordination of Cd-Br moieties is not innocent. It is noteworthy that, in the field of carbonyl clusters there is only two examples where the same metal cage can be stabilized by a different number of carbonyl ligands (see chapter 4.1).

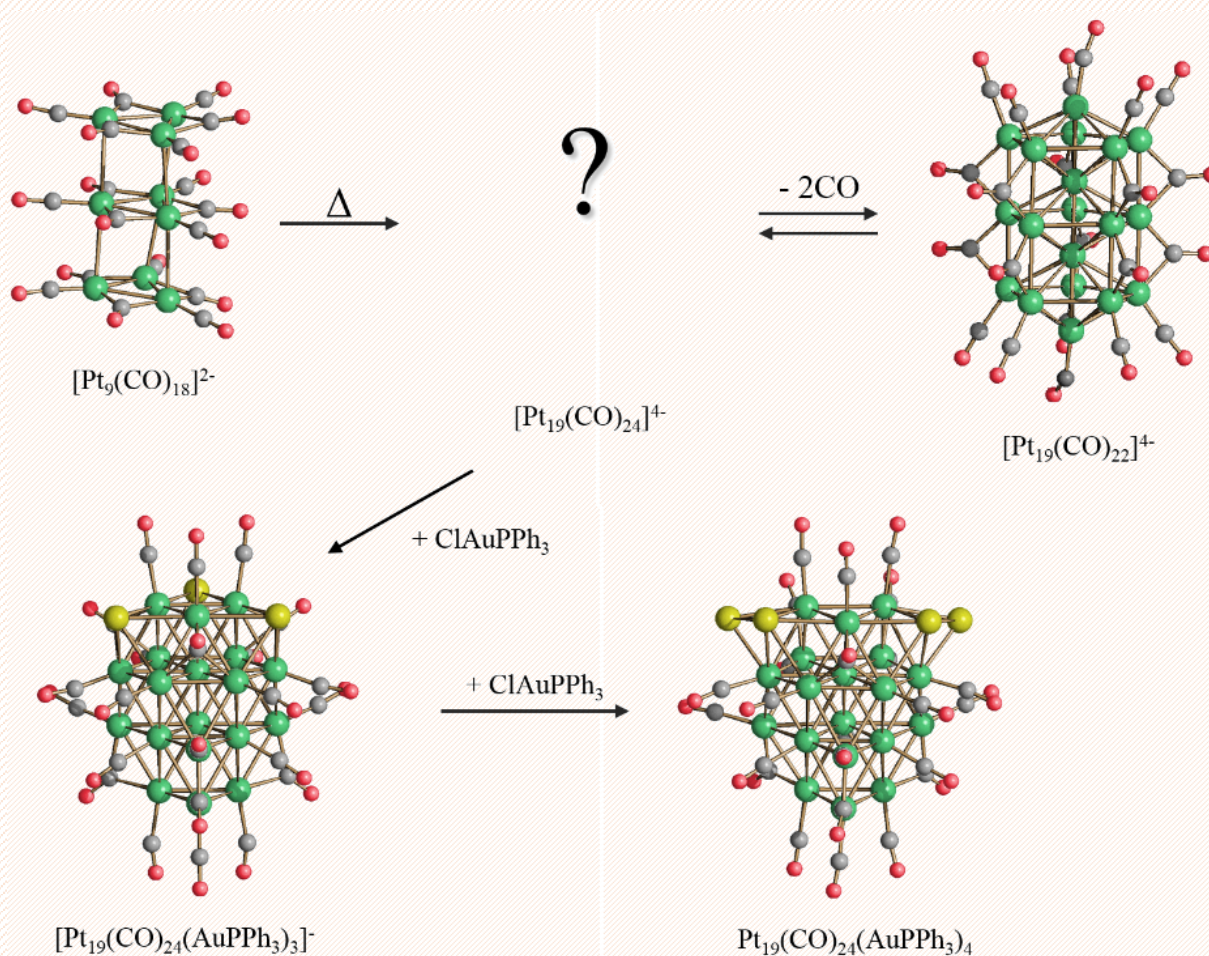


**Figure box 3.3.1.** Syntheses of  $[\text{Pt}_{19}(\text{CO})_{24}]^{4+}$  and its reactivity with  $[\text{AuPPh}_3]^+$ . For the sake of clarity the phosphines bonded to gold atoms are not represented (Pt, green; Au, yellow; C, grey; O, red).

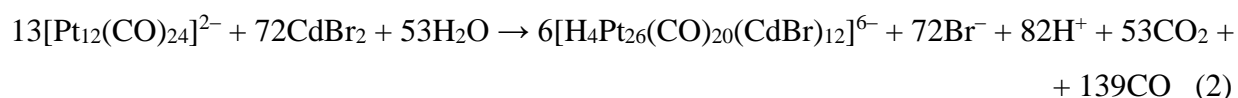
The unknown structure of  $[\text{Pt}_{19}(\text{CO})_{24}]^{4+}$  provides an illustrative examples that is subject of speculation. This high nuclearity compound can be obtained by a reversible carbonylation of  $[\text{Pt}_{19}(\text{CO})_{22}]^{4+}$  with CO at atmospheric pressure. In contrast to what is normally observed, the IR bands of the carbonylated product shift to lower wavenumbers, indicating an increased metal-to-ligand back-donation and suggesting that this uncharacterized species would be a better

electron donor toward electrophiles. This shift can be justified based on metal cage rearrangement. Despite the considerable efforts, the lack of structural characterization is due to fact that the crystallization of  $[\text{Pt}_{19}(\text{CO})_{24}]^{4-}$  [54] is hampered by its conversion into  $[\text{Pt}_{19}(\text{CO})_{22}]^{4-}$  during crystallization.

In the attempt to stabilize the unstable  $[\text{Pt}_{19}(\text{CO})_{24}]^{4-}$  by neutralization of its charge with  $[\text{AuPPh}_3]^+$  moieties, A. Ceriotti had investigated the reaction of  $[\text{Pt}_{19}(\text{CO})_{24}]^{4-}$  with  $\text{Au}(\text{PPh}_3)\text{Cl}$ . The Pt core present in the structures of both  $[\text{Pt}_{19}(\text{CO})_{24}\{\text{Au}(\text{PPh}_3)\}_3]^-$  and  $[\text{Pt}_{19}(\text{CO})_{24}\{\text{Au}_2(\text{PPh}_3)_2\}_2]$  is identical [55]. It indeed represents a chunk of *fcc* lattice but is based on a 3-6-7-3 four layers arrangement of Pt atoms. This raises the question if the Pt framework observed in the bimetallic compound is the same of  $[\text{Pt}_{19}(\text{CO})_{24}]^{4-}$  or if  $[\text{AuPPh}_3]^+$  induce a rearrangement of the Pt-core. Logic dictates that if the absorption of two carbonyl ligands leads to a change of the  $\text{Pt}_{19}$  metal framework, as shown by the shift of the IR bands, even the addition of  $\text{AuPPh}_3^+$  fragments can give another rearrangement.

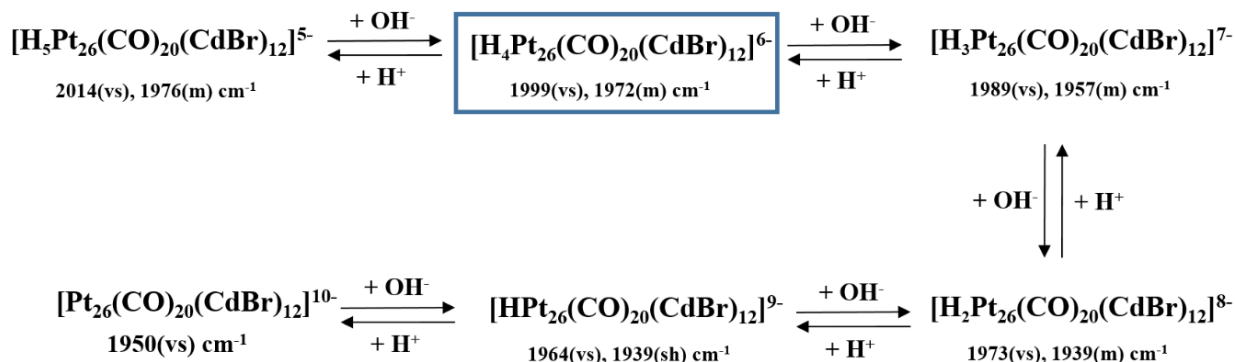
### 3.3.2. Synthesis of $[\text{H}_4\text{Pt}_{26}(\text{CO})_{20}(\text{CdBr})_{12}(\text{PtBr})_x]^{6-}$ ( $x = 0-2$ )

On the basis of the previous results obtained by the thermal degradation of  $[\text{Pt}_6(\text{CO})_{12}]^{2-}$  and  $[\text{Pt}_9(\text{CO})_{18}]^{2-}$  with  $\text{CdBr}_2 \cdot \text{H}_2\text{O}$ , we decided to investigate the same reaction starting from more oxidized clusters, *i.e.*,  $[\text{Pt}_{3n}(\text{CO})_{6n}]^{2-}$  ( $n = 4-6$ ). The reaction leads to the new  $[\text{H}_4\text{Pt}_{26}(\text{CO})_{20}(\text{CdBr})_{12}]^{6-}$   $[\text{H}_4\mathbf{1}]^{6-}$  cluster according to the equation (2) [56]:



This has been precipitated from dmf solutions by addition of water in the presence of the bromide salt of an appropriate quaternary phosphonium cation. The solid has been recovered by filtration and washed with water, iso-propanol and thf. Crystals suitable for X-ray analyses of  $[\text{PPh}_4]_8[\text{H}_4\mathbf{1}] \cdot 4\text{CH}_3\text{CN}$  are obtained by extraction of the cluster in  $\text{CH}_3\text{CN}$  followed by slow diffusion of di-iso-propyl-ether. Conversely the thermal degradation of  $[\text{Pt}_{15}(\text{CO})_{30}]^{2-}$  with  $\text{CdBr}_2 \cdot \text{H}_2\text{O}$  result in a mixture of  $[\text{H}_4\text{Pt}_{26}(\text{CO})_{20}(\text{CdBr})_{12}(\text{PtBr})_x]^{6-}$   $[\text{H}_4\mathbf{2}]^{6-}$  ( $x = 0-2$ ). Crystals suitable for X-ray analyses of  $[\text{PPh}_4]_6[\text{H}_4\mathbf{2}] \cdot (10+x)\text{dmf}$  ( $x = 0.56$ ) are obtained by extraction of the cluster in  $\text{CH}_3\text{CN}$  followed by slow diffusion of di-iso-propyl-ether. It must be remarked that only a few crystals of  $[\text{PPh}_4]_8[\text{H}_2\mathbf{1}] \cdot 4\text{CH}_3\text{CN}$  were obtained, whereas the majority of the precipitate was composed by an amorphous solid mainly composed of the  $[\text{H}_4\mathbf{1}]^{6-}$  hexa-anion. The octa-anion is, then, formed by partial deprotonation of the hexa-anion, which occurs during crystallisation due to accidental traces of bases in the solvent. In order to demonstrate this point,  $[\text{H}_4\mathbf{1}]^{6-}$  has been treated with increasing amounts of  $[\text{NBu}_4][\text{OH}]$  in dmf. On the basis of IR

evidence the deprotonation can be carried out in a reversible way up to the formation of  $[\mathbf{1}]^{10-}$  (scheme 3.3.1).



**Scheme 3.3.1** Protonation and deprotonation equilibria of  $[\text{H}_{10-n}\mathbf{1}]^{n-}$  ( $n = 5-10$ ). The  $\nu(\text{CO})$  signals have been recorded in dmf solution.

Indeed, further addition of  $[\text{NBu}_4][\text{OH}]$  to  $[\mathbf{1}]^{10-}$  results in its decomposition to yet uncharacterised products. This point has been taken as an indirect proof of the fact that the latter anion is fully deprotonated. Finally, acidification of a dmf solution of the hexa-anion  $[\text{H}_4\mathbf{1}]^{6-}$  results in the formation of a new species which can be formulated as the penta-anion  $[\text{H}_5\mathbf{1}]^{5-}$  on the basis of its  $\nu(\text{CO})$  bands. Therefore, the complete series of the structurally related polyhydrides  $[\text{H}_{10-n}\mathbf{1}]^{n-}$  ( $n = 5-10$ ) has been spectroscopically characterised and the species with  $n = 6$  and  $n = 8$  have been structurally determined by X-ray crystallography.

All attempts to directly confirm the hydride nature of  $[\text{H}_{10-n}\mathbf{1}]^{n-}$  ( $n = 5-10$ ) by  $^1\text{H}$  NMR failed under any experimental condition. Thus, their nature is indirectly inferred from the above protonation/deprotonation reactions joined to IR studies and the crystallographic determination of two different anions (see chapter 2.4).

#### *Crystal structures of $[\text{PPh}_4]_8[\text{H}_2\mathbf{1}] \cdot 4\text{CH}_3\text{CN}$ and $[\text{PPh}_4]_6[\text{H}_4\mathbf{2}] \cdot (10+x)\text{dmf}$ ( $x = 0.56$ )*

The  $[\text{H}_2\mathbf{1}]^{8-}$  anion is composed by a distorted cubic close packed (ccp)  $\text{Pt}_{26}\text{Cd}_{12}$  core, reminiscent of the structures of  $[\text{Pt}_{38}(\text{CO})_{44}]^{2-}$  and  $[\text{Ni}_{24}\text{Pt}_{14}(\text{CO})_{44}]^{4-}$  (figure 3.3.3). The anion can be viewed as a truncated- $v_3$ -octahedron, which encapsulates a fully interstitial  $\text{Pt}_6$  octahedron. The ccp  $\text{Pt}_{26}\text{Cd}_{12}$  core is composed by four compact ABCA layers, comprising 7, 12, 12, 7 metal atoms, respectively. Each layer contains three Cd-atoms, in a non-bonded triangular arrangement. The 20 non-interstitial Pt-atoms are coordinated to one terminal CO ligand each, whereas the Cd-atoms are bonded to terminal Br-atoms.

Alternatively, the cluster may be described as composed by a face centred cubic (fcc)  $\text{Pt}_{14}$ -core (figure 3.3.4) comprising the fully interstitial  $\text{Pt}_6$ -octahedron, even if the edges of the cube are considerably elongated and non-bonding.

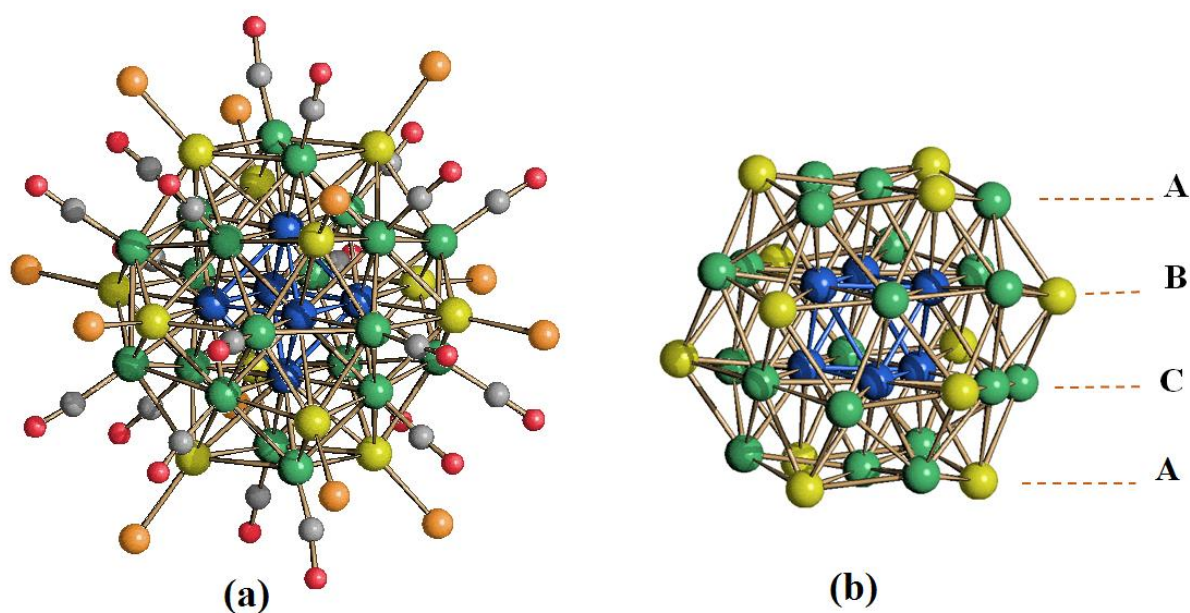


**Figure 3.3.3** (a) Molecular structure of  $[\text{H}_2\mathbf{1}]^{8-}$  and (b) its Pt-Cd core as found in  $[\text{PPh}_4]_8[\text{H}_2\mathbf{1}] \cdot 4\text{CH}_3\text{CN}$  ( $\text{Pt}_{\text{surface}}$ , green;  $\text{Pt}_{\text{interstitial}}$ , blue; Cd, yellow; Br, orange; C, grey; O, red).

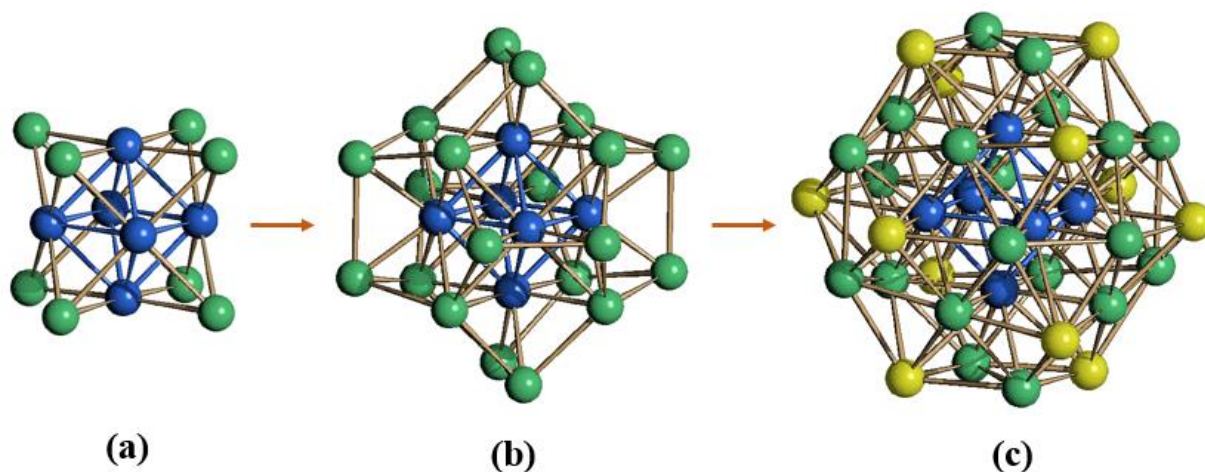


**Figure 3.3.4** Stepwise reconstruction of the structure of  $[\text{H}_2\mathbf{1}]^{8-}$ : (a) face centred cubic (fcc)  $\text{Pt}_{14}$ -core; (b)  $\text{Pt}_{26}$  framework obtained by adding six  $\text{Pt}_2$ -units to the vertexes of the interstitial  $\text{Pt}_6$ -octahedron and (c) the whole  $\text{Pt}_{26}\text{Cd}_{12}$  cage ( $\text{Pt}_{\text{surface}}$ , green;  $\text{Pt}_{\text{interstitial}}$ , blue; Cd, yellow).

Six  $\text{Pt}_2$ -units condense on the vertexes of the interstitial  $\text{Pt}_6$ -octahedron, resulting on a  $\text{Pt}_{26}$  fragment possessing 12 cyclo-pentane like pentagonal faces to which 12  $\text{CdBr}$  fragments are added. As a result, each of the six  $\text{Pt}_2$ -units is bonded to two Cd-atoms, resulting on six  $\text{Pt}_2\text{Cd}_2$  rhombuses covering the fcc  $\text{Pt}_{14}$ -core. It is noteworthy that as in the case of the heterometallic

$[\text{Pt}_{19}(\text{CO})_{17}\{\text{Cd}_5(\mu\text{-Br})_5\text{Br}_3(\text{Me}_2\text{CO})_2\}\{\text{Cd}_5(\mu\text{-Br})_5\text{Br}(\text{Me}_2\text{CO})_4\}]^{2-}$  cluster, even  $[\text{H}_2\mathbf{1}]^{8-}$  shows a platinum core different from the homometallic species  $[\text{Pt}_{26}(\text{CO})_{32}]^{2-}$ .

Finally, in the unit cell of  $[\text{PPh}_4]_6[\text{H}_4\mathbf{2}]\cdot(10+x)\text{dmf}$  ( $x = 0.56$ ), the fractionary indexes are due to disorder involving two free dmf molecules and the additional PtBr moieties present on the surface of the cluster. Apart from the charge and the presence of this additional groups, the structure of  $[\text{H}_4\mathbf{2}]^{6-}$  is almost identical to the one just described for  $[\text{H}_2\mathbf{1}]^{8-}$  for what concerns the geometry and connectivity of the  $\text{Pt}_{26}(\text{CO})_{20}(\text{CdBr})_{12}$  core and its bonding distances. As a matter of fact,  $[\text{H}_4\mathbf{2}]^{6-}$  may be viewed as deriving from  $[\text{H}_2\mathbf{1}]^{8-}$  by adding an additional PtBr fragment with refined occupancy factor 0.281(9) on the Pt-Pt edge of one of the above mentioned  $\text{Pt}_2\text{Cd}_2$  rhombuses (figure 3.3.5).

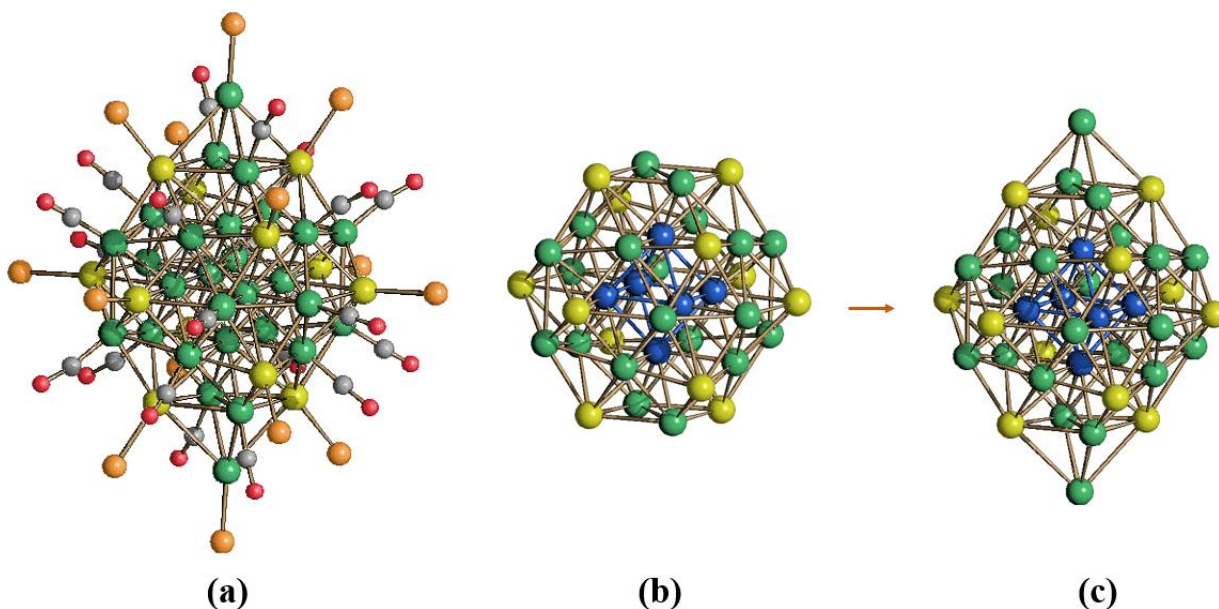


**Figure 3.3.5** (a) Molecular structure of  $[\text{H}_4\mathbf{2}]^{6-}$  in  $[\text{PPh}_4]_6[\text{H}_4\mathbf{2}]\cdot(10+x)\text{dmf}$  ( $x = 0.56$ ). Structural relationship between the (b)  $[\text{H}_2\mathbf{1}]^{8-}$  and (c)  $[\text{H}_4\mathbf{2}]^{6-}$  cages ( $\text{Pt}_{\text{surface}}$ , green;  $\text{Pt}_{\text{interstitial}}$ , blue; Cd, yellow).

Because of the presence of an inversion centre on the cluster, this PtBr fragment is present twice on opposite edges and displays an overall fractionary index of *ca.* 0.56. This can be justified by assuming that the crystal actually contains a mixture of three structurally related clusters, *i.e.*,  $[\text{H}_4\text{Pt}_{26}(\text{CO})_{20}(\text{CdBr})_{12}]^{6-}$ ,  $[\text{H}_4\text{Pt}_{26}(\text{CO})_{20}(\text{CdBr})_{12}(\text{PtBr})]^{6-}$  and  $[\text{H}_4\text{Pt}_{26}(\text{CO})_{20}(\text{CdBr})_{12}(\text{PtBr})_2]^{6-}$ .

This point is rather interesting, since it points out that closely related species displaying a common  $\text{Pt}_{26}(\text{CO})_{20}(\text{CdBr})_{12}$  structure and differing only for the charge and/or the presence of additional PtBr fragments may be obtained under very similar experimental conditions. From

this point of view, the herein reported PtCd carbonyl clusters are at the border between molecular (atomically defined) metal clusters and quasi-monodisperse metal nanoparticles.

### *Electron count*

Adopting the ionic approach,  $[\text{H}_2\mathbf{1}]^{8-}$  may be partitioned into a  $[\text{H}_2\text{Pt}_{26}(\text{CO})_{20}]^{20-}$  Pt-CO moiety which act as a Lewis base towards 12  $[\text{CdBr}]^+$  fragments. The former displays 322 CVE  $[26(\text{Pt}) \times 10 + 20(\text{CO}) \times 2 + 2(\text{H}) \times 1 + 20 = 322]$ . Analogously, using the covalent scheme, each CdBr fragment behaves as a pseudo-halide donating one electron to the  $[\text{H}_2\text{Pt}_{26}(\text{CO})_{20}]^{8-}$  core, which again adopts 322 CVE  $[26(\text{Pt}) \times 10 + 20(\text{CO}) \times 2 + 2(\text{H}) \times 1 + 2(\text{H}) \times 1 + 8 + 12(\text{CdBr}) \times 1 = 322]$ . Considering the whole  $\text{Pt}_{26}\text{Cd}_{12}$  metal cage of the cluster, this displays 466 CVE  $[26(\text{Pt}) \times 10 + 20(\text{CO}) \times 2 + 12(\text{Cd}) \times 12 + 12(\text{Br}) \times 1 + 2(\text{H}) \times 1 + 8 = 466]$ . By comparison the homonuclear and isostructural  $[\text{Pt}_{38}(\text{CO})_{44}]^{2-}$  anion possesses 470 CVE  $[38(\text{Pt}) \times 10 + 44(\text{CO}) \times 2 + 2 = 470]$ , which is not very dissimilar. In the case of  $[\text{H}_2\mathbf{2}]^{6-}$ , this may be derived from the hexa-anion  $[\text{H}_2\mathbf{1}]^{6-}$  by adding one or two PtBr fragments.

## Final Remarks

Section 3.1 reports the first examples of anionic Pt/CO/PR<sub>3</sub> clusters, obtained by CO/PPh<sub>3</sub> substitution in [Pt<sub>3n</sub>(CO)<sub>6n</sub>]<sup>2-</sup> (n = 2-6) Chini's clusters. Three of them, *i.e.*, [Pt<sub>12</sub>(CO)<sub>22</sub>(PPh<sub>3</sub>)<sub>2</sub>]<sup>2-</sup>, [Pt<sub>9</sub>(CO)<sub>16</sub>(PPh<sub>3</sub>)<sub>2</sub>]<sup>2-</sup> and [Pt<sub>6</sub>(CO)<sub>10</sub>(PPh<sub>3</sub>)<sub>2</sub>]<sup>2-</sup>, have been structurally characterized showing a close analogy to [Pt<sub>12</sub>(CO)<sub>24</sub>]<sup>2-</sup> and [Pt<sub>9</sub>(CO)<sub>18</sub>]<sup>2-</sup> for the first two clusters, whereas, due to steric repulsion, the third one significantly differs from the parent [Pt<sub>6</sub>(CO)<sub>12</sub>]<sup>2-</sup>. Two different structures of [Pt<sub>6</sub>(CO)<sub>10</sub>(PPh<sub>3</sub>)<sub>2</sub>]<sup>2-</sup> have been determined, showing that its metal cage can be easily deformed due to packing effects and van der Waals forces. Moreover, joined IR, <sup>31</sup>P{<sup>1</sup>H} NMR spectroscopy and ESI-MS studies have revealed the presence in solution of several other substitution products, obtained by replacing 1-3 CO ligands with PPh<sub>3</sub> in [Pt<sub>3n</sub>(CO)<sub>6n</sub>]<sup>2-</sup> (n = 2-6). Substitution is, then, followed by elimination of Pt<sub>3</sub>(CO)<sub>3</sub>(PPh<sub>3</sub>)<sub>3</sub> and formation of lower nuclearity clusters. These substitution/elimination reactions occur partially in parallel, leading to complex mixtures of products.

Conversely, the reaction of [Pt<sub>12</sub>(CO)<sub>24</sub>]<sup>2-</sup> with bidentate phosphines (section 3.2) leads to neutral compounds. The reaction with the peculiar P<sup>∧</sup>P (CH<sub>2</sub>=C(PPh<sub>2</sub>)<sub>2</sub>) bidentate phosphine leads to a rare case of a tetrahedral Pt-CO cluster, *i.e.*, Pt<sub>4</sub>(CO)<sub>4</sub>(P<sup>∧</sup>P)<sub>2</sub>. This neutral species is readily protonated by strong acids affording cationic hydride clusters which retain the same tetrahedral geometry of the Pt<sub>4</sub>-core, *i.e.*, [HPt<sub>4</sub>(CO)<sub>4</sub>(P<sup>∧</sup>P)<sub>2</sub>]<sup>+</sup> and [H<sub>2</sub>Pt<sub>4</sub>(CO)<sub>4</sub>(P<sup>∧</sup>P)<sub>2</sub>]<sup>2+</sup>. Cationic carbonyl clusters containing hydride ligands directly attached to metals become less well known as either/both: the positive charge on the cluster increases, or/and the size of the cluster increases. The structure and hydride nature of [H<sub>n</sub>Pt<sub>4</sub>(CO)<sub>4</sub>(P<sup>∧</sup>P)<sub>2</sub>]<sup>n+</sup> (n = 1, 2) has been corroborated by multinuclear NMR spectroscopy and directly confirmed by X-ray crystallography, thanks to the limited nuclearity of these clusters. Moreover, other bidentate phosphine have been employed and, even if they lead to different products, in all of the cases considered no substituted anionic clusters have been isolated. It seems, therefore, that bidentate phosphines favor the elimination of neutral Pt/CO/PP complexes or clusters with the concomitant formation of the homoleptic [Pt<sub>9</sub>(CO)<sub>18</sub>]<sup>2-</sup> anionic cluster. [H<sub>n</sub>Pt<sub>4</sub>(CO)<sub>4</sub>(P<sup>∧</sup>P)<sub>2</sub>]<sup>n+</sup> (n = 1, 2) show the expected electron count for a Pt tetrahedron (56 CVE) but two Pt-Pt contacts display distances (3.03-3.10 Å) which have sometime been considered in the literature to be non-bonding. This is contrasted by the bonding Pt-Pt intra-triangular contacts (3.02-3.10 Å) observed in several [Pt<sub>3n</sub>(CO)<sub>6n</sub>]<sup>2-</sup> (n = 2-8) clusters. If these distances are considered as (at least weak) bonds, the

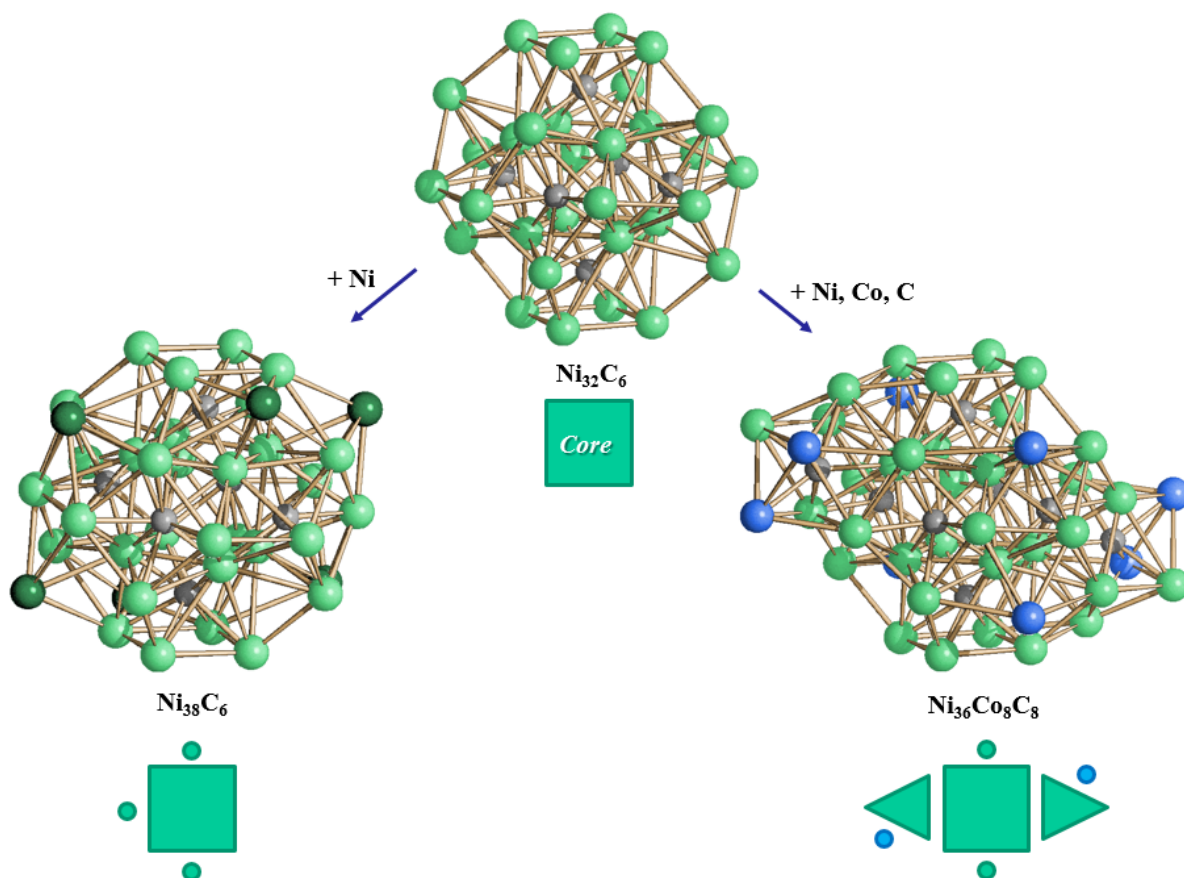
structures of some previously reported butterfly clusters (58 CVE) might be revised and considered as (at least incipient) tetrahedral (see box 3.2.1). Even if apparently simple systems, tetranuclear Pt<sub>4</sub>-clusters seem to require further experimental and theoretical investigations in order to fully understand their structural and bonding properties

Finally, the thermal degradation of [Pt<sub>12</sub>(CO)<sub>24</sub>]<sup>2-</sup> with CdBr<sub>2</sub>·H<sub>2</sub>O leads to the new high nuclearity cluster [H<sub>4</sub>Pt<sub>26</sub>(CO)<sub>20</sub>(CdBr)<sub>12</sub>]<sup>6-</sup> [H<sub>4</sub>1]<sup>6-</sup> (section 3.3). Conversely, starting from [Pt<sub>15</sub>(CO)<sub>30</sub>]<sup>2-</sup> the same reaction results in [H<sub>4</sub>Pt<sub>26</sub>(CO)<sub>20</sub>(CdBr)<sub>12</sub>(PtBr)<sub>x</sub>]<sup>6-</sup> [H<sub>4</sub>2]<sup>6-</sup> (x = 0.56), containing two PtBr fragments with fractional occupancy factors within the same crystal. This crystal disorder is particularly significant and may appear to be borderline between mixtures of molecular clusters or *quasi*-molecular clusters with very low polydispersity, whose structures (and thus polydispersity) have been crystallographically determined. Co-crystallization of slightly different MCCs is already well documented and other cases are reported in chapter 4. [H<sub>4</sub>1]<sup>6-</sup> and [H<sub>4</sub>2]<sup>6-</sup> clusters are based on a common cubic close packed (ccp) Pt<sub>26</sub>Cd<sub>12</sub> core. Conversely, the previously reported [Pt<sub>19</sub>(CO)<sub>17</sub>{Cd<sub>5</sub>(μ-Br)<sub>5</sub>Br<sub>3</sub>(Me<sub>2</sub>CO)<sub>2</sub>}{Cd<sub>5</sub>(μ-Br)<sub>5</sub>Br(Me<sub>2</sub>CO)<sub>4</sub>}]<sup>2-</sup> and [Pt<sub>13</sub>(CO)<sub>12</sub>{Cd<sub>5</sub>(μ-Br)<sub>5</sub>Br<sub>2</sub>(dmf)<sub>3</sub>}]<sub>2</sub><sup>2-</sup> display non-crystallographic metal icosahedral packings. It seems, therefore, that within this size regime the transition from icosahedral to close packed metal structures is not dictated by size but by the interactions between the metal kernels and the surface ligands and decorations. Hence, small changes in the experimental conditions are sufficient in order to pass from one structure to the other. Moreover, all the reported clusters may be interpreted in terms of Lewis acid-base theory and partitioned into a Pt-CO anionic kernel, *i.e.*, [Pt<sub>13</sub>(CO)<sub>12</sub>]<sup>8-</sup>, [Pt<sub>19</sub>(CO)<sub>17</sub>]<sup>8-</sup>, [H<sub>2</sub>Pt<sub>26</sub>(CO)<sub>20</sub>]<sup>20-</sup> and [H<sub>4</sub>Pt<sub>26</sub>(CO)<sub>20</sub>(PtBr)<sub>x</sub>]<sup>18-</sup> (x = 0, 1, 2) for [Pt<sub>13</sub>(CO)<sub>12</sub>{Cd<sub>5</sub>(μ-Br)<sub>5</sub>Br<sub>2</sub>(dmf)<sub>3</sub>}]<sub>2</sub><sup>2-</sup>, [Pt<sub>19</sub>(CO)<sub>17</sub>{Cd<sub>5</sub>(μ-Br)<sub>5</sub>Br<sub>3</sub>(Me<sub>2</sub>CO)<sub>2</sub>}{Cd<sub>5</sub>(μ-Br)<sub>5</sub>Br(Me<sub>2</sub>CO)<sub>4</sub>}]<sup>2-</sup>, [H<sub>4</sub>1]<sup>6-</sup> and [H<sub>4</sub>2]<sup>6-</sup>, respectively, decorated on the surface by {Cd<sub>5</sub>(μ-Br)<sub>5</sub>Br<sub>2</sub>(dmf)<sub>3</sub>}<sup>3+</sup>, {Cd<sub>5</sub>(μ-Br)<sub>5</sub>Br<sub>3</sub>(Me<sub>2</sub>CO)<sub>2</sub>}<sup>2+</sup>, {Cd<sub>5</sub>(μ-Br)<sub>5</sub>Br(Me<sub>2</sub>CO)<sub>4</sub>}<sup>4+</sup> and [CdBr]<sup>+</sup> motives.



# High Nuclearity Bimetallic Nickel Carbonyl Clusters

This chapter illustrates the synthesis and the electrochemical characterization of new bimetallic Ni-Co and Ni-Cu carbide clusters. The metal cores of some of these species are present in other known clusters revealing the existence of common metal frameworks that can be viewed as *starting seeds* for the growth of higher nuclearity clusters.





## Mixed Ni-Co Carbide Carbonyl Clusters

### 4.1.1 State of the art

Several bimetallic Ni-Co carbide and acetylide carbonyl clusters are known, *i.e.*,  $[\text{Co}_2\text{Ni}_{10}\text{C}(\text{CO})_{20}]^{2-}$ ,  $[\text{Co}_3\text{Ni}_9\text{C}(\text{CO})_{20}]^{n-}$  ( $n = 2, 3$ ),  $[\text{Co}_3\text{Ni}_7(\text{C}_2)(\text{CO})_{15}]^{3-}$ ,  $[\text{Co}_3\text{Ni}_7(\text{C}_2)(\text{CO})_{16}]^{n-}$  ( $n = 2, 3$ ) and  $[\text{Co}_6\text{Ni}_2(\text{C}_2)(\text{CO})_{16}]^{2-}$  [57] (figure 4.1.1 bottom). Their highest nuclearity is 12 and the Ni/Co ratio ranges from 0.33 to 5.<sup>17</sup> The wide variability of the Ni/Co composition of these clusters is due to the fact that both metals have similar properties. In particular, they display high affinity with the carbonyl ligands and weak M-M bonds. Indeed, the peculiar feature of these bimetallic clusters is the complete degradation under carbon monoxide into a mixture of  $\text{Ni}(\text{CO})_4$  and  $[\text{Co}(\text{CO})_4]^-$ . Moreover, the different composition of  $[\text{Co}_2\text{Ni}_{10}\text{C}(\text{CO})_{20}]^{2-}$  and  $[\text{Co}_3\text{Ni}_9\text{C}(\text{CO})_{20}]^{2-}$  does not affect the metal cage confirming the similar properties of the two metals. In the absence of interstitial hetero-atoms, high nuclearity homo- and bi-metallic clusters adopt compact (*ccp* and *hcp*) or poly-icosahedral structures. Conversely, the presence of interstitial hetero-atoms, such as carbon, perturbs the growth of the metal cages resulting in more complex and less regular structures. This may be related to the building-up of bulky carbide phases such as  $\text{Cr}_{23}\text{C}_6$  [58], as well as the formation of metal-carbide nano-alloys and the action of metal nanoparticles as catalysts for the preparation of carbon nanotubes or graphene sheets. In this regards, bimetallic Ni-Co nanoparticles are efficient catalysts for the growth of single-walled carbon nanotubes. This has been attributed to the efficiency of the initial nucleation and the subsequent growth of nanotube due to the presence of Co and Ni respectively [29, 59].

Moreover, the possibility to prepare bimetallic Ni-Co molecular clusters with very different Ni/Co compositions makes these clusters quite attractive for the preparation of bimetallic magnetic Ni-Co nanoparticles, allowing a gradual variation of their properties. A fine control of the composition of the resulting bimetallic nanoparticles might result in a better understanding of the relationships existing between composition and properties of the nanoparticles [29].

<sup>17</sup> Because X-ray are scattered by the electrons of an atom, an assignment of each of the metal atoms as either Ni or Co cannot be made *per se*. However, the disposition of each atoms had been assigned with the evaluation of their metal-carbonyl and metal-metal linkages supported by elemental analysis.

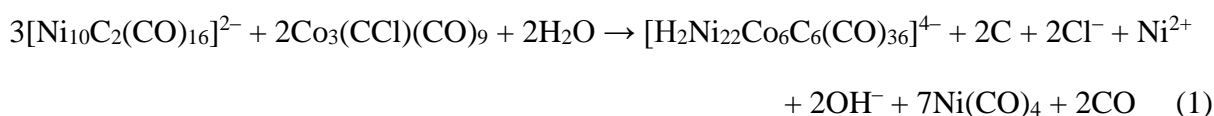
As depicted on the bottom of figure 4.1.1, the chemistry of this family of compounds is based on the redox condensation of  $\text{Co}_3(\mu_3\text{-CCl})(\text{CO})_9$  with  $[\text{Ni}_9\text{C}(\text{CO})_{17}]^{2-}$  or  $[\text{Ni}_6(\text{CO})_{12}]^{2-}$  as starting materials. Despite the presence of interstitial carbide atoms contributes to an extra-stabilization of the metal cage, only relatively low nuclearity Ni-Co clusters are known.<sup>18</sup> In addition to  $[\text{Ni}_9\text{C}(\text{CO})_{17}]^{2-}$ , other suitable precursors such as  $[\text{Ni}_{10}(\text{C}_2)(\text{CO})_{16}]^{2-}$  and  $[\text{Ni}_{16}(\text{C}_2)_2(\text{CO})_{23}]^{4-}$  are available, thus we started a re-investigation of Ni-Co carbide carbonyl clusters in order to obtain new higher nuclearity species.

#### 4.1.2 General results

As depicted on top of figure 4.1.1, the reaction between  $[\text{Ni}_{10}(\text{C}_2)(\text{CO})_{16}]^{2-}$  and  $\text{Co}_3(\text{CCl})(\text{CO})_9$  leads to the new hexa-carbides  $[\text{H}_{6-n}\text{Ni}_{22}\text{Co}_6\text{C}_6(\text{CO})_{36}]^{n-}$  ( $n = 3-6$ ) [60]. Their reactions with strong bases, such as  $[\text{NBu}_4][\text{OH}]$ , besides revealing the poly-hydride nature of these clusters, afforded the new mono-acetylide  $[\text{Ni}_9\text{Co}(\text{C}_2)(\text{CO})_{16-x}]^{3-}$  ( $x = 0, 1$ ) [60]. Moreover, the thermal decomposition in thf solution of  $[\text{H}_2\text{Ni}_{22}\text{Co}_6\text{C}_6(\text{CO})_{36}]^{4-}$  results in the new  $[\text{HNi}_{36}\text{Co}_8\text{C}_8(\text{CO})_{48}]^{5-}$  bimetallic Ni-Co octa-carbide, which can be converted into the closely related  $[\text{H}_{6-n}\text{Ni}_{36}\text{Co}_8\text{C}_8(\text{CO})_{48}]^{n-}$  ( $n = 3-6$ ) polyhydrides by means of acid-base reactions [61]. The Ni/Co compositions of these compounds has been determined on the basis of SEM-EDS analyses and their locations based on geometric considerations (M-M and M-CO connectivity). All these results will be described in details in the following sections.

#### 4.1.3 Synthesis and characterization of $[\text{H}_{6-n}\text{Ni}_{22}\text{Co}_6\text{C}_6(\text{CO})_{36}]^{n-}$ ( $n = 3-6$ )

The slow addition of an acetone solution of  $\text{Co}_3(\text{CCl})(\text{CO})_9$  to  $[\text{Ni}_{10}(\text{C}_2)(\text{CO})_{16}]^{2-}$  dissolved in acetone results in the formation of a considerable amount of  $\text{Ni}(\text{CO})_4$  together with a new brown species which has been isolated after removal of the solvent in *vacuo*, washing with water and toluene, and extraction of the residue in  $\text{CH}_3\text{CN}$ . After layering n-hexane and di-iso-propyl ether on the  $\text{CH}_3\text{CN}$  solution, crystals suitable for X-ray analysis of  $[\text{NEt}_4]_4[\text{H}_2\text{Ni}_{22}\text{Co}_6\text{C}_6(\text{CO})_{36}]$  were obtained. The formation of  $[\text{H}_2\text{Ni}_{22}\text{Co}_6\text{C}_6(\text{CO})_{36}]^{4-}$  is formally in agreement with equation (1):



<sup>18</sup> It is known that the highest nuclearity homometallic carbonyl cluster of Ni and Co is respectively 12 in  $[\text{H}_n\text{Ni}_{12}(\text{CO})_{21}]^{(4-n)-}$  ( $n = 0 - 2$ ) and 6 in  $[\text{H}_n\text{Co}(\text{CO})_{15}]^{(2-n)-}$  ( $n = 0 - 1$ ). For nickel carbonyl clusters, the presence of carbides results in an increase of nuclearity up to 38 in  $[\text{Ni}_{38}\text{C}_6(\text{CO})_{42}]^{6-}$ .



Compound	E°			
	-4/-5	-5/-6	-6/-7	-7/-8
$[\text{H}_2\text{Ni}_{22}\text{Co}_6\text{C}_6(\text{CO})_{36}]^{4-}$	-0.533	-0.833	-	-
$[\text{HNi}_{22}\text{Co}_6\text{C}_6(\text{CO})_{36}]^{5-}$	-	-0.961	-1.293	-1.666

**Table 4.1.1** Formal redox potentials (in V, referred to SCE) of the tetra-anion (in acetone) and the penta-anion (in  $\text{CH}_3\text{CN}$ ).

### Crystal structure

The molecular structures of  $[\text{H}_2\text{Ni}_{22}\text{Co}_6\text{C}_6(\text{CO})_{36}]^{4-}$  and  $[\text{Ni}_{22}\text{Co}_6\text{C}_6(\text{CO})_{36}]^{6-}$  have been determined as their  $[\text{NEt}_4]_4[\text{H}_2\text{Ni}_{22}\text{Co}_6\text{C}_6(\text{CO})_{36}]$  and  $[\text{NMe}_4]_6[\text{Ni}_{22}\text{Co}_6\text{C}_6(\text{CO})_{36}] \cdot 4\text{CH}_3\text{CN}$  salts, respectively (figure 4.1.2 and table 4.1.2). The two cluster anions are almost identical for what concerns the geometry of the metal core, the stereochemistry of the CO ligands and all bonding distances. The cluster comprises 28 metal atoms and the relative composition (22 Ni, 6 Co) has been independently confirmed by elemental and EDS-SEM analyses.

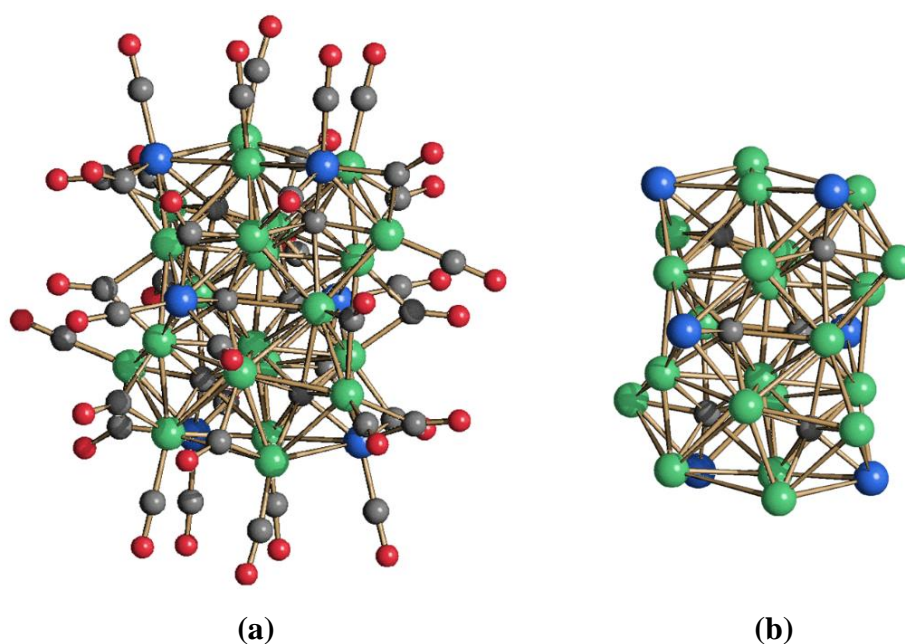


**Figure 4.1.2** Molecular structure (a) and the metal framework (b) of  $[\text{H}_{6-n}\text{Ni}_{22}\text{Co}_6\text{C}_6(\text{CO})_{36}]^{n-}$  ( $n = 4, 6$ ) (Ni, green; Co, blue; C, grey; O, red).

The assignment of the positions to Ni and Co have been based on the fact that there are six similar sites displaying the lowest M-M connectivity and highest M-CO coordination and these have been labeled as the six Co atoms.

The metal core of the  $[\text{H}_{6-n}\text{Ni}_{22}\text{Co}_6\text{C}_6(\text{CO})_{36}]^{n-}$  ( $n = 4, 6$ ) clusters is rather complex and formally results from the condensation of six  $\text{Ni}_7\text{CoC}$  distorted square antiprismatic C-centered

cages. Two of these Ni<sub>7</sub>CoC polyhedra are so highly distorted that the two Ni-atoms along the diagonal on one of the square faces are at bonding distance (3.03-3.05 Å) and, therefore, they may be alternatively described as two Ni<sub>5</sub>CoC trigonal prisms capped by two further Ni-atoms (figure 4.1.3 and figure 4.1.4).

	[H <sub>2</sub> Ni <sub>22</sub> Co <sub>6</sub> C <sub>6</sub> (CO) <sub>36</sub> ] <sup>4-</sup>	[Ni <sub>22</sub> Co <sub>6</sub> C <sub>6</sub> (CO) <sub>36</sub> ] <sup>6-</sup>
Ni–Ni	2.330(16)-3.2680(10) average 2.613(8)	2.337(3)-3.298(5) average 2.617(2)
Ni–Ni (inter.)*	2.330(16)	2.337(3)
Ni–Co	2.4283(11)-2.6315(11) average 2.524(4)	2.398(3)-2.652(3) average 2.525(9)
Ni–C	1.881(6)-2.328(6) average 2.08(3)	1.911(12)-2.368(13) average 2.09(5)
Co–C	1.925(6)-1.968(6) average 1.952(15)	1.858(13)-1.910(14) average 1.892(19)

**Table 4.1.2** Main bond distance (Å) for [H<sub>6-n</sub>Ni<sub>22</sub>Co<sub>6</sub>C<sub>6</sub>(CO)<sub>36</sub>]<sup>n-</sup> (n = 4, 6). \* This refers to the two fully interstitial Ni atoms.

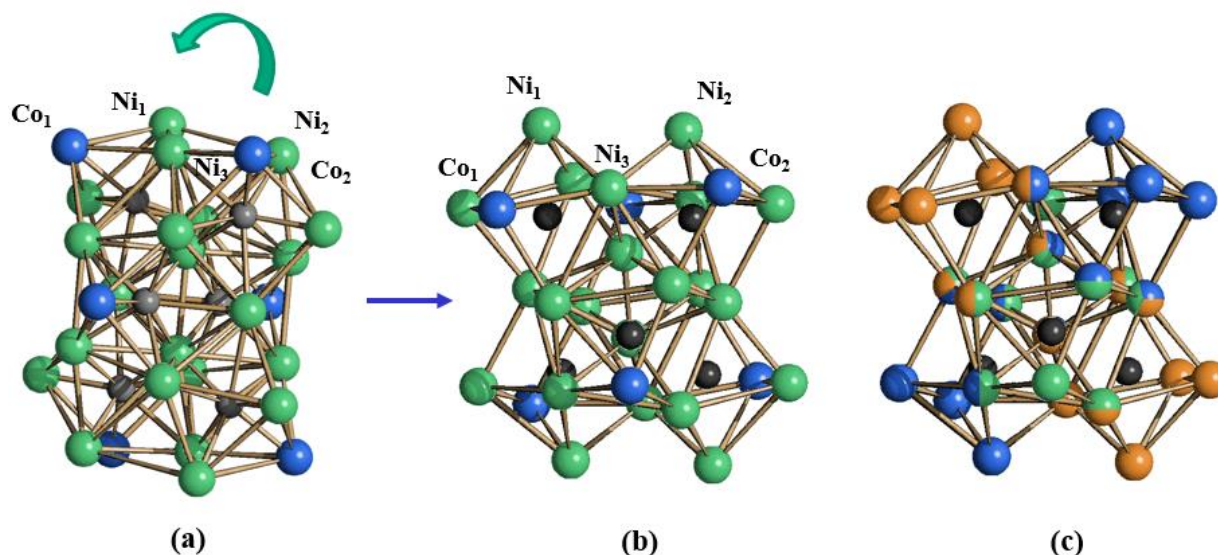


**Figure 4.1.3 (a-b)** Two views of the metal framework of [H<sub>6-n</sub>Ni<sub>22</sub>Co<sub>6</sub>C<sub>6</sub>(CO)<sub>36</sub>]<sup>n-</sup> (n = 4, 6) related by a rotation represented by a green arrow. **(c)** Multicolor representation of the same view of **(b)** in order to evidence the condensation of the six Ni<sub>7</sub>Co distorted antiprismatic square carbide centered cages. For sake of clarity in **(b)** and **(c)** the Ni-C, Co-C and the longer Ni-Ni (> 3 Å such as Ni<sub>1</sub>-Ni<sub>2</sub>) are not represented. The bicolor and tricolor atoms are respectively shared by two and three cages. The couple of cages with the same color are related by the inversion center.

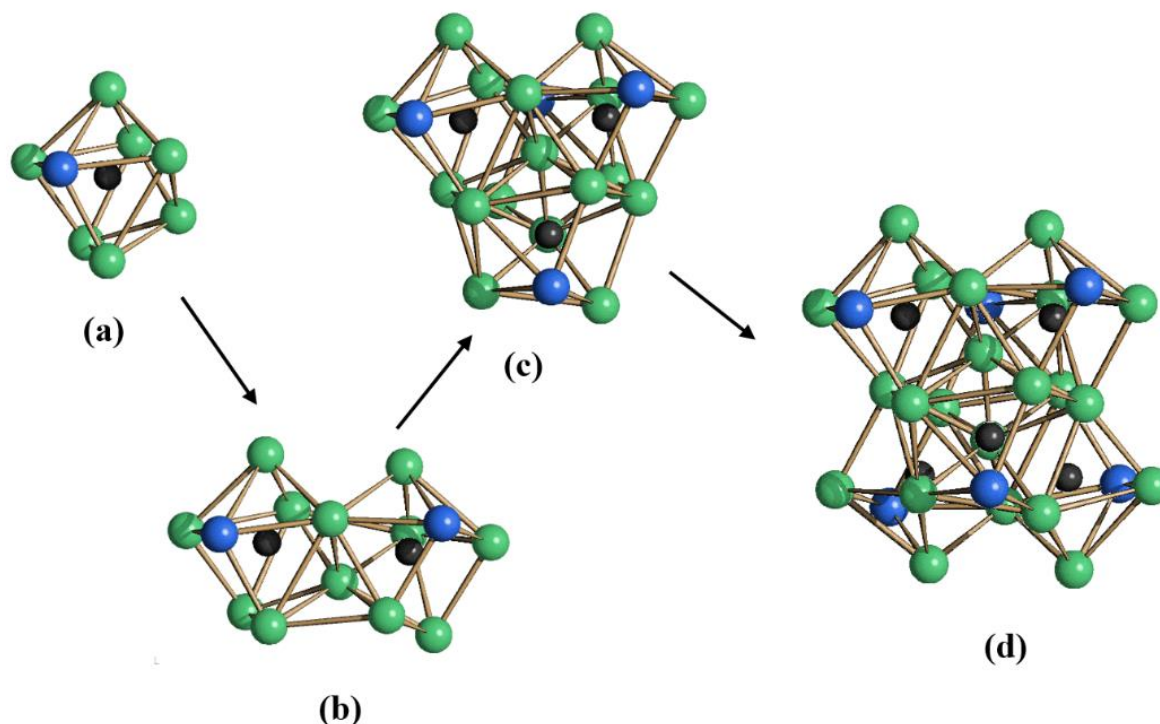


**Figure 4.1.4** Stepwise reconstruction of  $[\text{H}_{6-n}\text{Ni}_{22}\text{Co}_6\text{C}_6(\text{CO})_{36}]^{n-}$  ( $n = 4, 6$ ): (a)  $\text{Ni}_7\text{CoC}$  distorted antiprismatic square carbide centered cage; (b)  $\text{Ni}_{12}\text{Co}_2\text{C}_2$  framework obtained by the condensation of two  $\text{Ni}_7\text{Co}$  cages sharing a  $\text{Ni}_2$  edge; (c)  $\text{Ni}_{18}\text{Co}_4\text{C}_4$  framework obtained by the addition of two other  $\text{Ni}_7\text{Co}$  cages sharing two  $\text{Ni}_2$  edges each; (d) the final  $\text{Ni}_{22}\text{Co}_6\text{C}_6$  cage, the two added  $\text{Ni}_7\text{CoC}$  units share two square faces.

The average M-M connectivity is 5.93, resulting from very different situations. Thus, the six Co-atoms display the lowest number of M-M bonds, *i.e.* 4, plus one Co-C(carbide) bond. Conversely, there are two fully interstitial Ni atoms which display nine Ni-M bonding contacts and four Ni-C(carbide) bonds. It must be remarked that these two fully interstitial Ni atoms are tightly bonded together, showing the shortest Ni-Ni contact. The remaining 20 Ni-atoms display intermediate situations. A M-M connectivity of nine is close to the one found in bulk close packed metals (12) and similar to body centered cubic (8), suggesting (at least morphologically) metalization of these two atoms. Conversely, the situation for Co (4 M-M bonds) is similar to the one found in lower nuclearity molecular clusters (*e.g.*,  $\text{Co}_6(\text{CO})_{16}$ ).

The surface of the cluster is completed by 36 CO ligands, 16 terminal and 20 edge bridging. The CO/M ratio is 1.286, which, by considering the two interstitial Ni atoms, corresponds to a surface coverage  $\text{CO}/\text{M}_{\text{surface}}$  of 1.385. The six Co atoms display the highest number of CO ligands, one terminal and two edge bridging. This is a further (indirect) confirmation of our assignment of these sites as Co. Moreover, the addition of a further CO ligand formally results in the formation of  $[\text{Co}(\text{CO})_4]^-$ , suggesting a possible pathway for the CO-induced decomposition of the cluster.

## Electron count and EHMO analysis

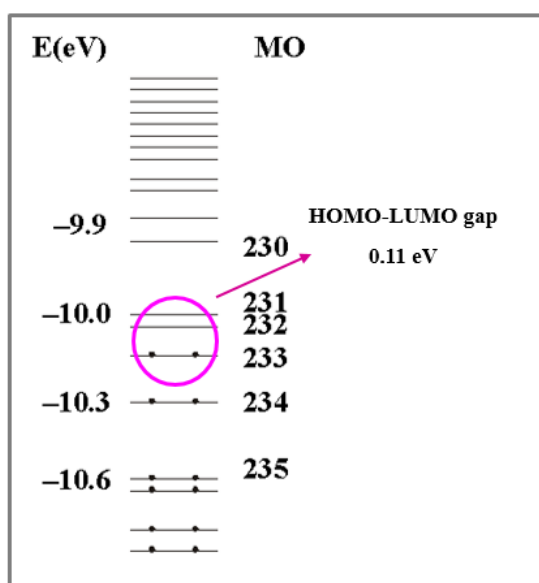


**Figure 4.1.5** Frontier region of EHMO diagram of  $[\text{Ni}_{22}\text{Co}_6\text{C}_6(\text{CO})_{36}]^{6-}$ .

The  $[\text{H}_{6-n}\text{Ni}_{22}\text{Co}_6\text{C}_6(\text{CO})_{36}]^{n-}$  ( $n = 3-6$ ) clusters possess 376 Cluster Valence Electrons (CVE) corresponding to 188 ( $6N + 20$ ;  $N =$  number of metal atoms) Cluster Valence Orbitals (CVO). This electron count is in keeping with other Ni polycarbide clusters which are usually electron rich, *i.e.*,  $[\text{Ni}_{32}\text{C}_6(\text{CO})_{36}]^{6-}$  [33] and  $[\text{Ni}_{38}\text{C}_6(\text{CO})_{42}]^{6-}$  ( $6N + 19$  CVO),  $[\text{Ni}_{36}\text{C}_8(\text{CO})_{36}(\text{Cd}_2\text{Cl}_3)]^{5-}$  ( $6N + 19$  CVO),  $[\text{Ni}_{42}\text{C}_8(\text{CO})_{44}(\text{CdCl})]^{7-}$  ( $6N + 22$  CVO). The electronic properties of  $[\text{Ni}_{22}\text{Co}_6\text{C}_6(\text{CO})_{36}]^{6-}$  have been investigated by means of Extended Hückel Molecular Orbital (EHMO) analysis, using the program CACAO [62] with its crystallographic

coordinates. The frontier regions (in the -11 - 9 eV interval of energy) of the EHMO diagram of  $[\text{Ni}_{22}\text{Co}_6\text{C}_6(\text{CO})_{36}]^{6-}$  is represented in figure 4.1.5. The diagram shows the presence of four closely spaced Molecular Orbitals (MOs 231-234) in an otherwise wide gap ( $\Delta\text{MO}(230-235) = 0.676$  eV). The HOMO (MO 233) – LUMO (MO 232) gap is, thus, very small (0.114 eV) and the LUMO (MO 232) and LUMO+1 (MO 231) are almost degenerate (0.048 eV). The small HOMO-LUMO gap as well as the presence of a very low energy LUMO+1 explain the propensity of these clusters towards reduction, as indicated by electrochemical studies.

#### 4.1.4 Synthesis and characterization of $[\text{Ni}_9\text{Co}(\text{C}_2)(\text{CO})_{16-x}]^{3-}$ ( $x = 0, 1$ )

The hexa-anion  $[\text{Ni}_{22}\text{Co}_6\text{C}_6(\text{CO})_{36}]^{6-}$  reacts with excess  $[\text{NBu}_4][\text{OH}]$  yielding the new mono-acetylide  $[\text{Ni}_9\text{Co}(\text{C}_2)(\text{CO})_{16-x}]^{3-}$  ( $x = 0, 1$ ).  $[\text{Ni}_9\text{Co}(\text{C}_2)(\text{CO})_{16-x}]^{3-}$  ( $x = 0, 1$ ) has been isolated in good yields after removal of the solvent *in vacuo*, washing the residue with water, thf and acetone and, then, extracted in  $\text{CH}_3\text{CN}$ . Crystals suitable for X-ray analyses of  $[\text{NEt}_4]_3[\text{Ni}_9\text{Co}(\text{C}_2)(\text{CO})_{16-x}]$  were obtained by slow diffusion of n-hexane and di-iso-propyl ether on the  $\text{CH}_3\text{CN}$  solution.

The fractional index of  $[\text{NEt}_4]_3[\text{Ni}_9\text{Co}(\text{C}_2)(\text{CO})_{16-x}]$  is due to the fact that within the same crystals, mixtures of structurally related  $[\text{Ni}_9\text{Co}(\text{C}_2)(\text{CO})_{16}]^{3-}$  and  $[\text{Ni}_9\text{Co}(\text{C}_2)(\text{CO})_{15}]^{3-}$  clusters are present. Their ratio varies from batch to batch depending on the experimental conditions as it has been confirmed by analyzing several crystals obtained from different batches. The crystals from the same batch show the same composition (*e.g.*,  $x = 0.84$  and  $0.82$ ), as expected from the statistical crystallization of the  $[\text{Ni}_9\text{Co}(\text{C}_2)(\text{CO})_{16}]^{3-}$  and  $[\text{Ni}_9\text{Co}(\text{C}_2)(\text{CO})_{15}]^{3-}$  mixtures present

in solution. Conversely, crystals from different batches display different compositions (*e.g.*,  $x = 0.84, 0.58$  and  $0.70$ ) indicating that the two species are formed in different ratios depending on slight variations of the experimental conditions. The chemical relationship between  $[\text{Ni}_9\text{Co}(\text{C}_2)(\text{CO})_{16}]^{3-}$  and  $[\text{Ni}_9\text{Co}(\text{C}_2)(\text{CO})_{15}]^{3-}$  may be formally viewed as an dissociation reaction of one carbonyl according to equation (2):



Nonetheless, this reaction is only a formal equilibrium and indeed,  $[\text{Ni}_9\text{Co}(\text{C}_2)(\text{CO})_{16}]^{3-}$  is stable under *vacuum*. Thus, the two products are likely formed in parallel during the reaction of  $[\text{Ni}_{22}\text{Co}_6\text{C}_6(\text{CO})_{36}]^{6-}$  with  $[\text{NBu}_4][\text{OH}]$ . Moreover, mixture of  $[\text{Ni}_9\text{Co}(\text{C}_2)(\text{CO})_{16-x}]^{3-}$  is decomposed under CO atmosphere, resulting in the formation of  $\text{Ni}(\text{CO})_4$  and  $[\text{Co}(\text{CO})_4]^-$ .

### Crystal structures and EHMO analysis

The molecular structure of the  $[\text{Ni}_9\text{Co}(\text{C}_2)(\text{CO})_{16-x}]^{3-}$  ( $x = 0, 1$ ) trianion has been determined as its  $[\text{NEt}_4]_3[\text{Ni}_9\text{Co}(\text{C}_2)(\text{CO})_{16-x}]$  salts (figure 4.1.6). Within the crystal, the two different trianions are generated by the fact that two edge bridging CO ligands related by a mirror plane and bonded to a common atom are partially vacant and replaced by a single terminal CO bonded to the same metal atom.

The single Co-atom has been assigned as disordered over two symmetry related positions in the central square of the cluster. Indeed, also the above mentioned disordered bridging-terminal CO ligands are bonded to these atoms.

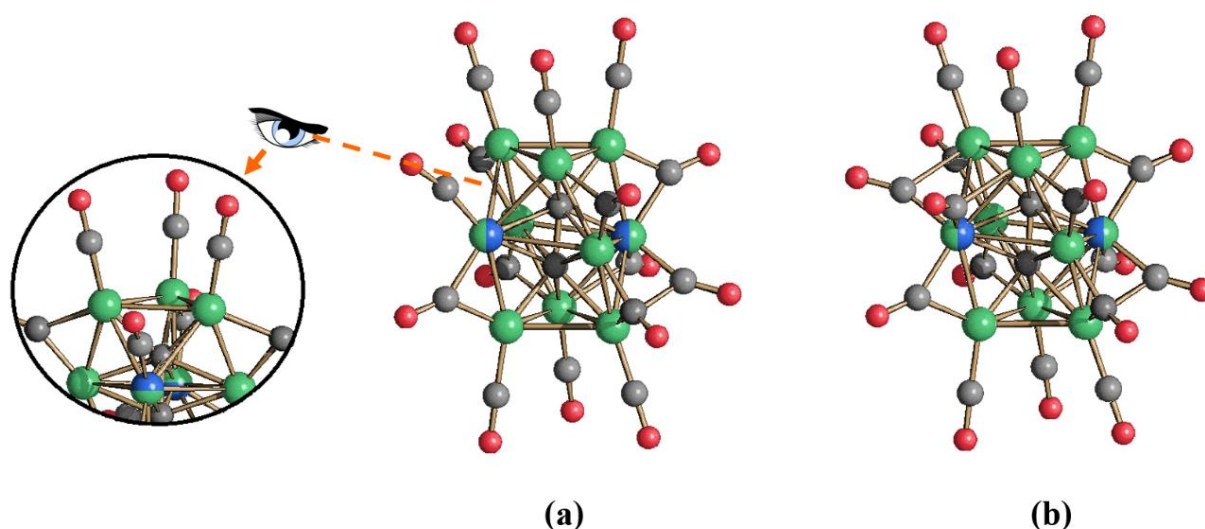


**Figure 4.1.6** Molecular structure of (a)  $[\text{Ni}_9\text{Co}(\text{C}_2)(\text{CO})_{15}]^{3-}$  and (b)  $[\text{Ni}_9\text{Co}(\text{C}_2)(\text{CO})_{16}]^{3-}$ . The different number of carbonyl ligands has no effect on the metal cage. (Ni, green; Co, blue;  $[\text{Ni}/\text{Co}]_{\text{disordered}}$ , bicolor green-blue).

The  $[\text{Ni}_9\text{Co}(\text{C}_2)(\text{CO})_{16-x}]^{3-}$  ( $x = 0, 1$ ) trianions are closely related to the previously reported  $[\text{Ni}_{10}(\text{C}_2)(\text{CO})_{16}]^{2-}$ ,  $[\text{Co}_3\text{Ni}_7(\text{C}_2)(\text{CO})_{15}]^{3-}$  and  $[\text{Co}_3\text{Ni}_7(\text{C}_2)(\text{CO})_{16}]^{n-}$  ( $n = 2, 3$ ). Their common metal polyhedron may be seen as being derived from the condensation of two (distorted) capped trigonal-prisms sharing a common square face. Overall, the metal framework consists of a 3,4,3 stack of metal atoms of  $C_{2h}$  idealized symmetry.

The interstitial C-atoms are lodged within mono-capped trigonal prismatic cavities, showing seven M-C contacts each. As a result of the fact that these two  $M_7C$  prisms share a common square face, the interstitial C-atoms display a very short C-C distance [1.455(12) Å], suggesting the presence of tightly bonded  $C_2$ -units. For what concerns the stereochemistry of the CO ligands,  $[\text{Ni}_9\text{Co}(\text{C}_2)(\text{CO})_{16}]^{3-}$  contains six terminal and ten edge bridging carbonyls, whereas  $[\text{Ni}_9\text{Co}(\text{C}_2)(\text{CO})_{15}]^{3-}$  possesses seven terminal and eight edge bridging ligands.

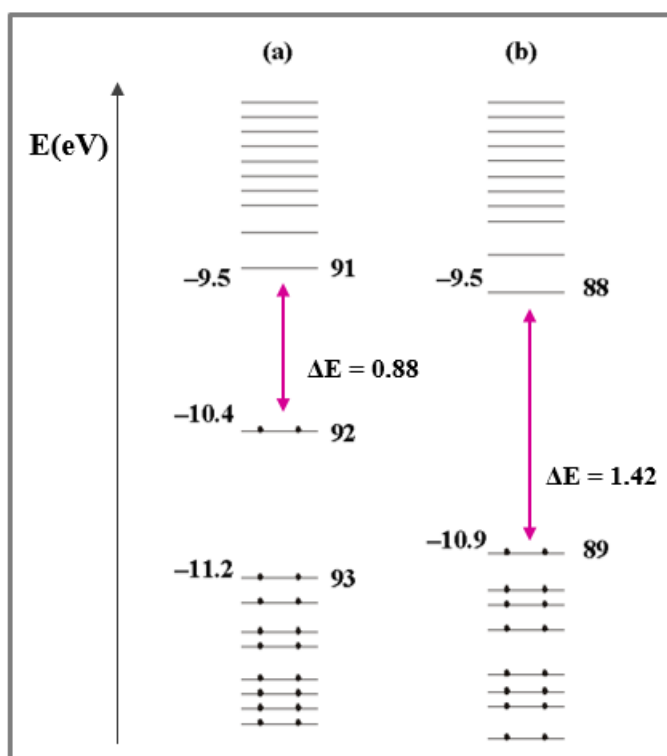


**Figure 4.1.7** Frontier region of EHMO diagrams of (a)  $[\text{Ni}_9\text{Co}(\text{C}_2)(\text{CO})_{16}]^{3-}$  and (b)  $[\text{Ni}_9\text{Co}(\text{C}_2)(\text{CO})_{15}]^{3-}$ .

EHMO calculations with CACAO [62] show that  $[\text{Ni}_9\text{Co}(\text{C}_2)(\text{CO})_{15}]^{3-}$  displays a rather wide HOMO-LUMO gap (1.416 eV) and possesses a close-shell electronic configuration (figure 4.1.7). The addition of a further CO in  $[\text{Ni}_9\text{Co}(\text{C}_2)(\text{CO})_{16}]^{3-}$  introduces an additional MO within this gap, reducing the HOMO-LUMO gap to 0.88 eV. The latter is isoelectronic with  $[\text{Ni}_{10}(\text{C}_2)(\text{CO})_{16}]^{2-}$ , possessing 142 CVE ( $6N + 11 \text{ CVO}$ ). Conversely,  $[\text{Ni}_9\text{Co}(\text{C}_2)(\text{CO})_{15}]^{3-}$  contains 140 CVE ( $6N + 10 \text{ CVO}$ ) being isoelectronic to  $[\text{Co}_3\text{Ni}_7(\text{C}_2)(\text{CO})_{16}]^{3-}$ . Finally, the previously reported  $[\text{Co}_3\text{Ni}_7(\text{C}_2)(\text{CO})_{15}]^{3-}$  displays only 138

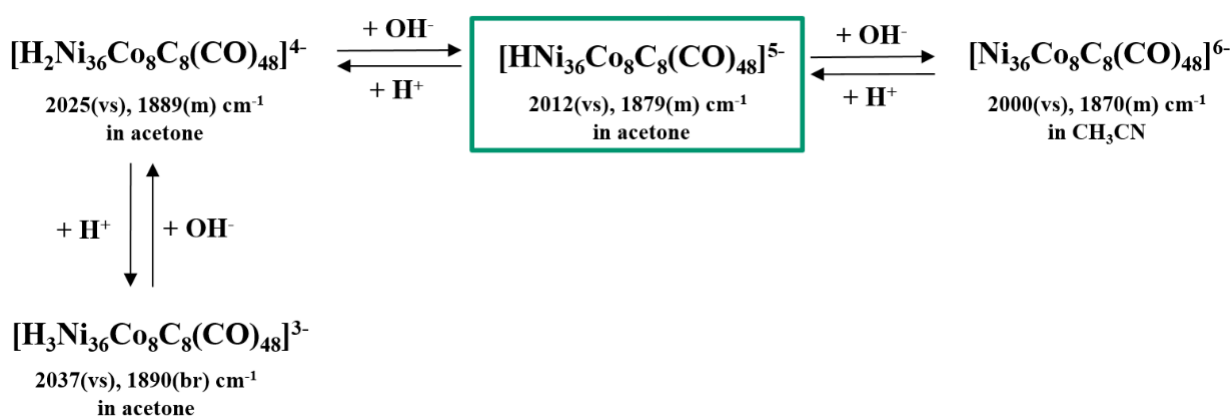
CVE ( $6N + 9 \text{ CVO}$ ) even if the metal cages are very similar. The different electron counts of these deca-nuclear mono-acetylide clusters possessing similar metal frameworks is probably due to distortions and loosening of the metal interactions.

#### 4.1.4 Synthesis and characterization of $[\text{H}_{6-n}\text{Ni}_{36}\text{Co}_8\text{C}_8(\text{CO})_{48}]^{n-}$ ( $n = 3-6$ )

The thermal decomposition in thf solution of  $[\text{H}_2\text{Ni}_{22}\text{Co}_6\text{C}_6(\text{CO})_{36}]^{4-}$  hexa-carbide results in a nearly colourless solution and a dark oily precipitate. The reaction takes *ca.* 2 hours and a longer heating time must be avoided since it favours the formation of  $[\text{Ni}_{132}\text{C}_6(\text{CO})_{36}]^{6-}$  [33] as side product. Single crystal suitable for X-ray analysis are obtained after layering n-hexane on the acetone solution (were the cluster is extracted after work-up), resulting in X-ray quality single crystals of the new  $[\text{NMe}_3(\text{CH}_2\text{Ph})]_6[\text{Ni}_{36}\text{Co}_8\text{C}_8(\text{CO})_{48}] \cdot 5\text{CH}_3\text{COCH}_3$  bimetallic octa-carbide. The IR analysis shows that deprotonation has occurred starting from the  $[\text{HNi}_{36}\text{Co}_8\text{C}_8(\text{CO})_{48}]^{5-}$  penta-anion present in acetone before crystallization. This has been fully corroborated by studying the reactivity of the cluster towards acids and bases and substantiated by electrochemical experiments.

Formation of  $[\text{HNi}_{36}\text{Co}_8\text{C}_8(\text{CO})_{48}]^{5-}$  from  $[\text{H}_2\text{Ni}_{22}\text{Co}_6\text{C}_6(\text{CO})_{36}]^{4-}$  requires cluster rearrangement. Yields are *ca.* 45 % based on Ni and 35 % based on Co, suggesting the formation of several by products. Unfortunately, these compounds are completely insoluble in all solvents, hampering their identification and making very difficult to speculate on the reactions occurring during the synthesis.

The  $[\text{Ni}_{36}\text{Co}_8\text{C}_8(\text{CO})_{48}]^{6-}$  hexa-anion is protonated by acids such as  $\text{HBF}_4$  resulting in the  $[\text{HNi}_{36}\text{Co}_8\text{C}_8(\text{CO})_{48}]^{5-}$  penta-anion mono-hydride (scheme 4.1.2). The latter is further protonated in acetone giving, first, the  $[\text{H}_2\text{Ni}_{36}\text{Co}_8\text{C}_8(\text{CO})_{48}]^{4-}$  tetra-anion di-hydride and, then, the  $[\text{H}_3\text{Ni}_{36}\text{Co}_8\text{C}_8(\text{CO})_{48}]^{3-}$  tri-anion tri-hydride. All these reactions are reversed after addition of stoichiometric amounts of bases such as  $[\text{NBu}_4][\text{OH}]$ .



**Scheme 4.1.2** Deprotonation and protonation of  $[\text{H}_{6-n}\text{Ni}_{36}\text{Co}_8\text{C}_8(\text{CO})_{48}]^{n-}$  ( $n = 3-6$ ) species. The  $[\text{HNi}_{36}\text{Co}_8\text{C}_8(\text{CO})_{48}]^{5-}$  species is the direct product of the thermal degradation of  $[\text{H}_2\text{Ni}_{22}\text{Co}_6\text{C}_6(\text{CO})_{36}]^{4-}$ .

As previously reported for high nuclearity platinum carbonyl clusters, all attempts to directly confirm the presence and numbers of hydride ligands by  $^1\text{H}$  NMR spectroscopy failed

under every experimental condition adopted (see chapter 2.4). The electrochemical studies on  $[\text{Ni}_{36}\text{Co}_8\text{C}_8(\text{CO})_{48}]^{6-}$  and  $[\text{HNi}_{36}\text{Co}_8\text{C}_8(\text{CO})_{48}]^{5-}$  show the presence only of complicated irreversible redox processes (figure 4.1.8). Both clusters undergo two irreversible oxidation processes, giving ill-defined broad peaks, whose potential can be only roughly estimated at  $-0.27$  and  $+0.55\text{V}$  in the case of  $[\text{Ni}_{36}\text{Co}_8\text{C}_8(\text{CO})_{48}]^{6-}$  and at  $+0.02$  and  $+0.41\text{V}$  in the case of  $[\text{HNi}_{36}\text{Co}_8\text{C}_8(\text{CO})_{48}]^{5-}$ .  $[\text{Ni}_{36}\text{Co}_8\text{C}_8(\text{CO})_{48}]^{6-}$  also shows an irreversible reduction at  $-1.32\text{V}$ .

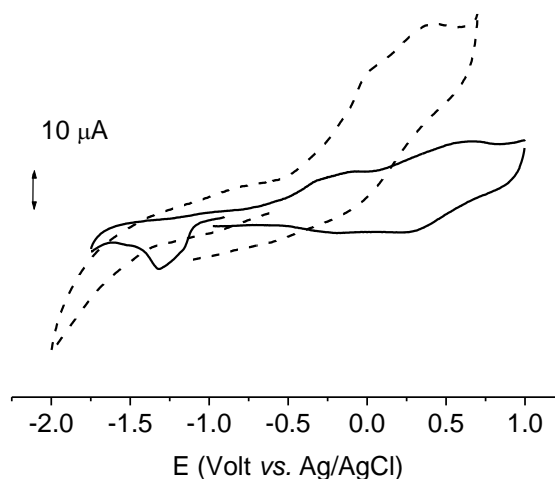


**Figure 4.1.8** Voltammogram of  $[\text{Ni}_{36}\text{Co}_8\text{C}_8(\text{CO})_{48}]^{6-}$  recorded at platinum electrode in a  $\text{CH}_3\text{CN}$  solution ( $0.8 \cdot 10^{-3}\text{ M}$ ; dashed line) comparing to that of the conjugate base  $[\text{HNi}_{36}\text{Co}_8\text{C}_8(\text{CO})_{48}]^{5-}$  ( $1.3 \cdot 10^{-3}\text{ M}$ ; full line).  $[\text{NBu}_4][\text{PF}_6]$  ( $0.2\text{ M}$ ) supporting electrolyte. Scan rate  $0.2\text{ V/s}$ .

Both samples have revealed to be highly difficult to characterise because of severe electrode poisoning, which could not be circumvented by using different electrode materials. The complete absence of reversible redox processes indicates that the different charges displayed by these clusters cannot be due to redox reactions, substantiating our hypothesis on their polyhydride nature.

The different  $[\text{H}_{6-n}\text{Ni}_{36}\text{Co}_8\text{C}_8(\text{CO})_{48}]^{n-}$  ( $n = 3-6$ ) anions as well as the parent  $[\text{HNi}_{22}\text{Co}_6\text{C}_6(\text{CO})_{36}]^{5-}$  display very similar and almost featureless UV-visible spectra and, thus, this technique revealed to be not very useful in order to distinguish the different species present in solution, as previously found for other large molecular clusters (figure 4.1.9). Moreover, these UV-visible spectra closely resemble those of small metal nanoparticles, pointing out the close relationship between large molecular clusters and small metal nanoparticles. At the same time, there is no noticeable change in the absorption spectra passing from nuclearity 28 to 44.

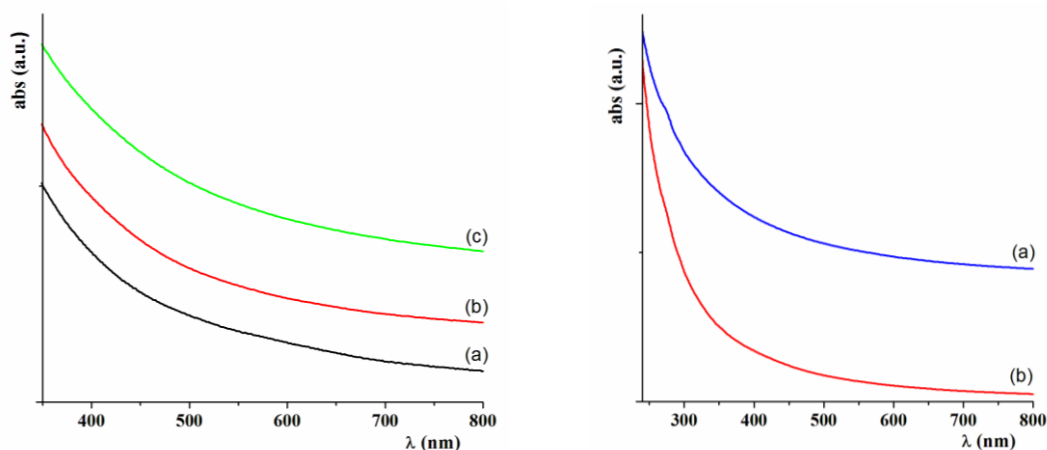


**Figure 4.1.9** (Left) Normalised UV-visible spectra of (a)  $[\text{Ni}_{36}\text{Co}_8\text{C}_8(\text{CO})_{48}]^{6-}$  (in  $\text{CH}_3\text{CN}$ ); (b)  $[\text{H}\text{Ni}_{36}\text{Co}_8\text{C}_8(\text{CO})_{48}]^{5-}$  (in  $\text{CH}_3\text{CN}$ ); (c)  $[\text{H}_2\text{Ni}_{36}\text{Co}_8\text{C}_8(\text{CO})_{48}]^{4-}$  (in acetone). (Right) Normalised UV-visible spectra of (a)  $[\text{H}\text{Ni}_{22}\text{Co}_6\text{C}_6(\text{CO})_{36}]^{5-}$  (in  $\text{CH}_3\text{CN}$ ); (b)  $[\text{H}\text{Ni}_{36}\text{Co}_8\text{C}_8(\text{CO})_{48}]^{5-}$  (in  $\text{CH}_3\text{CN}$ ). [Clusters] =  $10^{-5}$  M.

### Crystal structures

The molecular structure of the  $[\text{Ni}_{36}\text{Co}_8\text{C}_8(\text{CO})_{48}]^{6-}$  cluster has been determined in its  $[\text{NMe}_3(\text{CH}_2\text{Ph})]_6[\text{Ni}_{36}\text{Co}_8\text{C}_8(\text{CO})_{48}] \cdot 5\text{CH}_3\text{COCH}_3$  salts (see figure 4.1.10).

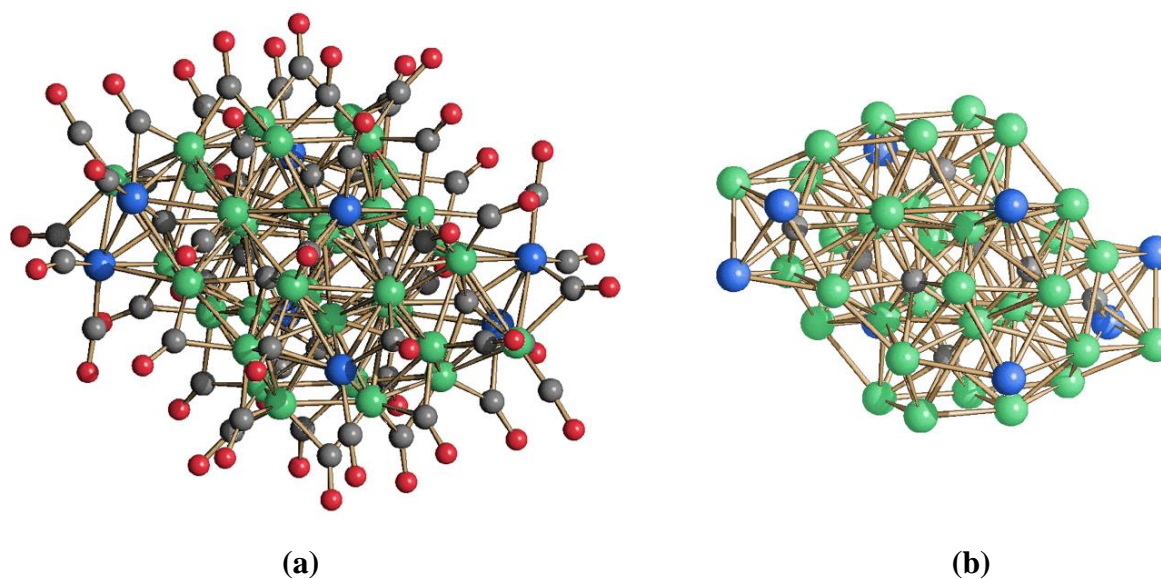


**Figure 4.1.10** Molecular structure (a) and the metal framework (b) of  $[\text{Ni}_{36}\text{Co}_8\text{C}_8(\text{CO})_{48}]^{6-}$  (Ni, green; Co, blue; C, grey; O, red).

The  $\text{Ni}_{36}\text{Co}_8\text{C}_8$  framework of the cluster anion may be rationalized as depicted in figure 4.1.11, which also shows the structural analogy between  $[\text{Ni}_{36}\text{Co}_8\text{C}_8(\text{CO})_{48}]^{6-}$  and the previously reported  $[\text{Ni}_{32}\text{C}_6(\text{CO})_{36}]^{6-}$  and  $[\text{H}\text{Ni}_{38}\text{C}_6(\text{CO})_{42}]^{5-}$  hexa-carbides. Thus, the core of the cluster is based on a cubic  $\text{Ni}_8\text{C}_6$  unit whose six square faces are capped by six carbide atoms. These carbides are encapsulated within six square anti-prismatic cages, after the addition of further four Ni-atoms on each carbide. This results on a  $\text{Ni}_{32}\text{C}_6$  framework, closely resembling the structure

of  $[\text{Ni}_{32}\text{C}_6(\text{CO})_{36}]^{6-}$ . The  $\text{Ni}_{32}\text{C}_6$  framework displays eight centred hexagonal  $\text{Ni}_7$  faces.  $[\text{HNi}_{38}\text{C}_6(\text{CO})_{42}]^{5-}$  formally arises from  $[\text{Ni}_{32}\text{C}_6(\text{CO})_{36}]^{6-}$  by adding six  $\text{Ni}(\text{CO})$  fragments on these faces. In the case of  $[\text{Ni}_{36}\text{Co}_8\text{C}_8(\text{CO})_{48}]^{6-}$ , four of these  $\text{Ni}_7$  centred hexagonal faces are capped by Co-atoms, which are not bonded to any carbide, resulting in a  $\text{Ni}_{32}\text{Co}_4\text{C}_6$  framework. Two other  $\text{Ni}_7$  centred hexagonal faces are not capped, whereas the remaining two faces are connected to two additional carbide atoms. The coordination sphere of these two carbides is completed by adding two further Ni and two Co atoms to each carbide, resulting in the final  $\text{Ni}_{36}\text{Co}_8\text{C}_8$  framework of the cluster. These additional carbides are, overall, encapsulated within mono-capped trigonal prismatic  $\text{Ni}_5\text{Co}_2\text{C}$  cages.

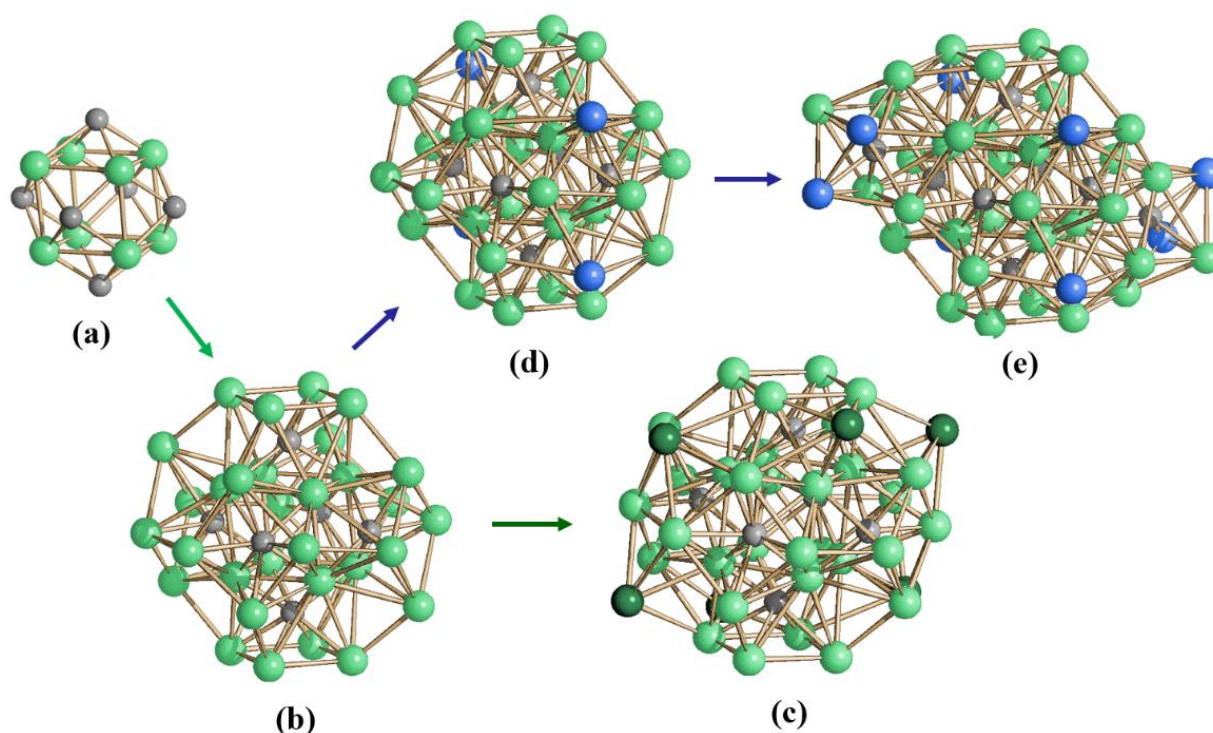


**Figure 4.1.11** Stepwise reconstruction of  $[\text{Ni}_{36}\text{Co}_8\text{C}_8(\text{CO})_{48}]^{6-}$ : (a)  $\text{Ni}_8\text{C}_6$  core; (b)  $\text{Ni}_{32}\text{C}_6$  framework; (c)  $\text{Ni}_{38}\text{C}_6$  framework obtained by adding six nickel atoms (dark green) non bonded to any carbide atom (d)  $\text{Ni}_{32}\text{Co}_4\text{C}_6$  framework obtained by adding four cobalt atoms; (e) the whole  $\text{Ni}_{36}\text{Co}_8\text{C}_8$  metal cage (Ni, green; Co, blue; C, grey).

The eight interstitial carbide atoms display rather different environments. Thus, two C-atoms are enclosed within regular  $\text{Ni}_8\text{C}$  square anti-prismatic cages showing eight Ni-C contacts similar to those found in  $[\text{Ni}_{32}\text{C}_6(\text{CO})_{36}]^{6-}$  and  $[\text{HNi}_{38}\text{C}_6(\text{CO})_{42}]^{5-}$ . Other four carbides are contained within irregular  $\text{Ni}_8\text{C}$  square anti-prismatic cages, formed by the four rhombic faces described above. The last two carbide atoms are enclosed within  $\text{Ni}_5\text{Co}_2\text{C}$  mono-capped trigonal prismatic cages and show normal Ni-C and Co-C contacts.

All the  $[\text{H}_{6-n}\text{Ni}_{36}\text{Co}_8\text{C}_8(\text{CO})_{48}]^{n-}$  ( $n = 3-6$ ) clusters are isoelectronic and possess 566 Cluster Valence Electrons (CVE) corresponding to  $283 (6N + 19; N = \text{number of metal atoms})$  Cluster Valence Orbitals (CVO). These clusters are considerably electron richer than isonuclear species which do not contain interstitial heteroatoms such as  $[\text{Ni}_{36}\text{Pd}_8(\text{CO})_{44}]^{6-}$  (534 CVE; 267  $(6N + 3)$  CVO). This electron count is in keeping with other Ni polycarbide clusters which are usually electron rich as it is observed for  $[\text{Ni}_{32}\text{C}_6(\text{CO})_{36}]^{6-}$  and  $[\text{Ni}_{38}\text{C}_6(\text{CO})_{42}]^{6-}$  ( $6N + 19$  CVO). This, in turn, is due to the presence of several interstitial carbide atoms which behave like “internal” ligands donating four electrons.

## Bimetallic Ni-Cu Carbide Carbonyl Clusters with Vacant Ni(CO) Fragments

### 4.2.1 Bimetallic Ni-Cu nanoparticles and clusters

Bimetallic alloys of the active Group 10 metals (Ni, Pd, Pt) and relatively inactive Group 11 metals (Cu, Ag, Au) have been the subject of many experimental and theoretical studies on their catalytic properties. In particular, the chemisorption of CO, H<sub>2</sub> and several hydrocarbons on Ni-Cu surfaces have been extensively investigated. Studies in the field of heterogeneous catalysis include [63]:

- experimental and theoretical investigation of the adsorption and desorption of carbon monoxide on Ni-Cu surfaces;
- the redox disproportionation of carbon monoxide ( $\text{CO} \rightarrow \text{C} + \text{CO}_2$ ),
- the methanation of carbon monoxide ( $\text{CO} + \text{H}_2 \rightarrow \text{CH}_4 + \text{H}_2\text{O}$ ),
- methanol synthesis from CO<sub>2</sub>, CO and H<sub>2</sub> on Ni/Cu (100) surfaces.

In the last two decades, the interest on this bimetallic alloys has moved in the nano-field due to higher catalytic activity and selectivity. Moreover, bimetallic Ni-Cu nanoparticles have been extensively studied because of their magnetic and optical properties that are dramatically influenced by variations of their Ni-Cu composition.

The close-packed  $[\text{Cu}_x\text{Ni}_{35-x}(\text{CO})_{40}]^{5-}$  ( $x = 3, 5$ ) cluster [64], obtained by the redox condensation of  $[\text{Ni}_6(\text{CO})_{12}]^{2-}$  with CuBr<sub>2</sub>, is the only example of bimetallic Ni-Cu MCC reported (figure 4.2.1).<sup>19</sup> The 35-atom metal core is composed of equilateral triangular layers containing 10/15/10 atoms that are stacked in a A:B:A close-packed conformation. It is noteworthy that the *hcp* arrangement of the metal core contains three fully interstitial copper atoms. Only few examples of other (lower nuclearity) clusters containing naked copper atoms are known, *e.g.*,  $[\text{Fe}_4\text{Cu}_5(\text{CO})_{16}]^{3-}$ . On the other hand, clusters containing edge-bridging or face-

<sup>19</sup> The synthesis of  $[\text{Cu}_x\text{Ni}_{35-x}(\text{CO})_{40}]^{5-}$  ( $x = 3$  or  $5$ ) is irreproducible and therefore, the investigation of alternatives routes is crucial in order to explore its chemical and electrochemical properties. Unfortunately, all attempts to find a new synthetic route such as the redox condensation of  $[\text{Ni}_6(\text{CO})_{12}]^{2-}$  with a suitable Cu salts have failed.

capping CuL fragments, where L is a two-electron donor ligands such as CH<sub>3</sub>CN or PR<sub>3</sub> (R = alkyl or aryl), are more common (figure 4.2.2).

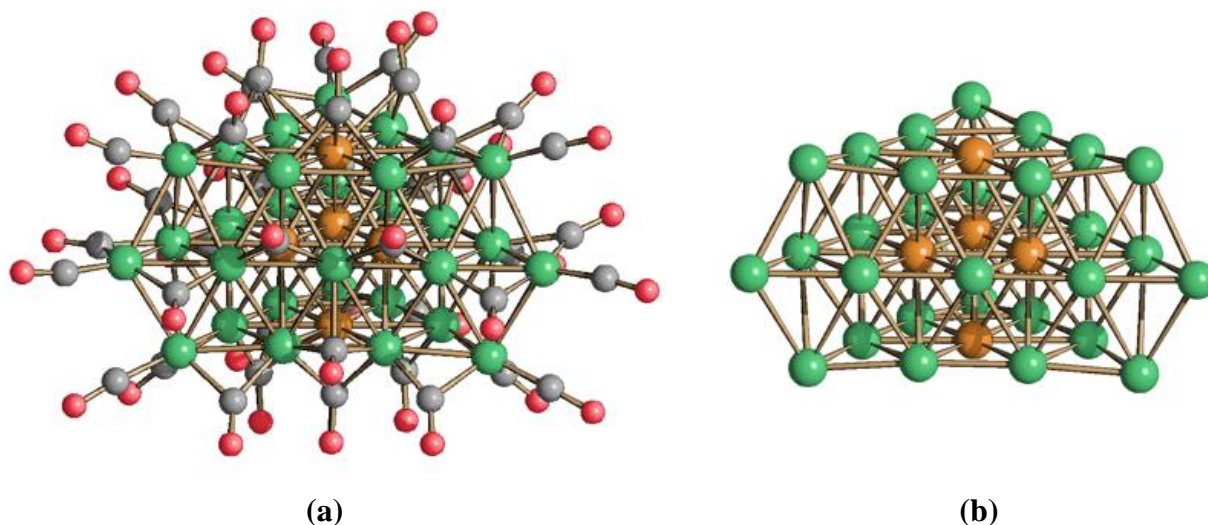


**Figure 4.2.1** (a) Molecular structure and (b) metal core of [Ni<sub>30</sub>Cu<sub>5</sub>(CO)<sub>40</sub>]<sup>5-</sup>. The *hcp* arrangement of the metal core contains three fully interstitial copper metal atoms. (Ni, green; Cu, orange; C, grey; O, red).

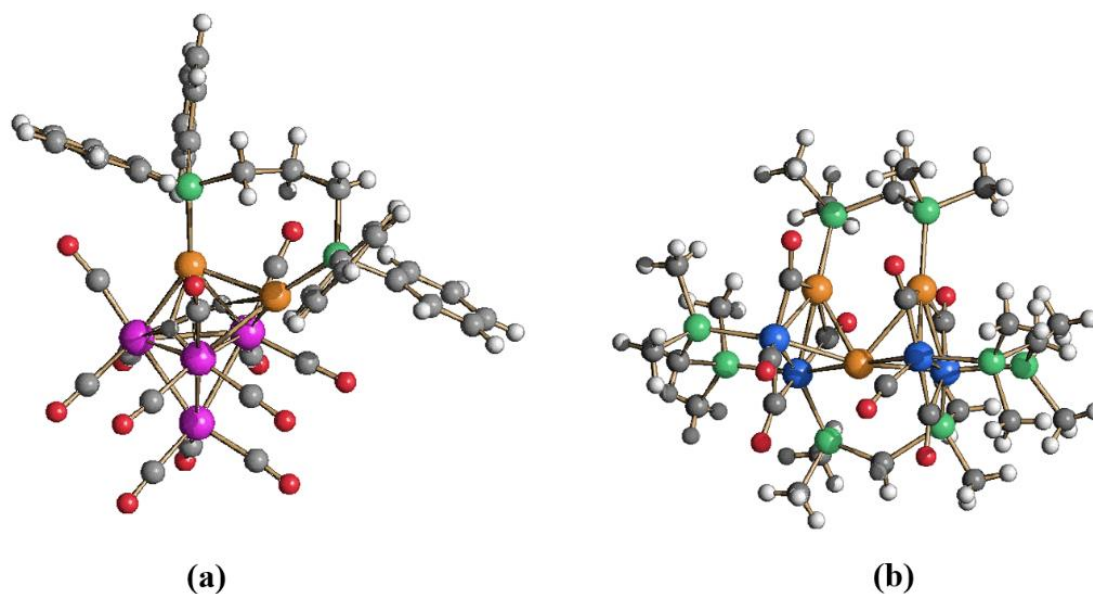


**Figure 4.2.2** Molecular structures of (a) H<sub>2</sub>Ru<sub>4</sub>(CO)<sub>12</sub>(Cu<sub>2</sub>PPh<sub>2</sub>CH<sub>2</sub>CH<sub>2</sub>PPh<sub>2</sub>) and (b) [Co<sub>4</sub>Cu(Cu<sub>2</sub>PPh<sub>2</sub>CH<sub>2</sub>PPh<sub>2</sub>)(PPh<sub>2</sub>CH<sub>2</sub>PPh<sub>2</sub>)<sub>3</sub>]<sup>+</sup>. It should be noted that only (b) contains a naked copper atom (Ru, purple; Co, blue, Cu, orange; P, green; C, grey; O, red; H, white).

On the basis of these considerations and recent studies on the synthesis of new high nuclearity Ni-Cd MCCs [65], we decided to explore the possible substitution of [CdX]<sup>+</sup> moieties with isoelectronic and isolobal [Cu(CH<sub>3</sub>CN)]<sup>+</sup> fragments. We tried, first, the exchange of [CdCl]<sup>+</sup> with [Cu(CH<sub>3</sub>CN)]<sup>+</sup> by reacting [H<sub>2</sub>Ni<sub>30</sub>C<sub>4</sub>(CO)<sub>34</sub>(CdX)<sub>2</sub>]<sup>4+</sup> with [Cu(CH<sub>3</sub>CN)<sub>4</sub>][BF<sub>4</sub>]. The results have been little rewarding owing to obtainment of rather complicated mixtures of

compounds, which could not be separated and crystallized. We, therefore, turned to investigate a reaction similar to the one affording  $[\text{H}_2\text{Ni}_{30}\text{C}_4(\text{CO})_{34}(\text{CdX})_2]^{4-}$ , namely the reaction of  $[\text{Ni}_9\text{C}(\text{CO})_{17}]^{2-}$  with  $[\text{Cu}(\text{CH}_3\text{CN})_4][\text{BF}_4]$ .

## 4.2.2 General results

The results described in detail in the following sections are herein briefly summarized (table 4.2.1) [66]. The reaction of  $[\text{Ni}_9\text{C}(\text{CO})_{17}]^{2-}$  with  $[\text{Cu}(\text{CH}_3\text{CN})_4][\text{BF}_4]$  (1.1-1.5 equivalents) afforded the first Ni-Cu carbide carbonyl cluster, *i.e.*,  $[\text{H}_2\text{Ni}_{30}\text{C}_4(\text{CO})_{34}\{\text{Cu}(\text{CH}_3\text{CN})\}_2]^{4-}$  ( $[\text{H}_2\mathbf{1}]^{4-}$ ). This has been crystallised in a pure form with miscellaneous  $[\text{NR}_4]^+$  (R = Me, Et) cations, as well as co-crystallised with  $[\text{H}_2\text{Ni}_{29}\text{C}_4(\text{CO})_{33}\{\text{Cu}(\text{CH}_3\text{CN})\}_2]^{4-}$  ( $[\text{H}_2\mathbf{2}]^{4-}$ ) which differs from  $[\text{H}_2\mathbf{1}]^{4-}$  by a missing Ni(CO).

Symbol	Formula	Isolated as
$[\text{H}_2\mathbf{1}]^{4-}$	$[\text{H}_2\text{Ni}_{30}\text{C}_4(\text{CO})_{34}\{\text{Cu}(\text{CH}_3\text{CN})\}_2]^{4-}$	pure compound
$[\text{H}_2\mathbf{2}]^{4-}$	$[\text{H}_2\text{Ni}_{29}\text{C}_4(\text{CO})_{33}\{\text{Cu}(\text{CH}_3\text{CN})\}_2]^{4-}$	mix $[\text{H}_2\mathbf{2}]^{4-}/[\text{H}_2\mathbf{1}]^{4-}$
$[\text{H}_2\mathbf{3}]^{2-}$	$[\text{H}_2\text{Ni}_{30}\text{C}_4(\text{CO})_{35}\{\text{Cu}(\text{CH}_3\text{CN})\}_2]^{2-}$	mix $[\text{H}_2\mathbf{3}]^{2-}/[\text{H}_2\mathbf{4}]^{2-}$
$[\text{H}_2\mathbf{4}]^{2-}$	$[\text{H}_2\text{Ni}_{29}\text{C}_4(\text{CO})_{34}\{\text{Cu}(\text{CH}_3\text{CN})\}_2]^{2-}$	pure compound
$[\text{H}_2\mathbf{5}]^{2-}$	$[\text{H}_2\text{Ni}_{29}\text{C}_4(\text{CO})_{32}(\text{CH}_3\text{CN})_2\{\text{Cu}(\text{CH}_3\text{CN})\}_2]^{2-}$	pure compound
$[\text{H}_2\mathbf{6}]^{3-}$	$[\text{H}_3\text{Ni}_{30}\text{C}_4(\text{CO})_{34}\{\text{Cu}(\text{NCC}_6\text{H}_4\text{CN})\}_2]^{3-}$	mix $[\text{H}_2\mathbf{6}]^{3-}/[\text{H}_2\mathbf{7}]^{3-}$
$[\text{H}_2\mathbf{7}]^{3-}$	$[\text{H}_3\text{Ni}_{29}\text{C}_4(\text{CO})_{33}\{\text{Cu}(\text{NCC}_6\text{H}_4\text{CN})\}_2]^{3-}$	mix $[\text{H}_2\mathbf{7}]^{3-}/[\text{H}_2\mathbf{6}]^{3-}$

**Table 4.2.1** List of new bimetallic Ni-Cu clusters with their related symbols. The clusters can be crystallized in a pure form or a mixture (mix) as indicated.

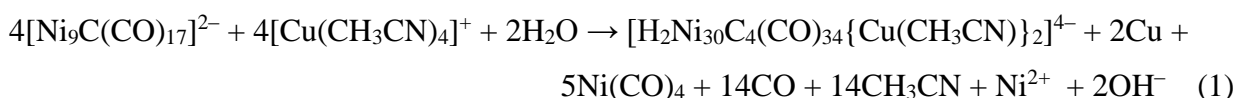
By increasing the  $[\text{Cu}(\text{CH}_3\text{CN})_4]^+ / [\text{Ni}_9\text{C}(\text{CO})_{17}]^{2-}$  ratio to 1.7-1.8, the closely related  $[\text{H}_2\text{Ni}_{30}\text{C}_4(\text{CO})_{35}\{\text{Cu}(\text{CH}_3\text{CN})\}_2]^{2-}$  ( $[\text{H}_2\mathbf{3}]^{2-}$ ),  $[\text{H}_2\text{Ni}_{29}\text{C}_4(\text{CO})_{34}\{\text{Cu}(\text{CH}_3\text{CN})\}_2]^{2-}$  ( $[\text{H}_2\mathbf{4}]^{2-}$ ), and  $[\text{H}_2\text{Ni}_{29}\text{C}_4(\text{CO})_{32}(\text{CH}_3\text{CN})_2\{\text{Cu}(\text{CH}_3\text{CN})\}_2]^{2-}$  ( $[\text{H}_2\mathbf{5}]^{2-}$ ) dianions have been obtained.  $[\text{H}_2\mathbf{4}]^{2-}$  and  $[\text{H}_2\mathbf{5}]^{2-}$  have been isolated in a pure form while  $[\text{H}_2\mathbf{3}]^{2-}$  has been isolated in mixture with  $[\text{H}_2\mathbf{4}]^{2-}$ . Replacement of Cu-bonded  $\text{CH}_3\text{CN}$  with *p*- $\text{NCC}_6\text{H}_4\text{CN}$  afforded, after protonation of the tetra-anion, mixtures of  $[\text{H}_3\text{Ni}_{30}\text{C}_4(\text{CO})_{34}\{\text{Cu}(\text{NCC}_6\text{H}_4\text{CN})\}_2]^{3-}$  ( $[\text{H}_3\mathbf{6}]^{3-}$ ) and  $[\text{H}_3\text{Ni}_{29}\text{C}_4(\text{CO})_{33}\{\text{Cu}(\text{NCC}_6\text{H}_4\text{CN})\}_2]^{3-}$  ( $[\text{H}_3\mathbf{7}]^{3-}$ ).

The species **1-7** display a common  $\text{Ni}_{28}\text{C}_4\text{Cu}_2$  core and differ for the charge, the presence of additional Ni atoms, the number and nature of the ligands, even though they are obtained under similar experimental conditions and often in mixtures.

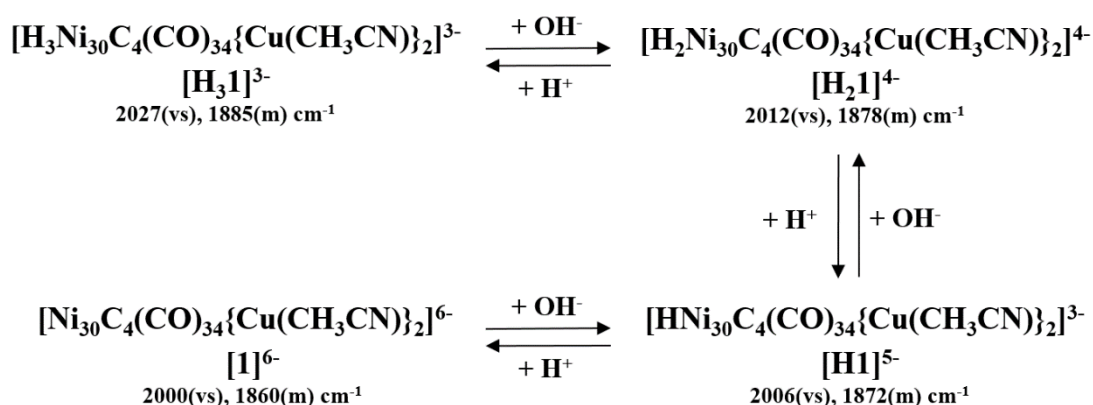
### 4.2.3 Synthesis and characterization of new bimetallic Ni-Cu clusters

The versatility of the  $[\text{Ni}_9\text{C}(\text{CO})_{17}]^{2-}$  dianion as a starting material for obtaining high nuclearity homo- and heterometallic carbonyl clusters is well documented (see chapters 4.1 and 7.1). In particular, its simple and high yield synthesis make this compound a perfect candidate to be reacted with  $[\text{Cu}(\text{CH}_3\text{CN})_4][\text{BF}_4]$  under different conditions.

The reaction of the  $[\text{Ni}_9\text{C}(\text{CO})_{17}]^{2-}$  dianion with a slight excess of  $[\text{Cu}(\text{CH}_3\text{CN})_4][\text{BF}_4]$  (1.1-1.5 equivalents) results in the formation of a new species of formula  $[\text{H}_2\text{Ni}_{30}\text{C}_4(\text{CO})_{34}\{\text{Cu}(\text{CH}_3\text{CN})\}_2]^{4-}$  ( $[\text{H}_2\mathbf{1}]^{4-}$ ) together with  $\text{Ni}(\text{CO})_4$  and a mirror of Cu-metal, in accord to equation (1):



The reaction is reminiscent of the one between  $[\text{Ni}_9\text{C}(\text{CO})_{17}]^{2-}$  and  $\text{CdX}_2$  ( $\text{X} = \text{Cl}, \text{Br}, \text{I}$ ) resulting in the formation of  $[\text{H}_{6-n}\text{Ni}_{30}\text{C}_4(\text{CO})_{34}(\text{CdX})_2]^{n-}$  ( $n = 3-6$ ), which contains the same  $\text{Ni}_{30}\text{C}_4(\text{CO})_{34}$  core. Since the  $\{\text{Cu}(\text{CH}_3\text{CN})\}^+$  fragment is isoelectronic to  $[\text{CdX}]^+$ , the product of reaction has been formulated as a di-hydride. Hydride ligands may arise from traces of  $\text{H}_2\text{O}$  present in the reaction medium. This is circumstantially confirmed by the fact that the tetra-anion is protonated in the same solvent by acids such as  $\text{HBF}_4$  yielding the tri-anion  $[\text{H}_3\mathbf{1}]^{3-}$ . Conversely, in the presence of bases, the tetra-anion is deprotonated yielding first the penta-anion  $[\text{H}\mathbf{1}]^{5-}$  and, then, the hexa-anion  $[\mathbf{1}]^{6-}$  (scheme 4.2.1)



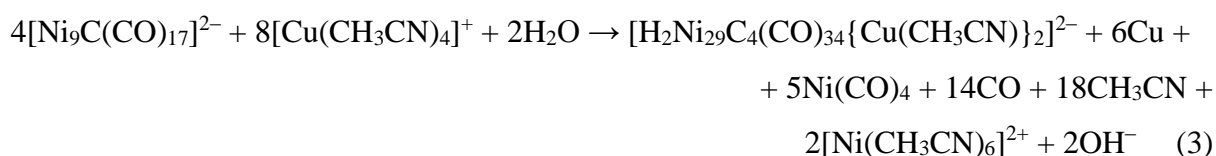
**Scheme 4.2.1** Protonation-deprotonation reactions of  $[\text{H}_2\mathbf{1}]^{4-}$  in  $\text{CH}_3\text{CN}$  solution.

Several attempts have been done on  $[\text{H}_{6-n}\mathbf{1}]^{n-}$  ( $n = 3-6$ ) in order to detect the hydrides *via*  $^1\text{H}$  NMR, but their spectra do not show any resonance a part those of the organic cations and solvents, even by changing the experimental conditions (see chapter 2.4).

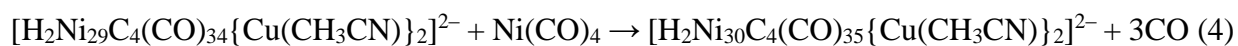
While investigating the protonation-deprotonation reactions, in the attempt to find the conditions to isolate other members of the  $[\text{H}_{6-n}\mathbf{1}]^{n-}$  ( $n = 3-6$ ) series, we noticed some minor but yet systematic differences in the IR spectra of anions with the same value of  $n$ . In order to shed more light on this point, we have attempted to crystallise several samples under different experimental conditions, resulting in X-ray quality single crystals of  $[\text{H}_2\mathbf{1}]^{4-}$  as well as co-crystallized mixtures of  $[\text{H}_2\mathbf{1}]^{4-}$  and the structurally related  $[\text{H}_2\mathbf{2}]^{4-}$ , *i.e.*, the  $[\text{NMe}_3(\text{CH}_2\text{Ph})]_4[\text{H}_2\text{Ni}_{30-x}\text{C}_4(\text{CO})_{34-x}\{\text{Cu}(\text{CH}_3\text{CN})\}_2] \cdot 2\text{CH}_3\text{CN}$  ( $x \sim 0.35$ ) salt. Formation of  $[\text{H}_2\mathbf{2}]^{4-}$  in mixture with  $[\text{H}_2\mathbf{1}]^{4-}$  may be justified by equation (2) in view of the fact that the required CO is formed during their synthesis:



Furthermore, by increasing the  $[\text{Cu}(\text{CH}_3\text{CN})_4]^+ / [\text{Ni}_9\text{C}(\text{CO})_{17}]^{2-}$  ratio to 1.7-1.8, probably owing to the more oxidizing conditions, the  $[\text{H}_2\mathbf{4}]^{2-}$  and  $[\text{H}_2\mathbf{5}]^{2-}$  dianions have been obtained according reaction (3):



In particular, the di-anion  $[\text{H}_2\mathbf{4}]^{2-}$  has been crystallised from acetone, whereas two CO ligands were replaced by two  $\text{CH}_3\text{CN}$  molecules during crystallisation from  $\text{CH}_3\text{CN}$  yielding the closely related species  $[\text{H}_2\mathbf{5}]^{2-}$ . It must be remarked that CO/ $\text{CH}_3\text{CN}$  substitution has been observed for these dianions but not for the above tetra-anions  $[\text{H}_2\mathbf{1}]^{4-}$ , in agreement with the greater basicity of the  $\text{CH}_3\text{CN}$  ligands. Conversely, metathesis of the  $[\text{Ni}(\text{CH}_3\text{COCH}_3)]^{2+}$  cation with  $[\text{NMe}_4]\text{Cl}$  led to isolation of a co-crystallized mixture of  $[\text{H}_2\mathbf{4}]^{2-}$  and  $[\text{H}_2\mathbf{3}]^{2-}$ , as present on the  $[\text{NMe}_4]_2[\text{H}_2\text{Ni}_{29+x}\text{C}_4(\text{CO})_{34+x}\{\text{Cu}(\text{CH}_3\text{CN})\}_2] \cdot 3.39\text{thf}$  ( $x \sim 0.3$ ) salt. The additional  $\text{Ni}(\text{CO})$  fragment present in  $[\text{H}_2\mathbf{3}]^{2-}$  probably arises from condensation between  $\text{Ni}(\text{CO})_4$  and  $[\text{H}_2\mathbf{4}]^{2-}$ , in accord to equation (4):



$[\text{H}_2\mathbf{3}]^{2-}$ ,  $[\text{H}_2\mathbf{4}]^{2-}$  and  $[\text{H}_2\mathbf{5}]^{2-}$  have been formulated as di-hydrides in order to be isoelectronic with  $[\text{H}_2\mathbf{1}]^{4-}$  and  $[\text{H}_2\mathbf{2}]^{4-}$ .

The co-crystallized mixture of the protonated  $[\text{H}_3\mathbf{6}]^{3-}$  and  $[\text{H}_3\mathbf{7}]^{3-}$  has been conversely characterized as the  $[\text{NMe}_4]_3[\text{H}_3\text{Ni}_{30-x}\text{C}_4(\text{CO})_{34-x}\{\text{Cu}(\text{NCC}_6\text{H}_4\text{CN})\}_2] \cdot 3.5\text{CH}_3\text{COCH}_3$  ( $x \sim 0.52$ ) salt, which contains  $\text{NCC}_6\text{H}_4\text{CN}$  bonded to Cu instead of  $\text{CH}_3\text{CN}$ , every time the tri-anion has been crystallized from acetone/iso-propanol in the presence of  $\text{NCC}_6\text{H}_4\text{CN}$  in excess.

Compounds **1-7** display very similar and almost featureless UV-visible spectra and, thus, this technique revealed to be not very useful in order to distinguish the different species present in solution.

### Crystal structures

The crystal structures of several salts containing bimetallic Ni-Cu carbonyl clusters have been determined by single crystal X-ray analyses (table 4.2.2). Their most relevant average bond distances are reported in table 4.2.3 where they are compared to the previously reported species which display similar structures. Herein, the structure of  $[\text{H}_2\mathbf{1}]^{4-}$  is described in some detail whereas we will focus only on the differences of all other anions.

Salt determined by single crystal X-ray analyses	Compounds
$[\text{NEt}_4]_4[\text{H}_2\text{Ni}_{30}\text{C}_4(\text{CO})_{34}\{\text{Cu}(\text{CH}_3\text{CN})\}_2] \cdot 6\text{CH}_3\text{CN}$	$[\text{H}_2\mathbf{1}]^{4-}$
$[\text{NMe}_4]_4[\text{H}_2\text{Ni}_{30}\text{C}_4(\text{CO})_{34}\{\text{Cu}(\text{CH}_3\text{CN})\}_2] \cdot 2\text{CH}_3\text{CN}$	$[\text{H}_2\mathbf{1}]^{4-}$
$[\text{NMe}_4]_4[\text{H}_2\text{Ni}_{30}\text{C}_4(\text{CO})_{34}\{\text{Cu}(\text{CH}_3\text{CN})\}_2] \cdot 6\text{CH}_3\text{COCH}_3$	$[\text{H}_2\mathbf{1}]^{4-}$
$[\text{NMe}_3(\text{CH}_2\text{Ph})]_4[\text{H}_2\text{Ni}_{30-x}\text{C}_4(\text{CO})_{34-x}\{\text{Cu}(\text{CH}_3\text{CN})\}_2] \cdot 2\text{CH}_3\text{CN}$ ( $x \sim 0.35$ )	$[\text{H}_2\mathbf{1}]^{4-}/[\text{H}_2\mathbf{2}]^{4-}$
$[\text{NMe}_4]_3[\text{H}_3\text{Ni}_{30-x}\text{C}_4(\text{CO})_{34-x}\{\text{Cu}(\text{NCC}_6\text{H}_4\text{CN})\}_2] \cdot 3.5\text{CH}_3\text{COCH}_3$ ( $x \sim 0.52$ )	$[\text{H}_2\mathbf{6}]^{3-}/[\text{H}_2\mathbf{7}]^{3-}$
$[\text{Ni}(\text{CH}_3\text{CN})_6][\text{H}_2\text{Ni}_{29}\text{C}_4(\text{CO})_{32}(\text{CH}_3\text{CN})_2\{\text{Cu}(\text{CH}_3\text{CN})\}_2] \cdot 4\text{CH}_3\text{CN}$	$[\text{H}_2\mathbf{5}]^{2-}$
$[\text{Ni}(\text{CH}_3\text{COCH}_3)_6][\text{H}_2\text{Ni}_{29}\text{C}_4(\text{CO})_{34}\{\text{Cu}(\text{CH}_3\text{CN})\}_2] \cdot 2\text{CH}_3\text{COCH}_3$	$[\text{H}_2\mathbf{4}]^{2-}$
$[\text{NMe}_4]_2[\text{H}_2\text{Ni}_{29+x}\text{C}_4(\text{CO})_{34+x}\{\text{Cu}(\text{CH}_3\text{CN})\}_2] \cdot 3.39\text{thf}$ ( $x \sim 0.3$ )	$[\text{H}_2\mathbf{3}]^{2-}/[\text{H}_2\mathbf{4}]^{2-}$

**Table 4.2.2** Crystal structures of several salts containing bimetallic Ni-Cu carbonyl clusters.

The  $[\text{H}_2\mathbf{1}]^{4-}$  tetra-anion is based on an inner  $\text{Ni}_{24}$  *quasi-regular* polyhedron which is based on a central heptagonal antiprism in which each of the heptagonal faces is joined to a  $\text{Ni}_5$  pentagon (figure 4.2.3). The resulting  $\text{Ni}_{24}$  polyhedron shows two pentagonal, four square and thirty triangular faces and displays 58 edges. It conforms, therefore, to the Euler rule ( $V-E+F=2$ ;  $V = 24$ ,  $E = 58$ ,  $F = 36$ ).

Deviations from regularity are mainly due to the fact that one edge of each pentagon is slightly elongated and that the inner angles of each heptagonal layer depart from the theoretical value of  $128.4^\circ$ . The above  $\text{Ni}_{24}$  polyhedron interstitially lodges 4 Ni atoms describing two edge-fused triangles and 4 carbide atoms describing a non-bonded square. The two pentagonal faces are capped by the two  $\text{Cu}(\text{CH}_3\text{CN})$  moieties, whereas two out of four square faces on opposite sides of the above polyhedron are capped by additional  $\text{Ni}(\text{CO})$  fragments.

	Ni–Ni	Ni–C (TP) <sup>[a]</sup>	Ni–C (CTP) <sup>[b]</sup>	Ni–M <sup>[c]</sup>
$[\text{H}_2\text{Ni}_{30}\text{C}_4(\text{CO})_{34}\{\text{Cu}(\text{CH}_3\text{CN})\}_2]^{4-}$	2.580	1.95	2.02	2.641
$[\text{H}_2\text{Ni}_{30}\text{C}_4(\text{CO})_{34}\{\text{Cu}(\text{CH}_3\text{CN})\}_2]^{4-}$	2.568	2.01	2.01	2.635
$[\text{H}_2\text{Ni}_{30}\text{C}_4(\text{CO})_{34}\{\text{Cu}(\text{CH}_3\text{CN})\}_2]^{4-}$	2.567	1.94	2.01	2.624
$[\text{H}_2\text{Ni}_{30-x}\text{C}_4(\text{CO})_{34-x}\{\text{Cu}(\text{CH}_3\text{CN})\}_2]^{4-}$	2.581	1.95	2.01	2.630
$[\text{H}_3\text{Ni}_{30-x}\text{C}_4(\text{CO})_{34-x}\{\text{Cu}(\text{NCC}_6\text{H}_4\text{CN})\}_2]^{3-}$	2.573	1.94	2.00	2.621
$[\text{H}_2\text{Ni}_{29}\text{C}_4(\text{CO})_{32}(\text{CH}_3\text{CN})_2\{\text{Cu}(\text{CH}_3\text{CN})\}_2]^{2-}$	2.583	1.95	2.01	2.645
$[\text{H}_2\text{Ni}_{29}\text{C}_4(\text{CO})_{34}\{\text{Cu}(\text{CH}_3\text{CN})\}_2]^{2-}$	2.572	1.94	2.01	2.644
$[\text{H}_2\text{Ni}_{29+x}\text{C}_4(\text{CO})_{34+x}\{\text{Cu}(\text{CH}_3\text{CN})\}_2]^{2-}$	2.560	1.94	2.01	2.657
$[\text{H}_2\text{Ni}_{30}\text{C}_4(\text{CO})_{34}(\text{CdI})_2]^{4-}$ <sup>[d]</sup>	2.581	1.96	2.00	2.772
$[\text{HNi}_{30}\text{C}_4(\text{CO})_{34}(\text{CdBr})_2]^{5-}$ <sup>[d]</sup>	2.583	2.00	2.02	2.765
$[\text{H}_2\text{Ni}_{32-y}\text{C}_4(\text{CO})_{36-y}(\text{CdBr})]^{5-}$ <sup>[d]</sup>	2.587	1.94	2.01	2.766
$[\text{HNi}_{33-y}\text{C}_4(\text{CO})_{37-y}(\text{CdCl})]^{6-}$ <sup>[d]</sup>	2.584	1.94	2.02	2.728
$[\text{H}_2\text{Ni}_{30}\text{C}_4(\text{CO})_{34}(\text{CdCl})_2]^{4-}$ <sup>[d]</sup>	2.593	1.94	2.01	2.764
$[\text{HNi}_{30}\text{C}_4(\text{CO})_{34}(\text{CdCl})_2]^{5-}$ <sup>[d]</sup>	2.596	1.95	2.01	2.768
$[\text{Ni}_{30}\text{C}_4(\text{CO})_{34}(\text{CdCl})_2]^{6-}$ <sup>[d]</sup>	2.599	1.92	2.02	2.757
$[\text{HNi}_{34}\text{C}_4(\text{CO})_{38}]^{5-}$	2.597	1.94	2.01	–
$[\text{Ni}_{35}\text{C}_4(\text{CO})_{38}]^{6-}$	2.596	1.94	2.03	–

**Table 4.2.3** Average bond distances (Å) of the new Ni-Cu tetracarbide carbonyl clusters compared to some previously reported compounds. <sup>[a]</sup> Average Ni-C distance in the trigonal prismatic cavities. <sup>[b]</sup> Average Ni-C distance in the capped trigonal prismatic cavities. <sup>[c]</sup> M = Cu, Cd. <sup>[d]</sup> See ref. [65].

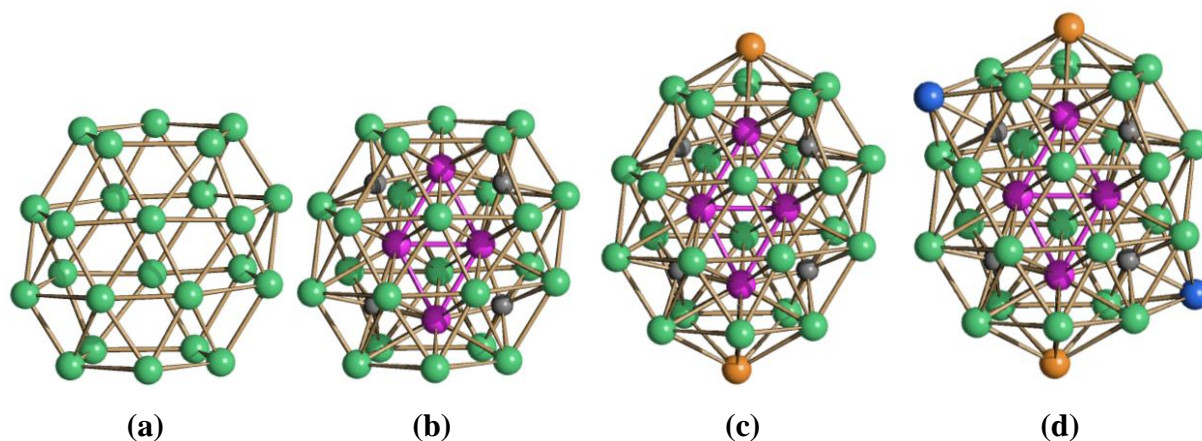


**Figure 4.2.3** Description of the structure of the  $\text{Ni}_{30}\text{C}_4\text{Cu}_2$  metal-carbide frame of  $[\text{H}_2\mathbf{I}]^{4-}$ : (a) The  $\text{Ni}_{24}$  polyhedron (Ni, green); (b) the  $\text{Ni}_{28}\text{C}_4$  core with the four interstitial Ni-atoms (purple) and the four carbides (grey); (c) the two Cu-atoms (orange) capping the two pentagonal faces of  $\text{Ni}_{28}\text{C}_4$ ; (d) the two additional Ni(CO) fragments (Ni, blue) capping two of the four square faces of  $\text{Ni}_{28}\text{C}_4\text{Cu}_2$ .

The overall metal frame is almost identical to that of  $[\text{H}_{6-n}\text{Ni}_{30}\text{C}_4(\text{CO})_{34}(\text{CdX})_2]^{n-}$  ( $n = 3-6$ ) and is also closely related to those of the homometallic tetra-carbides  $[\text{H}\text{Ni}_{34}\text{C}_4(\text{CO})_{38}]^{5-}$  [65] and  $[\text{Ni}_{35}\text{C}_4(\text{CO})_{39}]^{6-}$  (figure 4.2.4). Of the 34 CO ligands, 14 are terminal, 18 edge bridging and 2 face bridging. Two of the four interstitial carbide atoms are lodged into trigonal prismatic cavities, whereas the other two C-atoms are located in two mono-capped trigonal prismatic cavities (figure 4.2.5). The stepwise reconstruction of  $[\text{H}_2\mathbf{1}]^{4-}$  obtained by the formal condensation of  $\text{Ni}_6\text{C}$  cages is reported in figure 4.2.6.

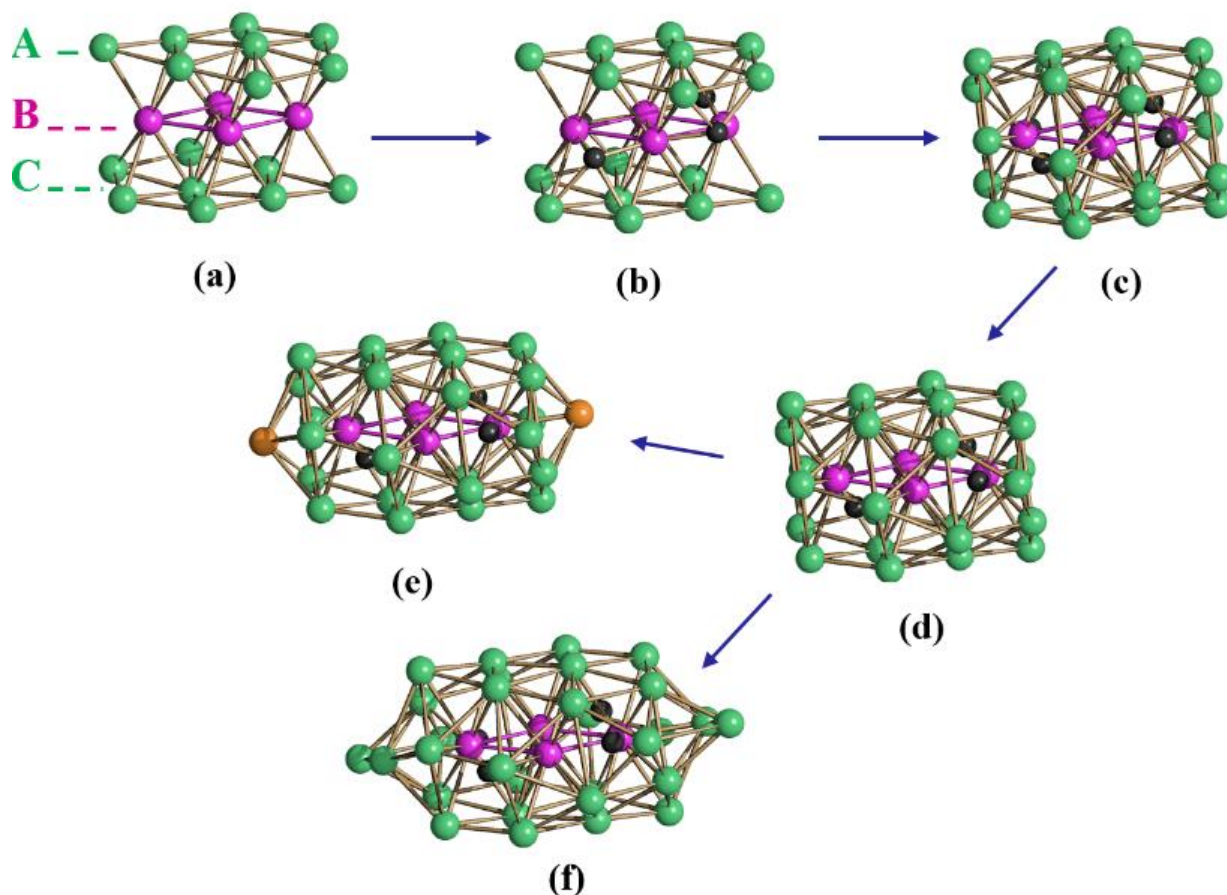


**Figure 4.2.4** Formal grow path of the metal cores of  $[\text{H}_{6-n}\mathbf{1}]^{n-}$  ( $n = 3-6$ ) and  $[\text{H}\text{Ni}_{34}\text{C}_4(\text{CO})_{38}]^{5-}$ : (a)  $\text{Ni}_{20}$  *ccp* core (A and C layers in green, B layer in purple); (b)  $\text{Ni}_{20}\text{C}_4$ ; (c)  $\text{Ni}_{28}\text{C}_4$  with the carbide atoms in trigonal prismatic cages; (d)  $\text{Ni}_{30}\text{C}_4$  after capping of two opposite trigonal prismatic cage; (e) the  $\text{Ni}_{30}\text{Cu}_2\text{C}_4$  core of  $[\text{H}_{6-n}\mathbf{1}]^{n-}$  ( $n = 3-6$ ) and (f)  $\text{Ni}_{34}\text{C}_4$  core of  $[\text{H}\text{Ni}_{34}\text{C}_4(\text{CO})_{38}]^{5-}$  [65] (Ni, green;  $\text{Ni}_{\text{interstitial}}$ , purple; Cu, orange; C, black).

The two additional  $\text{Ni}(\text{CO})$  fragments which cap two of the four square faces of the  $\text{Ni}_{24}$  polyhedron and form the two mono-capped trigonal prismatic cavities are fundamental in order to understand the structures of all this series of clusters, since they are present in  $[\text{H}_2\mathbf{1}]^{4-}$ , whereas they are partially absent in all other structures. The  $[\text{NMe}_3(\text{CH}_2\text{Ph})]_4[\text{H}_2\text{Ni}_{30-x}\text{C}_4(\text{CO})_{34-x}\{\text{Cu}(\text{CH}_3\text{CN})\}_2]\cdot 2\text{CH}_3\text{CN}$  ( $x \sim 0.35$ ) salt contains the  $[\text{H}_2\text{Ni}_{30-x}\text{C}_4(\text{CO})_{34-x}\{\text{Cu}(\text{CH}_3\text{CN})\}_2]^{4-}$  anion which is actually a mixture of  $[\text{H}_2\mathbf{1}]^{4-}$  and  $[\text{H}_2\mathbf{2}]^{4-}$  (figure 4.2.7). Similarly

$[\text{NMe}_4]_3[\text{H}_3\text{Ni}_{30-x}\text{C}_4(\text{CO})_{34-x}\{\text{Cu}(\text{NCC}_6\text{H}_4\text{CN})\}_2] \cdot 3.5\text{CH}_3\text{COCH}_3$  ( $x \sim 0.52$ ) contains  $[\text{H}_3\text{Ni}_{30-x}\text{C}_4(\text{CO})_{34-x}\{\text{Cu}(\text{NCC}_6\text{H}_4\text{CN})\}_2]^{3-}$ , *i.e.*,  $[\text{H}_3\mathbf{6}]^{3-}$  and  $[\text{H}_3\mathbf{7}]^{3-}$  (figure 4.2.8).

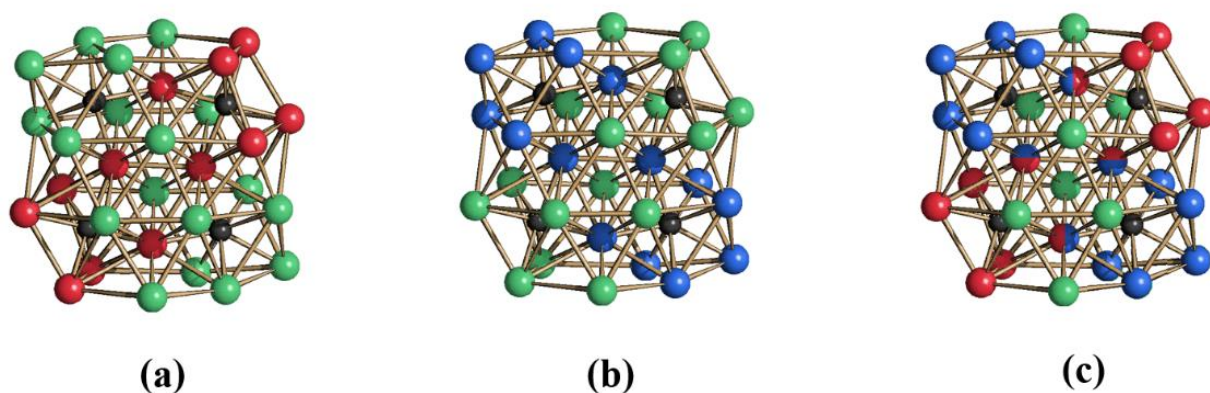


**Figure 4.2.5** In  $\text{Ni}_{30}\text{C}_4$  framework, two carbide atoms are located in trigonal prismatic (**a**, red) and trigonal prismatic mono-capped (**b**, blu) cages. An inversion centre relates the cages with the same colour. In the representation (**c**) the bicolour metals are shared between two cages ( $\text{Ni}_{\text{general}}$ , green; C, black).

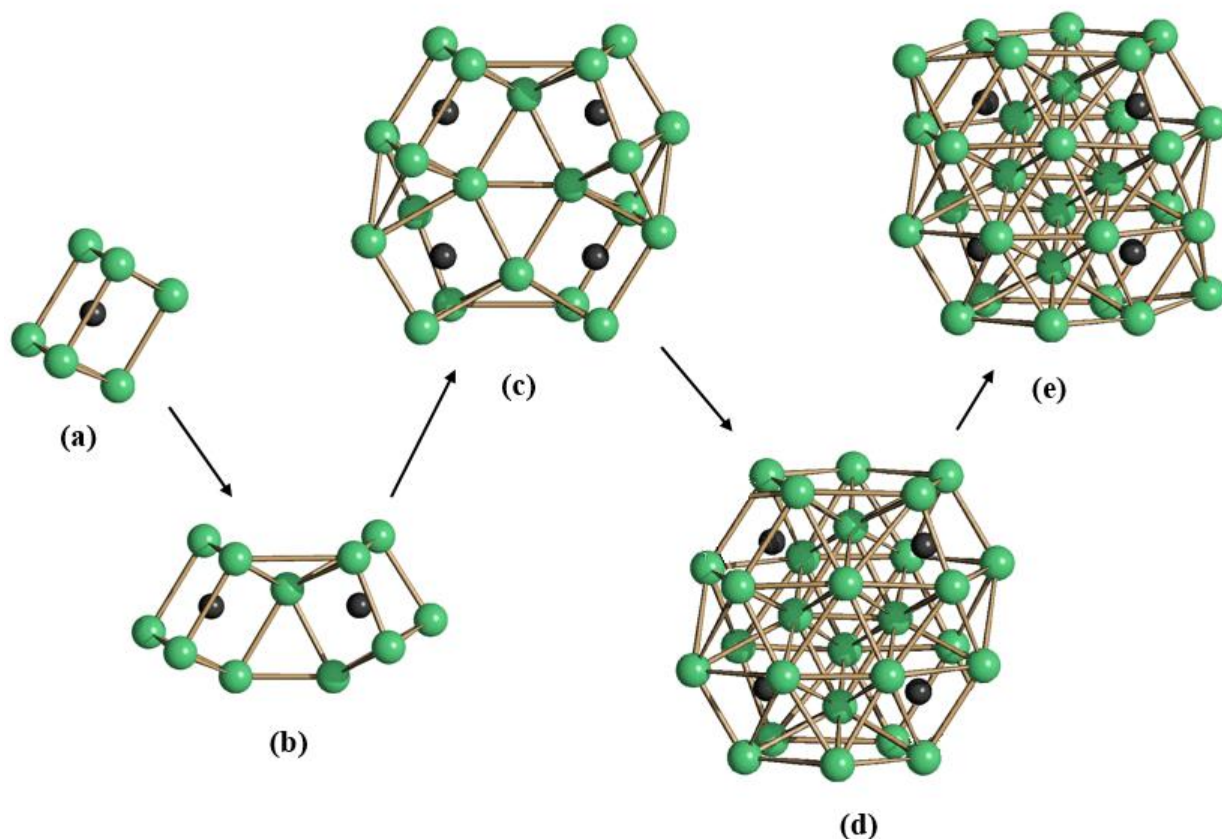


**Figure 4.2.6** Stepwise reconstruction of  $[\text{H}_2\mathbf{1}]^{4-}$ : (**a**)  $\text{Ni}_6\text{C}$  trigonal prismatic cage; (**b**)  $\text{Ni}_{11}\text{C}_2$  framework obtained by the condensation of two  $\text{Ni}_6\text{C}$  cages sharing the Ni corner; (**c**)  $\text{Ni}_{20}\text{C}_4$  framework obtained by the addition of two other  $\text{Ni}_6\text{C}$  cages sharing two Ni corners; (**d**) addition of further 8 nickel atoms shared between the different cages that results in  $\text{Ni}_{28}\text{C}_4$  framework; (**e**) the final  $\text{Ni}_{30}\text{C}_4$  structure (Ni, green; C, black).

They are closely related to  $[\text{H}_2\mathbf{1}]^{4-}$  displaying the same  $\text{Ni}_{30}\text{C}_4$  cage. The major difference is due to the fact that the two  $\text{Ni}(\text{CO})$  fragments which complete the two mono-capped  $\text{Ni}_7\text{C}$  trigonal prismatic cages have in these two salts fractional occupancy factors, since they comprise co-crystallised mixtures of  $\text{Ni}_{30}\text{C}_4(\text{CO})_{34}\text{Cu}_2$  and  $\text{Ni}_{29}\text{C}_4(\text{CO})_{33}\text{Cu}_2$  species.

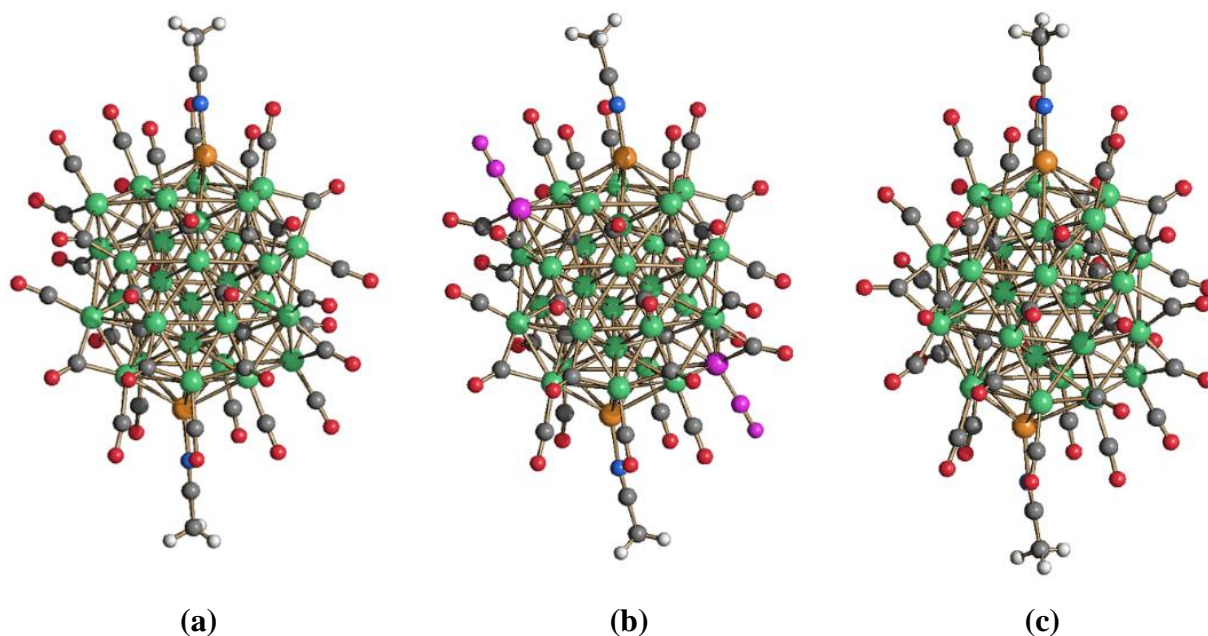


**Figure 4.2.7** Molecular structures of (a)  $[\text{H}_2\mathbf{1}]^{4-}$ , (b)  $[\text{H}_2\mathbf{2}]^{2-}$  and (c)  $[\text{H}_3\mathbf{4}]^{2-}$  (Ni, green; Cu, orange; N, blue; C, grey; O, red; H, white; Ni(CO) fragments with fractionary occupancy factors in purple).

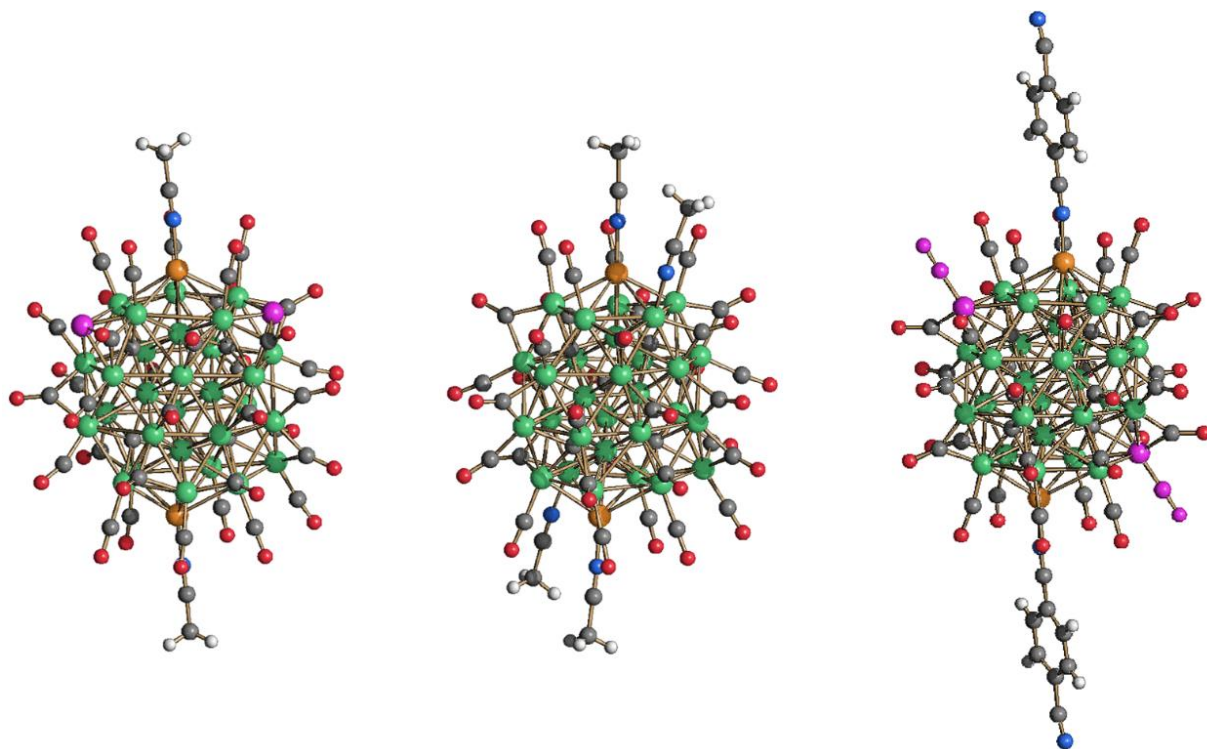


**Figure 4.2.8** Molecular structures of (a)  $[\text{H}_2\mathbf{3}]^{2-}$ , (b)  $[\text{H}_2\mathbf{5}]^{2-}$  and (c)  $[\text{H}_3\mathbf{6}]^{3-}/[\text{H}_3\mathbf{7}]^{3-}$  (Ni, green; Cu, orange; N, blue; C, grey; O, red; H, white; Ni(CO) fragments with fractionary occupancy factors in purple).

It must be remarked that in  $[\text{H}_3\mathbf{6}]^{3-}$  and  $[\text{H}_3\mathbf{7}]^{3-}$ ,  $\text{CH}_3\text{CN}$  has been replaced by  $\text{NCC}_6\text{H}_4\text{CN}$ , and this might be exploited in order to polymerise the clusters. Moreover, the  $[\text{H}_2\text{Ni}_{30-x}\text{C}_4(\text{CO})_{34-x}\{\text{Cu}(\text{CH}_3\text{CN})\}_2]^{4-}$  anions display the same stereochemistry of the CO ligands as in  $[\text{H}_2\mathbf{1}]^{4-}$ , whereas the  $[\text{H}_3\text{Ni}_{30-x}\text{C}_4(\text{CO})_{34-x}\{\text{Cu}(\text{NCC}_6\text{H}_4\text{CN})\}_2]^{3-}$  tri-anion shows some differences, since it displays 16 terminal CO, 16 edge bridging and two face bridging ligands.

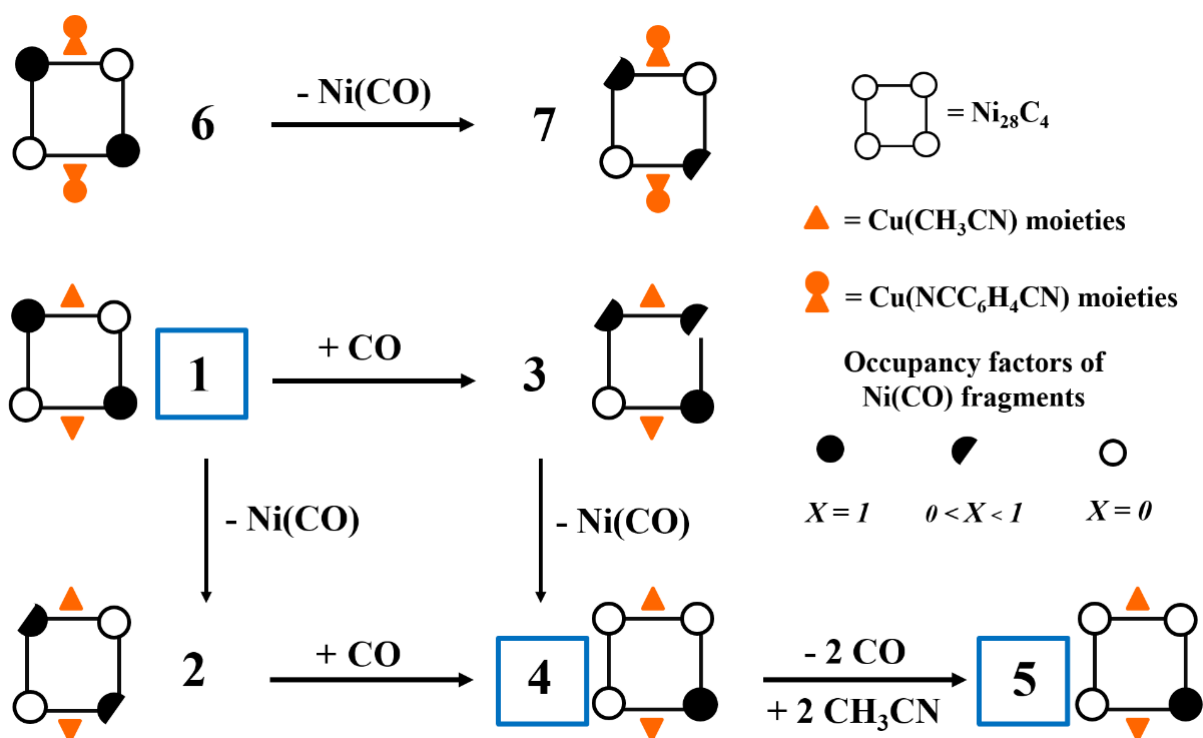
The  $[\text{H}_2\mathbf{5}]^{2-}$  and  $[\text{H}_2\mathbf{4}]^{2-}$  anions differ from the previous  $[\text{H}_2\mathbf{1}]^{4-}$ ,  $[\text{H}_2\mathbf{2}]^{4-}$ ,  $[\text{H}_3\mathbf{6}]^{3-}$  and  $[\text{H}_3\mathbf{7}]^{3-}$  compound since one of the two Ni atoms forming the two  $\text{Ni}_7\text{C}$  cages in  $[\text{H}_2\mathbf{1}]^{4-}$ , and corresponding to the  $\text{Ni}(\text{CO})$  fragments with fractional occupancy factors in the co-crystallised mixtures of  $[\text{H}_2\mathbf{1}]^{4-}/[\text{H}_2\mathbf{2}]^{4-}$  and  $[\text{H}_3\mathbf{6}]^{3-}/[\text{H}_3\mathbf{7}]^{3-}$  is now completely missing resulting in  $\text{Ni}_{29}$  clusters. Thus, the carbide atoms in  $[\text{H}_2\mathbf{4}]^{2-}$  and  $[\text{H}_2\mathbf{5}]^{2-}$  are enclosed within three trigonal prismatic  $\text{Ni}_6\text{C}$  cages and a single mono-capped trigonal prismatic  $\text{Ni}_7\text{C}$  cage. This results in a slight deformation of the metal cage of the clusters which allows the presence of 34 ligands attached to the 29 Ni-atoms. It must be remarked that if these two anions were simply derived from  $[\text{H}_2\mathbf{1}]^{4-}$  by missing a  $\text{Ni}(\text{CO})$  fragment, they should display 33 ligands attached to Ni. The presence of a further two-electrons ligand probably justify the fact that  $[\text{H}_2\mathbf{4}]^{2-}$  and  $[\text{H}_2\mathbf{5}]^{2-}$  are dianions and not tetra-anions as  $[\text{H}_2\mathbf{1}]^{4-}$ . Moreover, the reduced charge on these cluster anions makes the substitution of CO with  $\text{CH}_3\text{CN}$  easier than in the above tetra-anions. Thus, the  $[\text{H}_2\mathbf{4}]^{2-}$  anion contains 16 terminal, 16 edge bridging and 2 face bridging carbonyls bonded to Ni-atoms, whereas the stereochemistry of the ligands bonded to Ni in  $[\text{H}_2\mathbf{5}]^{2-}$  comprises 2 terminal  $\text{CH}_3\text{CN}$  as well as 14 terminal, 16 edge bridging and 2 face bridging CO ligands.

The structure of  $[\text{NMe}_4]_2[\text{H}_2\text{Ni}_{29+x}\text{C}_4(\text{CO})_{34+x}\{\text{Cu}(\text{CH}_3\text{CN})\}_2] \cdot 3.39\text{thf}$  ( $x \sim 0.3$ ) is closely related to  $[\text{H}_2\mathbf{4}]^{2-}$ , since the  $[\text{H}_2\text{Ni}_{29+x}\text{C}_4(\text{CO})_{34+x}\{\text{Cu}(\text{CH}_3\text{CN})\}_2]^{2-}$  cluster anion present within this salt is actually a co-crystallised mixture of  $[\text{H}_2\mathbf{4}]^{2-}$  and  $[\text{H}_2\mathbf{3}]^{2-}$ . The former displays 16 terminal, 16 edge bridging and 2 face bridging CO ligands. In addition, there are two  $\text{Ni}(\text{CO})$  fragments with fractional occupancy factors in positions corresponding to the capping of two trigonal prismatic  $\text{Ni}_6\text{C}$  cages, which generate the  $\text{Ni}_{30}\text{C}_4(\text{CO})_{35}$  cluster corresponding to  $[\text{H}_2\mathbf{3}]^{2-}$ . Scheme 4.2.2 reports the structural relationship between the bimetallic Ni-Cu frameworks of **1**, **2**, **3**, **4**, **5**, **6** and **7** clusters.

#### *Electrochemical studies and EHMO analysis*

The electrochemical behaviour of  $[\text{H}_{6-n}\mathbf{1}]^{n-}$  ( $n = 4, 5, 6$ ),  $[\text{H}_2\mathbf{4}]^{2-}$  and  $[\text{H}_2\mathbf{5}]^{2-}$ , which can be obtained as pure crystals, has been investigated by means of cyclic voltammetry (table 4.2.4). The solubility of these clusters is in all case rather limited in the presence of the supporting

electrolyte in large excess. Moreover, these species may undergo protonation/deprotonation equilibria in solution as previously described. As a result, the electrochemical patterns have never a high resolution, and their interpretation may be taken with some care. Rest potential has been directly measured by the potentiostat and the anodic/cathodic nature of the processes has been unambiguously established by hydrodynamic voltammetry (with periodic renewal of the diffusion layer obtained by the periodical percussion of the electrode).



**Scheme 4.2.2** Structural relationship between the bimetallic Ni-Cu frameworks of **1**, **2**, **3**, **4**, **5**, **6** and **7** clusters. The blue gridded species may be obtained as pure crystals while the other compounds are isolated as mixtures.

The  $[\text{H}_2\mathbf{1}]^{4-}$  tetra-anion shows one oxidation ( $E^{\circ}_{3-/4-} = -0.29$  V) and three reduction ( $E^{\circ}_{4-/5-} = -0.55$  V;  $E^{\circ}_{5-/6-} = -0.79$  V;  $E^{\circ}_{6-/7-} = -0.98$  V) processes with some features of chemical reversibility, but little electrochemical reversibility. Conversely, in the case of the  $[\text{H}\mathbf{1}]^{5-}$  penta-anion, only three reduction processes ( $E^{\circ}_{5-/6-} = -0.62$  V;  $E^{\circ}_{6-/7-} = -1.04$  V;  $E^{\circ}_{7-/8-} = -1.40$  V) with some features of chemical reversibility may be distinguished. Finally, the fully deprotonated hexa-anion  $[\mathbf{1}]^{6-}$  presents one oxidation ( $E^{\circ}_{5-/6-} = -0.45$  V) and three reduction processes ( $E^{\circ}_{6-/7-} = -0.83$  V;  $E^{\circ}_{7-/8-} = -1.03$  V;  $E^{\circ}_{8-/9-} = -1.44$  V).

The most relevant conclusion from these data is that species with different charges (and, thus, in our formulation, with a different number of hydrides) show a different voltammetric behaviour, indirectly confirming their nature of poly-hydrides and the protonation/deprotonation equilibria.

Compound	E°							Solvent
	2-/3-	3-/4-	4-/5-	5-/6-	6-/7-	7-/8-	8-/9-	
[H <sub>2</sub> 1] <sup>4-</sup>	-	-0.29	-0.55	-0.79	-0.98	-	-	Acetone
[H1] <sup>5-</sup>	-	-	-	-0.62	-1.04	-1.40	-	CH <sub>3</sub> CN
[1] <sup>6-</sup>	-	-	-	-0.45	-0.83	-1.03	-1.44	dmf
[H <sub>2</sub> 4] <sup>2-</sup>	-0.32	-0.68	-1.06	-1.34	-	-	-	Acetone
[H <sub>2</sub> 5] <sup>2-</sup>	-0.32	-0.60	-1.03	-1.67	-	-	-	CH <sub>3</sub> CN

**Table 4.2.4** Formal redox potential referred to SCE (in V) of the redox actives [H<sub>6-n</sub>1]<sup>n-</sup> (n = 4, 5, 6), [H<sub>2</sub>4]<sup>2-</sup> and [H<sub>2</sub>5]<sup>2-</sup> species. [Cluster] = 5·10<sup>-3</sup> M. [NBu<sub>4</sub>][BF<sub>4</sub>] (0.1 M) supporting electrolyte. Scan Rate 0.1 V/s.

Moreover, the electrochemical behaviour of [1]<sup>6-</sup> is somehow reminiscent of the one previously reported for the iso-structural and iso-electronic [Ni<sub>30</sub>C<sub>4</sub>(CO)<sub>34</sub>(CdCl)<sub>2</sub>]<sup>6-</sup> which displayed one oxidation (E°<sub>5-/6-</sub> = -0.49 V) and two reduction processes (E°<sub>6-/7-</sub> = -0.88 V; E°<sub>7-/8-</sub> = -1.28 V). This is probably due to the robustness and electronic status of their common Ni<sub>30</sub>C<sub>4</sub>(CO)<sub>34</sub> framework which makes them to behave as electron sinks. It must be remarked that only at very negative potentials Cu-reduction followed by anodic stripping occurs, further supporting the capacity of these clusters to delocalise and stabilise the added electrons preventing the deposition of Cu-metal. This was easily predictable for the analogous Ni-Cd tetra-carbides in view of the very electropositive nature of cadmium, whereas it is quite remarkable for a nobler metal such as copper. Furthermore, the [H<sub>6-n</sub>1]<sup>n-</sup> (n = 4, 5, 6) clusters display ΔE between consecutive redox couples of *ca.* 0.2-0.4 V, indicating the incipient metallisation of their metal cores.

The cyclic voltammogram of [H<sub>2</sub>4]<sup>2-</sup> displays four reduction processes (E°<sub>2-/3-</sub> = -0.32 V; E°<sub>3-/4-</sub> = -0.68 V; E°<sub>4-/5-</sub> = -1.06 V; E°<sub>5-/6-</sub> = -1.34 V) with features of chemical reversibility. Its first reduction occurs at less negative potentials than for [H<sub>2</sub>1]<sup>4-</sup> (E°<sub>4-/5-</sub> = -0.55 V) in agreement with its minor negative charge. It is noteworthy that [H<sub>2</sub>5]<sup>2-</sup> displays an electrochemical behaviour very similar to [H<sub>2</sub>4]<sup>2-</sup> indicating that the substitution of two CO ligands with two CH<sub>3</sub>CN molecules in such large clusters does not significantly alter their electrochemical properties.

Thus, the cyclic voltammetric profiles of [1]<sup>6-</sup>, [H1]<sup>5-</sup>, [H<sub>2</sub>1]<sup>4-</sup>, [H<sub>2</sub>5]<sup>2-</sup> and [H<sub>2</sub>4]<sup>2-</sup> display almost equally spaced redox waves. These correspond to oxidations and reductions steps with features of reversibility on the cyclic voltammetric time scale. As a result, the plots of their formal potential versus the charge z of the most reduced species involved in the redox couple display an almost perfect linear fit (figure 4.2.8).

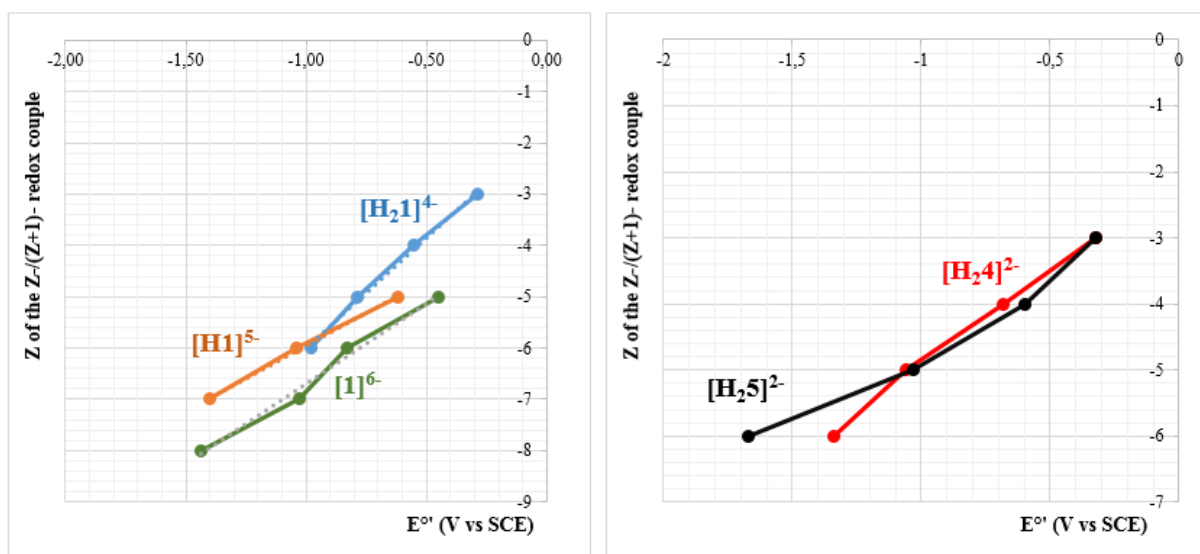


**Figure 4.2.8** Linear trend of  $z$ -plots vs formal redox potential ( $E^\circ$  vs SCE) of  $[\text{H}_{6-n}\mathbf{1}]^{z-}$  ( $z = 4, 5, 6$ ). The graphic indicates that the first reduction of the  $[\text{H}_{6-n}\mathbf{1}]^{z-}$  ( $z = 4, 5, 6$ ) clusters occurs at more negative potentials by increasing the value of  $z$ , in agreement with the more negative charge of the oxidised species.

The redox behaviour of the MCCs herein described prompted a study of their electronic status by means of Extended Hückel Molecular Orbital (EHMO) with CACAO [62]. Calculations have been performed for  $[\mathbf{1}]^{6-}$ ,  $[\mathbf{4}]^{4-}$  and  $[\mathbf{5}]^{4-}$ , which have been studied via electrochemistry. The diagram of  $[\mathbf{2}]^{6-}$  has been also calculated for comparison. The frontier region of the EHMO diagrams of these clusters is shown in figure 4.2.9.  $[\mathbf{1}]^{6-}$  and  $[\mathbf{2}]^{6-}$  clusters, which differ only for a missing Ni(CO) fragment in the latter, display very similar diagrams, with the last two electrons occupying two almost degenerate Molecular Orbitals (MOs). Above these semi-occupied orbitals, there is a nearly continuum of MOs without a well defined HOMO-LUMO gap. This is in keeping with the observed propensity of  $[\text{H}_{6-n}\mathbf{1}]^{n-}$  ( $n = 4, 5, 6$ ) to undergo both oxidation and reduction processes.

The cluster  $[\mathbf{4}]^{4-}$ , which is iso-electronic to  $[\text{H}_2\mathbf{4}]^{2-}$  and  $[\mathbf{2}]^{6-}$ , may be derived from the latter by adding a further CO ligand and reducing the charge of two units in order to maintain the same number of electrons. By comparing figures 4.2.9(b) and 4.2.9(c), it is clear that this operation makes the two almost degenerate semi-occupied MOs of  $[\mathbf{2}]^{6-}$  to be split introducing a HOMO-LUMO gap in  $[\mathbf{4}]^{4-}$  of 0.285 eV. This is still rather small and does not inhibit the redox properties of these clusters. Finally, the EHMO diagram of  $[\mathbf{5}]^{4-}$  indicates that substitution of two CO in  $[\mathbf{4}]^{4-}$  with two  $\text{CH}_3\text{CN}$  molecules to give  $[\mathbf{5}]^{4-}$  does not significantly alter the electronic status of the cluster, as also demonstrated by electrochemical studies.

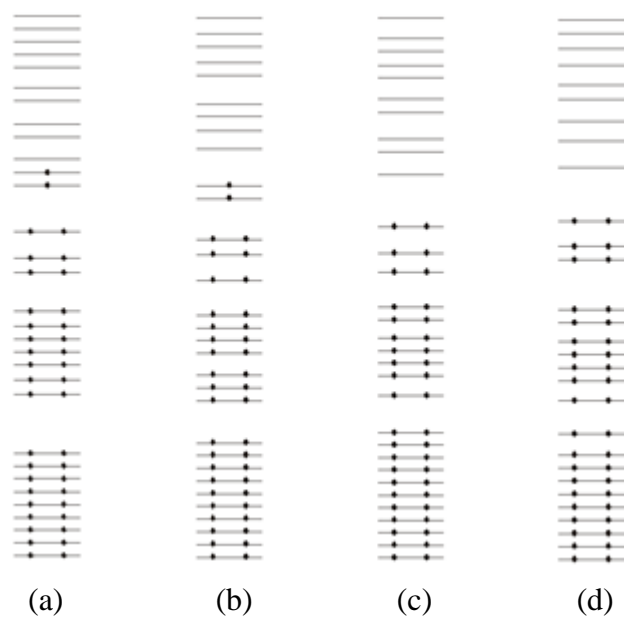


**Figure 4.2.9** Frontier region (in the  $-11$  to  $-9$  eV interval of energy) of the EHMO diagram of **(a)**  $[1]^{6-}$ ; **(b)**  $[2]^{6-}$ ; **(c)**  $[4]^{4-}$  and **(d)**  $[5]^{4-}$ .

## Final Remarks

In the absence of interstitial hetero-atoms, high nuclearity homo- and bi-metallic clusters adopt compact (*ccp*, *hcp* or a combination of the two) or poly-icosahedral structures. Conversely, the presence of interstitial hetero-atoms, such as carbon, perturbs the growth of the metal cages resulting in more complex and less regular structures. The stabilizing effect of interstitial main group elements in metal carbonyl clusters was demonstrated several years ago, and is exemplified by the preparation and characterization of numerous species containing a large variety of interstitial atoms.

In this chapter, the synthesis and the characterization of new bimetallic Ni-Co and Ni-Cu carbide clusters has been described. A renewed interest in this area arises from the possibility to get information on the building-up of bulky carbide phases, the formation of metal-carbide nano-alloys and the role of metal nanoparticles as catalysts for the preparation of carbon nanotubes or graphene sheets.

Our work point out the capacity of carbide atoms in Ni and Ni-Co carbonyl clusters to be lodged in rather different cavities as well as to form tightly bonded C<sub>2</sub>-units. In particular in the case of [H<sub>6-n</sub>Ni<sub>36</sub>Co<sub>8</sub>C<sub>8</sub>(CO)<sub>48</sub>]<sup>n-</sup> (n = 3-6) and [H<sub>6-n</sub>Ni<sub>22</sub>Co<sub>6</sub>C<sub>6</sub>(CO)<sub>36</sub>]<sup>n-</sup> (n = 3-6) the carbides are located within Ni<sub>5</sub>Co<sub>2</sub>C mono-capped trigonal prismatic and Ni<sub>7</sub>CoC square antiprismatic cages respectively. In the case of Ni-Cu carbide carbonyl clusters such as [H<sub>6-n</sub>Ni<sub>30</sub>C<sub>4</sub>(CO)<sub>34</sub>{Cu(CH<sub>3</sub>CN)}<sub>2</sub>]<sup>n-</sup> (n = 3-6) the carbides are encapsulated within trigonal prismatic and mono-capped trigonal prismatic cages. These clusters approach the nano-size regime showing an incipient metallization of their energy levels in the molecular orbital diagram and are multivalent.

The [Ni<sub>9</sub>Co(C<sub>2</sub>)(CO)<sub>16-x</sub>]<sup>3-</sup> (x = 0, 1) trianions are closely related to the previously reported [Ni<sub>10</sub>(C<sub>2</sub>)(CO)<sub>16</sub>]<sup>2-</sup>, [Co<sub>3</sub>Ni<sub>7</sub>(C<sub>2</sub>)(CO)<sub>15</sub>]<sup>3-</sup> and [Co<sub>3</sub>Ni<sub>7</sub>(C<sub>2</sub>)(CO)<sub>16</sub>]<sup>n-</sup> (n = 2, 3). These species display very complex and irregular metal cages, which are required in order to accommodate the interstitial carbon atoms confirming that the metal core in ligand-stabilized clusters is rather deformable and soft. It behaves more like a liquid metal drop that adapts itself to the surface and/or interstitial ligands rather than a solid close-packed metal chunk. It is, therefore, not surprising that the diffusion and mobility of carbon atoms into “nearly liquid” Co and Ni nanoparticles have been claimed as the basis of the growth of carbon nanotubes and other graphitic nanomaterials promoted by these catalysts.

It is noteworthy that the two monoacetylides with a different number of carbonyls show the same Ni<sub>9</sub>Co cage. This is rather rare in MCCs, being [Rh<sub>12</sub>Sn(CO)<sub>27-x</sub>]<sup>3-</sup> (x = 0-2) the most relevant example previously reported in the literature. It is noteworthy, that these Rh-Sn clusters were easily and reversibly interchanged via addition and thermal elimination of CO. Conversely, such an inter-change has not been observed in the case of [Ni<sub>9</sub>CoC<sub>2</sub>(CO)<sub>16</sub>]<sup>3-</sup> and [Ni<sub>9</sub>CoC<sub>2</sub>(CO)<sub>15</sub>]<sup>3-</sup> suggesting that these two clusters are formed together during the degradation of [Ni<sub>22</sub>Co<sub>6</sub>C<sub>6</sub>(CO)<sub>36</sub>]<sup>6-</sup>.

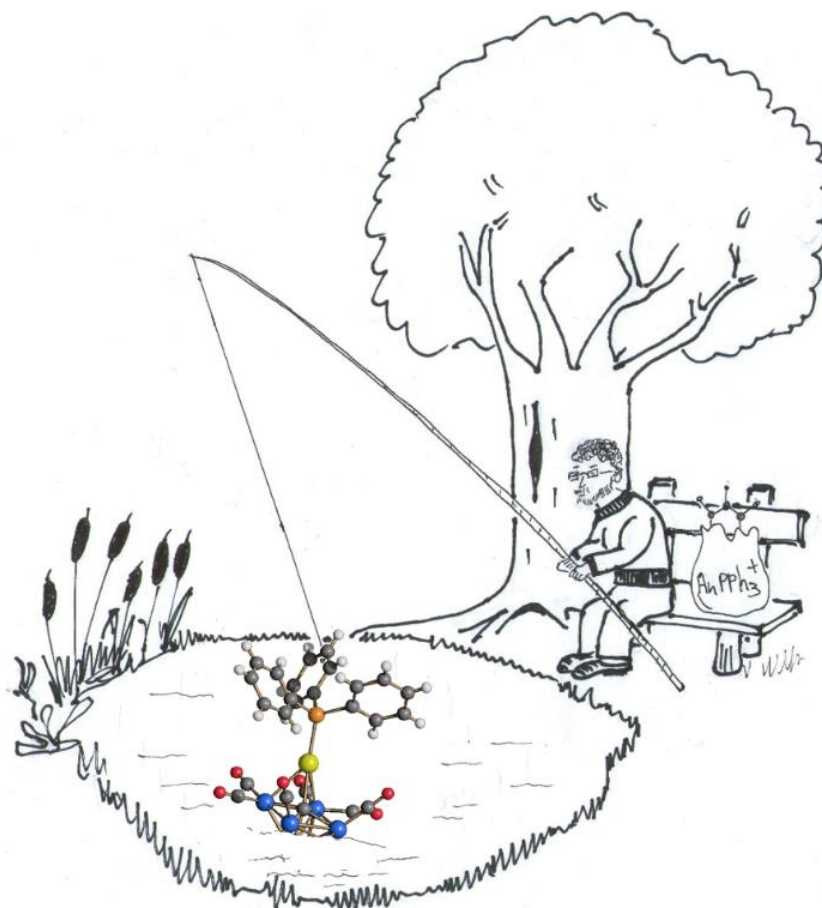
[H<sub>6-n</sub>Ni<sub>36</sub>Co<sub>8</sub>C<sub>8</sub>(CO)<sub>48</sub>]<sup>n-</sup> (n = 3-6) and [H<sub>6-n</sub>Ni<sub>30</sub>C<sub>4</sub>(CO)<sub>34</sub>{Cu(CH<sub>3</sub>CN)}<sub>2</sub>]<sup>n-</sup> (n = 3-6) display inner Ni<sub>32</sub>C<sub>6</sub> and Ni<sub>30</sub>C<sub>4</sub> cores, respectively, that are present in other known clusters such as [Ni<sub>32</sub>C<sub>6</sub>(CO)<sub>36</sub>]<sup>6-</sup> and [HNi<sub>38</sub>C<sub>6</sub>(CO)<sub>42</sub>]<sup>5-</sup> for the former, and [HNi<sub>34</sub>C<sub>4</sub>(CO)<sub>38</sub>]<sup>5-</sup> and [H<sub>6-n</sub>Ni<sub>30</sub>C<sub>4</sub>(CO)<sub>34</sub>{CdX}<sub>2</sub>]<sup>n-</sup> (n = 3-6; X = Cl, Br, I) for the Ni<sub>30</sub>C<sub>4</sub> kernel. These two metal cores can be viewed as *starting seeds* for the growth of higher nuclearity clusters. In particular, the [H<sub>6-n</sub>Ni<sub>36</sub>Co<sub>8</sub>C<sub>8</sub>(CO)<sub>48</sub>]<sup>n-</sup> (n = 3-6) clusters contain a second metal-carbide shell that starts to grow around the inner one, envisioning the possibility of preparing molecular polycarbide clusters containing different metal-carbide shells.

The growth of such starting seeds, which leads to nano-clusters, is not a trivial task as it has already been observed in chapter 2.2. Indeed, with the increase of the nuclearity, the incipient metallization leads to the disappearance of the molecular features giving a family of related compounds that differ for a few metal atoms as has been mentioned in the case of Ni-Cu tetra-carbides clusters. The observed crystal disorder in such bimetallic compounds is particularly significant and may appear to be borderline between mixtures of molecular clusters or *quasi*-molecular clusters with very low polydispersity.



# New Bimetallic Carbonyl Clusters Containing Au(I) Units

On the basis of their chemical-physical properties and their wide applications in different fields of chemistry and biology, gold nanoparticles represent a hot topic contributing to a continuous development of nanochemistry and nanotechnologies. New innovative approaches have allowed a great diversification of the research interests. In this chapter, two different routes for the synthesis of bimetallic Co-Au and Ni-Au carbonyl clusters are presented. In particular, the reactions of homometallic precursors with  $\text{Au}(\text{PPh}_3)\text{Cl}$  give different surface decorated compounds that seem to be an interesting platform in order to test aurophilicity.



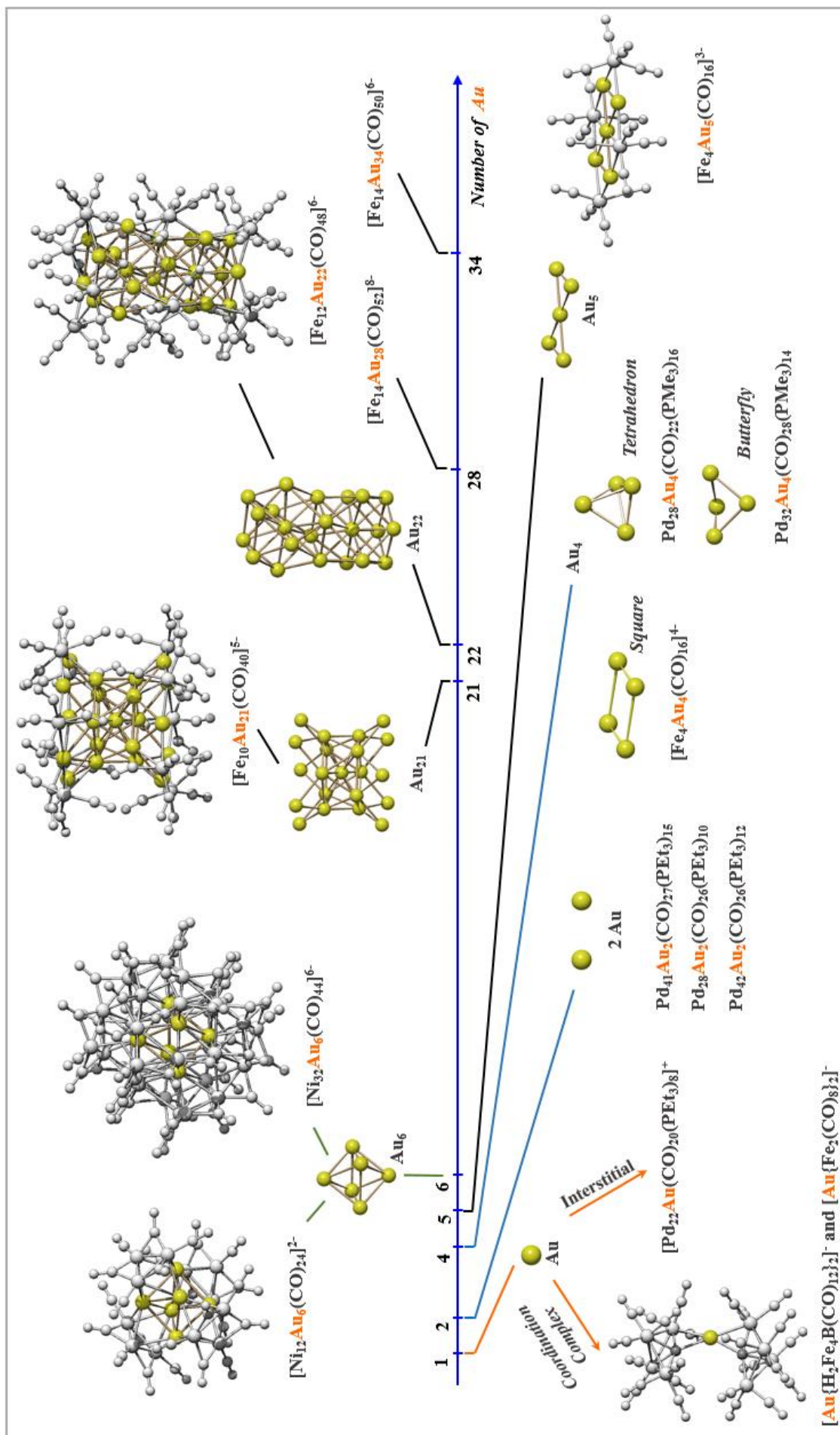


Figure 5.1.1 Known bimetallic carbonyl clusters containing naked gold atoms arranged on the basis of gold-nuclearity.

## Investigation on the Redox Condensation of $[\text{Ni}_6(\text{CO})_{12}]^{2-}$ with Au(III) Salts

### 5.1.1 Bimetallic carbonyl clusters containing naked gold atoms: an overview

Redox condensation is one of the main ways to generate bimetallic M-Au carbonyl clusters from commonly available gold salts and preformed metal carbonyls. Figure 5.1.1 reports some examples of bimetallic carbonyl clusters containing naked gold atoms divided into three main categories:

- bimetallic Ni-Au core-shell clusters (green line);
- surface decorated gold clusters (black line);
- bimetallic Pd-Au heteroleptic carbonyl clusters and coordination complex (orange line).

The synthesis of bimetallic Fe-Au clusters consists in the redox condensation between  $[\text{Fe}_3(\text{CO})_{11}]^{2-}$  and  $[\text{AuCl}_4]^-$  [67]. The first product is  $[\text{Fe}_4\text{Au}_5(\text{CO})_{16}]^{3-}$  followed by the formation of other bimetallic Au-Fe clusters with nanosized dimensions. Their metal frames consist of an inner Au core decorated by  $\text{Fe}(\text{CO})_4$  and  $\text{Fe}(\text{CO})_3$  fragments. With the exception of  $[\text{Fe}_{12}\text{Au}_{22}(\text{CO})_{48}]^{6-}$ , Au fragments of  $C_5$  local symmetry seem to dominate all structures. It is noteworthy that the metal cores of these nanosized Au-Fe carbonyl clusters contain a number of metal atoms in a zero oxidation state minor than in the formula.

Only two examples of carbonyl clusters containing a single naked Au-atom are known, *i.e.*,  $[\text{Au}\{\text{H}_2\text{Fe}_4\text{B}(\text{CO})_{12}\}_2]^-$  and  $[\text{Pd}_{22}\text{Au}(\text{CO})_{20}(\text{PEt}_3)_8]^+$ . The former may be viewed as a homoleptic Au(I) complex containing two  $[\text{H}_2\text{Fe}_4\text{B}(\text{CO})_{12}]^-$  clusters as ligands. Conversely, in  $[\text{Pd}_{22}\text{Au}(\text{CO})_{20}(\text{PEt}_3)_8]^+$  the Au atom is located in a fully interstitial position with a formal Au(I) oxidation state [46].<sup>20</sup> This compound is a versatile precursor for the preparation of other three bimetallic Au-Pd clusters, *i.e.*,  $\text{Pd}_{21}\text{Au}_2(\text{CO})_{20}(\text{PEt}_3)_{10}$ ,<sup>21</sup>  $\text{Pd}_{42}\text{Au}_2(\text{CO})_{30}(\text{PEt}_3)_{12}$  and  $\text{Pd}_{28}\text{Au}_2(\text{CO})_{26}(\text{PEt}_3)_{10}$  whose Au atoms are individually located in fully interstitial positions

<sup>20</sup> The  $\text{Au}^+$  configuration  $6s^0$  is electronically equivalent to that of the corresponding zerovalent Pd atoms  $5s^0$ , therefore the  $[\text{Pd}_{22}\text{Au}(\text{CO})_{20}(\text{PEt}_3)_8]^+$  cluster may be viewed as a formal substitution of the interstitial  $\mu_{12}$ -Pd with  $\text{Au}^+$  in  $\text{Pd}_{23}(\text{CO})_{20}(\text{PEt}_3)_8$ .

<sup>21</sup> On the basis of the different nature of one Au that is coordinated to  $\text{PEt}_3$  ligand,  $\text{Pd}_{21}\text{Au}_2(\text{CO})_{20}(\text{PEt}_3)_{10}$  is not reported in the figure 5.1.1. The other naked Au is located in fully interstitial position.

without direct Au-Au bonds [68]. Examples of clusters with semi-interstitial Au atoms are not known even if, for long time  $[\text{Pd}_{14}\text{Tl}_2(\text{CO})_9(\text{PEt}_3)_4]^{2+}$  and  $[\text{Pd}_9\text{Tl}(\text{CO})_9(\text{PEt}_3)_6]^+$  compounds had been reported as  $\text{Pd}_{14}\text{Au}_2$  and  $\text{Pd}_9\text{Au}$  clusters. The highest Au nuclearity for bimetallic Au-Pd clusters is four in  $\text{Pd}_{28}\text{Au}_4(\text{CO})_{22}(\text{PMe}_3)_{16}$  and  $\text{Pd}_{32}\text{Au}_4(\text{CO})_{28}(\text{PMe}_3)_{14}$  in which the Au cores display tetrahedral and butterfly framework, respectively.

### 5.1.2 Core-shell bimetallic Ni-Au carbonyl clusters: state of the art

It has been more than three decades since L. F. Dahl announced the discovery of  $[\text{Ni}_{12}\text{Au}_6(\text{CO})_{24}]^{2-}$ . It consists of a  $\text{Au}_6$  octahedral core decorated on the surface by four  $\text{Ni}_3(\text{CO})_{12}$  units. The product was isolate from the reaction of  $[\text{Ni}_6(\text{CO})_{12}]^{2-}$  with  $\text{Au}(\text{PPh}_3)\text{Cl}$  in the attempt to obtain a new surface decorated nickel carbonyl cluster [69a]:

*It was hoped that the trigonal faces of the trigonal-antiprismatic (pseudo-octahedral)  $[\text{Ni}_6(\text{CO})_{12}]^{2-}$  dianions would serve as viable sites for the coordination of  $[\text{AuPPh}_3]^+$  fragments. No such cluster adduct was isolated. Rather, in addition to small amounts of the known  $\text{Au}_{11}(\text{PPh}_3)_7\text{Cl}_3$  cluster, a new gold nickel cluster,  $[\text{Ni}_{12}\text{Au}_6(\text{CO})_{24}]^{2-}$ .*

In the light of the low Ni-Ni bond energy it is reasonable to consider  $[\text{Ni}_6(\text{CO})_{12}]^{2-}$  as a poor candidate as a platform in order to anchor  $[\text{AuPPh}_3]^+$  fragments. For instance, the presence of a carbide plays a key role in the stabilization of the final adduct as reported in the case of  $\text{Ni}_6\text{C}(\text{CO})_9(\text{AuPPh}_3)_4$  (see chapter 7.1).

The  $\text{Ni}_{12}\text{Au}_6$  core consists in a segregated bimetallic phase that may be envisioned as a molecular model for surface-science studies. Thermodynamic considerations concerning the “chemisorption-induced segregation” model predicts that in bimetallic nanoparticles, under ultrahigh vacuum, the metal component with the lower heat of sublimation should concentrate at the surface in order to lower the surface tension. This core-shell architecture can be reversed if an absorbate gas bind much more strongly to the other metal component with the higher heat of sublimation.

Thus, in the case of bimetallic Ni-Au nanoalloys<sup>22</sup> under *vacuum*, the gold atoms would concentrate at the surface based on a lower sublimation energy than nickel resulting in a nanoparticles with a Ni-core and a Au-shell (figure 5.1.2a). However, since CO chemisorbs on

<sup>22</sup> Bimetallic Ni-Au nanoalloys are well studied for catalytic steam reforming. They are more resistant than pure Ni particles toward carbon formation on the catalyst, which leads to catalysts deactivation. The resistance to carbon formation has been attributed to blocking of the high reactivity exposed edge and kink sites on the surface of the particle by larger Au atoms.

Ni much more strongly than on Au, an inverted configuration is expected in the presence of CO (Au-core and Ni-shell; figure 5.1.2b).

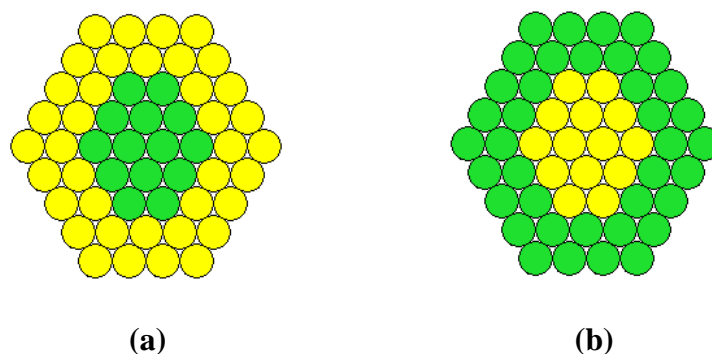


**Figure 5.1.2** Schematic representation of the two-inverted bimetallic Ni-Au core-shell architectures in (a) high vacuum and (b) CO atmosphere. The pictures show cross sections of the clusters (Au, yellow; Ni, green).

A few years later, the same author reported the synthesis of the higher nuclearity bimetallic Ni-Au compound  $[\text{Ni}_{32}\text{Au}_6(\text{CO})_{44}]^{6-}$  that displays a similar octahedral  $\text{Au}_6$  core.  $[\text{Ni}_{32}\text{Au}_6(\text{CO})_{44}]^{6-}$  was obtained in low yields by reacting  $\text{Au}(\text{PPh}_3)\text{Cl}$ ,  $\text{Ni}(\text{OAc})_2$  and  $[\text{Ni}_6(\text{CO})_{12}]^{2-}$  (molar ratio 1 : 3 : 2) in dmsO for 2 days [69b]. As shown by the comparison between the metal frameworks of  $[\text{Ni}_{32}\text{Au}_6(\text{CO})_{44}]^{6-}$  and  $[\text{Pt}_{38}(\text{CO})_{44}]^{2-}$ , the two clusters differ mainly in the top and bottom layers which in the former is a  $\mu_3$ -capped  $\nu_2$ - $\text{Ni}_6$  triangle, while in the other is a  $\text{Ni}_7$  centered hexagon (figure 5.1.3).

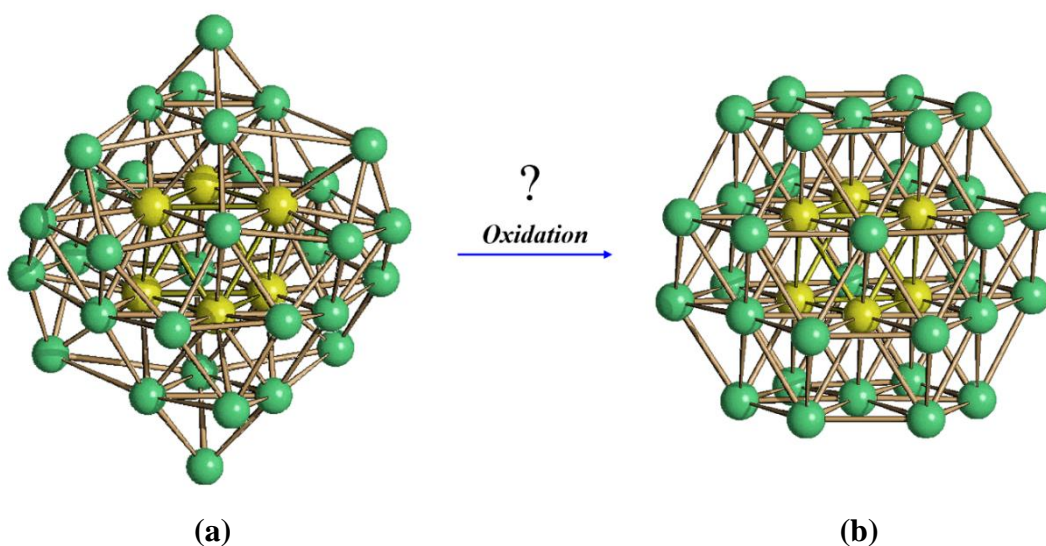


**Figure 5.1.3** Metal frameworks of (a)  $[\text{Ni}_{32}\text{Au}_6(\text{CO})_{44}]^{6-}$  and (b) its hypothetical oxidized product that is isoelectronic and isostructural to  $[\text{Pt}_{38}(\text{CO})_{44}]^{2-}$ . Very loose Ni-Ni contacts up to ca. 3.6 Å have been included in the drawing of the former for sake of clarity (Au, yellow; Ni, green).

The re-arrangement from **(b)** to **(a)** causes the loss of 6 M-M contacts. Probably as a consequence,  $[\text{Ni}_{32}\text{Au}_6(\text{CO})_{44}]^{6-}$  features 10 additional cluster valence electrons with respect to  $[\text{Pt}_{38}(\text{CO})_{44}]^{2-}$ . It was of interest to verify whether the structural conversion **(a)**  $\rightarrow$  **(b)** could occur upon oxidation of  $[\text{Ni}_{32}\text{Au}_6(\text{CO})_{44}]^{6-}$ , in view of the fact that it would only require sinking of the capping atoms in the centers of the  $v_2$  triangles with their swelling to give centered hexagons.

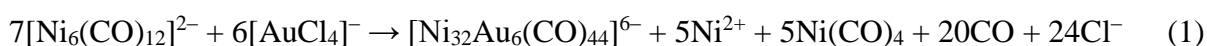
Unfortunately, the bimetallic metal carbonyl clusters  $[\text{Ni}_{32}\text{Au}_6(\text{CO})_{44}]^{6-}$  is isolable in low yield. Therefore the investigation of alternative routes is crucial in order to explore its chemical and electrochemical properties. On the basis of our experience gained on the synthesis of bimetallic high nuclearity metal carbonyl clusters, we decided to investigate the redox condensation of  $[\text{Ni}_6(\text{CO})_{12}]^{2-}$  with  $[\text{AuCl}_4]^-$  as a reasonable alternative reaction.

### 5.1.3 General Results

As expected, we found out that the redox condensation of  $[\text{Ni}_6(\text{CO})_{12}]^{2-}$  with  $[\text{AuCl}_4]^-$  leads to  $[\text{Ni}_{32}\text{Au}_6(\text{CO})_{44}]^{6-}$  as final product. Interestingly, the new  $[\text{Ni}_{12}\text{Au}(\text{CO})_{24}]^{3-}$  cluster has been isolated as intermediated compound [70]. The fact that both  $[\text{Ni}_{12}\text{Au}(\text{CO})_{24}]^{3-}$  and  $[\text{Ni}_{32}\text{Au}_6(\text{CO})_{44}]^{6-}$  have been obtained in high yields allowed us to investigate in detail their reactivity and electrochemical behavior. The results are summarized in figure 5.1.4. The reactions of  $[\text{Ni}_{12}\text{Au}(\text{CO})_{24}]^{3-}$  and  $[\text{Ni}_{32}\text{Au}_6(\text{CO})_{44}]^{6-}$  lead only to known species, *i.e.*,  $[\text{Ni}_5(\text{CO})_{12}]^{2-}$  and  $[\text{Ni}_6(\text{CO})_{12}]^{2-}$ . More interestingly,  $[\text{Ni}_{12}\text{Au}_6(\text{CO})_{24}]^{2-}$  has been spectroscopically identified as an intermediate in the CO induced degradation of  $[\text{Ni}_{32}\text{Au}_6(\text{CO})_{44}]^{6-}$ .

### 5.1.4 Synthesis and characterization of $[\text{Ni}_{32}\text{Au}_6(\text{CO})_{44}]^{6-}$

On the attempt to synthesize  $[\text{Ni}_{32}\text{Au}_6(\text{CO})_{44}]^{6-}$  in high yields, we have investigated the reaction of miscellaneous salts of  $[\text{Ni}_6(\text{CO})_{12}]^{2-}$  with  $[\text{AuCl}_4]^-$  in acetone, by adding increasing amounts of the Au(III) complex to the Ni carbonylate solution, and following the reaction *via* FT-IR. The highest yields of the target compound were obtained using *ca.* 0.9 moles of  $[\text{AuCl}_4]^-$  per mole of  $[\text{Ni}_6(\text{CO})_{12}]^{2-}$ , in accord to equation (1):



The compound was purified by removing the solvent *in vacuo*, washing the solid residue with water, toluene, thf and acetone, and extraction of pure  $[\text{Ni}_{32}\text{Au}_6(\text{CO})_{44}]^{6-}$  in  $\text{CH}_3\text{CN}$ . The resulting high yields (54% based on Au) confirms the versatility of the redox condensation reached for this synthesis.

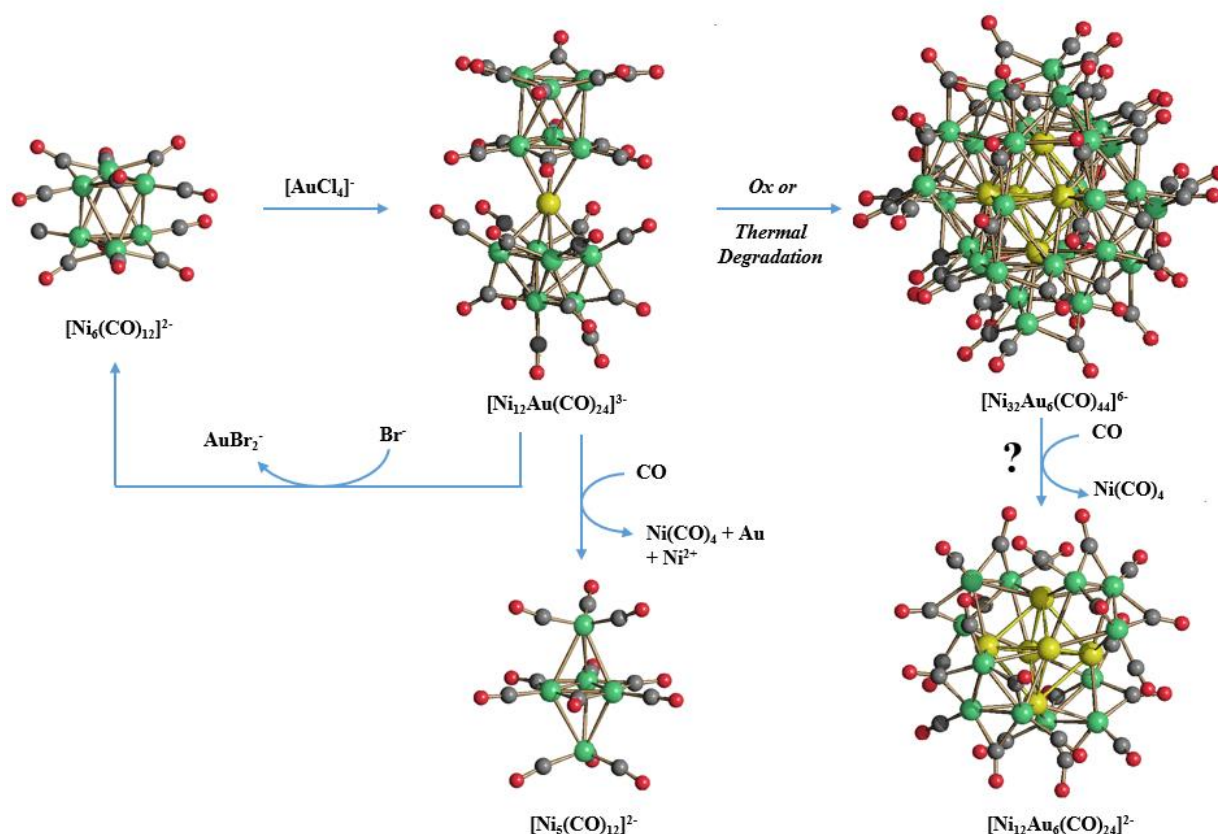
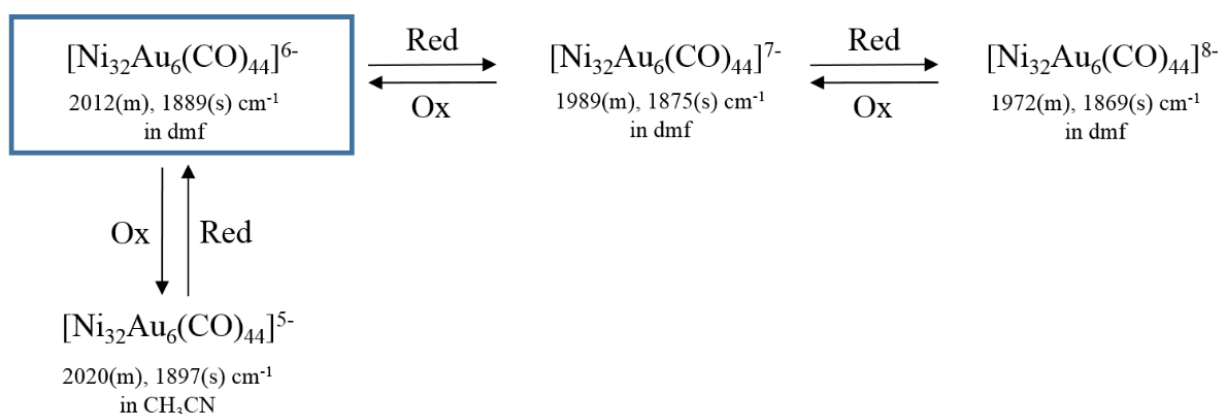


**Figure 5.1.4** Synthesis of the new  $[\text{Ni}_{12}\text{Au}(\text{CO})_{24}]^{3-}$  compound and its chemical relationship with other known clusters (Au, yellow; Ni, green; C, grey; O, red).

The availability in good yields of  $[\text{Ni}_{32}\text{Au}_6(\text{CO})_{44}]^{6-}$  made it possible to prompt an investigation of its chemical behavior. Thus,  $[\text{Ni}_{32}\text{Au}_6(\text{CO})_{44}]^{6-}$  is stepwise reduced to  $[\text{Ni}_{32}\text{Au}_6(\text{CO})_{44}]^{7-}$  and  $[\text{Ni}_{32}\text{Au}_6(\text{CO})_{44}]^{8-}$  by addition of Na/naphthalene in dmf (scheme 5.1.1).



**Scheme 5.1.1** Reversible reduction and oxidation reactions of  $[\text{Ni}_{32}\text{Au}_6(\text{CO})_{44}]^{n-}$  ( $n = 5-8$ ).  $[\text{Ni}_{32}\text{Au}_6(\text{CO})_{44}]^{6-}$  is the direct product of the redox condensation between  $[\text{Ni}_6(\text{CO})_{12}]^{2-}$  and  $[\text{AuCl}_4]^-$ . All  $[\text{Ni}_{32}\text{Au}_6(\text{CO})_{44}]^{n-}$  ( $n = 5-8$ ) species have been identified and characterized by means of IR spectroscopy and their nature further corroborated *via* electrochemical studies.

These reductions are chemically reversed by mild oxidizing agents. In view of the very negative potentials at which the reductions occur (see electrochemical studies), water is already a suitable oxidant and, thus, all attempts to isolate the reduced species failed. In fact, while trying to recover  $[\text{Ni}_{32}\text{Au}_6(\text{CO})_{44}]^{n-}$  ( $n = 7, 8$ ) from the dmf solutions by addition of aqueous  $[\text{NEt}_4]\text{Br}$ ,  $[\text{Ni}_{32}\text{Au}_6(\text{CO})_{44}]^{6-}$  was always obtained as the final product. Contrarily to initial expectations,  $[\text{Ni}_{32}\text{Au}_6(\text{CO})_{44}]^{6-}$  is only oxidized to a purported unstable  $[\text{Ni}_{32}\text{Au}_6(\text{CO})_{44}]^{5-}$  by means of  $[\text{C}_7\text{H}_7][\text{BF}_4]$ . Addition of this oxidizing agent in excess only led to complete decomposition.

$[\text{Ni}_{32}\text{Au}_6(\text{CO})_{44}]^{6-}$  reacts with carbon monoxide, eventually resulting in the formation of  $\text{Ni}(\text{CO})_4$  and Au metal. This decomposition process might be appealing since it seems to open the possibility of producing Au or Au-Ni clusters, rather than a gold mirror, once carried out in the presence of suitable ligands. Interestingly in the initial steps of the above degradation reaction the intermediate formation of a species showing IR absorptions very close to those of  $[\text{Ni}_{12}\text{Au}_6(\text{CO})_{24}]^{2-}$  could be observed. In spite of some efforts, we have been unable to stop the reaction at this stage and isolate this compound. Further studies might be carried out in order to isolate in satisfactory yields this elusive species.

### Electrochemical studies

The  $[\text{Ni}_{32}\text{Au}_6(\text{CO})_{44}]^{6-}$  nano-cluster undergoes five reductions at  $-0.74$  V,  $-1.06$  V,  $-1.30$  V,  $-1.58$  and  $-1.80$  V, with apparent features of reversibility and two irreversible oxidations at  $-0.36$  V and  $-0.18$  V (figure 5.1.5).

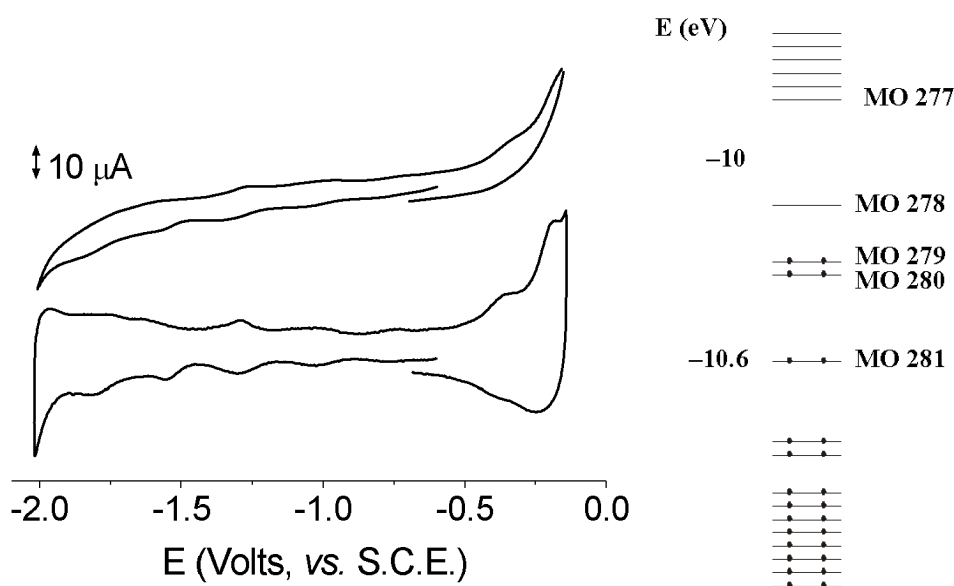


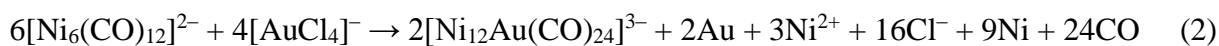
**Figure 5.1.5** Left: cyclic voltammogram (top) and deconvoluted cyclic voltammogram (bottom) recorded at a platinum electrode in acetonitrile solution of  $[\text{NBu}_4]_6[\text{Ni}_{32}\text{Au}_6(\text{CO})_{44}]$ , ( $1.1 \times 10^{-3}$  M).  $[\text{NBu}_4][\text{PF}_6]$  (0.2 M) supporting electrolyte. Scan rate 0.2 V/s. Right: frontier region (in the  $-11.5$  to  $-9.5$  eV interval of energy) of the EHMO diagram of  $[\text{Ni}_{32}\text{Au}_6(\text{CO})_{44}]^{6-}$ .

The peaks/current ratio would suggest that the number of electrons involved in the oxidations and in the third and fourth reductions could be the double of those involved in the first two reductions. Anyway, the low concentration obtained with this heavy cluster, which has also the property to foul the electrodes, as indicated by the fact that the signals are detected only with a platinum working electrode and with no other electrode material, deprives of true reliability any reasoning on the current intensity. Interestingly, all the redox processes are almost equally spaced by ~259 mV, which is a classic trait of interstitial clusters with this structural features. This value can be compared with the values of 400 and 300 mV respectively displayed by  $[\text{Pt}_{38}(\text{CO})_{44}]^{2-}$ ,  $[\text{H}_2\text{Ni}_{24}\text{Pt}_{14}(\text{CO})_{44}]^{4-}$  and  $[\text{HNi}_{38}\text{Pt}_6(\text{CO})_{48}]^{5-}$  which contain an encapsulated octahedron of Pt atoms and display an identical or slightly superior nuclearity.

The electronic properties of  $[\text{Ni}_{32}\text{Au}_6(\text{CO})_{44}]^{6-}$  have been investigated by means of Extended Hückel Molecular Orbital (EHMO) analysis, using the program CACAO [62] with its crystallographic coordinates. It is noteworthy that  $[\text{Ni}_{32}\text{Au}_6(\text{CO})_{44}]^{6-}$  displays a rather small HOMO-LUMO gap (0.196 eV), as usually found for multivalent metal carbonyl clusters (MCCs). Moreover, the propensity of  $[\text{Ni}_{32}\text{Au}_6(\text{CO})_{44}]^{6-}$  to be oxidized and reduced shown by these electrochemical experiments is in good agreement with its chemical behavior.

### 5.1.5 Synthesis and characterization of $[\text{Ni}_{12}\text{Au}(\text{CO})_{24}]^{3-}$

During the work up of  $[\text{Ni}_{32}\text{Au}_6(\text{CO})_{44}]^{6-}$ , the IR evidence of a new carbonyl species was observed in the acetone extraction. This new species becomes the major product by decreasing the amount of Au(III), *i.e.* 0.6-0.8 moles of  $[\text{AuCl}_4]^-$  per mole of  $[\text{Ni}_6(\text{CO})_{12}]^{2-}$ . This improved synthesis allowed the isolation and structural characterization of the new cluster, which resulted to be  $[\text{Ni}_{12}\text{Au}(\text{CO})_{24}]^{3-}$  as determined by single crystal X-ray diffraction as its  $[\text{NEt}_4]_3[\text{Ni}_{12}\text{Au}(\text{CO})_{24}]$  salt. Its formation requires 0.67 moles of  $[\text{AuCl}_4]^-$  per mole of  $[\text{Ni}_6(\text{CO})_{12}]^{2-}$  in a rather good agreement with the experiments:



In detail,  $[\text{NEt}_4][\text{AuCl}_4]$  is added in small portions to an acetone solution of  $[\text{NEt}_4]_2[\text{Ni}_6(\text{CO})_{12}]$  and the solvent removed *in vacuo* after two hours. The residue is washed with water, toluene and thf, and the crude product extracted in acetone. Crystals suitable for X-ray analysis of  $[\text{NEt}_4]_3[\text{Ni}_{12}\text{Au}(\text{CO})_{24}]$  were obtained by slow diffusion of isopropyl alcohol over the acetone solution. The formation of  $[\text{Ni}_{12}\text{Au}(\text{CO})_{24}]^{3-}$  is always accompanied by small amounts of  $[\text{Ni}_{32}\text{Au}_6(\text{CO})_{44}]^{6-}$ . Nonetheless, the two products can be easily separated since the former is soluble in acetone and the latter only in  $\text{CH}_3\text{CN}$ . The two clusters display distinct FT-

IR and electronic spectra (figure 5.1.6). In particular,  $[\text{Ni}_{12}\text{Au}(\text{CO})_{24}]^{3-}$  shows a strong absorption at 416 nm, whereas  $[\text{Ni}_{32}\text{Au}_6(\text{CO})_{44}]^{6-}$  displays a nearly featureless spectrum with a small shoulder at *ca.* 274 nm. These different electronic spectra are in keeping with the different nuclearities of these clusters. Thus, the smaller  $[\text{Ni}_{12}\text{Au}(\text{CO})_{24}]^{3-}$  shows a molecular-like spectrum, whereas  $[\text{Ni}_{32}\text{Au}_6(\text{CO})_{44}]^{6-}$  displays an UV-visible spectrum similar to those of small metal nanoparticles.

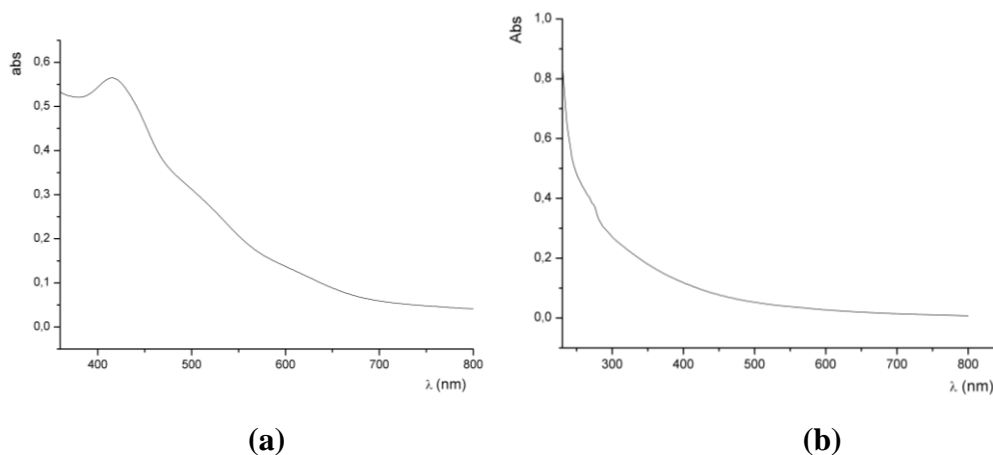
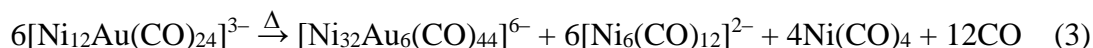


**Figure 5.1.6** UV-visible spectra of (a)  $[\text{Ni}_{12}\text{Au}(\text{CO})_{24}]^{3-}$  (in acetone) and (b)  $[\text{Ni}_{32}\text{Au}_6(\text{CO})_{44}]^{6-}$  (in  $\text{CH}_3\text{CN}$ ). Cluster concentration  $\approx 10^{-5}$  M.

$[\text{Ni}_{12}\text{Au}(\text{CO})_{24}]^{3-}$  is converted into  $[\text{Ni}_{32}\text{Au}_6(\text{CO})_{44}]^{6-}$  after addition of further  $[\text{AuCl}_4]^-$ .  $[\text{Ni}_{12}\text{Au}(\text{CO})_{24}]^{3-}$  is thermally unstable. In fact, after refluxing in acetone under  $\text{N}_2$  atmosphere, it is completely converted into a mixture of  $[\text{Ni}_{32}\text{Au}_6(\text{CO})_{44}]^{6-}$ ,  $[\text{Ni}_6(\text{CO})_{12}]^{2-}$  and  $\text{Ni}(\text{CO})_4$  in agreement with equation (3):



Similarly,  $[\text{Ni}_{12}\text{Au}(\text{CO})_{24}]^{3-}$  reacts with  $\text{HBF}_4$  yielding  $[\text{Ni}_{32}\text{Au}_6(\text{CO})_{44}]^{6-}$  and  $\text{Ni}(\text{CO})_4$ , as the only carbonyl products, in accord to equation (4):



In addition, the oxidation of  $[\text{Ni}_{12}\text{Au}(\text{CO})_{24}]^{3-}$  with  $[\text{C}_7\text{H}_7][\text{BF}_4]$  affords, once again,  $[\text{Ni}_{32}\text{Au}_6(\text{CO})_{44}]^{6-}$  which is further oxidized to  $[\text{Ni}_{32}\text{Au}_6(\text{CO})_{44}]^{5-}$ . Conversely, by treating an acetone solution of  $[\text{Ni}_{12}\text{Au}(\text{CO})_{24}]^{3-}$  under CO at room temperature,  $[\text{Ni}_5(\text{CO})_{12}]^{2-}$  and  $\text{Ni}(\text{CO})_4$  are formed as the only carbonyl products:



Indeed, as described in the crystal structure section,  $[\text{Ni}_{12}\text{Au}(\text{CO})_{24}]^{3-}$  may be viewed as a complex composed by two  $[\text{Ni}_6(\mu\text{-CO})_6(\text{CO})_6]^{2-}$  ligands coordinated to a central  $\text{Au}^+$  ion, and the CO-induced conversion of  $[\text{Ni}_6(\mu\text{-CO})_6(\text{CO})_6]^{2-}$  to  $[\text{Ni}_5(\text{CO})_{12}]^{2-}$  and  $\text{Ni}(\text{CO})_4$  is a well known process.

In agreement with the above hypothesis,  $[\text{Ni}_{12}\text{Au}(\text{CO})_{24}]^{3-}$  is converted into  $[\text{Ni}_6(\text{CO})_{12}]^{2-}$  after addition of an excess of  $\text{Br}^-$  ions. This reaction is likely to be a nucleophilic substitution where the two  $[\text{Ni}_6(\text{CO})_{12}]^{2-}$  coordinated to Au(I) in  $[\text{Ni}_{12}\text{Au}(\text{CO})_{24}]^{3-}$  are replaced by two bromide ions as follow:



### Crystal structure

The crystal structure of  $[\text{NEt}_4]_3[\text{Ni}_{12}\text{Au}(\text{CO})_{24}]$  has been determined by X-ray crystallography (figure 5.1.7). The  $[\text{Ni}_{12}\text{Au}(\text{CO})_{24}]^{3-}$  cluster anion can be described as being composed of two  $[\text{Ni}_6(\mu\text{-CO})_6(\text{CO})_6]^{2-}$  units coordinated to a central  $\text{Au}^+$  cation. It is remarkable that the two  $[\text{Ni}_6(\mu\text{-CO})_6(\text{CO})_6]^{2-}$  units display different structures and coordination modes to the Au(I) center.

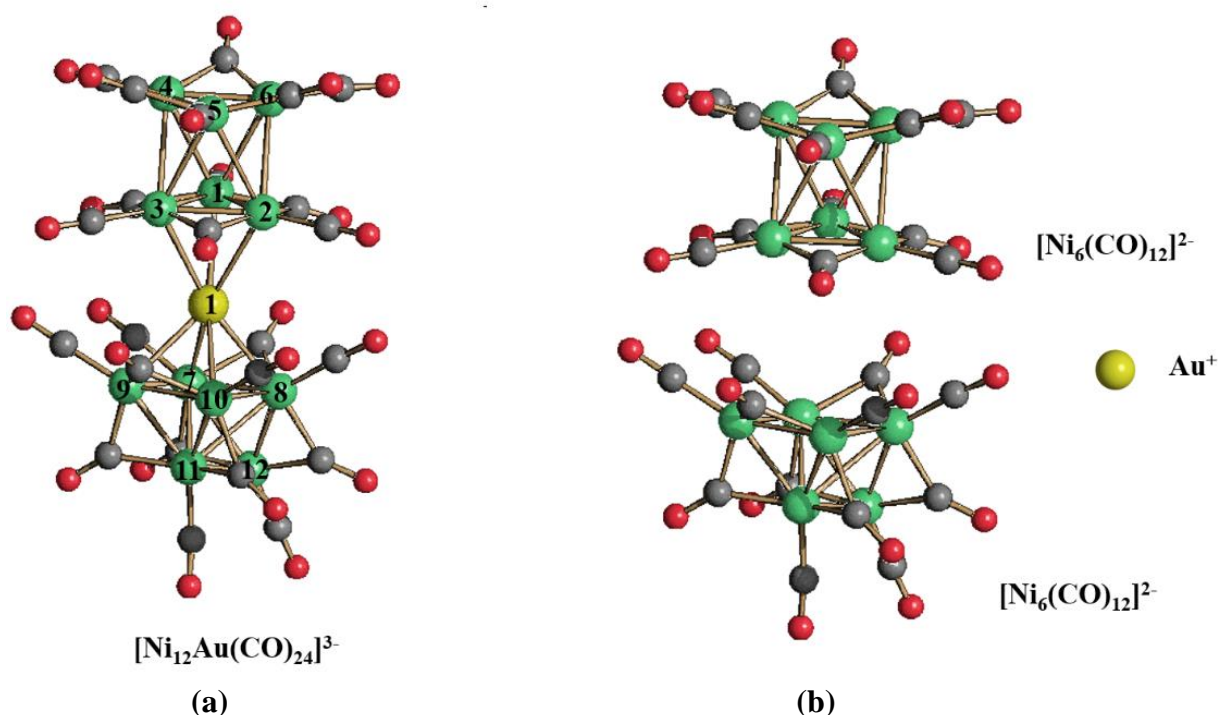


**Figure 5.1.7** (a) Molecular structure of  $[\text{Ni}_{12}\text{Au}(\text{CO})_{24}]^{3-}$  with key atoms labeled and (b) view of its separated components (Au, yellow; Ni, green; C, grey; O, red).

Thus, one  $[\text{Ni}_6(\mu\text{-CO})_6(\text{CO})_6]^{2-}$  unit adopts the usual trigonal anti-prismatic structure previously found in the parent  $[\text{Ni}_6(\mu\text{-CO})_6(\text{CO})_6]^{2-}$  free dianion. As for the free dianion, this  $[\text{Ni}_6(\mu\text{-CO})_6(\text{CO})_6]^{2-}$  unit contains six terminal CO ligands and six  $\mu\text{-CO}$  bridging the six edges of the two triangular bases of the trigonal anti-prism. This unit is coordinated to Au(I) *via* a  $\text{Ni}_3$  face, which is known to possess the character of a soft Lewis base.

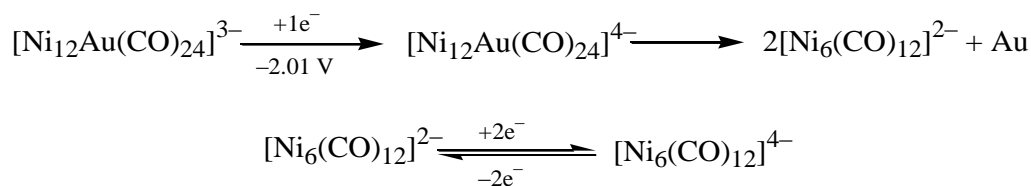
The second  $[\text{Ni}_6(\mu\text{-CO})_6(\text{CO})_6]^{2-}$  unit can be viewed as a distorted monocapped square pyramid. This unit is coordinated to Au(I) through the square base of the pyramid. Alternatively, this  $\text{Ni}_6$  framework may be described as a distorted trigonal prism, coordinated to Au(I) *via* a lateral square face and having the remaining two square faces heavily compressed along a diagonal. As a consequence, whereas in the trigonal anti-prismatic  $[\text{Ni}_6(\mu\text{-CO})_6(\text{CO})_6]^{2-}$  unit there were twelve Ni-Ni contacts at bonding distances, in this distorted trigonal prismatic unit there are only eleven contacts at bonding distances.

Also in this unit there are six terminal CO (one per Ni atom) and six  $\mu\text{-CO}$  bridging the edges of the two triangular bases of the trigonal prism. The angle formed between Au and the centroids of the  $\text{Ni}_3$  and  $\text{Ni}_4$  faces is  $173.77(2)^\circ$ , in agreement with the classical diagonal coordination of Au(I). A similar situation was found in  $[\text{H}_4\text{Fe}_8\text{AuB}_2(\text{CO})_{24}]^-$ , where the central  $\text{Au}^+$  cation was coordinated to two triangular  $[\text{H}_2\text{Fe}_4\text{B}(\text{CO})_{12}]^-$  units (figure 5.1.1).

### *Electrochemistry of $[\text{Ni}_{12}\text{Au}(\text{CO})_{24}]^{3-}$*

The trianion  $[\text{Ni}_{12}\text{Au}(\text{CO})_{24}]^{3-}$  undergoes both cathodic and anodic processes, which will be discussed separately (scheme 5.1.2, figure 5.1.8).

In the cathodic region, it undergoes a chemically irreversible mono-electronic reduction at  $-2.01$  V, followed by a chemically reversible two-electron reduction at  $-2.42$  V. This latter process is observed at the same potential for the free  $[\text{Ni}_6(\text{CO})_{12}]^{2-}$  cluster. Therefore, it is likely that  $[\text{Ni}_{12}\text{Au}(\text{CO})_{24}]^{3-}$  is irreversibly reduced at  $-2.01$  V to Au(0) and  $[\text{Ni}_6(\text{CO})_{12}]^{2-}$ , followed by the reversible reduction of the latter at  $-2.42$  V.



**Scheme 5.1.2** Irreversible mono-electron and reversible two-electrons reductions of  $[\text{Ni}_{12}\text{Au}(\text{CO})_{24}]^{3-}$  and  $[\text{Ni}_6(\text{CO})_{12}]^{2-}$ , respectively

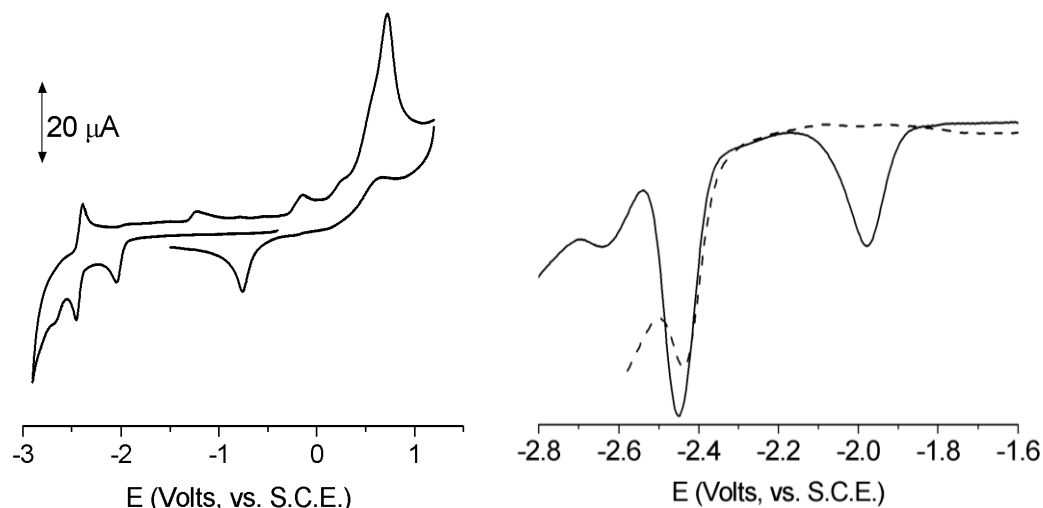


**Figure 5.1.8** Left: Cyclic voltammogram recorded at a gold electrode in thf solution of  $[\text{NBu}_4]_3[\text{Ni}_{12}\text{Au}(\text{CO})_{24}]$  ( $1.5 \times 10^{-3} \text{ M}$ ). Right: Osteryoung square-wave voltammograms recorded at a gold electrode in a thf solution of  $[\text{Ni}_{12}\text{Au}(\text{CO})_{24}]^{3-}$  before (full line) and after (dashed line) exhaustive electrolysis at  $E_w = -2.2 \text{ V}$ .  $[\text{NBu}_4][\text{PF}_6]$  (0.2 M) supporting electrolyte. Scan rate 0.2 V/s.

In agreement with this hypothesis, the frontier region of the EHMO diagram, calculated with CACAO, for  $[\text{Ni}_{12}\text{Au}(\text{CO})_{24}]^{3-}$  (figure 5.1.9) displays a rather large HOMO-LUMO gap (0.785 eV) and the LUMO receives contributions only from the two  $[\text{Ni}_6(\text{CO})_{12}]^{2-}$  moieties.

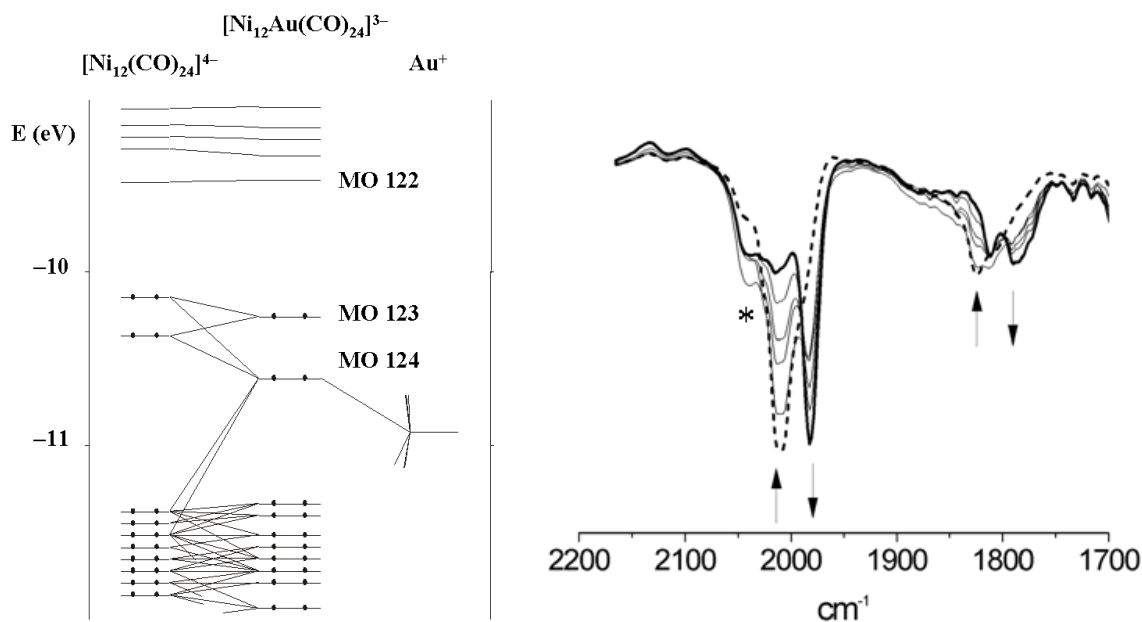


**Figure 5.1.9** Left: Frontier region (in the  $-11$  to  $-9 \text{ eV}$  interval of energy) of the EHMO diagram of  $[\text{Ni}_{12}\text{Au}(\text{CO})_{24}]^{3-}$ . Right: IR ex-situ spectroelectrochemistry showing the evolution of the probing  $\nu(\text{CO})$  stretching, from the original sample (dotted line) to the exhaustively electrolyzed one (full line), throughout the step-by-step reduction of  $[\text{Ni}_{12}\text{Au}(\text{CO})_{24}]^{3-}$ . \*,  $\uparrow$ ,  $\downarrow$  are the stretching of  $\text{NiCO}_4$ ,  $[\text{Ni}_{12}\text{Au}(\text{CO})_{24}]^{3-}$  and  $[\text{Ni}_6(\text{CO})_{12}]^{2-}$  respectively.

Thus, it is likely that, after reduction, the additional electron is delocalized over these Ni-CO units destabilizing the formal  $[\text{Ni}_{12}\text{Au}(\text{CO})_{24}]^{4-}$  adducts, which, in turn, undergoes an internal reduction to Au metal and  $[\text{Ni}_6(\text{CO})_{12}]^{2-}$ . The formation of  $[\text{Ni}_6(\text{CO})_{12}]^{2-}$ , obtaining after the reduction of  $[\text{Ni}_{12}\text{Au}(\text{CO})_{24}]^{3-}$ , has been confirmed by a bulk electrolysis experiment. In fact, the quantitative reduction ( $E_w = -2.2$  V) of the sample makes the brown solution of  $[\text{Ni}_{12}\text{Au}(\text{CO})_{24}]^{3-}$  to turn red, as expected for a solution of  $[\text{Ni}_6(\text{CO})_{12}]^{2-}$ , while the peak at  $-2.01$  V progressively disappears without altering the reduction process at  $-2.42$  V. Such a behavior is clearly illustrated in figure 5.1.8 in which the Osteryoung square wave voltammograms of the sample before and after the bulk electrolysis are compared.

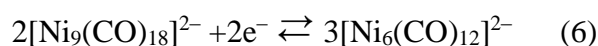
The unquestionable establishment of the nature of the product obtained after the irreversible reduction of  $[\text{Ni}_{12}\text{Au}(\text{CO})_{24}]^{3-}$  was obtained by IR *ex-situ* spectroelectrochemistry. Step-by step reduction reveals that the formation of  $[\text{Ni}_6(\text{CO})_{12}]^{2-}$  is not quantitative and is accompanied by the formation of side products such as the volatile complex  $\text{Ni}(\text{CO})_4$  (figure 5.1.9).

#### *Comparison of the electrochemical behavior of $[\text{Ni}_{12}\text{Au}(\text{CO})_{24}]^{3-}$ with other MCCs*

The features of the cathodic region of the cyclic voltammogram of  $[\text{Ni}_{12}\text{Au}(\text{CO})_{24}]^{3-}$  are more than evocative of what has been observed in the case of  $\{\text{Cd}_2\text{Cl}_3[\text{Ni}_6(\text{CO})_{12}]_2\}^{3-}$  and prompted a reinvestigation of the redox behavior of this latter, as well as that of the dianions  $[\text{Ni}_6(\text{CO})_{12}]^{2-}$  and  $[\text{Ni}_9(\text{CO})_{18}]^{2-}$ . In fact, in the paper describing the redox behavior of  $\{\text{Cd}_2\text{Cl}_3[\text{Ni}_6(\text{CO})_{12}]_2\}^{3-}$ , a reversible reduction at  $-2.43$  V was reported as also preceded by an ill-resolved irreversible peak, formerly interpreted as the sign of the presence of impurities.

Anyway, in the light of the present findings, a different interpretation appears to be more consistent. Really, once compared, as for the cathodic region in figure 5.1.10, the cyclic voltammograms of this family of clusters clearly reveal their relationships and may suggest that in all cases the one-electron irreversible reduction of  $[\text{X}\{\text{Ni}_6(\text{CO})_{12}\}_2]^{3-}$  ( $E_p = -2.01$  V for X=Au,  $E_p = -1.52$  V for X= $\text{Cd}_2\text{Cl}_3$ ) involves the detachment of the X unit connecting two  $[\text{Ni}_6(\text{CO})_{12}]^{2-}$  clusters, which subsequently undergo the expected reduction at about  $-2.42$  V.

Similarly, the irreversible reduction ( $E_p = -1.86$  V) of  $[\text{Ni}_9(\text{CO})_{18}]^{2-}$ , which is synthetically obtained by oxidation of  $[\text{Ni}_6(\text{CO})_{12}]^{2-}$ , is rapidly followed by the quantitative reformation of this latter, indicating the reversibility of the reaction as follow:



This interpretation of the redox behavior of this family of clusters is also consistent with the acid-base interaction existing between the soft Lewis base  $[\text{Ni}_6(\text{CO})_{12}]^{2-}$  and the acid fragment  $\text{X}^+$ . In fact, this interaction is broken as soon as the acidity of  $\text{X}^+$  is switched off by reduction. As in the previous work, the very negative cathodic value of the unique reversible process prevented any reliable coulometric determination of the number of electrons involved in this redox processes. Anyway, the second derivative of the Osteryoung square wave voltammograms indicates that, in all cases, the reversible reduction at about  $-2.42$  V, erroneously described as monoelectronic, actually involves the subsequent addition of two-electrons.

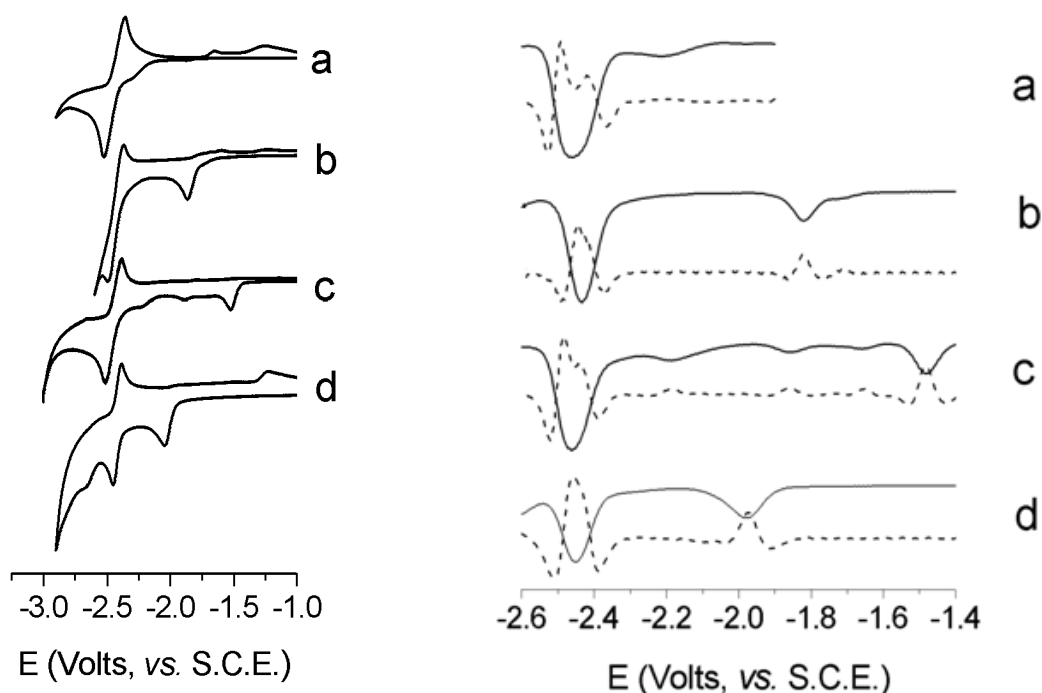


**Figure 5.1.10** (Left) Cyclic voltammograms and (right) osteryoung square-wave voltammograms (full line) with its second derivative (dashed line) recorded at a gold electrode in thf solution of: (a)  $[\text{Ni}_6(\text{CO})_{12}]^{2-}$ ; (b)  $[\text{Ni}_9(\text{CO})_{18}]^{2-}$ ; (c)  $\{\text{Cd}_2\text{Cl}_3[\text{Ni}_6(\text{CO})_{12}]_2\}^{3-}$ ; (d)  $[\text{Ni}_{12}\text{Au}(\text{CO})_{24}]^{3-}$ . Normalized currents of samples in mM concentration.  $[\text{NBu}_4][\text{PF}_6]$  (0.2 M) supporting electrolyte. Scan rate 0.2 V/s.

Finally, it may be noteworthy that a very similar behavior has been observed in the anodic region for all these compounds, which, after an unresolved multielectronic oxidation at  $\sim +0.7$  V generate a new, unidentified product which is reduced at  $-0.75$  V. An attempt to unambiguously identify this latter by IR spectroelectrochemistry performed on  $[\text{Ni}_{12}\text{Au}(\text{CO})_{24}]^{3-}$  had only modest success since the main difference between the IR spectrum of the original solution and that obtained after bulk electrolysis ( $E_w = +0.72$  V) is the appearance of a strong signal at  $2038\text{ cm}^{-1}$ , indicating the presence of  $\text{Ni}(\text{CO})_4$ . As a matter of fact, the electrolysis of  $[\text{Ni}_{12}\text{Au}(\text{CO})_{24}]^{3-}$  makes a brown powder to deposit on the electrode, so it is possible that the main product of the oxidation process is not detected by the IR technique.

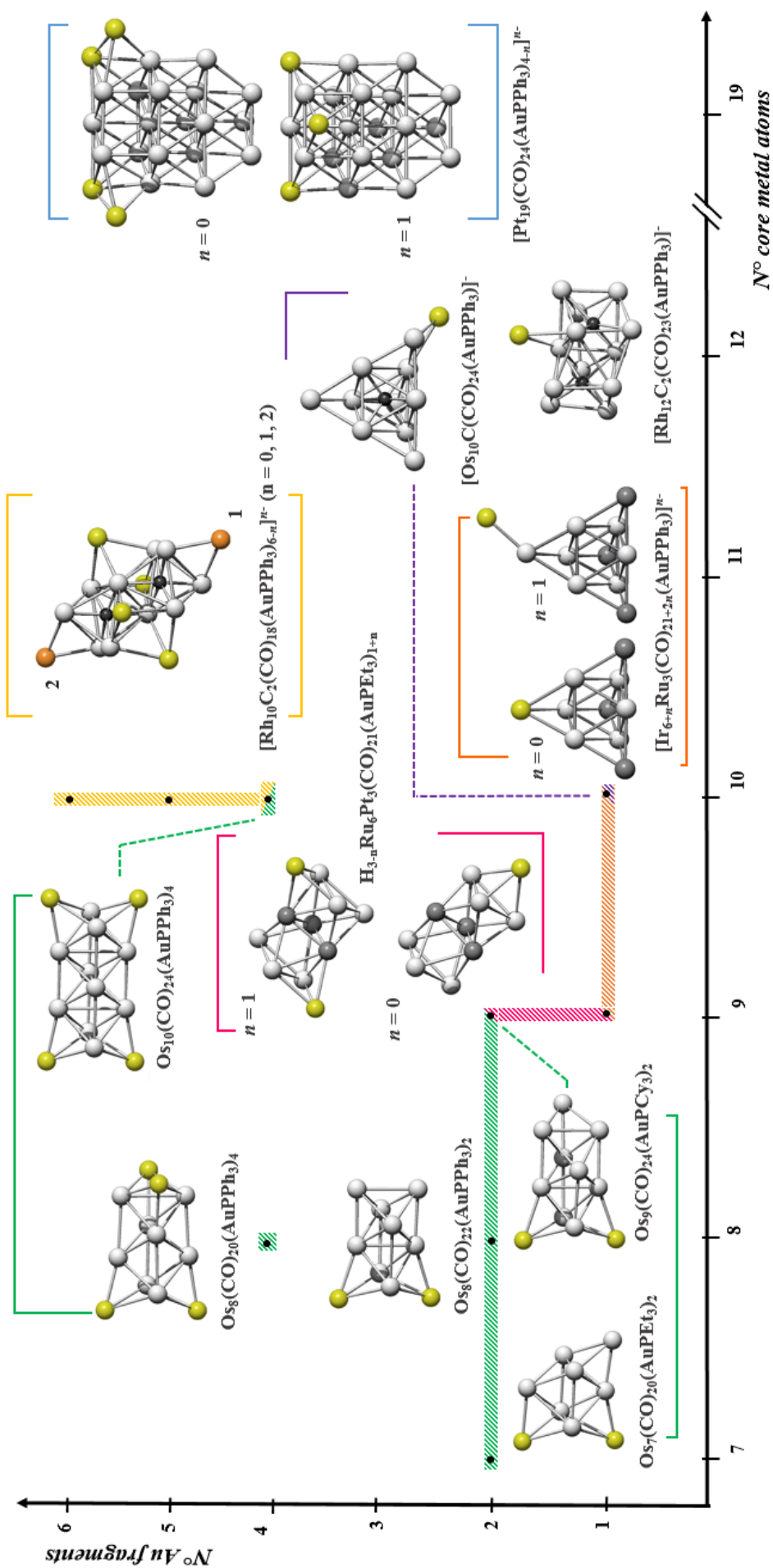


**Figure 5.2.1** Overview of homoleptic metal carbonyl clusters decorated on the surface by  $[\text{AuPPh}_3]^+$  fragments. The compounds are classified on the basis their metal core nuclearities without considering the contribution of the  $[\text{AuPPh}_3]^+$  fragments. The species belonging to the same family are limited by open rectangles. The phosphine units are not represented for the sake of clarity.

# Co<sub>6</sub>C Carbide Carbonyl Clusters Decorated by Gold(I) Phosphine Fragments

## 5.2.1 Introduction

Au(I) fragments have been widely employed as soft Lewis acids towards soft Lewis bases such as anionic metal carbonyl clusters in acid-base reactions resulting in the increase of nuclearity of the clusters. Several examples of such “fragment condensation”<sup>23</sup> are known in the literature. In these cases, the Au(I) fragment has been added to preformed anionic carbonyls in order to expand of a few units the nuclearity of the clusters. In other cases, on the basis of the isolobal analogy between [AuL]<sup>+</sup> and H<sup>+</sup>, the former have been used to have information on the protonation sites of anionic metal carbonyl clusters (see chapter 7.1.1). Alternatively, the reaction of carbonyl anions with Au(I) fragments may result in bimetallic species *via* redox condensation or homometallic clusters through oxidation (see chapter 5.1) [29].

Following the pioneering work of Nyholm *et al.*, most compounds, *e.g.*, V(CO)<sub>3</sub>(AuPPh<sub>3</sub>)<sub>3</sub> and Co<sub>3</sub>Ru(CO)<sub>12</sub>(AuPPh<sub>3</sub>) have been obtained by reaction of an anionic mononuclear or cluster complex with ClAuL [71]. The charge of the anionic cluster has a strong influence on its reactivity. The reaction can be facilitated with the formation of [AuL]<sup>+</sup> cations that can be generated *in situ* using a chloride abstractor or prepared separately. Moreover, the use of [AuL]<sup>+</sup> cations instead of the neutral chloride compound avoids the possibility of side reactions due to the nucleophilic Cl<sup>-</sup> anion.

When two or more Au(I) centers are present, they are often found at short Au...Au distances (2.7 – 3.3 Å) which are intermediate between the sum of covalent (2.72 Å) and van der Waals (3.32 Å) radii of Au. This effect has been called aurophilic attraction or aurophilicity by Schmidbaur. Theoretical calculations, including relativistic effects, have played a key role in understanding this unique behavior and the development of gold chemistry.

---

<sup>23</sup> It is noteworthy that the “fragments” are not necessarily the starting material of the reactions. These units can be unambiguously identified with a simple “retrosynthesis”. In general, these differences are due to the rearrangement of the cage induced by loss of one or more carbonyl ligands. For instance, the bimetallic Co-Au cluster Co<sub>6</sub>C(CO)<sub>13</sub>(AuPPh<sub>3</sub>)<sub>2</sub> can be obtained by the reaction of [Au(PPh<sub>3</sub>)]<sup>+</sup> with [Co<sub>6</sub>C(CO)<sub>15</sub>]<sup>2-</sup> or [Co<sub>6</sub>C(CO)<sub>13</sub>]<sup>2-</sup>. Only in the last case, the starting materials are both the fragments of the condensation.

These calculations have shown that bonding between closed-shell Au(I)  $d^{10}$  metal centers may be strongly enhanced by relativistic effects, and aurophilicity was accepted as a logical consequence of these contributions. Indeed, the short Au-Au contact would be more difficult to justify in terms of classical bonding on the basis of the closed shell  $5d^{10}$  configuration [72].

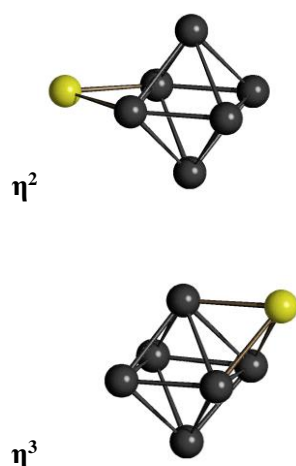
As demonstrated by a search in the Cambridge Structural Database, the highest nuclearity of the metal carbonyl clusters decorated on the surface by Au(I) fragments is 19 (without considering the contribution of  $[\text{AuL}]^+$  units) and the number of the  $[\text{AuL}]^+$  fragments ranges from 1 to 6. Figure 5.2.1 reports the correlation between the nuclearity of the metal carbonyl cores and the number of  $[\text{AuL}]^+$  of known clusters. Compounds with bidentate  $\text{Au}_2(\text{dppx})$  fragments or heteroleptic metal cores such as  $\text{Pt}_{13}(\text{CO})_{10}(\text{PPh}_3)_4(\text{AuPPh}_3)_4$  are not included in this survey [40].

The location of the gold fragments on the core are largely governed by steric factors and, excluding the case of  $[\text{Pt}_{19}(\text{CO})_{24}(\text{AuPPh}_3)_{4-n}]^{n-}$  ( $n = 0, 1$ ), the AuL units do not show any  $\text{Au}\cdots\text{Au}$  contacts [55]. The left part of the graph is dominated by the presence of bimetallic Os-Au adducts. The products are obtained by the reaction of the parent homometallic clusters with the same osmium nuclearity. Although the nuclearity is conserved, the metal core geometry can change proving that the coordination of  $[\text{AuL}]^+$  are not so innocent (see box 3.4.1). For instance, the osmium core framework of  $\text{Os}_8(\text{CO})_{22}(\text{AuPPh}_3)_2$  is the 1,5-isomer of the 1,3-bicapped octahedron found in its starting material  $[\text{Os}_8(\text{CO})_{22}]^{2-}$ . Curiously,  $\text{Os}_8(\text{CO})_{22}\text{Au}_2(\text{dppb})$  obtained by the analogous reaction shows the bicapped octahedral  $\text{Os}_8$  arrangement observed in the parent dianion  $[\text{Os}_8(\text{CO})_{22}]^{2-}$  [73].

Other two remarkable structures are  $\text{Rh}_{10}\text{C}_2(\text{CO})_{18}(\text{AuPPh}_3)_6$  and  $\text{Ir}_6\text{Ru}_3(\text{CO})_{21}(\text{AuPPh}_3)$  that respectively represent the carbonyl cluster with the highest number of  $[\text{AuL}]^+$  fragments and the unique example with a terminally coordinated Au atom.

### 5.2.2 $\text{M}_6$ octahedral clusters decorated by $[\text{AuL}]^+$ fragments: an overview

The  $\text{M}_6$  octahedral framework, present in several carbonyl clusters, seems to be an interesting platform to test aurophilicity especially when interstitial heteroatoms are present, as demonstrated in this chapter as well as in chapter 7.1. Indeed, in the presence of strong core interactions, the geometry of the  $\text{M}_6$  octahedron is retained whereas the arrangement of surface fragments may be governed by weaker forces such as aurophilic interactions, van der Waals and packing forces. A single  $[\text{AuPPh}_3]^+$  fragment has been found coordinated to an edge ( $\eta^2$ ) or a trigonal face ( $\eta^3$ ) in  $\text{M}_6$  octahedral clusters (table 5.2.1). At present, there is no example of terminally coordinated  $[\text{AuPPh}_3]^+$  fragments on  $\text{M}_6$  clusters.



Apticity	Compound	Ref.
$\eta^2$	$\text{Ru}_6\text{B}(\text{CO})_{17}(\text{AuPR}_3)^*$	[74]
	$\text{Ru}_4\text{Ir}_2\text{B}(\text{CO})_{16}(\text{AuPCy}_3)$	[75]
	$[\text{Ir}_6(\text{CO})_{15}(\text{AuPPh}_3)]^-$	[76]
	$[\text{Fe}_6\text{C}(\text{CO})_{16}(\text{AuPPh}_3)]^-$	[77]
$\eta^3$	$[\text{Co}_6\text{C}(\text{CO})_{13}(\text{AuPPh}_3)]^-$	[78]
	$[\text{Fe}_5\text{MoC}(\text{CO})_{17}(\text{AuPMe}_3)]^-$	[79]
	$[\text{Co}_5\text{MoN}(\text{CO})_{14}(\text{AuPPh}_3)]^-$	[80]
	$\text{Ru}_4\text{Rh}_2\text{B}(\text{CO})_{16}(\text{AuPPh}_3)$	[75]

**Table 5.2.1** Survey on octahedral homoleptic carbonyl clusters decorated by one  $[\text{AuPPh}_3]^+$  fragment. For the sake of clarity, phosphines and carbonyl groups are not represented. \* R = 2-methyl-Ph.

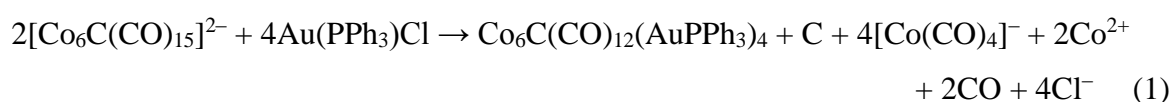
Moreover, when a second fragment is added, several options arise since it can coordinate to a site close or far from the first one. Auophilicity favors the proximity of the two Au(I) centers and formation of intramolecular  $d^{10}$ - $d^{10}$  interactions. The auophilic interaction may occur in several ways that can be classified on the basis of the gold-metal cage interactions as depicted in table 5.2.2.

In  $\text{Ru}_6\text{C}(\text{CO})_{16}(\text{AuPPh}_3)_2$  and  $\text{Ru}_5\text{PtC}(\text{CO})_{15}(\text{AuPPh}_3)_2$ , the two  $[\text{AuPPh}_3]^+$  fragments are coordinated on two opposite edges ( $\eta^2$ ,  $\eta^2$ ) of the octahedral metal core without any auophilic interaction. However, the survey is dominated by the cases where an Au-Au interaction is present and this leads to a wide variability of the coordination mode of the two Au atoms. It is noteworthy that,  $[\text{Ir}_6(\text{CO})_{15}(\text{AuPPh}_3)]^-$  and  $\text{Ir}_6(\text{CO})_{15}(\text{AuPPh}_3)_2$  are the only compounds found in this survey which do not contain any interstitial atom.

In the case of  $\text{M}_6$  octahedral cages stabilized by three  $[\text{AuPPh}_3]^+$  fragments, the number of entries come down to two. In the first example of table 5.2.3,  $\text{Ru}_4\text{Rh}_2\text{B}(\text{CO})_{15}(\text{AuPCy}_3)_3$  one  $[\text{AuPPh}_3]^+$  fragment is coordinated to an edge ( $\eta^2$ ) while the other two display the same arrangement observed in  $\text{HRu}_6\text{B}(\text{CO})_{16}(\text{AuPPh}_3)_2$ . Finally, in the case of  $\text{Ru}_6\text{B}(\text{CO})_{16}(\text{AuPPh}_3)_3$ , auophilic interactions are not present.

### 5.2.3 Synthesis of $\text{Co}_6\text{C}(\text{CO})_{12}(\text{AuPPh}_3)_4$ clusters

The new neutral cluster  $\text{Co}_6\text{C}(\text{CO})_{12}(\text{AuPPh}_3)_4$  [86] has been obtained by reacting  $[\text{Co}_6\text{C}(\text{CO})_{15}]^{2-}$  with 2-3 equivalents of  $\text{Au}(\text{PPh}_3)\text{Cl}$  according to the equations (1) and (2):





Au-Au Bond	Apticity	Compound	Ref.
0	$\eta^2, \eta^2$	$\text{Ru}_6\text{C}(\text{CO})_{16}(\text{AuL}_3)_2^*$	[81]
		$\text{Ru}_5\text{PtC}(\text{CO})_{15}(\text{AuPPh}_3)_2$	[82]
1	$\eta^3, \eta^3$	$\text{HRu}_6\text{B}(\text{CO})_{16}(\text{AuPPh}_3)_2$	[74]
	$\eta^1, \eta^3$	$\text{Ir}_6(\text{CO})_{15}(\text{AuPPh}_3)_2$	[83]
	$\eta^2, \eta^2$	$\text{Fe}_4\text{Rh}_2\text{C}(\text{CO})_{15}(\text{AuPPh}_3)_2$	[84]
	$\eta^2, \eta^3$	$\text{Co}_6\text{C}(\text{CO})_{13}(\text{AuPPh}_3)_2^\#$	[78]
	$\eta^2, \eta^3$	$\text{Ru}_5\text{WC}(\text{CO})_{17}(\text{AuPEt}_3)_2$	[81]

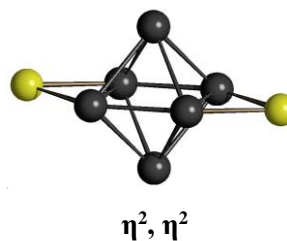
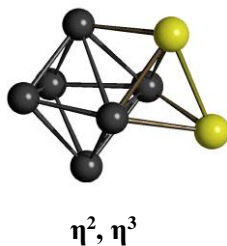
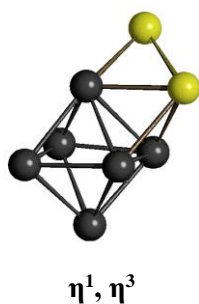
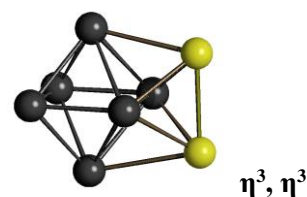
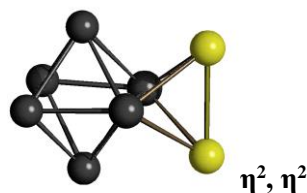


**Table 5.2.2** Survey on octahedral homoleptic carbonyl clusters decorated by two  $[\text{AuPPh}_3]^+$  fragments. For the sake of clarity, phosphines and carbonyl groups are not represented. # The isostructural  $\text{Rh}_6\text{C}(\text{CO})_{13}(\text{AuPPh}_3)_2$  cluster is also known. \*  $\text{L} = \text{PPh}_3$  or  $\text{PPh}_2\text{Me}$ .

Au-Au Bond	Apticity	Compound	Ref.
0	$\eta^2, \eta^3, \eta^3$	$\text{Ru}_4\text{Rh}_2\text{B}(\text{CO})_{15}(\text{AuPCy}_3)_3$	[85]
1	$\eta^2, \eta^2, \eta^3$	$\text{Ru}_6\text{B}(\text{CO})_{16}(\text{AuPPh}_3)_3$	[74]

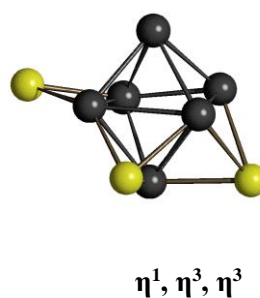
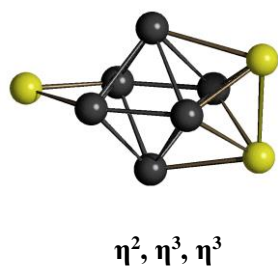


**Table 5.2.3** Survey on octahedral homoleptic carbonyl clusters decorated by  $[\text{AuPPh}_3]^+$  fragments. For the sake of clarity, phosphines and carbonyl groups are not represented.

The side-products  $[\text{Co}(\text{CO})_4]^-$  and  $\text{Co}^{2+}$  have been identified by IR spectroscopy and the typical pink color of the water extract during workup, respectively. Formation of a gold mirror on the reaction flask was also observed. The neutral cluster was purified by removing the solvent *in vacuo*, washing the residue with water and toluene, and finally extracted in thf. Crystallization by slow diffusion of n-hexane on the thf solutions affords three types of crystals, *i.e.*,  $\text{Co}_6\text{C}(\text{CO})_{12}(\text{AuPPh}_3)_4$  (**I**),  $\text{Co}_6\text{C}(\text{CO})_{12}(\text{AuPPh}_3)_4 \cdot \text{thf}$  (**II**) and  $\text{Co}_6\text{C}(\text{CO})_{12}(\text{AuPPh}_3)_4 \cdot 4\text{thf}$  (**III**), as single species and/or mixtures, depending on the experimental conditions. The use of toluene/n-hexane instead of thf/n-hexane for crystallization results in crystals of **I** as well as  $\text{Co}_6\text{C}(\text{CO})_{12}(\text{AuPPh}_3)_4 \cdot 4\text{toluene}$  closely related to **III**. Conversely, crystallization from  $\text{CH}_2\text{Cl}_2/\text{n-hexane}$  affords crystal of **I**. It is noteworthy that they are not merely different solvates of the same neutral cluster, but they contain three different isomers of  $\text{Co}_6\text{C}(\text{CO})_{12}(\text{AuPPh}_3)_4$  (see section 5.2.4). As discussed in the next section, all three isomers contain the same octahedral  $[\text{Co}_6\text{C}(\text{CO})_{12}]^{4-}$  carbido-carbonyl core differently decorated by four  $[\text{AuPPh}_3]^+$  fragments. As a consequence, the three crystals display different IR spectra in nujol mull. Crystals of **I-III** are poorly soluble in organic solvents and, in all cases, after dissolution they dissociate two  $[\text{AuPPh}_3]^+$  fragments resulting in the previously reported  $[\text{Co}_6\text{C}(\text{CO})_{12}(\text{AuPPh}_3)_2]^{2-}$  anion:



Thus, in solution the cluster is mostly ionized and  $[\text{Co}_6\text{C}(\text{CO})_{12}(\text{AuPPh}_3)_2]^{2-}$  condenses with two  $[\text{AuPPh}_3]^+$  during the crystallization. The presence in solution of dynamic equilibria has been demonstrated by variable temperature  $^{31}\text{P}\{^1\text{H}\}$  NMR experiments (figure 5.2.2).

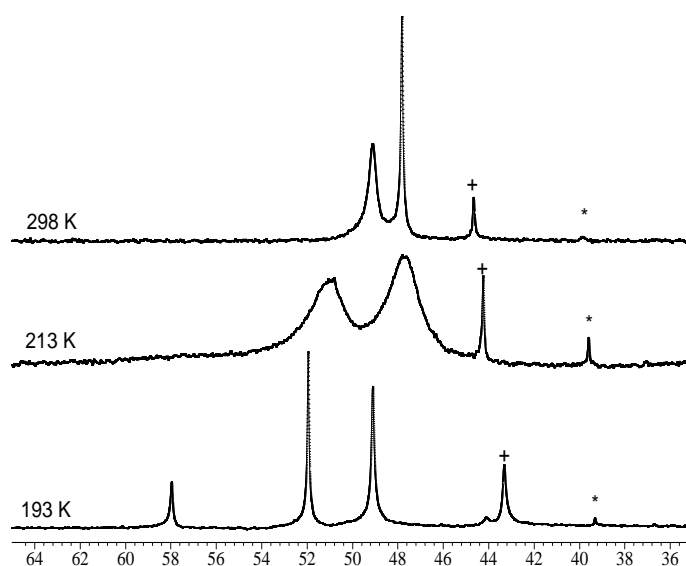


**Figure 5.2.2** Variable temperature  $^{31}\text{P}\{^1\text{H}\}$  NMR spectra of  $\text{Co}_6\text{C}(\text{CO})_{12}(\text{AuPPh}_3)_4$  in  $\text{CD}_2\text{Cl}_2$ . + and \* are impurities.

Two resonances at  $\delta_P$  49.1 (br) and 47.8 (s) ppm are present at 298 K, which broaden by lowering the temperature. The exchange is frozen at 193 K, as demonstrated by the presence of three sharp singlets at (relative intensities are given in parentheses)  $\delta_P$  49.1 (351), 51.9 (274) and 58.0 (100) ppm. The resonance at 51.9 ppm may be assigned to  $[\text{Co}_6\text{C}(\text{CO})_{12}(\text{AuPPh}_3)_2]^{2-}$  by comparison to literature data [78]. The resonance at 58.0 ppm may be tentatively assigned to a more dissociated  $[\text{Co}_6\text{C}(\text{CO})_{12}(\text{AuPPh}_3)]^{3-}$  species:



This is in agreement with the fact that a shift towards higher frequencies has been previously observed for  $\text{Co}_6\text{C}(\text{CO})_{13}(\text{AuPPh}_3)_2$  ( $\delta_P$  50.2 ppm) upon dissociation to  $[\text{Co}_6\text{C}(\text{CO})_{13}(\text{AuPPh}_3)]^-$  ( $\delta_P$  54.0 ppm) [78]. The major resonance at 49.1 ppm may be assigned to  $[\text{Co}_6\text{C}(\text{CO})_{12}(\text{AuPPh}_3)_3]^-$  or, more likely, to the free  $[\text{AuPPh}_3]^+$  fragments.

#### 5.2.4 Crystal structures of the three isomers of $\text{Co}_6\text{C}(\text{CO})_{12}(\text{AuPPh}_3)_4$

The structure of the neutral  $\text{Co}_6\text{C}(\text{CO})_{12}(\text{AuPPh}_3)_4$  cluster has been determined as its  $\text{Co}_6\text{C}(\text{CO})_{12}(\text{AuPPh}_3)_4$  (**I**),  $\text{Co}_6\text{C}(\text{CO})_{12}(\text{AuPPh}_3)_4 \cdot \text{thf}$  (**II**) and  $\text{Co}_6\text{C}(\text{CO})_{12}(\text{AuPPh}_3)_4 \cdot 4\text{thf}$  (**III**) solvates (figure 5.2.3 and table 5.2.4).

All the three isomers of  $\text{Co}_6\text{C}(\text{CO})_{12}(\text{AuPPh}_3)_4$  may be viewed as composed by an anionic  $[\text{Co}_6\text{C}(\text{CO})_{12}]^{4-}$  octahedral moiety decorated by four cationic  $[\text{AuPPh}_3]^+$  units. They mainly differ because of the arrangement of these cationic fragments which results in different  $\text{Co}_6\text{CAu}_4$  cores (figure 5.2.4).

Thus, in isomer **I**, Au(1) is  $\mu_3$ -bridging a triangular face of the  $\text{Co}_6\text{C}$  octahedron, generating a  $\text{Co}_3\text{Au}$  tetrahedron. The other three Au atoms are capping the three  $\text{Co}_2\text{Au}$  triangular faces of this tetrahedron. The resulting  $\text{Co}_6\text{CAu}_4$  core of **I** possesses a perfect  $C_{3v}$  symmetry with the 3-fold crystallographic axis passing through the interstitial carbide and Au(1). Isomer **I** presents three equivalent Au-Au bonding contacts involving the central Au(1) and the three lateral Au-atoms; conversely the contacts between the three lateral Au's are completely non-bonding. In the case of **II**, Au(1) is  $\mu_3$ -bridging the Co(1)-Co(2)-Co(3) triangular face of the  $\text{Co}_6\text{C}$  octahedron and Au(2) caps one triangular face of the resulting tetrahedron as in **I**.

Then, the other two Au-atoms are  $\mu$ -coordinated to two Co-Co edges of the opposite triangular  $\text{Co}_3$ -face of the octahedron, generating a  $\text{Co}_3\text{Au}_2$  square pyramid. The four Au-atoms are grouped into two isolated  $\text{Au}_2$ -dimers on opposite sides of the octahedron presenting very similar Au-Au bonding contacts.

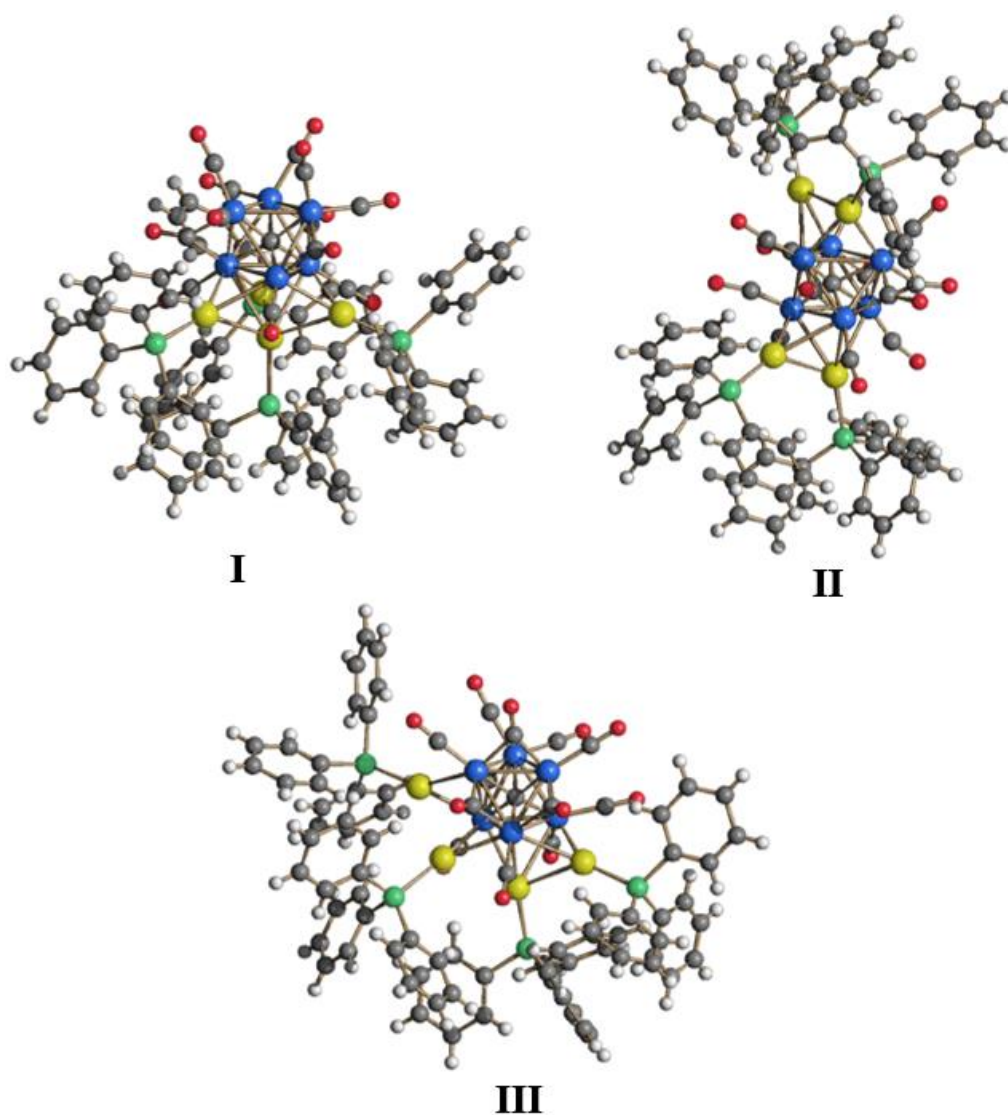


**Figure 5.2.3** Molecular structures of isomers **I**, **II** and **III** of  $\text{Co}_6\text{C}(\text{CO})_{12}(\text{AuPPh}_3)_4$  (Au, yellow; Co, blue; P, green; C, grey; O, red; H, white).

	<b>I</b>	<b>II</b>	<b>III</b>
Co-Co	2.5108(12)-2.7816(16) Average 2.652(5)	2.450(10)-2.804(9) Average 2.65(3)	2.500(5)-2.911(5) Average 2.653(17)
Co-C <sub>carbide</sub>	1.856(3)-1.901(4) Average 1.878(9)	1.78(4)-1.98(4) Average 1.88(9)	1.85(3)-1.91(2) Average 1.88(5)
Co-Au	2.6087(11)-2.7902(11) Average 2.718(3)	2.584(7)-2.765(7) Average 2.70(2)	2.597(3)-2.869(4) Average 2.714(11)
Au-P	2.2874(14)-2.326(2) Average 2.297(3)	2.254(13)-2.304(14) Average 2.28(3)	2.289(7)-2.310(7) Average 2.299(14)
Au-Au	2.8708(12)	2.840(3)-2.844(3) Average 2.84(2)	2.8358(15)-2.9336(15) Average 2.889(3)

**Table 5.2.4** Comparison of the most relevant bond lengths (Å) in the three isomers of  $\text{Co}_6\text{C}(\text{CO})_{12}(\text{AuPPh}_3)_4$  as found in  $\text{Co}_6\text{C}(\text{CO})_{12}(\text{AuPPh}_3)_4$  (**I**),  $\text{Co}_6\text{C}(\text{CO})_{12}(\text{AuPPh}_3)_4 \cdot \text{thf}$  (**II**) and  $\text{Co}_6\text{C}(\text{CO})_{12}(\text{AuPPh}_3)_4 \cdot 4\text{thf}$  (**III**).

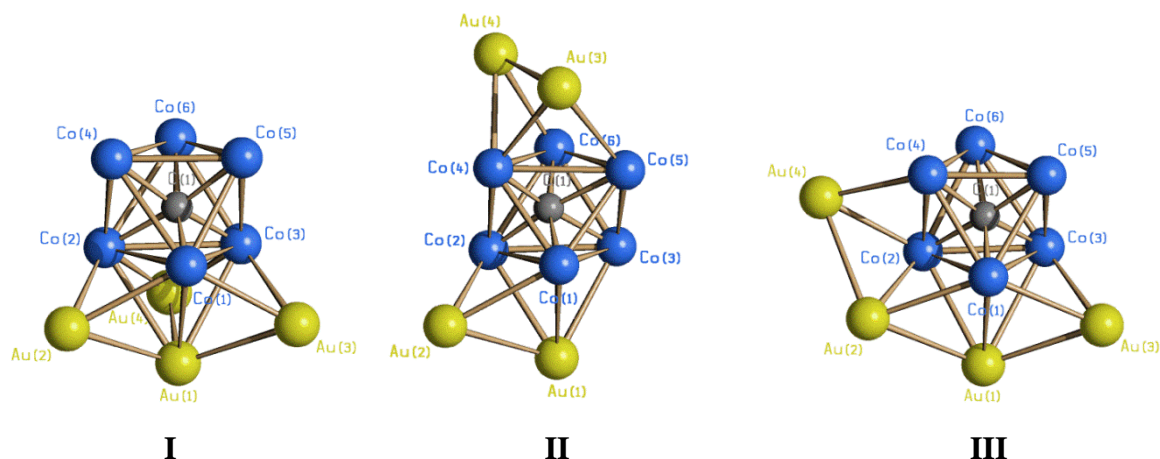


**Figure 5.2.4** The  $\text{Co}_6\text{CAu}_4$  cores of isomers **I**, **II** and **III** (Au, yellow; Co, blue).

In the case of isomer **III**, three Au-atoms show the same coordination as in **I**. Thus, Au(1) is  $\mu_3$ -bridging the Co(1)-Co(2)-Co(3) triangular face of the  $\text{Co}_6\text{C}$  octahedron, whereas Au(2) and Au(3) are capping two  $\text{Co}_2\text{Au}$  faces of the resulting  $\text{Co}_3\text{Au}$  tetrahedron. Then, Au(4) is bonded to Au(2), Co(2) and Co(4). Overall, the  $\text{Co}_6\text{CAu}_4$  core of **III** possesses  $C_1$  symmetry. The cluster displays three Au-Au bonding contacts and nine Co-Au bonds. It must be remarked that, despite the different structures, all isomers contain nine Co-Au bonds with very similar bonding parameters.

The  $[\text{Co}_6\text{C}(\text{CO})_{12}]^{4-}$  fragment in the three isomers displays the same C-centered octahedral structure with very similar Co-Co and Co- $\text{C}_{\text{carbide}}$  bonding contacts. Conversely, the stereochemistry of the 12 CO ligands is sensibly different (figure 5.2.5). Thus, the more symmetric isomer **I** contains 9 terminal and 3 edge bridging carbonyls, whereas both isomer **II** and **III** contain 8 terminal and 4 edge bridging CO ligands, even if distributed differently around the octahedron. Moreover, the CO ligands show some weak  $\text{Au}\cdots\text{C}$  contacts, that are well above the sum of the covalent radii of Au and C (2.04 Å) but still below the sum of their van der Waals radii (3.36 Å). In particular, **I** contains six  $\text{Au}\cdots\text{C}(\text{O})$  contacts in the range 2.771(5)-2.850(5) Å, **II** eight  $\text{Au}\cdots\text{C}(\text{O})$  contacts in the range 2.73(4)-2.96(6) Å, and **III** five  $\text{Au}\cdots\text{C}(\text{O})$  contacts in the range 2.75(3)-2.92(3) Å.

Overall, the three isomers of  $\text{Co}_6\text{C}(\text{CO})_{12}(\text{AuPPh}_3)_4$  display very similar bonding parameters (number of bonds and distances) when the stronger Co-Co, Co- $\text{C}_{\text{carbide}}$ , Co-Au and Au-P interactions are considered. The differences are mainly focused on the weaker Au-Au and  $\text{Au}\cdots\text{C}(\text{O})$  interactions, as well as the stereochemistry of the carbonyls and, above all, the spatial rearrangement of the four  $[\text{AuPPh}_3]^+$  fragments. We might expect that these isomers have very similar internal energies, and thus, small differences in the van der Waals forces due to the

interactions with a variable amount of cocrystallized solvent molecules that causes the formation in the solid state of **I**, **II** and **III**. This prompted a theoretical investigation (see next section).

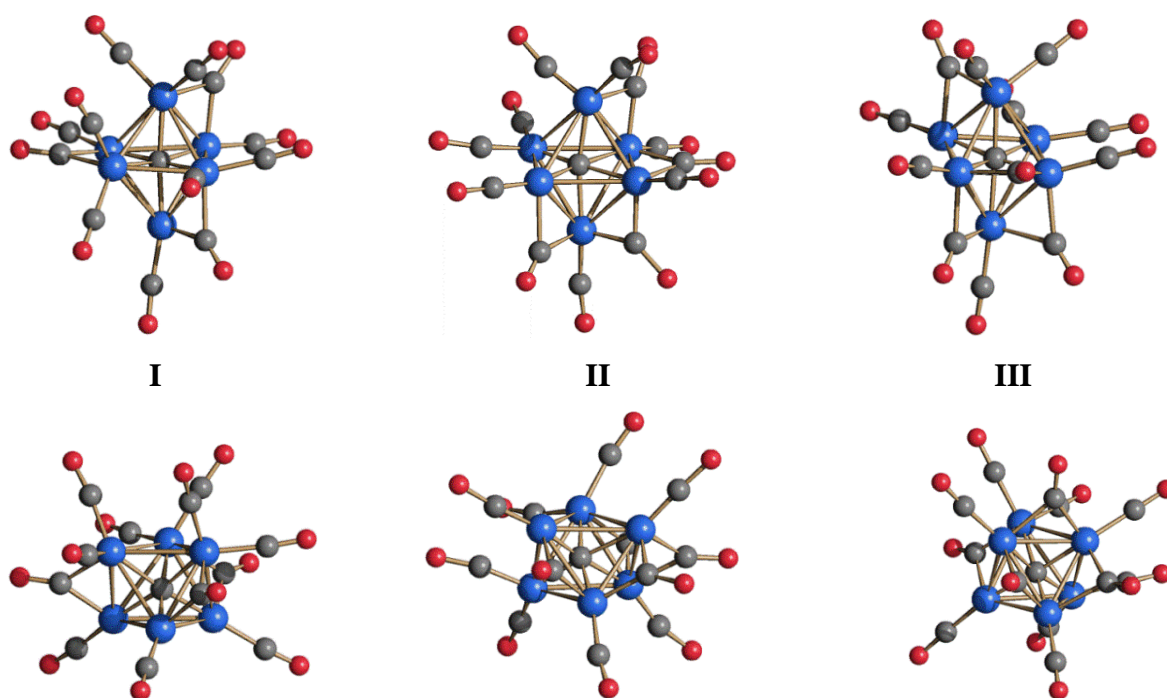


**Figure 5.2.5** The  $[\text{Co}_6\text{C}(\text{CO})_{12}]^{4+}$  fragment of isomer **I**, isomer **II** and isomer **III** of  $\text{Co}_6\text{C}(\text{CO})_{12}(\text{AuPPh}_3)_4$ . Two views are reported per each isomer in order to better appreciate its octahedral structure (Co, blue; C, grey; O, red).

### 5.2.5 Theoretical Investigation

In order to shed some light on the isomers **I**, **II** and **III** found in the solid state, a series of DFT optimizations were performed using the B97D functional with the inclusion of the dispersion forces that in principle could help to reproduce the different stability of the isomers. In the first attempts we used simplified models starting from the crystallographic coordinates with  $\text{PH}_3$  in substitution of bulky  $\text{PPh}_3$  ligands and by neglecting the co-crystallized molecules.

Although this kind of approach gave satisfactory results in the investigation of the  $\text{Ni}_6\text{C}(\text{CO})_9(\text{AuPPh}_3)_4$  cluster (see chapter 7.1), it appears insufficient in the present case. In fact, during the optimizations the  $\text{AuPH}_3$  fragments move away from the original positions and the obtained models were unsatisfactory. In the second series of calculations, we decided to include in the models also the phenyl rings. The general features of the models were conserved but it was impossible to obtain the convergence for isomers **I** and **II**, likely imputed to the complex nature of the considered molecule. Nevertheless some useful information from the calculations could be obtained. First of all, qualitative single point calculations on the crystallographic structures revealed that **I** is 14 kcal/mol and 2.5 kcal/mol more stable than **II** and **III** respectively.

The energy differences are reasonably small and existence of the isomers in the crystals is consistent with solid-state packing effects, neglected during the modelling of a single isolated molecule. More intriguing fact is the incapacity of the PH<sub>3</sub> models in simulating the experimental structures. We can conclude that the aurophilic interactions alone are not able to stabilize the models. The  $\pi$ - $\pi$  and  $\pi$ -H interactions have also a stabilizing role in the clusters. In particular the number of such interactions and the stability of the clusters seem to be correlated and they change in the same order ( $\text{I} \cong \text{III} < \text{II}$ ). In any case, for the isomer **III** we were able to complete the geometry optimization of the whole compound and a comparison between the optimized and the experimental structures was pointed out in table 5.2.5. The Co<sub>6</sub>-C core is satisfactorily reproduced except for a slight overestimation mainly attributable to the usage of the *pseudo*-potential, especially for the two equatorial Co centres with a bridging Au atom (3.05 vs. the experimental value of 2.83 Å). An opposite trend may be pointed out for the Au-Au distances, being two of them shorter than the X-ray ones (2.84 vs. crystallographic 2.93 and 2.90 Å). The main discrepancy concerns the Co-Au bonding pattern, since only eight rather than nine (in the X-ray structure) Co-Au bonding distances have been predicted by the optimization, being the Au<sub>1</sub>-Co<sub>3</sub> significantly elongated (0.4 Å).

	Experimental	Calculated
Co-Co	2.500(5)-2.911(5); Av. 2.653(17)	2.512-3.054; Av. 2.688
Co-C <sub>carbide</sub>	1.85(3)-1.91(2); Av. 1.88(5)	1.879-1.949; 1.910
Co-Au	2.597(3)-2.869(4); Av. 2.714(11)	2.639-2.977; Av. 2.802
Au-P	2.289(7)-2.310(7); Av. 2.299(14)	2.319-2.324; Av. 2.320
Au-Au	2.8358(15)-2.9336(15); Av. 2.889(3)	2.842-2.860; Av. 2.852

**Table 5.2.5** Comparison of the most relevant bond lengths (Å) between the Co<sub>6</sub>C(CO)<sub>12</sub>(AuPPh<sub>3</sub>)<sub>4</sub>·4thf (**III**) and the calculated structure.

The gap between the highest occupied molecular orbital (HOMO, figure 5.2.6 a) and the lowest unoccupied one (LUMO, figure 5.2.6 b) has been estimated to be 1.29 eV. Both HOMO and the LUMO are largely located on the Co atoms rather than on the Au (69.6 and 60.7 vs. 8.04 and 11.3 % for HOMO and LUMO, respectively). Only in the LUMO+2 (figure 5.2.6 c), +0.38 eV higher in energy than the LUMO, the contribution from the gold is only slightly bigger than the Co one (32.3 vs. 29.7).

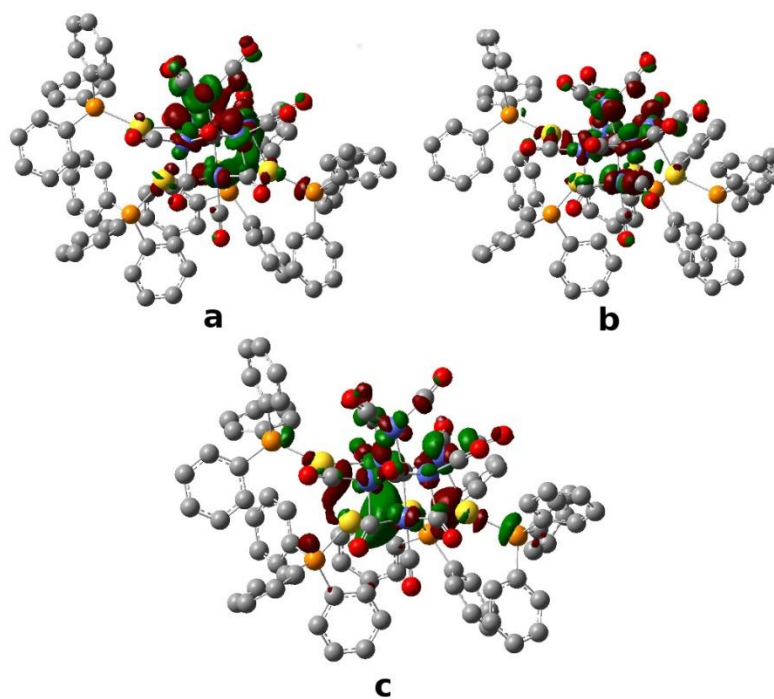


**Figure 5.2.6** Graphical plots (isosurface = 0.03) of the a) HOMO, b) LUMO and c) LUMO+2 of  $\text{Co}_6\text{C}(\text{CO})_{15}(\text{AuPPh}_3)_4$ .

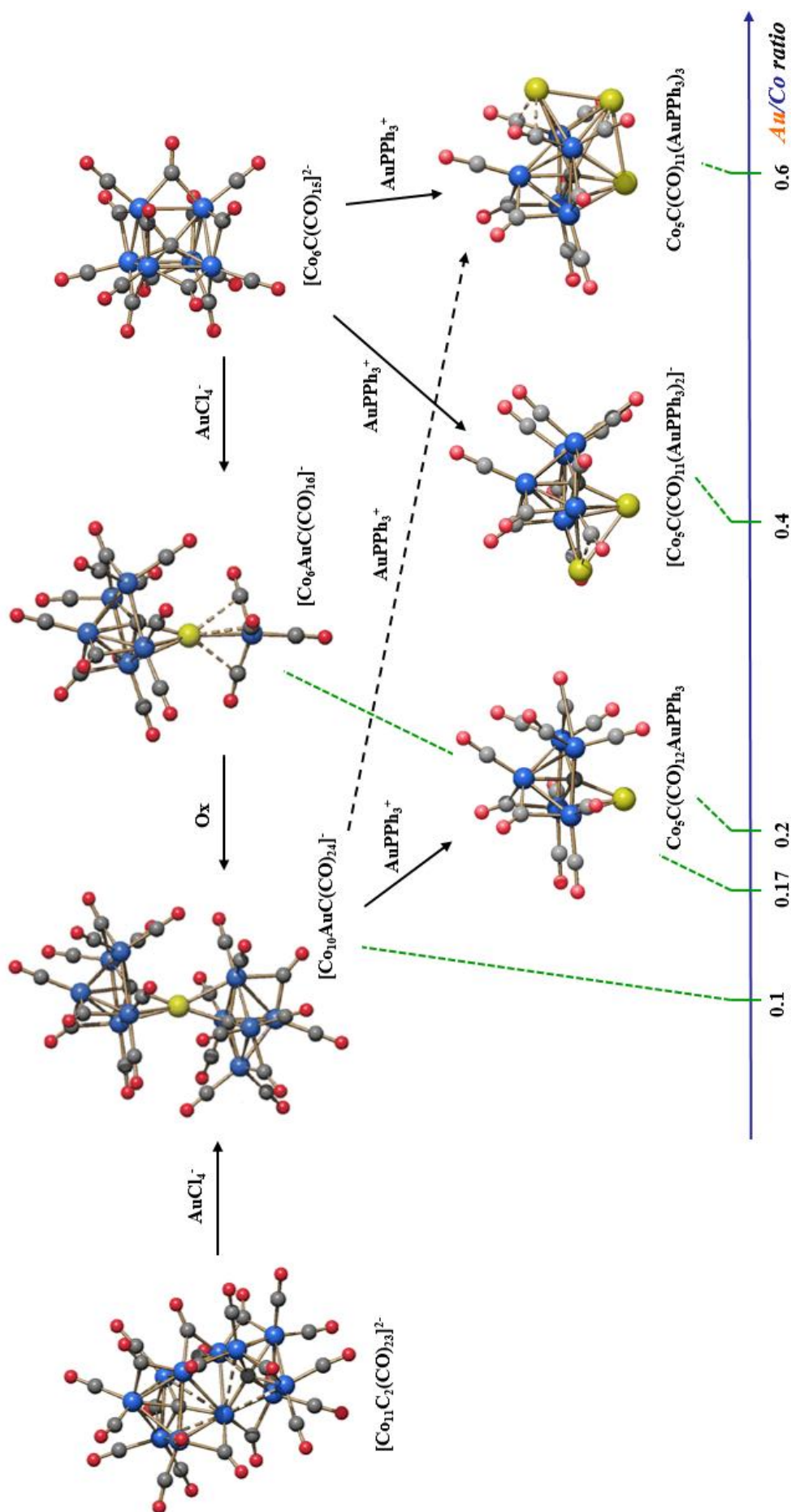


**Figure 5.3.1** Synthesis of new bimetallic Co-Au carbonyl clusters containing  $\text{Co}_5\text{C}$  square-pyramidal fragment. The bimetallic compounds are arranged on the basis of their Au/Co ratios. For the sake of clarity, the phosphine ligands are not represented.

## Isolation of Unprecedented $\text{Co}_5\text{C}$ Square-Pyramidal Clusters

### 5.3.1 Square-pyramidal clusters decorated by $[\text{AuL}]^+$ fragments

A search of the Cambridge Crystallographic Data Base reveals only a relatively small group of  $\text{M}_5\text{E}(\text{CO})_x(\text{AuL})_y$  (E = main group atom; M = transition metal) clusters with a  $\text{M}_5$  square-pyramid geometry. The  $\text{Ru}_5\text{B}(\text{CO})_{15}(\text{AuPPh}_3)$  molecular cluster represents the only example of  $\text{M}_5$  square pyramid geometry stabilized by one  $[\text{AuPPh}_3]^+$  unit [87]. It is noteworthy that the  $[\text{AuPPh}_3]^+$  fragment is not symmetrically bonded to the square base of the  $[\text{Ru}_5\text{B}(\text{CO})_{15}]^-$  unit, which would have resulted in a  $\text{Ru}_5\text{Au}$  octahedron. Conversely, it is bridging to the  $\text{Ru}_2$  edge and further interacting with the boride atom ( $\eta^3$  bond). The resulting structure can be referred as an open octahedron or a hinged square-based pyramid.

The isolation of  $\text{Ru}_5\text{B}(\text{CO})_{15}(\text{AuPPh}_3)$  (figure 5.3.2 a) by J. Lewis provides an illustrative example on how the change of the chemical-physical properties of the  $\text{AuPPh}_3$ -adduct, obtained from the related anionic cluster, would make their isolation easier [88]. Indeed,  $[\text{Ru}_5\text{B}(\text{CO})_{15}]^-$  was originally obtained by the Cambridge group in mixture with  $[\text{Ru}_6\text{B}(\text{CO})_{17}]^-$ . The anionic nature of the two clusters hampers their chromatographic separation as result of the decomposition of  $[\text{Ru}_5\text{B}(\text{CO})_{15}]^-$  on the silica gel.<sup>24</sup> Differently, the separation of  $\text{Ru}_5\text{B}(\text{CO})_{15}(\text{AuPPh}_3)$  and  $\text{Ru}_6\text{B}(\text{CO})_{17}(\text{AuPPh}_3)$  by thin layer chromatography is facile. After the purification,  $\text{Ru}_5\text{B}(\text{CO})_{15}(\text{AuPPh}_3)$  has been isolated in a crystalline state and structurally characterized via X-ray crystallography.<sup>25</sup>  $\text{Fe}_5\text{C}(\text{CO})_{14}(\text{AuPEt}_3)_2$  (figure 5.3.2 b) and  $\text{Os}_5\text{C}(\text{CO})_{14}(\text{AuPPh}_3)_2$  (figure 5.3.2 c) represent fascinating examples where the  $\text{M}_5\text{E}$  core is

<sup>24</sup> In general, the chromatographic separation of mixtures of neutral derivatives is much easier. The systematic different approach of the Cambridge group (see chapter 1) is due to the different properties of the clusters. Probably the use of chromatographic separation is both cause and consequence of the isolation of neutral compounds.

<sup>25</sup> The assumption that the addition of the  $[\text{AuPPh}_3]^+$  fragments to  $[\text{Ru}_5\text{B}(\text{CO})_{15}]^-$  takes place with little perturbation of the  $\text{Ru}_5\text{B}$  square-pyramidal boride core is not in conflict with the consideration showed in the case of two  $[\text{Pt}_{19}(\text{CO})_{24}(\text{AuPPh}_3)_{4+n}]^n$  ( $n = 0, 1$ ) clusters (see box 3.3.1) where, instead, the presence of different structural isomers must be taken into account.

decorated by two  $[\text{AuPPh}_3]^+$  units that adopt different structures in the solid state [81]. In the later, the two  $[\text{AuPPh}_3]^+$  units are bonded to  $\text{Os}_2$  edges ( $\eta^2$  bond) including the apical atom of the square-pyramidal cage. Conversely, in the case of  $\text{Fe}_5\text{C}(\text{CO})_{14}(\text{AuPEt}_3)_2$ , one  $[\text{AuPPh}_3]^+$  fragment is symmetrically bonded to the square base of  $\text{Fe}_5$  core and the other to the  $\text{Fe}_2$  edge ( $\eta^2$  bond).

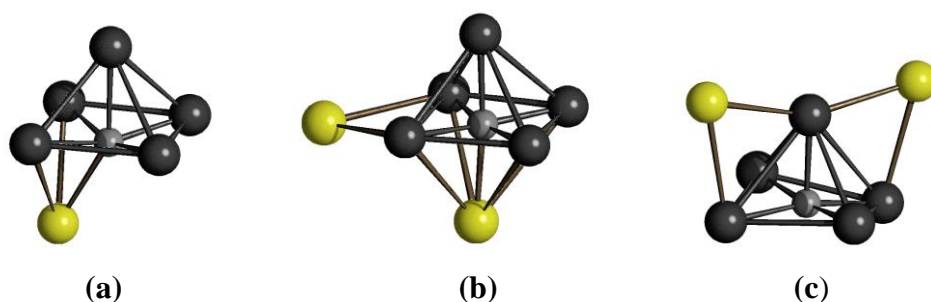


**Figure 5.3.2** Examples of known square-pyramidal homoleptic carbonyl clusters decorated by gold phosphine units: (a)  $\text{Ru}_5\text{B}(\text{CO})_{15}(\text{AuPPh}_3)$ ; (b)  $\text{Fe}_5\text{C}(\text{CO})_{14}(\text{AuPEt}_3)_2$  and (c)  $\text{Os}_5\text{C}(\text{CO})_{14}(\text{AuPPh}_3)_2$ . For the sake of clarity in the phosphine and the carbonyl groups are not represented.

Another interesting example is the molecular structure of the neutral compound  $\text{Ru}_5\text{B}(\text{CO})_{14}(\text{AuPPh}_3)_3$  of which is reported only a preliminary low quality X-ray diffraction study. However, the heavy-atom connectivity was unambiguously established showing the presence of a  $\text{Ru}_5$  square-based pyramid core. One  $\text{AuPPh}_3$  group caps a triangular  $\text{Ru}_3$  face, while the other two Au atoms form a  $(\text{AuPPh}_3)_2$  staple motif which is positioned under the square face of the  $\text{Ru}_5$ -core.

### 5.3.2 $\text{M}_5\text{C}$ square-pyramidal carbide carbonyl clusters

The  $\text{Fe}_5\text{C}(\text{CO})_{15}$  square-pyramidal cluster, whose structure was determined by Dahl in 1962, represented the first high nuclearity carbide carbonyl cluster (figure 5.3.3) [89]. Since then, several other  $\text{M}_5\text{C}$  square-pyramidal carbide carbonyl clusters have been characterised, *i.e.*,  $[\text{M}_5\text{C}(\text{CO})_{15}]$  ( $\text{M} = \text{Ru}, \text{Os}$ ),  $[\text{M}_5\text{C}(\text{CO})_{14}]^{2-}$  ( $\text{M} = \text{Fe}, \text{Ru}, \text{Os}$ ),  $[\text{Fe}_4\text{MC}(\text{CO})_{14}]^-$  ( $\text{M} = \text{Co}, \text{Rh}$ ), and  $[\text{HRe}_5\text{C}(\text{CO})_{16}]^{2-}$ . All these clusters possess 74 Cluster Valence Electrons (CVE) in agreement with the inert gas rule. It is noteworthy that, with the only exception of rhenium, all other  $\text{M}_5\text{C}$  carbonyls are based on group VIII metals. The hypothetical  $[\text{Co}_5\text{C}(\text{CO})_{12}]^-$  cluster is isoelectronic with the above species, but it has never been observed before. Probably the non existence of  $[\text{Co}_5\text{C}(\text{CO})_{12}]^-$  as free species is due to the lower number of carbonyls that favors nucleophilic substitution. This led us to move our attention to the synthesis of new carbonyl clusters contained the  $\text{Co}_5\text{C}$  core decorated by Au(I) units.

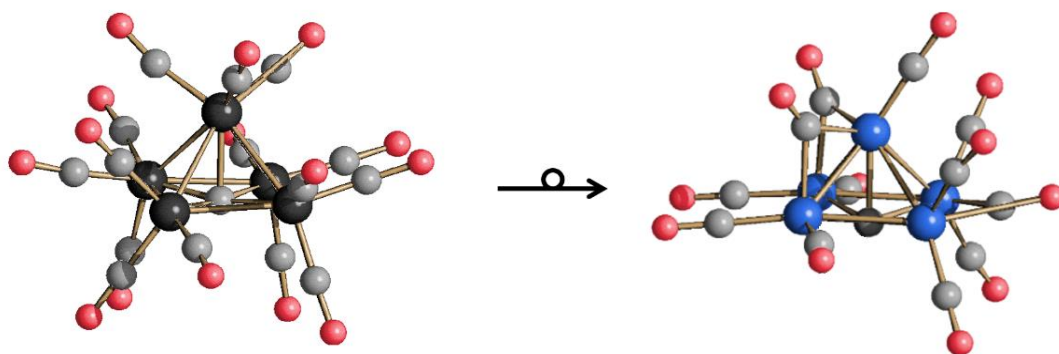


**Figure 5.3.3** Structural relationship between  $\text{Fe}_5\text{C}(\text{CO})_{15}$  and the unknown  $[\text{Co}_5\text{C}(\text{CO})_{12}]^-$  as free species. The molecular structure of the latter is depicted using the crystallographic data of  $\text{Co}_5\text{C}(\text{CO})_{12}(\text{AuPPh}_3)$  (Au, yellow; Co, blue; Fe, black; C, grey; O, red).

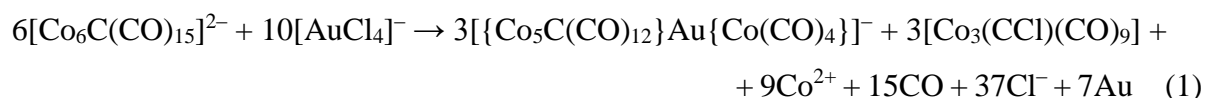
### 5.3.3 General results

The following sections (5.3.4 and 5.3.5) report the characterisation of the new  $[\{\text{Co}_5\text{C}(\text{CO})_{12}\}\text{Au}\{\text{Co}(\text{CO})_4\}]^-$ , **[1]**<sup>-</sup>, and  $[\{\text{Co}_5\text{C}(\text{CO})_{12}\}_2\text{Au}]^-$ , **[2]**<sup>-</sup> clusters obtained from the redox condensation of  $[\text{AuCl}_4]^-$  with  $[\text{Co}_6\text{C}(\text{CO})_{15}]^{2-}$  and  $[\text{Co}_{11}\text{C}_2(\text{CO})_{23}]^{2-}$ , respectively [90]. Electrochemical and spectroelectrochemical studies of **[1]**<sup>-</sup> and **[2]**<sup>-</sup> are reported in section 5.3.6.

Moreover, the new derivatives  $[\text{Co}_5\text{C}(\text{CO})_{12}(\text{AuPPh}_3)]$ , **3**,  $[\text{Co}_5\text{C}(\text{CO})_{11}(\text{AuPPh}_3)_2]^-$ , **4**,  $[\text{Co}_5\text{C}(\text{CO})_{11}(\text{AuPPh}_3)_3]$ , **5** obtained from the reaction of  $[\{\text{Co}_5\text{C}(\text{CO})_{12}\}_2\text{Au}]^-$  and  $[\text{Co}_6\text{C}(\text{CO})_{15}]^{2-}$  with  $\text{Au}(\text{PPh}_3)\text{Cl}$  are presented. All these results are summarized in figure 5.3.1.

### 5.3.4 Synthesis, reactivity and structure of $[\{\text{Co}_5\text{C}(\text{CO})_{12}\}\text{Au}\{\text{Co}(\text{CO})_4\}]^-$ , **[1]**<sup>-</sup>

$[\text{Co}_6\text{C}(\text{CO})_{15}]^{2-}$  reacts with two equivalents of  $[\text{AuCl}_4]^-$  affording the new  $[\{\text{Co}_5\text{C}(\text{CO})_{12}\}\text{Au}\{\text{Co}(\text{CO})_4\}]^-$ , **[1]**<sup>-</sup>, cluster, in accord to the equation (1):



If less  $[\text{AuCl}_4]^-$  is used, the main product is the previously reported  $[\text{Co}_6\text{C}(\text{CO})_{14}]^-$  paramagnetic mono-anion, as inferred by IR analysis.<sup>26</sup> Carbon monoxide evolution and formation of a gold mirror are observed.  $[\text{Co}_3(\text{CCl})(\text{CO})_9]$  (further removed with toluene) was detected by IR spectroscopy, whereas Co(II) salts have been extracted in  $\text{H}_2\text{O}$  during work-up. Crystals suitable for X-ray analyses of  $[\text{NEt}_4][\{\text{Co}_5\text{C}(\text{CO})_{12}\}\text{Au}\{\text{Co}(\text{CO})_4\}]^-$ ,  $[\text{NEt}_4][\mathbf{1}]^-$ , were obtained by slow diffusion of n-hexane into the thf solution. The same compound may be

<sup>26</sup> Regardless of the nature of the oxidant, the oxidation of  $[\text{Co}_6\text{C}(\text{CO})_{15}]^{2-}$  leads to  $[\text{Co}_6\text{C}(\text{CO})_{14}]^-$  as first product. Another example is reported in chapter 6.2.

obtained using  $[\text{Co}_8\text{C}(\text{CO})_{18}]^{2-}$  instead of  $[\text{Co}_6\text{C}(\text{CO})_{15}]^{2-}$ .  $[\text{AuCl}_4]^-$  may be replaced with  $[\text{Au}(\text{Et}_2\text{S})\text{Cl}]$ , but the yields are lower.

The ESI-MS spectrum in  $\text{CH}_3\text{CN}$  solution displays peaks at  $m/z$  (relative intensity in parentheses) 1024 (5), 1011 (100), 983 (20), 658 (10), 644 (10) and 171 (50) attributable to  $[\text{M}(-\text{CO}, +\text{CH}_3\text{CN})]^-$ ,  $[\text{M}]^-$ ,  $[\text{M}(-\text{CO})]^-$ ,  $[\text{Co}_{11}\text{C}_2(\text{CO})_{23}]^{2-}$ ,  $[\text{Co}_5\text{C}(\text{CO})_{12}]^-$  and  $[\text{Co}(\text{CO})_4]^-$ , respectively ( $\text{M} = \{\text{Co}_5\text{C}(\text{CO})_{12}\}\text{Au}\{\text{Co}(\text{CO})_4\}$ ). The major peak in the mass spectrum corresponds to the molecular ion  $[\mathbf{1}]^-$ , confirming its presence in solution. Its fragmentation path is interesting, since it indicates that the cluster may lose CO ligands or break down into  $[\text{Co}_5\text{C}(\text{CO})_{12}]^-$  and  $[\text{Co}(\text{CO})_4]^-$ , as suggested by the solid state structure. Traces of  $[\text{Co}_{11}\text{C}_2(\text{CO})_{23}]^{2-}$  are probably formed during ionisation because of partial oxidation.

$[\mathbf{1}]^-$  is stable under CO atmosphere, whereas it reacts with oxidants such as  $\text{HBF}_4$  and  $[\text{FeCp}_2]^+$  affording the new  $[\{\text{Co}_5\text{C}(\text{CO})_{12}\}_2\text{Au}]^-$ ,  $[\mathbf{2}]^-$ , cluster (see below). Conversely, further addition of  $[\text{AuCl}_4]^-$  results in the formation of a mixture of  $\text{Co}_3(\text{CCl})(\text{CO})_9$  and  $[\mathbf{2}]^-$ .  $[\mathbf{1}]^-$  is not stable after refluxing in  $\text{CH}_3\text{CN}$ , where it affords, after work-up,  $[\text{Co}_{11}\text{C}_2(\text{CO})_{23}]^{2-}$ . The reduction of  $[\mathbf{1}]^-$  with Na/naphtalene (or  $\text{NaBH}_4$ ) has been studied since it was believed that it might have been resulted in the reduction of Au(I) into Au(0) with concomitant release of  $[\text{Co}(\text{CO})_4]^-$  and the unprecedented  $[\text{Co}_5\text{C}(\text{CO})_{12}]^-$ . Conversely, the only products detected were  $[\text{Co}(\text{CO})_4]^-$  and  $[\text{Co}_6\text{C}(\text{CO})_{15}]^{2-}$ .

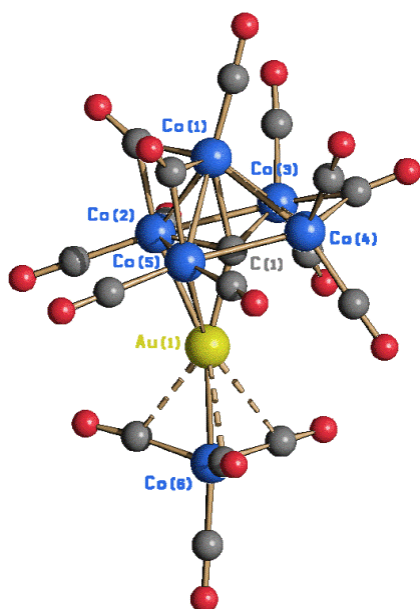


**Fig. 5.3.4** Molecular structure of  $[\mathbf{1}]^-$ , with key atoms labelled.

### Crystal structure

The molecular structure of  $[\mathbf{1}]^-$  has been determined as its  $[\text{NEt}_4][\mathbf{1}]$  salt (figure 5.3.4 table 5.3.1). The cluster anion may be viewed as a heteroleptic Au(I) complex containing  $[\text{Co}(\text{CO})_4]^-$  and  $[\text{Co}_5\text{C}(\text{CO})_{12}]^-$  as ligands. The latter “cluster ligand” is  $\eta^3$ -coordinated to Au(I) *via* Co(2), Co(5) and the carbide C(1). Considering it as a single ligand, the Au(1) centre displays an almost linear coordination  $[\text{Co}(6)\text{-Au}(1)\text{-Centroid}_{\text{Co}(2)\text{Co}(5)\text{C}(1)} 172.2(4)^\circ]$  as often found for Au(I) complexes. The Au(1)-Co(6) distance [2.503(16) Å] is significantly shorter than Au(1)-Co(2) [2.656(16) Å] and Au(1)-Co(5) [2.681(14) Å], in view of the fact that the former is a 2c-2e single bond, whereas the latter ones are delocalised “allyl-like” bonds. For comparison, the Au-Co

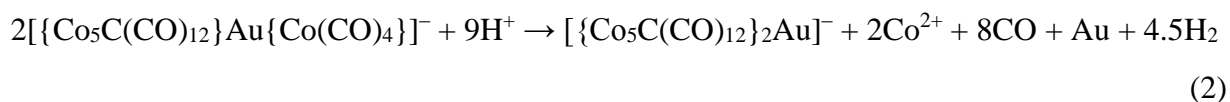
distance is 2.503 Å in  $\text{Au}(\text{PPh}_3)\{\text{Co}(\text{CO})_4\}$  and 2.509 Å in  $[\text{Au}\{\text{Co}(\text{CO})_4\}_2]^-$  which contain a

2c-2e  $\sigma$ -bond, whereas values in the range 2.61-2.90 Å are reported for Au atoms simultaneously bonded to two or more Co-atoms. In addition, there are three weak Au $\cdots$ C(O) interactions [2.68(2)-2.91(2) Å], involving three carbonyls of the [Co(CO)<sub>4</sub>]<sup>-</sup> anion.

The coordinated [Co(CO)<sub>4</sub>]<sup>-</sup> anion displays a trigonal bipyramidal geometry, with three carbonyls in equatorial positions, whereas the axial positions are occupied by the fourth CO and Au(1). The [Co<sub>5</sub>C(CO)<sub>12</sub>]<sup>-</sup> fragment shows a square pyramidal geometry, with the C(1) carbide slightly below the basal plane. It possesses 12 CO ligands, nine terminal and three edge bridging. The Co-Co distances compare very well to those previously reported for Co-carbide carbonyl clusters. As expected, the shortest contacts are those bridged by CO ligands, whereas the longest is Co(2)-Co(5) bridged by Au(1).

### 5.3.5 Synthesis and characterization of [{Co<sub>5</sub>C(CO)<sub>12</sub>]<sub>2</sub>Au]<sup>-</sup>, [2]<sup>-</sup>

The new [{Co<sub>5</sub>C(CO)<sub>12</sub>]<sub>2</sub>Au]<sup>-</sup>, [2]<sup>-</sup>, mono-anion was obtained from the reaction of [1]<sup>-</sup> with HBF<sub>4</sub> (ca. 7 equivalents), according to the equation (2):

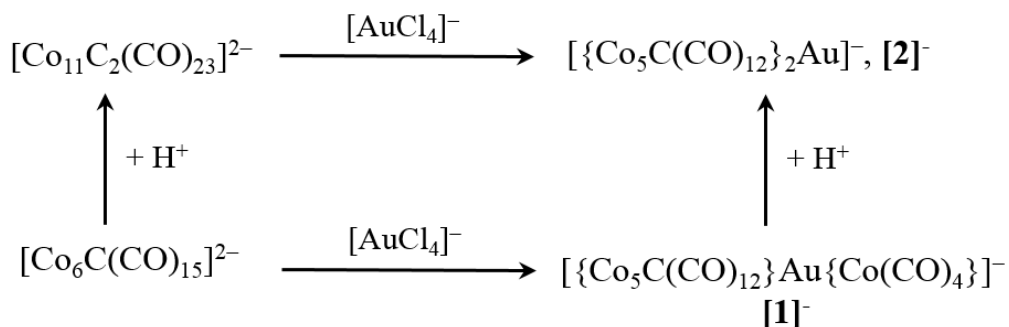


Crystals suitable for X-ray analyses of [NEt<sub>4</sub>][2] and [NMe<sub>3</sub>(CH<sub>2</sub>Ph)][2] have been obtained after work-up by slow diffusion of n-hexane into their CH<sub>2</sub>Cl<sub>2</sub> solutions. The ESI-MS spectrum in CH<sub>3</sub>CN solution displays negative peaks at *m/z* (relative intensity in parentheses) 1495 (90), 1482 (100), 1454 (80), 741 (10), 727 (20), 658 (25), 644 (25), 171 (30) attributable to [M(-CO, +CH<sub>3</sub>CN)]<sup>-</sup>, [M]<sup>-</sup>, [M(-CO)]<sup>-</sup>, [M]<sup>2-</sup>, [M(-CO)]<sup>2-</sup>, [Co<sub>11</sub>C<sub>2</sub>(CO)<sub>23</sub>]<sup>2-</sup>, [Co<sub>5</sub>C(CO)<sub>12</sub>]<sup>-</sup> and [Co(CO)<sub>4</sub>]<sup>-</sup>, respectively (M = {Co<sub>5</sub>C(CO)<sub>12</sub>]<sub>2</sub>Au).

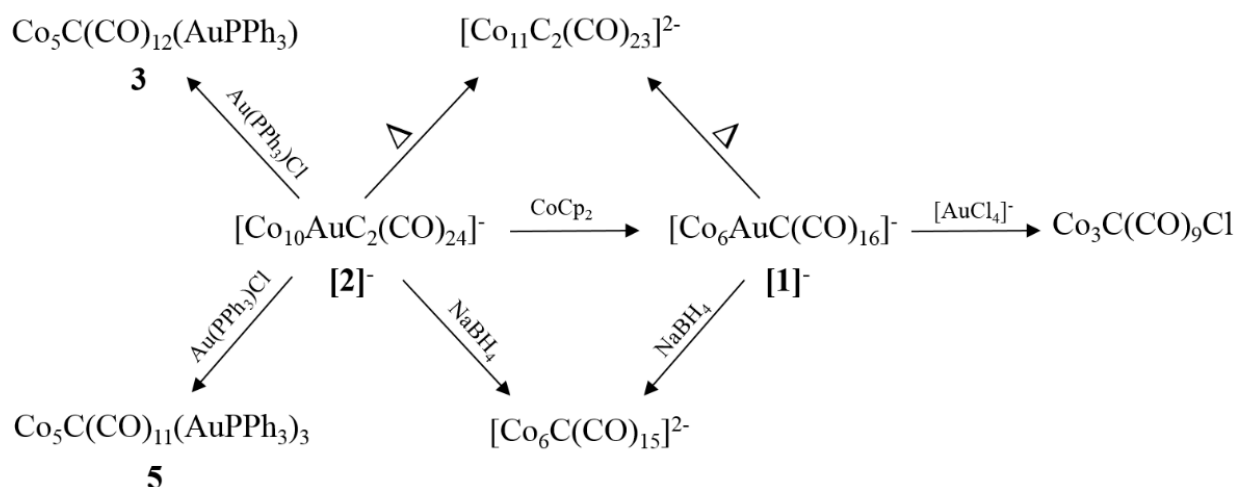
Alternatively, [2]<sup>-</sup> can be obtained from the reaction of [Co<sub>11</sub>C<sub>2</sub>(CO)<sub>23</sub>]<sup>2-</sup> with two equivalents of [AuCl<sub>4</sub>]<sup>-</sup> (scheme 5.3.1). In turn, [Co<sub>11</sub>C<sub>2</sub>(CO)<sub>23</sub>]<sup>2-</sup> is obtained by the oxidation of [Co<sub>6</sub>C(CO)<sub>15</sub>]<sup>2-</sup> with HBF<sub>4</sub>, as previously reported. Thus, the three clusters [1]<sup>-</sup>, [Co<sub>11</sub>C<sub>2</sub>(CO)<sub>23</sub>]<sup>2-</sup> and [2]<sup>-</sup> may be all obtained starting from [Co<sub>6</sub>C(CO)<sub>15</sub>]<sup>2-</sup> and adding [AuCl<sub>4</sub>]<sup>-</sup> and/or HBF<sub>4</sub> in the correct order. This sort of “commutative property” is not common in metal carbonyl clusters although other examples are known. [2]<sup>-</sup> is stable under CO (1 bar) and does not react with PPh<sub>3</sub>. Conversely, [Co<sub>11</sub>C<sub>2</sub>(CO)<sub>23</sub>]<sup>2-</sup> is obtained after refluxing [2]<sup>-</sup> in CH<sub>3</sub>CN. Its reduction with [CoCp<sub>2</sub>] results in the formation of [1]<sup>-</sup>, first, and, then [Co<sub>6</sub>C(CO)<sub>15</sub>]<sup>2-</sup>. Finally, the new derivatives [Co<sub>5</sub>C(CO)<sub>12</sub>(AuPPh<sub>3</sub>)], **3**, and [Co<sub>5</sub>C(CO)<sub>11</sub>(AuPPh<sub>3</sub>)<sub>3</sub>], **5**, have been obtained by reacting [2]<sup>-</sup> with two and four equivalents of [Au(PPh<sub>3</sub>)Cl], respectively. The reactivity of both [1]<sup>-</sup> and [2]<sup>-</sup> are summarized in scheme 5.3.2.

	[1] <sup>-</sup>	[2] <sup>-</sup>	3	4	5A	5B
Co-Co	2.47(2)-2.701(19) Average 2.56(6)	2.4687(9)-2.7003(9) Average 2.552(4)	2.468(4)-2.668(4) Average 2.551(11)	2.4716(16)-2.9147(15) Average 2.582(4)	2.478(3)-2.860(3) Average 2.594(8)	2.4694(13)-2.8349(12) Average 2.600(4)
Co-C <sub>carbide</sub>	1.88(9)-2.04(10) Average 1.92(19)	1.883(4)-2.068(5) Average 1.924(13)	1.87(2)-1.993(16) Average 1.90(4)	1.883(8)-1.961(8) Average 1.908(18)	1.882(13)-1.982(14) Average 1.91(3)	1.863(6)-1.993(6) Average 1.918(13)
Co-Au	2.503(16)-2.656(16) Average 2.58(2)	2.6756(7)-2.6834(7) Average 2.6799(14)	2.723(2)-2.760(3) Average 2.741(4)	2.612(1)-3.369(2) Average 2.784(5)	2.589(2)-3.143(2) Average 2.828(6)	2.636(1)-3.348(2) Average 2.798(9)
Au-C <sub>carbide</sub>	2.11(10)	2.167(4)-2.180(5) Average 2.174(6)	2.117(15)	2.118(8)	2.027(14)	2.102(6)
Au-Au	-	-	-	3.1219(5)	2.8587(12) and 3.1447(11)	2.8394(2) and 4.160(2)
Au-P	-	-	2.281(4)	2.277(2)-2.292(2) Average 2.284(3)	2.262(5)-2.312(4) Average 2.287(9)	2.2887(18)-2.3007(16) Average 2.293(7)
Co <sub>apex</sub> -C <sub>carbide</sub> -Au	154(5)°	151.4(2) and 151.3(2)°	160.0(10)°	154.1(4)	168.8(8)°	157.8(3)
Deviation of C <sub>carbide</sub> from the Co <sub>4</sub> square basal plane	0.38(9)	0.384(5) and 0.409(4)	0.331(15)	0.281(12)	0.276(14)	0.271(13)

**Table 5.3.1** Main bonding parameters (Å and °) of [ $\text{Co}_5\text{C}(\text{CO})_{12}\text{Au}\{\text{Co}(\text{CO})_4\}$ ]<sup>-</sup>, [1]<sup>-</sup>, [ $\text{Co}_5\text{C}(\text{CO})_{12}\text{Au}$ ]<sup>-</sup>, [2]<sup>-</sup>, [ $\text{Co}_5\text{C}(\text{CO})_{12}(\text{AuPPh}_3)_3$ ]<sup>-</sup>, [3], [ $\text{Co}_5\text{C}(\text{CO})_{11}(\text{AuPPh}_3)_2$ ]<sup>-</sup>, [4] and [ $\text{Co}_5\text{C}(\text{CO})_{11}(\text{AuPPh}_3)_3$ ]<sup>-</sup>, [5].



**Scheme 5.3.1** Different routes for the synthesis of the bimetallic Co-Au  $[\mathbf{2}]^-$ .  $[\mathbf{2}]^-$  can be obtained from the redox condensation of  $[\text{AuCl}_4]^-$  and  $[\text{Co}_{11}\text{C}_2(\text{CO})_{23}]^{2-}$  or by the oxidation of  $[\mathbf{1}]^-$ .



**Scheme 5.3.2** Reactivity of  $[\mathbf{1}]^-$  and  $[\mathbf{2}]^-$ .

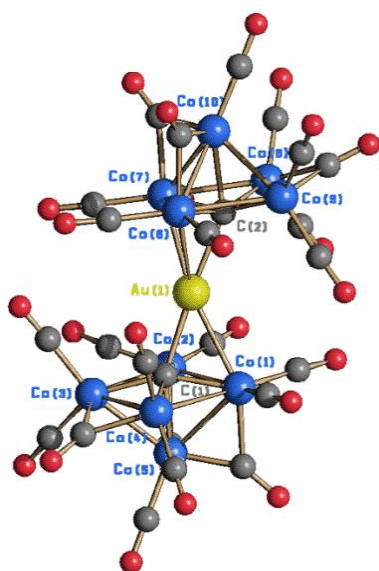


**Figure 5.3.5** Molecular structure of  $[\mathbf{2}]^-$ , with key atoms labelled.

### Crystal structure

Two almost identical structures of  $[\mathbf{2}]^-$  have been determined as its  $[\text{NEt}_4][\mathbf{2}]$  and  $[\text{NMe}_3(\text{CH}_2\text{Ph})][\mathbf{2}]$  salts (figure 5.3.5 and table 5.3.1). The molecular anion  $[\mathbf{2}]^-$  is a homoleptic Au(I) complex composed by two  $[\text{Co}_5\text{C}(\text{CO})_{12}]^-$  anionic cluster ligands  $\eta^3$ -coordinated to Au(I). The two  $[\text{Co}_5\text{C}(\text{CO})_{12}]^-$  fragments are almost identical to the one found in  $[\mathbf{1}]^-$ , for what concerns the geometry of the metal cage, the bonding parameters and the stereochemistry of the CO ligands. Au(I) forms two Au-Co bonds with each  $[\text{Co}_5\text{C}(\text{CO})_{12}]^-$  fragment as well as one Au-C<sub>carbide</sub> bond; the Au-Co distances are comparable to those found in  $[\mathbf{1}]^-$ . The Au(1)⋯Co(3), Au(1)⋯Co(4), Au(1)⋯Co(8) and Au(1)⋯Co(9) interactions are essentially non-bonding.

### 5.3.6 Electrochemistry and IR spectroelectrochemistry of [1]<sup>-</sup> and [2]<sup>-</sup>

[2]<sup>-</sup> exhibits a rich redox activity in CH<sub>2</sub>Cl<sub>2</sub>/[N<sup>n</sup>Bu<sub>4</sub>][PF<sub>6</sub>] solution, in that it undergoes two oxidations and four reductions (figure 5.3.6 and table 5.3.2). The oxidation at +0.84 V is multi-electronic and irreversible, while the anodic process at +0.32 V and the first two reductions (-1.02 and -1.30 V) possess features of chemical reversibility in the cyclic voltammetric timescale, and involve identical numbers of electrons, as inferred from hydrodynamic voltammetry. The most cathodic steps at -1.81 and -2.11 V are partially chemically reversible and the number of involved electrons is ill-defined. By comparison with the [FeCp<sub>2</sub>]/[FeCp<sub>2</sub>]<sup>+</sup> couple ( $\Delta E_p = 75$  mV at 0.1 V/s) and on the basis of the dependence of the peak currents from scan rate (0.02-1.0 V/s) the oxidation step at +0.32 V and the reductions at -1.02 and -1.30 V may be described as electrochemically reversible, whereas the electrochemical quasi-reversibility of the processes at -1.81 and -2.11 V can be inferred from their peak-to-peak separations (110 and 160 mV, respectively, measured at 0.1 V/s).

In the attempt to determine the electron stoichiometry of the process occurring at -1.02 V, we subjected a solution of [2]<sup>-</sup> to constant-potential bulk-electrolysis ( $E_w = -1.2$  V). By monitoring the electrolysis progress by cyclic and hydrodynamic voltammetry, the shift of the current axis of the cathodic wave was accompanied by a progressive decrease of the total concentration of the [2]<sup>-</sup>/[2]<sup>n-</sup> couple, indicating that the reduced species was not stable in the time of exhaustive electrolysis.

	Oxidation processes			Reduction processes							
	$E^{\circ}_1$	$E^{\circ}_2$	$\Delta E_p^a$	$E^{\circ}_3$	$\Delta E_p^a$	$E^{\circ}_4$	$\Delta E_p^a$	$E^{\circ}_5$	$\Delta E_p^a$	$E^{\circ}_6$	$\Delta E_p^a$
[2] <sup>-b</sup>	0.84 <sup>c</sup>	0.32	80	-1.02	75	-1.30	81	-1.81 <sup>d</sup>	110	-2.02 <sup>d</sup>	160
	0.45	0.71		-0.63		-0.91		-1.42		-1.72	
[1] <sup>-b</sup>	0.40 <sup>e</sup>	0.27 <sup>e</sup>		-1.16	80	-1.70	130				
	0.79	0.66		-0.77		-1.31					
[1] <sup>-c</sup>				-1.15	80	-1.84	140	-2.53	150	-3.09 <sup>e</sup>	

**Table 5.3.2** Formal electrode potentials [V vs. [FeCp<sub>2</sub>] (blue) vs. SCE (red)] and peak-to-peak separations (mV) for the redox processes exhibited in CH<sub>2</sub>Cl<sub>2</sub> or thf solution by [2]<sup>-</sup> and [1]<sup>-</sup>. <sup>a</sup> Measured at 0.1 V/s. <sup>b</sup> In CH<sub>2</sub>Cl<sub>2</sub>/[N<sup>n</sup>Bu<sub>4</sub>][PF<sub>6</sub>] solution. <sup>c</sup> In thf/[N<sup>n</sup>Bu<sub>4</sub>][PF<sub>6</sub>] solution. <sup>d</sup> Coupled to relatively fast chemical reactions. <sup>e</sup> Peak potential value for irreversible processes.

The process was proved to be mono-electronic by monitoring the reduction of [2]<sup>-</sup>, carried out with an equimolar amount of [CoCp<sub>2</sub>], by hydrodynamic voltammetry recorded immediately after the addition of the reducing agent: the expected anodic shift of the current axis

of the process at  $-1.02$  V, that remained unchanged as far as the height of the wave is concerned, pointed out the quantitative formation of the  $[2]^{2-}$  dianionic cluster ( $E_{1-/2-}^{\circ} = -1.02$  V).

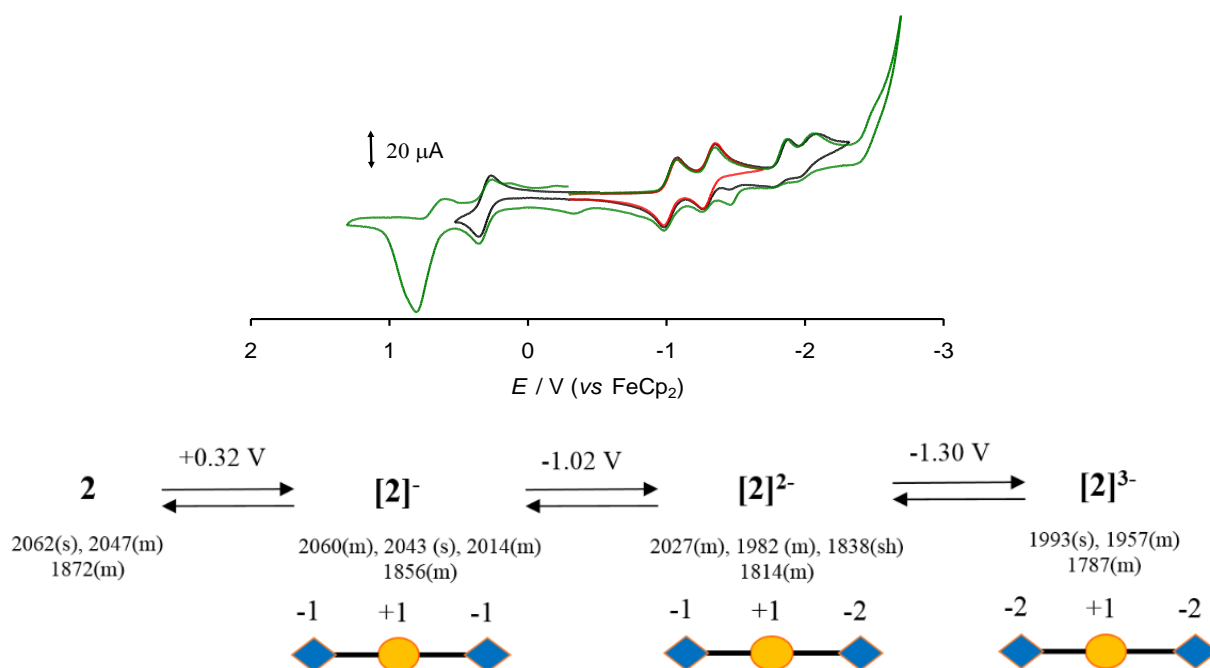


**Figure 5.3.6** Top: cyclic voltammograms (green, black and red) recorded at a platinum electrode in a  $\text{CH}_2\text{Cl}_2$  solution of  $[2]^-$ .  $[\text{N}^n\text{Bu}_4][\text{PF}_6]$  (0.2 M) as supporting electrolyte. Scan rates: 0.1 V/s. Bottom: reversible reduction oxidation equilibria of the  $[2]^{n-}$  ( $n = 0-3$ ). The reductions are centred on the  $[\text{Co}_5\text{C}(\text{CO})_{12}]^-$  units as sketched ( $\bullet$ ,  $\text{Au}^+$ ;  $\blacklozenge$ ,  $[\text{Co}_5\text{C}(\text{CO})_{12}]^-$ ).

$[2]^{2-}$ , in turn, is reversibly reduced to  $[2]^{3-}$  ( $E_{2-/3-}^{\circ} = -1.30$  V), whereas the first anodic process ( $E_{0/1-}^{\circ} = +0.32$  V) corresponds to the formation of the neutral **2** species. Thus, the four  $[\{\text{Co}_5\text{C}(\text{CO})_{12}\}_2\text{Au}]^{n-}$  ( $n = 0-3$ ) clusters are stable in the timescale of cyclic voltammetry, and the electrochemical reversibility of the associate redox transfers suggests that only slight distortions of the geometry of the cluster occur during these electrochemical processes.

The one-electron oxidation and the two consecutive one-electron reductions of  $[2]^-$  have been followed by IR spectroelectrochemistry in  $\text{CH}_2\text{Cl}_2/[\text{N}^n\text{Bu}_4][\text{PF}_6]$  solution (figure 5.3.7). The CO stretching absorptions of  $[2]^-$  are gradually replaced, upon the one-electron oxidation, by new peaks at higher frequencies, accordingly to the formation of the neutral cluster **2**. Upon reduction, the CO stretching absorptions of  $[2]^-$  undergo two gradual downshifts according to the formation of  $[2]^{2-}$  as  $[2]^{3-}$ , respectively. In all cases, the spectral changes pointed out the appearance of well-defined isosbestic points. On the time scale of the IR experiment, however, both the complete oxidation and the complete reductions are accompanied by partial decomposition, more severe in the case of the  $-2/-3$  redox change, which did not allow the complete recovery of the starting compound in the backward potential scan.

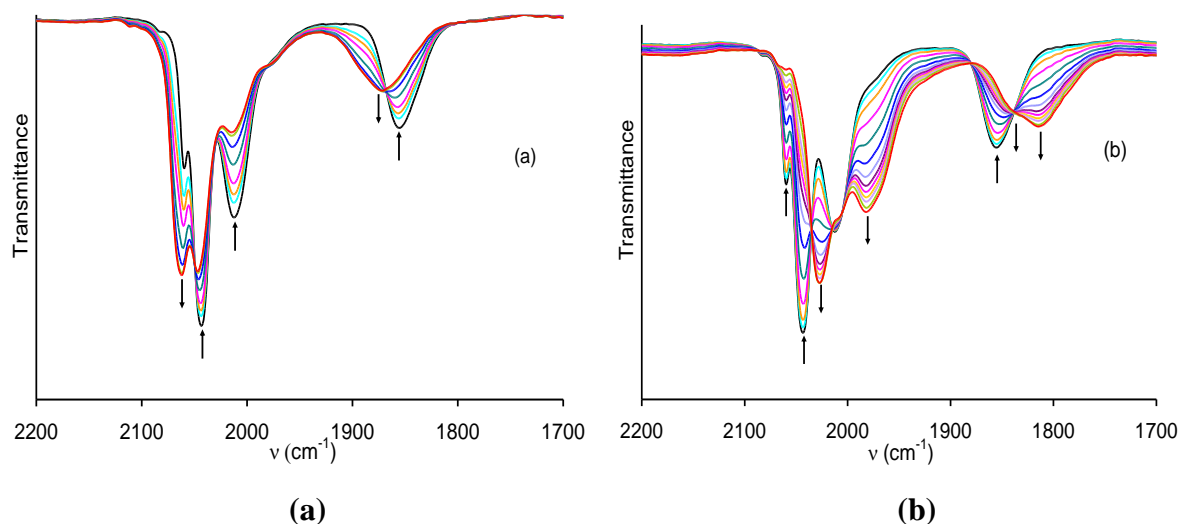


**Figure 5.3.7** IR spectral changes recorded in an OTTLE cell during the progressive (a) one-electron oxidation, and (b) one-electron reductions of  $[2]^-$  in  $\text{CH}_2\text{Cl}_2$  solution (only the spectra collected before the disappearance of isosbestic points are reported).  $[\text{N}^n\text{Bu}_4][\text{PF}_6]$  (0.2 M) as the supporting electrolyte.

DFT calculations using the hybrid EDF2 functional on  $[2]^-$  (figure 5.3.8) point out the presence of two closely spaced empty molecular orbitals [-1.53 and -1.36 eV] corresponding to the LUMO and LUMO+1 ( $\Delta = 0.17$  eV), well above the HOMO [-3.71 eV] (HOMO-LUMO gap 2.18 eV). Both LUMO and LUMO+1 are mainly centred on the two  $[\text{Co}_5\text{C}(\text{CO})_{12}]^-$  moieties of  $[2]^-$  (figure 5.3.9). Therefore, we may conclude that the two extra-electrons involved in the first two reduction steps of  $[2]^-$  are added to the  $[\text{Co}_5\text{C}(\text{CO})_{12}]^-$  fragments which are reduced to  $[\text{Co}_5\text{C}(\text{CO})_{12}]^{2-}$ . The limited stability of  $[2]^{n-}$  ( $n = 2, 3$ ), which hampers their chemical isolation, might be due to intra-molecular redox reactions, which lead to Au(0) and  $[\text{Co}_5\text{C}(\text{CO})_{12}]^-$ , with concomitant fragmentation of the cluster. This process is likely to be favoured by the addition of further electrons during the third and fourth cathodic reactions which, therefore, are not reversible. Conversely, the HOMO receives some significant contribution also from the Au(I) centre, suggesting that the reversible oxidation leading to **2** involves the whole cluster.

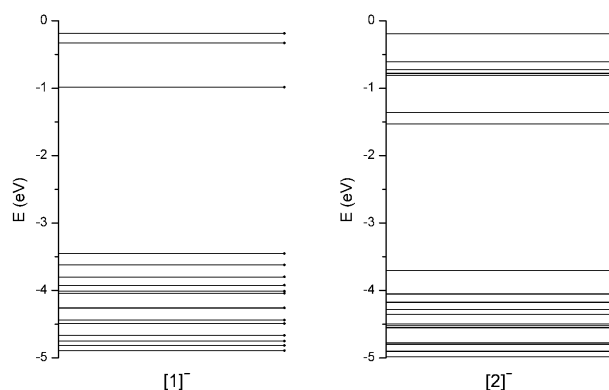


**Figure 5.3.8** Energies (eV) of the Kohn-Sham molecular orbitals in the frontier regions for  $[1]^-$  and  $[2]^-$ .

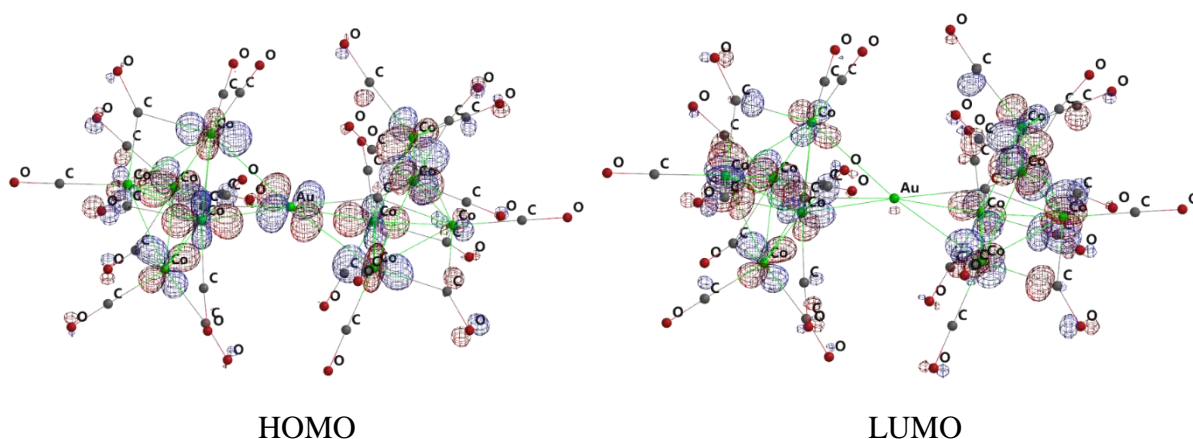


**Figure 5.3.9** HOMO and LUMO of  $[2]^-$ . DFT EDF2 calculations, isovalue = 0.04 a.u.

Figure 5.3.10 shows the voltammetric profile exhibited by  $[1]^-$  in  $\text{CH}_2\text{Cl}_2/[\text{N}^n\text{Bu}_4][\text{PF}_6]$  solution. In the anodic region four irreversible processes are observed at the potentials of  $-0.42$ ,  $-0.20$ ,  $+0.27$  and  $+0.40$  V, respectively; only the oxidations at  $+0.27$  and  $+0.40$  V can be attributed to the starting compound, while the processes at  $-0.42$  and  $-0.20$  V appear to be related to decomposition products formed during the reduction scan.

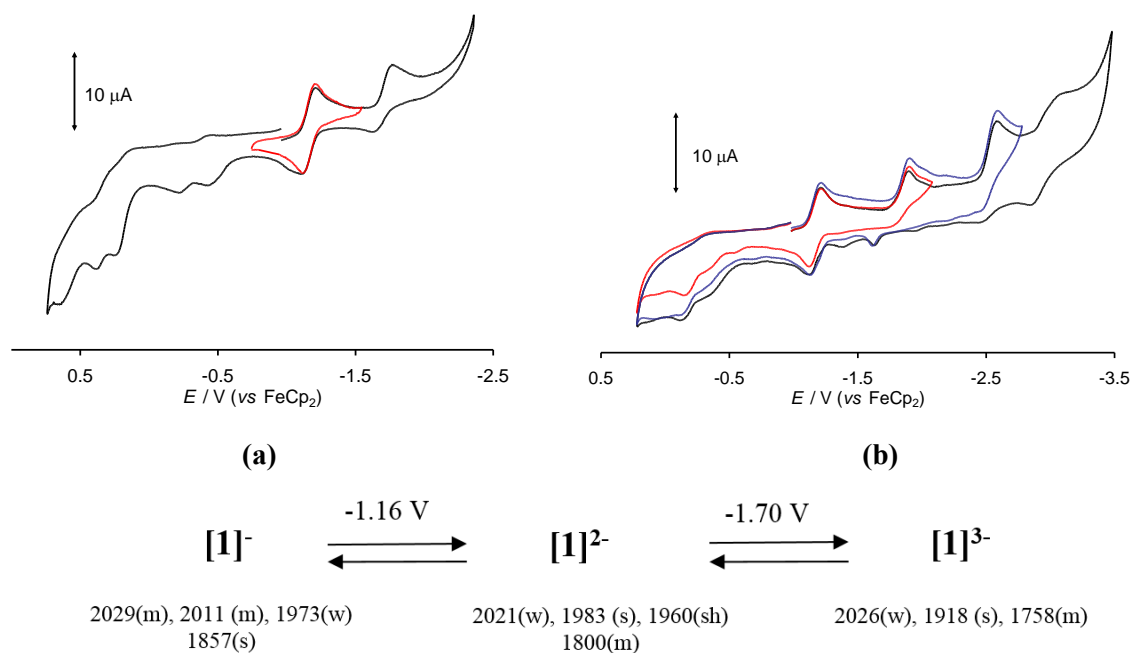


**Figure 5.3.10** Cyclic voltammograms recorded at a platinum electrode of  $[1]^-$  (a) in  $\text{CH}_2\text{Cl}_2$  and (b) in thf solutions.  $[\text{N}^n\text{Bu}_4][\text{PF}_6]$  (0.2 M) as supporting electrolyte. Scan rates: 0.1 V/s.

In the cathodic region, one reduction at  $-1.16$  V, with features of chemical reversibility in the cyclic voltammetry time scale, is followed by a further, partially chemically reversible reduction at  $-1.70$  V. By comparison with the hydrodynamic voltammetric response of the  $[2]^-/[2]^{2-}$  couple, the two cathodic processes involve both the consumption of one electron per

molecular unit. Analysis of the cyclic voltammetric responses of the reductions with scan rates progressively increasing from 0.02 to 1.0 V/s confirmed that the reduction at  $-1.16$  V is a simple, chemically and electrochemically reversible process, while the second one at  $-1.70$  V appears electrochemically quasi-reversible, and complicated by subsequent chemical reactions.

If compared to  $[2]^-$ ,  $[1]^-$  in  $\text{CH}_2\text{Cl}_2$  solution exhibits a poorer redox activity. In spite of the similarity in the redox aptitude of the two mono-anionic clusters to give the  $-2$  charged species, a second electron is accommodated by  $[2]^-$  more easily than  $[1]^-$  ( $-1.30$  V and  $-1.70$  V, respectively), and further reductions are no more observable for the latter, due to the discharge of the solvent. Thus, we carried out the cyclovoltammetric analysis of  $[1]^-$  in  $\text{thf}/[\text{N}^n\text{Bu}_4][\text{PF}_6]$  solution: four reduction processes were observed also for this cluster anion. As in  $\text{CH}_2\text{Cl}_2$  solution, only the first process is electrochemically and chemically reversible in the time scale of the cyclic voltammetry, whereas the three subsequent cathodic processes appear as electrochemically quasi-reversible and coupled to chemical complications, as showed by the appearance of oxidation processes in the back scan toward positive potentials.

The IR spectroelectrochemical changes following the stepwise two-electron reduction of the  $[1]^-$  cluster anion in  $\text{CH}_2\text{Cl}_2$  are shown in figure 5.3.11.

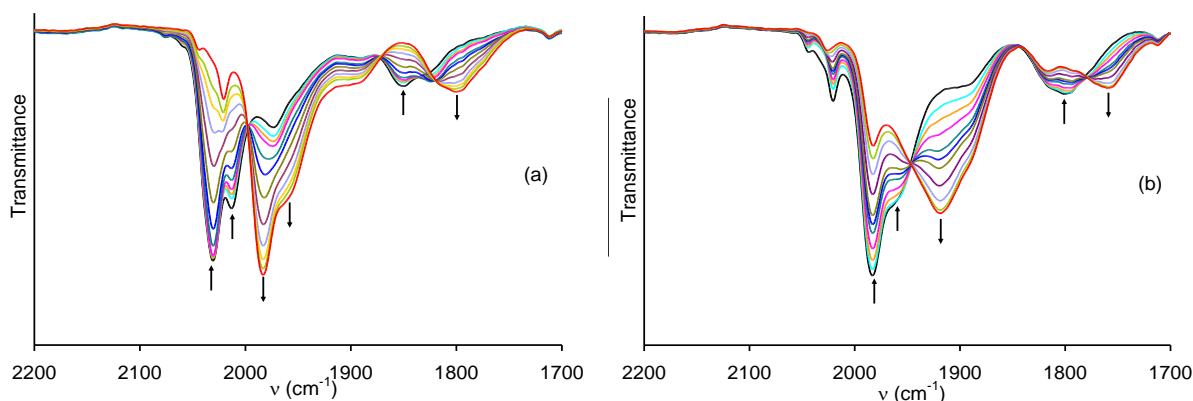


**Figure 5.3.11** IR spectral changes recorded in an OTTLE cell during the two consecutive one-electron reductions of  $[1]^-$  in  $\text{CH}_2\text{Cl}_2$  solution;  $[\text{N}^n\text{Bu}_4][\text{PF}_6]$  (0.2 M) as the supporting electrolyte.

The additions of the first and second electron are accompanied by the downshift of the stretching vibrations of the terminal, and bridging carbonyl groups of  $[1]^-$ , according to the gradual formation of  $[1]^{2-}$  and  $[1]^{3-}$  species. On the time scale of the IR experiment, however, both the clusters  $[1]^{2-}$  and  $[1]^{3-}$  undergo a partial decomposition that hampers the complete recovery of the starting compound in the backward potential scan. Accordingly, not all the isosbestic points persist until the end of the reduction processes and in the spectra of  $[1]^{2-}$  and

$[\mathbf{1}]^{3-}$ , the presence of other stretching vibrations can be tentatively attribute to  $[\text{Co}(\text{CO})_4]^-$  and  $[\text{Co}_6\text{C}(\text{CO})_{15}]^{2-}$ .

As in the case of  $[\mathbf{2}]^-$ , also in  $[\mathbf{1}]^-$  the LUMO (-0.98 eV) is mainly centred on the  $[\text{Co}_5\text{C}(\text{CO})_{12}]^-$  fragment (figure 5.3.12), which is reduced to  $[\text{Co}_5\text{C}(\text{CO})_{12}]^{2-}$  and  $[\text{Co}_5\text{C}(\text{CO})_{12}]^{3-}$ , respectively, after the first and second reduction step. On the other hand, all the cobalt and gold centres contribute to the HOMO (-3.45 eV), which is well-separated from the unoccupied orbitals. The instability of  $[\mathbf{1}]^{n-}$  ( $n = 2, 3$ ) is likely to be due to intra-molecular redox reactions which lead to Au(0) and oxidation of  $[\text{Co}_5\text{C}(\text{CO})_{12}]^{n-}$ , with concomitant fragmentation of the cluster.

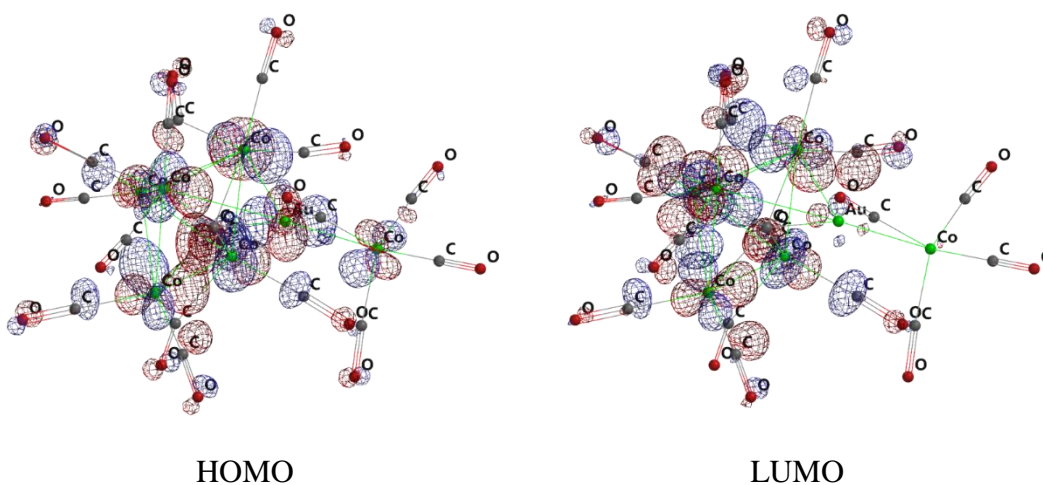


**Figure 5.3.12** HOMO and LUMO of  $[\mathbf{1}]^-$ . DFT EDF2 calculations, isovalue = 0.04 a.u.

### 5.3.7 Synthesis and structure of $[\text{Co}_5\text{C}(\text{CO})_{12}(\text{AuPPh}_3)]$ , **3**

The new derivative **3** has been obtained by reacting  $[\mathbf{2}]^-$  with two equivalents of  $\text{Au}(\text{PPh}_3)\text{Cl}$ . Its structure is very similar to  $[\mathbf{1}]^-$ , being composed by an  $\text{Au}^+$  centre coordinated by  $\text{PPh}_3$  and one  $\eta^3\text{-}[\text{Co}_5\text{C}(\text{CO})_{12}]^-$  anionic cluster ligand (figure 5.3.13). Alternatively, it may be viewed as a  $[\text{Co}_5\text{C}(\text{CO})_{12}]^-$  cluster anion stabilised by a  $[\text{AuPPh}_3]^+$  fragment. The  $[\text{Co}_5\text{C}(\text{CO})_{12}]^-$  fragment found in **3** is very similar to those present in  $[\mathbf{1}]^-$  and  $[\mathbf{2}]^-$  (see table 5.3.1). The Co(5)-C(1)-Au(1) angle of  $160.0(10)^\circ$  is sensibly larger than in  $[\mathbf{1}]^-$  and  $[\mathbf{2}]^-$ , indicating that in this case Au(1) occupies a slightly more central position. Therefore, the bonding Au(1)-Co(2) and Au(1)-Co(4) interactions in  $\text{Co}_5\text{C}(\text{CO})_{12}(\text{AuPPh}_3)$  are longer than in  $[\mathbf{1}]^-$  and  $[\mathbf{2}]^-$ , whereas the non-bonding Au(1) $\cdots$ Co(3) and Au(1) $\cdots$ Co(6) interactions are shorter. In this sense, this structure may be viewed as intermediate between the open ( $\eta^3$ ) and closo ( $\eta^5$ ) octahedron.

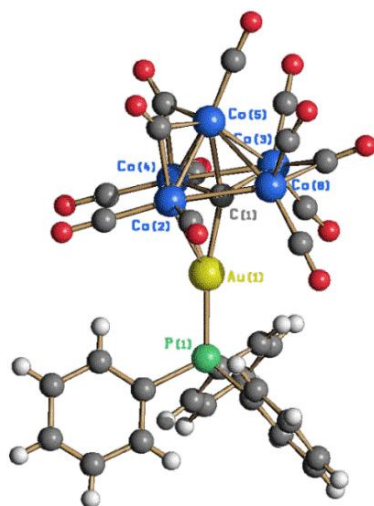


**Figure 5.3.13** Molecular structure of **3**, with key atoms labelled (Au, yellow; Co, blue; P, green; C, grey; O, red; H, white).

### 5.3.8 Synthesis and structure of $[\text{Co}_5\text{C}(\text{CO})_{11}(\text{AuPPh}_3)_2]^-$ , **4**

The closely related mono-anion  $[\text{Co}_5\text{C}(\text{CO})_{11}(\text{AuPPh}_3)_2]^-$ , **4**, has been obtained in moderate yields by reacting  $[\text{Co}_6\text{C}(\text{CO})_{15}]^{2-}$  in thf with two equivalents of  $[\text{Au}(\text{PPh}_3)\text{Cl}]$  and one equivalent of  $\text{PPh}_3$ . The latter, probably, is needed in order to help the elimination of one Co-atom from the cluster.

The structure of the **4** mono-anion has been determined as its  $[\text{NEt}_4][\mathbf{4}] \cdot 2\text{CH}_2\text{Cl}_2$  salt (figure 5.3.14 and table 5.3.1). This anion formally derives from **5**, by removing one  $[\text{AuPPh}_3]^+$  fragment. Indeed, it contains the same  $[\text{Co}_5\text{C}(\text{CO})_{11}]^{3-}$  anionic framework bonded to two  $[\text{AuPPh}_3]^+$  fragments. The  $[\text{Co}_5\text{C}(\text{CO})_{11}]^{3-}$  anionic framework displays the same square pyramidal structure found in **5** with similar bonding parameters.

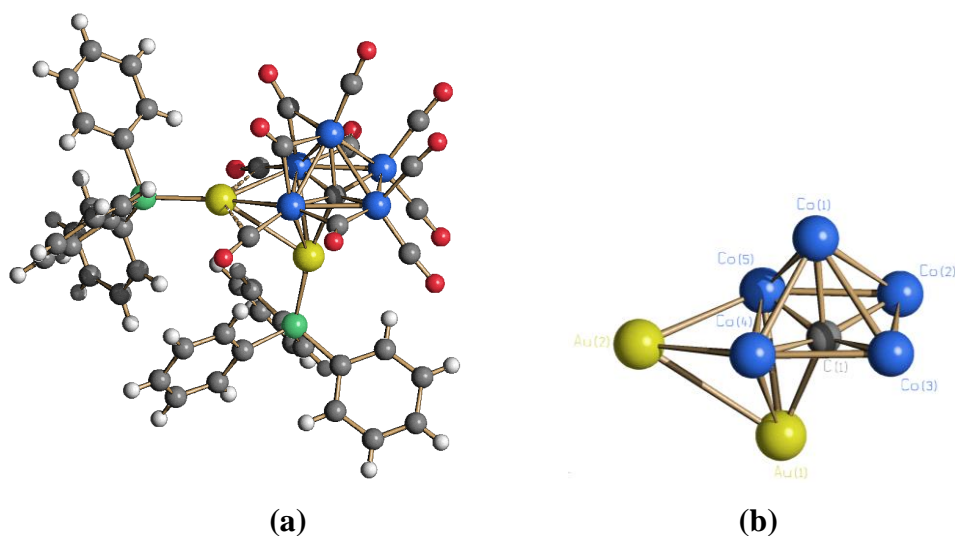


**Figure 5.3.14** (a) Molecular structure and (b) metal cage framework of **4** (Au, yellow; Co, blue; P, green; C, grey; O, red; H, white).

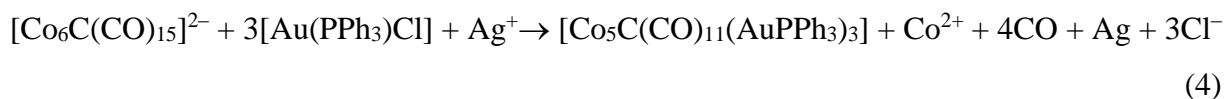
Nonetheless, the stereochemistry of the CO ligands is different, probably in order to accommodate a different number of  $[\text{AuPPh}_3]^+$  fragments. Thus, **4** contains seven terminal carbonyls and four edge bridging CO's, whereas **5** displays eight terminal and three  $\mu$ -CO ligands. Finally, the two equatorial carbonyls bonded to Co(4) and Co(5) form two weak  $\text{Au}\cdots\text{C}(\text{O})$  interactions [2.796(11) and 2.800(10) Å] with Au(2).

### 5.3.9 Synthesis and structure of $[\text{Co}_5\text{C}(\text{CO})_{11}(\text{AuPPh}_3)_3]$ , **5**

The neutral  $[\text{Co}_5\text{C}(\text{CO})_{11}(\text{AuPPh}_3)_3]$ , **5**, cluster was isolated for the first time in very low yields as  $\mathbf{5}\cdot\text{thf}\cdot 0.5\text{C}_6\text{H}_{14}$  whilst studying the reaction of  $[\{\text{Co}_5\text{C}(\text{CO})_{12}\}_2\text{Au}]^-$  with four equivalents of  $[\text{Au}(\text{PPh}_3)\text{Cl}]$ . In the search for a better synthesis of **5**, we have found that the target compound can be obtained in moderate yields by using four equivalents of the Au(I) reagent per mole of  $[\text{Co}_6\text{C}(\text{CO})_{15}]^{2-}$ , in according to equation (3):



Only three moles of  $[\text{Au}(\text{PPh}_3)\text{Cl}]$  are actually used for the decoration of **5**, whereas the fourth one is used as an oxidant. Indeed, the same product can be also obtained from the reaction of  $[\text{Co}_6\text{C}(\text{CO})_{15}]^{2-}$  with 3 equivalents of  $[\text{Au}(\text{PPh}_3)\text{Cl}]$  in the presence of an oxidant such as  $\text{Ag}^+$  or  $\text{HBF}_4$ , as depicted by equation (4):



Alternatively, the more oxidized  $[\text{Co}_6\text{C}(\text{CO})_{14}]^-$  may be used as starting material, requiring *ca.* 3 equivalent of  $[\text{Au}(\text{PPh}_3)\text{Cl}]$  (5):



Two different isomers of **5**, showing significant structural differences may be obtained depending on the crystallization conditions. Thus, crystals of  $\mathbf{5}\cdot\text{thf}\cdot 0.5\text{C}_6\text{H}_{14}$ , containing isomer **5-A**, have been obtained, after work-up, by slow diffusion of n-hexane on its thf solutions (figure 5.3.15 and table 5.3.1). Conversely, crystals of  $\mathbf{5}\cdot\text{CH}_3\text{CN}$ , containing the new isomer **5-B**, have been obtained by slow diffusion of n-hexane and di-isopropyl-ether on a  $\text{CH}_3\text{CN}$  solution. These crystals are almost insoluble in all organic solvents and IR analysis in solid as nujol mulls shows different spectra in view of the different structures of isomers **5-A** and **5-B**.

The molecular structure of isomer **5-A** may be viewed as composed by a  $[\text{Co}_5\text{C}(\text{CO})_{11}]^{3-}$  anionic framework stabilised by three  $[\text{AuPPh}_3]^+$  fragments. The  $[\text{Co}_5\text{C}(\text{CO})_{11}]^{3-}$  anion is

isoelectronic with  $[\text{Co}_5\text{C}(\text{CO})_{12}]^-$ , and the two anions show the same square pyramidal structure of the  $\text{Co}_5\text{C}$  cage. The  $[\text{Co}_5\text{C}(\text{CO})_{11}]^{3-}$  anion contains 8 terminal and 3 edge bridging carbonyls.

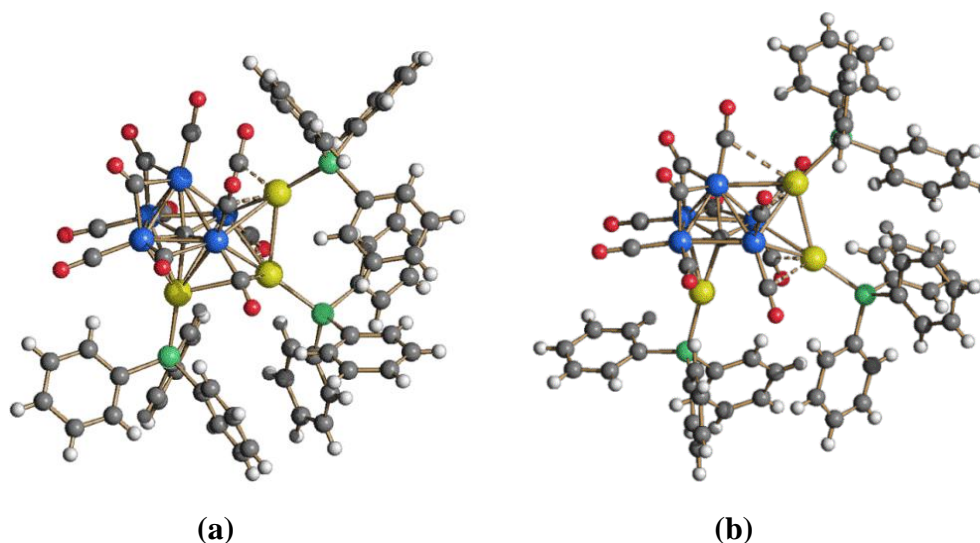


**Figure 5.3.15** Molecular structure of the isomer (a) **5-A** and (b) **5-B**. Weak  $\text{Au}\cdots\text{C}(\text{O})$  interactions (2.65(2)-2.74(2) Å) are represented with fragmented lines (Au, yellow; Co, blue; P, green; C, grey; O, red; H, white).

The  $\text{Co}_5\text{C}$  framework of **5-A** is  $\eta^5$ -coordinated to Au(1) resulting in a distorted  $\text{Co}_5\text{CAu}$  closo octahedron. The Au(2)Au(3) dimer is directly bonded to Au(I) *via* Au(2). The cluster contains two Au-Au contacts which may be considered bonding, one shorter [Au(2)-Au(3) 2.8587(12) Å] and one longer [Au(1)-Au(2) 3.1447(11) Å] (figure 5.3.16 a).

The molecular structure of isomer **5-B** shows some differences compared to **5-A** mainly regarding the three  $[\text{AuPPh}_3]^+$  fragments. Indeed  $[\text{Co}_5\text{C}(\text{CO})_{11}]^{3-}$  is  $\eta^3$ -coordinated to Au(1) in **5-B** and Au(1) is not bonded to any other Au-atom (figure 5.3.16 b).

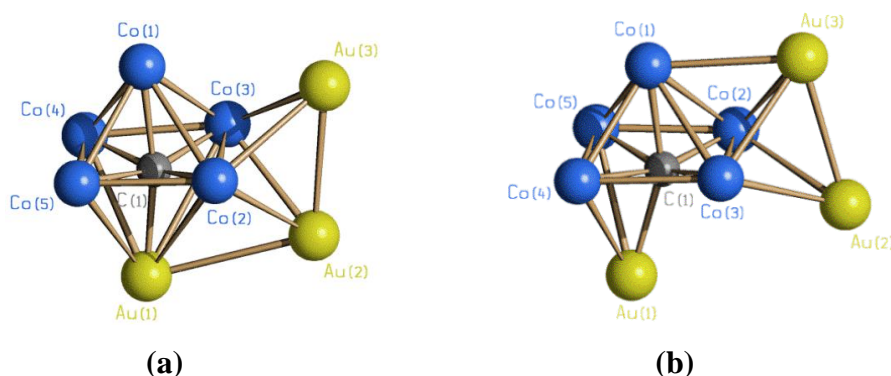


**Figure 5.3.16** Metal cage framework of the isomers (a) **5-A** and (b) **5-B** with key atoms labelled (Au, yellow; Co, blue).

Conversely a direct bond is present between Au(2) and Au(3). Then, as a consequence of the different position of Au(1), the Au(2)Au(3) fragment is moved towards Co(1) in **5-B** whereas

it is weakly bonded to Au(1) in **5-A**. The Au(1)···Au(2) contact is non-bonding in **5-B**. In addition, **5-A** contains five Au···C(O) weak contacts [2.69(7)-2.97(3) Å].

## Final Remarks

In this chapter two different approaches for the synthesis of bimetallic Ni-Au and Co-Au carbonyl clusters have been described. Starting from suitable preformed carbonyl clusters, their redox condensation with  $[\text{AuCl}_4]^-$  lead to Au(I) complexes containing cluster ligands, *i.e.*,  $[\text{Ni}_{12}\text{Au}(\text{CO})_{24}]^{3-}$ ,  $[\{\text{Co}_5\text{C}(\text{CO})_{12}\}\text{Au}\{\text{Co}(\text{CO})_4\}]^-$  and  $[\{\text{Co}_5\text{C}(\text{CO})_{12}\}_2\text{Au}]^-$ . The two  $[\text{Ni}_6(\text{CO})_{12}]^{2-}$  anions coordinated to  $\text{Au}^+$  adopt different geometries, suggesting the large flexibility of the metal cores of metal carbonyl clusters. Instead, the interstitial carbide confers rigidity and directionality of coordination on the basal plane of  $[\text{Co}_5\text{C}(\text{CO})_{12}]^-$  units. It is noteworthy that  $[\text{Ni}_6(\text{CO})_{12}]^{2-}$  is a very stable cluster whereas the  $[\text{Co}_5\text{C}(\text{CO})_{12}]^-$  fragment is not known as a free species. This leads to different electrochemical behaviors. Indeed,  $[\text{Ni}_{12}\text{Au}(\text{CO})_{24}]^{3-}$  is irreversibly reduced to Au(0) and  $[\text{Ni}_6(\text{CO})_{12}]^{2-}$  and the next reduction is centered on the hexa-nuclear homoleptic cluster, whereas the electrochemical studies of  $[\{\text{Co}_5\text{C}(\text{CO})_{12}\}\text{Au}\{\text{Co}(\text{CO})_4\}]^-$  and  $[\{\text{Co}_5\text{C}(\text{CO})_{12}\}_2\text{Au}]^-$  show a very rich reversible redox chemistry centred on the coordinated  $[\text{Co}_5\text{C}(\text{CO})_{12}]^-$  fragments. The limited stability of all species apart from the two mono-anions, which hampers their chemical isolation, is likely to be due to intra-molecular redox reactions, which lead to the formation of Au(0) and fragmentation of the clusters. This, in turn, is an interesting example of inner sphere redox reactions occurring in metal complexes, which may be viewed as the opposite of the redox condensation reactions widely employed for the synthesis of homo- and hetero-metallic carbonyl clusters.

The availability in good yields of  $[\text{Ni}_{32}\text{Au}_6(\text{CO})_{44}]^{6-}$  obtained as final product of the redox condensation of  $[\text{Ni}_6(\text{CO})_{12}]^{2-}$  and  $[\text{AuCl}_4]^-$  have prompted an investigation of its chemical and electrochemical behavior. This high nuclearity compound is multivalent and it may be viewed as a molecular nanocapacitor. Comparable values of  $\Delta E$  between consecutive redox couples in the 260-400 mV range have also been reported for  $\text{Au}_{144}(\text{SR})_{60}$ , even if the nuclearity of this gold nanocluster stabilized by thiolates is more than three times bigger than  $[\text{Ni}_{32}\text{Au}_6(\text{CO})_{44}]^{6-}$ . Such a delayed metallization of the gold thiolate finds justification in our earlier suggestion that these Au nanocluster consist of a positively charged core of Au atoms, featuring a nuclearity well inferior than implicated by the formula, which are stabilized by negative  $[\text{Au}_n(\text{SR})_{n+1}]^-$  anions behaving as 4-e donor. In such a view, the structurally characterized  $\text{Au}_{25}(\text{SR})_{18}$  and  $\text{Au}_{38}(\text{SR})_{24}$  will respectively contain only 8 and 14 Au(0), whereas the purported  $\text{Au}_{144}(\text{SR})_{60}$  may end up in containing only 60-80 Au(0). These heavily reduced nuclearities make these two distinct families

of clusters fairly comparable not only in their electronic configuration (*viz.* electron count) but also in their properties (*viz.* metallization with nuclearity).

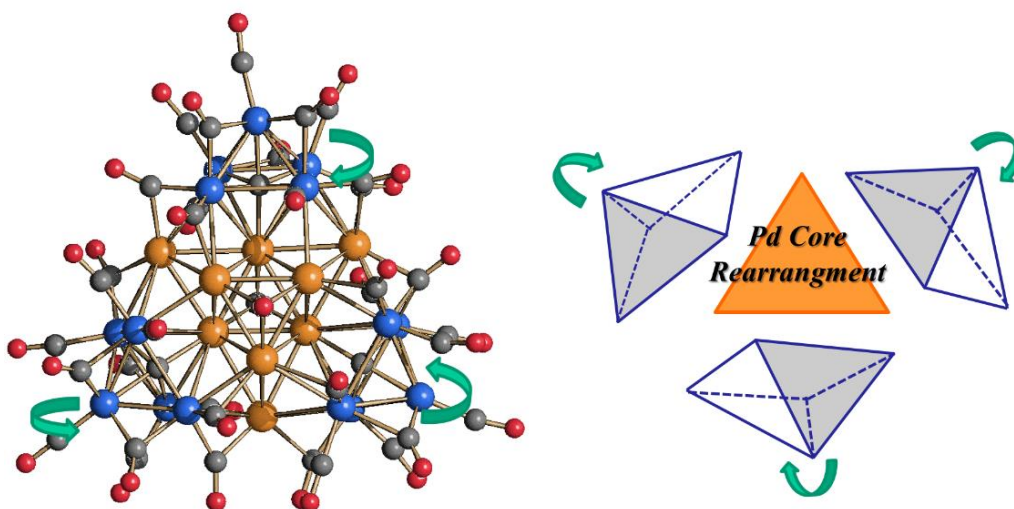
The reactions of the homometallic  $[\text{Co}_6\text{C}(\text{CO})_{15}]^{2-}$  and the heterometallic  $[\{\text{Co}_5\text{C}(\text{CO})_{12}\}_2\text{Au}]^-$  with  $\text{AuPPh}_3\text{Cl}$  consist in alternative simpler approaches for the stabilization of the unprecedented  $[\text{Co}_5\text{C}(\text{CO})_{12}]^-$  and  $[\text{Co}_5\text{C}(\text{CO})_{11}]^{3-}$  clusters. Moreover, the structural characterization of the different isomers of the new  $\text{Co}_6\text{C}(\text{CO})_{12}(\text{AuPPh}_3)_4$  shows that these  $\text{Co}_6\text{C}$  clusters decorated by Au-fragments are very good platforms in order to test aurophilicity and other weak forces, since their different energies are dictated only by the weak interactions on the surfaces, whereas the stronger core-interactions are almost constant. At the same time, this explains why different isomers are formed in the solid state as the consequence of a different solvation of the solid and packing forces. Theoretical investigations suggest that the formation in the solid state of the three isomers during crystallization is governed by packing and van der Waals forces, as well as aurophilic and weak  $\pi$ - $\pi$  and  $\pi$ -H interactions.



# Metal Segregation in Bimetallic Co-Pd Carbide Carbonyl Clusters

The rare case of 3D cluster-in-cluster architecture

In this chapter, the synthesis and characterization of new bimetallic Co-Pd carbide nanoclusters are described. Comparisons with some other bimetallic Pd clusters are illustrated in the attempt to shed light on the relationship between molecular structure and choice of starting material and type of reaction. Finally, speculative hypothesis of the peculiar chemical properties of some compounds as result of their molecular structures is given.



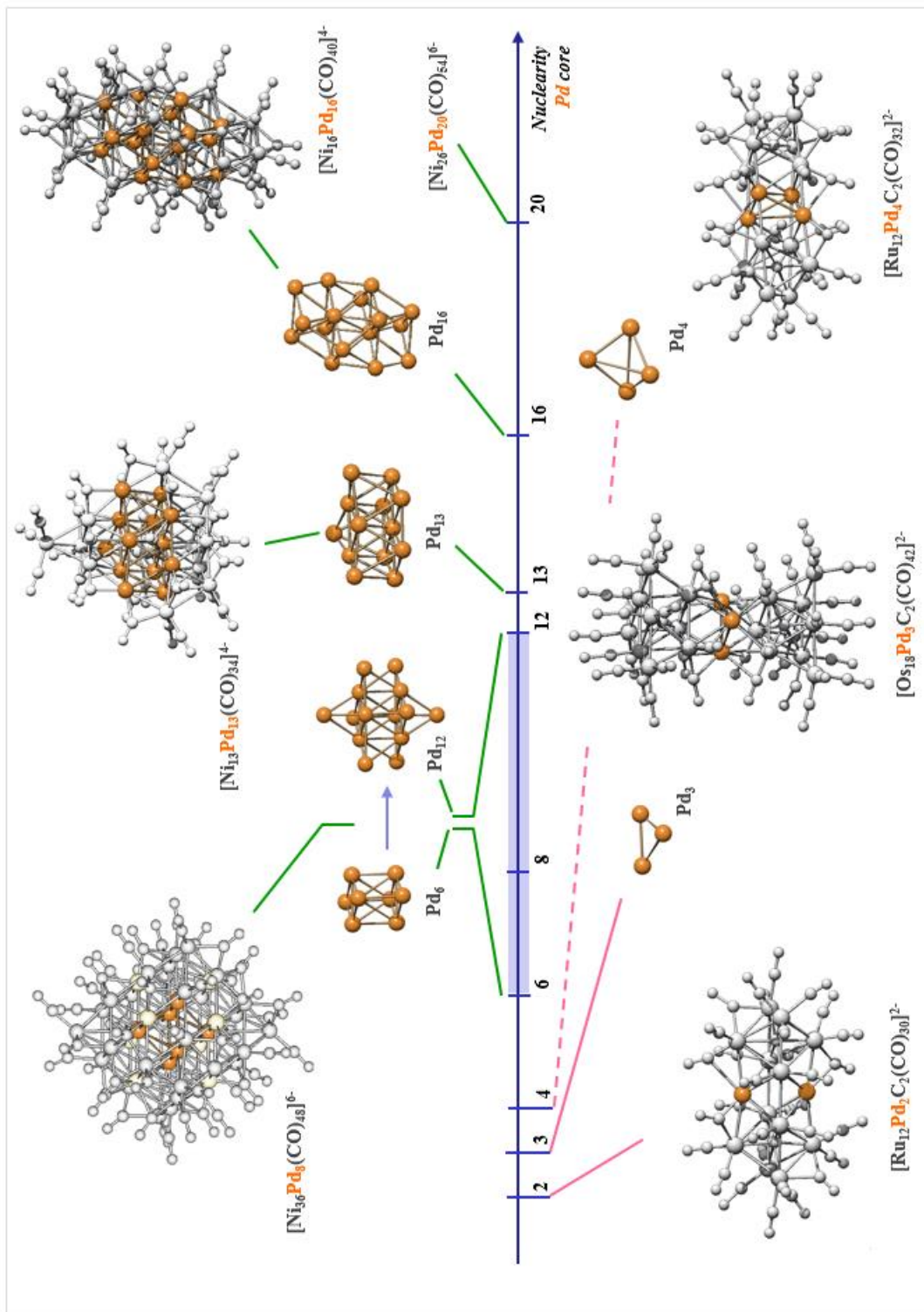


**Figure 6.1** Known bimetallic Ni-Pd, Ru-Pd and Os-Pd carbonyl clusters ordered on the basis of their palladium core nuclearity. The nuclearity of the Pd core in  $[\text{Ni}_{36}\text{Pd}_8(\text{CO})_{48}]^{6-}$  ranges from 6 (octahedral) to 12 (hexa-capped octahedral) with an average of 8. In the whole molecular structure only the octahedral core is highlighted.

## 6.1 Introduction

The structures of bimetallic metal carbonyl clusters (MCCs) are the result of a subtle compromise between optimisation of M-M, M-M', M'-M', M-CO and M'-CO interactions. Most of the reported high-nuclearity bimetallic clusters containing Pd exhibit a clear-cut site and composition preference of the noble metal atoms that results in stoichiometric and ordered structures. In part, this is due to low affinity of Pd to CO. Indeed, examples of terminal carbonyl ligands bonded to palladium are not known.<sup>27</sup> On the top of figure 6.1 there are reported some examples of bimetallic Ni-Pd homoleptic clusters ordered on the basis of their Pd-nuclearities. Generally, the structures of the above species show that interactions among similar atoms are maximised and Pd tends to occupy the core of the cluster. The presence of partial metal segregation as well as substitutional disorder has also been sometimes evidenced, as in the case of  $[\text{Ni}_{136}\text{Pd}_8(\text{CO})_{48}]^{6-}$  [92].

Bimetallic Ni-Pd nanoclusters are synthesized by redox condensation of  $[\text{Ni}_6(\text{CO})_{12}]^{2-}$  with Pd(II) compounds. These reactions lead to considerable fragmentation and recombination of the  $[\text{Ni}_6(\text{CO})_{12}]^{2-}$ .

The structures of bimetallic metal carbonyl clusters may be further complicated by the introduction of interstitial main group elements, such as carbides, in view of the formation of additional M-C<sub>carbide</sub> and M'-C<sub>carbide</sub> interactions. In this field the most fascinating results are the bimetallic Ru-Pd and Os-Pd “sandwich clusters”, where the Pd cores act like a “glue” holding together Ru or Os carbonyl units (figure 6.1 bottom). The presence of the carbide gives an extra-stability to the starting material leading only to no or only partial fragmentation of the metal cage.<sup>28</sup> For example, the reaction of  $[\text{Ru}_6\text{C}(\text{CO})_{16}]^{2-}$  with  $[\text{Pd}(\text{CH}_3\text{CN})_4]^{2+}$  yields the  $[\text{Ru}_{12}\text{Pd}_4\text{C}_2(\text{CO})_{32}]^{2-}$  product containing a Pd<sub>4</sub> core stabilised by two Ru<sub>6</sub>C clusters [93]. On the basis of geometrical constraints, the stabilization of cluster fragments can hardly lead to high nuclearity compounds. In this regard, it makes sense to envisage that the stabilization of small cluster fragments with big palladium cores may be the key of success. This should lead to the three-dimensional growth of the cluster over the palladium core.

Moreover, at the molecular level, the synergic effect of two metals with complementary properties and/or the stabilising effect of an interstitial hetero-element results in larger and more stable MCCs. The increased stability of bimetallic and poly-carbide MCCs may result in the appearance of peculiar physical properties, such as multivalence (*i.e.*, the capacity of a cluster to

<sup>27</sup> It is noteworthy that in a xenon matrix, Pd(CO)<sub>4</sub> exists up to 80 K [91].

<sup>28</sup> However, redox condensations with considerable fragmentation and recombination of carbide clusters are known. For example, the reaction of  $[\text{Co}_6\text{C}(\text{CO})_{15}]^{2-}$  with  $\text{PtCl}_2(\text{Et}_2\text{S})_2$  leads  $[\text{Co}_8\text{Pt}_4\text{C}_2(\text{CO})_{24}]^{2-}$  where the Co<sub>6</sub>C unit or its derivatives, such as Co<sub>5</sub>C fragment, are not retained [37].

undergo several reversible redox processes) and paramagnetism in both odd and even electrons molecular clusters. The highest nuclearity palladium core in homoleptic carbonyl clusters is 20, *i.e.*,  $[\text{Ni}_{26}\text{Pd}_{20}(\text{CO})_{54}]^{6-}$  [25], conversely palladium CO/ $\text{PPh}_3$ -ligated homo- and heterometallic clusters contain up to 165 metal atoms [46].

## 6.2 General results

The following sections report the synthesis of the nanometric Co-Pd bimetallic  $[\text{H}_{6-n}\text{Co}_{20}\text{Pd}_{16}\text{C}_4(\text{CO})_{48}]^{n-}$  ( $n = 4-6$ ) carbide carbonyl clusters obtained by the redox condensation of  $[\text{Co}_6\text{C}(\text{CO})_{15}]^{2-}$  and  $\text{PdCl}_2(\text{Et}_2\text{S})_2$  [94-95] (figure 6.2)

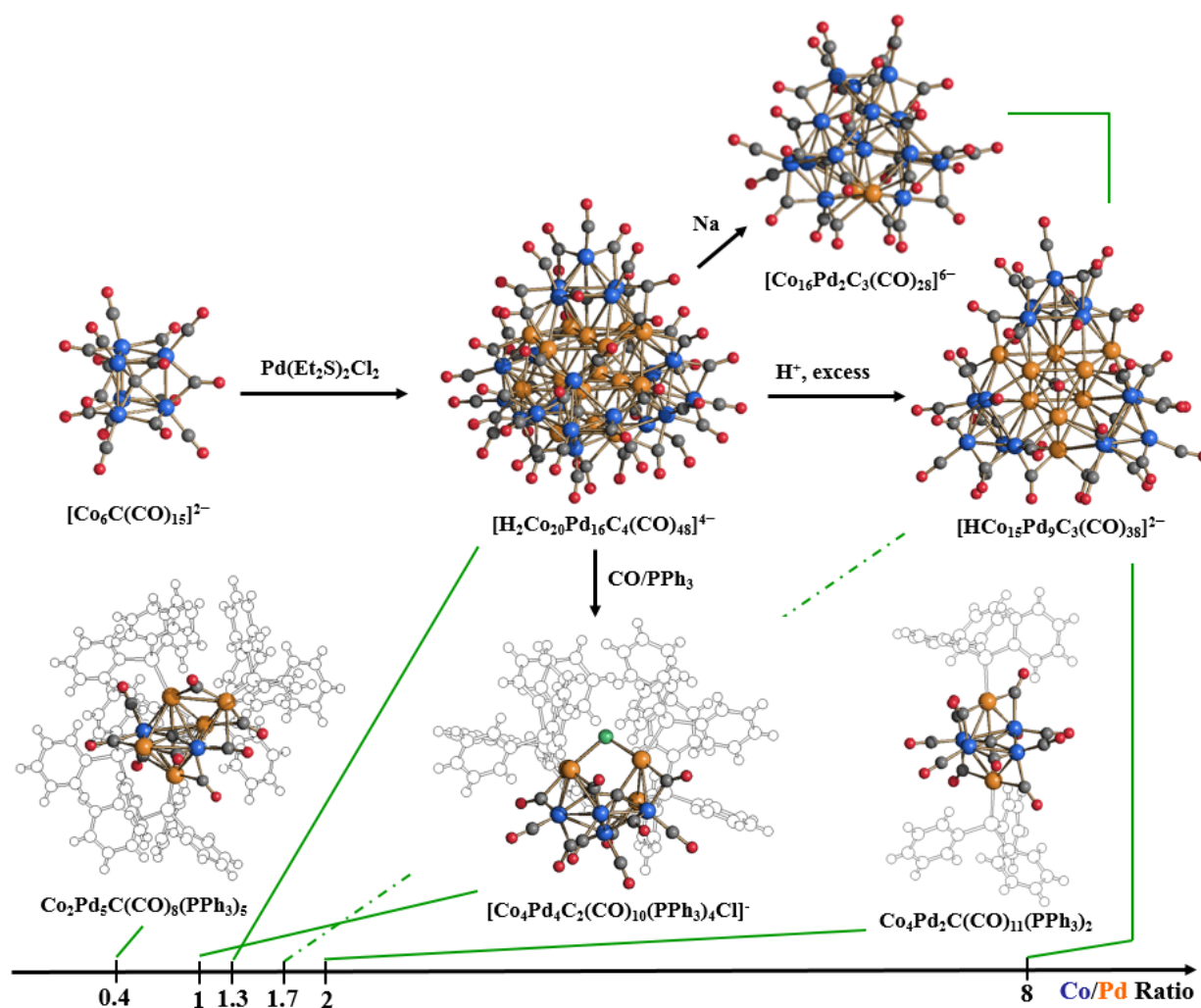


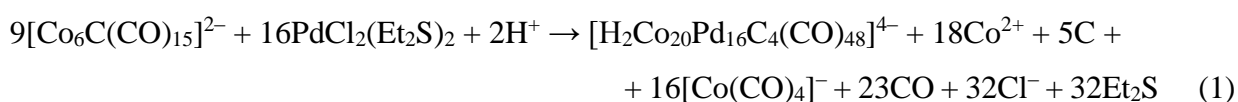
**Figure 6.2** Synthesis and reactivity of  $[\text{H}_2\text{Co}_{20}\text{Pd}_{16}\text{C}_4(\text{CO})_{48}]^{4-}$ . The products are ordered on the basis of their Co/Pd ratios. Except  $[\text{Co}_{16}\text{Pd}_2\text{C}_3(\text{CO})_{28}]^{6-}$ , these new bimetallic clusters display Co/Pd ratios comprised in a narrow range. The atoms of phosphine ligands are represented as grey open spheres (Co, blue; Pd, orange; C, grey; O, red).

In turn, this compound is a useful starting material for the synthesis of other bimetallic Co-Pd clusters. Indeed, the new species  $[\text{H}_{6-n}\text{Co}_{16}\text{Pd}_2\text{C}_3(\text{CO})_{28}]^{n-}$  ( $n = 5, 6$ ),

$\text{Co}_4\text{Pd}_2\text{C}(\text{CO})_{11}(\text{PPh}_3)_2$ ,  $\text{Co}_2\text{Pd}_5\text{C}(\text{CO})_8(\text{PPh}_3)_5$  and  $[\text{Co}_4\text{Pd}_4\text{C}_2(\text{PPh}_3)_4(\text{CO})_{10}\text{Cl}]^-$  have been obtained from the reactions of  $[\text{H}_{6-n}\text{Co}_{20}\text{Pd}_{16}\text{C}_4(\text{CO})_{48}]^{n-}$  ( $n = 4-6$ ) with Na/naphthalene and  $\text{PPh}_3/\text{CO}$ , respectively. Finally, the oxidation of  $[\text{H}_{6-n}\text{Co}_{20}\text{Pd}_{16}\text{C}_4(\text{CO})_{48}]^{n-}$  ( $n = 3-6$ ) with an excess of acid leads to the synthesis of  $[\text{H}_{3-n}\text{Co}_{15}\text{Pd}_9\text{C}_3(\text{CO})_{38}]^{n-}$  ( $n = 0-3$ ) clusters.

### 6.3 Synthesis and characterization of $[\text{H}_{6-n}\text{Co}_{20}\text{Pd}_{16}\text{C}_4(\text{CO})_{48}]^{n-}$ ( $n = 4-6$ )

The new bimetallic  $[\text{H}_2\text{Co}_{20}\text{Pd}_{16}\text{C}_4(\text{CO})_{48}]^{4-}$  cluster is obtained from the reaction in thf of  $[\text{Co}_6\text{C}(\text{CO})_{15}]^{2-}$  with 1.8 equivalents or more of  $\text{PdCl}_2(\text{Et}_2\text{S})_2$ . The reaction is rather slow at room temperature and it is completely accomplished after stirring the mixture for 2-3 days or refluxing for 3 hours. Carbon monoxide evolution is observed and the other major side-products detected are  $\text{Co}^{2+}$  salts and  $[\text{Co}(\text{CO})_4]^-$  according to equation (1):



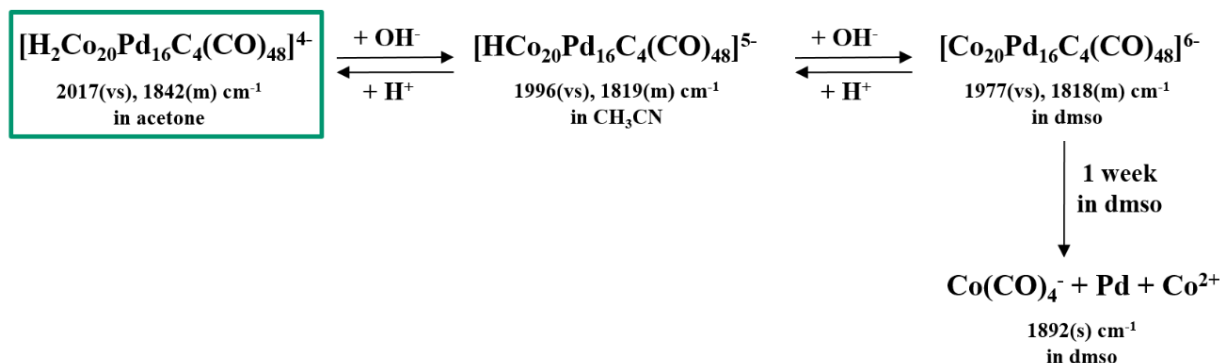
If less than 1.8 equivalents of  $\text{PdCl}_2(\text{Et}_2\text{S})_2$  are used,  $[\text{Co}_6\text{C}(\text{CO})_{15}]^{2-}$  is oxidised to  $[\text{Co}_6\text{C}(\text{CO})_{14}]^-$ .<sup>29</sup> The  $[\text{H}_2\text{Co}_{20}\text{Pd}_{16}\text{C}_4(\text{CO})_{48}]^{4-}$  tetra-anion was recovered by removing the solvent *in vacuo* and washing the residue with water and toluene, in order to extract Co(II) salts and  $[\text{Co}(\text{CO})_4]^-$ . Crude  $[\text{H}_2\text{Co}_{20}\text{Pd}_{16}\text{C}_4(\text{CO})_{48}]^{4-}$  was extracted in acetone and crystals of  $[\text{NEt}_4]_4[\text{H}_2\text{Co}_{20}\text{Pd}_{16}\text{C}_4(\text{CO})_{48}] \cdot 4\text{CH}_3\text{COCH}_3$  suitable for X-ray analyses were obtained by slow diffusion of *iso*-propanol into the acetone solution.

After addition of  $[\text{NBu}_4][\text{OH}]$  to an acetone solution of  $[\text{H}_2\text{Co}_{20}\text{Pd}_{16}\text{C}_4(\text{CO})_{48}]^{4-}$ , the carbonyl stretchings appear at lower wave-numbers in agreement with formation of the penta-anion  $[\text{HCo}_{20}\text{Pd}_{16}\text{C}_4(\text{CO})_{48}]^{5-}$  (scheme 6.1). A similar shift of the  $\nu(\text{CO})$  bands is observed after dissolving the  $[\text{H}_2\text{Co}_{20}\text{Pd}_{16}\text{C}_4(\text{CO})_{48}]^{4-}$  tetra-anion in  $\text{CH}_3\text{CN}$  and dmf, in agreement with its deprotonation to the penta-anion  $[\text{HCo}_{20}\text{Pd}_{16}\text{C}_4(\text{CO})_{48}]^{5-}$  due to the greater basicity of these solvents compared to thf and acetone. The dmf and dmsO solutions of the penta-anion are not stable and after standing at room temperature for one night the hexa-anion  $[\text{Co}_{20}\text{Pd}_{16}\text{C}_4(\text{CO})_{48}]^{6-}$  is observed as well as degradation to  $[\text{Co}(\text{CO})_4]^-$ . The latter is the major product formed after standing in solution for longer time.

$[\text{HCo}_{20}\text{Pd}_{16}\text{C}_4(\text{CO})_{48}]^{5-}$  can be converted back to  $[\text{H}_2\text{Co}_{20}\text{Pd}_{16}\text{C}_4(\text{CO})_{48}]^{4-}$  by addition of acids such as  $\text{HBF}_4$  in acetone solution. Further addition of acids results in the formation of  $[\text{H}_{3-n}\text{Co}_{15}\text{Pd}_9\text{C}_3(\text{CO})_{38}]^{n-}$  ( $n = 0-3$ ) clusters (see section 6.6). These acid-base reactions together the

<sup>29</sup> Regardless of the nature of the oxidant, the oxidation of  $[\text{Co}_6\text{C}(\text{CO})_{15}]^{2-}$  leads to  $[\text{Co}_6\text{C}(\text{CO})_{14}]^-$  as first product. Other examples are reported in chapter 5.3.

electrochemical studies give support to the poly-hydride nature of these  $[\text{H}_{6-n}\text{Co}_{20}\text{Pd}_{16}\text{C}_4(\text{CO})_{48}]^{n-}$  ( $n = 4-6$ ) clusters.



**Scheme 6.1** Deprotonation and protonation of  $[\text{H}_{6-n}\text{Co}_{20}\text{Pd}_{16}\text{C}_4(\text{CO})_{48}]^{n-}$  ( $n = 4-6$ ). The  $[\text{H}_2\text{Co}_{20}\text{Pd}_{16}\text{C}_4(\text{CO})_{48}]^{4-}$  species is the direct product of the redox condensation of  $[\text{Co}_6\text{C}(\text{CO})_{15}]^{2-}$  and  $\text{Cl}_2\text{Pd}(\text{Et}_2\text{S})_2$ . The hexa-anion decomposes to  $[\text{Co}(\text{CO})_4]^-$  after standing in dmsO or dmf solution for a week.

The pattern of the cyclic voltammogram of the bi-protonated tetra-anion in acetone is very rich and highly complicated (figure 6.3 and table 6.1).

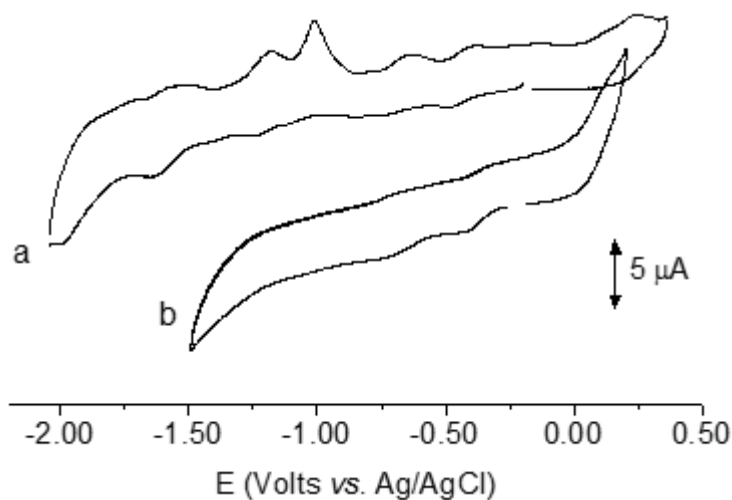


**Figure 6.3** Cyclic voltammograms recorded at a gold electrode in acetone (a) and  $\text{CH}_3\text{CN}$  (b) solutions of  $[\text{H}_2\text{Co}_{20}\text{Pd}_{16}\text{C}_4(\text{CO})_{48}]^{4-}$ .

One oxidation process and four reduction processes, the third of which further complicated by adsorption phenomena, are observed. On the other side, by using  $\text{CH}_3\text{CN}$  as a solvent, the cyclic voltammogram has a much simpler pattern and only the first two of the four reductions remain, while the last two disappear and no oxidation process is observed. This remarkable change of the redox profiles gives a further evidence of the acid-base reactions between the cluster and the solvent. Indeed, this is confirmed by the comparison of the redox profiles of  $[\text{H}_2\text{Co}_{20}\text{Pd}_{16}\text{C}_4(\text{CO})_{48}]^{4-}$  in  $\text{CH}_3\text{CN}$  with that of a pristine sample of

$[\text{HCo}_{20}\text{Pd}_{16}\text{C}_4(\text{CO})_{48}]^{5-}$  in the same solvent (with  $[\text{NBu}_4][\text{PF}_6]$  0.2 M as supporting electrolyte, in both cases). Their square wave voltammeteries perfectly overlap and this undeniably confirms the deprotonation of  $[\text{H}_2\text{Co}_{20}\text{Pd}_{16}\text{C}_4(\text{CO})_{48}]^{4-}$  in the presence of  $\text{CH}_3\text{CN}$ . Thus, we may assign the first two reductions observed in the acetone solution of  $[\text{H}_2\text{Co}_{20}\text{Pd}_{16}\text{C}_4(\text{CO})_{48}]^{4-}$  also to the presence of a certain amount of  $[\text{HCo}_{20}\text{Pd}_{16}\text{C}_4(\text{CO})_{48}]^{5-}$ . This observation denotes the establishment of a  $[\text{H}_2\text{Co}_{20}\text{Pd}_{16}\text{C}_4(\text{CO})_{48}]^{4-}/[\text{HCo}_{20}\text{Pd}_{16}\text{C}_4(\text{CO})_{48}]^{5-}$  equilibrium in this solvent.

Compound	E°					Solvent
	7-/8-	6-/7-	5-/6-	4-/5-	4-/3-	
$[\text{H}_2\text{Co}_{20}\text{Pd}_{16}\text{C}_4(\text{CO})_{48}]^{4-}$	-1.62	-1.24	-0.68	-0.40	+0.19	acetone
$[\text{H}_2\text{Co}_{20}\text{Pd}_{16}\text{C}_4(\text{CO})_{48}]^{4-}$	-	-	-0.70	-0.38	-	$\text{CH}_3\text{CN}$
$[\text{HCo}_{20}\text{Pd}_{16}\text{C}_4(\text{CO})_{48}]^{5-}$	-	-0.70	-0.38	-	-	$\text{CH}_3\text{CN}$

**Table 6.1** Formal redox potentials (V vs. Ag/AgCl) for the redox processes (orange, reductions; blue oxidations) exhibited by  $[\text{H}_{6-n}\text{Co}_{20}\text{Pd}_{16}\text{C}_4(\text{CO})_{48}]^{n-}$  ( $n = 4, 5$ ) clusters.  $[\text{NBu}_4][\text{PF}_6]$  (0.2 M) supporting electrolyte. Scan rate 0.2 V/s.

#### *Crystal structure of $[\text{H}_{6-n}\text{Co}_{20}\text{Pd}_{16}\text{C}_4(\text{CO})_{48}]^{n-}$ ( $n = 4-5$ )*

The molecular structures of the  $[\text{H}_2\text{Co}_{20}\text{Pd}_{16}\text{C}_4(\text{CO})_{48}]^{4-}$  and  $[\text{HCo}_{20}\text{Pd}_{16}\text{C}_4(\text{CO})_{48}]^{5-}$  anions have been determined as their  $[\text{NEt}_4]_4[\text{H}_2\text{Co}_{20}\text{Pd}_{16}\text{C}_4(\text{CO})_{48}] \cdot 4\text{CH}_3\text{COCH}_3$  and  $[\text{NMe}_3(\text{CH}_2\text{Ph})][\text{NMe}_4]_4[\text{HCo}_{20}\text{Pd}_{16}\text{C}_4(\text{CO})_{48}] \cdot 5\text{CH}_3\text{COCH}_3$  salts, respectively (figure 6.4 and table 6.2). Apart from the charge, the two anions have almost identical geometries and bonding parameters.

The  $\text{Co}_{20}\text{Pd}_{16}\text{C}_4$  framework of the  $[\text{H}_{6-n}\text{Co}_{20}\text{Pd}_{16}\text{C}_4(\text{CO})_{48}]^{n-}$  ( $n = 4, 5$ ) anions may be described as composed by an inner *ccp*  $\text{Pd}_{16}$  core fused with four  $\text{Co}_5\text{PdC}$  octahedral fragments. The *ccp*  $\text{Pd}_{16}$  core is a truncated tetrahedron of frequency 3, composed by three ABC layers containing seven, six and three Pd-atoms, respectively.

This displays four triangular and four centered hexagonal (111) faces. Under  $T_d$  symmetry the 16 Pd-atoms consist of four equivalent atoms at the center of the four (111) faces describing a tetrahedron, and 12 equivalents Pd-atoms on the edges of the hexagonal faces (figure 6.5.a). The same *ccp*  $\text{Pd}_{16}$  core has been previously found in  $[\text{Ni}_4\text{Pd}_{16}(\text{CO})_{22}(\text{PPh}_3)_4]^{2-}$ , in which the four Ni-atoms were added to the triangular faces completing the  $v_3$ -tetrahedron (figure 6.5b). Conversely, the  $\text{Co}_{20}\text{Pd}_{16}\text{C}_4$  framework of the present clusters is obtained by adding four square-pyramidal  $\text{Co}_5\text{C}$  fragments to the centered hexagonal (111) faces. Each carbide atom is bonded to five Co atoms and the central Pd of each (111) face, resulting in four  $\text{Co}_5\text{PdC}$  octahedral

fragments. The structure of this bimetallic cluster displays a perfect segregation of the two metals, with Pd-atoms occupying the compact core of the cluster and the Co-atoms on its surface. Moreover, the Pd atoms form a compact metal framework, maximizing the Pd-Pd interactions and, at the same time, minimizing the Pd-CO and Pd-C<sub>carbide</sub> contacts.

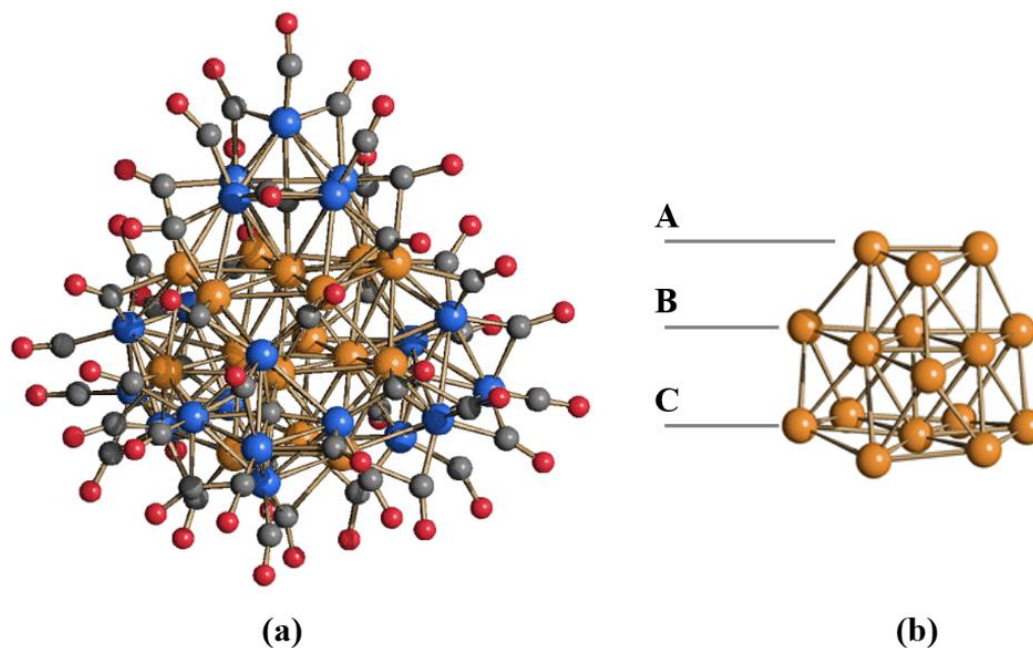


**Figure 6.4** (a) Molecular structure of  $[\text{H}_{6-n}\text{Co}_{20}\text{Pd}_{16}\text{C}_4(\text{CO})_{48}]^{n-}$  ( $n = 4, 5$ ) and (b) its *ccp*  $\text{Pd}_{16}$  core (Co, blue; Pd, orange; C, grey; O, red).

	$[\text{H}_2\text{Co}_{20}\text{Pd}_{16}\text{C}_4(\text{CO})_{48}]^{4-}$	$[\text{HCo}_{20}\text{Pd}_{16}\text{C}_4(\text{CO})_{48}]^{5-}$
Co-Co	2.490(6)-2.783(7) average 2.626	2.481(3)-2.800(3) average 2.632
Co-Pd	2.598(7)-3.012(6) average 2.744	2.596(2)-3.022(3) average 2.745
Pd-Pd	2.730(4)-3.141(4) average 2.848	2.7458(17)-2.9860(16) average 2.849
Co-C <sub>carbide</sub>	1.77(4)-2.04(4) average 1.91	1.891(16)-1.962(14) average 1.93
Pd-C <sub>carbide</sub>	1.91(3)-2.09(4) average 2.03	1.943(14)-1.978(14) average 1.96

**Table 6.2** Most relevant bonding distances (Å) of  $[\text{H}_{6-n}\text{Co}_{20}\text{Pd}_{16}\text{C}_4(\text{CO})_{48}]^{n-}$  ( $n = 4, 5$ ).

The  $\text{Co}_{20}\text{Pd}_{16}$  metal core of these clusters presents 124 M-M contacts which can be considered within bonding distances, 32 Co-Co, 48 Pd-Pd and 44 Co-Pd. The structure is completed by 48 CO ligands, 12 terminal, 32 edge bridging and 4 face bridging. All terminal CO ligands are bonded to Co atoms, whereas the  $\mu$ -CO ligands are bridging Co-Co (12) or Co-Pd (20) edges.

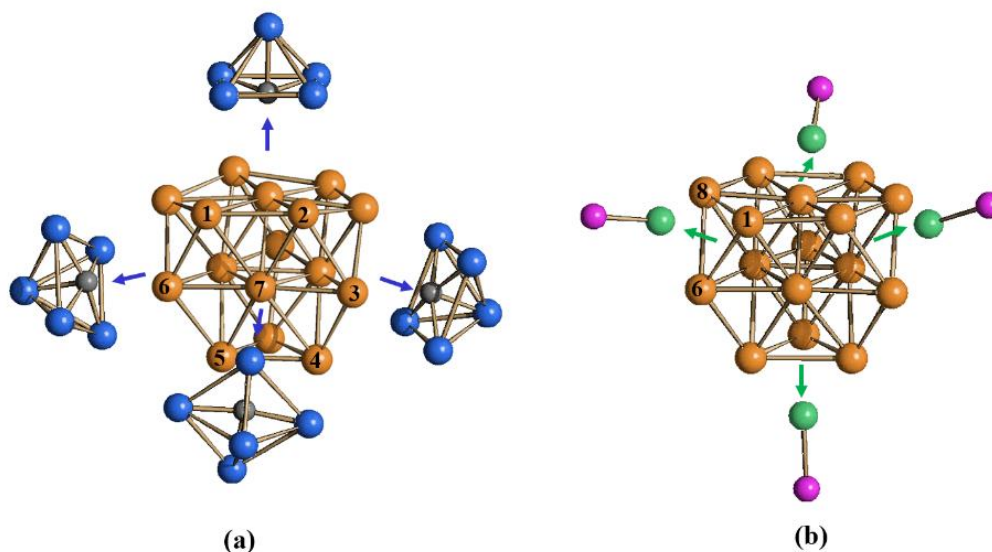


**Figure 6.5** Views of the (a)  $\text{Pd}_{16}(\text{Co}_5\text{C})_4$  and (b)  $\text{Pd}_{16}(\text{NiP})_4$  frameworks observed in  $[\text{H}_{6-n}\text{Co}_{20}\text{Pd}_{16}\text{C}_4(\text{CO})_{48}]^{n-}$  ( $n = 4, 5$ ) and  $[\text{Ni}_4\text{Pd}_{16}(\text{CO})_{22}(\text{PPh}_3)_4]^{2-}$  respectively. The  $\text{Co}_5\text{C}$  fragments are coordinated on the centered hexagonal faces of the Pd-core. In  $[\text{Ni}_4\text{Pd}_{16}(\text{CO})_{22}(\text{PPh}_3)_4]^{2-}$  the NiP fragments are coordinated on the triangular faces completing the  $\nu_3$  tetrahedron (Co, blue; Pd, orange; Ni, green; P, purple; C, grey; O, red).

The four  $\mu_3$ -CO ligands are located on  $\text{CoPd}_2$  faces. Within the inner *ccp*  $\text{Pd}_{16}$  core of the clusters there are four Pd-atoms, describing a tetrahedron and corresponding to the centers of the four (111) faces, which are completely interstitial and form only Pd-Pd, Pd-Co and Pd- $\text{C}_{\text{carbide}}$  contacts. The cluster may be viewed as a *supracluster* composed by an inner *ccp*  $[\text{Pd}_{16}]^{n-}$  ( $n = 0-2$ ) core decorated by four  $[\text{Co}_5\text{C}(\text{CO})_{12}]^-$  organometallic ligands.

#### 6.4 Synthesis and crystal structures of heteroleptic bimetallic Co-Pd clusters

The  $[\text{H}_{6-n}\text{Co}_{20}\text{Pd}_{16}\text{C}_4(\text{CO})_{48}]^{n-}$  ( $n = 3-6$ ) anions are stable under CO atmosphere, and do not react with stoichiometric amounts of  $\text{PPh}_3$ . Conversely, the reaction of  $[\text{H}_2\text{Co}_{20}\text{Pd}_{16}\text{C}_4(\text{CO})_{48}]^{4-}$  with a large excess of  $\text{PPh}_3$  under CO atmosphere results in complex mixtures of products, whose nature depends on the amount of  $\text{PPh}_3$  added and the reaction time.

Among these,  $\text{Co}_4\text{Pd}_2\text{C}(\text{CO})_{11}(\text{PPh}_3)_2$ ,  $\text{Co}_2\text{Pd}_5\text{C}(\text{CO})_8(\text{PPh}_3)_5$  and  $[\text{Co}_4\text{Pd}_4\text{C}_2(\text{PPh}_3)_4(\text{CO})_{10}\text{Cl}]^-$  have been structurally characterised. They have been obtained in low yields (10 %) by reacting  $[\text{H}_2\text{Co}_{20}\text{Pd}_{16}\text{C}_4(\text{CO})_{48}]^{4-}$  under CO atmosphere with 3, 5 and 10 equivalents of  $\text{PPh}_3$ , respectively; reaction times were 4, 1 and 2 days, respectively.

The molecular structure of the neutral  $\text{Co}_4\text{Pd}_2\text{C}(\text{CO})_{11}(\text{PPh}_3)_2$  cluster has been determined as its  $\text{Co}_4\text{Pd}_2\text{C}(\text{CO})_{11}(\text{PPh}_3)_2 \cdot 1.5\text{thf}$  solvate (figure 6.6 a).  $\text{Co}_4\text{Pd}_2\text{C}(\text{CO})_{11}(\text{PPh}_3)_2$  displays a distorted octahedral geometry of the metal core, with a fully interstitial carbide atom.

This structure is rather common for  $M_6C$  clusters and more than 300 examples are present in the Cambridge Structural Database.

The molecular structure of the neutral  $Co_2Pd_5C(CO)_8(PPh_3)_5$  cluster has been determined as its  $Co_2Pd_5C(CO)_8(PPh_3)_5 \cdot 2thf$  solvate (figure 6.6 b). The cluster molecule displays a mono-capped octahedral geometry, with the carbide atom in the centre of the *trans*- $Co_2Pd_4$  octahedron. The fifth Pd-atoms caps a triangular  $CoPd_2$  face and is not bonded to the interstitial carbide. A similar structure has been previously found in other  $M_7C$  clusters, *e.g.*,  $Pd_2Ru_5C(CO)_{15}(PBU^t)_2$ ,  $[Re_7C(CO)_{22}]^-$ ,  $[Re_7C(CO)_{21}]^{3-}$ .

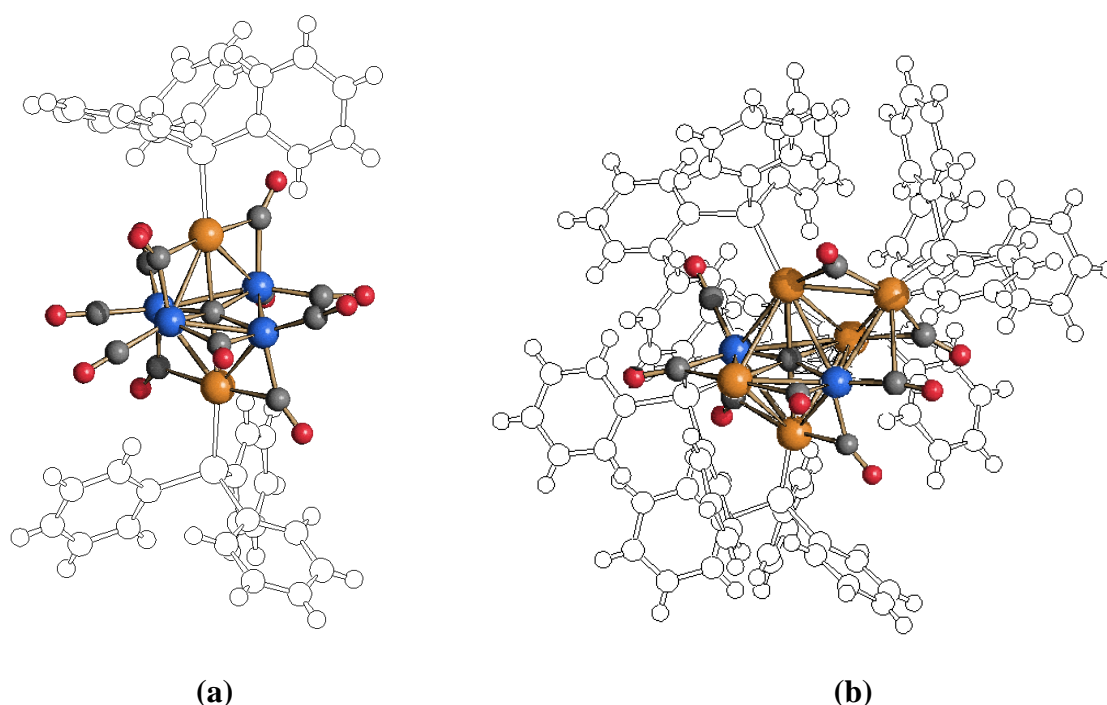


**Figure 6.6** Molecular structure of (a)  $Co_4Pd_2C(CO)_{11}(PPh_3)_2$  and (b)  $Co_2Pd_5C(CO)_8(PPh_3)_5$  clusters. The atoms of  $PPh_3$  ligands are represented as grey open spheres (Co, blue; Pd, orange; C, grey; O, red).

The molecular structure of the  $[Co_4Pd_4C_2(PPh_3)_4(CO)_{10}Cl]^-$  anion has been determined as its  $[NMe_3(CH_2Ph)][Co_4Pd_4C_2(PPh_3)_4(CO)_{10}Cl] \cdot 2CH_3COCH_3$  salt (figure 6.7). The cluster may be viewed as composed by a  $Co_4Pd_4C_2$  mono-acetylide core deriving from two  $Co_3Pd_2C$  fragments sharing a common  $Co_2$  edge. This results in a bond between the two interstitial C-atoms and, thus, the cluster is better described as a mono-acetylide. The two  $Co_3Pd_2C$  fragments may be viewed as heavily distorted square-pyramids with one Co-atom in the vertex and two Co and two Pd-atoms on the C-centered square base. The latter is so distorted that only three contacts are bonding whereas the fourth Pd-Co contact is non-bonding.

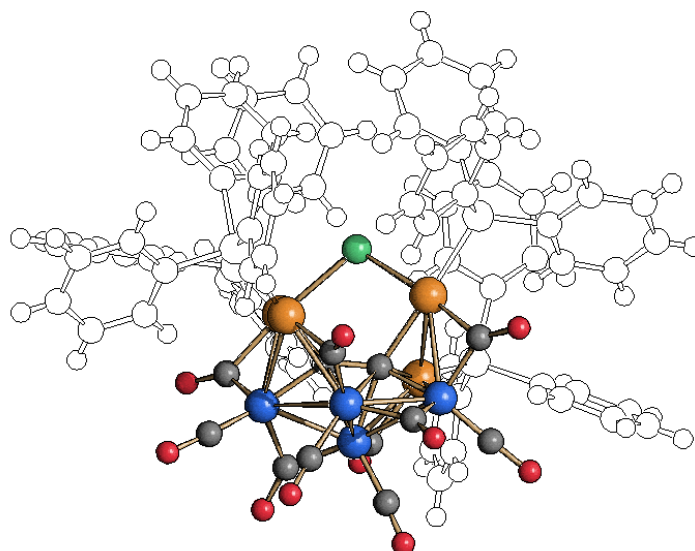


**Figure 6.7** Molecular structure of  $\text{Co}_2\text{Pd}_5\text{C}(\text{CO})_8(\text{PPh}_3)_5$ . The atoms of the  $\text{PPh}_3$  ligands are represented as grey open spheres (Co, blue; Pd, orange; Cl, green; C, grey; O, red).

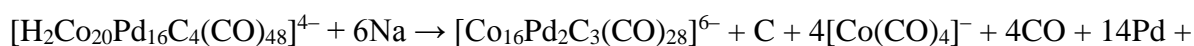
The structure of the cluster is completed by adding one  $\text{PPh}_3$  ligand per each Pd-atom, one Cl-ligand bridging two Pd atoms and 10 CO ligands. Four carbonyls are terminal, two  $\mu$ -CO bridge Co-Co edges and four CO ligands are  $\mu$ -coordinated to four Co-Pd edges.

The  $\text{C}_2$ -acetylide fragment is semi-exposed in view of the fact that the metal cage is rather open. Homoleptic MCCs containing semi-exposed acetylide fragments are rather rare, a few examples being  $[\text{Co}_5\text{FeC}_2(\text{CO})_{17}]^-$  and  $[\text{Co}_3\text{Fe}_3\text{C}_2(\text{CO})_{18}]^-$ . Conversely several heteroleptic MCCs containing semi-exposed  $\text{C}_2$ -units are known, that contain ancillary ligands beside CO. Among these, the complexes  $\text{Ru}_5\text{Co}_4\text{C}_2(\text{CO})_{18}(\text{PPh}_2)_2(\text{SMe})_2$  and  $\text{Ru}_6\text{Co}_2\text{C}_2(\text{CO})_{17}(\text{PPh}_2)_2(\text{SMe})_2$  are of particular interest to the present work, since they show a coordination of the  $\text{C}_2$ -fragment similar to the one found in  $[\text{Co}_4\text{Pd}_4\text{C}_2(\text{PPh}_3)_4(\text{CO})_{10}\text{Cl}]^-$ .

### 6.5 Synthesis and characterization of $[\text{H}_{6-n}\text{Co}_{16}\text{Pd}_2\text{C}_3(\text{CO})_{28}]^{n-}$ ( $n = 5, 6$ )

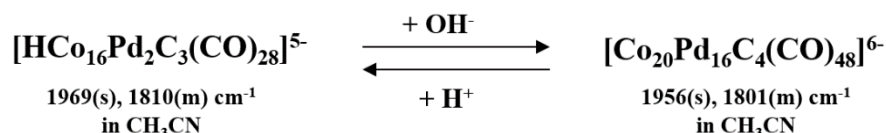
The reduction of  $[\text{H}_2\text{Co}_{20}\text{Pd}_{16}\text{C}_4(\text{CO})_{48}]^{4-}$  in thf solution with Na/naphthalene results, after work-up, into the isolation of the new tri-carbide  $[\text{HCo}_{16}\text{Pd}_2\text{C}_3(\text{CO})_{28}]^{5-}$ , which has been structurally characterised as its  $[\text{NEt}_4]_5[\text{HCo}_{16}\text{Pd}_2\text{C}_3(\text{CO})_{28}] \cdot 1.5\text{CH}_3\text{CN}$  salt.  $[\text{H}_{6-n}\text{Co}_{16}\text{Pd}_2\text{C}_3(\text{CO})_{28}]^{n-}$  ( $n = 5, 6$ ) and  $[\text{H}_{3-n}\text{Co}_{15}\text{Pd}_9\text{C}_3(\text{CO})_{38}]^{n-}$  ( $n = 0-3$ , see next section) are the first examples of MCCs containing isolated atoms. Reversible deprotonation to the  $[\text{Co}_{16}\text{Pd}_2\text{C}_3(\text{CO})_{28}]^{6-}$  hexa-anion is observed after treatment with strong bases such as  $[\text{NBu}_4][\text{OH}]$ .

Formation of  $[\text{Co}_{16}\text{Pd}_2\text{C}_3(\text{CO})_{28}]^{6-}$  from  $[\text{H}_2\text{Co}_{20}\text{Pd}_{16}\text{C}_4(\text{CO})_{48}]^{4-}$  and Na may be explained on the basis of equation (2):





This is in agreement with the fact that  $[\text{Co}_{16}\text{Pd}_2\text{C}_3(\text{CO})_{28}]^{6-}$  and  $[\text{Co}(\text{CO})_4]^-$  are the only carbonyl species detected during the reaction. Protonation of the hexa-anion to give the  $[\text{HCo}_{16}\text{Pd}_2\text{C}_3(\text{CO})_{28}]^{5-}$  mono-hydride penta-anion occurs, then, during work-up due to the use of  $\text{H}_2\text{O}$  for precipitation (scheme 6.2).



**Scheme 6.2** Deprotonation and protonation of  $[\text{H}_{6-n}\text{Co}_{16}\text{Pd}_2\text{C}_3(\text{CO})_{28}]^{n-}$  ( $n = 5, 6$ ).

The redox profile of  $[\text{HCo}_{16}\text{Pd}_2\text{C}_3(\text{CO})_{28}]^{5-}$  reveals one oxidation and two reductions (table 6.3). A comparison of their redox potentials values with those of  $[\text{HCo}_{20}\text{Pd}_{16}\text{C}_4(\text{CO})_{48}]^{5-}$  indicates that both the oxidation and the first reduction of  $[\text{HCo}_{16}\text{Pd}_2\text{C}_3(\text{CO})_{28}]^{5-}$  appear at the same potential of the two reduction processes observed for  $[\text{HCo}_{20}\text{Pd}_{16}\text{C}_4(\text{CO})_{48}]^{5-}$ . This suggests that a certain amount of  $[\text{HCo}_{20}\text{Pd}_{16}\text{C}_4(\text{CO})_{48}]^{6-}$  is present. In other words, the mono-protonated  $[\text{HCo}_{20}\text{Pd}_{16}\text{C}_4(\text{CO})_{48}]^{n-}$  cluster seems to be present in its reduced hexa-anionic form, as indicated by the fact that the redox process observed at  $\sim -0.37$  V is now an oxidation, while in the case of  $[\text{HCo}_{20}\text{Pd}_{16}\text{C}_4(\text{CO})_{48}]^{5-}$  it was a reduction. These findings are in agreement with the origin of  $[\text{HCo}_{16}\text{Pd}_2\text{C}_3(\text{CO})_{28}]^{5-}$ , which is obtained by the chemical reduction of  $[\text{H}_2\text{Co}_{20}\text{Pd}_{16}\text{C}_4(\text{CO})_{48}]^{4-}$ .

Compound	E°					Solvent
	7-/8-	6-/7-	5-/6-	4-/5-	4-/3-	
$[\text{HCo}_{16}\text{Pd}_2\text{C}_3(\text{CO})_{28}]^{5-}$	-	-1.41	-0.72	-0.37	-	$\text{CH}_3\text{CN}$
$[\text{HCo}_{20}\text{Pd}_{16}\text{C}_4(\text{CO})_{48}]^{5-}$	-	-0.70	-0.38	-	-	$\text{CH}_3\text{CN}$

**Table 6.3** Formal redox potentials (V vs. Ag/AgCl) for the redox processes (orange, reductions; blue oxidations) exhibited by the clusters  $[\text{HCo}_{16}\text{Pd}_2\text{C}_3(\text{CO})_{28}]^{5-}$  compared to  $[\text{HCo}_{20}\text{Pd}_{16}\text{C}_4(\text{CO})_{48}]^{5-}$ .  $[\text{NBu}_4][\text{PF}_6]$  (0.2 M) supporting electrolyte. Scan rate 0.2 V/s.

#### *Crystal structure of $[\text{HCo}_{16}\text{Pd}_2\text{C}_3(\text{CO})_{28}]^{5-}$*

The molecular structure of the  $[\text{HCo}_{16}\text{Pd}_2\text{C}_3(\text{CO})_{28}]^{5-}$  anion has been determined as its  $[\text{NEt}_4]_5[\text{HCo}_{16}\text{Pd}_2\text{C}_3(\text{CO})_{28}] \cdot 1.5\text{CH}_3\text{CN}$  salt (figure 6.8). The  $\text{Co}_{16}\text{Pd}_2\text{C}_3$  metal carbide cage of the cluster may be formally reconstructed as depicted in figure 6.9. Two carbide atoms are enclosed within two  $\text{Co}_6\text{C}$  distorted octahedral cages which share a common vertex resulting,

thus, in a  $\text{Co}_{11}\text{C}_2$  fragment. The third carbide atom is enclosed within a mono-capped trigonal prismatic  $\text{Co}_7\text{C}$  cage sharing three Co-atoms with the above  $\text{Co}_{11}\text{C}_2$  fragment resulting in a  $\text{Co}_{15}\text{C}_3$  unit. The additional sixteenth Co-atom and the two Pd-atoms are, then, added to this unit affording the final  $\text{Co}_{16}\text{Pd}_2\text{C}_3$  metal carbide cage. It must be remarked that the Co and Pd atoms added in this last step are not bonded to any carbide atom.

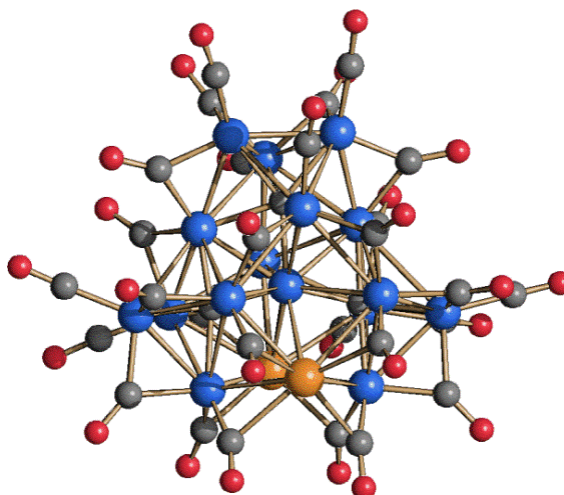


**Figure 6.8** Molecular structure of  $[\text{HCo}_{16}\text{Pd}_2\text{C}_3(\text{CO})_{28}]^{5-}$  (Co, blue; Pd, orange; C, grey; O, red).

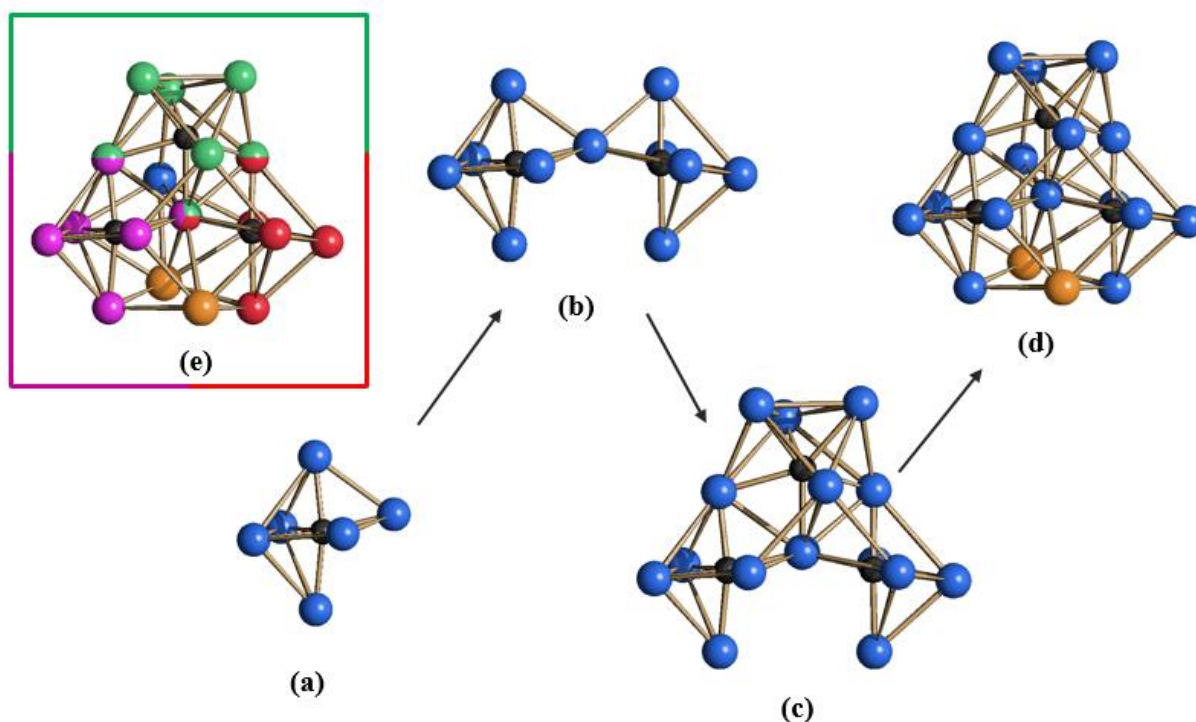


**Figure 6.9** Stepwise reconstruction of  $[\text{HCo}_{16}\text{C}_3(\text{CO})_{28}]^{5-}$ : (a)  $\text{Co}_6\text{C}$  distorted octahedral carbide centered cage; (b)  $\text{Co}_{11}\text{C}_2$  framework obtained by the condensation of two  $\text{Co}_6\text{C}$  octahedrons sharing a common vertex; (c)  $\text{Ni}_{15}\text{C}_3$  framework obtained by the addition of a monocapped trigonal prismatic  $\text{Co}_7\text{C}$  unit to  $\text{Co}_{11}\text{C}_2$  sharing three vertices; (d) the final  $\text{Co}_{16}\text{Pd}_2\text{C}_3$  core. (e) Multicolor representation of  $\text{Co}_{16}\text{Pd}_2\text{C}_3$  core: the  $\text{Co}_6$  cage is represented in three different colors, the bicolor and tricolor atoms are respectively shared by two and three cages.

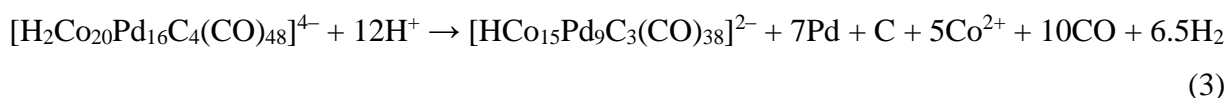
The three carbide atoms of  $[\text{HCo}_{16}\text{Pd}_2\text{C}_3(\text{CO})_{28}]^{5-}$  display different environments, since two are enclosed within  $\text{Co}_6\text{C}$  distorted octahedral cages and the third in a mono-capped trigonal prismatic  $\text{Co}_7\text{C}$  cage, showing looser Co-C<sub>carbide</sub> contacts in view of the larger size of the trigonal prismatic cavity.

The  $\text{Co}_{16}\text{Pd}_2$  metal core of the cluster presents 55 M-M contacts which can be considered within bonding distances, 44 Co-Co, and 11 Co-Pd. The structure is completed by 28 CO ligands, 7 terminal and 21 edge bridging. Each Pd atoms is bonded to four  $\mu$ -CO, whereas one Pd forms five Co-Pd bonds and the other six Co-Pd bonds. The 16 Co-atoms have rather different environments, with only one Co-atom which is fully interstitial and does not bind to any CO. This interstitial cobalt is connected to six other Co-atoms, two Pd-atoms and three carbides. It must be remarked that  $[\text{HCo}_{16}\text{Pd}_2\text{C}_3(\text{CO})_{28}]^{5-}$  is the first example of a MCC containing three interstitial carbide atoms.

## 6.6 Synthesis and characterization of $[\text{H}_{3-n}\text{Co}_{15}\text{Pd}_9\text{C}_3(\text{CO})_{38}]^{n-}$ ( $n = 0-3$ )

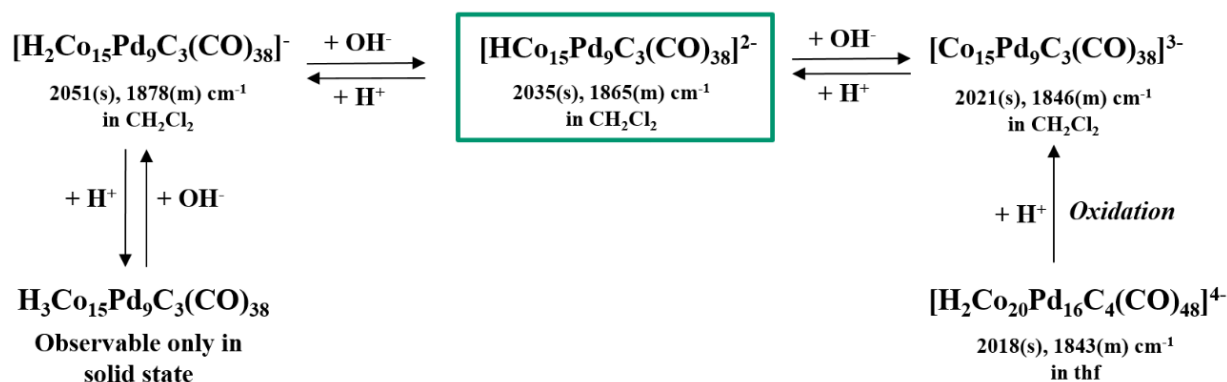
The reaction of  $[\text{H}_2\text{Co}_{20}\text{Pd}_{16}\text{C}_4(\text{CO})_{48}]^{4-}$  with an excess of  $\text{HBF}_4 \cdot \text{Et}_2\text{O}$  in thf results in the formation of  $[\text{H}_3\text{Co}_{20}\text{Pd}_{16}\text{C}_4(\text{CO})_{48}]^{3-}$ , as previously described in section 6.3. After removing the solvent *in vacuo* and dissolving the residue in  $\text{CH}_2\text{Cl}_2$ , crystals of  $[\text{NMe}_3(\text{CH}_2\text{Ph})]_2[\text{HCo}_{15}\text{Pd}_9\text{C}_3(\text{CO})_{38}] \cdot \text{C}_6\text{H}_{14}$  have been obtained in good yields after slow diffusion of n-hexane on the  $\text{CH}_2\text{Cl}_2$  solution (scheme 6.3).

Formation of  $[\text{HCo}_{15}\text{Pd}_9\text{C}_3(\text{CO})_{38}]^{2-}$  requires an excess of acid and the use of  $\text{CH}_2\text{Cl}_2$  as solvent, whereas the same product is not obtained in thf. It is likely that the lower ability of  $\text{CH}_2\text{Cl}_2$  to interact with  $\text{H}^+$  compared to thf makes the acid more reactive and induces the reaction.  $[\text{HCo}_{15}\text{Pd}_9\text{C}_3(\text{CO})_{38}]^{2-}$  is the only carbonyl species detected at the end of the reaction in solution as indicated by IR spectroscopy. A Pd mirror is also formed on the reaction flask and Co(II) salts may be extracted in water after removing the organic solvent *in vacuo*. On the basis of these data, we may explain the formation of  $[\text{HCo}_{15}\text{Pd}_9\text{C}_3(\text{CO})_{38}]^{2-}$  from  $[\text{H}_2\text{Co}_{20}\text{Pd}_{16}\text{C}_4(\text{CO})_{48}]^{4-}$  and  $\text{HBF}_4 \cdot \text{Et}_2\text{O}$  accordingly to equation (3):



The  $[\text{HCo}_{15}\text{Pd}_9\text{C}_3(\text{CO})_{38}]^{2-}$  mono-hydride di-anion is deprotonated to the  $[\text{Co}_{15}\text{Pd}_9\text{C}_3(\text{CO})_{38}]^{3-}$  tri-anion after the addition of a stoichiometric amount of  $[\text{NBu}_4][\text{OH}]$  (scheme 6.3). Its structure has been confirmed by X-ray crystallography on the  $[\text{NEt}_4]_3[\text{Co}_{15}\text{Pd}_9\text{C}_3(\text{CO})_{38}] \cdot \text{thf}$  salt, obtained by slow diffusion of n-hexane on a  $\text{CH}_2\text{Cl}_2$  solution of  $[\text{Co}_{15}\text{Pd}_9\text{C}_3(\text{CO})_{38}]^{3-}$  containing some thf to help crystallisation.  $[\text{HCo}_{15}\text{Pd}_9\text{C}_3(\text{CO})_{38}]^{2-}$  reacts

with  $\text{HBF}_4 \cdot \text{Et}_2\text{O}$  (1.5-2 equivalents) affording the  $[\text{H}_2\text{Co}_{15}\text{Pd}_9\text{C}_3(\text{CO})_{38}]^-$  di-hydride mono-anion, as corroborated by the shift of the  $\nu(\text{CO})$  bands towards higher wave numbers and fully confirmed by X-ray crystallography as the  $[\text{NEt}_4][\text{H}_2\text{Co}_{15}\text{Pd}_9\text{C}_3(\text{CO})_{38}] \cdot 0.5\text{C}_6\text{H}_{14}$  salt.



**Scheme 6.3** Deprotonation and protonation of  $[\text{H}_{3-n}\text{Co}_{15}\text{Pd}_9\text{C}_3(\text{CO})_{38}]^{n-}$  ( $n = 0-3$ ) clusters obtaining from the oxidation of the higher nuclearity compound  $[\text{H}_2\text{Co}_{20}\text{Pd}_{16}\text{C}_4(\text{CO})_{48}]^{4-}$ . A large excess of  $\text{HBF}_4 \cdot \text{Et}_2\text{O}$  of ca. 15-20 equiv. leads to the  $[\text{HCo}_{15}\text{Pd}_9\text{C}_3(\text{CO})_{38}]^{2-}$  species. An increase or decrease amount of acid directly leads to the mono- or the three-anion respectively. The neutral  $\text{H}_3\text{Co}_{15}\text{Pd}_9\text{C}_3(\text{CO})_{38}$  compound is observed only in solid state, whereas its dissolution in  $\text{CH}_2\text{Cl}_2$  leads to the mono-anion.

Apparently, no reaction occurs also after adding a large excess of acid (8-10 equivalents) to  $[\text{H}_2\text{Co}_{15}\text{Pd}_9\text{C}_3(\text{CO})_{38}]^-$ , as indicated by the fact that no significant shift of the  $\nu(\text{CO})$  bands is observed in the IR spectrum. Nonetheless, slow diffusion of n-hexane on a  $\text{CH}_2\text{Cl}_2$  solution of the mono-anion containing an excess of acid and some thf afforded crystals of the  $\text{H}_3\text{Co}_{15}\text{Pd}_9\text{C}_3(\text{CO})_{38} \cdot 2\text{thf}$  solvate, which contains the neutral tri-hydride cluster. The solid is soluble in  $\text{CH}_2\text{Cl}_2$  where it shows the same carbonyl stretchings of  $[\text{H}_2\text{Co}_{15}\text{Pd}_9\text{C}_3(\text{CO})_{38}]^-$ . Thus, it is likely that protonation results in only an undetectable amount of the neutral species to be formed, presumably in equilibrium with the mono-anion. This is less soluble in the solvent mixture used and crystallises out. Similarly, when  $\text{H}_3\text{Co}_{15}\text{Pd}_9\text{C}_3(\text{CO})_{38} \cdot 2\text{thf}$  is dissolved in  $\text{CH}_2\text{Cl}_2$  the same equilibrium is shifted towards the formation of  $[\text{H}_2\text{Co}_{15}\text{Pd}_9\text{C}_3(\text{CO})_{38}]^-$ , which is the only species detected in solution by IR spectroscopy.

The electrochemical behaviour of the  $[\text{H}_{3-n}\text{Co}_{15}\text{Pd}_9\text{C}_3(\text{CO})_{38}]^{n-}$  ( $n = 1-3$ ) anions has been investigated by means of cyclic voltammetry (figure 6.10 and table 6.4). Conversely, the electrochemical properties of the neutral cluster  $\text{H}_3\text{Co}_{15}\text{Pd}_9\text{C}_3(\text{CO})_{38}$  have not been studied, since it readily deprotonates in solution affording the mono-anion  $[\text{H}_2\text{Co}_{15}\text{Pd}_9\text{C}_3(\text{CO})_{38}]^-$ .

The  $[\text{H}_2\text{Co}_{15}\text{Pd}_9\text{C}_3(\text{CO})_{38}]^-$  di-hydride mono-anion shows two oxidations ( $E^{\circ}_{1-0} = +0.104 \text{ V}$ ;  $E^{\circ}_{0/+1} = +0.600 \text{ V}$ ) with features of chemical reversibility. Also the fully deprotonated  $[\text{Co}_{15}\text{Pd}_9\text{C}_3(\text{CO})_{38}]^{3-}$  tri-anion displays two reversible oxidations ( $E^{\circ}_{3-/2-} = +0.002 \text{ V}$ ;  $E^{\circ}_{2-/1-} = +0.347 \text{ V}$ ), whereas the  $[\text{HCo}_{15}\text{Pd}_9\text{C}_3(\text{CO})_{38}]^{2-}$  mono-hydride di-anion presents three oxidation

processes with features of chemical reversibility ( $E^{\circ\prime}_{2-/1-} = +0.067$  V;  $E^{\circ\prime}_{1-/0} = +0.398$  V;  $E^{\circ\prime}_{0/+1} = +0.899$  V). Conversely, the three species do not show any cathodic process, further supporting their formulation as poly-hydrides. If this was not the case, for instance, the di-anion should have shown at least one reduction to give the tri-anion.

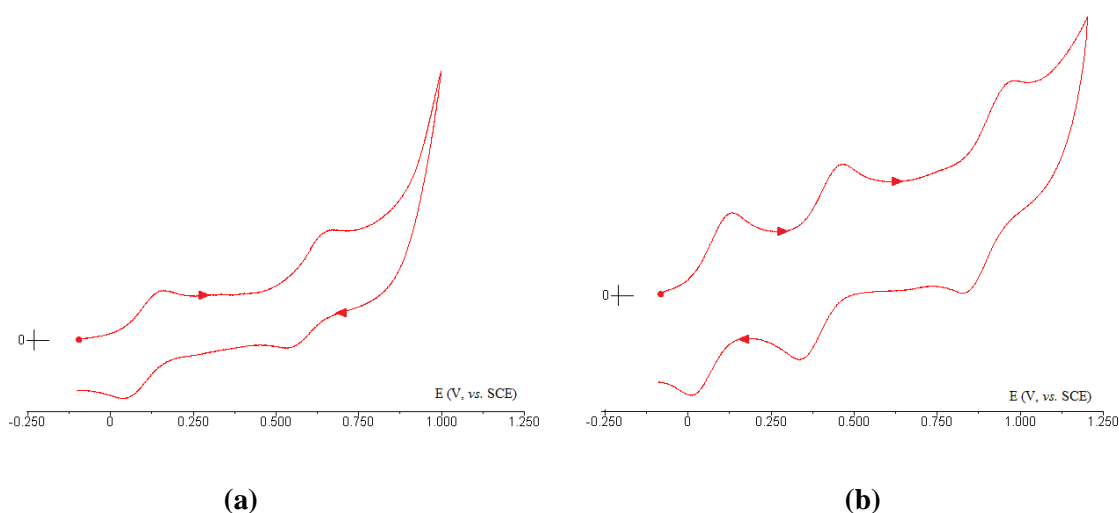


**Figure 6.10** Cyclic voltammograms recorded at a glassy carbon electrode in  $\text{CH}_2\text{Cl}_2$  of (a)  $[\text{H}_2\text{Co}_{15}\text{Pd}_9\text{C}_3(\text{CO})_{38}]^-$  and (b)  $[\text{HCo}_{15}\text{Pd}_9\text{C}_3(\text{CO})_{38}]^{2-}$ .

$n$	$E^{\circ\prime}$			
	3-/2-	2-/1-	1-/0	0/+1
1	-	-	+ 0.104	+ 0.600
2	-	+ 0.067	+ 0.398	+ 0.899
3	+ 0.002	+ 0.347	-	-

**Table 6.4** Formal electrode potentials (in V, vs. S.C.E.) for the redox changes exhibited by  $[\text{H}_{3-n}\text{Co}_{15}\text{Pd}_9\text{C}_3(\text{CO})_{38}]^{n-}$  ( $n = 1-3$ ) in  $\text{CH}_2\text{Cl}_2$ .  $[\text{NBu}_4][\text{BF}_4]$  (0.1 M) supporting electrolyte. Scan rate 0.2 V/s. Rest potential has been directly measured by the potentiostat and the anodic/cathodic nature of the processes has been unambiguously established by hydrodynamic voltammetry.

The three  $[\text{H}_{3-n}\text{Co}_{15}\text{Pd}_9\text{C}_3(\text{CO})_{38}]^{n-}$  ( $n = 1-3$ ) clusters display two or three reversible redox processes with  $\Delta E$  between consecutive redox couples of *ca.* 0.2-0.4 V, indicating the incipient metalisation of their metal cores. Moreover, the data summarised in table 6.3 indicate that the first oxidation of the  $[\text{H}_{3-n}\text{Co}_{15}\text{Pd}_9\text{C}_3(\text{CO})_{38}]^{n-}$  ( $n = 1-3$ ) clusters occurs at more positive potentials by decreasing the value of  $n$ , in agreement with the less negative charge of the reduced species. A similar trend is observed also for the second oxidation process.

In addition, SQUID measurements on a crystalline sample of  $[\text{NMe}_3(\text{CH}_2\text{Ph})_2][\text{HCo}_{15}\text{Pd}_9\text{C}_3(\text{CO})_{38}] \cdot \text{C}_6\text{H}_{14}$  (figure 6.11) show that its ground state has total spin  $S=1$ , corresponding to two unpaired electrons. This, in turn, indicates that the cluster anion must possess an even number of electrons and, thus, at least one hydride ligand must be present.

The magnetic properties of  $[\text{NMe}_3(\text{CH}_2\text{Ph})]_2[\text{HCo}_{15}\text{Pd}_9\text{C}_3(\text{CO})_{38}] \cdot \text{C}_6\text{H}_{14}$  give a further support to previous findings on the intrinsic paramagnetism of other even electron MCCs.

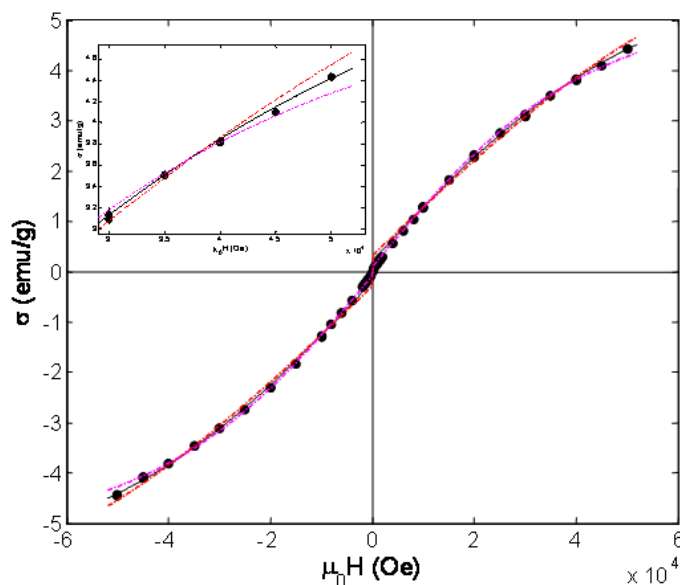


**Figure 6.11** Magnetization in function of field of  $[\text{NMe}_3(\text{CH}_2\text{Ph})]_2[\text{HCo}_{15}\text{Pd}_9\text{C}_3(\text{CO})_{38}] \cdot \text{C}_6\text{H}_{14}$  as measured at 5K (black dots). The data were fitted with the Brillouin function for different  $S$  values and Landé  $g$ -factor of free electron. Dashed lines are the best fits for  $S=1/2$  (red) and  $S=3/2$  (magenta). The black solid line represents the best-fitting curve from least-squares analysis for  $S=1$ . Inset: zoom of the high field region.

### Crystal structures

The molecular structures of the four  $[\text{H}_{3-n}\text{Co}_{15}\text{Pd}_9\text{C}_3(\text{CO})_{38}]^{n-}$  ( $n = 0-3$ ) clusters have been determined as their  $\text{H}_3\text{Co}_{15}\text{Pd}_9\text{C}_3(\text{CO})_{38} \cdot 2\text{thf}$ ,  $[\text{NEt}_4][\text{H}_2\text{Co}_{15}\text{Pd}_9\text{C}_3(\text{CO})_{38}] \cdot 0.5\text{C}_6\text{H}_{14}$ ,  $[\text{NMe}_3(\text{CH}_2\text{Ph})]_2[\text{HCo}_{15}\text{Pd}_9\text{C}_3(\text{CO})_{38}] \cdot \text{C}_6\text{H}_{14}$  and  $[\text{NEt}_4]_3[\text{Co}_{15}\text{Pd}_9\text{C}_3(\text{CO})_{38}] \cdot \text{thf}$  solids and salts (figure 6.12 and table 6.5)

The structures of the four  $[\text{H}_{3-n}\text{Co}_{15}\text{Pd}_9\text{C}_3(\text{CO})_{38}]^{n-}$  ( $n = 0-3$ ) clusters may be described as composed by an inner  $[\text{Pd}_9(\mu_3\text{-CO})_2]^{n+}$  ( $n = 0-3$ ) core decorated on its surface by three  $[\text{Co}_5\text{C}(\text{CO})_{12}]^-$  clusters. The same organometallic fragments have been previously found in the parent  $[\text{H}_{6-n}\text{Co}_{20}\text{Pd}_{16}\text{C}_4(\text{CO})_{48}]^{n-}$  ( $n = 3-6$ ) clusters, suggesting that they are not altered during the synthesis.

It is, thus, likely, that the transformation of  $[\text{H}_2\text{Co}_{20}\text{Pd}_{16}\text{C}_4(\text{CO})_{48}]^{4-}$  into  $[\text{HCo}_{15}\text{Pd}_9\text{C}_3(\text{CO})_{38}]^{2-}$  occurs *via* a proton induced degradation of the  $\text{Pd}_{16}$ -core of the former to give a  $\text{Pd}_9$  metal kernel stabilised by the same  $\text{Co}_5\text{C}(\text{CO})_{12}$  organometallic fragments (figure 6.13).

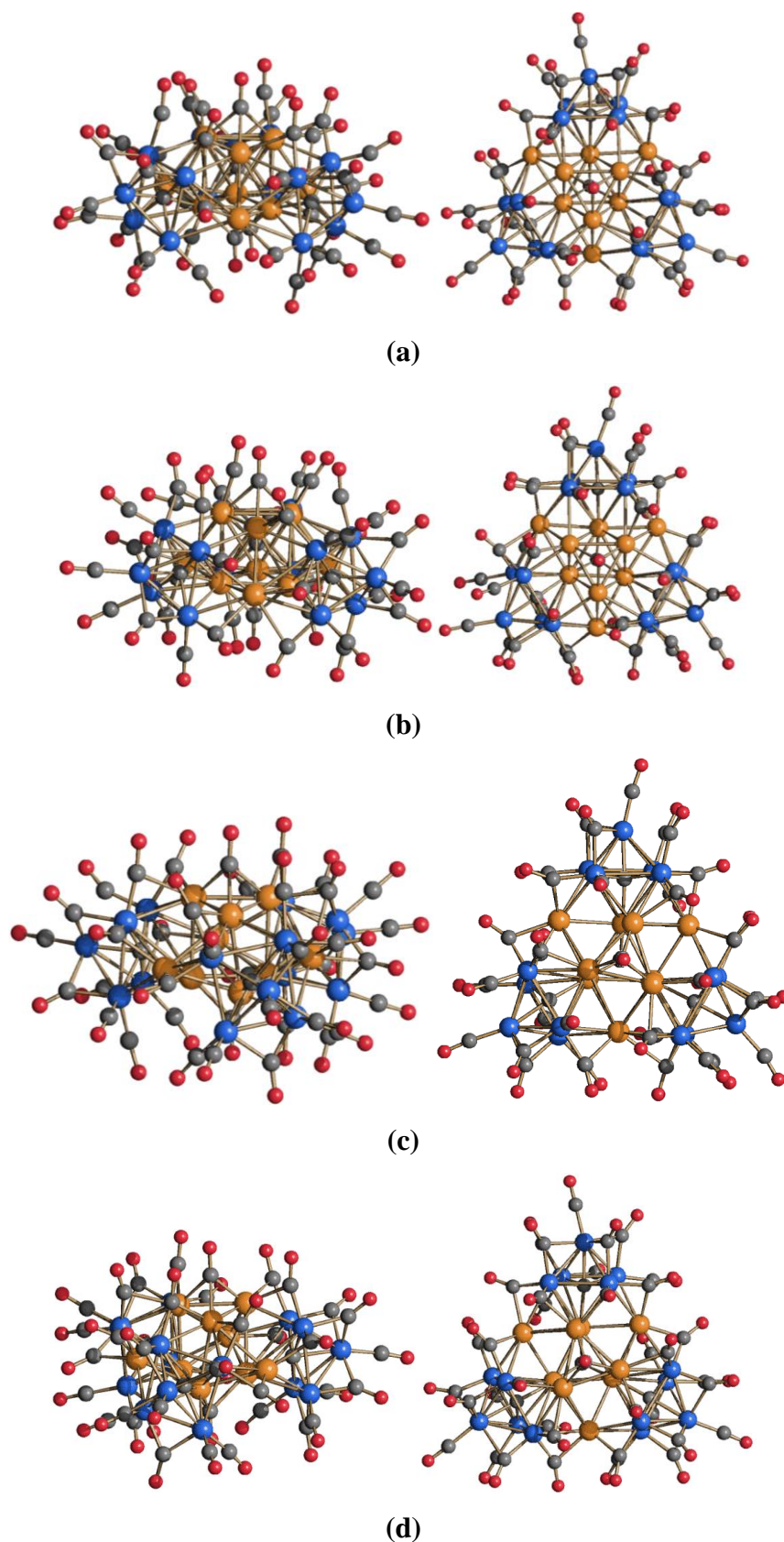


**Figure 6.12** Two different views of the molecular structures of (a)  $\text{H}_3\text{Co}_{15}\text{Pd}_9\text{C}_3(\text{CO})_{38}$ , (b)  $[\text{H}_2\text{Co}_{15}\text{Pd}_9\text{C}_3(\text{CO})_{38}]^-$ , (c)  $[\text{HCo}_{15}\text{Pd}_9\text{C}_3(\text{CO})_{38}]^{2-}$  and (d)  $[\text{Co}_{15}\text{Pd}_9\text{C}_3(\text{CO})_{38}]^{3-}$ . Left: the side views show that they have a "bent" structure, with the concave surface on top of the representation and the convex one on bottom. Right: the top views show the presence of a *pseudo*- $C_3$  symmetry axis (Co, blue; Pd, orange; C, grey; O, red).

$n$		0	1	2	3
M-M		75	74	67	68
Co-Co		24	24	24	24
Co-Pd		30	29	24	26
Pd-Pd		21	21	19	18
Co-C <sub>carbide</sub>		15	15	15	15
Pd-C <sub>carbide</sub>		3	3	3	3
t-CO		19	20	19	12
$\mu$ -CO	(Co-Co)	7	6	7	12
	(Co-Pd)	9	7	8	12
$\mu_3$ -CO	Pd <sub>3</sub>	2	2	2	2
$\square$	Co <sub>2</sub> Pd	1	3	2	-

**Table 6.5** Numbers of M-M bonds and CO ligands grouped by categories for  $[\text{H}_{3-n}\text{Co}_{15}\text{Pd}_9\text{C}_3(\text{CO})_{38}]^{n-}$  ( $n = 0-3$ ).

Partial degradation should also occur in order to free the two CO ligands which complete the coordination of the Pd<sub>9</sub>-kernel. Then, further rearrangements of the Pd<sub>9</sub> kernel are induced by the protonation-deprotonation reactions which originate the different  $[\text{H}_{3-n}\text{Co}_{15}\text{Pd}_9\text{C}_3(\text{CO})_{38}]^{n-}$  ( $n = 0-3$ ) clusters (see below).

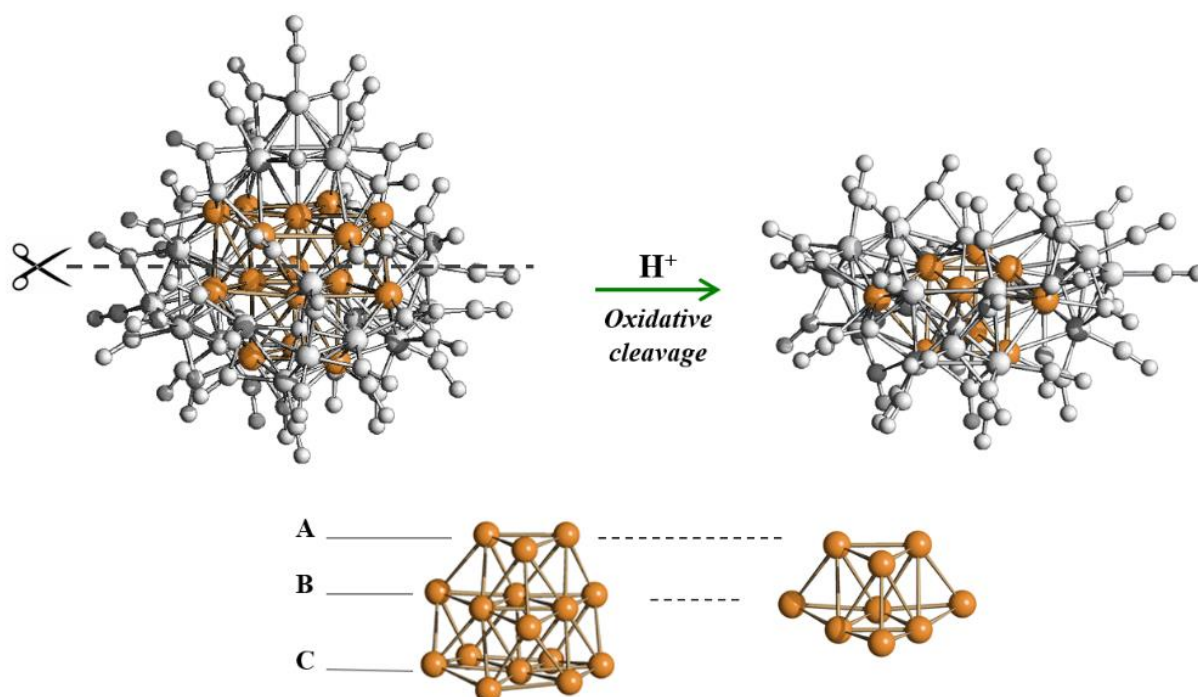


**Figure 6.13** Structural relationship of the whole structures (top) and Pd-cores (bottom) between  $[\text{H}_{6-n}\text{Co}_{20}\text{Pd}_{16}\text{C}_4(\text{CO})_{48}]^{n-}$  ( $n = 3-6$ ) and  $[\text{H}_2\text{Co}_{15}\text{Pd}_9\text{C}_3(\text{CO})_{38}]^{n-}$ .

In the final structures, the three carbide atoms are encapsulated within Co<sub>5</sub>PdC octahedral frameworks, resulting from the interaction of the three Co<sub>5</sub>C square pyramids with one Pd atom of the Pd<sub>9</sub>-kernel. The Co-C<sub>carbide</sub> and Pd-C<sub>carbide</sub> distances are very similar in the four  $[\text{H}_{3-n}$

${}^n\text{Co}_{15}\text{Pd}_9\text{C}_3(\text{CO})_{38}]^{n-}$  ( $n = 0-3$ ) clusters, indicating that the  $\text{Co}_5\text{PdC}$  octahedral cavities are not very much affected by the charge of the cluster.

Major differences among the four  $[\text{H}_{3-n}\text{Co}_{15}\text{Pd}_9\text{C}_3(\text{CO})_{38}]^{n-}$  ( $n = 0-3$ ) clusters arise when their  $\text{Pd}_9$ -kernel is considered. Thus, this is a tri-capped octahedron in  $\text{H}_3\text{Co}_{15}\text{Pd}_9\text{C}_3(\text{CO})_{38}$  and  $[\text{H}_2\text{Co}_{15}\text{Pd}_9\text{C}_3(\text{CO})_{38}]^-$ , whereas a distorted tri-capped trigonal prism is present in  $[\text{HCo}_{15}\text{Pd}_9\text{C}_3(\text{CO})_{38}]^{2-}$  and  $[\text{Co}_{15}\text{Pd}_9\text{C}_3(\text{CO})_{38}]^{3-}$  (figure 6.14).

In detail, the  $\text{Pd}_9$ -core of  $\text{H}_3\text{Co}_{15}\text{Pd}_9\text{C}_3(\text{CO})_{38}$  and  $[\text{H}_2\text{Co}_{15}\text{Pd}_9\text{C}_3(\text{CO})_{38}]^-$  is a close packed two layers (AB) arrangement of Pd-atoms, containing three and six atoms, respectively. Alternatively, it may be viewed as a distorted tri-capped octahedron, possessing idealised  $C_{3v}$  symmetry and displaying overall 21 Pd-Pd bonds. This compact  $\text{Pd}_9$ -kernel may be derived from the *ccp* (ABC 3+6+7)  $\text{Pd}_{16}$ -core of the parent  $[\text{H}_{6-n}\text{Co}_{20}\text{Pd}_{16}\text{C}_4(\text{CO})_{48}]^{n-}$  ( $n = 3-6$ ) by eliminating the compact C layer composed of seven Pd-atoms (figure 6.13).

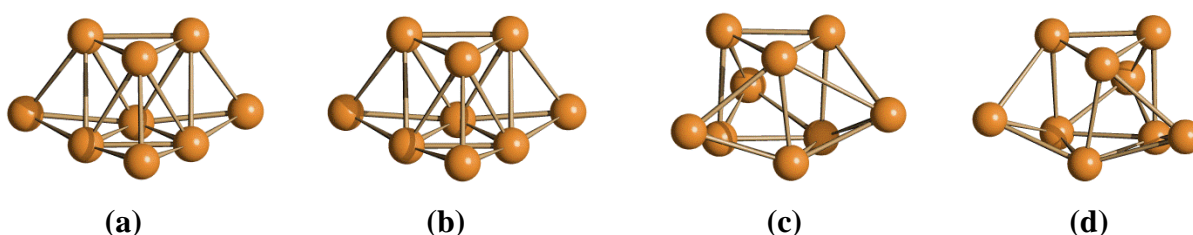


**Figure 6.14** The  $\text{Pd}_9$  core of (a)  $\text{H}_3\text{Co}_{15}\text{Pd}_9\text{C}_3(\text{CO})_{38}$ , (b)  $[\text{H}_2\text{Co}_{15}\text{Pd}_9\text{C}_3(\text{CO})_{38}]^-$ , (c)  $[\text{HCo}_{15}\text{Pd}_9\text{C}_3(\text{CO})_{38}]^{2-}$  and (d)  $[\text{Co}_{15}\text{Pd}_9\text{C}_3(\text{CO})_{38}]^{3-}$ .

The nine Pd-atoms may be divided into three groups composed each of three equivalent atoms: a) the three Pd-atoms of the A layer; b) the three Pd's of the B layer defining the bottom triangle of the octahedron; c) the three capping atoms, completing the B layer. The three  $\text{Co}_5\text{C}(\text{CO})_{12}$  fragments are, then, added in the way that the three Pd-atoms of group (b) complete the three octahedral  $\text{Co}_5\text{PdC}$  cages. The geometries of the  $\text{Co}_{15}\text{Pd}_9\text{C}_3$  frameworks as well as the M-M and M- $\text{C}_{\text{carbide}}$  bonds in both  $\text{H}_3\text{Co}_{15}\text{Pd}_9\text{C}_3(\text{CO})_{38}$  and  $[\text{H}_2\text{Co}_{15}\text{Pd}_9\text{C}_3(\text{CO})_{38}]^-$  are almost identical, whereas some minor differences are detected on the stereochemistry of the CO ligands (table 6.5).

On passing to the more charged  $[\text{HCo}_{15}\text{Pd}_9\text{C}_3(\text{CO})_{38}]^{2-}$  and  $[\text{Co}_{15}\text{Pd}_9\text{C}_3(\text{CO})_{38}]^{3-}$  clusters, an inversion from octahedral to trigonal prismatic of the  $\text{Pd}_9$ -core is observed. In addition, the tri-capped trigonal prismatic  $\text{Pd}_9$ -core of these two clusters is considerably distorted, in the sense that the three capping atoms are moved from the centres of the rectangular faces of the prism. As a consequence, in the fully deprotonated  $[\text{Co}_{15}\text{Pd}_9\text{C}_3(\text{CO})_{38}]^{3-}$  trianion, each capping atom

forms only three Pd-Pd bonds instead of the four expected for a regular tri-capped trigonal prism. Thus, the total number of Pd-Pd bonding contacts in  $[\text{Co}_{15}\text{Pd}_9\text{C}_3(\text{CO})_{38}]^{3-}$  is only 18 and not 21 as expected. Conversely, the mono-protonated  $[\text{HCo}_{15}\text{Pd}_9\text{C}_3(\text{CO})_{38}]^{2-}$  dianion shows 19 Pd-Pd bonds, in view of the fact that one capping Pd-atom forms four Pd-Pd bonds and the other two only three as in the tri-anion. In this way,  $[\text{HCo}_{15}\text{Pd}_9\text{C}_3(\text{CO})_{38}]^{2-}$  contains a  $\text{Pd}_5$ -square pyramidal cavity which is not present in  $[\text{Co}_{15}\text{Pd}_9\text{C}_3(\text{CO})_{38}]^{3-}$ .

#### *Possible location of the hydride ligands*

It is matter of speculation if the structural changes of  $[\text{H}_{3-n}\text{Co}_{15}\text{Pd}_9\text{C}_3(\text{CO})_{38}]^{n-}$  ( $n = 0-3$ ) clusters are due to the different charges of the clusters or to some stereochemical effect of the hydride ligands. By considering first the two almost isostructural  $\text{H}_3\text{Co}_{15}\text{Pd}_9\text{C}_3(\text{CO})_{38}$  and  $[\text{H}_2\text{Co}_{15}\text{Pd}_9\text{C}_3(\text{CO})_{38}]^-$  clusters, it is interesting to find out that they possess three square-pyramidal  $\text{Co}_2\text{Pd}_3$  cavities related by a 3-fold axis on their concave surface. It must be remarked that the two hydrides in  $[\text{H}_2\text{Rh}_{13}(\text{CO})_{24}]^{3-}$  have been located by neutron diffraction in the same type of cavities. The centres of these three  $\text{Co}_2\text{Pd}_3$  cavities in  $\text{H}_3\text{Co}_{15}\text{Pd}_9\text{C}_3(\text{CO})_{38}$  and  $[\text{H}_2\text{Co}_{15}\text{Pd}_9\text{C}_3(\text{CO})_{38}]^-$  display distances from the five metal atoms (1.80-2.03 Å), which are acceptable for Co-H and Pd-H bonds in interstitial hydrides (figure 6.15).

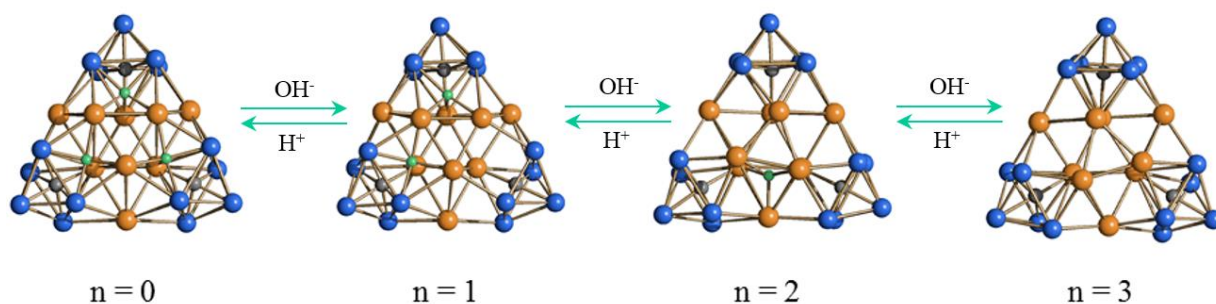


**Figure 6.15** Possible location of the hydride ligands in the  $[\text{H}_{3-n}\text{Co}_{15}\text{Pd}_9\text{C}_3(\text{CO})_{38}]^{n-}$  ( $n = 0-3$ ) clusters.

The inversion of the  $\text{Pd}_9$ -kernel from octahedral to trigonal prismatic on passing from  $[\text{H}_{3-n}\text{Co}_{15}\text{Pd}_9\text{C}_3(\text{CO})_{38}]^{n-}$  ( $n = 0, 1$ ) to  $[\text{H}_{3-n}\text{Co}_{15}\text{Pd}_9\text{C}_3(\text{CO})_{38}]^{n-}$  ( $n = 2, 3$ ) removes these three square pyramidal cavities. Nonetheless, the major difference between  $[\text{HCo}_{15}\text{Pd}_9\text{C}_3(\text{CO})_{38}]^{2-}$  and  $[\text{Co}_{15}\text{Pd}_9\text{C}_3(\text{CO})_{38}]^{3-}$  is represented by the presence in the former of an internal  $\text{Pd}_5$  cavity possessing a square pyramidal geometry, whereas this is absent in the latter. The centre of this  $\text{Pd}_5$  square pyramidal cavity shows contacts in the range 1.79-2.12 Å from the five Pd-atoms. This seems to be the most likely location for the unique hydride in  $[\text{HCo}_{15}\text{Pd}_9\text{C}_3(\text{CO})_{38}]^{2-}$ .

Conversely,  $[\text{Co}_{15}\text{Pd}_9\text{C}_3(\text{CO})_{38}]^{3-}$  does not contain any square pyramidal cavity, in agreement with its formulation as a fully deprotonated non-hydride species. Even if these

considerations are more speculations than a conclusive proofs, it seems reasonable that the hydride ligands exert some stereochemical effects in the  $[\text{H}_{3-n}\text{Co}_{15}\text{Pd}_9\text{C}_3(\text{CO})_{38}]^{n-}$  ( $n = 0-3$ ) clusters causing their structural rearrangements after protonation-deprotonation reactions .

## Final Remarks

$[\text{H}_{3-n}\text{Co}_{15}\text{Pd}_9\text{C}_3(\text{CO})_{38}]^{n-}$  ( $n = 0-3$ ) and  $[\text{H}_{6-n}\text{Co}_{20}\text{Pd}_{16}\text{C}_4(\text{CO})_{48}]^{n-}$  ( $n = 3-6$ ) represent the first examples of homoleptic bimetallic Co-Pd carbide carbonyl clusters. This must be contrasted with other group 10 metals, which form several bimetallic MCCs with Co, such as bimetallic Ni-Co (see chapter 4.1) and Co-Pt carbide clusters. It is noteworthy that all these clusters contain interstitial carbide atoms, which seem to be essential in order to stabilise their metal cages.

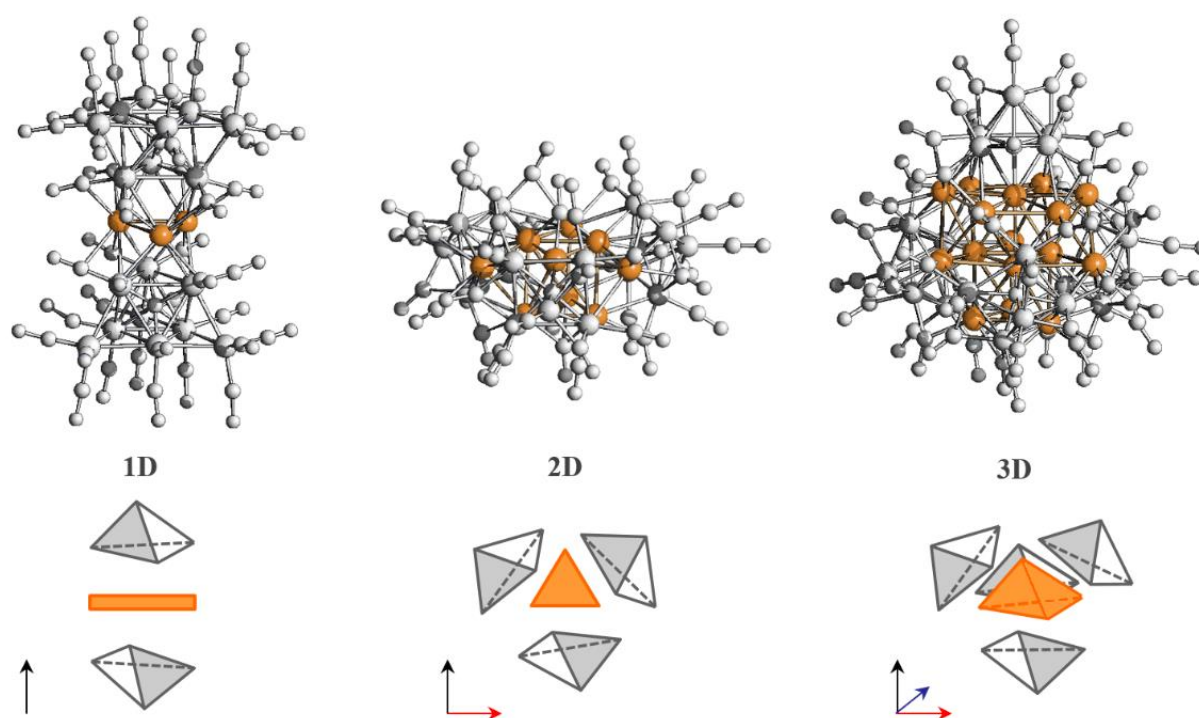


**Figure 6.16** Mono-, bi- and three-dimensional cluster-in-cluster architectures. From left to right: molecular structure of  $[\text{Os}_{18}\text{Pd}_3\text{C}_2(\text{CO})_{42}]^{2-}$ ,  $[\text{H}_2\text{Co}_{15}\text{Pd}_9\text{C}_3(\text{CO})_{38}]^-$  and  $[\text{H}_2\text{Co}_{20}\text{Pd}_{16}\text{C}_4(\text{CO})_{48}]^{4-}$  clusters.

These structures display a perfect segregation of the two metals, with an inner  $[\text{Pd}_9(\mu_3\text{-CO})_2]^{n+}$  ( $n = 0-3$ ) or  $[\text{Pd}_{16}]^{n-}$  ( $n = 0-2$ ) kernel stabilised by three or four  $[\text{Co}_5\text{C}(\text{CO})_{12}]^-$  fragments, respectively. These represent a further example of new clusters containing the unprecedented  $[\text{Co}_5\text{C}(\text{CO})_{12}]^-$  molecular units (see chapter 5.3). The metal segregation is due to the greater propensity of Co compared to Pd to form M-CO and M-C<sub>carbide</sub> bonds. These new results show how the nuclearity of the palladium core affects the final architecture of the bimetallic framework.

Previous to our work, the highest Pd-nuclearity in related species was four, *e.g.*,  $[\text{Ru}_{12}\text{Pd}_4\text{C}_2(\text{CO})_{32}]^{2-}$ , and this core was too small to coordinate more than two fragments. Thus,  $[\text{Ru}_{12}\text{Pd}_4\text{C}_2(\text{CO})_{32}]^{2-}$  displays a sandwich structure (mono-dimensional cluster-in-cluster) (figure 5.16). As the Pd nuclearity increases, additional fragments can be coordinated resulting in bi-

and tri-dimensional cluster-in-cluster structures as observed in  $[\text{H}_{3-n}\text{Co}_{15}\text{Pd}_9\text{C}_3(\text{CO})_{38}]^{n-}$  ( $n = 0-3$ ) and  $[\text{H}_{6-n}\text{Co}_{20}\text{Pd}_{16}\text{C}_4(\text{CO})_{48}]^{n-}$  ( $n = 3-6$ ) respectively (figure 5.1.16).

The most relevant result is represented by the fact that, for the first time, significant rearrangements of the metal cage of a large MCC have been observed as the consequence of the change of one unit of their charges, due to simple and reversible acid-base reactions. Beside every speculation, this further points out that the metal core in ligand-stabilized clusters is rather deformable. The fact that these structural rearrangements are caused by protonation-deprotonation of the clusters seems to suggest that the hydride ligands may have some stereochemical effects. This was previously documented only in a single case for lower nuclearity MCCs, *i.e.*,  $[\text{Fe}_4(\text{CO})_{13}]^{2-}$  and  $[\text{HFe}_4(\text{CO})_{13}]^-$ . We can suppose that the metal cages of  $[\text{H}_{3-n}\text{Co}_{15}\text{Pd}_9\text{C}_3(\text{CO})_{38}]^{n-}$  ( $n = 0-3$ ) change in order to create suitable cavities to accommodate the hydride ligands. This, in turn, is favoured by the very rigid and stable  $\text{Co}_5\text{C}(\text{CO})_{12}$  fragments which follow the movements and stabilize the inner "soft"  $\text{Pd}_9$  kernels. In other words, this unprecedented inner core deformation, hardly imaginable in a core-shell architecture, shall be rendered possible by the cluster-in-cluster structure. Indeed, the considerable rearrangement of the  $\text{Pd}_9$  kernel leads to a little reorientation of the  $\text{Co}_5\text{C}(\text{CO})_{12}$  fragments resulting in a different stereochemical CO coordination.

Another point of interest is the fact that, as determined by SQUID measurements, the even electron  $[\text{HCo}_{15}\text{Pd}_9\text{C}_3(\text{CO})_{38}]^{2-}$  mono-hydride di-anion is paramagnetic because of two unpaired electrons. This confirms that even electron MCCs may be paramagnetic and lends support to the mono-hydride nature of  $[\text{HCo}_{15}\text{Pd}_9\text{C}_3(\text{CO})_{38}]^{2-}$ . Finally, the  $[\text{H}_{6-n}\text{Co}_{16}\text{Pd}_2\text{C}_3(\text{CO})_{28}]^{n-}$  ( $n = 5, 6$ ) and  $[\text{H}_{3-n}\text{Co}_{15}\text{Pd}_9\text{C}_3(\text{CO})_{38}]^{n-}$  ( $n = 0-3$ ) clusters represent the first MCCs containing three carbide atoms.

## CHAPTER 7

# Carbides and Hydrides Contained in Small Cages

This chapter illustrates cases of carbide and hydride atoms enclosed within small metal cages of carbonyl clusters stabilized by  $[\text{AuPPh}_3]^+$  units. In particular, two examples of carbides encapsulated in octahedral  $\text{Ni}_6$ -cages and the first case of a hydride enclosed in a  $\text{Fe}_4$ -tetrahedral cavity of a low valent cluster are reported and related to other known compounds. Finally, the first molecular cluster containing one carbide atom and one tightly bonded  $\text{C}_2$ -unit with sub-van der Waals interactions is presented.



## Surface Decorated Nickel Carbide Carbonyl Clusters

### 7.1.1 Interstitial monocarbide carbonyl clusters

Polyhedral clusters contain cavities, the size and shape of which is dependent on the geometry of the metal core and the covalent radii of the metals. Theoretically, the geometry of a cavity defines the size of the atoms that can be encapsulated, based on the radii of the metal atoms ( $r_{\text{met}}$ ) and the interstitial atoms ( $r_{\text{int}}$ ) [96]. However, the metal framework and the interstitial atom tend to be “soft” enough so that a less than perfect fit can be accommodated. In this regard, carbon and other main group elements such as boron and nitrogen are particularly flexible. Indeed, an octahedral cavity should only be able to contain atoms with  $r_{\text{int}}/r_{\text{met}} \leq 0.41$ , but C is commonly found in octahedral cavities despite a bigger radius ratio (figure 7.1.1).

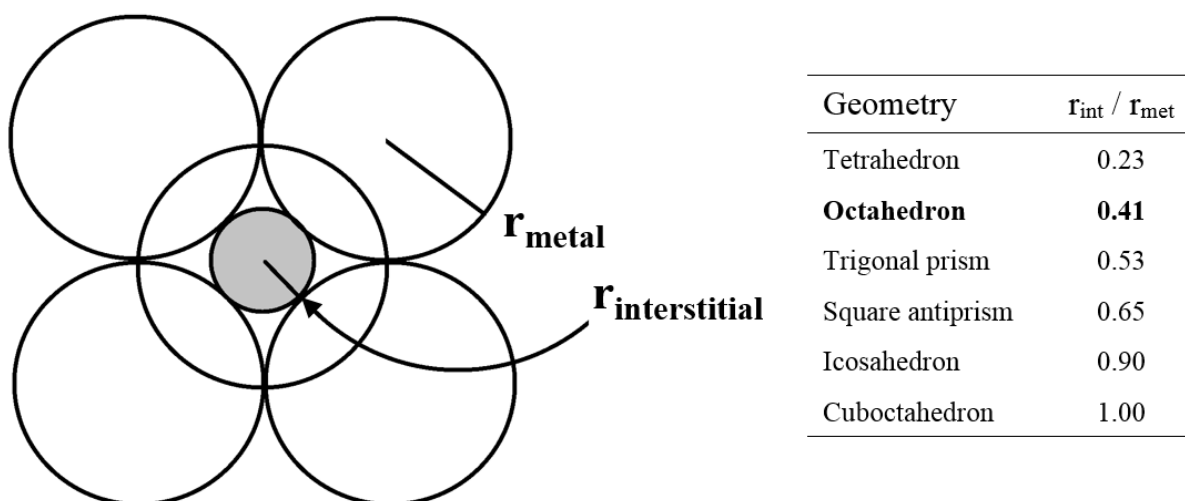


**Figure 7.1.1** Interstitial cavity of an octahedral cluster with a list of cavities of different geometries related with their  $r_{\text{int}}/r_{\text{met}}$  ratios.

Several structurally characterized metal carbonyl clusters containing a single isolated interstitial atom are known. In the field of homometallic nickel clusters, the carbides are encapsulated in mono-capped trigonal prismatic or square-antiprismatic cavities. Indeed, the carbon atom is too large to fit into an octahedral nickel cage and the carbide cluster with lower nuclearity, *i.e.*,  $[\text{Ni}_7\text{C}(\text{CO})_{12}]^{2-}$  [97], displays a monocapped trigonal prismatic cage. It is

noteworthy than, despite many efforts, all attempts to obtain a hexanuclear Ni<sub>6</sub>C carbide by means of decapping of the eptanuclear cluster have failed.<sup>30</sup>

Conversely, [Fe<sub>6</sub>C(CO)<sub>16</sub>]<sup>2-</sup> [98] displays an octahedral cage according to the larger size of Fe compared to Ni (figure 7.1.2). In the case of cobalt, which shows an intermediate radius between iron and nickel, both octahedral and trigonal prismatic metal cages are known, *i.e.*, [Co<sub>6</sub>C(CO)<sub>13</sub>]<sup>2-</sup> [99] and [Co<sub>6</sub>C(CO)<sub>15</sub>]<sup>2-</sup> [100].

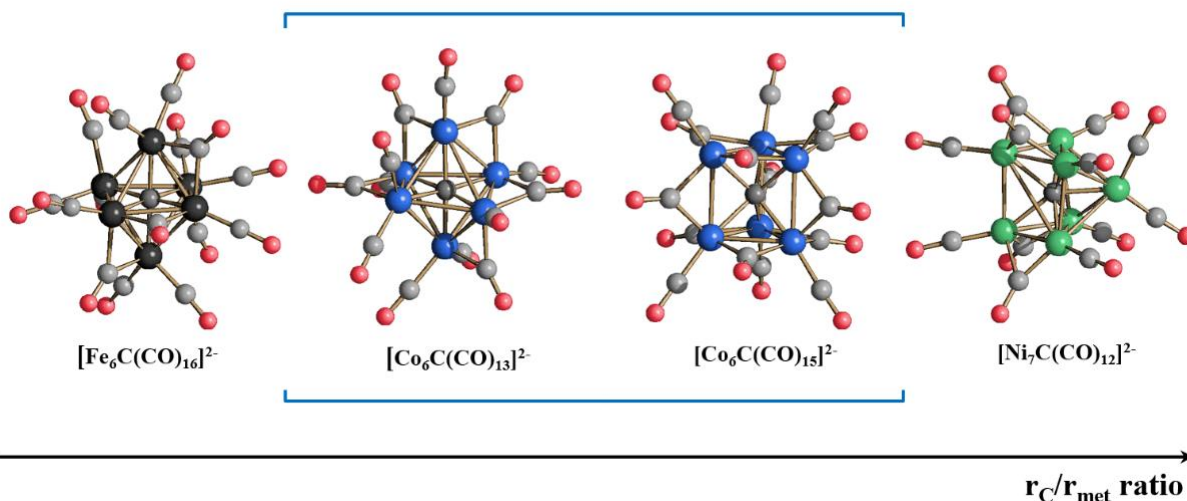


**Figure 7.1.2** Molecular structures of the lower nuclearity mono-carbido iron, cobalt and nickel carbonyl clusters ordered on the basis of the ratio of carbon and metal radii (Ni, green; Co, blue; Fe, black; C, grey; O, red).

### 7.1.2 General results

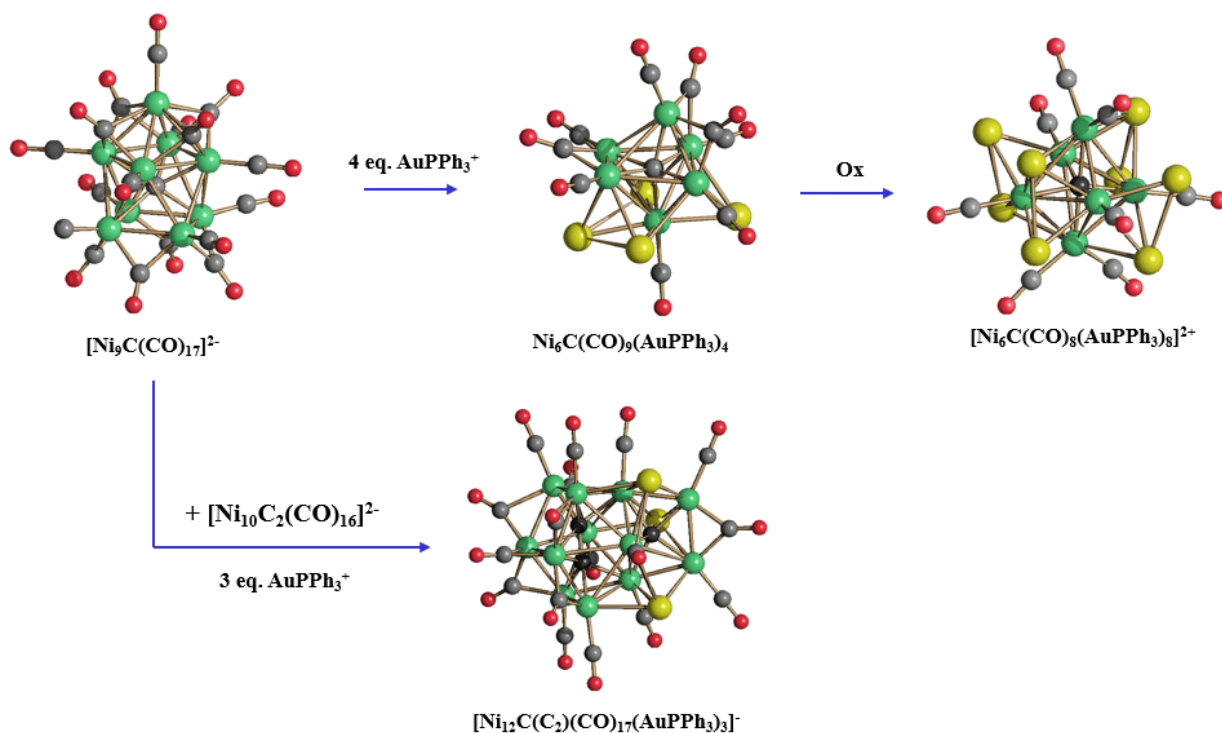
The following sections report the investigation of the reaction of [Ni<sub>9</sub>C(CO)<sub>17</sub>]<sup>2-</sup> with an increasing amount of Au(PPh<sub>3</sub>)Cl. The reaction led to the isolation of the new bimetallic cluster Ni<sub>6</sub>C(CO)<sub>9</sub>(AuPPh<sub>3</sub>)<sub>4</sub> [101]. In turn, Ni<sub>6</sub>C(CO)<sub>9</sub>(AuPPh<sub>3</sub>)<sub>4</sub> reacts with an excess of HBF<sub>4</sub>·Et<sub>2</sub>O to give the new [Ni<sub>6</sub>C(CO)<sub>8</sub>(AuPPh<sub>3</sub>)<sub>8</sub>]<sup>2+</sup> cationic species. Moreover, the reaction of a mixture of [Ni<sub>9</sub>C(CO)<sub>17</sub>]<sup>2-</sup>, [Ni<sub>10</sub>C<sub>2</sub>(CO)<sub>16</sub>]<sup>2-</sup> and Au(PPh<sub>3</sub>)Cl in a 1 : 1 : 3 ratio results in the new [Ni<sub>12</sub>C(C<sub>2</sub>)(CO)<sub>17</sub>(AuPPh<sub>3</sub>)<sub>3</sub>]<sup>-</sup> cluster [102]. These results are summarized in scheme 7.1.1.

### 7.1.3 Synthesis and characterization of Ni<sub>6</sub>C(CO)<sub>9</sub>(AuPPh<sub>3</sub>)<sub>4</sub>

The neutral cluster Ni<sub>6</sub>C(CO)<sub>9</sub>(AuPPh<sub>3</sub>)<sub>4</sub> was obtained in low yields from the reaction of [Ni<sub>9</sub>C(CO)<sub>17</sub>]<sup>2-</sup> with Au(PPh<sub>3</sub>)Cl (*ca.* 2 equivalents) in thf. Formation of Ni<sub>6</sub>C(CO)<sub>9</sub>(AuPPh<sub>3</sub>)<sub>4</sub> is accompanied by several by-products, such as Ni(CO)<sub>4</sub>, Ni<sup>2+</sup>, Ni(CO)<sub>3</sub>(PPh<sub>3</sub>), [Ni<sub>8</sub>C(CO)<sub>16</sub>]<sup>2-</sup>, Au

<sup>30</sup> These attempts consist mainly in the reaction of [Ni<sub>7</sub>C(CO)<sub>12</sub>]<sup>2-</sup> with a large excess of PPh<sub>3</sub> under CO.

metal and unreacted  $[\text{Ni}_9\text{C}(\text{CO})_{17}]^{2-}$ . All the carbonyl by-products have been identified through IR spectroscopy by comparison with the spectra reported in the literature.



**Scheme 7.1.1** Synthesis of new bimetallic Ni-Au carbide clusters. For the sake of clarity, the phosphines are not represented (Ni, green; Au, yellow; C, grey; O, red).

Purification was accomplished by removing the solvent *in vacuo*, washing the residue with water and toluene. The residue was, then, extracted in thf and re-crystallized from thf/toluene and thf/n-hexane resulting in X-ray quality crystals of  $\text{Ni}_6\text{C}(\text{CO})_9(\text{AuPPh}_3)_4 \cdot \text{thf}$  and  $\text{Ni}_6\text{C}(\text{CO})_9(\text{AuPPh}_3)_4 \cdot \text{thf} \cdot 0.5\text{C}_6\text{H}_{14}$ , respectively. Under these conditions, anionic species such as  $[\text{Ni}_8\text{C}(\text{CO})_{16}]^{2-}$  and  $[\text{Ni}_9\text{C}(\text{CO})_{17}]^{2-}$  preferentially remained in solution or precipitated as amorphous solids. Crystals for X-ray analyses were, therefore, mechanically separated from the amorphous material before further proceeding with the analyses. These crystals are almost insoluble in all organic solvents, hampering any further chemical, spectroscopic or physical study. The crystals show  $\nu(\text{CO})$  in nujol mull at 2027(ms), 1984(vs), 1970(s), 1851(m), 1832(ms)  $\text{cm}^{-1}$ .

### Crystal structures

$\text{Ni}_6\text{C}(\text{CO})_9(\text{AuPPh}_3)_4$  displays similar structures in both two solvates, even if there are some differences especially regarding the weak  $\text{Au} \cdots \text{Au}$  contacts (figure 7.1.3 and table 7.1.1)

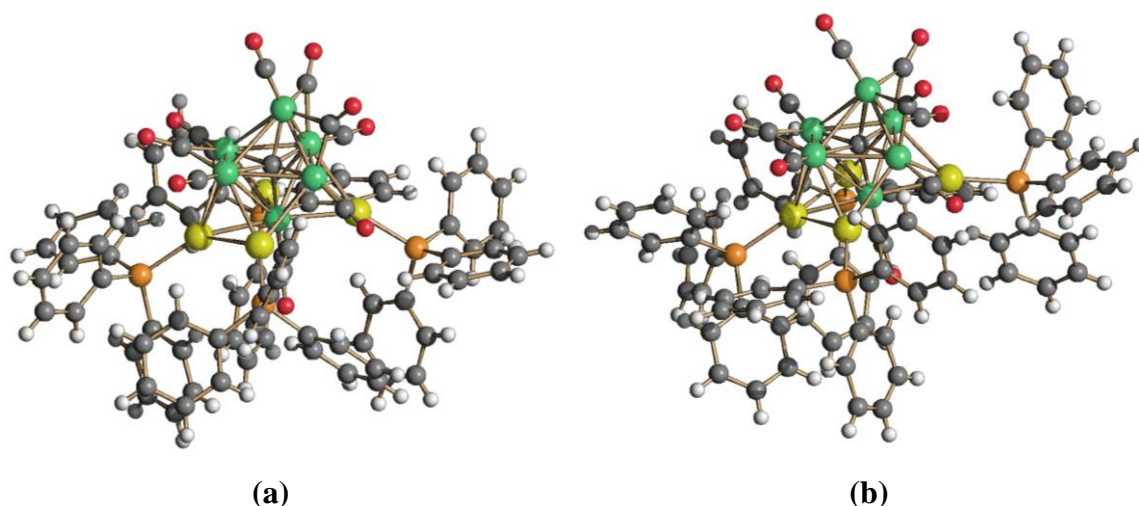


**Figure 7.1.3** Molecular structure of  $\text{Ni}_6\text{C}(\text{CO})_9(\text{AuPPh}_3)_4$  as found in  $\text{Ni}_6\text{C}(\text{CO})_9(\text{AuPPh}_3)_4 \cdot \text{thf}$  (a) and  $\text{Ni}_6\text{C}(\text{CO})_9(\text{AuPPh}_3)_4 \cdot \text{thf} \cdot 0.5\text{C}_6\text{H}_{14}$  (b) (Ni, green; Au, yellow; C, grey; O, red, H, white).

	$\text{Ni}_6\text{C}(\text{CO})_9(\text{AuPPh}_3)_4 \cdot \text{thf}$	$\text{Ni}_6\text{C}(\text{CO})_9(\text{AuPPh}_3)_4 \cdot \text{thf} \cdot 0.5\text{C}_6\text{H}_{14}$
Ni-Ni	2.3891(12)-2.8687(12) Average 2.678(4)	2.3847(18)-2.9875(18) Average 2.682(6)
Ni-C <sub>carbide</sub>	1.811(6)-1.931(6) Average 1.893(16)	1.816(9)-1.920(9) Average 1.89(2)
Ni-Au	2.5625(8)-2.9323(9) Average 2.696(3)	2.5738(12)-2.8615(14) Average 2.702(5)
Au-P	2.2836(19)-2.2914(19) Average 2.289(4)	2.287(3)-2.298(3) Average 2.294(6)
Au...Au	3.5922(5), 3.0509(5), 4.2721(5), 3.6648(5) Average 3.6450(10)	3.1701(7), 2.9889(7), 4.3230(7), 4.0611(7) Average 3.6358(14)

**Table 7.1.2** Comparison of the most relevant bond lengths (Å) in  $\text{Ni}_6\text{C}(\text{CO})_9(\text{AuPPh}_3)_4 \cdot \text{thf}$  and  $\text{Ni}_6\text{C}(\text{CO})_9(\text{AuPPh}_3)_4 \cdot \text{thf} \cdot 0.5\text{C}_6\text{H}_{14}$ .

The  $\text{Ni}_6\text{C}(\text{CO})_9(\text{AuPPh}_3)_4$  cluster contains a C-centered distorted  $\text{Ni}_6\text{C}$  octahedral core. The four  $\text{Au}(\text{PPh}_3)$  fragments are  $\mu_3$ -bonded to four contiguous triangular faces (related by a 4-fold) of the octahedron, formally reducing the symmetry from  $O_h$  to  $C_{4v}$ . For what concerns the nine CO ligands, six are terminally coordinated one per each Ni-atom, whereas the remaining three carbonyls are edge bridging, one in the equatorial plane of the cluster and the other two on two edges spanning from the equatorial plane toward the apical Ni non-bonded to any Au-atom.

The four Ni-atoms in the equatorial plane of the cluster as well as the carbide atom are almost coplanar whereas the other two nickels are in apical positions, one bonded to four Au-atoms and the other to none. The cluster may be partitioned into an anionic  $[\text{Ni}_6\text{C}(\text{CO})_9]^{4-}$  moiety decorated by four cationic  $[\text{AuPPh}_3]^+$  units. The resulting octahedral cages are very distorted

with the twelve Ni-Ni edges very different, in virtue of the fact that the interstitial carbide atom is rather big to be accommodated in a regular octahedron (figure 7.1.4).

Four Au...Au contacts are present in the cluster, displaying similar average values in the two solvates but distributed in a rather different manner. Thus, in  $\text{Ni}_6\text{C}(\text{CO})_9(\text{AuPPh}_3)_4\cdot\text{thf}$ , only one contact may be considered at bonding distance [3.0509(5) Å], whereas the other three contacts [3.5922(5), 3.6648(5) and 4.2721(5) Å] are well above the sum of the van der Waals radii of Au [sum of covalent radii 2.72 Å; sum of the van der Waals radii 3.32 Å]. Conversely, in  $\text{Ni}_6\text{C}(\text{CO})_9(\text{AuPPh}_3)_4\cdot\text{thf}\cdot 0.5\text{C}_6\text{H}_{14}$ , two contiguous Au...Au contacts are at bonding distances [2.9889(7) and 3.1701(7) Å], whereas the other two are non-bonding [4.0611(7) and 4.3230(7) Å].

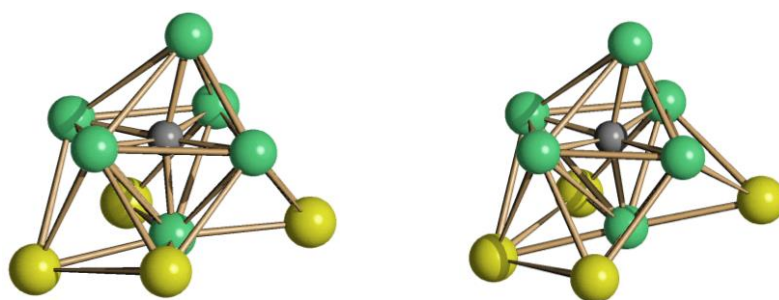


**Figure 7.1.4** The  $\text{Ni}_6\text{CAu}_4$  cores of  $\text{Ni}_6\text{C}(\text{CO})_9(\text{AuPPh}_3)_4$  as found in  $\text{Ni}_6\text{C}(\text{CO})_9(\text{AuPPh}_3)_4\cdot\text{thf}$  (a) and  $\text{Ni}_6\text{C}(\text{CO})_9(\text{AuPPh}_3)_4\cdot\text{thf}\cdot 0.5\text{C}_6\text{H}_{14}$  (b) (Ni, green; Au, yellow; C, grey).

### Theoretical investigation

In order to better understand the factors that rule such a dichotomy found in the solid state, a theoretical investigation was performed at B3LYP-DFT/6-31+G(d,p) level of theory with the Stuttgart-Dresden *pseudo*-potential for both Au and Ni centers. Two simplified models were built from the X-ray structures upon substitution of the bulky  $\text{PPh}_3$  with simpler  $\text{PH}_3$  and by neglecting the co-crystallized solvent molecule. Single point energy calculations on the structure models revealed that the structure found in  $\text{Ni}_6\text{C}(\text{CO})_9(\text{AuPPh}_3)_4\cdot\text{thf}\cdot 0.5\text{C}_6\text{H}_{14}$  is more stable by 4.95 kcal/mol than the one present in  $\text{Ni}_6\text{C}(\text{CO})_9(\text{AuPPh}_3)_4\cdot\text{thf}$ . This difference in stability is consistent either with a solid state packing effect or with weak Au-Au interactions. The optimization of both these models converged to the same structure with an angle  $\text{Ni}_{\text{ap}}\text{-C-Ni}_{\text{ap}}$  of  $159.5^\circ$  and very similar to the one found in  $\text{Ni}_6\text{C}(\text{CO})_9(\text{AuPPh}_3)_4\cdot\text{thf}\cdot 0.5\text{C}_6\text{H}_{14}$  (figure 7.1.5). This suggests that the more stable geometry is the one found in  $\text{Ni}_6\text{C}(\text{CO})_9(\text{AuPPh}_3)_4\cdot\text{thf}\cdot 0.5\text{C}_6\text{H}_{14}$ , with two short and two long Au...Au distances. Conversely, the one present in  $\text{Ni}_6\text{C}(\text{CO})_9(\text{AuPPh}_3)_4\cdot\text{thf}$  with a single short Au...Au contact is less stable (by *ca.* 5 kcal/mol). The presence in the solid state of this structure may be justified by assuming that packing effects compensate its minor stability as isolated molecule.

In the optimized structure, the Ni-Ni contacts spread over a large range (2.39-3.04 Å) and they can be divided in three different sets: the in-plane ones (2.42-3.04 Å), the Ni<sub>ap</sub>-Ni<sub>eq</sub> not involved in interactions with Au centers (2.39-2.80 Å) and the one in the Au-capping half (2.59-2.92 Å). The calculated Ni-C<sub>carbide</sub> distances are 1.93 Å with the only exception of the one between the apical Ni, interacting with the Au atoms (1.83 Å). Although some overestimation by the calculations, likely imputed to the usage of a *pseudo*-potential for the metal atoms and a simplified model, the computed structure satisfactorily reproduces the Ni<sub>6</sub>C core. Interestingly, the four capping Au and the apical Ni lie all in the same plane as in Ni<sub>6</sub>C(CO)<sub>9</sub>(AuPPh<sub>3</sub>)<sub>4</sub>·thf·0.5C<sub>6</sub>H<sub>14</sub>. The Au···Au distances are in pair: two short (3.14 Å) and two long (4.22 Å), quite resembling the structure of Ni<sub>6</sub>C(CO)<sub>9</sub>(AuPPh<sub>3</sub>)<sub>4</sub>·thf·0.5C<sub>6</sub>H<sub>14</sub>.

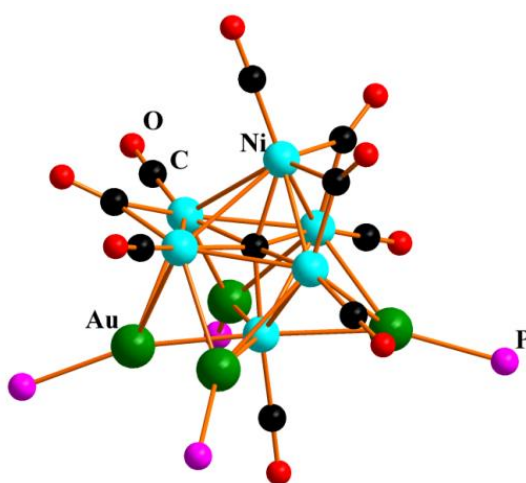


**Figure 7.1.5** Optimized structure of Ni<sub>6</sub>(CO)<sub>9</sub>(Au(PH<sub>3</sub>)<sub>4</sub>) at B3LYP-DFT level of theory.

The HOMO-LUMO gap was estimated to be 2.54 eV. The HOMO is calculated to be mainly localized on the Ni<sub>6</sub> core otherwise the LUMO has a strong contribution from the gold and apical Ni centers (figure 7.1.6). The main contributions to metal bonding come from the interaction between fully occupied d orbitals combinations of the Ni atoms with the empty sp hybrids on the gold centers.

In principle a functional with the inclusion of the dispersion forces as the B97D could help to reproduce the two isomers in the case that structural differences between the two experimental structures are given by variable Au···Au interactions. As occurred for B3LYP functional, the calculations converged into the same structure with quite short Au···Au distances in between 3.59 and 3.85 Å. Although some slight differences in the obtained Ni-Ni distances, especially for those involving the Ni bonded to gold atoms, the other main features remain quite unaltered. The HOMO-LUMO gap calculated with B97D functional was 1.58 eV. Since also the inclusion of dispersion corrections is not able to reproduce the double minimum features of the

Potential Energy Surface, such behavior could be reasonably imputed to solid state packing in the crystal due to the weak interaction with the co-crystallized solvent molecules.

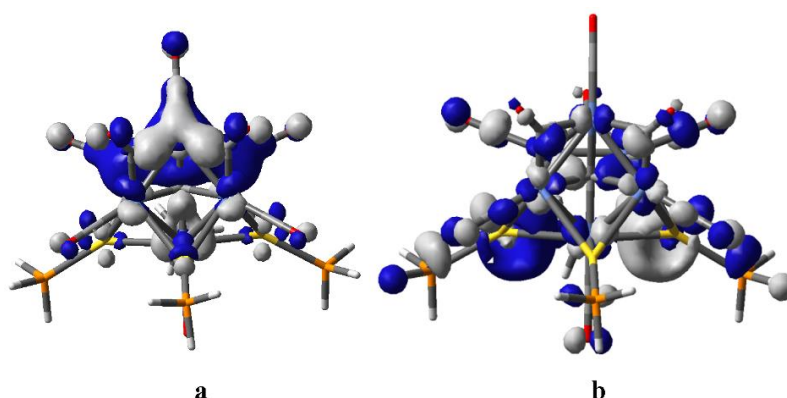


**Figure 7.1.6** Graphical plot of (a) HOMO and (b) LUMO orbitals of  $\text{Ni}_6(\text{CO})_9(\text{Au}(\text{PH}_3)_4)$ .

The experimental IR spectrum in nujol mull displays five main peaks at 2027, 1984, 1970, 1851 and 1832  $\text{cm}^{-1}$ , respectively. Through the frequencies calculations, performed within Gaussian 09 package on the optimized geometries, we attempted in the assignment of the different carbonyl stretching (table 7.1.2). In fact, although slightly different in the position and sometimes deriving from a complex vibrational pattern, they can be simply attributed to the different carbonyl moieties. The first three peaks could be assigned to the terminal CO: the high energy one to CO bonded to the apical Ni without interaction with the gold centers, the second to the in-plane ones and the last to the remaining apical one. The calculated stretchings of the bridging CO ligands occur at 1935 and 1970  $\text{cm}^{-1}$ , respectively for the in- and out-plane carbonyl ligands.

Assignment	Multiplicity	Experimental*	Calculated
t-CO $\text{Ni}_{\text{ap}}$ (no Au)	1	2027(ms)	2114
t-CO $\text{Ni}_{\text{eq}}$	4	1984(vs)	2062
t-CO $\text{Ni}_{\text{ap}}$ (Au)	1	1970(s)	2038
$\mu$ -CO $\text{Ni}_{\text{eq}}$	1	1851(m)	1972
$\mu$ -CO $\text{Ni}_{\text{ap}}$	2	1832(ms)	1935

**Table 7.1.2** Experimental and calculated  $\nu(\text{CO})$  stretchings ( $\text{cm}^{-1}$ ) of  $\text{Ni}_6\text{C}(\text{CO})_9(\text{AuPPh}_3)_4$ .

### 7.1.4 Synthesis and characterization of $[\text{Ni}_6\text{C}(\text{CO})_8(\text{AuPPh}_3)_8]^{2+}$

$\text{Ni}_6\text{C}(\text{CO})_9(\text{AuPPh}_3)_4$  reacts with an excess of  $\text{HBF}_4 \cdot \text{Et}_2\text{O}$  resulting in the cationic species  $[\text{Ni}_6\text{C}(\text{CO})_8(\text{AuPPh}_3)_8]^{2+}$  which has been structurally characterized in the solid state as its  $[\text{Ni}_6\text{C}(\text{CO})_8(\text{AuPPh}_3)_8][\text{BF}_4]_2$  salt (figure 7.1.7). A single resonance at  $\delta_{\text{P}}$  55.0 ppm is present in the  $^{31}\text{P}$  NMR spectrum recorded in  $\text{CD}_2\text{Cl}_2$  at 203 K, indicating equivalence of the eight  $\text{PPh}_3$  ligands in solution.

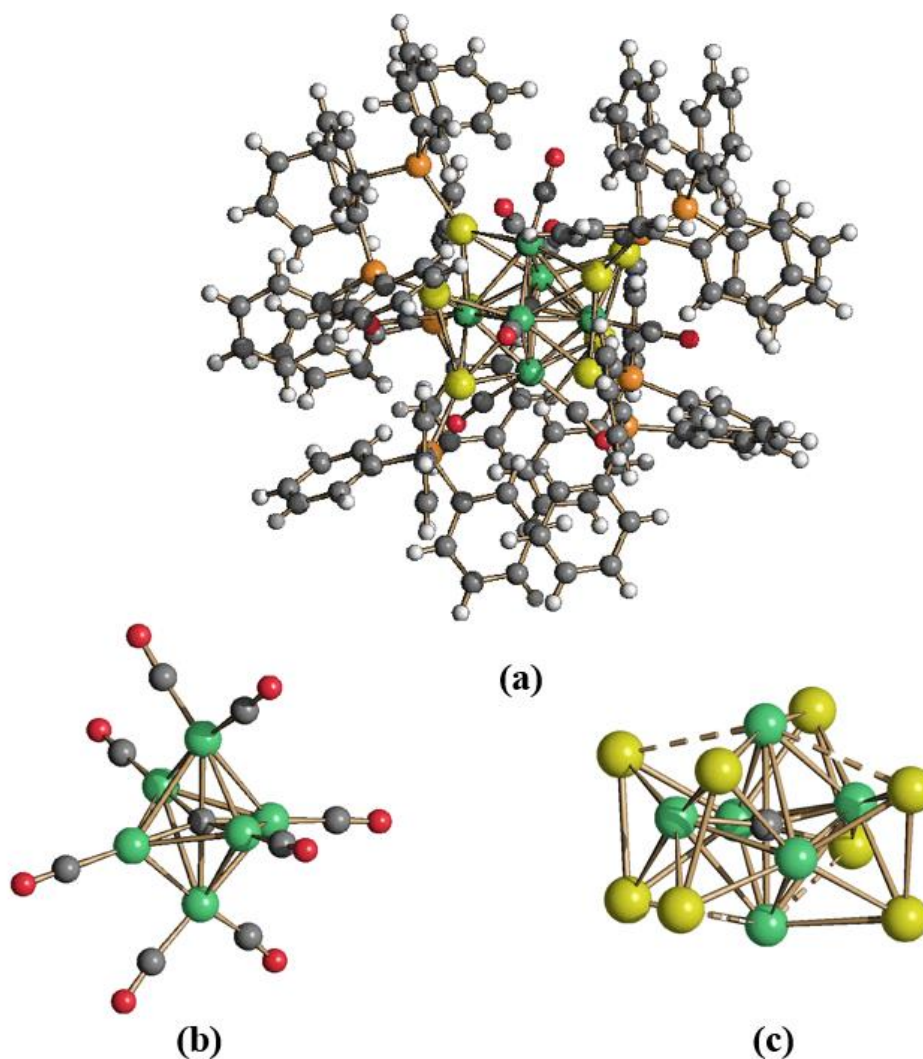


**Figure 7.1.7** (a) Molecular structure, (b)  $[\text{Ni}_6\text{C}(\text{CO})_8]^{6-}$  core and (c)  $\text{Ni}_6\text{CAu}_8$  cage of  $[\text{Ni}_6\text{C}(\text{CO})_8(\text{AuPPh}_3)_8]^{2+}$  (Ni, green; Au, yellow; C, grey; O, red, H, white).

In the solid state, the cation displays crystallographic  $\bar{4}$  ( $S_4$ ) symmetry, with the  $\bar{4}$ -axis passing through the apical Ni and the interstitial carbide atoms. The cluster may be viewed as composed by a distorted octahedral  $[\text{Ni}_6\text{C}(\text{CO})_8]^{6-}$  core decorated by four  $[\text{PPh}_3\text{Au}-\text{AuPPh}_3]^{2+}$  fragments. The octahedral core is highly distorted, in virtue of the fact that the interstitial carbide

atom is rather big to be accommodated in a regular Ni<sub>6</sub>-octahedron. The cluster contains eight terminal CO ligands, two bonded to each apical Ni, and one per each Ni in equatorial position.

The [PPh<sub>3</sub>Au-AuPPh<sub>3</sub>]<sup>2+</sup> fragments are μ<sub>5</sub>-bonded to two contiguous triangular faces of the Ni<sub>6</sub>-octahedron, with one Au forming three Ni-Au bonds and the other only two. A short Au-Au interaction is present within each [PPh<sub>3</sub>Au-AuPPh<sub>3</sub>]<sup>2+</sup> fragment [2.8291(10) Å], whereas all the Au...Au contacts between adjacent fragments [3.915(1) and 4.792(1) Å] are non-bonding. The eight Au atoms are located at the vertices of a very distorted cube, centered by the Ni<sub>6</sub>C-octahedron. [Ni<sub>6</sub>C(CO)<sub>8</sub>]<sup>6-</sup> possesses 86 cluster valence electrons (CVE), as expected for an octahedral low valent cluster.

The HOMO-LUMO gap, as computed by means of DFT M06 calculations, is very large in accord with the electron precise nature of the cluster. Charge distribution analyses indicate the presence of a partial negative charge on the carbide atom. HOMO is mainly composed by a p-type orbital of the carbide and d-type orbitals of the Ni centre (figure 7.1.8)

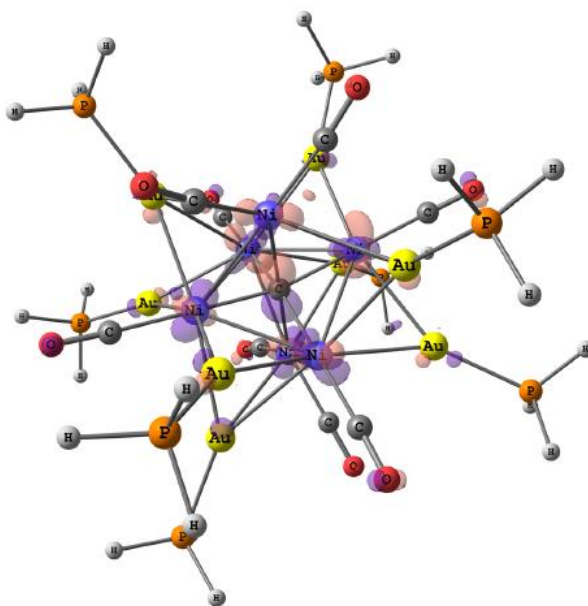


**Figure 7.1.8** HOMO of [Ni<sub>6</sub>(C)(CO)<sub>8</sub>(AuPPh<sub>3</sub>)<sub>8</sub>]<sup>2+</sup> (surface isovalue = 0.055 a.u., M06/LANL2DZ calculations).

### 7.1.5 Synthesis and characterization of [Ni<sub>12</sub>(C<sub>2</sub>)(C)(CO)<sub>17</sub>(AuPPh<sub>3</sub>)<sub>3</sub>]<sup>-</sup>

The [Ni<sub>12</sub>(C<sub>2</sub>)(C)(CO)<sub>17</sub>(AuPPh<sub>3</sub>)<sub>3</sub>]<sup>-</sup> carbide carbonyl cluster was obtained originally on the attempt to optimize the synthesis of Ni<sub>6</sub>C(CO)<sub>8</sub>(AuPPh<sub>3</sub>)<sub>4</sub>. The structure has been fully elucidated by means of X-ray crystallography on its [NEt<sub>4</sub>][Ni<sub>12</sub>(C<sub>2</sub>)(C)(CO)<sub>17</sub>(AuPPh<sub>3</sub>)<sub>3</sub>]<sup>-</sup>·thf salt (figure 7.1.9). On the basis of the structural evidence, the serendipitous synthesis was replaced by another one employing [Ni<sub>9</sub>C(CO)<sub>17</sub>]<sup>2-</sup>, [Ni<sub>10</sub>(C<sub>2</sub>)(CO)<sub>16</sub>]<sup>2-</sup> and Au(PPh<sub>3</sub>)Cl in a 1 : 1 : 3 ratio. The crystals display ν(CO) bands in nujol mull at 2002(s), 1971(sh), 1938(m), 1824(m)

$\text{cm}^{-1}$ , whereas  $\nu(\text{CO})$  stretchings at 2009(s), 1975(m), 1945(sh), 1888(w), 1832(w)  $\text{cm}^{-1}$  are observed in thf solution. Two resonances at  $\delta_{\text{P}}$  49.0 and 48.2 ppm with relative intensities 2 : 1 are present in the  $^{31}\text{P}$  NMR spectrum of  $[\text{Ni}_{12}(\text{C}_2)(\text{C})(\text{CO})_{17}(\text{AuPPh}_3)_3]^-$  recorded in  $\text{d}^8\text{-thf}$ , as expected on the basis of the solid state structure.

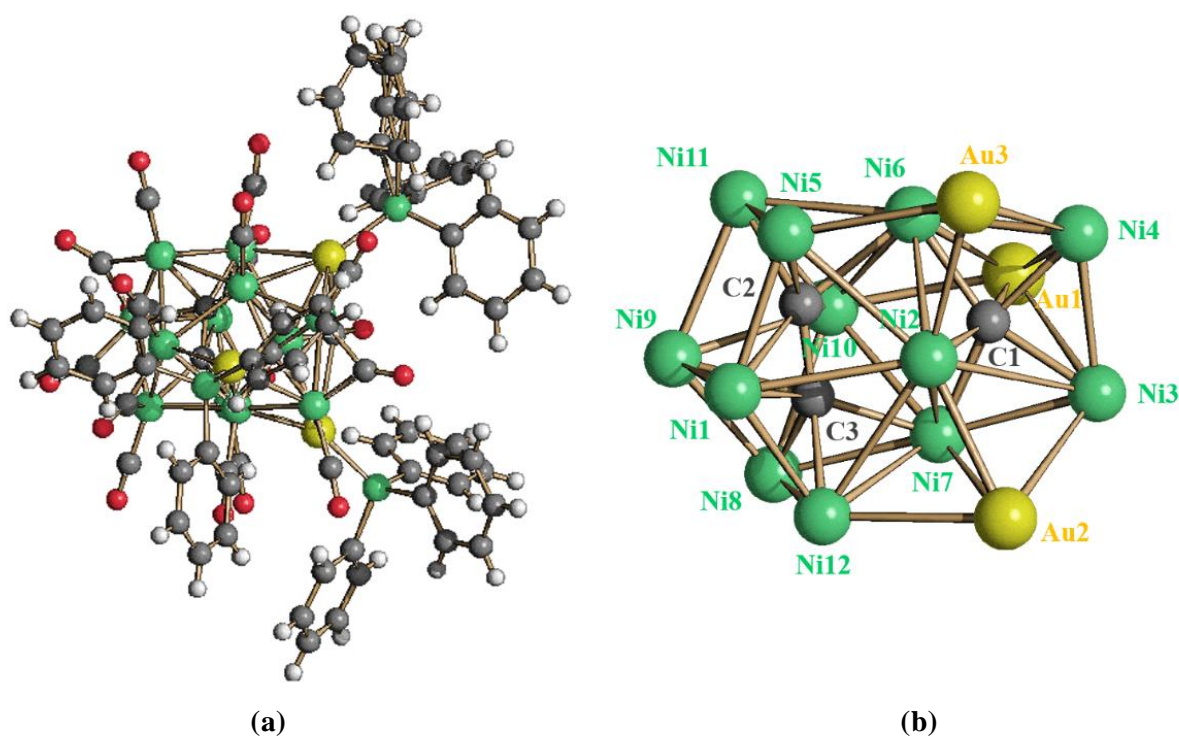


**Figure 7.1.9** (a) Molecular structure of  $[\text{Ni}_{12}(\text{C})(\text{C}_2)(\text{CO})_{17}(\text{AuPPh}_3)_3]^-$  and (b) its  $\text{Ni}_{12}(\text{C})(\text{C}_2)\text{Au}_3$  cage with key atoms labeled (Ni, green; Au, yellow; C, grey; O, red, H, white).

The cluster may be viewed as composed by a  $\text{Ni}_{10}(\text{C}_2)$  mono-acetylide fragment fused with a  $\text{Ni}_5\text{CAu}$  octahedron (figure 7.1.10 and figure 7.1.11), and sharing three Ni-atoms (Ni(2), Ni(6) and Ni(7)) arranged on an open triangle (V-shaped). The metal cage of the cluster is completed by two further Au-atoms capping two  $\text{Ni}_4$ -butterfly surfaces with Ni(2) in common. The structure of the  $\text{Ni}_{10}(\text{C}_2)$  fragment is very similar to the one of the parent  $[\text{Ni}_{10}(\text{C}_2)(\text{CO})_{16}]^{2-}$  cluster (figure 7.1.10), whose metal polyhedron is composed by two  $\mu_4$ -Ni capped trigonal-prisms sharing a common square face. The major difference is the fact that the  $\text{Ni}(10)\cdots\text{Ni}(2)$  contact in  $[\text{Ni}_{12}(\text{C}_2)(\text{C})(\text{CO})_{17}(\text{AuPPh}_3)_3]^-$  [ $3.743(2)\text{\AA}$ ] is considerably elongated and non-bonding in order to accommodate the  $\text{Ni}_5\text{CAu}$  octahedron. Moreover, the interstitial  $\text{C}_2$ -unit forms only 12 Ni-C bonds, whereas 14 were present in  $[\text{Ni}_{10}(\text{C}_2)(\text{CO})_{16}]^{2-}$ . The cluster is completed by 17 CO ligands on the Ni-atoms, 10 terminal and 7 edge bridging, as well as three  $\text{PPh}_3$  ligands, one per each Au. In addition, there are also two weak  $\text{Au}\cdots\text{C}(\text{O})$  contacts [ $2.833(8)$  and  $2.859(8)\text{\AA}$ ].

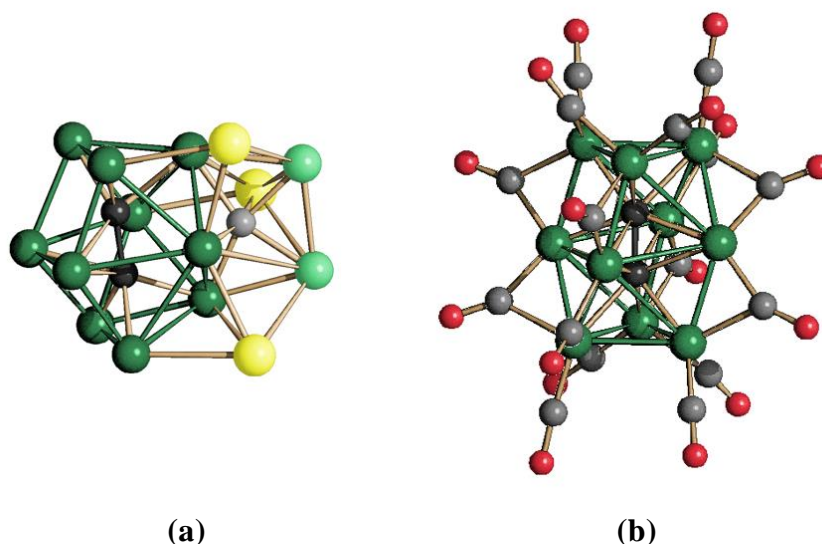


**Figure 7.1.10** (a)  $\text{Ni}_{10}(\text{C}_2)$  (in dark) fragment of  $[\text{Ni}_{12}(\text{C})(\text{C}_2)(\text{CO})_{17}(\text{AuPPh}_3)_3]^-$  compared to (b) the molecular structure of  $[\text{Ni}_{10}\text{C}_2(\text{CO})_{16}]^{2-}$  (Ni, green; Au, yellow; C, grey; O, red, H, white).

The Ni-Ni [2.4110(14)-3.053(3) Å, average 2.626 (7) Å] and Ni-Au [2.5884(10)-2.9185(11) Å, average 2.746(4) Å] contacts are rather spread, in virtue of the interpenetrated and distorted geometry of the cluster, but in keeping with the values reported in the literature for other Ni-carbide and Ni-Au clusters. As expected, the Ni- $\text{C}_{\text{carbide}}$  interactions within the octahedral cage [1.905(7)-1.938(7) Å, average 1.922(16) Å] are considerably shorter than those involving the Ni- $(\text{C}_2)$  acetylide unit [1.953(7)-2.217(7) Å, average 2.09(2) Å]. The mono-carbide atom interacts also with one Au atom [Au(1)-C(1) 2.139(7) Å]. The C(2) and C(3) atoms within the  $\text{C}_2$ -unit are tightly bonded [1.402(10) Å], as previously found in other mono- and poly-acetylide clusters.

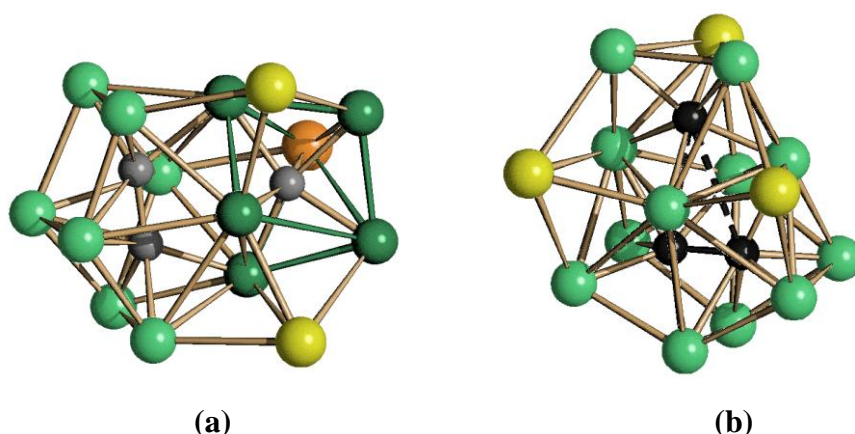


**Figure 7.1.11** Representations of  $[\text{Ni}_{12}(\text{C})(\text{C}_2)(\text{CO})_{17}(\text{AuPPh}_3)_3]^-$  showing (a) its  $\text{Ni}_5\text{CAu}$  octahedral moiety and (b) the weak  $\text{C}\cdots(\text{C}_2)$  sub van der Waals interactions (Ni, green; Au, yellow and orange; C, grey; O, red, H, white).

The most interesting feature of  $[\text{Ni}_{12}(\text{C})(\text{C}_2)(\text{CO})_{17}(\text{AuPPh}_3)_3]^-$  is that it is the first molecular cluster that contains at the same time a mono-carbide atom as well as a tightly bonded

C<sub>2</sub>-unit. These three C-atoms are enclosed within a very large metal cage and no metal atom is interposed between them (figure 7.1.11b). As a result, C(1) and C(2)-C(3) are in close contact [C(1)⋯C(2) 2.781(11) Å; C(1)⋯C(3) 2.798(11) Å]; for comparison the sum of the covalent and van der Waals radii of C are 1.36 and 3.4 Å, respectively. These values are in keeping with those reported in the literature for weak C⋯C interactions, which have been experimentally and theoretically investigated. Such contacts range between 2.7 and 3.4 Å, with calculated interaction energies between -6.0 and -22.8 kJ/mol, resulting from different contributions, *i.e.*, polarization, electrostatic, exchange, charge transfer. From the other side, ultralong covalent C-C bonds up to 1.8 Å have been reported. The C⋯C contacts between the carbide and acetylide units are far longer than these ultralong covalent bonds, but at the lowest limit of the sub van der Waals contacts. This might suggest the incipient formation of more extended C-C bonding within the cavity of the metal cluster.

Further information about the electronic structure of [Ni<sub>12</sub>(C)(C<sub>2</sub>)(CO)<sub>17</sub>(AuPPh<sub>3</sub>)<sub>3</sub>]<sup>-</sup> was obtained by means of DFT calculations. A quite large HOMO-LUMO gap was computed and the HOMO shows the π-bonding interaction between the carbon atoms of the acetylide unit (figure 7.1.12)

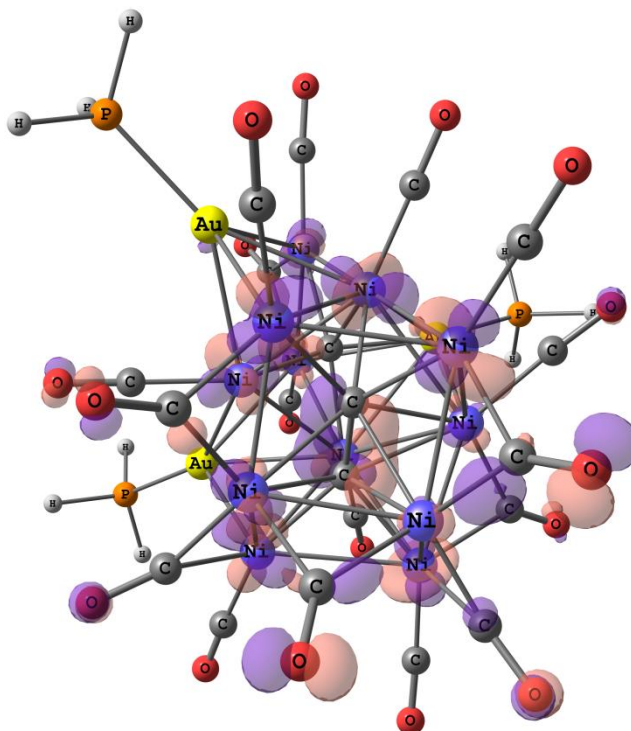


**Figure 7.1.12** HOMO of the model system [Ni<sub>12</sub>(C)(C<sub>2</sub>)(CO)<sub>17</sub>(AuPPh<sub>3</sub>)<sub>3</sub>]<sup>-</sup> (M06/6-31G(d,p)+LANL2TZ(f) calculations, surface isovalue = 0.05 a.u.).

The comparison of the partial charges derived from Mulliken population analyses strongly indicates a partial negative charge on the carbon atoms in the cluster core, in particular

for the carbide unit. Electron density values between the two carbon atoms of the acetylide unit suggest the presence of a partial multiple bond, while a direct covalent interaction between the carbide and acetylide units appears negligible. This last result is confirmed by Mulliken bond orders near zero. On the other hand, the presence of a bond order greater than one in the C<sub>2</sub> fragment is indicated by the computed bond order values. The orbitals of the carbide and acetylide fragments participate simultaneously to the formation of several occupied molecular orbitals, in particular HOMO-75, HOMO-76 and HOMO-77. The interaction between these two groups through the orbitals of the metal centres is however scarce. Therefore, as stated above, the C···C contacts displayed in [Ni<sub>12</sub>(C<sub>2</sub>)(C)(CO)<sub>17</sub>(AuPPh<sub>3</sub>)<sub>3</sub>]<sup>-</sup> between the carbide and acetylide units have no a covalent nature, but are better viewed as sub van der Waals contacts.

## Interstitial Hydride into Tetrahedral Cavity

### 7.2.1 Hydride ligands and the isolobal analogy with $[\text{AuPPh}_3]^+$

Metal hydrides are of fundamental importance in chemistry, both as solid-state materials and molecular compounds. They are key intermediates in various catalytic reactions and have promising applications for hydrogen storage. Moreover, it is known that porous palladium metal is used for purification and isotope separation of hydrogen. In this respect the isolation of  $\text{H}_{12}\text{Pd}_{28}(\text{PtPMe}_3)(\text{PtPPh}_3)_{12}(\text{CO})_{27}$  [38] provides an useful model as it was demonstrated by treating the cluster with  $\text{D}_2$  and following the exchange reaction by NMR spectroscopy which showed that 80% of the hydrogens were replaced by deuterium. Moreover, hydrogen displays a unique chemistry, in view of its small mass, the presence of a single 1s valence orbital, the absence of core and non-bonding valence electron, and an anomalously high electronegativity.

Hydride atoms in molecular clusters may display several coordination modes, since they can be coordinated to the surface of the cluster as terminal, edge or face bridging ligands, as well as located in semi-interstitial or fully interstitial positions. Terminal M-H bonds can be considered as localized two centre/two electron interactions. Conversely, when the hydride interacts with more than one metal atom, a delocalized description is required. A three centre/two electron description accounts for edge-bridging hydride ligands (figure 7.2.1 a) and it is in agreement with the experimental observation that hydride-bridged M-M bonds are slightly elongated (see the case of  $[\text{H}_n\text{Pt}_4(\text{CO})_4(\text{P}^{\wedge}\text{P})_2]^{n+}$  ( $n = 1, 2$ ); chapter 3.2). Indeed, this phenomenon is sometimes employed to locate hydride ligands in X-ray structures from the heavy atom position.<sup>31</sup>

Concerning fully interstitial hydrides in bulky material, four-coordinate hydrogen in tetrahedral sites and six-coordinate hydrogen in octahedral sites are those most commonly observed in intermetallic hydrides. However, for very long-time only molecular clusters containing six-coordinate hydrogen in an octahedral cavity were known (figure 7.2.1 b, c), and

<sup>31</sup> With the increasing of the nuclearity these structural evaluations lose their efficacy and neutron diffraction is the only technique able to unambiguously locate hydrides. In this respect, the hydrides location in the  $[\text{Os}_{10}\text{H}_4(\text{CO})_{24}]^{2-}$  cluster represents an illustrative example. Originally, it was thought that one of the four hydride ligands would be in the central octahedral cavity. However, the neutron diffraction studies showed that all the hydride ligands are on the surface of the cluster, two in  $\mu_3$ - and two in  $\mu_2$ -sites.

it was only in 2008 that the first molecular species containing a 4-coordinate hydrogen in the tetrahedral cavity of  $[(C_5Me_4SiMe_3)YH_2]_4(thf)$  was fully characterized [103]. Some other examples of tetrahedral  $\mu_4-H$  are also known, including  $[\{PhP(CH_2)_3Fe\}_4(\mu_4-H)]^-$  [104], but they are all compounds containing metals in positive oxidation states.

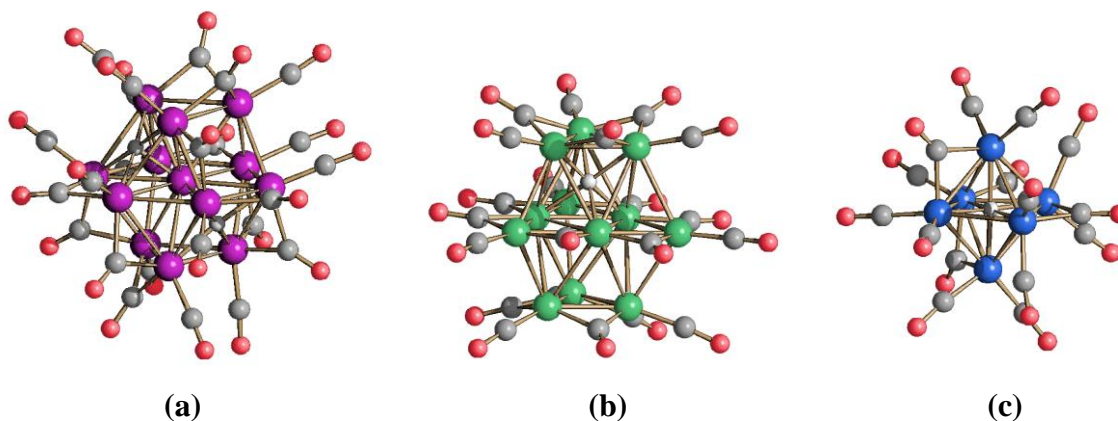


**Figure 7.2.1** Molecular structures of (a)  $[H_2Rh_{13}(CO)_{24}]^{3-}$  [105], (b)  $[HNi_{12}(CO)_{21}]^-$  [106] and (c)  $[HCo_6(CO)_{15}]^-$  [107]. In the case (a) the H atoms are situated in square-pyramidal cavities, almost coplanar with the surface rhodiums, but very slightly displaced towards the central Rh atom. In the  $[HCo_6(CO)_{15}]^-$  cluster (c) the hydride is located in the center of the  $Co_6$  octahedron. Conversely, in the case of  $[HNi_{12}(CO)_{21}]^-$  (b), the hydrogen atom is significantly off-centered (Co, blue; Ni, green; Rh, purple; C, grey; O, red; H, white).

It is known that  $H^+$  is isolobal with the  $[AuPPh_3]^+$  fragment. In the case of species containing a single  $AuPPh_3$  unit, this very often occupies the same site as in the related monohydride. Conversely, in the case of poly-hydrides, usually the replacement of  $H^+$  ions with isolobal  $[AuPPh_3]^+$  fragments results in significant structural changes.

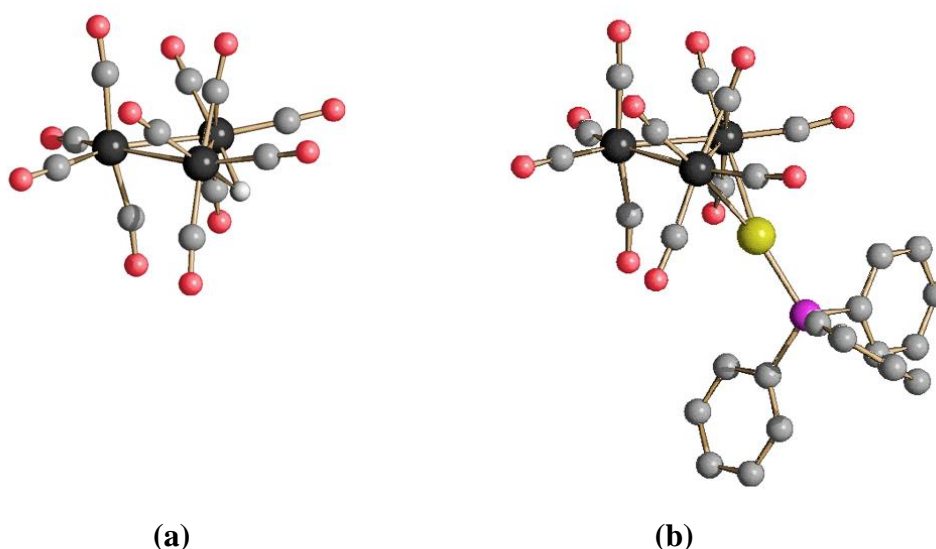


**Figure 7.2.2** The molecular structure of (a)  $[HFe_3(CO)_{11}]^-$  and (b)  $[(PPh_3Au)Fe_3(CO)_{11}]^-$  showing the isolobal relationship between the edge-bridging hydride ligand and  $[AuPPh_3]^+$  unit. Note the hydrogen atoms of the phenyl rings omitted for clarity (Fe, black; Au, gold; P, purple; C, grey; O, red; H, white).

These are mainly due to the fact that Au(I) units tend to give weak aurophilic interactions (see chapter 6.1 and 6.2), whereas hydrides are always isolated.

## 7.2.2 General results

The reaction of  $[\text{HFe}_4(\text{CO})_{12}]^{3-}$  with two equivalents of  $\text{Au}(\text{PPh}_3)\text{Cl}$  results in the new bimetallic Fe-Au hydride cluster  $[\text{HFe}_4(\text{CO})_{12}(\text{AuPPh}_3)_2]^-$  which represents a direct adduct of the two reagents [108]. This is, in turn, transformed into the neutral  $\text{HFe}_4(\text{CO})_{12}(\text{AuPPh}_3)_3$  upon addition of a third  $[\text{AuPPh}_3]^+$  fragment, with concomitant migration of the unique hydride from the surface of the cluster to its tetrahedral cavity (figure 7.2.3).

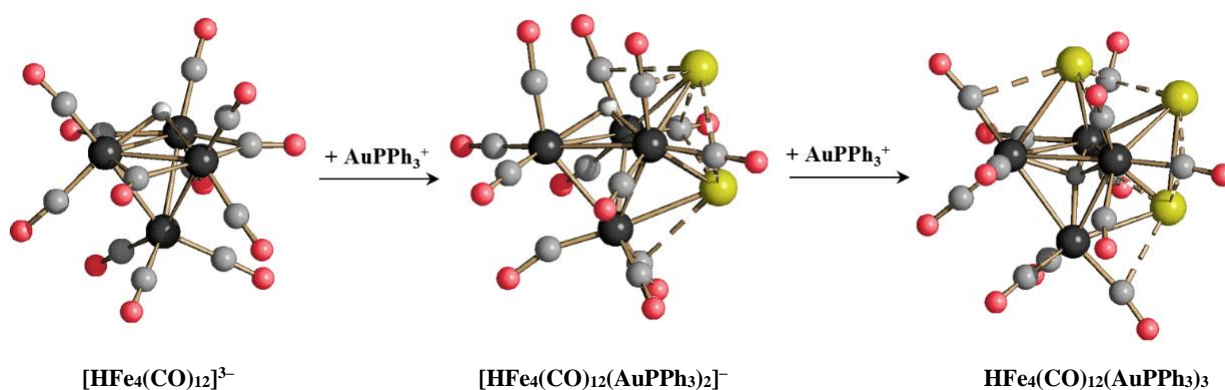


**Figure 7.2.3** Synthesis of new hydride bimetallic Fe-Au clusters (Fe, black; Au, gold; C, grey; O, red; H, white).

## 7.2.3 Synthesis and characterization of $[\text{HFe}_4(\text{CO})_{12}(\text{AuPPh}_3)_2]^-$

The  $[\text{HFe}_4(\text{CO})_{12}(\text{AuPPh}_3)_2]^-$  mono-anion was obtained in moderate yields from the reaction of  $[\text{HFe}_4(\text{CO})_{12}]^{3-}$  with two equivalents of  $\text{Au}(\text{PPh}_3)\text{Cl}$ , according to equation (1):



The new compound has been fully characterized by means of IR,  $^1\text{H}$  and  $^{31}\text{P}\{^1\text{H}\}$  NMR spectroscopies, and ESI-MS.  $^{13}\text{C}\{^1\text{H}\}$  NMR data have been obtained on a  $^{13}\text{CO}$ -enriched sample,  $[\text{HFe}_4(^{13}\text{CO})_{12}(\text{AuPPh}_3)_2]^-$  ( $^{13}\text{CO}$  ca. 30%), prepared from  $[\text{HFe}_4(^{13}\text{CO})_{12}]^{3-}$ . Moreover, its molecular structure has been fully elucidated *via* X-ray crystallography on single crystals of  $[\text{NEt}_4][\text{HFe}_4(\text{CO})_{12}(\text{AuPPh}_3)_2]$ .

### *Molecular structure and theoretical investigation*

The cluster is composed of a tetrahedral  $[\text{HFe}_4(\text{CO})_{12}]^{3-}$  core decorated by two  $[\text{AuPPh}_3]^+$  fragments (figure 7.2.4). The former retains the tetrahedral structure of the parent cluster with a

$\mu_3$ -H hydride. Conversely, the stereochemistry of the CO ligands is changed, in order to permit the coordination of the two  $[\text{AuPPh}_3]^+$  fragments. The hydride ligand has been located in the final Fourier Difference Map and its position is in correspondence with the minimum of the non-bonded potential energy surface of the cluster as located by the program XHYDEX [109]. The hydride atom has been included in the final refinement of the structure. The hydride location has been also confirmed by means of geometry optimizations carried out at DFT level, starting from the experimental X-Ray structure. In particular, EDF2 calculations have been carried out on the  $[\text{HFe}_4(\text{CO})_{12}(\text{AuPPh}_3)_2]^-$  anion, while the hyper-GGA M06 functional has been used for the optimization of the model system  $[\text{HFe}_4(\text{CO})_{12}(\text{AuPH}_3)_2]^-$ . The computed geometries are comparable to the experimental one. Despite a slight underestimation of the Fe-H distances with respect to the X-Ray data, DFT optimizations confirm the position of the hydride as surface  $\mu_3$ -H.

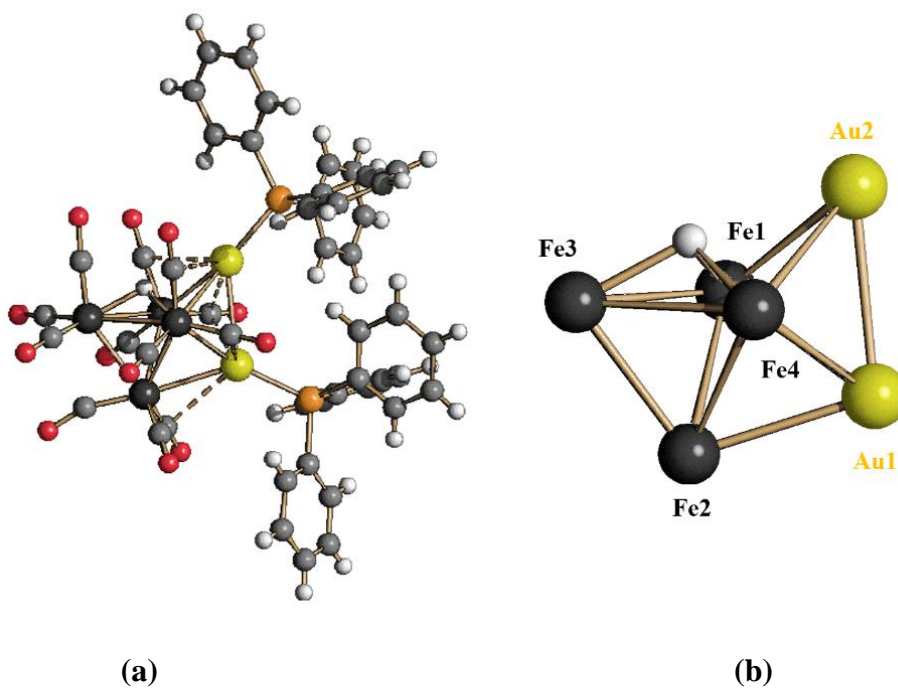


**Figure 7.2.4** Views of (a) molecular structure and (b)  $\text{HFe}_4\text{Au}_2$  hydride-metal core of  $[\text{HFe}_4(\text{CO})_{12}(\text{AuPPh}_3)_2]^-$  (Fe, black; Au, gold; P, orange; C, grey; O, red; H, white).

Au(1) is  $\mu_3$ -coordinated to the Fe(1)-Fe(2)-Fe(4) face of the tetrahedron, adjacent to the face capped by the  $\mu_3$ -H hydride (figure 7.2.4). Au(2) is, then, added to the nearby Au(1)-Fe(1)-Fe(4) face, resulting in a  $\text{Fe}_2\text{Au}_2$  tetrahedron. In this respect, the cluster may be viewed as a  $\text{Fe}_4\text{Au}$  trigonal bipyramid capped by Au(2), or as composed by three face-sharing tetrahedra ( $\text{Fe}_4$ ,  $\text{Fe}_3\text{Au}$  and  $\text{Fe}_2\text{Au}_2$ ). In all cases, it obeys to the inert gas rule, which predicts 60 Cluster Valence Electron (CVE) for a tetrahedron, and 84 CVE for a mono-capped trigonal bipyramid.

The 12 CO ligands bonded to the four Fe atoms of  $[\text{HFe}_4(\text{CO})_{12}(\text{AuPPh}_3)_2]^-$  are all terminals, even if two may be considered as very unsymmetrically edge bridging. By comparison, the parent  $[\text{HFe}_4(\text{CO})_{12}]^{3-}$  presented 9 terminal and 3 edge bridging carbonyls. In addition there are seven weak  $\text{Au}\cdots\text{CO}$  interactions. The cluster contains five Au-Fe contacts and one Au-Au bond [2.9560(9) Å].

### *NMR spectroscopic characterization*

The presence of a hydride ligand is confirmed by a singlet at  $\delta_{\text{H}} -19.5$  ppm in the  $^1\text{H}$  NMR spectrum of  $[\text{HFe}_4(\text{CO})_{12}(\text{AuPPh}_3)_2]^-$  in deuterated acetone. The hydride displays a long longitudinal relaxation time ( $T_1 = 23$  s), as also found in the parent  $[\text{HFe}_4(\text{CO})_{12}]^{3-}$  ( $T_1 = 21$  s). Allowing a long delay between scans (200 s) the expected 30 : 1 ratio between the integrals of the phenyl protons and hydride atom has been measured. Both  $^{31}\text{P}\{^1\text{H}\}$  and  $^{13}\text{C}\{^1\text{H}\}$  (in the carbonyl region) NMR spectra show only one singlet each at all temperatures considered (193–298 K), *i.e.*  $\delta_{\text{P}} 57.3$  ppm and  $\delta_{\text{CO}} 222.4$  ppm (at 298 K), indicating a very rapid exchange of the ligands at all temperatures. As suggested by the structure of the  $\text{HFe}_4(\text{CO})_{12}(\text{AuPPh}_3)_3$  neutral mono-hydride discussed below, this rapid exchange is likely to occur *via* the movement of the hydride from one triangular face to the other of the  $\text{Fe}_4$ -cage passing through its tetrahedral cavity with concomitant rearrangement of the  $[\text{AuPPh}_3]^+$  fragments and CO ligands (figure 7.2.6).

### **7.2.4 Synthesis and characterization of $\text{HFe}_4(\text{CO})_{12}(\text{AuPPh}_3)_3$**

Aiming at preparing a purported  $\text{H}_2\text{Fe}_4(\text{CO})_{12}(\text{AuPPh}_3)_2$  neutral di-hydride, we have investigated the reaction of  $[\text{HFe}_4(\text{CO})_{12}(\text{AuPPh}_3)_2]^-$  with one equivalent of  $\text{H}^+$  in  $\text{CH}_3\text{CN}$ . Unexpectedly, this resulted in the  $\text{HFe}_4(\text{CO})_{12}(\text{AuPPh}_3)_3$  neutral mono-hydride species, which can be recovered in moderate yields after work-up. The use of a deuterated acid such as  $\text{D}_2\text{SO}_4$  results in the same  $\text{HFe}_4(\text{CO})_{12}(\text{AuPPh}_3)_3$  hydride and not in the  $\text{DFe}_4(\text{CO})_{12}(\text{AuPPh}_3)_3$  deuteride. This indicates that the hydride ligand remains bonded to the cluster during the reaction.

It is likely that the acid causes the decomposition of part of the starting cluster with release of some  $[\text{AuPPh}_3]^+$  fragments, which are intercepted by the unreacted  $[\text{HFe}_4(\text{CO})_{12}(\text{AuPPh}_3)_2]^-$  cluster. The resulting  $\text{HFe}_4(\text{CO})_{12}(\text{AuPPh}_3)_3$  species is not soluble in  $\text{CH}_3\text{CN}$  and precipitates out, preventing further decomposition. The same neutral cluster may be also obtained by reacting  $[\text{HFe}_4(\text{CO})_{12}(\text{AuPPh}_3)_2]^-$  with a mild oxidant, such as  $[\text{C}_7\text{H}_7][\text{BF}_4]$  in  $\text{CH}_3\text{CN}$ . Alternatively,  $\text{HFe}_4(\text{CO})_{12}(\text{AuPPh}_3)_3$  is formed after the addition of  $\text{Au}(\text{PPh}_3)(\text{NO}_3)$  to  $[\text{HFe}_4(\text{CO})_{12}(\text{AuPPh}_3)_2]^-$ , further confirming that the origin of the hydride ligand is endogenous.

*Molecular structure and theoretical investigation*

The molecular structure of  $\text{HFe}_4(\text{CO})_{12}(\text{AuPPh}_3)_3$  may be derived from the one of  $[\text{HFe}_4(\text{CO})_{12}(\text{AuPPh}_3)_2]^-$ , after the addition of a third  $[\text{AuPPh}_3]^+$  fragment 8 (figure 7.2.5). This is  $\mu_3$ -coordinated to the Fe(1)-Fe(3)-Fe(4) face, to which the hydride was coordinated in  $[\text{HFe}_4(\text{CO})_{12}(\text{AuPPh}_3)_2]^-$  (figure 7.2.5). As a result, the hydride ligand is forced to move in the centre of the  $\text{Fe}_4$ -tetrahedron. As above, the hydride ligand has been located in the final Fourier Difference Map and its position is in correspondence with the minimum of the non-bonded potential energy surface of the cluster as located by the program XHYDEX [109]. The hydride atom has been included in the final refinement of the structure. As for  $[\text{HFe}_4(\text{CO})_{12}(\text{AuPPh}_3)_2]^-$ , the hydride location has been confirmed by means of DFT calculations on both  $\text{HFe}_4(\text{CO})_{12}(\text{AuPPh}_3)_3$  and  $\text{HFe}_4(\text{CO})_{12}(\text{AuPH}_3)_3$ . The DFT-optimized structures are closely comparable to the experimental one.

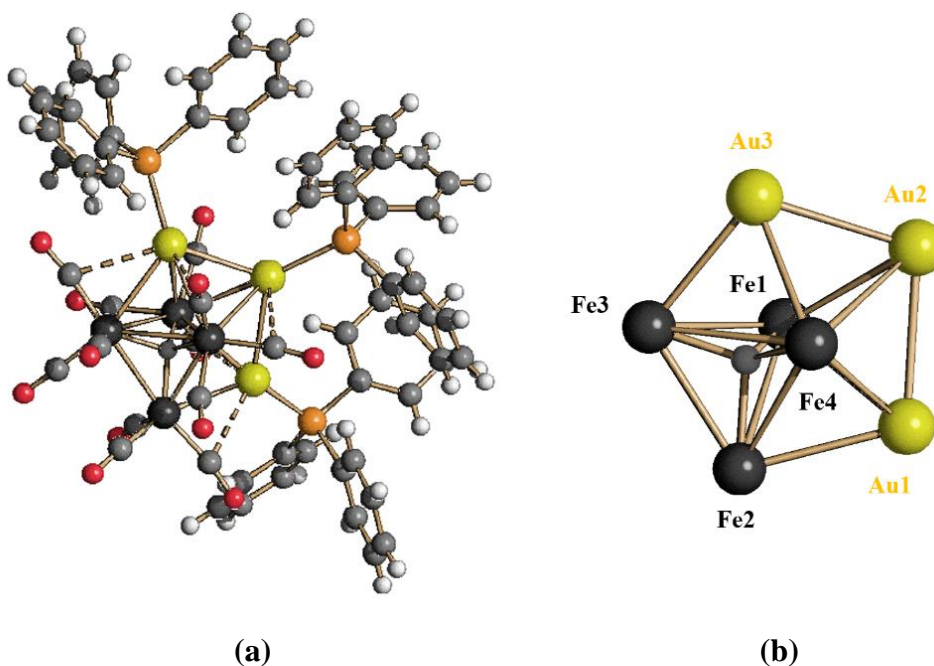


**Figure 7.2.5** Views of (a) molecular structure and (b)  $\text{HFe}_4\text{Au}_3$  hydride-metal core of  $\text{HFe}_4(\text{CO})_{12}(\text{AuPPh}_3)_3$  (Fe, black; Au, gold; P, orange; C, grey; O, red; H, white).

The addition of a third  $[\text{AuPPh}_3]^+$  fragment as well as the presence of an interstitial  $\mu_4\text{-H}$  causes a further swelling of the  $\text{Fe}_4$ -tetrahedron compared to the parent  $[\text{HFe}_4(\text{CO})_{12}(\text{AuPPh}_3)_2]^-$ .  $\text{HFe}_4(\text{CO})_{12}(\text{AuPPh}_3)_3$  displays two Au-Au bonding contacts [ $\text{Au}(1)\text{-Au}(2)$  2.9083(3) Å;  $\text{Au}(2)\text{-Au}(3)$  2.8766(3) Å] as well as eight weak  $\text{Au}\cdots\text{CO}$  interactions. 11 CO ligands are terminal, one edge bridging. The coordination site of Au(3) is dictated by steric effects as well as aurophilic interactions.

If partitioned into a  $[\text{HFe}_4(\text{CO})_{12}]^{3-}$  tetrahedron decorated by three  $[\text{AuPPh}_3]^+$  fragments, the former possesses 60 CVE as expected for a tetrahedral cluster. Alternatively,  $\text{HFe}_4(\text{CO})_{12}(\text{AuPPh}_3)_3$  may be viewed as composed of five tetrahedra ( $\text{Fe}_4$ ,  $\text{Fe}_3\text{Au}$ ,  $\text{Fe}_2\text{Au}_2$ ,  $\text{Fe}_2\text{Au}_2$ ,  $\text{Fe}_3\text{Au}$ ) sharing five triangular faces and resulting in a pentagonal bipyramid. It displays 96 CVE, as previously found in the isostructural  $\text{Ru}_5(\text{CO})_{15}\text{Au}_2(\text{dppm})$ ,  $\text{Ru}_3\text{Ir}(\text{CO})_{12}(\text{AuPPh}_3)_3$ ,  $\text{Os}_5(\text{CO})_{15}\text{Au}_2(\text{dppm})$  and  $\text{Os}_4\text{Ru}(\text{CO})_{12}(\text{C}_6\text{H}_6)\text{Au}_2(\text{dppm})$

### *NMR spectroscopic characterization*

The new  $\text{HFe}_4(\text{CO})_{12}(\text{AuPPh}_3)_3$  cluster has been fully characterized by spectroscopic methods (IR,  $^1\text{H}$ ,  $^{31}\text{P}\{^1\text{H}\}$  and  $^{13}\text{C}\{^1\text{H}\}$  NMR) and its structure crystallographically determined. X-ray crystallographic studies have been performed both at 295 and 100 K, giving almost coincident results. As above, the presence of a hydride ligand is confirmed by a singlet at  $\delta_{\text{H}} -19.1$  ppm in the  $^1\text{H}$  NMR spectrum of  $\text{HFe}_4(\text{CO})_{12}(\text{AuPPh}_3)_3$  in  $\text{CD}_2\text{Cl}_2$ , whereas VT  $^{31}\text{P}\{^1\text{H}\}$  and  $^{13}\text{C}\{^1\text{H}\}$  NMR studies indicate fluxionality in solution which makes the  $\text{PPh}_3$  and CO ligands equivalent at all temperatures [ $\delta_{\text{P}} 56.4$  ppm and  $\delta_{\text{CO}} 218.0$  ppm (at 298 K)].

Dissociation to  $[\text{HFe}_4(\text{CO})_{12}(\text{AuPPh}_3)_2]^-$  and  $[\text{AuPPh}_3]^+$  occurs in solution depending on the polarity of the solvent (figure 7.2.6)

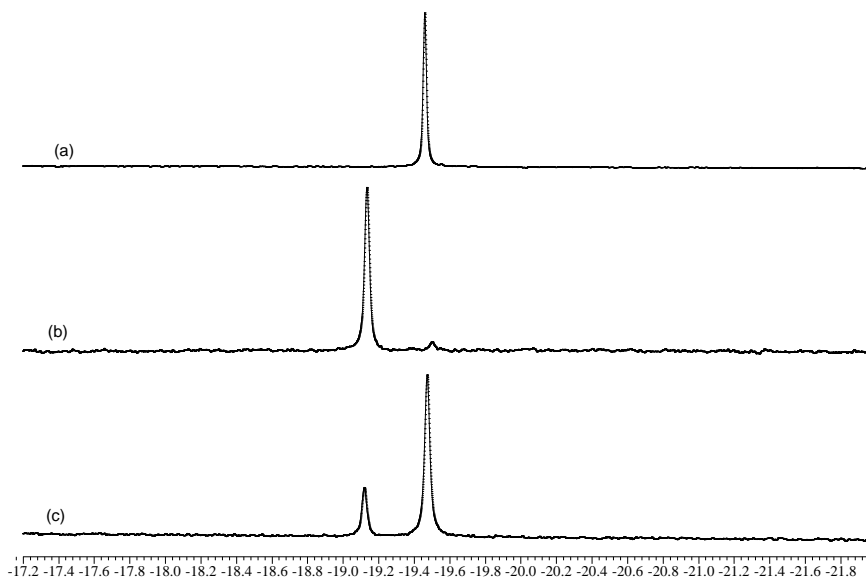


**Figure 7.2.6**  $^1\text{H}$  NMR spectra (298 K) in the hydride region of (a)  $[\text{HFe}_4(\text{CO})_{12}(\text{AuPPh}_3)_2]^-$  in  $\text{d}^6$ -acetone, (b)  $\text{HFe}_4(\text{CO})_{12}(\text{AuPPh}_3)_3$  in  $\text{CD}_2\text{Cl}_2$  and (c)  $\text{HFe}_4(\text{CO})_{12}(\text{AuPPh}_3)_3$  in  $\text{d}^6$ -acetone. Spectrum (c) indicates that  $\text{HFe}_4(\text{CO})_{12}(\text{AuPPh}_3)_3$  is mainly dissociated to give  $[\text{HFe}_4(\text{CO})_{12}(\text{AuPPh}_3)_2]^-$  in  $\text{d}^6$ -acetone. Conversely, dissociation is considerably more limited in  $\text{CD}_2\text{Cl}_2$  as demonstrated by spectrum (b).

Thus,  $[\text{HFe}_4(\text{CO})_{12}(\text{AuPPh}_3)_2]^-$  is the main species in polar solvents such as acetone, whereas  $\text{HFe}_4(\text{CO})_{12}(\text{AuPPh}_3)_3$  is predominant in  $\text{CH}_2\text{Cl}_2$ . A dissociative mechanism may be

invoked in order to explain the fluxionality of this neutral cluster. Also the hydride of  $\text{HFe}_4(\text{CO})_{12}(\text{AuPPh}_3)_3$  shows a rather long longitudinal relaxation time ( $T_1 = 16$  s), and reliable integrals between the phenyl protons and hydride (experimental 47.5 : 1; expected 45 : 1) have been obtained using 200 s delay between scans.

## Final Remarks

The new bimetallic  $\text{Ni}_6\text{C}(\text{CO})_9(\text{AuPPh}_3)_4$  and  $[\text{Ni}_6\text{C}(\text{CO})_8(\text{AuPPh}_3)_8]^{2+}$  compounds represent the first examples of octahedral Ni mono-carbide carbonyl clusters since, due to steric effects, C-atoms are usually lodged into larger cavities in Ni mono-carbide clusters, *i.e.*, trigonal prismatic or square anti-prismatic. This results in heavy distortions of the octahedral geometry, as recently found in the heavy distorted octahedral  $\text{Ni}_6\text{C}(\text{Cp})_6$  cyclopentadienyl mono-carbide cluster. The  $[\text{Ni}_6\text{C}(\text{CO})_9]^{4-}$  core of  $\text{Ni}_6\text{C}(\text{CO})_9(\text{AuPPh}_3)_4$  possesses 86 Cluster Valence Electrons (CVE) as expected for an octahedral cluster. Conversely,  $\text{Ni}_6\text{C}(\text{Cp})_6$  is considerably electron richer and displays 94 CVE. This increase in CVE results in the opening of the octahedral cage of  $\text{Ni}_6\text{C}(\text{Cp})_6$  by breaking two Ni-Ni edges. Conversely, in the case of  $\text{Ni}_6\text{C}(\text{CO})_9(\text{AuPPh}_3)_4$ , even if the  $\text{Ni}_6\text{C}$  octahedron is rather distorted, the 12 Ni-Ni contacts are all at bonding distances, in keeping with its electron count. The structure of  $\text{Ni}_6\text{C}(\text{CO})_9(\text{AuPPh}_3)_4$  has been determined in two different solvates, which mainly differ in the distribution of the four  $\text{Au}\cdots\text{Au}$  contacts. DFT calculations clearly point out that these deformations arise from packing effects due to Van der Waals interactions of the neutral clusters with the co-crystallized solvent molecules. The fact that the Au-atoms are the ones more affected by these weak forces, confirms that  $\text{Au}\cdots\text{Au}$   $d^{10}$ - $d^{10}$  interactions are rather soft and, thus, influenced also by weak forces.

Steric effects as well as aurophilicity seem to play a fundamental role in the stabilization of interstitial atoms in small cages. Similarly, to what is observed in the case of bimetallic Ni-Au carbide clusters, the presence of  $\text{AuPPh}_3$  units plays a key role for the confinement of the hydride in a tetrahedral cage. In this regard,  $\text{HFe}_4(\text{CO})_{12}(\text{AuPPh}_3)_3$  represents the first example of a low valent transition metal cluster containing an interstitial four-coordinate hydrogen in a tetrahedral site. The presence of hydride atoms in the tetrahedral cavities of low valent transition metal clusters and hydride migration on and through their metal cages may help the understanding of the structures of larger clusters and nanoparticles, as well as the mechanism of their interaction with hydrogen.

$[\text{Ni}_{12}(\text{C})(\text{C}_2)(\text{CO})_{17}(\text{AuPPh}_3)_3]^-$  is the first molecular cluster containing at the same time one carbide atom and one tightly bonded  $\text{C}_2$ -unit. Moreover, sub-van der Waals contacts are present between the carbide and acetylide units, suggesting the incipient formation of more

extended C-C bonding. It must be remarked that metal surfaces, metal crystallites and metal nanoparticles are active catalysts in several chemical reactions as well as for the preparation of carbon nanotubes and other nanostructured carbon-based materials (figure 7.3.1). All along these processes, the formation of carbide atoms on the surface or interstices of the metals, their interaction with metal cages and the formation of C-C bonds play a fundamental role. Thus, the study of molecular carbide clusters such as  $[\text{Ni}_{12}(\text{C})(\text{C}_2)(\text{CO})_{17}(\text{AuPPh}_3)_3]^-$  may contribute also to a better understanding of the formation of C-C bonds within a metal cage.

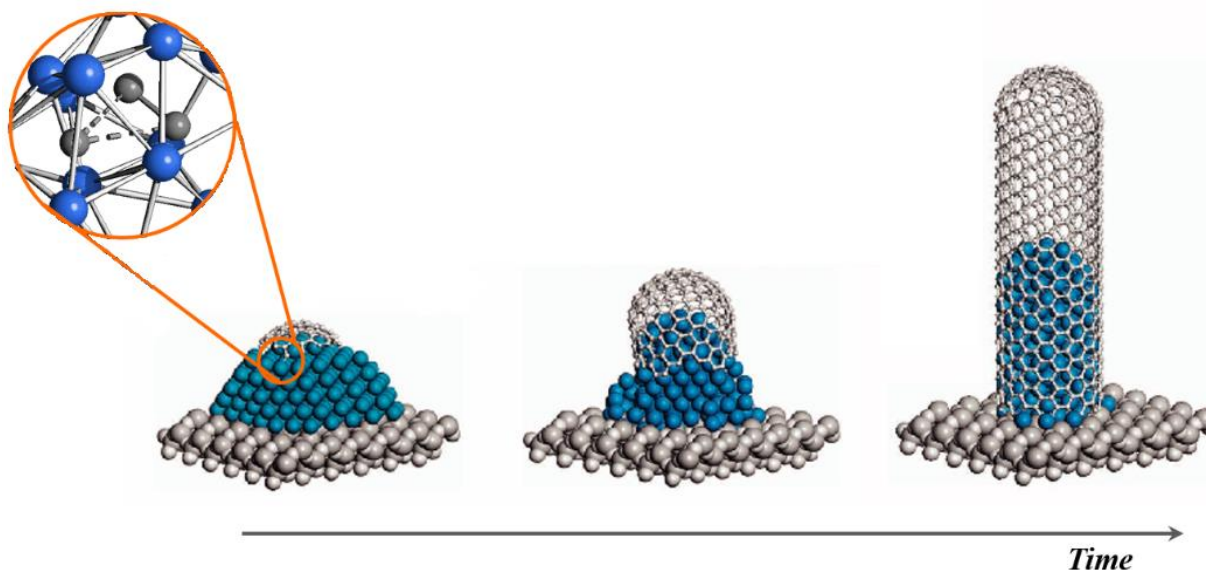


**Figure 7.3.1** Sequence Ni-catalyzed carbon nanotube root growth. In the picture, the incipient formation of the C-C bonds in the carbon nanotube is related to the sub-van der Waals contacts presented in  $[\text{Ni}_{12}(\text{C})(\text{C}_2)(\text{CO})_{17}(\text{AuPPh}_3)_3]^-$ .

In conclusion, three new Ni carbide and two Fe hydride clusters decorated by Au(I)-PPh<sub>3</sub> fragments have been reported. This confirms the ability of anionic carbonyl clusters to act as soft Lewis bases. Moreover, surface decoration of metal clusters with miscellaneous Au(I) fragments seems a rather general phenomenon, as for instance found in the staple motives present in Au-thiolate clusters.

## CHAPTER 8

# Final Remarks

During my Ph.D. period, several new metal carbonyl clusters (MCCs) have been synthesized and characterized. Table 9.1 reports the list of new MCCs ordered on the basis of the chapter where they have been discussed. The list may be divided into three main categories on the basis of their structural properties:

- hydride clusters;
- carbide clusters;
- clusters containing  $\text{Co}_5\text{C}$  units.

### *Hydride Clusters*

In the case of high nuclearity clusters (entries 6-9, 11-17 and 25-27) the hydride nature has been indirectly inferred from joined chemical and electrochemical experiments. Indeed, NMR measurements apparently show the complete absence of any proton resonances in the hydride region. Probably, this is due to the fact that their resonance become so broad to be lost in the baseline of the spectrum, even if at the moment, there is not a satisfactory physical explanation for this phenomenon (see chapter 2.4). In the case of  $[\text{H}_{3-n}\text{Co}_{15}\text{Pd}_9\text{C}_3(\text{CO})_{38}]^{n-}$  ( $n = 0, 1, 2, 3$ ), the most relevant result is represented by the fact that, for the first time, significant rearrangements of the metal cage of a large MCC have been observed as the consequence of the change of one unit of their charges, due to simple and reversible acid-base reactions. Beside every speculation, this further points out that the metal core in ligand-stabilized clusters is rather deformable. The fact that these structural rearrangements are caused by protonation-deprotonation of the clusters seems to suggest that the hydride ligands may have some stereochemical effects. This, in turn, is favoured by the very rigid and stable  $\text{Co}_5\text{C}(\text{CO})_{12}$  fragments which follow the movements and stabilize the inner "soft"  $\text{Pd}_9$  kernels.

Entry	Compound	Chapter
1	$[\text{Pt}_{12}(\text{CO})_{20}(\text{PPh}_3)_2]^{2-}$	3.1
2	$[\text{Pt}_9(\text{CO})_{16}(\text{PPh}_3)_2]^{2-}$	3.1
3	$[\text{Pt}_6(\text{CO})_{10}(\text{PPh}_3)_2]^{2-}$	3.1
4	$[\text{H}_n\text{Pt}_4(\text{CO})_4(\text{P}^\wedge\text{P})_2]^{n+}$ (n = <b>1, 2, 3</b> )	3.2
5	$\text{Pt}_6(\text{CO})_6(\text{dppm})_3$	3.2
6	$[\text{H}_{10-n}\text{Pt}_{26}(\text{CO})_{20}(\text{CdBr})_{12}]^{n-}$ (n = 5, 6, 7, <b>8, 9, 10</b> )	3.3
7	$[\text{H}_4\text{Pt}_{26}(\text{CO})_{20}(\text{CdBr})_{12}(\text{PtBr})_x]^{6-}$ (x = 0-2)	3.3
8	$[\text{H}_{6-n}\text{Ni}_{36}\text{Co}_8\text{C}_8(\text{CO})_{48}]^{n-}$ (n = 3, 4, 5, <b>6</b> )	4.1
9	$[\text{H}_{6-n}\text{Ni}_{22}\text{Co}_6\text{C}_6(\text{CO})_{36}]^{n-}$ (n = 3, <b>4, 5, 6</b> )	4.1
10	$[\text{Ni}_9\text{Co}(\text{C})_2(\text{CO})_{16-x}]^{3-}$ (x = 0.58)	4.1
11	$[\text{H}_{6-n}\text{Ni}_{30}\text{C}_4(\text{CO})_{34}\{\text{Cu}(\text{CH}_3\text{CN})\}_2]^{4-}$ (n = 3, <b>4, 5, 6</b> )	4.2
12	$[\text{H}_2\text{Ni}_{29}\text{C}_4(\text{CO})_{33}\{\text{Cu}(\text{CH}_3\text{CN})\}_2]^{4-}$	4.2
13	$[\text{H}_2\text{Ni}_{30}\text{C}_4(\text{CO})_{33}\{\text{Cu}(\text{CH}_3\text{CN})\}_2]^{2-}$	4.2
14	$[\text{H}_2\text{Ni}_{29}\text{C}_4(\text{CO})_{34}\{\text{Cu}(\text{CH}_3\text{CN})\}_2]^{2-}$	4.2
15	$[\text{H}_2\text{Ni}_{29}\text{C}_4(\text{CO})_{32}(\text{CH}_3\text{CN})_2\{\text{Cu}(\text{CH}_3\text{CN})\}_2]^{2-}$	4.2
16	$[\text{H}_3\text{Ni}_{30}\text{C}_4(\text{CO})_{34}\{\text{Cu}(\text{NCC}_6\text{H}_4\text{CN})\}_2]^{3-}$	4.2
17	$[\text{H}_3\text{Ni}_{29}\text{C}_4(\text{CO})_{33}\{\text{Cu}(\text{NCC}_6\text{H}_4\text{CN})\}_2]^{3-}$	4.2
18	$[\text{Ni}_{12}\text{Au}(\text{CO})_{24}]^{3-}$	5.1
19	$\text{Co}_6\text{C}(\text{CO})_{12}(\text{AuPPh}_3)_4$	5.2
20	$[\{\text{Co}_5\text{C}(\text{CO})_{12}\}\text{Au}\{\text{Co}(\text{CO})_4\}]^-$	5.3
21	$[\{\text{Co}_5\text{C}(\text{CO})_{12}\}_2\text{Au}]^-$	5.3
22	$\text{Co}_5\text{C}(\text{CO})_{12}(\text{AuPPh}_3)$	5.3
23	$[\text{Co}_5\text{C}(\text{CO})_{11}(\text{AuPPh}_3)_2]^-$	5.3
24	$\text{Co}_5\text{C}(\text{CO})_{11}(\text{AuPPh}_3)_3$	5.3
25	$[\text{H}_{6-n}\text{Co}_{20}\text{Pd}_{16}\text{C}_4(\text{CO})_{48}]^{n-}$ (n = 3, <b>4, 5, 6</b> )	6
26	$[\text{H}_{3-n}\text{Co}_{15}\text{Pd}_9\text{C}_3(\text{CO})_{38}]^{n-}$ (n = <b>0, 1, 2, 3</b> )	6
27	$[\text{H}_{6-n}\text{Co}_{16}\text{Pd}_2\text{C}_3(\text{CO})_{28}]^{n-}$ (n = <b>5, 6</b> )	6
28	$\text{Co}_2\text{Pd}_5\text{C}(\text{CO})_8(\text{PPh}_3)_5$	6
29	$\text{Co}_4\text{Pd}_2\text{C}(\text{CO})_{11}(\text{PPh}_3)_2$	6
30	$[\text{Co}_4\text{Pd}_4\text{C}_2(\text{PPh}_3)_4(\text{CO})_{10}\text{Cl}]^-$	6
31	$\text{Ni}_6\text{C}(\text{CO})_9(\text{AuPPh}_3)_4$	7.1
32	$[\text{Ni}_6\text{C}(\text{CO})_8(\text{AuPPh}_3)_8]^{2+}$	7.1
33	$[\text{Ni}_{12}(\text{C}_2)(\text{C})(\text{CO})_{17}(\text{AuPPh}_3)_3]^-$	7.1
34	$[\text{HFe}_4(\text{CO})_{12}(\text{AuPPh}_3)_2]^-$	7.2
35	$\text{HFe}_4(\text{CO})_{12}(\text{AuPPh}_3)_3$	7.2

**Table 9.1** New metal carbonyl clusters (MCCs) synthesized and fully characterized during my work. All the species present as single entries have been structurally characterized. In the case of polyhydride MCCs (multiple entries), n values in bold indicate the species structurally characterized.

In other words, this unprecedented inner core deformation, hardly imaginable in a core-shell architecture, shall be rendered possible by the cluster-in-cluster structure. Indeed, the considerable rearrangement of the Pd<sub>9</sub> kernel leads to a little reorientation of the Co<sub>5</sub>C(CO)<sub>12</sub> fragments resulting in a different stereochemical CO coordination (see chapter 6).

Conversely, the <sup>1</sup>H NMR spectra of lower nuclearity clusters, *i.e.*, [H<sub>n</sub>Pt<sub>4</sub>(CO)<sub>4</sub>(P<sup>^</sup>P)<sub>2</sub>]<sup>n+</sup> (n = 0, 1, 2), [HFe<sub>4</sub>(CO)<sub>12</sub>(AuPPh<sub>3</sub>)<sub>2</sub>]<sup>-</sup> and HFe<sub>4</sub>(CO)<sub>12</sub>(AuPPh<sub>3</sub>)<sub>3</sub>, are diagnostic for the presence of hydride ligands and, in the former case, support the IR evidences in demonstrating the occurrence in solution of protonation-deprotonation equilibria (see chapter 3.2).

HFe<sub>4</sub>(CO)<sub>12</sub>(AuPPh<sub>3</sub>)<sub>3</sub> represents the first example of a low valent transition metal cluster containing an interstitial four-coordinate hydrogen in a tetrahedral site. The hydride migration from the surface, in [HFe<sub>4</sub>(CO)<sub>12</sub>(AuPPh<sub>3</sub>)<sub>2</sub>]<sup>-</sup>, to the tetrahedral cavity, in HFe<sub>4</sub>(CO)<sub>12</sub>(AuPPh<sub>3</sub>)<sub>3</sub> may help the understanding of the structures of larger clusters and nanoparticles, as well as the mechanism of their interaction with hydrogen.

The Pd<sub>9</sub> core rearrangement of [H<sub>3-n</sub>Co<sub>15</sub>Pd<sub>9</sub>C<sub>3</sub>(CO)<sub>38</sub>]<sup>n-</sup> (n = 0-3) and the HFe<sub>4</sub>(CO)<sub>12</sub>(AuPPh<sub>3</sub>)<sub>3</sub> cluster indicate that hydride ligands may play a fundamental role for the stabilization of MCCs.

### Carbide clusters

Table 9.1 is dominated by the presence of interstitial carbide carbonyl clusters (entries 8-17 and 19-33). It is known that the presence of interstitial carbide atoms contributes to an extra-stabilization of the metal cage of the cluster. Indeed, the highest nuclearity homometallic carbonyl cluster of Ni and Co is 12, *i.e.*, [H<sub>n</sub>Ni<sub>12</sub>(CO)<sub>21</sub>]<sup>(4-n)-</sup> (n = 0 - 2) and 6, *i.e.*, [H<sub>n</sub>Co(CO)<sub>15</sub>]<sup>(2-n)-</sup> (n = 0 - 1), respectively. Conversely, the presence of carbides combined to the bimetallic composition have resulted in an increase of nuclearity up to 44 in [Hi<sub>36</sub>Co<sub>8</sub>C<sub>8</sub>(CO)<sub>48</sub>]<sup>6-</sup>.

In the case of bimetallic Ni-Cu tetra-carbide clusters, the nanosize dimensions are primary due to the presence of the carbide atoms rather than the bimetallic composition. [Cu(L)]<sup>+</sup> (L = CH<sub>3</sub>CN, NCC<sub>6</sub>H<sub>4</sub>CN) fragments intercept the growth of the clusters without significant change on the nuclearity. This is confirmed by the fact that the same Ni<sub>30</sub>C<sub>4</sub> metal-carbide kernel present in these new Ni-Cu clusters has been previously found in other clusters, *i.e.*, [HNi<sub>34</sub>C<sub>4</sub>(CO)<sub>38</sub>]<sup>5-</sup> and [H<sub>6-n</sub>Ni<sub>30</sub>C<sub>4</sub>(CO)<sub>34</sub>{CdX}<sub>2</sub>]<sup>n-</sup> (n = 3-6; X = Cl, Br, I). In similar way, [H<sub>6-n</sub>Ni<sub>36</sub>Co<sub>8</sub>C<sub>8</sub>(CO)<sub>48</sub>]<sup>n-</sup> (n = 3, 4, 5, 6) displays a Ni<sub>32</sub>C<sub>6</sub> core isostructural to those observed in [Ni<sub>32</sub>C<sub>6</sub>(CO)<sub>36</sub>]<sup>6-</sup> and [HNi<sub>38</sub>C<sub>6</sub>(CO)<sub>42</sub>]<sup>5-</sup>. However, in the case of [H<sub>6-n</sub>Ni<sub>36</sub>Co<sub>8</sub>C<sub>8</sub>(CO)<sub>48</sub>]<sup>n-</sup> (n = 3, 4, 5, 6), the presence of Co seems to play a key role in order to increase the nuclearity.

Indeed,  $[\text{Hi}_{36}\text{Co}_8\text{C}_8(\text{CO})_{48}]^{6-}$  is composed by an inner  $\text{Ni}_{32}\text{C}_6$  core to which are added two further carbide atoms encapsulated within  $\text{Ni}_5\text{Co}_2\text{C}$  mono-capped trigonal prismatic cages. This may be viewed as a second metal-carbide shell that starts to grow on the inner one, envisioning the possibility of preparing molecular polycarbide clusters containing different metal-carbide shells. Thus,  $\text{Ni}_{30}\text{C}_4$  and  $\text{Ni}_{32}\text{C}_6$  metal cores may be viewed as *starting seeds* for the growth of higher nuclearity clusters.

Concerning low nuclearity clusters, it is noteworthy that  $\text{Ni}_6\text{C}(\text{CO})_9(\text{AuPPh}_3)_4$  and  $[\text{Ni}_6\text{C}(\text{CO})_8(\text{AuPPh}_3)_8]^{2+}$  represent the first examples of octahedral Ni mono-carbide carbonyl clusters since, due to steric effects, C-atoms are usually lodged into larger cavities in Ni mono-carbide clusters, *i.e.*, trigonal prismatic or square anti-prismatic. Steric effects as well as aurophilicity seem to play a fundamental role in the stabilization of interstitial atoms in small cages. Indeed,  $[\text{Ni}_{12}(\text{C})(\text{C}_2)(\text{CO})_{17}(\text{AuPPh}_3)_3]^-$  is the first molecular cluster containing at the same time one carbide atom and one tightly bonded  $\text{C}_2$ -unit. Moreover, sub-van der Waals contacts are present between the carbide and acetylide units, suggesting the incipient formation of more extended C-C bonding. The study of molecular carbide clusters such as  $[\text{Ni}_{12}(\text{C})(\text{C}_2)(\text{CO})_{17}(\text{AuPPh}_3)_3]^-$  may contribute also to a better understanding of the formation of C-C bonds within a metal cage.

#### *Clusters containing $\text{Co}_5\text{C}$ units*

Several clusters containing  $[\text{Co}_5\text{C}(\text{CO})_{12}]^-$  and  $[\text{Co}_5\text{C}(\text{CO})_{11}]^{3-}$  fragments have been synthesized and characterized (table 9.1, entries 20-26). Probably, the no-existence of these  $\text{Co}_5\text{C}$  clusters as free species is due to their lower number of carbonyls that favors nucleophilic substitution. The reaction of  $[\text{Co}_6\text{C}(\text{CO})_{15}]^{2-}$  with  $\text{Au}(\text{PPh}_3)\text{Cl}$  (see chapter 5.3) represents the simplest approach in order to prepare  $[\text{Co}_5\text{C}(\text{CO})_{12}]^-$  and  $[\text{Co}_5\text{C}(\text{CO})_{11}]^{3-}$  clusters stabilized by  $[\text{AuPPh}_3]^+$  fragments. This resulted in the preparation of bimetallic Co-Au clusters, *i.e.*,  $\text{Co}_5\text{C}(\text{CO})_{12}(\text{AuPPh}_3)$ ,  $[\text{Co}_5\text{C}(\text{CO})_{11}(\text{AuPPh}_3)_2]^-$  and  $\text{Co}_5\text{C}(\text{CO})_{11}(\text{AuPPh}_3)_3$  where the  $\text{Co}_5\text{C}$  cores are decorated by  $[\text{AuPPh}_3]^+$  units. From a structural point of view, it is noteworthy to observe that in the case of bimetallic Co-Au clusters, the  $\text{Co}_5\text{C}$  unit is object rather than agent of decoration as found in the case of bimetallic Co-Pd clusters. The  $\text{Co}_5\text{C}$  units represent a useful building block in order to obtain new bimetallic nanoclusters as confirmed by the synthesis of  $[\{\text{Co}_5\text{C}(\text{CO})_{12}\}\text{Au}\{\text{Co}(\text{CO})_4\}]^-$  and  $[\{\text{Co}_5\text{C}(\text{CO})_{12}\}_2\text{Au}]^-$  that represent Au(I) complexes containing one and two  $[\text{Co}_5\text{C}(\text{CO})_{12}]^-$  fragments respectively. The two bimetallic Co-Au clusters show a very rich reversible redox chemistry centred on the coordinated  $[\text{Co}_5\text{C}(\text{CO})_{12}]^-$  fragments. The limited stability of all species apart from the two mono-anions, which hampers

their chemical isolation, is likely to be due to intra-molecular redox reactions, which lead to the formation of Au(0) and fragmentation of the clusters. This, in turn, is an interesting example of inner sphere redox reactions occurring in metal complexes, which may be viewed as the opposite of the redox condensation reactions widely employed for the synthesis of homo- and hetero-metallic carbonyl clusters.

In this thesis, the syntheses and the characterizations of several new bimetallic carbonyl clusters have been outlined. X-ray crystallography is a key technique in order to elucidate their structures which can be related to their chemical and physical properties. In particular, electrochemical studies are very useful in order to understand how the physical properties of metal aggregates change with increasing size and when the molecular behavior fades into bulk behavior. Moreover, the incipient metallization of the cluster has been assessed (not measured) via UV-vis analyses even if this technique revealed to be not very useful in order to distinguish the different species present in solution. Overall, this work demonstrates that molecular nanoclusters are ideal models in order to better understand the structures and properties of ultrasmall metal nanoparticles.

## Scientific Production

1. I. Ciabatti, C. Femoni, M. C. Iapalucci, G. Longoni, S. Zacchini, "Bimetallic Nickel-Cobalt Hexacarbido Carbonyl Clusters  $[H_{6-n}Ni_{22}Co_6C_6(CO)_{36}]^{n-}$  ( $n = 3-6$ ) Possessing Polyhydride Nature and their Base-Induced Degradation to the Monoacetylide  $[Ni_9CoC_2(CO)_{16-x}]^{3-}$  ( $x = 0, 1$ )", *Organometallics* **2012**, *31*, 4593-4600.
2. I. Ciabatti, C. Femoni, M. C. Iapalucci, G. Longoni, S. Zacchini, S. Zarra, "Surface Decorated Platinum Carbonyl Clusters", *Nanoscale* **2012**, *4*, 4166-4177.
3. I. Ciabatti, C. Femoni, M. C. Iapalucci, G. Longoni, S. Zacchini, S. Fedi, F. Fabrizi de Biani, "Synthesis, Structure, and Electrochemistry of the Ni-Au Carbonyl Cluster  $[Ni_{12}Au(CO)_{24}]^{3-}$  and its Relation to  $[Ni_{32}Au_6(CO)_{44}]^{6-}$ ", *Inorg. Chem.* **2012**, *51*, 11753-11761.
4. A. Bernardi, I. Ciabatti, C. Femoni, M. C. Iapalucci, G. Longoni, S. Zacchini, "Ni-Cu tetracarbide carbonyls with vacant Ni(CO) fragments as borderline compounds between molecular and quasi-molecular cluster", *Dalton Trans.* **2013**, *42*, 407-421.
5. I. Ciabatti, C. Femoni, M. C. Iapalucci, G. Longoni, T. Lovato, S. Zacchini, "PPh<sub>3</sub>-Derivatives of  $[Pt_{3n}(CO)_{6n}]^{2-}$  ( $n = 2-6$ ) Chini's Clusters: Syntheses, Structures, and <sup>31</sup>P NMR Studies", *Inorg. Chem.* **2013**, *52*, 4384-4395.
6. I. Ciabatti, C. Femoni, M. C. Iapalucci, G. Longoni, S. Zacchini, F. Fabrizi de Biani, "Selective synthesis of the  $[Ni_{36}Co_8C_8(CO)_{48}]^{6-}$  octa-carbide carbonyl cluster by thermal decomposition of the  $[H_2Ni_{22}Co_6C_6(CO)_{36}]^{4-}$  hexa-carbide", *Dalton Trans.* **2013**, *42*, 9662-9670.
7. I. Ciabatti, C. Femoni, M. C. Iapalucci, A. Ienco, G. Longoni, G. Manca, S. Zacchini, "Intramolecular d<sup>10</sup>-d<sup>10</sup> Interactions in a Ni<sub>6</sub>C(CO)<sub>9</sub>(AuPPh<sub>3</sub>)<sub>4</sub> Bimetallic Nickel-Gold Carbide Carbonyl Cluster", *Inorg. Chem.* **2013**, *52*, 10559-10565.
8. I. Ciabatti, C. Femoni, M. C. Iapalucci, G. Longoni, S. Zacchini, "Tetrahedral  $[H_nPt_4(CO)_4(P^AP)_2]^{n+}$  ( $n = 1, 2$ ; P^A P = CH<sub>2</sub>=C(PPh<sub>2</sub>)<sub>2</sub>) Cationic Mon- and Dihydrido Carbonyl Clusters Obtained by Protonation of the Neutral Pt<sub>4</sub>(CO)<sub>4</sub>(P^A P)<sub>2</sub>", *Organometallics* **2013**, *32*, 5180-5189.

9. I. Ciabatti, C. Femoni, M. C. Iapalucci, G. Longoni, S. Zacchini, "Platinum Carbonyl Clusters Chemistry: Four Decades of Challenging Nanoscience", *J. Cluster Sci.* **2014**, *25*, 115-146.
10. I. Ciabatti, F. Fabrizi de Biani, C. Femoni, M. C. Iapalucci, G. Longoni, S. Zacchini "Metal Segregation in Bimetallic Co-Pd Carbide Carbonyl Clusters: Synthesis, Structure, Reactivity and Electrochemistry of  $[H_{6-n}Co_{20}Pd_{16}C_4(CO)_{48}]^{n-}$  ( $n=3-6$ )", *ChemPlusChem* **2013**, *78*, 1456-1465.
11. I. Ciabatti, C. Femoni, M. C. Iapalucci, G. Longoni, D. Pontiroli, M. Riccò, S. Zacchini, "Structural rearrangements induced by acid-base reactions in metal carbonyl clusters: the case of  $[H_{3-n}Co_{15}Pd_9C_3(CO)_{38}]^{n-}$  ( $n = 0-3$ )", *Dalton Trans.* **2014**, *43*, 4388-4399.
12. I. Ciabatti, C. Femoni, M. Hayatifar, M. C. Iapalucci, G. Longoni, C. Pinzino, S. Zacchini, M. V. Solmi, "The Redox Chemistry of  $[Co_6C(CO)_{15}]^{2-}$ : A Synthetic Route to New Co-Carbide Carbonyl Clusters", *Inorg. Chem.* **2014**, *53*, 3818-3831.
13. M. Bortoluzzi, I. Ciabatti, C. Femoni, M. Hayatifar, M. C. Iapalucci, G. Longoni, S. Zacchini, "Hydride Migration from a Triangular Face to a Tetrahedral Cavity in Tetranuclear Iron Carbonyl Clusters upon Coordination of  $[AuPPh_3]^+$  Fragments", *Angew. Chem. Int. Ed.* **2014**, *53*, 7233-7237.
14. M. Bortoluzzi, I. Ciabatti, C. Femoni, T. Funaioli, M. Hayatifar, M. C. Iapalucci, G. Longoni, S. Zacchini, "Homoleptic and Heteroleptic Au(I) Complexes Containing the new  $[Co_5C(CO)_{12}]^-$  Cluster as Ligand", *Dalton Trans.* **2014**, *43*, 9633-9646.
15. C. Femoni, M. C. Iapalucci, G. Longoni, S. Zacchini, I. Ciabatti, R. G. Della Valle, M. Mazzani, M. Riccò, "The Chemistry of Ni-Sb Carbonyl Clusters Synthesis and Characterization of the  $[Ni_{19}Sb_4(CO)_{26}]^{4-}$  Tetraanion and the Vialogen Salts of  $[Ni_{13}Sb_2(CO)_{24}]^{4-}$  Carbonyl Clusters", *EurJIC* **2014**, *25*, 4151-4158.
16. M. Bortoluzzi, I. Ciabatti, C. Femoni, M. Hayatifar, M. C. Iapalucci, G. Longoni, S. Zacchini, "Peraurated Nickel Carbide Carbonyl Clusters: the Cationic  $[Ni_6(C)(CO)_8(AuPPh_3)_8]^{2+}$  Monocarbide and the  $[Ni_2(C)(C_2)(CO)_{17}(AuPPh_3)_3]^-$  Anion Containing one Carbide and one Acetylide Unit", *Dalton Trans.* **2014**, *43*, 13471-13475.
17. M. Bortoluzzi, I. Ciabatti, C. Femoni, M. Hayatifar, M. C. Iapalucci, G. Longoni, S. Zacchini, "Octahedral Co-carbide Carbonyl Clusters Decorated by  $[AuPPh_3]^+$  Fragments: Synthesis,

- Structural Isomerism and Auophilic Interactions of  $\text{Co}_6\text{C}(\text{CO})_{12}(\text{AuPPh}_3)_4$ ”, *Inorg. Chem.* **2014**, *53*, 9761-9770.
18. M. Bortoluzzi, I. Ciabatti, C. Femoni, M. Hayatifar, M. C. Iapalucci, G. Longoni, S. Zacchini, “[ $\text{H}_{3-n}\text{Fe}_4(\text{CO})_{12}(\text{IrCOD})$ ]<sup>n-</sup> (n = 1, 2) and [ $\text{H}_2\text{Fe}_3(\text{CO})_{10}(\text{IrCOD})$ ]<sup>-</sup> Bimetallic Fe-Ir Hydride Carbonyl Clusters”, *Organometallics* **2015**, *34*, 189-197.
19. I. Ciabatti, “Dalla Scoperta del Nichel Tetracarbonile alla Sintesi di Nanocondensatori Molecolari ad Elevata Nuclearità”, *Rendiconti Accademia Nazionale delle Scienze detta dei XL, Memorie di Scienze Chimiche Naturali* **2014**, 45–57.
20. I. Ciabatti, C. Femoni, M. Hayatifar, M. C. Iapalucci, G. Longoni, “ $\text{Co}_5\text{C}$  and  $\text{Co}_4\text{C}$  Carbido Carbonyl Clusters Stabilized by [ $\text{AuPPh}_3$ ]<sup>+</sup> Fragments”, *Inorg. Chim. Acta* **2015**, *418*, 203-211.

## CHAPTER 9

# Experimental Section

All reactions and sample manipulations were carried out using standard Schlenk techniques under nitrogen and in dried solvents. The “difficulty levels” for the synthesis, manipulation and crystallization of each product as reported in its procedure are indicated with a number between 1 and 3. In the case of the synthesis, the effort in order to carry out the reaction is classified as follow:



- 1** The reaction leads always to the same product. No specific skill is needed.
- 2** The reaction is quite difficult to reproduce. Experience on similar reactions is recommended.
- 3** The reaction is difficult to reproduce and/or special care must be taken.

Manipulation is referred to the stability in solution of the cluster:



- 1** Very stable. It is limitedly affected by the presence of oxygen. The solvent of the solution can be removed *in vacuo* and the solid dissolved for many times without any significant degradation.
- 2** Fairly stable.
- 3** Instable. Very sensible to oxygen and readily degradable with any treatment (*e.g.*, solvent removed *in vacuo*)

Finally, the probability to obtain single crystals suitable for X-ray crystallography is classified as follow:



- 1 Crystals of good quality can be obtained under several conditions (*i.e.*, solvent and counteraction).
- 2 Crystals can be obtained in limited conditions. Some attempts are required.
- 3 Crystals are hardly obtained. Several attempts are required.

All the reagents were commercial products (Aldrich) of the highest purity available and used as received, except the following compounds which have been prepared according to the literature (table 9.1).

Compound	Ref.
$[\text{AR}_3]_2[\text{Pt}_{3n}(\text{CO})_{6n}]$ ( $n = 2-6$ )	[44]
$[\text{AR}_3]_2[\text{Ni}_9\text{C}(\text{CO})_{17}]$	[110]
$[\text{AR}_3]_2[\text{Ni}_{10}(\text{C})_2(\text{CO})_{16}]$	[111]
$[\text{AR}_3]_2[\text{Ni}_6(\text{CO})_{12}]$	[112]
$[\text{AR}_3]_2[\text{Co}_6\text{C}(\text{CO})_{15}]$	[100]
$\text{Co}_3(\text{C})_2(\text{CO})_9$	[113]
$[\text{AR}_3]_3[\text{HFe}_4(\text{CO})_{12}]$	[115]

**Table 9.1** Clusters prepared according to literature methods. A = N or P; R = Me, Et, Bu, Ph and  $\text{CH}_2\text{Ph}$ .

IR spectra were recorded on a Perkin Elmer SpectrumOne interferometer in  $\text{CaF}_2$  cells with 0.1 mm thickness.

$^1\text{H}$ ,  $^{13}\text{C}\{^1\text{H}\}$  and  $^{31}\text{P}\{^1\text{H}\}$  NMR measurements were performed on a Varian Mercury Plus 400 MHz instrument. The proton and carbon chemical shifts were referenced to the non deuterated aliquot of the solvent, whereas the phosphorous chemical shifts were referenced to external  $\text{H}_3\text{PO}_4$  (85% in  $\text{D}_2\text{O}$ ).

ESI mass spectra were recorded on a Waters Micromass ZQ4000/ZMD instrument and in all cases the solvent is acetonitrile. Analyses of C, H and N were obtained with a ThermoQuest FlashEA 1112NC instrument.

Cyclic voltammetry was performed in a three-electrode cell containing a platinum or gold working electrode surrounded by a platinum-spiral counter electrode, and an aqueous saturated calomel reference electrode (SCE) mounted with a Luggin capillary. All the potential values are referred to the saturated calomel electrode (SCE).  $[\text{NBu}_4][\text{BF}_4]$  0.1 M was used as supporting

electrolyte. Part of the electrochemical studies have been carried out by Tiziana Funaioli (Università di Pisa) and Fabrizia Fabrizi de Biani (Università di Siena).

Analysis of Ni and Co (chapter 4) were performed by atomic absorption on a Pye-Unicam instrument. The content of Ni and Co on single crystals was determined using an EVO 50 EP (ZEISS) Scanning Electron Microscope (SEM) with an OXFORD INCA 350 EDS.

The diffraction experiments were carried out on a Bruker APEX II diffractometer equipped with a CCD detector using Mo-K $\alpha$  radiation. Data were corrected for Lorentz polarization and absorption effects (empirical absorption correction SADABS) [115]. Structures were solved by direct methods and refined by full-matrix least-squares based on all data using  $F^2$  [116]. Hydrogen atoms were fixed at calculated positions and refined by a riding model. All non-hydrogen atoms were refined with anisotropic displacement parameters. Structure drawings have been performed with SCHAKAL99 [117].

Extended Hückel Molecular Orbital (EHMO) analyses have been performed using the program CACAO with crystallographic coordinates. Theoretical DFT calculations have been carried out by Marco Bortoluzzi (Università di Venezia), Andrea Ienco and Gabriele Manca (Università di Firenze).

## Homometallic and bimetallic Pt clusters (chapter 3)

### Synthesis of $[\text{NEt}_4]_2[\text{Pt}_{12}(\text{CO})_{20}(\text{PPh}_3)_2]$



Solid  $\text{PPh}_3$  (0.205 g, 0.782 mmol) was added in small portions to an acetone (20 mL) solution of  $[\text{NEt}_4]_2[\text{Pt}_{12}(\text{CO})_{24}]$  (1.28 g, 0.391 mmol).

The solution was stirred at room temperature under nitrogen for 30 minutes. Then, the solvent was removed *in vacuo*, the solid washed with water (40 mL) and toluene (40 mL) and extracted in acetone (20 mL). Crystals of  $[\text{NEt}_4]_2[\text{Pt}_{12}(\text{CO})_{22}(\text{PPh}_3)_2]$  suitable for X-ray analyses were obtained by slow diffusion of n-hexane (40 mL). The crystals of  $[\text{NEt}_4]_2[\text{Pt}_{12}(\text{CO})_{22}(\text{PPh}_3)_2]$  were obtained in mixture with an

amorphous powder containing  $[\text{Pt}_9(\text{CO})_{16}(\text{PPh}_3)_2]^{2-}$  and  $[\text{Pt}_9(\text{CO})_{17}(\text{PPh}_3)]^{2-}$  in a 1.5 : 1 : 1.1 ratio, as determined by  $^{31}\text{P}\{^1\text{H}\}$  NMR. Therefore, it has not been possible to calculate the yield.

IR (acetone, 293 K)  $\nu(\text{CO})$ : 2036(vs), 1848(m)  $\text{cm}^{-1}$ . IR (nujol mull, 293 K)  $\nu(\text{CO})$ : 2032(s), 2002(w), 1825(s), 1780(s)  $\text{cm}^{-1}$ .  $^{31}\text{P}\{^1\text{H}\}$  NMR ( $\text{CD}_3\text{COCD}_3$ , 298 K):  $\delta_{\text{P}}$  50.6 ppm,  $^1\text{J}_{\text{Pt-P}}$  5102 Hz,  $^2\text{J}_{\text{Pt-P}}$  551 Hz.

### Synthesis of $[\text{NBu}_4]_2[\text{Pt}_9(\text{CO})_{16}(\text{PPh}_3)_2]$

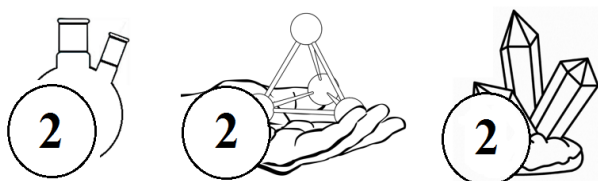


Solid  $\text{PPh}_3$  (0.217 g, 0.830 mmol) was added in small portions to an acetone (20 mL) solution of  $[\text{NBu}_4]_2[\text{Pt}_9(\text{CO})_{18}]$  (1.14 g, 0.415 mmol). The solution was stirred at room

temperature under nitrogen for 30 minutes. Then, the solvent was removed *in vacuo*, the solid washed with water (40 mL) and toluene (40 mL) and extracted in acetone (20 mL). Crystals of  $[\text{NBu}_4]_2[\text{Pt}_9(\text{CO})_{16}(\text{PPh}_3)_2]$  suitable for X-ray analyses were obtained by slow diffusion of n-hexane (40 mL) (yield 0.60 g, 45% based on Pt).

$\text{C}_{84}\text{H}_{102}\text{N}_2\text{O}_{16}\text{P}_2\text{Pt}_9$  (3213.43): calcd. C 31.39, H 3.20, N 0.87, Pt 54.64; found: C 31.52, H 3.02, N 0.71, Pt 54.89. IR (thf, 293 K)  $\nu(\text{CO})$ : 2017(s), 1828(m)  $\text{cm}^{-1}$ . IR (acetone, 293 K)  $\nu(\text{CO})$ : 2015(vs), 1823(m)  $\text{cm}^{-1}$ . IR ( $\text{CH}_3\text{CN}$ , 293 K)  $\nu(\text{CO})$ : 2018(vs), 1820(m)  $\text{cm}^{-1}$ . IR (dmf, 293 K)  $\nu(\text{CO})$ : 2014(vs), 1822(m)  $\text{cm}^{-1}$ . IR (nujol mull, 293 K)  $\nu(\text{CO})$ : 2021(vs), 2007(s), 1988(m), 1814(vs), 1769(m)  $\text{cm}^{-1}$ .  $^{31}\text{P}\{^1\text{H}\}$  NMR ( $\text{CD}_3\text{COCD}_3$ , 298 K):  $\delta_{\text{P}}$  54.3 ppm,  $^1\text{J}_{\text{Pt-P}}$  5144 Hz,  $^2\text{J}_{\text{Pt-P}}$  556 Hz.

### Synthesis of $[\text{NBu}_4]_2[\text{Pt}_6(\text{CO})_{10}(\text{PPh}_3)_2]$ and $[\text{NBu}_4]_2[\text{Pt}_6(\text{CO})_{10}(\text{PPh}_3)_2] \cdot 2\text{thf}$



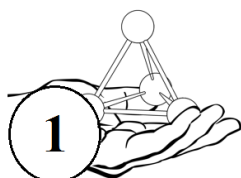
Solid  $\text{PPh}_3$  (1.50 g, 5.72 mmol) was added in small portions to an acetone (20 mL) solution of  $[\text{NBu}_4]_2[\text{Pt}_6(\text{CO})_{12}]$  (1.14 g, 0.572 mmol). The solution was stirred at room temperature

under nitrogen for 30 minutes. Then, the solvent was removed *in vacuo*, the solid washed with water (40 mL) and toluene (40 mL) and extracted in acetone (20 mL). Crystals of  $[\text{NBu}_4]_2[\text{Pt}_6(\text{CO})_{10}(\text{PPh}_3)_2]$  suitable for X-ray analyses were obtained by slow diffusion of n-hexane (40 mL). Indeed, crystals of  $[\text{NBu}_4]_2[\text{Pt}_6(\text{CO})_{10}(\text{PPh}_3)_2] \cdot 2\text{thf}$  can be obtained by slow diffusion of n-hexane (40 mL) on a thf solution. Only a few crystals of  $[\text{NBu}_4]_2[\text{Pt}_6(\text{CO})_{10}(\text{PPh}_3)_2]$  and  $[\text{NBu}_4]_2[\text{Pt}_6(\text{CO})_{10}(\text{PPh}_3)_2] \cdot 2\text{thf}$  were obtained, whereas the majority of the solid was

composed of amorphous  $[\text{Pt}_6(\text{CO})_{12}]^{2-}$  with traces of  $[\text{Pt}_9(\text{CO})_{16}(\text{PPh}_3)_2]^{2-}$ ,  $[\text{Pt}_9(\text{CO})_{15}(\text{PPh}_3)_3]^{2-}$  and  $[\text{Pt}_6(\text{CO})_{11}(\text{PPh}_3)]^{2-}$ . Therefore, it has not been possible to calculate the yield.

IR (nujol mull, 293 K)  $\nu(\text{CO})$ : 1973(s), 1960(vs), 1794(m), 1756(vs)  $\text{cm}^{-1}$ .  $^{31}\text{P}\{^1\text{H}\}$  NMR ( $\text{CD}_3\text{COCD}_3$ , 298 K):  $\delta_{\text{P}}$  56.5 ppm,  $^1\text{J}_{\text{Pt-P}}$  5301 Hz,  $^2\text{J}_{\text{Pt-P}}$  566 Hz.

### Synthesis of $\text{Pt}_4(\text{CO})_4(\text{P}^{\wedge}\text{P})_2$ ( $\text{P}^{\wedge}\text{P} = \text{CH}_2=\text{C}(\text{PPh}_2)_2$ )

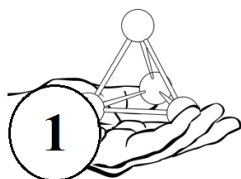


$\text{P}^{\wedge}\text{P}$  (0.095 g, 0.240 mmol) was added as a solid to a solution of  $[\text{NBu}_4]_2[\text{Pt}_{12}(\text{CO})_{24}]$  (0.70 g, 0.200 mmol) in acetone (20 mL) and the mixture stirred at room

temperature for 2 days. At this point, an orange precipitate of  $\text{Pt}_4(\text{CO})_4(\text{P}^{\wedge}\text{P})_2$  started to form and the precipitation was completed by addition of dmf (20 mL). The solid was recovered by filtration, washed with  $\text{CH}_3\text{CN}$  ( $2 \times 20$  mL) and dried under *vacuum* (yields 0.18 g, 18% based on Pt). Crystals of  $\text{Pt}_4(\text{CO})_4(\text{P}^{\wedge}\text{P})_2$  suitable for X-ray analyses have been obtained directly from the acetone solution by slow diffusion of n-hexane (40 mL).

$\text{C}_{56}\text{H}_{44}\text{O}_4\text{P}_4\text{Pt}_4$  (1685.15): calcd. C 39.91, H 2.63, Pt 46.31; found: C 39.74, H 2.89, Pt 46.05. IR (nujol, 293 K)  $\nu(\text{CO})$ : 1979(s), 1954(m)  $\text{cm}^{-1}$ . IR ( $\text{CH}_2\text{Cl}_2$ , 293 K)  $\nu(\text{CO})$ : 1979(s), 1954(m)  $\text{cm}^{-1}$ .  $^1\text{H}$  NMR ( $\text{CD}_2\text{Cl}_2$ , 298 K)  $\delta$  (ppm): 7.1-7.8 (m, 40H, Ph), 5.56 (m, 4H, =CH<sub>2</sub>).  $^{31}\text{P}\{^1\text{H}\}$  NMR ( $\text{CD}_2\text{Cl}_2$ , 298 K)  $\delta$  (ppm): 28.1 (m,  $^1\text{J}_{\text{PtP}} = 2406$  Hz;  $^2\text{J}_{\text{PtP}} = 696, 570$  and 104 Hz;  $\text{J}_{\text{PP}} = 25$  and 60 Hz).

### Synthesis of $[\text{HPt}_4(\text{CO})_4(\text{P}^{\wedge}\text{P})_2][\text{BF}_4] \cdot x\text{CH}_2\text{Cl}_2$ ( $x = 1.47$ ) ( $\text{P}^{\wedge}\text{P} = \text{CH}_2=\text{C}(\text{PPh}_2)_2$ )



$\text{HBF}_4 \cdot \text{Et}_2\text{O}$  (0.029 g, 0.179 mmol) was added to a solution of  $\text{Pt}_4(\text{CO})_4(\text{P}^{\wedge}\text{P})_2$  (0.256 g, 0.152 mmol) in  $\text{CH}_2\text{Cl}_2$  (20 mL) and the mixture stirred at room

temperature for 2 hours. Then, the solution was filtered and the filtrate layered with n-hexane (40 mL) resulting in orange crystals of  $[\text{HPt}_4(\text{CO})_4(\text{P}^{\wedge}\text{P})_2][\text{BF}_4] \cdot x\text{CH}_2\text{Cl}_2$  ( $x = 1.47$ ) suitable for X-ray crystallography (yields 0.257 g, 89% based on Pt). It must be remarked that sometimes, a few crystals of  $[\text{HPt}_4(\text{CO})_4(\text{P}^{\wedge}\text{P})_2][\text{B}_2\text{F}_7]$  have been obtained as side-product due to the accidental formation of  $[\text{B}_2\text{F}_7]^-$ .

$\text{C}_{57.47}\text{H}_{47.93}\text{BCl}_{2.93}\text{F}_4\text{O}_4\text{P}_4\text{Pt}_4$  (1897.39): calcd. C 36.38, H 2.55, Pt 41.12; found: C 36.65, H 2.19, Pt 41.46. IR (nujol, 293 K)  $\nu(\text{CO})$ : 2049(w), 2044(w), 2020(s), 2009(w)  $\text{cm}^{-1}$ . IR ( $\text{CH}_2\text{Cl}_2$ , 293

K)  $\nu(\text{CO})$ : 2057(w), 2043(w), 2030(s), 2008(w)  $\text{cm}^{-1}$ .  $^1\text{H}$  NMR ( $\text{CD}_2\text{Cl}_2$ , 298 K)  $\delta$  (ppm): 7.0-8.0 (m, 40H, Ph), 6.00 (m, 4H, =CH<sub>2</sub>), -2.40 (m, 1H,  $^{\text{av}}J_{\text{PtH}} = 286$  Hz,  $^{\text{av}}J_{\text{PH}} = 37$  Hz,  $\mu\text{-H}$ ).  $^{31}\text{P}\{^1\text{H}\}$  NMR ( $\text{CD}_2\text{Cl}_2$ , 298 K)  $\delta$  (ppm): 16.8 (m,  $^1J_{\text{PtP}} = 3010$  Hz).  $^{31}\text{P}\{^1\text{H}\}$  NMR ( $\text{CD}_2\text{Cl}_2$ , 173 K)  $\delta$  (ppm): 6.4 (br), 23.4 (br).

### Synthesis of $[\text{H}_2\text{Pt}_4(\text{CO})_4(\text{P}^{\wedge}\text{P})_2][(\text{BF}_4)_2\text{H}]_2$ ( $\text{P}^{\wedge}\text{P} = \text{CH}_2=\text{C}(\text{PPh}_2)_2$ )



$\text{HBF}_4 \cdot \text{Et}_2\text{O}$  (0.105 g, 0.651 mmol) was added to a solution of  $\text{Pt}_4(\text{CO})_4(\text{P}^{\wedge}\text{P})_2$  (0.256 g, 0.152 mmol) in  $\text{CH}_2\text{Cl}_2$  (20 mL) and the mixture stirred at

room temperature for 2 hours. Then, the solution was filtered and the filtrate layered with n-hexane (40 mL) resulting in orange crystals of  $[\text{H}_2\text{Pt}_4(\text{CO})_4(\text{P}^{\wedge}\text{P})_2][(\text{BF}_4)_2\text{H}]_2$  suitable for X-ray crystallography (yields 0.282 g, 91% based on Pt).

$\text{C}_{56}\text{H}_{48}\text{B}_4\text{F}_{16}\text{O}_4\text{P}_4\text{Pt}_4$  (2036.42): calcd. C 33.03, H 2.38, Pt 38.32; found: C 32.89, H 2.26, Pt 38.48. IR (nujol, 293 K)  $\nu(\text{CO})$ : 2080(sh), 2077(s)  $\text{cm}^{-1}$ . IR ( $\text{CH}_2\text{Cl}_2$ , 293 K)  $\nu(\text{CO})$ : 2083(s)  $\text{cm}^{-1}$ .  $^1\text{H}$  NMR ( $\text{CD}_2\text{Cl}_2$ , 298 K)  $\delta$  (ppm): 9.52 (br, 2H  $[(\text{BF}_4)_2\text{H}]^-$ ), 7.1-8.1 ppm (m, 40H, Ph), 6.36 ppm (m, 4H, =CH<sub>2</sub>), -4.00 ppm (m, 2H,  $^1J_{\text{PtH}} = 579$  Hz,  $^2J_{\text{PtH}} = 128$  Hz,  $^2J_{\text{PH}} = 64$  Hz,  $^3J_{\text{PH}} = 11$  Hz,  $\mu\text{-H}$ ).  $^{31}\text{P}\{^1\text{H}\}$  NMR ( $\text{CD}_2\text{Cl}_2$ , 298 K)  $\delta$  (ppm): 4.6 (m,  $^1J_{\text{PtP}} = 3178$  Hz).

### Synthesis of $\text{Pt}_6(\text{CO})_6(\text{dppm})_3$ ( $\text{dppm} = \text{Ph}_2\text{PCH}_2\text{PPh}_2$ )

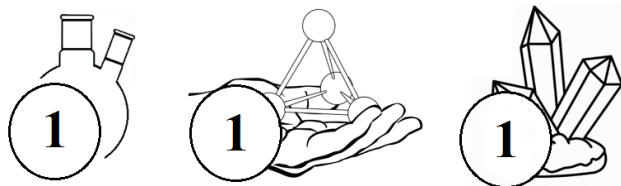


dppm (0.177 g, 0.460mmol) was added to a solution of  $[\text{NBu}_4][\text{Pt}_{12}(\text{CO})_{24}]$  (0.70 g, 0.200 mmol) in acetone (20 mL) and the mixture stirred at room temperature for 2

hours. At this point, an orange precipitate of  $\text{Pt}_6(\text{CO})_6(\text{dppm})_3$  started to form and the precipitation was completed by addition of dmf (20 mL). The solid was recovered by filtration, washed with  $\text{CH}_3\text{CN}$  ( $2 \times 20$  mL) and dried under *vacuum* (yields 0.20 g, 20% based on Pt). Crystals of  $\text{Pt}_6(\text{CO})_6(\text{dppm})_3$  suitable for X-ray analyses have been obtained directly from the acetone solution by slow diffusion of n-hexane (40 mL).

$\text{C}_{81}\text{H}_{66}\text{O}_6\text{P}_6\text{Pt}_6$  (2491.70): calcd. C 39.04, H 2.67, Pt 46.97; found: C 39.51, H 2.97, Pt 47.11. IR (nujol, 293 K)  $\nu(\text{CO})$ : 1832(m), 1787(s), 1775(m), 1763(m)  $\text{cm}^{-1}$ . IR ( $\text{CH}_2\text{Cl}_2$ , 293 K)  $\nu(\text{CO})$ : 1836(w), 1795(s), 1751(m)  $\text{cm}^{-1}$ .

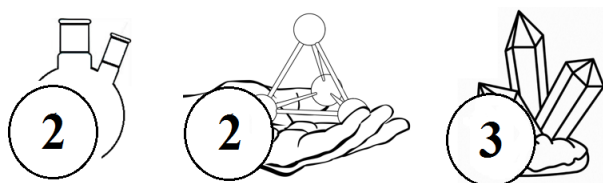
### Synthesis of $\text{Pt}(\text{dppb})_2$ ( $\text{dppb} = o\text{-C}_6\text{H}_4(\text{PPh}_2)_2$ )



$\text{dppb}$  (0.901 g, 2.02 mmol) was added to a solution of  $[\text{NBu}_4]_2[\text{Pt}_{12}(\text{CO})_{24}]$  (0.70 g, 0.200 mmol) in acetone (20 mL) and the mixture stirred at room temperature for 2

hours. At this point, an orange precipitate of  $\text{Pt}(\text{dppb})_2$  started to form and this was separated from the red solution by filtration. The acetone solution was layered with *n*-hexane (40 mL) resulting in a mixture of crystals of  $[\text{NBu}_4]_2[\text{Pt}_9(\text{CO})_{18}]$  (major product) and  $[\text{Pt}(\text{dppb})_2][\text{Pt}_9(\text{CO})_{18}] \cdot 2\text{CH}_3\text{COCH}_3$  (a few crystals). The solid was dissolved in  $\text{CH}_2\text{Cl}_2$  (20 mL) and crystals of  $\text{Pt}(\text{dppb})_2$  have been obtained after slow diffusion of *n*-hexane (yields 0.18 g, 7% based on Pt).

### Synthesis of $[\text{PPh}_4]_8[\text{H}_2\text{Pt}_{26}(\text{CO})_{20}(\text{CdBr})_{12}] \cdot 4\text{CH}_3\text{CN}$

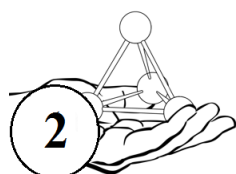


$\text{CdBr}_2 \cdot \text{H}_2\text{O}$  (2.60 g, 8.97 mmol) was added as a solid to a solution of  $[\text{NMe}_4]_2[\text{Pt}_{12}(\text{CO})_{24}]$  (1.16 g, 0.365 mmol) in *dmf* (30 mL) and the resulting suspension stirred at 120 °C under

nitrogen for 8 hours. The solution turned from green to brown and gas evolution was observed. This was, then, allowed to cool to room temperature and solid  $[\text{PPh}_4]\text{Br}$  (1.50 g, 3.59 mmol) was added. The crude compound was finally precipitated by addition of water (50 mL). The residue was recovered by filtration, washed with water (30 mL), *iso*-propanol (30 mL), *thf* (30 mL), acetone (30 mL) and dried in vacuum. The final compound was, then, extracted in  $\text{CH}_3\text{CN}$  (20 mL). The IR spectrum of this solution showed that the major species present was the hexa-anion  $[\text{H}_4\text{Pt}_{26}(\text{CO})_{20}(\text{CdBr})_{12}]^{6-}$ . Crystals suitable for X-ray analysis of  $[\text{PPh}_4]_8[\text{H}_2\text{Pt}_{26}(\text{CO})_{20}(\text{CdBr})_{12}] \cdot 4\text{CH}_3\text{CN}$  were obtained by slow diffusion of *n*-hexane (5 mL) and *di*-*iso*-propyl ether (40 mL) on the  $\text{CH}_3\text{CN}$  solution. It must be remarked that after diffusion the solution was still partially coloured (indicating that only part of the cluster was precipitated) and the solid was composed by a major amorphous component containing the hexa-anion  $[\text{PPh}_4]_6[\text{H}_4\text{Pt}_{26}(\text{CO})_{20}(\text{CdBr})_{12}]$  and a few crystals of the octa-anion  $[\text{PPh}_4]_8[\text{H}_2\text{Pt}_{26}(\text{CO})_{20}(\text{CdBr})_{12}] \cdot 4\text{CH}_3\text{CN}$ . The formulation of the two species is based on their IR spectra on *nujol* mull as well as X-ray crystallography on the latter. Since it was not possible to completely separate the two solids, the yields have not been calculated. The total amount of solid recovered after work-up was 0.44 g.

[PPh<sub>4</sub>]<sub>8</sub>[H<sub>2</sub>Pt<sub>26</sub>(CO)<sub>20</sub>(CdBr)<sub>12</sub>].4CH<sub>3</sub>CN (single crystal) IR (nujol, 293 K)  $\nu(\text{CO})$ : 1970(vs), 1938(br) cm<sup>-1</sup>. [PPh<sub>4</sub>]<sub>6</sub>[H<sub>4</sub>Pt<sub>26</sub>(CO)<sub>20</sub>(CdBr)<sub>12</sub>] (amorphous powder) IR (nujol, 293 K)  $\nu(\text{CO})$ : 1992(vs), 1959(br) cm<sup>-1</sup>. IR (CH<sub>3</sub>CN, 293 K)  $\nu(\text{CO})$ : 2000(vs), 1990(sh), 1975(m) cm<sup>-1</sup>. IR (dmf, 293 K)  $\nu(\text{CO})$ : 1999(vs), 1972(m) cm<sup>-1</sup>.

### Synthesis of [PPh<sub>4</sub>]<sub>6</sub>[H<sub>4</sub>Pt<sub>26</sub>(CO)<sub>20</sub>(CdBr)<sub>12</sub>(PtBr)<sub>x</sub>].(10+x)dmf (x = 0.56)



CdBr<sub>2</sub>·H<sub>2</sub>O (2.30 g, 7.94 mmol) was added as a solid to a solution of [NBu<sub>4</sub>]<sub>2</sub>[Pt<sub>15</sub>(CO)<sub>30</sub>] (1.20 g, 0.282 mmol) in dmf (30 mL) and the resulting suspension stirred at 120 °C under

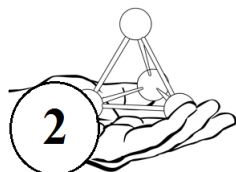
nitrogen for 6 hours. The solution turned from green to brown and gas evolution was observed. This was, then, allowed to cool to room temperature and solid [PPh<sub>4</sub>]<sub>6</sub>Br (1.50 g, 3.59 mmol) was added. The crude compound was finally precipitated by addition of water (50 mL). The residue was recovered by filtration, washed with water (30 mL), iso-propanol (30 mL), thf (30 mL), acetone (30 mL) and dried in vacuum. The final compound was, then, extracted in dmf (20 mL) and crystals suitable for X-ray analysis of [PPh<sub>4</sub>]<sub>6</sub>[H<sub>4</sub>Pt<sub>26</sub>(CO)<sub>20</sub>(CdBr)<sub>12</sub>(PtBr)<sub>x</sub>].(10+x)dmf (x = 0.56) were obtained by slow diffusion of iso-propanol (40 mL) (yield 0.62 g, 35% based on Pt).

C<sub>195.7</sub>H<sub>193.96</sub>Br<sub>12.57</sub>Cd<sub>12</sub>N<sub>10.57</sub>O<sub>30.57</sub>P<sub>6</sub>Pt<sub>26.57</sub> (10905.70): calcd. C 21.53, H 1.79, N 1.36, Cd 12.53, Pt 47.50; found. C 21.72, H 1.48, N 1.19, Cd 12.65, Pt 47.23.

IR (nujol, 293 K)  $\nu(\text{CO})$ : 1992(vs), 1966(br) cm<sup>-1</sup>. IR (dmf, 293 K)  $\nu(\text{CO})$ : 1999(vs), 1973(m) cm<sup>-1</sup>.

## Bimetallic Ni-Co and Ni-Cu clusters (chapter 4)

### Synthesis of [NEt<sub>4</sub>]<sub>4</sub>[H<sub>2</sub>Ni<sub>22</sub>Co<sub>6</sub>C<sub>6</sub>(CO)<sub>36</sub>]



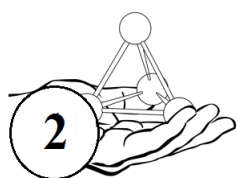
A solution of Co<sub>3</sub>( $\mu$ -3-CCl)(CO)<sub>9</sub> (0.224 g, 0.471 mmol) in acetone (15 mL) was added dropwise to a solution of [NEt<sub>4</sub>]<sub>2</sub>[Ni<sub>10</sub>(C<sub>2</sub>)(CO)<sub>16</sub>] (1.05 g, 0.818 mmol)

in acetone (25 mL). An evolution of gas was immediately observed and the solution was further

stirred under nitrogen for 2 hours. Then, the solvent was removed *in vacuo*, the solid washed with water (40 mL) and toluene (40 mL) and extracted in CH<sub>3</sub>CN (20 mL). Crystals of [NEt<sub>4</sub>]<sub>4</sub>[H<sub>2</sub>Ni<sub>22</sub>Co<sub>6</sub>C<sub>6</sub>(CO)<sub>36</sub>] suitable for X-ray analyses were obtained by slow diffusion of n-hexane (5 mL) and di-iso-propyl ether (40 mL) (yield 0.62 g, 52 % based on Ni, 82 % based on Co).

C<sub>74</sub>H<sub>80</sub>Co<sub>6</sub>N<sub>4</sub>Ni<sub>22</sub>O<sub>36</sub> (3228.63): calcd. C 27.50, H 2.50, N 1.73, Co 10.95, Ni 39.48; found: C 27.68, H 2.50, N 1.59, Co 11.12, Ni 39.64. IR (thf, 293 K)  $\nu(\text{CO})$ : 2023(s), 1859(m) cm<sup>-1</sup>. IR (acetone, 293 K)  $\nu(\text{CO})$ : 2018(vs), 1857(m) cm<sup>-1</sup>.

### Synthesis of [NMe<sub>3</sub>(CH<sub>2</sub>Ph)]<sub>6</sub>[Ni<sub>36</sub>Co<sub>8</sub>C<sub>8</sub>(CO)<sub>48</sub>]·5CH<sub>3</sub>COCH<sub>3</sub>

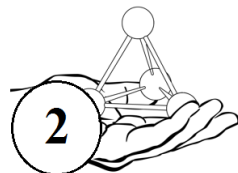


[NMe<sub>3</sub>(CH<sub>2</sub>Ph)]<sub>4</sub>[H<sub>2</sub>Ni<sub>22</sub>Co<sub>6</sub>C<sub>6</sub>(CO)<sub>36</sub>] (0.85 g, 0.28 mmol) was refluxed in thf (20 mL) under nitrogen for 2 hours. The solution became nearly colourless and a dark-brown

oily precipitate separated out. Then, the precipitate was recovered by filtration, washed with thf (20 mL) and dried *in vacuo*. The solid was washed with water (40 mL) and toluene (40 mL), and extracted in acetone (20 mL). Crystals of [NMe<sub>3</sub>(CH<sub>2</sub>Ph)]<sub>6</sub>[Ni<sub>36</sub>Co<sub>8</sub>C<sub>8</sub>(CO)<sub>48</sub>]·5CH<sub>3</sub>COCH<sub>3</sub> suitable for X-ray analyses were obtained by slow diffusion of n-hexane (40 mL) on the acetone solution (yield 0.38 g, 45 % based on Ni, 35 % based on Co).

C<sub>131</sub>H<sub>126</sub>Co<sub>8</sub>N<sub>6</sub>Ni<sub>36</sub>O<sub>53</sub> (5217.38): calcd. C 30.16, H 2.43, N 1.61, Co 9.04, Ni 40.50; found: C 30.34, H 2.21, N 1.85, Co 9.19, Ni 40.23. IR (nujol mull, 293 K)  $\nu(\text{CO})$ : 2002(s), 1857(m) cm<sup>-1</sup>. IR (CH<sub>3</sub>CN, 293 K)  $\nu(\text{CO})$ : 2000(vs), 1870(m) cm<sup>-1</sup>. The <sup>1</sup>H NMR spectrum does not show any resonance a part those of the [NMe<sub>3</sub>(CH<sub>2</sub>Ph)]<sup>+</sup> cation.

### Synthesis of [NEt<sub>4</sub>]<sub>3</sub>[Ni<sub>9</sub>Co(C<sub>2</sub>)(CO)<sub>16-x</sub>] (x = 0.58)



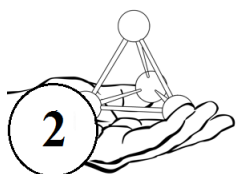
A solution of [NBu<sub>4</sub>][OH] (0.348 g, 1.34 mmol) in CH<sub>3</sub>CN (15 mL) was added dropwise to a solution of [NEt<sub>4</sub>]<sub>4</sub>[H<sub>2</sub>Ni<sub>22</sub>Co<sub>6</sub>C<sub>6</sub>(CO)<sub>36</sub>] (0.868 g, 0.269

mmol) in CH<sub>3</sub>CN (20 mL) over a period of 3 hours. Then, the solvent was removed *in vacuo*, the solid washed with water (40 mL), thf (20 mL) and acetone (20 mL), and extracted in CH<sub>3</sub>CN (20 mL). Crystals of [NEt<sub>4</sub>]<sub>3</sub>[Ni<sub>9</sub>Co(C<sub>2</sub>)(CO)<sub>16-x</sub>] (x = 0.58) suitable for X-ray analyses were obtained by slow diffusion of n-hexane (5 mL) and di-iso-propyl ether (40 mL) (yield 0.59 g,

63 % based on Ni, 25 % based on Co). The value of x varies from batch to batch. The CIF files of other three crystals obtained from different reaction batches are included to support this point. They show  $x = 0.70, 0.84$  and  $0.82$ .

$C_{41.42}H_{60}CoN_3Ni_9O_{15.42}$  (1434.00): calcd. C 34.70, H 4.22, N 2.93, Co 4.11, Ni 36.74; found: C 34.55, H 4.40, N 2.78, Co 4.02, Ni 36.85. IR (nujol, 293 K)  $\nu(CO)$ : 2043(w), 2005(w), 1958(vs), 1920(m), 1832(ms), 1772(m)  $cm^{-1}$ . IR (acetone, 293 K)  $\nu(CO)$ : 1976(vs), 1942(sh), 1840(br)  $cm^{-1}$ . IR ( $CH_3CN$ , 293 K)  $\nu(CO)$ : 1979(vs), 1948(sh), 1874(ms), 1829(m)  $cm^{-1}$ .

### Synthesis of $[NEt_4]_4[H_2Ni_{30}C_4(CO)_{34}\{Cu(CH_3CN)\}_2] \cdot 6CH_3CN$

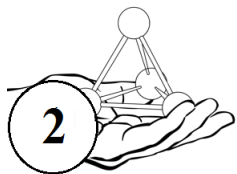


$[Cu(CH_3CN)_4][BF_4]$  (0.36 g, 1.14 mmol) was added as a solid to a solution of  $[NEt_4]_2[Ni_9C(CO)_{17}]$  (1.16 g, 0.91 mmol) in thf (20 mL) over a period of 2 hours. The

resulting mixture was further stirred at room temperature for two days and, then, the solvent removed *in vacuo*. The residue was washed with water (40 mL), dried under *vacuum* and extracted with  $CH_3CN$  (20 mL). Crystals of  $[NEt_4]_4[H_2Ni_{30}C_4(CO)_{34}\{Cu(CH_3CN)\}_2] \cdot 6CH_3CN$  suitable for X-ray analyses were obtained by layering n-hexane (5 mL) and di-iso-propyl ether (40 mL) on the  $CH_3CN$  solution (yield 0.38 g, 37 % based on Ni).

$C_{86}H_{106}Cu_2N_{12}Ni_{30}O_{34}$  (3739.72): calcd. C 27.62, H 2.86, N 4.49, Cu 3.40, Ni 47.08; found: C 27.49, H 2.92, N 4.33, Cu 3.61, Ni 47.25. IR ( $CH_3CN$ , 293 K)  $\nu(CO)$ : 2012(vs), 1878(ms)  $cm^{-1}$ .

### Synthesis of $[NMe_4]_4[H_2Ni_{30}C_4(CO)_{34}\{Cu(CH_3CN)\}_2] \cdot 2CH_3CN$



$[Cu(CH_3CN)_4][BF_4]$  (0.36 g, 1.14 mmol) was added as a solid to a solution of  $[NMe_4]_2[Ni_9C(CO)_{17}]$  (1.06 g, 0.91 mmol) in thf (20 mL) over a period of 2 hours. The

resulting mixture was further stirred at room temperature for two days and, then, the solvent removed *in vacuo*. The residue was washed with water (40 mL), dried under *vacuum* and extracted with  $CH_3CN$  (20 mL). Crystals of  $[NMe_4]_4[H_2Ni_{30}C_4(CO)_{34}\{Cu(CH_3CN)\}_2] \cdot 2CH_3CN$  suitable for X-ray analyses were obtained by layering n-hexane (5 mL) and di-iso-propyl ether (40 mL) on the  $CH_3CN$  solution (yield 0.32 g, 45 % based on Ni).

$C_{62}H_{62}Cu_2N_8Ni_{30}O_{34}$  (3351.07): calcd. C 22.22, H 1.86, N 3.34, Cu 3.79, Ni 52.54; found: C 22.36, H 1.71, N 3.48, Cu 3.95, Ni 52.76. IR (CH<sub>3</sub>CN, 293 K)  $\nu(CO)$ : 2012(vs), 1878(ms) cm<sup>-1</sup>.

### Synthesis of $[NMe_4]_4[H_2Ni_{30}C_4(CO)_{34}\{Cu(CH_3CN)\}_2] \cdot 6CH_3COCH_3$



$[Cu(CH_3CN)_4][BF_4]$  (0.36 g, 1.14 mmol) was added as a solid to a solution of  $[NMe_4]_2[Ni_9C(CO)_{17}]$  (1.06 g, 0.91 mmol) in thf (20 mL) over a period of 2 hours. The

resulting mixture was further stirred at room temperature for two days and, then, the solvent removed *in vacuo*. The residue was washed with water (40 mL), dried under vacuum and extracted with acetone (20 mL). Crystals of  $[NMe_4]_4[H_2Ni_{30}C_4(CO)_{34}\{Cu(CH_3CN)\}_2] \cdot 6CH_3COCH_3$  suitable for X-ray analyses were obtained by layering iso-propanol (40 mL) on the acetone solution (yield 0.37 g, 38 % based on Ni).

$C_{76}H_{92}Cu_2N_6Ni_{30}O_{40}$  (3617.45): calcd. C 25.23, H 2.56, N 2.32, Cu 3.51, Ni 48.68; found: C 25.09, H 2.42, N 2.79, Cu 3.52, Ni 48.58. IR (acetone, 293 K)  $\nu(CO)$ : 2011(vs), 1879(ms) cm<sup>-1</sup>.

### Synthesis of $[NMe_3(CH_2Ph)]_4[H_2Ni_{30-x}C_4(CO)_{34-x}\{Cu(CH_3CN)\}_2] \cdot 2CH_3CN$ (x ~ 0.35)



$[Cu(CH_3CN)_4][BF_4]$  (0.31 g, 0.99 mmol) was added as a solid to a solution of  $[NMe_4]_2[Ni_9C(CO)_{17}]$  (1.10 g, 0.84 mmol) in thf (20 mL) over a period of 1 hour. The

resulting mixture was further stirred at room temperature for 4 hours and, then, the solvent removed *in vacuo*. The residue was washed with water (40 mL), dried under vacuum and extracted with CH<sub>3</sub>CN (20 mL). Crystals of  $[NMe_3(CH_2Ph)]_4[H_2Ni_{30-x}C_4(CO)_{34-x}\{Cu(CH_3CN)\}_2] \cdot 2CH_3CN$  (x ~0.35) suitable for X-ray analyses were obtained by layering n-hexane (5 mL) and di-iso-propyl ether (40 mL) on the CH<sub>3</sub>CN solution (yield 0.29 g, 32 % based on Ni).

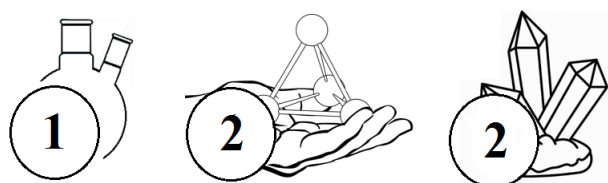
$C_{85.65}H_{78}Cu_2N_8Ni_{29.65}O_{33.66}$  (3625.28): calcd. C 28.38, H 2.17, N 3.09, Cu 3.51, Ni 48.00; found: C 28.56, H 1.98, N 3.23, Cu 3.74, Ni 48.25. IR (CH<sub>3</sub>CN, 293 K)  $\nu(CO)$ : 2010(vs), 1876(ms) cm<sup>-1</sup>.

**Synthesis of  $[\text{NMe}_4]_3[\text{H}_3\text{Ni}_{30-x}\text{C}_4(\text{CO})_{34-x}\{\text{Cu}(\text{NCC}_6\text{H}_4\text{CN})\}_2] \cdot 3.5\text{CH}_3\text{COCH}_3$  ( $x \sim 0.52$ )**


$[\text{Cu}(\text{CH}_3\text{CN})_4][\text{BF}_4]$  (0.57 g, 1.81 mmol) was added as a solid to a solution of  $[\text{NMe}_4]_2[\text{Ni}_9\text{C}(\text{CO})_{17}]$  (1.21 g, 1.04 mmol) in thf (20 mL) over a period of 2 hours. The

resulting mixture was further stirred at room temperature for 4 hours and, then, the solvent removed *in vacuo*. The residue was washed with water (40 mL), dried under vacuum and extracted with acetone (20 mL). At this stage, the species present in solution was the tetra-anion  $[\text{H}_2\text{Ni}_{30}\text{C}_4(\text{CO})_{34}\{\text{Cu}(\text{CH}_3\text{CN})\}_2]^{4-}$ , which was converted into the tri-anion  $[\text{H}_3\text{Ni}_{30}\text{C}_4(\text{CO})_{34}\{\text{Cu}(\text{CH}_3\text{CN})\}_2]^{3-}$  after addition of  $\text{HBF}_4 \cdot \text{Et}_2\text{O}$ .  $\text{NCC}_6\text{H}_4\text{CN}$  was, then, added in large excess to the acetone solution and, after stirring at room temperature for one night, the solution was layered with iso-propanol (40 mL) yielding crystals of  $[\text{NMe}_4]_3[\text{H}_3\text{Ni}_{30-x}\text{C}_4(\text{CO})_{34-x}\{\text{Cu}(\text{NCC}_6\text{H}_4\text{CN})\}_2] \cdot 3.5\text{CH}_3\text{COCH}_3$  ( $x \sim 0.52$ ) suitable for X-ray analyses (yield 0.35 g, 32 % based on Ni).

$\text{C}_{75.98}\text{H}_{68}\text{Cu}_2\text{N}_7\text{Ni}_{29.48}\text{O}_{36.98}$  (3528.19): calcd. C 25.86, H 1.94, N 2.78, Cu 3.60, Ni 49.04; found: C 25.57, H 2.04, N 3.01, Cu 3.45, Ni 49.25. IR (acetone, 293 K)  $\nu(\text{CO})$ : 2023(vs), 1883(ms)  $\text{cm}^{-1}$ .

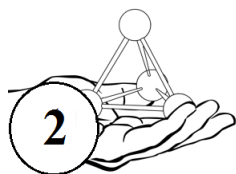
**Synthesis of  $[\text{Ni}(\text{CH}_3\text{CN})_6][\text{H}_2\text{Ni}_{29}\text{C}_4(\text{CO})_{32}(\text{CH}_3\text{CN})_2\{\text{Cu}(\text{CH}_3\text{CN})\}_2] \cdot 4\text{CH}_3\text{CN}$** 


$[\text{Cu}(\text{CH}_3\text{CN})_4][\text{BF}_4]$  (0.57 g, 1.81 mmol) was added as a solid to a solution of  $[\text{NMe}_4]_2[\text{Ni}_9\text{C}(\text{CO})_{17}]$  (1.21 g, 1.04 mmol) in thf (20 mL) over a period of 2 hours. The

resulting mixture was further stirred at room temperature for one night and, then, the solvent removed *in vacuo*. The residue was washed with water (40 mL), dried under vacuum and extracted with  $\text{CH}_3\text{CN}$  (20 mL). Crystals of  $[\text{Ni}(\text{CH}_3\text{CN})_6][\text{H}_2\text{Ni}_{29}\text{C}_4(\text{CO})_{32}(\text{CH}_3\text{CN})_2\{\text{Cu}(\text{CH}_3\text{CN})\}_2] \cdot 4\text{CH}_3\text{CN}$  suitable for X-ray analyses were obtained by layering n-hexane (5 mL) and di-iso-propyl ether (40 mL) on the  $\text{CH}_3\text{CN}$  solution (yield 0.38 g, 36 % based on Ni).

$\text{C}_{64}\text{H}_{44}\text{Cu}_2\text{N}_{14}\text{Ni}_{30}\text{O}_{32}$  (3409.0): calcd. C 22.55, H 1.30, N 5.75, Cu 3.73, Ni 51.65; found: C 22.88, H 1.06, N 5.91, Cu 3.65, Ni 51.49. IR ( $\text{CH}_3\text{CN}$ , 293 K)  $\nu(\text{CO})$ : 2030(vs), 1876(ms)  $\text{cm}^{-1}$ .

### Synthesis of $[\text{Ni}(\text{CH}_3\text{COCH}_3)_6][\text{H}_2\text{Ni}_{29}\text{C}_4(\text{CO})_{34}\{\text{Cu}(\text{CH}_3\text{CN})\}_2]\cdot 2\text{CH}_3\text{COCH}_3$

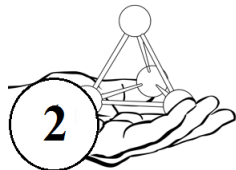


$[\text{Cu}(\text{CH}_3\text{CN})_4][\text{BF}_4]$  (0.57 g, 1.81 mmol) was added as a solid to a solution of  $[\text{NMe}_4]_2[\text{Ni}_9\text{C}(\text{CO})_{17}]$  (1.21 g, 1.04 mmol) in thf (20 mL) over a period of 2 hours. The

resulting mixture was further stirred at room temperature for one night and, then, the solvent removed *in vacuo*. The residue was washed with water (40 mL), dried under vacuum and extracted with acetone (20 mL). Crystals of  $[\text{Ni}(\text{CH}_3\text{COCH}_3)_6][\text{H}_2\text{Ni}_{29}\text{C}_4(\text{CO})_{34}\{\text{Cu}(\text{CH}_3\text{CN})\}_2]\cdot 2\text{CH}_3\text{COCH}_3$  suitable for X-ray analyses were obtained by layering isopropanol (40 mL) on the acetone solution (yield 0.37 g, 33 % based on Ni).

$\text{C}_{66}\text{H}_{56}\text{Cu}_2\text{N}_2\text{Ni}_{30}\text{O}_{42}$  (3437.03): calcd. C 23.06, H 1.64 N 0.82, Cu 3.70, Ni 51.23; found: C 23.12, H 1.71, N 1.01, Cu 3.52, Ni 51.12. IR (acetone, 293 K)  $\nu(\text{CO})$ : 2029(vs), 1875(ms)  $\text{cm}^{-1}$ .

### Synthesis of $[\text{NMe}_4]_2[\text{H}_2\text{Ni}_{29+x}\text{C}_4(\text{CO})_{34+x}\{\text{Cu}(\text{CH}_3\text{CN})\}_2]\cdot 3.79\text{thf}$ ( $x \sim 0.3$ )



$[\text{Cu}(\text{CH}_3\text{CN})_4][\text{BF}_4]$  (0.57 g, 1.81 mmol) was added as a solid to a solution of  $[\text{NMe}_4]_2[\text{Ni}_9\text{C}(\text{CO})_{17}]$  (1.21 g, 1.04 mmol) in thf (20 mL) over a period of 2 hours. The

resulting mixture was further stirred at room temperature for 4 hours and, then, the solvent removed *in vacuo*. The residue was dissolved in dmf (15 mL) and the crude product precipitated after addition of a water solution (40 mL) saturated with  $[\text{NMe}_4]\text{Cl}$ . The residue was recovered by filtration, washed with water (40 mL), dried under vacuum and extracted with thf (20 mL).

Crystals of  $[\text{NMe}_4]_2[\text{H}_2\text{Ni}_{29+x}\text{C}_4(\text{CO})_{33+x}\{\text{Cu}(\text{CH}_3\text{CN})\}_2]\cdot 3.39\text{thf}$  suitable for X-ray analyses were obtained by layering n-hexane (40 mL) on the thf solution (yield 0.24 g, 23 % based on Ni).

$\text{C}_{63.56}\text{H}_{57.11}\text{Cu}_2\text{N}_4\text{Ni}_{29.33}\text{O}_{37.39}$  (3324.25): calcd. C 22.97, H 1.73, N 1.69, Cu 3.82, Ni 51.79; found: C 23.42, H 1.68, N 1.86, Cu 4.03, Ni 51.14. IR (thf, 293 K)  $\nu(\text{CO})$ : 2028(vs), 1877(ms)  $\text{cm}^{-1}$ .

## Bimetallic Ni-Au and Co-Au clusters (chapter 5)

### Synthesis of $[\text{NEt}_4]_3[\text{Ni}_{12}\text{Au}(\text{CO})_{24}]$



Solid  $[\text{NEt}_4][\text{AuCl}_4]$  (0.89 g, 1.90 mmol) was added in small portions to an acetone (30 mL) solution of  $[\text{NEt}_4]_2[\text{Ni}_6(\text{CO})_{12}]$  (2.21 g, 2.33 mmol) over a period of 1 hour. The solution

was stirred at room temperature for a further hour and, then, the solvent removed *in vacuo*. The residue was washed with water (40 mL), toluene (40 mL) and thf (20 mL). The crude product was extracted in acetone (20 mL) and crystals suitable for X-ray analysis were obtained by slow diffusion of isopropyl alcohol (40 mL) over the acetone solution of the product (yields 0.92 g, 24.7 % based on Au, 40.2 % based on Ni).

$\text{C}_{48}\text{H}_{60}\text{Au}_3\text{Ni}_{12}\text{O}_{24}$  (1964.48): calcd. C 29.35, H 3.08, N 2.14, Ni 35.86, Au 10.03; found: C 29.48, H 2.92, N 2.26, Ni 35.99, Au 9.89. IR (acetone, 293 K)  $\nu(\text{CO})$ : 2010(vs), 1986(sh), and 1822(ms)  $\text{cm}^{-1}$ . IR (nujol, 293 K)  $\nu(\text{CO})$ : 1995(vs), 1833(sh), 1815(ms), 1775(m)  $\text{cm}^{-1}$ .

### Synthesis of $[\text{NEt}_4]_6[\text{Ni}_{32}\text{Au}_6(\text{CO})_{44}]$



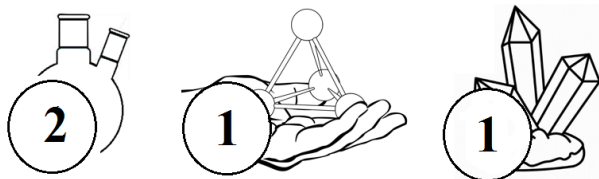
Solid  $[\text{NEt}_4][\text{AuCl}_4]$  (1.04 g, 2.22 mmol) was added in small portions to an acetone (30 mL) solution of  $[\text{NEt}_4]_2[\text{Ni}_6(\text{CO})_{12}]$  (2.21 g, 2.33 mmol) over a period of 1 hour.

The solution was stirred at room temperature for a further hour and, then, the solvent removed *in vacuo*. The residue was washed with water (40 mL), toluene (40 mL), thf (20 mL) and acetone (20 mL). The crude product was extracted in  $\text{CH}_3\text{CN}$  (20 mL) and a microcrystalline powder of  $[\text{NEt}_4]_6[\text{Ni}_{32}\text{Au}_6(\text{CO})_{44}]$  was obtained after addition of di-iso-propyl-ether (50 mL) (yields 0.87 g, 54.2 % based on Au, 39.2 % based on Ni).

$\text{C}_{92}\text{H}_{120}\text{Au}_6\text{N}_6\text{Ni}_{32}\text{O}_{44}$  (5073.94): calcd. C 21.78, H 2.38, N 1.66, Ni 37.02, Au 23.29; found: C 21.86, H 2.20, N 1.54, Ni 36.81, Au 23.06. IR ( $\text{CH}_3\text{CN}$ , 293 K)  $\nu(\text{CO})$ : 2012(m), 1889(vs)  $\text{cm}^{-1}$ .

1.

### Synthesis of $\text{Co}_6\text{C}(\text{CO})_{12}(\text{AuPPh}_3)_4$ (I-III)

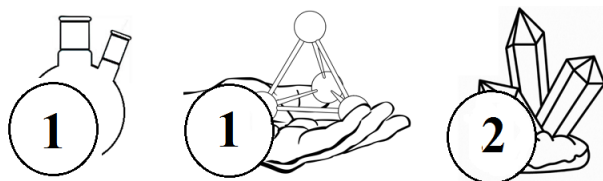


$\text{Au}(\text{PPh}_3)\text{Cl}$  (1.41 g, 2.82 mmol) was added as a solid to a solution of  $[\text{NMe}_3(\text{CH}_2\text{Ph})]_2[\text{Co}_6\text{C}(\text{CO})_{15}]$  (1.02 g, 0.94 mmol) in thf (30 mL) over a period of 2 h. The resulting

mixture was further stirred at room temperature for 4 h and, then, the solvent removed *in vacuo*. The residue was washed with water (40 mL), and extracted with thf (20 mL). A crystalline material was obtained by layering n-hexane (40 mL) on the thf solution (yield 0.2-0.4 g). This solid may contain one or a mixture of the three solvate crystals  $\text{Co}_6\text{C}(\text{CO})_{12}(\text{AuPPh}_3)_4$  (**I**),  $\text{Co}_6\text{C}(\text{CO})_{12}(\text{AuPPh}_3)_4 \cdot \text{thf}$  (**II**),  $\text{Co}_6\text{C}(\text{CO})_{12}(\text{AuPPh}_3)_4 \cdot 4\text{thf}$  (**III**). The different content of co-crystallized thf makes meaningless elemental analyses or the determination of the yield.

IR (nujol, 293 K)  $\nu(\text{CO})$ :  $\text{Co}_6\text{C}(\text{CO})_{12}(\text{AuPPh}_3)_4$  (**I**) 2034(s), 2004(vs), 1966(s), 1921(vs), 1879(sh) and 1799(vs)  $\text{cm}^{-1}$ ;  $\text{Co}_6\text{C}(\text{CO})_{12}(\text{AuPPh}_3)_4 \cdot \text{thf}$  (**II**) 2009(vs), 19810(s), 1941(m), 1834(m) and 1812(m)  $\text{cm}^{-1}$ ;  $\text{Co}_6\text{C}(\text{CO})_{12}(\text{AuPPh}_3)_4 \cdot 4\text{thf}$  (**III**) 2022(m), 2008(m), 1965(s), 1939(w), 1875(w), 1857(w), 1834(w), 1821(m) and 1796(w)  $\text{cm}^{-1}$ .

### Synthesis of $[\text{NEt}_4][\{\text{Co}_5\text{C}(\text{CO})_{12}\}\text{Au}\{\text{Co}(\text{CO})_4\}]$

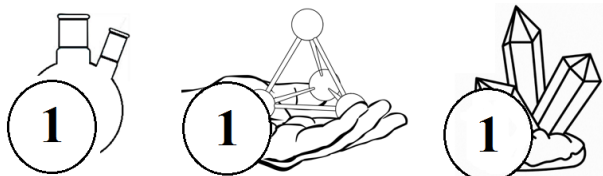


$[\text{NEt}_4][\text{AuCl}_4]$  (1.06 g, 2.26 mmol) was added as a solid to a solution of  $[\text{NEt}_4]_2[\text{Co}_6\text{C}(\text{CO})_{15}]$  (1.18 g, 1.13 mmol) in thf (20 mL) over a period of 1 h. Gas evolution (likely CO) and

formation of a gold mirror are observed. The solvent was, then, removed *in vacuo*, and the residue washed with water (20 mL) and toluene (40 mL), and, finally, extracted in thf (20 mL). Crystals of  $[\text{NEt}_4][\{\text{Co}_5\text{C}(\text{CO})_{12}\}\text{Au}\{\text{Co}(\text{CO})_4\}]$  suitable for X-ray analyses were obtained by layering n-hexane (40 mL) on the thf solution (yield 0.44 g, 34% based on Co, 17% based on Au).

$\text{C}_{25}\text{H}_{20}\text{AuCo}_6\text{NO}_{16}$  (1140.97): calcd. C 26.32, H 1.77, Au 17.26, Co 30.99; found: C 26.55, H 1.61, Au 17.05, Co 31.18. IR (nujol, 293 K)  $\nu(\text{CO})$ : 2029(m), 2014(s), 1991(w), 1973(m), 1939(w), 1841(m), 1830(w)  $\text{cm}^{-1}$ . IR (thf, 293 K)  $\nu(\text{CO})$ : 2029(s), 2011(m), 1973(w), 1857(m)  $\text{cm}^{-1}$ . IR ( $\text{CH}_2\text{Cl}_2$ , 293 K)  $\nu(\text{CO})$ : 2029(s), 2011(m), 1973(w), 1857(m)  $\text{cm}^{-1}$ . ESI-MS ( $\text{CH}_3\text{CN}$ ): ES-  $m/z$  (relative intensity in parentheses): 1024 (5), 1011(100), 983(20), 658 (10), 644(10), 171(50).

### Synthesis of $[\text{NEt}_4][\{\text{Co}_5\text{C}(\text{CO})_{12}\}_2\text{Au}]$



$\text{HBF}_4 \cdot \text{Et}_2\text{O}$  (362  $\mu\text{L}$ , 2.64 mmol) was added to a solution of  $[\text{NEt}_4][\{\text{Co}_5\text{C}(\text{CO})_{12}\}_2\text{Au}\{\text{Co}(\text{CO})_4\}]$  (0.43 g, 0.377 mmol) in  $\text{CH}_2\text{Cl}_2$  (20 mL) over a period

of 1 h. The solvent was, then, removed *in vacuo*, and the residue washed with water (20 mL) and toluene (20 mL), and, finally, extracted in  $\text{CH}_2\text{Cl}_2$  (20 mL). Crystals of  $[\text{NEt}_4][\{\text{Co}_5\text{C}(\text{CO})_{12}\}_2\text{Au}]$  suitable for X-ray analyses were obtained by layering n-hexane (40 mL) on the  $\text{CH}_2\text{Cl}_2$  solution (yield 0.25 g, 69% based on Co, 41% based on Au).

$\text{C}_{34}\text{H}_{20}\text{AuCo}_{10}\text{NO}_{24}$  (1612.78): calcd. C 25.32, H 1.25, Au 12.21, Co 36.54; found: C 25.12, H 0.94, Au 12.51, Co 36.86. IR (nujol, 293 K)  $\nu(\text{CO})$ : 2032(s), 2011(s), 1991(w), 2003(sh), 1979(m), 1879(w), 1844(w)  $\text{cm}^{-1}$ . IR ( $\text{CH}_2\text{Cl}_2$ , 293 K)  $\nu(\text{CO})$ : 2060(m), 2045(s), 2041(s), 2014(m), 1856(m)  $\text{cm}^{-1}$ . ESI-MS ( $\text{CH}_3\text{CN}$ ): ES-  $m/z$  (relative intensity in parentheses): 1495 (90), 1482 (100), 1454 (80), 741 (10), 727 (20), 658 (25), 644 (25), 171 (30).

### Synthesis of $\text{Co}_5\text{C}(\text{CO})_{12}(\text{AuPPh}_3)$



$[\text{Au}(\text{PPh}_3)\text{Cl}]$  (0.32 g, 0.64 mmol) was added as a solid to a solution of  $[\text{NEt}_4][\{\text{Co}_5\text{C}(\text{CO})_{12}\}_2\text{Au}]$  (0.52 g, 0.32 mmol) in thf (20 mL) over a period of 1 h. The

solution was, then, filtered and crystals of  $\text{Co}_5\text{C}(\text{CO})_{12}(\text{AuPPh}_3)$  suitable for X-ray analyses were obtained by layering n-hexane (40 mL) on the thf solution (yield 0.11 g, 16% based on Co, 10% based on Au).

$\text{C}_{31}\text{H}_{15}\text{AuCo}_5\text{O}_{12}\text{P}$  (1102.02): calcd. C 33.79, H 1.37, Au 17.87, Co 26.74; found: C 33.04, H 1.51, Au 19.09, Co 26.45. IR (nujol, 293 K)  $\nu(\text{CO})$ : 2075(w), 2040 (m), 2028 (m), 2017(s), 2009(s), 2003(s), 1996(m), 1976(m), 1960(m), 1873(m), 1963 (sh), 1857(m)  $\text{cm}^{-1}$ . The crystals are almost insoluble in all organic solvents.

### Synthesis of $[\text{Co}_5\text{C}(\text{CO})_{11}(\text{AuPPh}_3)_3] \cdot \text{thf} \cdot 0.5\text{C}_6\text{H}_{14}$ (A)

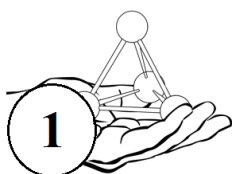


$[\text{Au}(\text{PPh}_3)\text{Cl}]$  (1.89 g, 3.82 mmol) was added as solid to a solution of  $[\text{NMe}_3(\text{CH}_2\text{Ph})]_2[\text{Co}_6\text{C}(\text{CO})_{15}]$  (1.02 g, 0.94 mmol) in thf (30 mL) over a period of 2 h. The

resulting mixture was further stirred at room temperature for 18 h and, then, the solvent removed *in vacuo*. The residue was washed with water (40 mL), and extracted with thf (20 mL). Crystals of  $[\text{Co}_5\text{C}(\text{CO})_{11}(\text{AuPPh}_3)_3]\cdot\text{thf}\cdot 0.5\text{C}_6\text{H}_{14}$  suitable for X-ray analyses were obtained by slow diffusion of n-hexane (40 mL) on the thf solution (yield 0.29 g, 12% based on Co, 11% based on Au). Alternatively,  $[\text{Au}(\text{PPh}_3)\text{Cl}]$  (0.81 g, 1.64 mmol) was added as a solid to a solution of  $[\text{NEt}_4][\{\text{Co}_5\text{C}(\text{CO})_{12}\}_2\text{Au}]$  (0.66 g, 0.409 mmol) in thf (20 mL) over a period of 1 hour. The solution was, then, filtered and crystals of  $[\text{Co}_5\text{C}(\text{CO})_{11}(\text{AuPPh}_3)_3]\cdot\text{thf}\cdot 0.5\text{C}_6\text{H}_{14}$  suitable for X-ray analyses were obtained by layering n-hexane (40 mL) on the thf solution (yield 0.10 g, 6% based on Co, 7% based on Au).

$\text{C}_{73}\text{H}_{60}\text{Au}_3\text{Co}_5\text{O}_{12}\text{P}_3$  (2107.67): calcd. C 41.60, H 2.87, Au 28.03, Co 13.98; found: C 41.94, H 2.99, Au 27.78, Co 14.18. IR (nujol, 293 K)  $\nu(\text{CO})$ : 2017(m), 2011(m), 1979(sh), 1962(s), 1945(s), 1938(s), 1916(sh), 1811(m)  $\text{cm}^{-1}$ . The crystals are almost insoluble in all organic solvents.

#### Synthesis of $[\text{Co}_5\text{C}(\text{CO})_{11}(\text{AuPPh}_3)_3]\cdot\text{CH}_3\text{CN}$ (B)

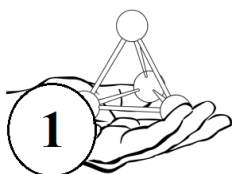


$[\text{Au}(\text{PPh}_3)\text{Cl}]$  (1.89 g, 3.82 mmol) was added as solid to a solution of  $[\text{NMe}_3(\text{CH}_2\text{Ph})]_2[\text{Co}_6\text{C}(\text{CO})_{15}]$  (1.02 g, 0.94 mmol) in thf (30 mL) over a period of 2 h. The

resulting mixture was further stirred at room temperature for 18 h and, then, the solvent removed *in vacuo*. The residue was washed with water (40 mL), and extracted with thf (20 mL). The resulting thf solution was filtered, the solvent removed *in vacuo* and the residue dissolved in  $\text{CH}_3\text{CN}$  (20 mL). Crystals of  $[\text{Co}_5\text{C}(\text{CO})_{11}(\text{AuPPh}_3)_3]\cdot\text{CH}_3\text{CN}$  suitable for X-ray analyses were obtained by slow diffusion of n-hexane (3 mL) and di-isopropyl ether (40 mL) on the  $\text{CH}_3\text{CN}$  solution (yield 0.26 g, 11% based on Co, 10% based on Au).

$\text{C}_{68}\text{H}_{48}\text{Au}_3\text{Co}_5\text{NO}_{11}\text{P}_3$  (2033.53): calcd. C 40.14, H 2.38, Au 29.07, Co 14.50; found: C 40.02, H 2.53, Au 28.91, Co 14.75. IR (nujol, 293 K)  $\nu(\text{CO})$ : 2026(s), 1980(m), 1960(m), 1852(w), 1832(m), 1820(w)  $\text{cm}^{-1}$ . The crystals are almost insoluble in all organic solvents.

#### Synthesis of $[\text{NEt}_4][\text{Co}_5\text{C}(\text{CO})_{11}(\text{AuPPh}_3)_2]\cdot 2\text{CH}_2\text{Cl}_2$



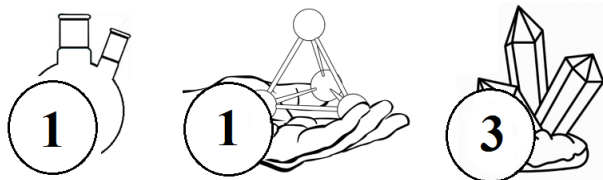
$[\text{Au}(\text{PPh}_3)\text{Cl}]$  (0.90 g, 1.82 mmol) was added as solid to a solution of  $[\text{NEt}_4]_2[\text{Co}_6\text{C}(\text{CO})_{15}]$  (0.87 g, 0.88 mmol) and  $\text{PPh}_3$  (0.24 g, 0.92

mmol) in thf (30 mL) over a period of 2 h. The resulting mixture was further stirred at room temperature for 18 h and, then, the solvent removed *in vacuo*. The residue was washed with water (40 mL) and toluene (20 mL), and extracted with CH<sub>2</sub>Cl<sub>2</sub> (15 mL). Crystals of [NEt<sub>4</sub>][Co<sub>5</sub>C(CO)<sub>11</sub>(AuPPh<sub>3</sub>)<sub>2</sub>] $\cdot$ 2CH<sub>2</sub>Cl<sub>2</sub> suitable for X-ray analyses were obtained by slow diffusion of n-hexane (30 mL) on the CH<sub>2</sub>Cl<sub>2</sub> solution (yield 0.41 g, 21% based on Co, 25% based on Au).

C<sub>58</sub>H<sub>54</sub>Au<sub>2</sub>Cl<sub>4</sub>Co<sub>5</sub>NO<sub>11</sub>P<sub>2</sub> (1833.35): calcd. C 38.02, H 2.97, Au 21.52, Co 19.10; found: C 38.23, H 3.11, Au 21.81, Co 18.92. IR (nujol, 293 K)  $\nu$ (CO): 2013(m), 1969(s), 1961(s), 1934(w), 1916(w), 1811(s) cm<sup>-1</sup>. IR (thf, 293 K)  $\nu$ (CO): 2012(m), 1982(s), 1947(w), 1815(vs) cm<sup>-1</sup>. IR (acetone, 293 K)  $\nu$ (CO): 2013(m), 1980(s), 1972(ms), 1945(m), 1825(s) cm<sup>-1</sup>. IR (CH<sub>3</sub>CN, 293 K)  $\nu$ (CO): 2014(m), 1979(s), 1945(m), 1917(w), 1823(s), 1779(w) cm<sup>-1</sup>.

## Bimetallic Co-Pd clusters (chapter 6)

### Synthesis of [NEt<sub>4</sub>]<sub>4</sub>[H<sub>2</sub>Co<sub>20</sub>Pd<sub>16</sub>C<sub>4</sub>(CO)<sub>48</sub>] $\cdot$ 4CH<sub>3</sub>COCH<sub>3</sub>



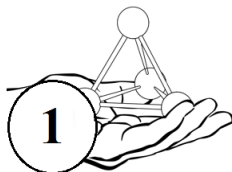
PdCl<sub>2</sub>(Et<sub>2</sub>S)<sub>2</sub> (0.932 g, 2.90 mmol) was added as a solid in small portions over a period of 2 h to a solution of [NEt<sub>4</sub>]<sub>2</sub>[Co<sub>6</sub>C(CO)<sub>15</sub>] (1.32 g, 1.27 mmol) in thf (20 mL) and the mixture

was refluxed for 3 h. The solvent was, then, removed *in vacuo* and the solid residue washed with water (2  $\times$  20 mL) and toluene (2  $\times$  20 mL) in order to remove Co(II) salts and [Co(CO)<sub>4</sub>]<sup>-</sup>. Crude [H<sub>2</sub>Co<sub>20</sub>Pd<sub>16</sub>C<sub>4</sub>(CO)<sub>48</sub>]<sup>4-</sup> was extracted in acetone (20 mL) and crystals of [NEt<sub>4</sub>]<sub>4</sub>[H<sub>2</sub>Co<sub>20</sub>Pd<sub>16</sub>C<sub>4</sub>(CO)<sub>48</sub>] $\cdot$ 4CH<sub>3</sub>COCH<sub>3</sub> suitable for X-ray analyses were obtained by slow diffusion of *iso*-propanol (40 mL) (yields 0.48 g, 53% based on Pd).

C<sub>96</sub>H<sub>106</sub>Co<sub>20</sub>N<sub>4</sub>O<sub>52</sub>Pd<sub>16</sub> (5029.25): calcd. C 22.93, H 2.12, N 1.11, Co 23.44, Pd 33.86; found: C 22.78, H 2.21, N 1.03, Co 23.58, Pd 33.95. IR (nujol, 293 K)  $\nu$ (CO): 2005(s), 1826(m) cm<sup>-1</sup>. IR (thf, 293 K)  $\nu$ (CO): 2018(s), 1843(m) cm<sup>-1</sup>. IR (acetone, 293 K)  $\nu$ (CO): 2017(s), 1842(m) cm<sup>-1</sup>.

Note: [NMe(CH<sub>2</sub>Ph)]<sub>4</sub>[H<sub>2</sub>Co<sub>20</sub>Pd<sub>16</sub>C<sub>4</sub>(CO)<sub>48</sub>] may be similarly obtained, using [NMe(CH<sub>2</sub>Ph)]<sub>2</sub>[Co<sub>6</sub>C(CO)<sub>15</sub>] instead of [NEt<sub>4</sub>]<sub>2</sub>[Co<sub>6</sub>C(CO)<sub>15</sub>].

### Synthesis of $[\text{NMe}_3(\text{CH}_2\text{Ph})][\text{NMe}_4]_4[\text{HCo}_{20}\text{Pd}_{16}\text{C}_4(\text{CO})_{48}] \cdot 5\text{CH}_3\text{COCH}_2$



$\text{PdCl}_2(\text{Et}_2\text{S})_2$  (0.820 g, 2.55 mmol) was added as a solid in small portions over a period of 2 h to a solution of  $[\text{NMe}_3(\text{CH}_2\text{Ph})]_2[\text{Co}_6\text{C}(\text{CO})_{15}]$  (1.24 g, 1.15 mmol) in thf (20 mL) and the mixture was refluxed for 3 h. The solvent was, then, removed *in vacuo* and the solid residue washed with water ( $2 \times 20$  mL) and toluene ( $2 \times 20$  mL) in order to remove Co(II) salts and  $[\text{Co}(\text{CO})_4]^-$ . Crude  $[\text{HCo}_{20}\text{Pd}_{16}\text{C}_4(\text{CO})_{48}]^{5-}$  was extracted in dmf (20 mL) and precipitated with a saturated solution of  $[\text{NMe}_4]\text{Cl}$  in water (50 mL). The solid was recovered by filtration, washed with water ( $2 \times 20$  mL) to remove excess  $[\text{NMe}_4]\text{Cl}$  and extracted in acetone (20 mL). Crystals of  $[\text{NMe}_3(\text{CH}_2\text{Ph})][\text{NMe}_4]_4[\text{HCo}_{20}\text{Pd}_{16}\text{C}_4(\text{CO})_{48}] \cdot 5\text{CH}_3\text{COCH}_2$  suitable for X-ray analyses were obtained by slow diffusion of *iso*-propanol (40 mL) on the acetone solution (yields 0.41 g, 51% based on Pd).

$\text{C}_{93}\text{H}_{95}\text{Co}_{20}\text{N}_5\text{O}_{53}\text{Pd}_{16}$  (5012.14): calcd. C 22.29, H 1.91, N 1.40, Co 23.52, Pd 33.97; found: C 22.05, H 1.96, N 1.52, Co 23.37, Pd 34.09. IR (nujol, 293 K)  $\nu(\text{CO})$ : 1994(s), 1819(br)  $\text{cm}^{-1}$ . IR (thf, 293 K)  $\nu(\text{CO})$ : 2000(s), 1832(m)  $\text{cm}^{-1}$ . IR (acetone, 293 K)  $\nu(\text{CO})$ : 1998(s), 1828(m)  $\text{cm}^{-1}$ . IR ( $\text{CH}_3\text{CN}$ , 293 K)  $\nu(\text{CO})$ : 1996(s), 1819(m)  $\text{cm}^{-1}$ . IR (dmf, 293 K)  $\nu(\text{CO})$ : 1989(s), 1819(m)  $\text{cm}^{-1}$ . The cluster is not very stable in dmf solution after standing for long time.

### Synthesis of $[\text{NMe}_3(\text{CH}_2\text{Ph})]_2[\text{HCo}_{15}\text{Pd}_9\text{C}_3(\text{CO})_{38}] \cdot \text{C}_6\text{H}_{14}$



$\text{HBF}_4 \cdot \text{Et}_2\text{O}$  (240  $\mu\text{L}$ , 1.74 mmol) was added dropwise to a solution of  $[\text{NMe}_3(\text{CH}_2\text{Ph})]_4[\text{H}_2\text{Co}_{20}\text{Pd}_{16}\text{C}_4(\text{CO})_{48}]$  (0.45 g, 0.092 mmol) in thf (20 mL) and the solvent removed *in vacuo* after 10 min. The residue was, then, dissolved in  $\text{CH}_2\text{Cl}_2$  (20 mL), the suspension filtered and the solution layered with *n*-hexane (40 mL), affording crystals suitable for X-ray analyses of  $[\text{NMe}_3(\text{CH}_2\text{Ph})]_2[\text{HCo}_{15}\text{Pd}_9\text{C}_3(\text{CO})_{38}] \cdot \text{C}_6\text{H}_{14}$  (yields 0.27 g, 66% based on Co; 50% based on Pd). The related  $[\text{NEt}_4]_2[\text{HCo}_{15}\text{Pd}_9\text{C}_3(\text{CO})_{38}]$  may be obtained following the same procedure using  $[\text{NEt}_4]_4[\text{H}_2\text{Co}_{20}\text{Pd}_{16}\text{C}_4(\text{CO})_{48}]$  as starting material.

$\text{C}_{67}\text{H}_{46}\text{Co}_{15}\text{N}_2\text{O}_{38}\text{Pd}_9$  (3328.61): calcd. C 24.17, H 1.39, N 0.84, Co 26.56, Pd 28.77; found: C 23.31, H 1.12, N 0.64, Co 27.01, Pd 29.92. IR (nujol, 293 K)  $\nu(\text{CO})$ : 2035(s), 1850(m)  $\text{cm}^{-1}$ . IR ( $\text{CH}_2\text{Cl}_2$ , 293 K)  $\nu(\text{CO})$ : 2035(s), 1865(m)  $\text{cm}^{-1}$ .

**Synthesis of  $[\text{NEt}_4]_3[\text{Co}_{15}\text{Pd}_9\text{C}_3(\text{CO})_{38}]\cdot\text{thf}$** 


$[\text{NBu}_4][\text{OH}]$  (330 mg, 0.412 mmol) was added as solid to a solution of  $[\text{NEt}_4]_2[\text{HCo}_{15}\text{Pd}_9\text{C}_3(\text{CO})_{38}]$  (0.44 g, 0.136 mmol) in  $\text{CH}_2\text{Cl}_2$  (20 mL) and the solution

stirred at room temperature for 1 h. Then, the suspension was filtered and the solution layered with n-hexane (40 mL) in the presence of some thf (5 mL), affording crystals suitable for X-ray analyses of  $[\text{NEt}_4]_3[\text{Co}_{15}\text{Pd}_9\text{C}_3(\text{CO})_{38}]\cdot\text{thf}$  (yields 0.41 g, 89% based on Co; 89% based on Pd).  $\text{C}_{69}\text{H}_{68}\text{Co}_{15}\text{N}_3\text{O}_{39}\text{Pd}_9$  (3404.81): calcd. C 24.34, H 2.01, N 1.23, Co 25.96, Pd 28.13; found: C 24.05, H 1.87, N 1.45, Co 26.11, Pd 28.29. IR (nujol, 293 K)  $\nu(\text{CO})$ : 2026(s), 1818(m)  $\text{cm}^{-1}$ . IR ( $\text{CH}_2\text{Cl}_2$ , 293 K)  $\nu(\text{CO})$ : 2021(s), 1846(m)  $\text{cm}^{-1}$ .

**Synthesis of  $[\text{NEt}_4][\text{H}_2\text{Co}_{15}\text{Pd}_9\text{C}_3(\text{CO})_{38}]\cdot 0.5\text{C}_6\text{H}_{14}$** 


$\text{HBF}_4\cdot\text{Et}_2\text{O}$  (32  $\mu\text{L}$ , 0.234 mmol) was added dropwise to a solution of  $[\text{NEt}_4]_2[\text{HCo}_{15}\text{Pd}_9\text{C}_3(\text{CO})_{38}]$  (0.40 g, 0.125 mmol) in  $\text{CH}_2\text{Cl}_2$  (20 mL) and the solution

stirred at room temperature for 1 h. Then, the suspension was filtered and the solution layered with n-hexane (40 mL), affording crystals suitable for X-ray analyses of  $[\text{NEt}_4][\text{H}_2\text{Co}_{15}\text{Pd}_9\text{C}_3(\text{CO})_{38}]\cdot 0.5\text{C}_6\text{H}_{14}$  (yields 0.34 g, 88% based on Co; 88% based on Pd).  $\text{C}_{52}\text{H}_{27}\text{Co}_{15}\text{NO}_{38}\text{Pd}_9$  (3115.30): calcd. C 20.05, H 0.87, N 0.45, Co 28.37, Pd 30.74; found: C 19.25, H 0.56, N 0.61, Co 28.12, Pd 30.41. IR ( $\text{CH}_2\text{Cl}_2$ , 293 K)  $\nu(\text{CO})$ : 2051(s), 1878(m)  $\text{cm}^{-1}$ .

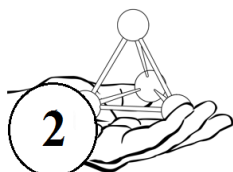
**Synthesis of  $\text{H}_3\text{Co}_{15}\text{Pd}_9\text{C}_3(\text{CO})_{38}\cdot 2\text{thf}$** 


$\text{HBF}_4\cdot\text{Et}_2\text{O}$  (263  $\mu\text{L}$ , 1.02 mmol) was added dropwise to a solution of  $[\text{NEt}_4]_2[\text{HCo}_{15}\text{Pd}_9\text{C}_3(\text{CO})_{38}]$  (0.40 g, 0.125 mmol) in  $\text{CH}_2\text{Cl}_2$  (20 mL) and the solution

stirred at room temperature for 1 h. Then, the suspension was filtered and the solution layered with n-hexane (40 mL) in the presence of some thf (3 mL), affording crystals suitable for X-ray analyses of  $\text{H}_3\text{Co}_{15}\text{Pd}_9\text{C}_3(\text{CO})_{38}\cdot 2\text{thf}$  (yields 0.28 g, 74% based on Co; 74% based on Pd).

$C_{49}H_{16}Co_{15}O_{40}Pd_9$  (3086.17): calcd. C 19.07, H 0.52, Co 28.64, Pd 31.03; found: C 18.88, H 0.68, Co 28.41, Pd 31.25. IR (nujol, 293 K)  $\nu(CO)$ : 2065(s), 1860(br)  $cm^{-1}$ . IR ( $CH_2Cl_2$ , 293 K)  $\nu(CO)$ : 2051(s), 1878(m)  $cm^{-1}$ .

### Synthesis of $[NEt_4]_5[HC_{16}Pd_2C_3(CO)_{28}] \cdot 1.5CH_3CN$

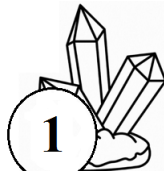
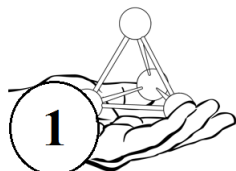


$[NEt_4]_4[H_2Co_{20}Pd_{16}C_4(CO)_{48}] \cdot 4CH_3COCH_3$  (0.44 g, 0.088 mmol) dissolved in thf (20 mL) was treated with a solution of Na/naphthalene in thf and the reaction

monitored by IR. When the starting material was completely reacted and the IR spectrum showed only the typical  $\nu(CO)$  of  $[Co(CO)_4]^-$  (1889  $cm^{-1}$ ) and a new band at 1953  $cm^{-1}$ , tentatively assigned to  $[Co_{16}Pd_2C_3(CO)_{28}]^{6-}$ , the solvent was removed *in vacuo* and the residue dissolved in dmsO (20 mL). The dmsO solution displayed three  $\nu(CO)$  bands attributable to  $[Co_{16}Pd_2C_3(CO)_{28}]^{6-}$  (1950(s) and 1801(m)  $cm^{-1}$ ) and  $[Co(CO)_4]^-$  (1889  $cm^{-1}$ ). Then, a saturated solution of  $[NEt_4]Br$  in water (60 mL) was added up to complete precipitation of the carbonyl species. The solid was recovered by filtration, washed with water ( $2 \times 20$  mL), toluene ( $2 \times 20$  mL), thf (20 mL) and acetone (20 mL) in order to remove Co(II) salts, excess  $[NEt_4]Br$ ,  $[Co(CO)_4]^-$  and naphthalene. The crude product was extracted in  $CH_3CN$  (20 mL) and crystals of  $[NEt_4]_5[HC_{16}Pd_2C_3(CO)_{28}] \cdot 1.5CH_3CN$  suitable for X-ray analyses were obtained by slow diffusion of *n*-hexane (5 mL) and di-*iso*-propyl ether (50 mL) on the  $CH_3CN$  solution (yields 0.14 g, 46% based on Co; 7.4% based on Pd).

$C_{74}H_{105.5}Co_{16}N_{6.5}O_{28}Pd_2$  (2689.93): calcd. C 33.04, H 3.95, N 3.38, Co 35.05, Pd 7.91; found: C 33.21, H 3.78, N 3.19, Co 34.94, Pd 8.05. IR (nujol, 293 K)  $\nu(CO)$ : 1969(s), 1808(m)  $cm^{-1}$ . IR ( $CH_3CN$ , 293 K)  $\nu(CO)$ : 1969(s), 1810(m)  $cm^{-1}$ .

### Synthesis of $Co_2Pd_5C(CO)_8(PPh_3)_5 \cdot 2thf$



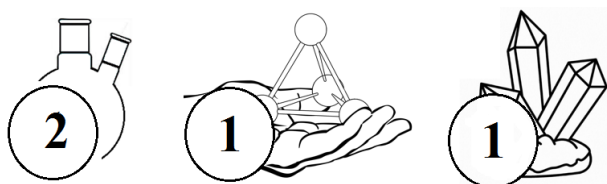
$PPh_3$  (0.16 g, 0.611 mmol) was added as a solid to a solution of  $[NMe(CH_2Ph)]_4[H_2Co_{20}Pd_{16}C_4(CO)_{48}]$  (0.65 g, 0.133 mmol) in thf (20 mL) under CO

atmosphere and the mixture stirred under CO for 6 h. The solvent was, then, removed *in vacuo* and the residue extracted in toluene (20 mL), leaving a solid containing a mixture of products not yet fully identified. After filtration, the toluene solution was dried under *vacuo* and the

residue dissolved in thf (20 mL). Crystals of  $\text{Co}_2\text{Pd}_5\text{C}(\text{CO})_8(\text{PPh}_3)_5 \cdot 2\text{thf}$  suitable for X-ray analyses were obtained by slow diffusion of n-hexane (40 mL) on the thf solution (yields 0.040 g, 1.3% based on Co; 4% based on Pd).

$\text{C}_{107}\text{H}_{91}\text{Co}_2\text{O}_{10}\text{P}_5\text{Pd}_5$  (2341.51): calcd. C 54.88, H 3.92, Co 5.03, Pd 22.72; found: C 55.03, H 3.67, Co 4.76, Pd 22.95. IR (nujol, 293 K)  $\nu(\text{CO})$ : 1963(s), 1903(w), 1865(w), 1857(m), 1839(vs)  $\text{cm}^{-1}$ . IR (thf, 293 K)  $\nu(\text{CO})$ : 1963(s), 1903(w), 1865(w), 1857(m), 1839(vs)  $\text{cm}^{-1}$ .

### Synthesis of $\text{Co}_4\text{Pd}_2\text{C}(\text{CO})_{11}(\text{PPh}_3)_2 \cdot 1.5\text{thf}$



$\text{PPh}_3$  (0.105 g, 0.401 mmol) was added as a solid to a solution of  $[\text{NMe}(\text{CH}_2\text{Ph})]_4[\text{H}_2\text{Co}_{20}\text{Pd}_{16}\text{C}_4(\text{CO})_{48}]$  (0.65 g, 0.133 mmol) in thf (20 mL) under CO

atmosphere and the mixture stirred under CO for 4 d. The solvent was, then, removed *in vacuo* and the residue extracted in toluene (20 mL), leaving a solid containing a mixture of products not yet fully identified. After filtration, the toluene solution was dried under *vacuo* and the residue dissolved in thf (20 mL). Crystals of  $\text{Co}_4\text{Pd}_2\text{C}(\text{CO})_{11}(\text{PPh}_3)_2 \cdot 1.5\text{thf}$  suitable for X-ray analyses were obtained by slow diffusion of n-hexane (40 mL) on the thf solution (yields 0.047 g, 5% based on Co; 3% based on Pd).

$\text{C}_{54}\text{H}_{42}\text{Co}_4\text{O}_{12.5}\text{P}_2\text{Pd}_2$  (1401.34): calcd. C 46.28, H 3.02, Co 16.82, Pd 15.19; found: C 46.09, H 3.25, Co 17.07, Pd 15.47. IR (nujol, 293 K)  $\nu(\text{CO})$ : 2002(s), 1960(sh), 1890(m), 1879(m)  $\text{cm}^{-1}$ . IR (thf, 293 K)  $\nu(\text{CO})$ : 2002(s), 1887(m)  $\text{cm}^{-1}$ .

### Synthesis of $[\text{NMe}_3(\text{CH}_2\text{Ph})][\text{Co}_4\text{Pd}_4\text{C}_2(\text{PPh}_3)_4(\text{CO})_{10}\text{Cl}] \cdot 2\text{CH}_3\text{COCH}_3$



$\text{PPh}_3$  (0.421 g, 1.61 mmol) was added as a solid to a solution of  $[\text{NMe}(\text{CH}_2\text{Ph})]_4[\text{H}_2\text{Co}_{20}\text{Pd}_{16}\text{C}_4(\text{CO})_{48}]$  (0.65 g, 0.133 mmol) in thf (20 mL) under CO

atmosphere and the mixture stirred under CO for 2 d. The solvent was, then, removed *in vacuo* and the residue extracted in toluene (20 mL), leaving a solid containing a mixture of products not yet fully identified. After filtration, the toluene solution was dried under *vacuo* and the residue dissolved in acetone (20 mL). Crystals of  $[\text{NMe}_3(\text{CH}_2\text{Ph})][\text{Co}_4\text{Pd}_4\text{C}_2(\text{PPh}_3)_4(\text{CO})_{10}\text{Cl}] \cdot 2\text{CH}_3\text{COCH}_3$  suitable for X-ray analyses were obtained by slow diffusion of n-hexane (40 mL) on the acetone solution (yields 0.11 g, 7% based on Co; 9% based on Pd).

$C_{100}H_{88}ClCo_4NO_{12}P_4Pd_4$  (2316.36): calcd. C 51.85, H 3.83, N 0.60, Co 10.18, Pd18.38; found: C 51.97, H 3.51, N 0.42, Co 10.02, Pd18.59. IR (nujol, 293 K)  $\nu(CO)$ : 1968(s), 1834(w)  $cm^{-1}$ . IR (thf, 293 K)  $\nu(CO)$ : 1965(s), 1865(w)  $cm^{-1}$ .

## Bimetallic Ni-Au and Fe-Au clusters (chapter 7)

### Synthesis of $Ni_6C(CO)_9(AuPPh_3)_4 \cdot thf$



$[Au(PPh_3)Cl]$  (0.52 g, 1.04 mmol) was added as a solid to a solution of  $[NEt_4]_2[Ni_9C(CO)_{17}]$  (0.664 g, 0.520 mmol) in thf (30 mL) over a period of two hours.

The resulting mixture was further stirred at room temperature for six hours and, then, the solvent removed *in vacuo*. The residue was washed with water (40 mL), toluene (40 mL), dried *in vacuo* and extracted with thf (20 mL). Crystals of  $Ni_6C(CO)_9(AuPPh_3)_4 \cdot thf$  suitable for X-ray analyses were obtained after layering toluene (40 mL) on the thf solution (yield 0.24 g, 12 % based on Ni).

$C_{86}H_{68}Au_4Ni_6O_{10}P_4$  (2525.41): calcd. C 40.90, H 2.71, Au 31.20, Ni 13.94; found: C 40.71, H 2.94, Au 31.35, Ni 14.09. IR (nujol, 293 K)  $\nu(CO)$ : 2027(ms), 1984(vs), 1970(s), 1851(m), 1832(ms)  $cm^{-1}$ .

### Synthesis of $Ni_6C(CO)_9(AuPPh_3)_4 \cdot thf \cdot 0.5C_6H_{14}$



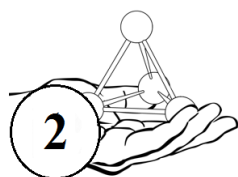
$[Au(PPh_3)Cl]$  (0.57 g, 1.15 mmol) was added as a solid to a solution of  $[NEt_4]_2[Ni_9C(CO)_{17}]$  (0.730 g, 0.572 mmol) in thf (30 mL) over a period of two hours.

The resulting mixture was further stirred at room temperature for six hours and, then, the solvent removed *in vacuo*. The residue was washed with water (40 mL), toluene (40 mL), dried *in vacuo* and extracted with thf (20 mL). Crystals of  $Ni_6C(CO)_9(AuPPh_3)_4 \cdot thf \cdot 0.5C_6H_{14}$  suitable for X-

ray analyses were obtained after layering n-hexane (40 mL) on the thf solution (yield 0.22 g, 10 % based on Ni).

$C_{89}H_{74}Au_4Ni_6O_{10}P_4$  (2567.49): calcd. C 41.64, H 2.91, Au 30.69, Ni 13.72; found: C 41.51, H 3.02, Au 30.81, Ni 13.64. IR (nujol, 293 K)  $\nu(CO)$ : 2027(ms), 1984(vs), 1970(s), 1851(m), 1832(ms)  $cm^{-1}$ .

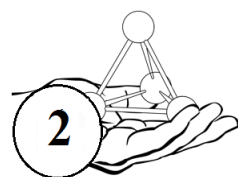
### Synthesis of $[Ni_6(C)(CO)_8(AuPPh_3)_8][BF_4]_2$



(158  $\mu$ L, 1.16 mmol) was added drop-wise to a solution of  $Ni_6(C)(CO)_9(AuPPh_3)_4$  (0.580 g, 0.236 mmol) in  $CH_2Cl_2$  (20 mL), and the resulting mixture stirred at room temperature

for 4 h. The solvent was removed in vacuo and the residue washed with water (40 mL), and extracted in  $CH_2Cl_2$  (20 mL). Crystals of  $[Ni_6(C)(CO)_8(AuPPh_3)_8][BF_4]_2$  suitable for X-ray analysis were obtained by slow diffusion of n-hexane (40 mL) on the  $CH_2Cl_2$  solution (yield 0.210 g, 20% based on Ni, 40% based on Au).  $C_{153}H_{120}Au_8B_2F_8Ni_6O_8P_8$  (4435.86): calcd. C 41.44, H 2.73, Ni 7.85, Au 35.57; found: C 41.21, H 2.95, Ni 7.59, Au 35.88. IR (nujol, 293 K)  $\nu(CO)$ : 1977(s), 1847(w), 1638(w)  $cm^{-1}$ . IR ( $CH_2Cl_2$ , 293 K)  $\nu(CO)$ : 2000(m), 1979(s), 1862(w), 1773(w)  $cm^{-1}$ .  $^{31}P\{^1H\}$  NMR ( $CD_2Cl_2$ , 298 K)  $\delta$  (ppm): 56.4 (s).  $^{31}P\{^1H\}$  NMR ( $CD_2Cl_2$ , 203 K)  $\delta$  (ppm): 55.0 (s)

### Synthesis of $[NEt_4][Ni_{12}(C)(C_2)(CO)_{17}(AuPPh_3)_3]\cdot thf$



$[Au(PPh_3)Cl]$  (1.05 g, 2.10 mmol) was added as a solid to a solution of  $[NEt_4]_2[Ni_9(C)(CO)_{17}]$  (0.894 g, 0.700 mmol) and  $[NEt_4]_2[Ni_{10}(C_2)(CO)_{16}]$  (0.910 g, 0.700

mmol) in thf (20 mL), and the resulting mixture stirred at room temperature for 6 h. The solvent was removed in vacuo and the residue washed with water (40 mL), and extracted in thf (20 mL). Crystals of  $[NEt_4][Ni_{12}(C)(C_2)(CO)_{17}(AuPPh_3)_3]\cdot thf$  suitable for X-ray analysis were obtained by slow diffusion of n-hexane (40 mL) on the thf solution (yield 0.611 g, 20% based on Ni, 31% based on Au).  $C_{86}H_{73}Au_3NNi_{12}O_{18}P_3$  (2796.78): calcd. C 37.04, H 2.64, N 0.50, Ni 24.95, Au 21.21; found: C 36.85, H 2.92, N 0.84, Ni 25.12, Au 21.06. IR (nujol, 293 K)  $\nu(CO)$ : 2002(s), 1971(sh), 1938(m), 1824(m)  $cm^{-1}$ . IR (thf, 293 K)  $\nu(CO)$ : 2009(s), 1975(m), 1945(sh), 1888(w), 1832(w)  $cm^{-1}$ .  $^{31}P\{^1H\}$  NMR ( $d^8$ -thf, 298 K)  $\delta$  (ppm): 49.0 (s, 2P), 48.2 (s, 1P).

### Synthesis of $[\text{NEt}_4][\text{HFe}_4(\text{CO})_{12}(\text{AuPPh}_3)_2]$



$[\text{Au}(\text{PPh}_3)\text{Cl}]$  (0.603 g, 1.22 mmol) was added as a solid to a solution of  $[\text{NEt}_4]_3[\text{HFe}_4(\text{CO})_{12}]$  (0.580 g, 0.610 mmol) in  $\text{CH}_3\text{CN}$  (25 mL), and the resulting mixture

stirred at room temperature for 24 h. The solvent was removed *in vacuo* and the residue washed with water (40 mL) and toluene (40 mL), and extracted in thf (20 mL). Crystals of  $[\text{NEt}_4][\text{HFe}_4(\text{CO})_{12}(\text{AuPPh}_3)_2]$  suitable for X-ray analysis were obtained by slow diffusion of n-hexane (40 mL) on the thf solution (yield 0.260 g, 26% based on Fe, 26% based on Au). The residue insoluble in thf was further extracted in acetone (20 mL) and afforded crystals of the known  $[\text{NEt}_4]_2[\text{Fe}_4(\text{CO})_{13}]$  (90 mg) after slow diffusion of n-hexane (40 mL).

$\text{C}_{56}\text{H}_{51}\text{Au}_2\text{Fe}_4\text{NO}_{12}\text{P}_2$  (1609.25): calcd. C 41.79, H 3.19, N 0.87, Fe 13.88, Au 24.48; found: C 41.98, H 2.94, N 1.08, Fe 13.56, Au 24.69. ESI-MS ( $\text{CH}_3\text{CN}$ ) multiplets centred at  $m/z$  (relative intensity in parentheses): 1479(100) ( $[\text{HFe}_4(\text{CO})_{12}(\text{AuPPh}_3)_2]^-$ ), 935(30) ( $[\text{Fe}_3(\text{CO})_{11}(\text{AuPPh}_3)]^-$ ) and 795(50) ( $[\text{Fe}_2(\text{CO})_8(\text{AuPPh}_3)]^-$ ). IR (nujol, 293 K)  $\nu(\text{CO})$ : 2016(vs), 1958(sh), 1937(vs), 1919(sh), 1880(m)  $\text{cm}^{-1}$ . IR (thf, 293 K)  $\nu(\text{CO})$ : 2016(vs), 1955(vs), 1944(sh), 1890(m)  $\text{cm}^{-1}$ . IR (acetone, 293 K)  $\nu(\text{CO})$ : 2017(vs), 1957(vs), 1944(sh), 1890(m)  $\text{cm}^{-1}$ . IR ( $\text{CH}_3\text{CN}$ , 293 K)  $\nu(\text{CO})$ : 2017(vs), 1955(vs), 1889(m)  $\text{cm}^{-1}$ . IR (dmf, 293 K)  $\nu(\text{CO})$ : 2015(vs), 1954(vs), 1942(sh), 1888(m)  $\text{cm}^{-1}$ .  $^1\text{H}$  NMR ( $\text{CD}_3\text{COCD}_3$ , 298 K)  $\delta$  (ppm): 7.43-7.16 (m, 30H, *Ph*), 3.35 (q,  $^3J_{\text{HH}} = 7.2$  Hz, 8H,  $\text{NCH}_2\text{CH}_3$ ), 1.26 (t,  $^3J_{\text{HH}} = 7.2$  Hz, 12H,  $\text{NCH}_2\text{CH}_3$ ), -19.54 (s, 1H, hydride).

$T_1$  for the hydride proton ( $\text{CD}_3\text{COCD}_3$ , 298 K): 23 s.  $^{31}\text{P}\{^1\text{H}\}$  NMR ( $\text{CD}_3\text{COCD}_3$ , 298 K)  $\delta$  (ppm): 57.3 (s).  $^{31}\text{P}\{^1\text{H}\}$  NMR ( $\text{CD}_3\text{COCD}_3$ , 193 K)  $\delta$  (ppm): 55.7 (s).  $^{13}\text{C}\{^1\text{H}\}$  NMR ( $\text{CD}_3\text{COCD}_3$ , 298 K)  $\delta$  (ppm)  $^{13}\text{C}$  enriched sample (only the CO region is given): 222.4 (s).  $^{13}\text{C}\{^1\text{H}\}$  NMR NMR ( $\text{CD}_3\text{COCD}_3$ , 193 K)  $\delta$  (ppm): 222.5 (s).

### Synthesis of $\text{HFe}_4(\text{CO})_{12}(\text{AuPPh}_3)_3$



$\text{HBF}_4 \cdot \text{Et}_2\text{O}$  (30  $\mu\text{L}$ , 0.22 mmol) was added dropwise to a solution of  $[\text{NEt}_4][\text{HFe}_4(\text{CO})_{12}(\text{AuPPh}_3)_2]$  (0.330 g, 0.205 mmol) in  $\text{CH}_3\text{CN}$  (30 mL) and the

resulting mixture stirred at room temperature for 1 h. The solvent was removed *in vacuo* and the residue washed with water (20 mL) and toluene (20 mL), and extracted in  $\text{CH}_2\text{Cl}_2$  (10 mL).

Crystals of  $\text{HFe}_4(\text{CO})_{12}(\text{AuPPh}_3)_3$  suitable for X-ray analysis were obtained by slow diffusion of n-hexane (30 mL) on the  $\text{CH}_2\text{Cl}_2$  solution (yield 0.050 g, 13% based on Fe, 19% based on Au). The same  $\text{HFe}_4(\text{CO})_{12}(\text{AuPPh}_3)_3$  hydride has been obtained using  $\text{D}_2\text{SO}_4$  instead of  $\text{HBF}_4 \cdot \text{Et}_2\text{O}$ . This confirms that the hydride ligand in the final neutral cluster derives from the starting  $[\text{NEt}_4][\text{HFe}_4(\text{CO})_{12}(\text{AuPPh}_3)_2]$  anion.

The compound is soluble in  $\text{CH}_2\text{Cl}_2$  and thf, whereas it mainly dissociates to  $[\text{HFe}_4(\text{CO})_{12}(\text{AuPPh}_3)_2]^-$  in more polar solvents, such as acetone and  $\text{CH}_3\text{CN}$ . The compound decomposes during ESI-MS analyses.

$\text{C}_{66}\text{H}_{46}\text{Au}_3\text{Fe}_4\text{O}_{12}\text{P}_3$  (1938.24): calcd. C 40.90, H 2.39, Fe 11.54, Au 30.49; found: C 40.64, H 2.07, Fe 11.89, Au 30.78. IR (nujol, 293 K)  $\nu(\text{CO})$ : 2029(vs), 1982(s), 1967(w), 1965(m), 1946(sh), 1938(w), 1929(w), 1920(m), 1899(vs), 1872(w), 1857(w)  $\text{cm}^{-1}$ . IR ( $\text{CH}_2\text{Cl}_2$ , 293 K)  $\nu(\text{CO})$ : 2015(vs), 1985(w), 1956(m)  $\text{cm}^{-1}$ . IR (thf, 293 K)  $\nu(\text{CO})$ : 2035(w), 2014(vs), 1986(w), 1960(m), 1943(m), 1895(sh)  $\text{cm}^{-1}$ .  $^1\text{H}$  NMR ( $\text{CD}_2\text{Cl}_2$ , 298 K)  $\delta$  (ppm): 7.24 (m, 45H, *Ph*), -19.14 (s, 1H, hydride).  $T_1$  for the hydride proton ( $\text{CD}_2\text{Cl}_2$ , 298 K): 16 s.  $^{31}\text{P}\{^1\text{H}\}$  NMR ( $\text{CD}_2\text{Cl}_2$ , 298 K)  $\delta$  (ppm): 56.4 (s).  $^{31}\text{P}\{^1\text{H}\}$  NMR ( $\text{CD}_2\text{Cl}_2$ , 203 K)  $\delta$  (ppm): 55.0 (s).  $^{13}\text{C}\{^1\text{H}\}$  NMR ( $\text{CD}_2\text{Cl}_2$ , 298 K)  $\delta$  (ppm)  $^{13}\text{CO}$  enriched sample (only the CO region is given): 218.0 (s).  $^{13}\text{C}\{^1\text{H}\}$  NMR ( $\text{CD}_2\text{Cl}_2$ , 203 K)  $\delta$  (ppm): 218.2 (s).

## References

- [1] (a) J. von Liebig, *Pogg. Ann.* **1834**, *30*, 90-95; (b) B. C. Brodie, *Q. J. Chem. Soc.* **1860**, *12*, 269-272.
- [2] R. Nietzki, T. Benckiser, *Ber.* **1885**, *18*, 499-515.
- [3] P. Schützenberger, *Bull. Soc. Chim. Paris* **1868**, 188-192.
- [4] P. Schützenberger, *J. Chem. Soc.* **1871**, *24*, 1009-1014.
- [5] P. Calderazzo, R. Ercoli, G. Natta in *Organic Synthesis via Metal Carbonyls*, Vol. 1 (Eds. I. Wender and P. Pino), Interscience Publishers, New York, **1968**, p. 216.
- [6] L. Mond, C. Langer, F. Quinke, *J. Chem. Soc.* **1890**, *57*, 749-753.
- [7] (a) L. Mond, *Nature* **1898**, *59*, 63-64; (b) L. Mond, *J. Soc. Chem. Ind.* **1895**, *14*, 945-946.
- [8] L. Mond, *Minutes of the Proceedings* **1899**, *135*, 45-52.
- [9] (a) M. Berthelot, *Compl. Rend.* **1891**, *112*, 1343-1348; (b) L. Mond, F. Quinke, *J. Chem. Soc.* **1891**, *59*, 604-607.
- [10] (a) A. Job, A. Cassal, *Bull. Soc. Chim. France* **1927**, *41*, 1041-1046; (b) A. Job, J. Rouvillois, *C. R. Hebd. Sc. Acad. Sci. Paris* **1928**, *187*, 564-566.
- [11] (a) W. O. Hieber, *Angew. Chem.* **1961**, *73*, 364-368. (b) W. O. Hieber, *Angew. Chem.* **1952**, *64*, 465-470.
- [12] W. O. Hieber, *Adv. Organomet. Chem.* **1970**, *8*, 1-28.
- [13] W. E. Trout, *J. Chem. Educ.* **1937**, *14*, 575-581.
- [14] W. O. Hieber, F. Sonnekalb, *Ber. Dtsch. Chem. Ges.* **1928**, *61*, 558-565.
- [15] F. Hein, *Chemische Koordinationslehre* (S. Hirzel Verlag), Leipzig, **1950**, pag. 339.
- [16] H. M. Powell, R. V. G. Ewens, *J. Chem. Soc.* **1939**, 286-292.
- [17] J. C. Green, M. L. H. Green, G. Parkin, *Chem. Commun.* **2012**, *48*, 11481-11503.
- [18] L. F. Dahl, E. Ishishi, R. E. Rundle, *J. Chem. Phys.* **1957**, *26*, 1750-1751.
- [19] C. F. Campana, I. A. Guzei, E. G. Mednikov, L. F. Dahl, *J. Clust. Sci.* **2014**, *25*, 205-224.
- [20] L. F. Dahl, J. F. Blount, *Inorg. Chem.* **1965**, *4*, 1373-1375.
- [21] F. A. Cotton, J. M. Troup, *J. Am. Chem. Soc.* **1974**, *96*, 7155-7169.
- [22] F. Calderazzo, *J. Organomet. Chem.* **1981**, *213*, ix-xii.
- [23] P. Chini, *J. Organomet. Chem.* **1980**, *200*, 37-61.
- [24] W. O. Hieber, E. H. Schubert, *Z. Anorg. Allg. Chem.* **1965**, *32*, 338-347.
- [25] C. Femoni, M. C. Iapalucci, G. Longoni, P. H. Svensson, *Chem. Commun.* **2004**, 2274-2275.
- [26] P. Chini, G. Longoni, V. G. Albano, *Adv. Organomet. Chem.* **1976**, *14*, 285-344.
- [27] V. Albano, P. Chini, V. Scatturin, *Chem. Commun.* **1968**, *15*, 163-164.
- [28] F. A. Cotton, *Q. Rev. Chem. Soc.* **1966**, *20*, 389-401.
- [29] S. Zacchini, *Eur. J. Inorg. Chem.* **2011**, *27*, 4125-4145.

- [30] C. Femoni, M. C. Iapalucci, F. Kaswalder, G. Longoni, S. Zacchini, *Coord. Chem. Rev.* **2006**, *250*, 1580-1604.
- [31] B. K. Teo, *J. Cluster Sci.* **2014**, *25*, 5-28.
- [32] (a) A. W. Castleman, S. N. Khanna, *J. Phys. Chem.* **2009**, *113*, 2664-2675. (b) S. N. Khanna, P. Jena, *Phys. Rev. B.* **1995**, *51*, 13705-13716.
- [33] (a) F. Calderoli, F. Demartin, F. Fabrizi de Biani, C. Femoni, M. C. Iapalucci, G. Longoni, P. Zanello, *Eur. J. Inorg. Chem.* **1999**, 663-671. (b) F. Calderoli, F. Demartin, M. C. Iapalucci, G. Longoni, P. Zanello, *Angew. Chem. Int. Ed. Engl.* **1996**, *35*, 2225-2226.
- [34] (a) M. Zhu, C. M. Aikens, F. J. Hollander, G. C. Schatz, R. Jin, *J. Am. Chem. Soc.* **2008**, *130*, 5883-5885. (b) M. W. Heaven, A. Dass, P. S. White, K. M. Holt, R. W. Murray, *J. Am. Chem. Soc.* **2008**, *130*, 3754-3755.
- [35] H. Qian, W. T. Eckenhoff, Y. Zhu, T. Pintauer, R. Jin, *J. Am. Chem. Soc.* **2010**, *132*, 8280-8281.
- [36] P. D. Jadzinsky, G. Calero, C. J. Ackerson, D. A. Bushnell, R. D. Kornberg, *Science*, **2007**, *318*, 430-433.
- [37] (a) C. Femoni, M. C. Iapalucci, G. Longoni, J. Wolowska, S. Zacchini, P. Zanello, S. Fedi, M. Riccò, D. Pontiroli, M. Mazzani, *J. Am. Chem. Soc.* **2010**, *132*, 2919-2927. (b) C. Femoni, M. C. Iapalucci, G. Longoni, S. Zacchini, S. Fedi, F. Fabrizi de Biani, *Eur. J. Inorg. Chem.* **2012**, 2243-2250.
- [38] J. M. Bemis, L. F. Dahl, *J. Am. Chem. Soc.* **1997**, *119*, 4545-4546.
- [39] A. Bernardi, C. Femoni, M. C. Iapalucci, G. Longoni, S. Zacchini, *Dalton Trans.* **2009**, 4245-4251.
- [40] I. Ciabatti, C. Femoni, M. C. Iapalucci, G. Longoni, S. Zacchini, *J. Cluster Sci.* **2014**, *25*, 115-146.
- [41] R. D. Adams, B. Captain, *J. Org. Chem.* **2004**, *689*, 4521-4529.
- [42] V. G. Albano, A. Ceriotti, P. Chini, G. Ciani, S. Martinengo, M. Anker, *J. Chem. Soc., Chem. Commun.* **1975**, 859-860.
- [43] (a) G. Longoni, P. Chini, *J. Am. Chem. Soc.* **1976**, *98*, 7225-7231. (b) J. C. Calabrese, L. F. Dahl, P. Chini, G. Longoni, S. Martinengo, *J. Am. Chem. Soc.* **1974**, *96*, 2614-2616.
- [44] C. Femoni, F. Kaswalder, M. C. Iapalucci, G. Longoni, M. Mehlstäubl, S. Zacchini, *Chem. Commun.* **2005**, *46*, 5769-5771.
- [45] A. Ceriotti, G. Longoni, M. Manassero, N. Masciocchi, G. Piro, L. Resconi, M. Sansoni, *J. Chem. Soc., Chem. Commun.* **1985**, 1402-1403.
- [46] E. G. Mednikov, L. F. Dahl, *Phil. Trans. R. Soc. A*, **2010**, *368*, 1301-1332.
- [47] I. Ciabatti, C. Femoni, M. C. Iapalucci, G. Longoni, T. Lovato, S. Zacchini, *Inorg. Chem.* **2013**, *52*, 4384-4395.
- [48] (a) M. R. Churchill, R. A. Lashewycz, *Inorg. Chem.* **1978**, *17*, 1950-1957. (b) M. R. Churchill, R. A. Lashewycz, J. R. Shapley, S. I. Richter, *Inorg. Chem.* **1980**, *19*, 1277-1285.
- [49] V. Moberg, P. Homanen, S. Selva, R. Persson, M. Haukka T. A. Pakkanen, M. Monari, E. Nordlander, *Dalton Trans.*, **2006**, 279-288.

- [50] I. Ciabatti, C. Femoni, M. C. Iapalucci, G. Longoni, S. Zacchini, *Organometallics* **2013**, *32*, 5180-5189.
- [51] R. G. Vranka, L. F. Dahl, P. Chini, J. Chatt, *J. Am. Chem. Soc.* **1969**, *91*, 1574-1576.
- [52] C. Femoni, F. Kaswalder, M. C. Iapalucci, G. Longoni, S. Zacchini, *Chem. Commun.* **2006**, 2135-2137.
- [53] C. Femoni, M. C. Iapalucci, G. Longoni, S. Zacchini, S. Zarra, *J. Am. Chem. Soc.* **2011**, *133*, 2406-2409.
- [54] A. Ceriotti, N. Masciocchi, P. Macchi, G. Longoni, *Angew. Chem. Int. Ed.* **1999**, *38*, 3724-3727.
- [55] A. Ceriotti, P. Macchi, A. Sironi, S. El Afefey, M. Daghetta, S. Fedi, F. F. de Biani, R. D. Pergola, *Inorg. Chem.* **2013**, *52*, 1960-1964.
- [56] I. Ciabatti, C. Femoni, M. C. Iapalucci, G. Longoni, S. Zacchini, S. Zarra, *Nanoscale* **2012**, *4*, 4166-4177.
- [57] (a) A. Ceriotti, R. Della Pergola, G. Longoni, M. Manassero, N. Masciocchi, M. Sansoni, *J. Organomet. Chem.* **1987**, *330*, 237-252. (b) A. Ceriotti, R. Della Pergola, G. Longoni, M. Manassero, M. Sansoni, *J. Chem. Soc Dalton Trans.* **1984**, 1181-1187. (c) A. Arrigoni, A. Ceriotti, R. Della Pergola, G. Longoni, M. Manassero, M. Sansoni, *J. Organomet. Chem.* **1985**, *296*, 243-253. (d) G. Longoni, A. Ceriotti, R. Della Pergola, M. Manassero, M. Perego, G. Piro, M. Sansoni, *Phil. Trans. R. Soc. Lond. A* **1982**, *308*, 47-57. (e) A. Arrigoni, A. Ceriotti, R. Della Pergola, M. Manassero, N. Masciocchi, M. Sansoni, *Angew. Chem. Int. Ed.* **1984**, *23*, 322-323.
- [58] A. L. Bowman, G. P. Arnold, E. K. Storms, N. G. Nereson, *Acta Cryst.* **1972**, *B28*, 3102-3103.
- [59] S. Hofmann, R. Sharma, C. Ducati, G. Du, C. Mattevi, C. Cepek, M. Cantoro, S. Pisana, A. Parvez, F. Cervantes-Sodi, A. C. Ferrari, R. Dunin-Borkowski, S. Lizzit, L. Petaccia, A. Goldoni, J. Robertson, *Nano Lett.* **2007**, *7*, 602-608.
- [60] I. Ciabatti, C. Femoni, M. C. Iapalucci, G. Longoni, S. Zacchini, *Organometallics* **2012**, *31*, 4593-4600.
- [61] I. Ciabatti, C. Femoni, M. C. Iapalucci, G. Longoni, S. Zacchini, F. Fabrizi de Biani, *Dalton Trans.* **2013**, *42*, 9662-9670.
- [62] C. Mealli, D. M. Proserpio, *J. Chem. Educ.* **1990**, *67*, 399-402.
- [63] (a) J. C. Harberts, A. F. Bourgonje, J. J. Stephan, V. Ponec, *J. Catal.* **1977**, *47*, 92-98. (b) M. T. Tavares, I. Alstrup, C. A. Bernardo, J. R. Rostrup-Nielsen, *J. Catal.* **1994**, *147*, 525-534. (c) J. Nerlov, I. Chorkendorff, *J. Catal.* **1999**, *181*, 271-279.
- [64] P. D. Mynek, M. Kawano, M. A. Kozee, L. F. Dahl, *J. Clust. Sci.* **2001**, *12*, 313-318.
- [65] (a) A. Bernardi, C. Femoni, M. C. Iapalucci, G. Longoni, F. Ranuzzi, S. Zacchini, P. Zanello, S. Fedi, *Chem. Eur. J.* **2008**, *14*, 1924-1934. (b) A. Bernardi, C. Femoni, M. C. Iapalucci, G. Longoni, S. Zacchini, *Inorg. Chim. Acta* **2009**, *362*, 1239-1246.
- [66] A. Bernardi, I. Ciabatti, C. Femoni, M. C. Iapalucci, G. Longoni, S. Zacchini, *Dalton Trans.* **2013**, *42*, 407-421.

- [67] (a) C. Femoni, M. C. Iapalucci, G. Longoni, C. Tiozzo, S. Zacchini, *Angew. Chem. Inte. Ed.* **2008**, *47*, 6666-6669. (b) V. G. Albano, F. Calderoni, M. C. Iapalucci, G. Longoni, M. Monari, *Chem. Comm.* **1995**, *4*, 433-434.
- [68] E. G. Mednikov, L. F. Dahl, *Inorg. Chem.* **2015**, *54*, 1145-1151.
- [69] (a) A. J. Whoolery, L. F. Dahl, *J. Am. Chem. Soc.* **1991**, *113*, 6683-6685. (b) N. T. Tran, M. Kawano, D. R. Powell, R. K. Hayashi, C. F. Campana, L. F. Dahal, *J. Am. Chem. Soc.* **1999**, *121*, 5945-5952.
- [70] I. Ciabatti, C. Femoni, M. C. Iapalucci, G. Longoni, S. Zacchini, S. Fedi, F. Fabrizi de Biani, *Inorg. Chem.* **2012**, *51*, 11753-11761.
- [71] E. C. Coffey, J. Lewis, R. S. Nyholm, *J. Chem. Soc. (A)* **1964**, 1741-1742.
- [72] (a) H. Schmidbaur, A. Schier, *Chem. Soc. Rev.* **2012**, *41*, 370-412. (b) Z. N. Chen, N. Zhao, Y. Fan, J. Ni, *Coord. Chem. Rev.* **2009**, *253*, 1-20. (c) H. Schmidbaur, A. Schier, *Chem. Soc. Rev.* **2008**, *37*, 1931-1951.
- [73] J. Lewis, P. R. Raithby, in *Metal Clusters in Chemistry*, Vol. 1, (Eds.: P. Braunstein, L. A. Oro, P. R. Raithby), Wiley-VCH, Weinheim, **1999**, pag. 348-379.
- [74] C. E. Housecroft, D. M. Matthews, A. Waller, A. J. Edwards, A. L. Rheingold, *J. Chem. Soc., Dalton Trans.* **1993**, 3059-3070.
- [75] J. R. Galsworthy, A. D. Hattersley, C. E. Housecroft, A. L. Rheingold, A. Waller, *J. Chem. Soc., Dalton Trans.* **1995**, 549-557.
- [76] R. Della Pergola, F. Demartin, L. Garlaschelli, M. Manassero, S. Martinengo, N. Masciocchi, M. Sansoni, *Organometallics* **1991**, *10*, 2239-2247.
- [77] O. Rossell, M. Seco, G. Segales, S. Alvarez, M. A. Pellinghelli, A. Tiripicchio, D. de Montauzon, *Organometallics* **1997**, *16*, 236-245.
- [78] R. Reina, O. Riba, O. Rossell, M. Seco, D. de Montauzon, M. A. Pellinghelli, A. Tiripicchio, M. Font-Bardia, X. Solans, *J. Chem. Soc., Dalton Trans.* **2000**, 4464-4469.
- [79] R. Reina, L. Rodriguez, O. Rossell, M. Seco, M. Font-Bardia, X. Solans, *Organometallics* **2001**, *20*, 1575-1579.
- [80] R. D. Pergola, A. Fumagalli, F. F. de Biani, L. Garlaschelli, F. Laschi, M. C. Malatesta, M. Manassero, E. Roda, M. Sansoni, P. Zanello, *Eur. J. Inorg. Chem.* **2004**, *19*, 3901-3906.
- [81] P. Braunstein, J. Rose, *Gold Bull.* **1985**, *18*, 17-30.
- [82] T. Khimiyak, B. F. G. Johnson, S. Hermans, A. D. Bond, *Dalton Trans.* **2003**, *13*, 2651-2657.
- [83] A. Ceriotti, R. D. Pergola, L. Garlaschelli, M. Manassero, N. Masciocchi, *Dalton Trans.* **1995**, *14*, 186-193.
- [84] L. A. Polyakova, S. P. Gubin, A. V. Churakov, L. G. Kuzmina, *Koord. Khim. (Russ.) (Coord. Chem.)* **1999**, *25*, 761-770.
- [85] A. D. Hattersley, C. E. Housecroft, A. L. Rheingold, *Collect. Czech. Chem. Commun.* **1999**, *64*, 959-970.

- [86] M. Bortoluzzi, I. Ciabatti, C. Femoni, M. Hayatifar, M. C. Iapalucci, G. Longoni, S. Zacchini, *Inorg. Chem.* **2014**, *53*, 9761-9770.
- [87] C. E. Housecroft, D. M. Matthews, A. L. Rheingold, *Organometallics*, **1992**, *11*, 2959-2961.
- [88] C. E. Housecroft, D. M. Nixon, A. L. Rheingold, *J. Cluster Sci.* **2001**, *12*, 89-98.
- [89] E. H. Braye, L. F. Dahl, W. Hubel and D. L. Wampler, *J. Am. Chem. Soc.*, **1962**, *84*, 4633-4639.
- [90] M. Bortoluzzi, I. Ciabatti, C. Femoni, T. Funaioli, M. Hayatifar, M. C. Iapalucci, G. Longoni, S. Zacchini, *Dalton Trans.* **2014**, *43*, 9633-9646.
- [91] J. H. Darling, J. S. Ogden, *Inorg. Chem.* **1972**, *11*, 666-667.
- [92] C. Femoni, M. C. Iapalucci, G. Longoni, P. H. Svensson, P. Zanello, F. F. de Biani, *Chem. -Eur. J.* **2004**, *10*, 2318-2326.
- [93] T. Nakajima, A. Ishiguro, Y. Wakatsuki, *Angew. Chem. Inte. Ed.* **2000**, *39*, 1131-1134.
- [94] I. Ciabatti, F. Fabrizi de Biani, C. Femoni, M. C. Iapalucci, G. Longoni, S. Zacchini, *ChemPlusChem* **2013**, *78*, 1456-1465.
- [95] I. Ciabatti, C. Femoni, M. C. Iapalucci, G. Longoni, D. Pontiroli, M. Riccò, S. Zacchini, *Dalton Trans.* **2014**, *43*, 4388-4399.
- [96] B. F. G. Johnson, C. M. Martin, in *Metal Clusters in Chemistry*, Vol. 2, (Eds.: P. Braunstein, L. A. Oro, P. R. Raithby), Wiley-VCH, Weinheim, **1999**, pag. 877-911.
- [97] A. Ceriotti, G. Piro, M. Manassero, N. Masciocchi, M. Sansoni, *New J. Chem.* **1988**, *12*, 501-504.
- [98] M. R. Churchill, J. Wormald, *J. Chem. Soc., Dalton Trans.* **1974**, 2410-2414.
- [99] V. G. Albano, D. Braga, S. Martinengo, *J. Chem. Soc., Dalton Trans.*, **1986**, 981-984.
- [100] V. G. Albano, P. Chini, S. Martinengo, M. Sansoni, D. Strumolo, *J. Chem. Soc., Chem. Comm.* **1974**, 299-300.
- [101] I. Ciabatti, C. Femoni, M. C. Iapalucci, A. Ienco, G. Longoni, G. Manca, S. Zacchini, *Inorg. Chem.* **2013**, *52*, 10559-10565.
- [102] M. Bortoluzzi, I. Ciabatti, C. Femoni, M. Hayatifar, M. C. Iapalucci, G. Longoni, S. Zacchini, *Dalton Trans.* **2014**, *43*, 13471-13475.
- [103] M. Yousufuddin, M. J. Gutmann, J. Baldamus, O. Tardif, Z. Hou, S. A. Mason, G. J. McIntyre, R. Bau, *J. Am. Chem. Soc.* **2008**, *130*, 3888-3891.
- [104] C. B. Serrano, R. J. Less, M. McPartlin, V. Naseri, D. S. Wright, *Organometallics* **2010**, *29*, 5754-5756.
- [105] T. Bau, M. H. Drabnis, L. Garlaschelli, W. T. Klooster, Z. W. Xie, T. F. Koetzle, S. Martinengo, *Science* **1997**, *275*, 1099-1102.
- [106] R. W. Broach, L. F. Dahl, G. Longoni, P. Chini, A. J. Schultz, J. M. Williams, *Adv. Chem. Ser.* **1978**, *167*, 93-110.
- [107] D. W. Hart, R. G. Teller, C. Y. Wei, R. Bau, G. Longoni, S. Campanella, P. Chini, T. F. Koetzle, *Angew. Chem. Inte. Ed.* **1979**, *18*, 80-81.

- [108] M. Bortoluzzi, I. Ciabatti, C. Femoni, M. Hayatifar, M. C. Iapalucci, G. Longoni, S. Zacchini, *Angew. Chem. Inte. Ed.* **2014**, *53*, 7233-7237.
- [109] A. G. Orpen, *J. Chem. Soc., Dalton Trans.* **1980**, 2509-2516.
- [110] A. Ceriotti, G. Longoni, M. Manassero, M. Perego, M. Sansoni, *Inorg. Chem.* **1985**, *24*, 117-124.
- [111] A. Ceriotti, G. Longoni, M. Manassero, N. Masciocchi, L. Resconi, M. Sansoni, *Chem. Commun.* **1985**, 181-182.
- [112] (a) G. Longoni, P. Chini, L. D. Lower, L. F. Dahl, *J. Am. Chem. Soc.* **1975**, *97*, 5034-5036. (b) G. Longoni, P. Chini, A. Cavalieri, *Inorg. Chem.* **1976**, *15*, 3025-3029.
- [113] (a) R. Ercoli, E. Santambrogio, G. T. Casagrande, *Che. Ind. (Milan)* **1962**, *44*, 1344-1349. (b) W. T. Dent, L. A. Duncanson, R. G. Guy, H. W. R. Reed, B. L. Shaw, *Chemistry & Industry* **1961**, 169-170.
- [114] C. Femoni, M. C. Iapalucci, G. Longoni, S. Zacchini, S. Zarra, *Inorg. Chem.* **2009**, *48*, 1599-1605.
- [115] Sheldrick, G. M. *SADABS*, Program for empirical absorption correction, University of Göttingen, Germany, **1996**.
- [116] Sheldrick, G. M. *SHELX97*, Program for crystal structure determination, University of Göttingen, Germany, **1997**.
- [117] Keller, E. *SCHAKAL99*, University of Freiburg, Germany, **1999**.